

How does cement influence the mechanical properties of sand and sandstones?

Lisa Anne Millar

2019

A Thesis presented for the Degree of Doctor of Philosophy

Department of Civil and Environmental Engineering

University of Strathclyde

Declaration

This thesis is the result of the author's original research. It has been composed by the author and has not been previously submitted for examination which has led to the award of a degree.

The copyright of this thesis belongs to the author under the terms of the United Kingdom Copyright Acts as qualified by University of Strathclyde Regulation 3.50. Due acknowledgement must always be made to the use of any material contained in, or derived from, this thesis.

Signed:

Date:

Acknowledgements

I would like to thank my supervisors Andrea Hamilton and Zoe Shipton for their advice, interdisciplinary ideas and fun, thought provoking scientific conversations.

Thanks also goes to the Engineering and Physical Sciences Research Council (EPSRC) for funding my PhD research.

Mara Knapp, John Carlin, Chris Bonner, Derek McNee and Gavin Gibson for all assistance in the Civil and Environmental Engineering labs. Fiona Sillars and Tiziana Marrocco from the Advanced Materials Research Laboratory (AMRL). John Gilleece for making my thin sections.

A special thank you to my fellow PhD students for all their support throughout my PhD. In particular, my desk buddy Becky Punton, and Lovisa Andersson for helping me to finally move out of the lab.

Thanks to my parents, my grandmother and fiancé Jamie for their endless love, support and encouragement.

This thesis is dedicated to my mum,

Carole Millar,

for always understanding and encouraging me to do my best.

Abstract

Deformation bands can act as barriers and baffles in sandstone reservoirs. An increasing number of deformation bands have been studied in poorly cemented sandstones, yet there are questions about how grains can break (rather than slide past one another) in such loose sediments/rocks. The strength and distribution of cement may provide an answer. Detailed 3D observations are required to understand the cement and porosity variability that may control the formation of deformation bands. Integrating x-ray microtomography (X-CT) with microscopic observations, the first part of this thesis analyses cement and porosity distribution across deformation band samples from Utah, Hungary and Arran by comparing 2D slice to 3D sub-volume analysis methods.

Characterisation of cement in outcrops of sand(stone)s is complex due to variable mineralogy and multiple periods of cementation. The second half of this thesis strips back the compositional complexities of sand(stone)s to recreate poorly cemented synthetic sandstones in the laboratory. Here gypsum and calcite were used as cementing phases with percentage of cement in the synthetic samples ranging from 3.5 – 26.7%. X-CT analysis shows that gypsum cement forms a network of needles encasing the sand grains meanwhile the calcite (formed by microbially induced calcite precipitation) forms at point contacts between the sand grains.

In order to quantify the strength of each of the synthetic sandstones a series of shear box, uniaxial compression testing (UCS) and triaxial experiments were carried out. The results from these experiments show that as the percentage of cement increased the shear and compressive strengths of these samples also increased. The maximum shear strengths of the synthetic samples produced ranged from 103 to 458 kPa. Meanwhile, maximum UCS results ranged from 139 to 2408 kPa. In addition, the mineralogy of these poorly cemented synthetic sandstones was shown to impact the mechanics and hydraulics of the synthetic sandstones.

Contents

Author’s Declaration	ii
Acknowledgements	iii
Abstract	v
Table of Contents	vi
List of Figures	xi
List of Tables	xx
Chapter 1 – Introduction	1
1.1 Aims and Objectives	1
1.2 Thesis Outline	1
Chapter 2 – Literature review	4
2.1 Rationale	4
2.2 Faults	4
2.3 Deformation bands	5
2.3.1 Deformation band characteristics.....	6
2.3.2 Deformation mechanisms.....	11
2.3.3 Deformation band kinematics	13
2.3.4 Review of deformation bands in sand and sandstone	15
2.3.5 Laboratory studies of deformation bands.....	16
2.4 Cement in sandstones.....	23
2.4.1 Types of cement	25
2.4.2 Cement distribution.....	25
2.4.3 Cement textures.....	28
2.4.4 Cement strength	29
2.4.5 Cement, grain and porosity interactions.....	30
2.5 Sampling consolidated and poorly consolidated sandstones	30
2.6 Summary	31

Chapter 3 - X-ray Computed Microtomography	33
3.1 Rationale	33
3.2 Types of X-CT	33
3.3 How the X-CT works	34
3.4 X-CT Limitations	35
3.4.1 Beam hardening and ring artefacts.....	36
3.5 Use of X-CT in geological research.....	38
3.6 X-CT at Strathclyde	40
3.7 Use of X-CT in this study	40
3.8 X-CT Process	41
3.8.1 Sample preparation for X-CT.....	41
3.8.2 Sampling for analysis.....	41
3.8.3 Image processing and analysis.....	42
3.8.4 Background removal	42
3.8.5 Image segmentation	45
3.8.6 Impact of resolution	49
3.9 Summary	52
Chapter 4 - Geological history of field sites	54
4.1 Rationale	54
4.2 Methods.....	56
4.2.1 Field data collection	56
4.2.2 Microscopy.....	56
4.2.3 X-ray diffraction.....	56
4.2.4 Grainsize	56
4.3 Utah.....	57
4.3.1 Geological context of the Iron Wash fault zone.....	57
4.3.2 Iron Wash field site	60
4.4 Hungary.....	62
4.4.1 Geological history of The Pannonian Basin.....	63
4.4.2 Etes field site	64
4.5 Scotland.....	68

4.5.1 Geological Context of the Arran site	69
4.5.2 Arran field site.....	69
4.6 Summary	71
Chapter 5 – Cement and porosity variation across deformation bands	72
5.1 Rationale	72
5.1.1 Data sampling.....	73
5.2 Deformation bands from Iron Wash Fault, Utah	73
5.2.1 Outcrop.....	74
5.2.2 Thin section analysis	74
5.2.3 Avizo® analysis	81
5.3 Deformation bands in Etes	93
5.3.1 Outcrop.....	93
5.3.2 Thin section analysis	94
5.3.3 Avizo® analysis	96
5.4 Deformation bands in Arran.....	108
5.4.1 Outcrop.....	108
5.4.2 Thin section analysis	108
5.4.3 Avizo® analysis	116
5.5 Discussion	128
5.5.1 Full sample analysis	128
5.5.2 2D Slice analysis	129
5.5.3 Sub-volume analysis	130
5.5.4 Cement and Porosity Calculations	130
5.5.5 Connectivity of cement and porosity	132
5.5.6 Impact of cement on the mechanical deformation	135
5.6 Summary	136
Chapter 6 - Calcium sulphate phases	138
6.1 Rationale	138
6.2 Review of calcium sulphate literature.....	139
6.2.1 Calcium Sulphate Mineralogy and Formation	140

6.2.2 Calcium Sulphate in the construction industry	140
6.2.3 Dehydration pathway	142
6.2.4 Hydration pathways	144
6.3 Characterisation of materials/Experimental methods	145
6.3.1 Sample preparation.....	145
6.3.2 Thermogravimetric analysis/ Differential scanning calorimetry (TGA/ DSC).....	145
6.3.3 Synchrotron XRD analysis.....	146
6.3.4 Crystal growth analysis	147
6.4 Results and discussion.....	149
6.4.1 The dehydration of calcium sulphate	149
6.4.2 The hydration of calcium sulphate: gypsum growth and kinetics.....	160
6.5 Summary	165
Chapter 7 – Making synthetic sandstones	167
7.1 Rationale	167
7.2 Literature review: synthetic sandstones	168
7.2.1 Gypsum cemented sandstones.....	168
7.2.2 MICP cemented sandstones	169
7.3 Synthetic sandstone procedure	172
7.3.1 Sand.....	172
7.3.2 Cementation of the synthetic sandstones	174
7.4 Discussion	226
7.4.1 Naturally formed sandstones.....	226
7.4.2 Mineral segmentation.....	228
7.4.3 Sampling technique.....	229
7.5 Summary	230
Chapter 8 - Mechanical deformation	232
8.1 Rationale	232
8.2 Direct Shear box test	233
8.2.1 Test apparatus.....	234

8.2.2 Shear box procedure.....	236
8.2.3 Previous shear box studies on MICP cemented sands	237
8.2.4 Shear box results	238
8.2.5 Shear box summary.....	270
8.3 Uniaxial compression strength tests.....	272
8.3.1 Gypsum cemented sandstone results.....	275
8.3.2 MICP cemented sandstone results	281
8.3.3 UCS summary	287
8.4 Triaxial testing	289
8.4.1 Choosing the most relevant deformation conditions.....	290
8.4.2 Triaxial sample preparation and test procedure	294
8.4.3 Triaxial results.....	297
8.4.4 Triaxial deformation summary.....	302
8.5 Comparison between cement and deformation techniques.....	303
8.5.1 Effect of cement	303
8.5.2 Comparison of deformation techniques	305
8.6 Summary	307
Chapter 9 -Discussion, Conclusions and Future work	308
9.1 Discussion.....	308
9.1.1 Cement distribution and mineralogy is important for mechanics and hydraulics	308
9.1.2 Timing of cementation in natural rocks	315
9.1.3 Comparing synthetic rocks to real rocks.....	316
9.1.4 Heterogeneity	328
9.2 Conclusions and Future work.....	332
References	335
Appendices	362
Appendix 1.....	362
Appendix 2	363
Appendix 3	364

List of Figures

Figure number	Description	Page
Figure 2.1	Fault zone model modified from Sibson (1983), Scholz (2002) and Fagereng and Toy (2011).	5
Figure 2.2	Increased strain localization during the stages of deformation band formation.	8
Figure 2.3	Examples of deformation bands in poorly consolidated sandstone from France and Hungary.	9
Figure 2.4	Simplified DB burial diagram demonstrates that DB bands require 10% porosity to form and the minimum burial depth for cataclasis to occur is ~500m. After Fulljames et al. (1997).	13
Figure 2.5	Maximum burial depth (km) and depositional environments of deformation band outcrops in poorly consolidated sandstones.	14
Figure 2.6	Plane polarised light thin sections of cataclastic deformation as categorised by Beke et al. (2019).	15
Figure 2.7	Deformation band properties summarised from published studies on sandstone and poorly consolidated sandstone.	17
Figure 2.8	Types of grain fracture which can occur with estimated depths. From Fossen (2010).	18
Figure 2.9	From Kimura et al. (2018) this figure shows the development of shear zones in sand (Tohoku silica sand No. 7) as displacement continues under high (e.g. 8 MPa) and low (e.g. 1 MPa) vertical stress from ring shear tests.	20
Figure 2.10	Process of consolidation. In this classification there are two end members: unconsolidated and consolidated.	24
Figure 2.11	Cement distribution A) Grain supported packed sand with closed pore throats in 2D. B) Cement on grain to grain contacts holding the grains together. C) Primarily cement supported grains. D) All pore space filled with cement.	26
Figure 2.12	Isopachous (uniform thickness) and meniscus cement fabrics from Scholle and Ulmer-Scholle (1979).	27
Figure 2.13	Two methods for removing poorly consolidated sandstones.	31
Figure 3.1	X-CT configurations a) Fan beam b) Cone beam c) Parallel beam from Landis and Keane (2010) (Landis and Keane 2010).	33
Figure 3.2	Images from PRO 3D software (© 2004- 2016 Nikon Metrology) reconstruction software.	37
Figure 3.3	A) X-ray source, stage and detector setup inside the Nikon XT H 320/225. B) X-CT control station.	40
Figure 3.4	Flowchart for X-CT analysis using Avizo®.	41

Figure 3.5	Three methods of sampling used to analyse the natural deformation band samples.	43
Figure 3.6	Object background removal during post processing of the X-CT scan.	44
Figure 3.7	Image segmentation of sample HN11 to show three phases: grains, cement and porosity.	45
Figure 3.8	Impact of erosion and dilation by 1 voxel on porosity phase (blue) from sample AR01.	46
Figure 3.9	Volume fraction of each segmented phase for each of full volume deformation band samples.	46
Figure 3.10	Separate objects module in Avizo®.	47
Figure 3.11	3D Separate objects module applied to sample AR01.s	48
Figure 3.12	Labelling of porosity from sample HN11.	49
Figure 3.13	Sub volume sample from AR01 before (A) and after (B) resolution analysis filter applied.	50
Figure 3.14	X-CT greyscale and segmented 2D slices from HN11 sample scanned at 4, 7 and 10µm resolution.	52
Figure 4.1	Simplified geological map of Utah.	58
Figure 4.2	Location map of field area UT02 along the Iron Wash Fault zone. Image from Google Earth (2018).	59
Figure 4.3	Stratigraphy of Utah study area from Richey (2013).	60
Figure 4.4	Sample UT02 host rock analysis.	61
Figure 4.5	A) Location map of Hungary in Europe. B) Zoomed in location map of northern Hungary field area. C) Aerial photograph of hillside field site Etes. Photos from Google Earth (2018).	62
Figure 4.6	Geological map of Hungary field area. From Beke et al. (2019).	64
Figure 4.7	Lithostratigraphic column of Hungary. Adapted from Petrik et al. (2014).	65
Figure 4.8	Summary of field site and sample from Etes, Hungary.	66
Figure 4.9	Sample HN11 host rock analysis	67
Figure 4.10	A) Simplified geological map of Arran with highlighted outcrop location (from Arran Museums 2015). B) Map of Scotland with location of Arran shown. C) East coast of Arran at Merkland Point. D) Zoomed location of coastal outcrop. Images from Google Earth (2018).	68
Figure 4.11	Sample AR01 host rock analysis.	70
Figure 5.1	Three methods used to sample data in this chapter. A) Full volume. B) 2D slices. 3) 3D sub volumes.	73
Figure 5.2	UT02 deformation bands from the field.	75
Figure 5.3	Thin section of sample UT02 deformation bands (PPL and XPL).	77
Figure 5.4	Sample UT02 grain length distributions along the long (blue graphs) and short axis (grey graphs) in each of the three areas described in Figure 5.2; host, deformation band and intermediate zone.	78

Figure 5.5	Zoomed PPL and XPL images of UT02 with focus on hematite ring and calcite cement inside deformation band between grains.	79
Figure 5.6	Zoomed in image of UT02 and focus on dots of oil (<25µm in diameter).	80
Figure 5.7	UT02 segmented slices showing: A) original grey image, B) Grains phase, C) Cement phase and D) Pores phase.	81
Figure 5.8	A) 2D vertical slice through a 6x2x2mm sub-sample of UT02: grain (blue), cement (purple) and porosity (green) percentage. B) Corresponding values of percentage grains, cement and porosity percentage for each horizontal slice along the z axis of the subsample.	86
Figure 5.9	Sample UT02 full volume segmented in Avizo®.	87
Figure 5.10	Cement and porosity connectivity in sample UT02.	88
Figure 5.11	Histogram showing the number of connected cement volumes from five 0.125 mm ³ sub volumes in the UT02 deformation bands.	89
Figure 5.12	Histogram showing the number of connected cement volumes from five 0.125 mm ³ sub volumes in the UT02 host rock.	90
Figure 5.13	Histogram showing the number of connected pore volumes from five 0.125 mm ³ sub volumes in the UT02 deformation bands.	91
Figure 5.14	Histogram showing the number of connected pore volumes from five 0.125 mm ³ sub volumes in the UT02 host rock.	92
Figure 5.15	Summary of field site and sample from Etes, Hungary.	93
Figure 5.16	Thin section of deformation band in PPL and XPL of HN11.	95
Figure 5.17	Sample HN11 grain length distributions along the long (blue graphs) and short axis (grey graphs) of fifty grains in both the host rock and the deformation band (see Figure 5.16).	96
Figure 5.18	Three phases of HN11 segmented.	97
Figure 5.19	A) 2D vertical slice through a 6x2x2mm sub-sample of HN11: grain (blue), cement (purple) and porosity (green) percentage. B) Corresponding values of percentage grains, cement and porosity percentage for each horizontal slice along the z axis of the subsample.	101
Figure 5.20	Sample HN11 full volume segmented in Avizo®.	102
Figure 5.21	Cement and porosity connectivity in sample HN11.	103
Figure 5.22	Histogram showing the number of connected cement volumes from five 0.125 mm ³ sub volumes in the HN11 deformation bands.	104
Figure 5.23	Histogram showing the number of connected cement volumes from five 0.125 mm ³ sub volumes in the HN11 host rock.	105
Figure 5.24	Histogram showing the number of connected pore volumes from five 0.125 mm ³ sub volumes in the HN11 deformation bands.	106
Figure 5.25	Histogram showing the number of connected pore volumes from five 0.125 mm ³ sub volumes in the HN11 host rock.	107
Figure 5.26	Photos of deformation bands on Arran.	111

Figure 5.27	Arran deformation band sample AR01.	112
Figure 5.28	AR01 thin section in PPL and XPL.	113
Figure 5.29	Sample AR01 grain length distributions along the long (blue graphs) and short axis (grey graphs) of fifty grains in each of the five areas shown in Figure 5.27.	114
Figure 5.30	Fe oxide and clay coating grains of sample AR01.	115
Figure 5.31	Three phases from AR01 segmentation.	116
Figure 5.32	A) 2D vertical slice through a 6x2x2mm sub-sample of AR01: grain (blue), cement (purple) and porosity (green) percentage. B) Corresponding values of percentage grains, cement and porosity percentage for each horizontal slice along the z axis of the subsample.	121
Figure 5.33	Sample AR01 full volume segmented in Avizo®.	122
Figure 5.34	Cement and porosity connectivity across sample AR01.	123
Figure 5.35	Histogram showing the number of connected cement volumes from five 0.125 mm ³ sub volumes in the AR01 deformation bands.	124
Figure 5.36	Histogram showing the number of connected cement volumes from five 0.125 mm ³ sub volumes in the HN11 host rock.	125
Figure 5.37	Histogram showing the number of connected pore volumes from five 0.125 mm ³ sub volumes in the AR01 deformation bands.	126
Figure 5.38	Histogram showing the number of connected pore volumes from five 0.125 mm ³ sub volumes in the AR01 host rock.	127
Figure 5.39	Volume fraction of each segmented phase for all deformation band samples (6 x 2 x 2 mm).	129
Figure 5.40	X-ray linear attenuation coefficient calculated for each listed mineral using MuCalc (Hanna and Ketcham 2017).	131
Figure 5.41	Schematic summary of deformation bands.	134
Figure 5.42	Schematic of cement connectivity through deformation bands.	136
Figure 6.1	Formation of gypsum crystals from hydrated basanite.	144
Figure 6.2	Gypsum calcinated at 160°C to form β -basanite and subsequently hydrated to show gypsum needle growth.	148
Figure 6.3	Bassanite displaying channel structure. From Berthold et al. (2011).	154
Figure 6.4	Synchrotron XRD pattern of gypsum heated to 105°C.	155
Figure 6.5	A magnified version of Figure 6.4, showing γ -anhydrite (ICSD collection code 86316) reflection positions marked in green.	155
Figure 6.6	XRD pattern of calcium sulphate samples from session 1.	156
Figure 6.7	Thermogravimetric analysis of gypsum powder.	158
Figure 6.8	TGA analysis where the horizontal dashed lines at 0.8430 and 0.7907 show the theoretical fractional mass content of bassanite and anhydrite.	159
Figure 6.9	Average crystal lengths for each calcination temperature after set time periods (10, 20, 30 mins. etc.)	162

Figure 6.10	Binary images demonstrating how calcination temperatures (120, 140, 160, 180 and 200°C) impacts the rate and size of gypsum crystal growth.	164
Figure 6.11	For each calcination temperature three steps of gypsum crystal growth were identified: initiation, acceleratory period and completion of hydration.	165
Figure 7.1	Microscope image in (A) plane polarised light and (B) cross polarised light of sand from Alloa Quarry. (C) QFL diagram of sand shows it is arkosic in composition. (D) Grain size distribution along the longest axis shows the predominant grain length to be 100-120 µm. E) Grain size distribution along the shortest axis shows the predominant shortest axis to be 60-80µm.	173
Figure 7.2	Schematic of gypsum cemented sandstone sample preparation in cuboid and cylinder moulds.	176
Figure 7.3	Photographs of gypsum cemented sandstone samples.	177
Figure 7.4	Gypsum cemented (10, 15, 20 and 25 wt % bassanite added) sandstone PPL and XPL microscope images. Red scale bar is 50µm. When viewed in thin section it is difficult to identify porosity.	182
Figure 7.5	2D X-CT slices of the four gypsum cemented samples.	185
Figure 7.6	X-ray linear attenuation coefficient calculated for quartz and gypsum using MuCalc (Hanna and Ketcham 2017).	186
Figure 7.7	Weka probability maps for gypsum sample 10B, slice 71.	187
Figure 7.8	Analysis of WEKA segmentation on sample 10B.	187
Figure 7.9	X-CT segmented 3D images of a 1mm ³ data sub volume from sample 10B.	190
Figure 7.10	Sample 10B (10% wt) cement and porosity connectivity.	191
Figure 7.11	X-CT segmented 3D images of a 1mm ³ data sub volume from sample 15B.	192
Figure 7.12	Sample 15B (15% wt) cement and porosity connectivity.	193
Figure 7.13	X-CT segmented 3D images of a 1mm ³ data sub volume from sample 20B.	194
Figure 7.14	Sample 20B (20% wt) cement and porosity connectivity.	195
Figure 7.15	X-CT segmented 3D images of a 1mm ³ data sub volume from sample 25B.	196
Figure 7.16	Sample 25B (25% wt) cement and porosity connectivity.	197
Figure 7.17	Volume of each segmented phases for all four gypsum cemented samples A) 10% B) 15% C) 20% D) 25% from erosion and dilation calculations (see Chapter 3).	198
Figure 7.18	Histogram showing the number of connected cement and pore volumes from each of the four gypsum cemented 1 mm ³ samples.	199
Figure 7.19	Schematic of MICP cemented sandstone sample preparation in cuboid and cylinder moulds.	205

Figure 7.20	Photographs of MICP cemented sandstone samples.	206
Figure 7.21	Sub sample for measuring CaCO ₃ content of MICP samples.	206
Figure 7.22	MICP cemented thin sections in plane polarised light (PPL) and cross polarised light (XPL). Due to their pale, high order interference colours the balls of calcite can be more readily identified in XPL light. At 120ml feed less calcite balls can be identified than at higher volumes of feed.	211
Figure 7.23	Slice through 3D X-CT image of MICP samples at (A) 120ml feed (B) 160ml feed (C) 200ml feed. Here the calcite balls and grain 'halos' can be identified in bright white.	212
Figure 7.24	X-ray linear attenuation coefficient calculated for quartz and calcite using MuCalc (Hanna and Ketcham 2017).	213
Figure 7.25	X-CT segmented 3D images of a 1 mm ³ data sub volume from MICP cemented sample L7 (120ml).	216
Figure 7.26	Sample L7 (120 ml) cement and porosity connectivity.	217
Figure 7.27	X-CT segmented 3D images of a 1mm ³ data sub volume from MICP cemented sample M7 (160ml).	218
Figure 7.28	Sample M7 (160 ml) cement and porosity connectivity.	219
Figure 7.29	X-CT segmented 3D images of a 1 mm ³ data sub volume from MICP cemented sample H6 (200ml).	220
Figure 7.30	Sample H6 (200 ml) cement and porosity connectivity.	221
Figure 7.31	Summary of phases (grains, cement and porosity) present in the MICP cemented sub volumes. A) 120 ml B) 160 ml C) 200ml.	222
Figure 7.32	Histogram showing the number of connect cement (purple) and pore(green) volumes for the 1 mm ³ MICP samples 120, 160 and 200ml.	223
Figure 7.33	Schematic diagram of cement growth between grains. Each of these diagrams have been modified from Cheng et al. (2013). Schematics have been created based on thin section and X-CT samples from this study.	225
Figure 7.34	Example of calcite cemented Devonian aged Caithness Flagstone in PPL (A) and XPL (B and C). Image from Andrea Hamilton.	226
Figure 7.35	Thins sections for comparison with gypsum cement. A) Beachrock from Mauz et al. (2015). No scale is provided. B) An example of clay cemented sand grains from Wooldridge et al. (2018).	227
Figure 7.36	X-ray linear attenuation coefficient calculated for quartz, gypsum and calcite using MuCalc (Hanna and Ketcham 2017).	228
Figure 8.1	Schematic cross section of shear box set up. Modified from Knappett & Craig (2012).	234
Figure 8.2	Schematic stress-strain curves from shear box tests. Edited from Osano (2012).	234
Figure 8.3	Shear box set up at the University of Strathclyde.	235
Figure 8.4	Components of the direct shear box.	236

Figure 8.5	Artefacts of shear box tests.	240
Figure 8.6	Artefacts from sample M5 (160 ml).	241
Figure 8.7	Repeatability test showing the response of untreated sand samples to shearing.	242
Figure 8.8	Vertical vs horizontal displacement of the three sheared sand samples.	243
Figure 8.9	Shear stress vs horizontal displacement for gypsum cemented sandstones (10, 15, 20 and 25%) deformed at 95.38 kPa normal load.	249
Figure 8.10	Shear stress vs horizontal displacement for gypsum cemented sandstones with 20% and 25% gypsum cement at A) 27.25 kPa and B) 163.50 kPa normal load.	250
Figure 8.11	20 and 25% gypsum cement sandstones maximum and ultimate shear stress plotted again the normal applied stress.	251
Figure 8.12	Gypsum shear box sample	252
Figure 8.13	Shear stress vs horizontal displacement for MICP cemented sandstones shear results of all samples at normal stresses of 95.38 kPa.	259
Figure 8.14	Shear stress vs horizontal displacement for MICP cemented sandstones shear results of all samples at normal stresses of A) 27.25 kPa and B) 163.50 kPa.	260
Figure 8.15	Maximum and ultimate shear stress of MICP shear samples (120, 160 and 200 ml) at normal stresses of 27.25, 95.38 and 163.50 kPa.	261
Figure 8.16	Images of MICP 120ml, 160ml and 200 ml feed samples before and after deformation.	262
Figure 8.17	Thin section evidence from MICP 120 ml sample of fractured calcite cement after shearing.	264
Figure 8.18	Thin section evidence of fractured grains after shearing the 160 ml feed MICP synthetic sandstone. Shearing took place at 95.38 kPa.	265
Figure 8.19	Thin section evidence of fractured grains after shearing the 200 ml MICP synthetic sandstone. Shearing took place at 95.38 kPa.	266
Figure 8.20	Comparison of maximum shear strength results vs normal stress of the MICP cemented sandstone results in this study and those listed in Table 8.2.	268
Figure 8.21	Comparison of the ultimate shear stress vs normal stress of the MICP cemented sandstone results in this study and those listed in Table 8.2.	269
Figure 8.22	Uniaxial compression testing rig at the university of Strathclyde's Geotechnics Laboratory.	272
Figure 8.23	A typical uniaxial compression strength (UCS) test deformation curve from Saxena et al. (2018).	273
Figure 8.24	Uniaxial compression testing modes of sample failure from Szwedzicki (2007).	273

Figure 8.25	UCS graphs for gypsum cemented synthetic sandstones (10, 15, 20 and 25%).	275
Figure 8.26	UCS and porosity vs gypsum content for each of the gypsum cemented sandstone samples.	276
Figure 8.27	Thin section evidence of transgranular fracture and grain spalling of gypsum cemented sandstones during uniaxial compaction testing.	278
Figure 8.28	UCS test result for 100% gypsum cylinder sample.	279
Figure 8.29	Uniaxial compression strength test results showing variation of stress over time for 120, 160 and 200ml MICP samples.	281
Figure 8.30	Photos of MICP samples before and after UCS deformation.	283
Figure 8.31	CaCO ₃ content and unconfined compressive strength for all MICP samples with standard error.	284
Figure 8.32	CaCO ₃ content and unconfined compressive strength of MICP cemented sandstone samples from van Paassen et al. (2010), El Mountassir et al. (2018), Mahawish et al. (2018), Terzis & Laloui (2018) and this thesis.	285
Figure 8.33	Schematic representation of the impact of saturation on the location of calcite growth.	286
Figure 8.34	Triaxial schematic response modified from Dewhurst et al. (2011) shows that differential stress increases with increased confining pressure.	289
Figure 8.35	Triaxial rig set up at the University of Edinburgh.	294
Figure 8.36	100% gypsum triaxial sample fitted with a heat shrink sleeve (A) before, and (B) after deformation.	295
Figure 8.37	Triaxial rig plumbing diagram built by Iain Butler and Michael Flynn, Geosciences Department, University of Edinburgh, figure courtesy of Iain Butler.	295
Figure 8.38	Triaxial results showing the comparison of 15% gypsum samples with and without a sleeve at 4000 psi.	298
Figure 8.39	Triaxial deformation results of A) 20 and B) 25% gypsum cemented sandstones.	300
Figure 8.40	Summary of triaxial results for gypsum cemented sandstones.	301
Figure 8.41	Triaxial results from A) 100% gypsum sample. B) Shows a typical sandstone sample. C) Comparison between all samples.	302
Figure 9.1	The strength of a rock is affected by cement in two ways.	309
Figure 9.2	Schematic displaying some of the cement types and distributions from silica, carbonate and clay cemented rocks.	311
Figure 9.3	Dunham classification of carbonate rocks (Dunham 1962).	313
Figure 9.4	Schematic of the cement distribution observed in the natural and synthetic sandstones.	314
Figure 9.5	Summary diagram of 3D analysis showing the location of cement in real and synthetic rocks from this thesis.	320

Figure 9.6	Summary maximum and ultimate shear stress results for gypsum and MICP cemented sandstones.	323
Figure 9.7	UCS and porosity (%) measurements from both MICP and gypsum cemented sandstones.	324
Figure 9.8	Results from triaxial testing for gypsum cemented sandstones replicated from Figure 8.40.	324

List of Tables

Table number	Description	Page
Table 2.1	Summary of deformation band terminology used in literature.	10
Table 2.2	Description of the level of cementation in coarse soils by ASTM D2488 Standard Practice for Description and Identification of Soils (Visual Manual Procedure).	29
Table 3.1	Average volume percentage and standard error from 5 sub volumes of 0.5 mm ³ inside the host rock and deformation band (DB).	51
Table 4.1	Summary of field locations used in this study. Includes previous literature which studies this area and geological setting.	55
Table 5.1	Average percentage of grains, cement and porosity for each zone (defined by the 2D slice numbers – see Figure 5.6) in UT02. DB = deformation band zone, H = host rock zone.	83
Table 5.2	Percentage of grains, cement and porosity from UT02 0.125mm ³ sub volumes inside the deformation band and the host rock.	84
Table 5.3	Average percentage of grains, cement and porosity for each 2D slices zone in HN11. DB = deformation band zone, H = host rock zone.	98
Table 5.4	Percentage of grains, cement and porosity from HN11 0.125mm ³ sub volumes inside the deformation band and the host rock.	99
Table 5.5	Average percentage of grains, cement and porosity for each 2D slices zone in AR01.	118
Table 5.6	Percentage of grains, cement and porosity from AR01 0.125mm ³ sub volumes inside the deformation band and the host rock.	119
Table 6.1	Jacques et al. (2009) uses a standard heating rate of (10K/min) shows how the temperatures transition (°C) during the dehydration of gypsum is affected by different sample environments (e.g. sealed, not sealed).	142
Table 6.2	Crystallographic information files used in the analysis and Rietveld refinement of the gypsum XRD results.	147
Table 6.3	Rietveld refinement results using TOPAS.	152
Table 6.4	TGA gypsum- bassanite transition temperatures with heating rate.	157
Table 7.1	Gypsum and MICP synthetic samples were created in the following shapes in preparation for mechanical testing (Chapter 8).	167
Table 7.2	Confining pressures used to form synthetic gypsum sandstone from previous gypsum studies.	168
Table 7.3	Summary of all cylindrical gypsum cemented sandstones and their properties.	178
Table 7.4	Summary of all cuboid gypsum cemented sandstones and their properties.	179

Table 7.5	Summary of gypsum cemented samples scanned in X-CT for micro analysis.	184
Table 7.6	Optical density (OD) and specific ureolytic activity results for each diluted bacterial solution used to make the MICP cemented synthetic sandstones.	200
Table 7.7	Summary of all MICP cemented cylinders and their properties. See Chapter 8 for a description of the cylinders deformation by uniaxial compression testing (UCS).	201
Table 7.8	Summary of all MICP cemented cuboids and their properties prior to deformation (see Chapter 8)	202
Table 7.9	Measured calcite content of sampled sub slice from the cylindrical MICP cemented sandstone core.	208
Table 7.10	Average total number of times pores were filled by bacterial and cementing solutions for each MICP cylinder sample.	209
Table 7.11	List of MICP samples scanned in X-CT for micro analysis.	224
Table 7.12	Pros and cons of gypsum vs MICP cement.	229
Table 8.1	Vertical mass applied to shear box and calculated equivalent normal stress. These conversions can be applied to all of Chapter 8.	237
Table 8.2	Summary of maximum and ultimate shear stress results from previous MICP shear box test.	237
Table 8.3	Summary of all sheared gypsum cemented sandstones and the normal load conditions at which they were sheared.	244
Table 8.4	Summary of all sheared MICP cemented sandstones and the normal load conditions at which they were sheared.	254
Table 8.5	Feed volume (ml) and corresponding average calcite content (wt%) per sample.	258
Table 8.6	Range of average maximum shear stress for each applied normal stress during all of the MICP feeds tested in this chapter.	270
Table 8.7	Average maximum and ultimate shear stress per sample group.	271
Table 8.8	Typical range of unconfined compressive strength of intact rocks. Edited from Zhang (2017).	274
Table 8.9	Summary of each gypsum cemented sandstone sample deformed by UCS. All samples were deformed at a strain rate of 1mm/min.	280
Table 8.10	Summary of each MICP sample deformed by UCS. All samples were deformed at a strain rate of 1mm/min.	282
Table 8.11	Comparison of some variables in selected MICP UCS studies.	288
Table 8.12	Summary of previous triaxial studies and determination of which type of deformation band has been formed.	292
Table 8.13	Summary of samples (gypsum cemented sandstones, sandstone and 100% gypsum sample) tested by triaxial deformation.	296
Table 8.14	Summary of average results from shear box and UCS tests on the synthetic sandstones.	304

Table 8.15	Summary describing the effects of increasing gypsum and MICP cement volume on the mechanical deformation of synthetic sandstones.	305
Table 9.1	Summary of each field site with focus on the periods of potential deformation band formation, cement type, and porosity.	316
Table 9.2	Summary of grain, cement and porosity phases from X-CT analysis of naturally formed sandstones, gypsum cemented sandstones, and MICP cemented sandstones.	319
Table 9.3	Moduli of selected minerals used in this study.	321
Table 9.4	Summary describing the effects of increasing cement volume on the mechanical deformation of synthetic sandstones.	325
Table 9.5	Summary describing the effects of increasing cement volume on the mechanical deformation of synthetic sandstones.	326

Chapter 1 – Introduction

1.1 Aims and Objectives

The primary aims of this thesis are to analyse the distribution of cement across deformation bands, and by reducing the mineralogical and structural variability of sandstones test the impact of cement volume on the deformation of sandstones.

In order to achieve these aims the following objectives were determined:

- Characterise the cement and porosity distribution of deformation bands in natural sandstones.
- Design, test and review methodology for 2D and 3D analysis of deformation band petrophysical parameters in both consolidated and poorly consolidated sandstones.
- Create simplified poorly consolidated synthetic sandstones in the laboratory with varying percentages of cement.
- Determine the impact of cement mineralogy, distribution and quantity on the deformation of poorly cemented sandstones.
- Determine if grain crushing can occur in poorly consolidated synthetic sandstones when mechanically deformed in the laboratory.

1.2 Thesis Outline

The thesis is divided into nine chapters.

Chapter 2: *Literature Review*

Reviews the background literature to the key areas of research in this thesis. It summarises the literature on deformation bands in sandstone and poorly consolidated sandstone.

Chapter 1 - Introduction

Chapter 3: *X-ray computed microtomography (X-CT)*

Reviews previous X-CT studies, describes X-CT methodology used in this thesis and compares the impact of scan resolution on segmentation analysis specifically for the scanner used in this thesis.

Chapter 4: *Geological history*

Outlines the geological history, tectonic setting, stratigraphy and host rock lithology for each of the three field areas where deformation bands were examined.

Chapter 5: *Deformation bands in sandstone*

Analyses each of the deformation band samples collected from Utah, Hungary and Scotland. In addition, this chapter creates a methodology for non-destructive quantification of the petrophysical properties of deformation band samples using X-CT.

Chapter 6: *Calcium sulphate phases*

Investigates the transition between the calcium sulphate phases and the growth of gypsum crystals by hydrating basanite to determine the impact of basanite calcination temperature on gypsum crystal formation and the stability of gypsum at varying temperatures.

Chapter 7: *Making synthetic sandstones*

Investigates the formation and properties of synthetic sandstones using gypsum and microbial induced calcite precipitation (MICP) as cementing agents. This chapter focusses on the formation of synthetic sandstones using varying volumes of cement.

Chapter 8: *Mechanical deformation*

Use mechanical deformation techniques (shearbox, unconfined compression strength testing and triaxial) to deform the synthetic sandstones under comparable conditions to deformation band forming conditions in the earth and previous laboratory experiments. In addition, this chapter tests the impact of varying volumes of cement on the mechanical properties of the synthetic sandstones.

Chapter 1 - Introduction

Chapter 9: *Discussion, Conclusions and Future work*

The discussion includes the impact of heterogeneities in all sandstones, comparing and contrasting the cement and porosity in the synthetic sandstones to the real sandstone samples and the use of the X-CT as an analysis technique. Thesis conclusions and future work are also listed.

Chapter 2 - Literature review

2.1 Rationale

This chapter reviews the geological formation of deformation bands and the type, distribution, strength and impact of cement in sandstones.

2.2 Faults

Faults begin as fractures in low porosity rock which develop in the brittle upper crust as a result of applied stress. This fracture or set of fractures can then propagate to form a fault. The majority of faults form along the edge of tectonic plates where most movement is accumulated. In porous sandstones faults can develop by pore collapse and grain crushing during the formation of deformation bands (Antonellini 1994). It has been proven that the orientation of the deformation bands control the initial and propagation direction of the fault (Johnson 1995; Johansen et al. 2005; Okubo and Schultz 2006).

However, fault characteristics and deformation mechanisms also vary with depth (Figure 2.1). An overarching goal of research in this area has been to improve the predictability of the flow and mechanical properties of faults with depth but there are many variables which remain. Fagereng and Toy (2011)'s diagram builds on the original model of a shear zone by Sibson 1983. In Sibson (1983) shear zone model the $T < 300^{\circ}\text{C}$ zone is blub shaped whereas in Fagereng and Toy (2011) they keep the width of the fault zone constant above 300°C . They also extend the friction rate behaviour and more clearly define the shear strength curve down to 450°C . Of particular interest to this study is the $T < 300^{\circ}\text{C}$ zone. Here Fagereng and Toy (2011) acknowledge the impact of diagenesis on soft sediments in shallow burial conditions by expanding the level of detail in this zone.

However, both diagrams do not reflect the mineralogy, fluid flow or fluid pressures over which deformation occurs. Further work in this zone of less than 300°C would include more details and be subdivided based on a better understanding of processes in this zone. This would allow studies to better constrain the parameters of granular flow, dissolution and frictional faulting therefore summarising deformation band

research to date. This thesis looks to apply case studies of deformation bands from Utah, Arran and Hungary to expand the understanding of faulted sandstones in the shallow crust (<3 km depth – highlighted in Figure 2.1).

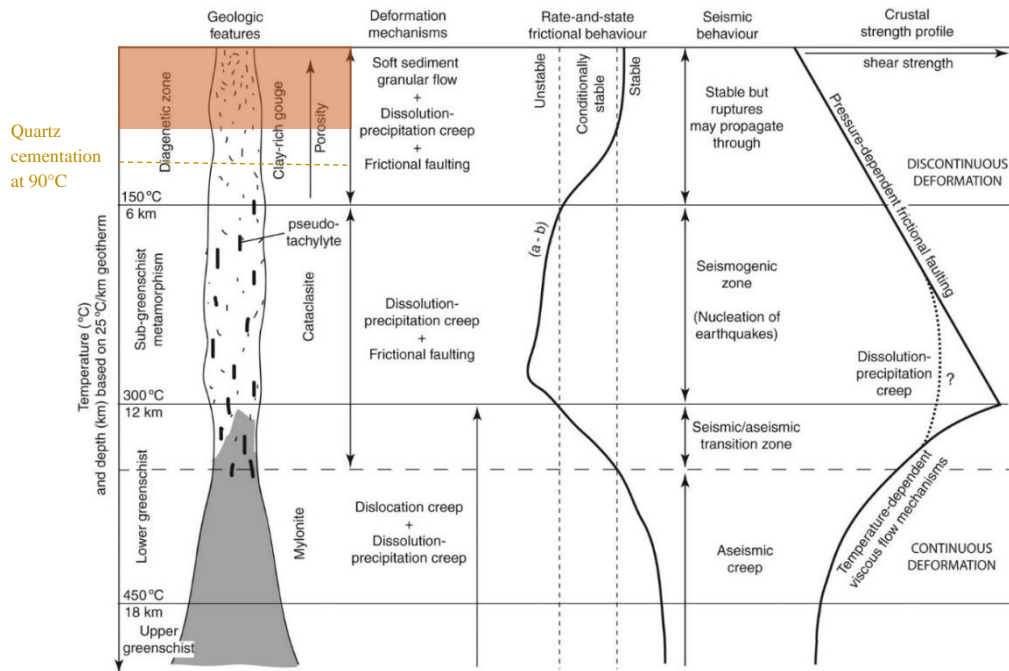


Figure 2.1: Fault zone model modified from (Sibson 1983; Scholz 2002; Fagereng and Toy 2011). This model is drawn assuming a 25°C/km geothermal gradient. In order to achieve quartz cementation at lower burial depths the geothermal gradient must be higher (30°C/km or above) or a groundwater silcrete is present. Shallow conditions (<3 km depth) are highlighted in orange.

2.3 Deformation bands

A deformation band is a naturally occurring tabular zone formed within bodies of rock/granular material displaying porosity greater than 10% (Holcomb et al. 2007). The zone is composed of the same lithology as the host rock however, the fabric of the rock has been mechanically altered. Despite a high volume of research into deformation bands (Aydin and Johnson 1978; Underhill and Woodcock 1987; Rykkelid and Skurtveit 2018; Zuluaga et al. 2018), there is less research into deformation bands in poorly consolidated sediments (Skurtveit et al. 2013; Alikarami

et al. 2014; Torabi 2014). Deformation bands are precursors to faults and are often found in the fault zone.

Primarily deformation bands have been studied as they act as a barrier or baffle in reservoir rocks (Edwards et al. 1993; Ogilvie and Glover 2001; Lothe et al. 2002; Cavailhes et al. 2009; Busch et al. 2017; Qu and Tveranger 2017; Griffiths et al. 2018). However, defining how and when deformation bands form in shallow vs deep burial depths allows deformation bands to be used as a chronological indicator (e.g. Petrik et al. 2014), and a method to measure diagenetic alteration (Busch et al. 2017). Cashman and Cashman (2000), Balsamo and Storti (2010) and Shipton et al. (2017) raise the possibility that grain fracturing in the shallow subsurface may indicate coseismic behaviour. If this is the case then the desecry of deformation bands in shallow sediments may alter future building codes.

2.3.1 Deformation band characteristics

Deformation bands can appear as millimetre to centimetre wide singular bands, zones of singular bands or anastomosing zones (Aydin 1978; Aydin and Johnson 1978; Underhill and Woodcock 1987). It is common to see cross cutting relationships between deformation bands therefore indicating two separate deformation band forming events. Deformation bands can vary in width, field studies suggest that widths are generally <2 cm (Du Bernard et al. 2002; Sigda and Wilson 2003; Johansen et al. 2005; Exner and Tschegg 2012; Torabi 2014). Johansen et al. (2005) suggests that deformation band width could be related to the available pore space in the host sediment, whereby thicker deformation bands are present in sandstones with a higher porosity, and those with thinner deformation bands are from sandstones with a lower host porosity.

Aydin (1978) and Underhill and Woodcock (1987) divides deformation bands into three zones; parent sandstone, outer and the inner. The parent sandstone has a high porosity and cement (although this is not always present) can be visibly acting as a contact between grains. The outer zone encompasses the edges of the inner zone where there is an overall reduction in porosity, there is evidence of some grain fracturing and there are increased grain to grain contact in comparison to the host rock as the cement holding the grains together is destroyed. The inner zone consists

Chapter 2 - Literature review

of predominantly angular, fractured grains (and cement) with only a few residual undeformed grains resulting in an overall smaller average grain size and low porosity. Within the majority of deformation bands there is a general decrease in porosity and permeability in comparison to the host rock. However, the porosity/permeability properties along a deformation band are inconsistent and vary depending on which part of the deformation band the measurement is taken from (Torabi & Fossen 2009).

Generally deformation bands, in particular cataclastic deformation bands, are stronger, and therefore more resistant than the original host rock from which they are formed (Mair et al. 2000; Kaproth et al. 2010).

Deformation bands can stretch for up to 10's of metres in length (Fossen et al. 2007; Tembe et al. 2008). Offsets on a single band are rarely more than a few mm, but have been observed up to 1 m (Lommatzsch et al. 2015). Deformation bands prove difficult to identify using geophysical techniques e.g. they are below seismic resolution, therefore the majority of studies to date focus on deformation bands from outcrops.

Deformation bands can form parallel to bedding (Tondi et al. 2006; Zuluaga et al. 2014) or in conjugate sets (Soliva et al. 2013). Studies of deformation bands in poorly consolidated sandstone report branch like features which form at the termination point of each band.

There are three key stages in the development of deformation bands (Figure 2.2). The initial stage is singular band development. As strain localization increases it leads to the formation of a deformation band zone and finally the formation of a slip surface (Aydin 1978; Aydin and Johnson 1978; Shipton and Cowie 2001). Aydin (1978) suggest that zones of deformation bands are formed due to a combination of strain localization in the sample and individual band strain hardening.

The conditions which control deformation band formation include the properties of the host rock (pore space, grain size/grain size distribution, grain shape, sorting, cementation), burial depth, tectonic environment, and pore fluid pressure (Cheung et al. 2012). However, with so many variables and many field examples there remains

ambiguity over the main properties which control deformation band formation. As a result, this area of research still requires considerable focus. My thesis will focus on quantifying the distribution of porosity and cement in deformation bands and investigate the impact of levels of weak cementation on sandstones during deformation. The majority of work so far on deformation bands shows their formation and impact in sandstone (Fossen et al. 2007).

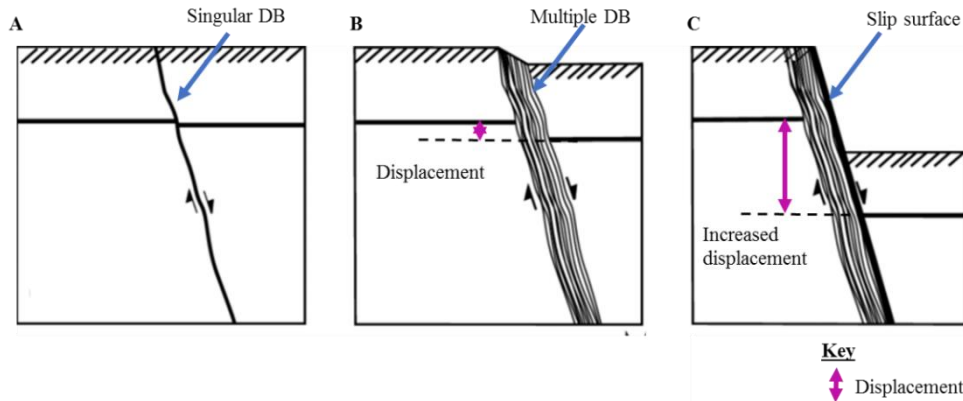


Figure 2.2: Increased strain localization during the stages of deformation band formation. A) Stage 1 - Single DB formed due to localisation of strain. B) Zone of DFB formed due to continued localisation of strain. C) Zone of DBs form a slip surface and displacement increases. Fault surface is formed. Image modified from Shipton et al. (2005).

However, deformation bands can also form in poorly cemented sands (Figure 2.3) (Cashman and Cashman 2000; Rawling and Goodwin 2003; Wen and Aydin 2004; Ballas et al. 2012; Petrik et al. 2014; Shipton et al. 2017), carbonate grainstone (Tondi et al. 2006); ignimbrite (Wilson et al. 2003), basalt (Adelinet et al. 2013) and basaltic tuff (Hoffman and Tewksbury, 2006). It has been shown that the majority of deformation bands studied in poorly consolidated sandstone are in extensional tectonic regimes (at the time of deformation band formation) (Fossen 2017).



Figure 2.3: Examples of deformation bands in poorly consolidated sandstone from France and Hungary. A) Cataclastic deformation bands from Riedseltz, France. Photo credit: Zoe Shipton. B) Three generations of cross-cutting deformation bands from Szilvasvarad, Hungary. C) A single deformation band cross cutting bedding in clay rich sediment from Novaj, Hungary.

Despite the volume of studies carried out to date the terminology used remains inconsistent across both field and lab studies which makes summarising previous studies challenging. In this study we use the term deformation band (DB) to describe all forms of bands e.g. compaction, shear, cataclastic etc. The terminology in this chapter follows that of Fossen et al. (2007). Table 2.1 summarises the deformation band properties (deformation mechanisms, kinematics and appearance) from a selection of previously published literature on sandstone and sand outcrops.

Table 2.1: Summary of deformation band terminology used in literature.

Type of deformation band	Abbreviation	Example of study using abbreviation
Pure compaction band	PCB	Eichhubl et al. (2010); Fossen et al. (2011, 2017); Ma and Haimson (2013)
Compaction band	CB	Olsson (1999); (Schultz 2009)
Cataclastic shear band	CSB	Cavailles et al. (2009); Fossen et al. (2015); Lommatzsch et al. (2015); Philit et al. (2015)
Cataclastic deformation band	CB/CDB	Fossen et al. (2007); Mesdeiros et al. (2010); Sallet and Wibberley (2013); Tindall (2014)
Dilation band	None used	Du Bernard et al. (2002)
Dilation shear band	DSB	Fossen et al. (2017)
Pure dilation band	PDB	Fossen et al. (2017)
Shear band	SB	Desrues and Viggiani (2004); Borja et al. (2013); Lin et al (2015)
Simple shear band	SSB	Fossen et al. (2017)
Shear enhanced compaction band	SECB	Eichhubl et al. (2010); Wong and Baud (2012); Ballas et al. (2013); Klimczak and Schultz (2013); Skurtveit et al. (2013)
Shear enhanced dilation band	SEDB	Fossen et al. (2017)

2.3.2 Deformation mechanisms

There are three deformation mechanisms reported in the literature by which deformation bands form: cataclasis, disaggregation and dissolution. The deformation mechanisms control the microfabric of deformation bands.

2.3.2.1 Cataclastic DB

Cataclastic bands are formed as a result of grain fracture and/or breakage (Aydin 1978, Aydin & Johnson 1983). Cataclasis appears to impact grains of 0.3-0.8 mm in size in sandstones (Mollema & Antonellini 1996). During grain fracturing the interlocking of grains increases the likelihood of strain hardening (Fossen et al. 2007). Cataclastic bands can be identified by a general reduction in grain and pore size and display offsets up to 3-4 cm (Fossen et al. 2007). As a result of the grain breakage these bands often exhibit compaction and a reduction in permeability. Permeability in cataclastic bands can be reduced by up to six orders of magnitudes in comparison to the host rock (Pittman 1981; Jamison and Stearns 1982, Harper and Moftah 1985; Knott 1993; Antonellini and Aydin 1994; Gibson 1994, 1998; Knipe et al. 1997; Crawford 1998; Antonellini et al. 1999; Fisher and Knipe 2001; Jourde et al. 2002; Shipton et al. 2002; Fossen 2007; SAILLET 2013).

Studies have shown that in general the degree of cataclasis increases with increasing burial depth (Fossen et al. 2007, Beke et al, 2019). However, cataclasis has also been found within shallowly buried sand(stones) (Cashman and Cashman 2000; Rawling and Goodwin 2003; Balsamo and Storti 2010a; Ballas et al. 2012; Torabi 2014; Shipton et al. 2017). It has been suggested that cataclastic bands in sandstone form after lithification between 1.5- 2.5km depth but before uplift (Fossen et al. 2007). However, this may not be the case for poorly/unconsolidated sediments displaying deformation bands.

2.3.2.2 Disaggregation DB/ Particulate flow

Disaggregation bands can form within grain breakage due to grain boundary sliding, grain rotation or breaks in cement resulting in the development of disaggregation bands. This process is known as either granular (Twiss and Moores 1992) or particulate flow (Rawling and Goodwin 2003).

Disaggregation bands can either increase or decrease porosity depending on their kinematic component (e.g. dilation or compaction). Some studies report up to 10% porosity increase in the bands compared to the host rock (Antonellini et al 1994; Du Bernard et al. 2002;). Other studies report disaggregation bands with porosity reduced by 25% (Mollema & Antonellini 1996).

2.3.2.3 Dissolution DB

Secondary deformation can occur in deformation bands syn or post deformation. Dissolution can take place in the shallow subsurface (<3km) or at depth (Walderhaug 1996) and is more likely to take place (and at a faster rate) when clay minerals are present around grain boundaries because they can retain a water boundary at the grain surface (Renard et al. 1997).

2.3.2.4 Burial depth

Fulljames et al. (1997) suggested that burial depth (confining pressure) and porosity are the primary controls on cataclasis in sandstones, but clearly there are other factors that promote cataclasis in shallow settings (Figure 2.4). When comparing estimated burial depths of poorly consolidated sandstones containing cataclastic deformation bands five studies (Cashman and Cashman 2000; Exner and Tschegg 2012; Kristensen et al. 2013; Torabi 2014; Shipton et al. 2017) suggest that their maximum burial depth is below 500 m (Figure 2.5). This implies that the minimum burial depth for cataclasis to occur is lower than previously believed. One possible explanation for cataclasis in shallow buried sediments is mineralogy. Feldspar and clay minerals will break preferentially over quartz. Feldspar has a hardness of 6, meanwhile quartz has a hardness of 7 in the Mohs hardness scale.

Furthermore, as clay content increases clay smears can develop and it is more likely that slip surfaces will form as opposed to deformation bands. Kristensen et al. (2013) describe 'intense' cataclasis in both sand and clay layers at their Galgeløkke site in Denmark (Jurassic aged sediments). They conclude that cataclasis at shallow depth is controlled by burial depth and mineralogy, and an increased clay content can reduce the level of cataclasis observed. However, Torabi (2014) conclude that 'intense'

cataclasis at shallow burial depths is not controlled by mineralogy.

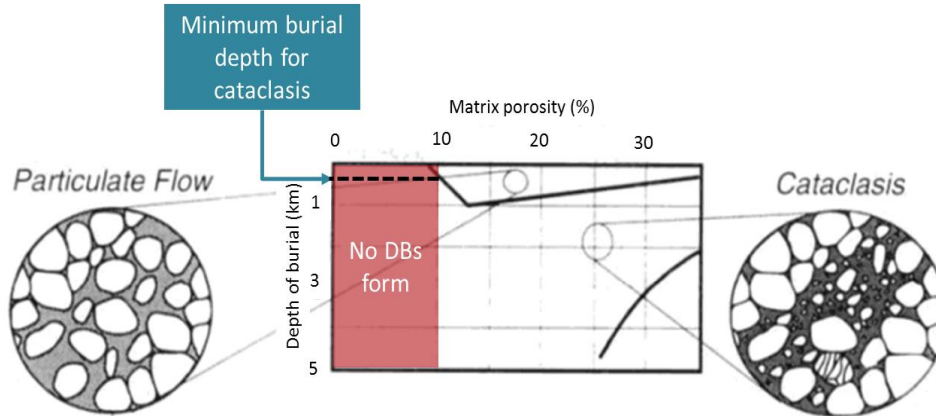


Figure 2.4: Simplified DB burial diagram demonstrates that DB bands require 10% porosity to form and the minimum burial depth for cataclasis to occur is ~500m. After Fulljames et al. (1997).

Meanwhile, Cashman and Cashman (2000) and Shipton et al. (2017) speculate that seismic slip may be required in order to achieve cataclasis at shallow burial depths (where overburden pressure is limited).

Beke et al. (2019) use samples from across Hungary to demonstrate the impact of progressive burial on deformation mechanism. They show that with increasing depth deformation bands progress from forming disaggregation bands, to cataclastic (weak-advanced), before finally developing a slip surface. Weak vs advanced cataclasis is qualitatively defined based upon the grain breakage mechanism (e.g. flaking, trangranular) and the pore size inside the deformation bands (Figure 2.6). This same classification is applied to the deformation bands described in Chapter 5.

2.3.3 Deformation band kinematics

Kinematically there are three end members of deformation band: shear, compaction and dilation. Shear bands display a macroscopic offset with respect to the surrounding rock, compaction bands display evidence of a volume decrease, and dilation bands display evidence of a volume increase. It is also suggested that there can be hybrid or intermediate versions of these (Aydin et al. 2006; Fossen et al.

2017) e.g. shear-enhanced compaction band (Table 2.1).

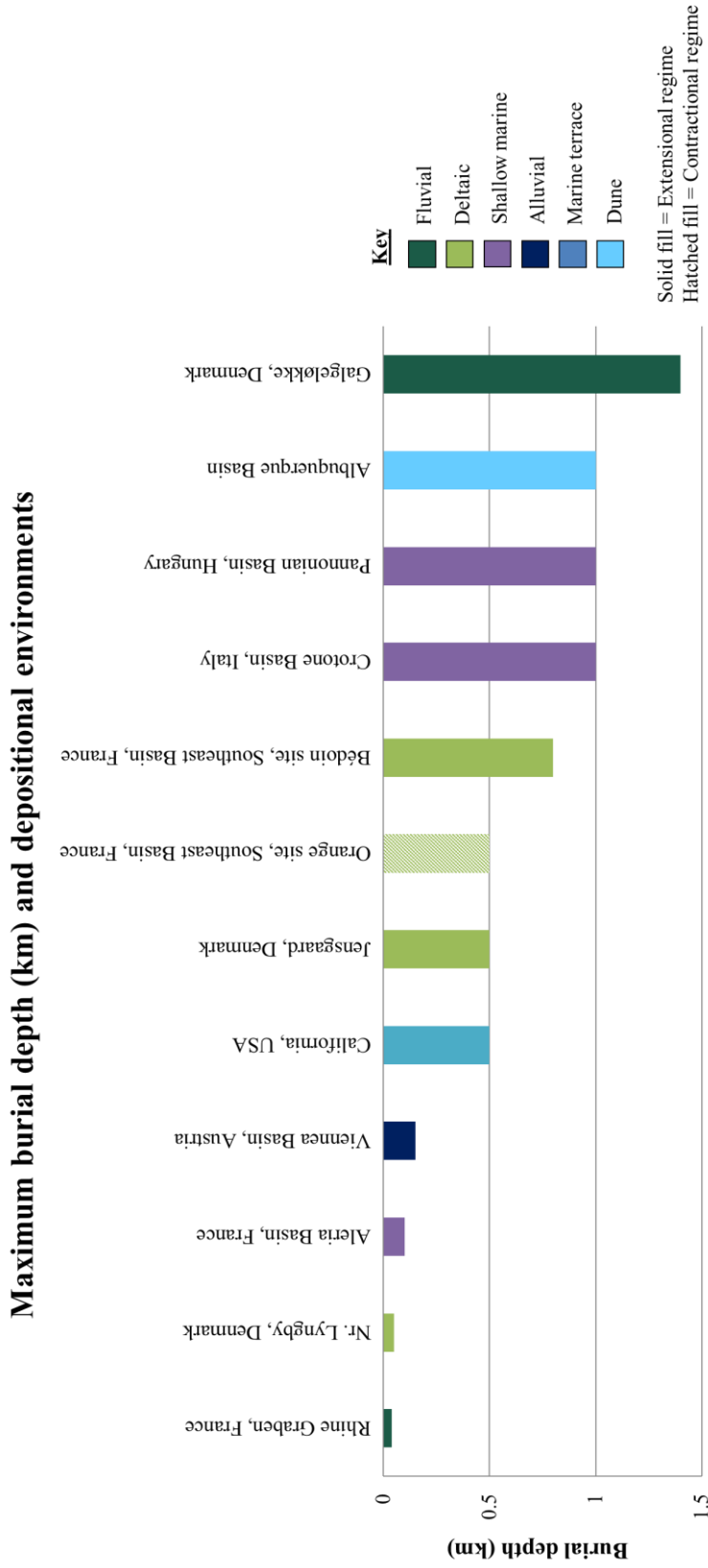


Figure 2.5: Maximum burial depth (km) and depositional environments of deformation band outcrops in poorly consolidated sandstones (Cashman and Cashman 2000; Rawling and Goodwin 2003; Balsamo and Storti 2010a; Exner and Tschegg 2012; Kristensen et al. 2013; Sallet and Wibberley 2013; Petrik et al. 2014; Torabi 2014; Shipton et al. 2017).

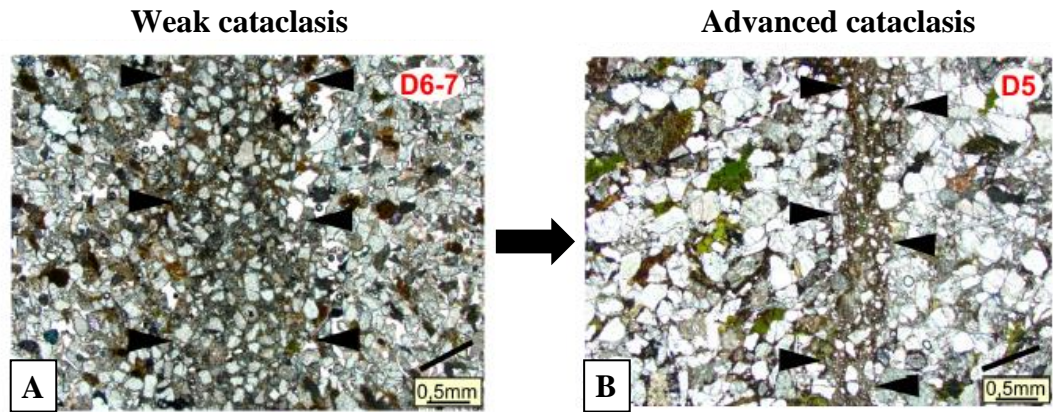


Figure 2.6: Plane polarised light thin sections of cataclastic deformation as categorised by Beke et al. (2019). Weak vs advanced cataclasis is defined by the grain breakage mechanism (e.g. flaking, trangranular) and the pore size inside the deformation bands. A) Weakly cataclastic deformation band from TaNe, Hungary. Quartz grains are fairly uniform in size across both the host rock and the deformation band zone with deformation primarily occurring where quartz grains are in contact. The deformation band zone is highlighted by an increase in phyllosilicates. B) Advanced cataclastic deformation band from Ha, Hungary 375 -1100m burial depth. Quartz grains inside deformation band are considerably smaller than the quartz grains of the host sediment. Images from Beke et al. (2019).

2.3.4 Review of deformation bands in sand and sandstone

This section summarises the deformation mechanism and kinematics of deformation band data collated from 66 deformation bands described in sandstone and poorly consolidated sandstone literature (Figure 2.7).

From Figure 2.7 it is clear that the majority of DB studies published describe the dominant deformation mechanism as being cataclasis in both consolidated and poorly consolidated sandstone states. One possible suggestion for the noted occurrence of cataclastic deformation bands at shallow depths is the influence of the surrounding tectonic regime (Fossen et al. 2017). For example, the majority of studies on deformation bands in poorly consolidated sandstones are in extensional

regimes (Figure 2.5). However, this could be due to the preferential selection of geological studies in extensional regimes as opposed to contractional. It is also possible that the greater number of cataclastic band descriptions are because cataclastic bands can be easier to identify in the field (in comparison to disaggregation and dissolution bands).

The DB studies referenced in Figure 2.7 indicate shear bands are the most studied kinematic class. However, in poorly cemented sandstone studies shear is the most common kinematic class in field studies. Intriguingly 30% of papers on deformation bands in poorly consolidated sandstone do not report the kinematics. It is possible this lack of data is as a result of the confusion or misuse of kinematic descriptions.

2.3.5 Laboratory studies of deformation bands

Lab studies have focussed on the conditions that control the formation of deformation bands in both sand and sandstones (e.g. Wong et al. 1997; Mair et al. 2000; Andò et al. 2015). Variables investigated include the properties of the host rock (pore space, grain size, grain shape, sorting, cementation), burial depth (confining pressure) and pore fluid pressure.

There has been a lot of research into the deformation and failure, of granular materials in geomechanical research (Brok et al. 1997; Alshibli and Sture 2000; Desrues and Viggiani 2004; Saidi et al. 2005; Alshibli and Alramahi 2006). There is also increasing work on grain fracture in brittle deformation mechanics e.g. under what conditions grains break. This is particularly relevant when trying to understand the conditions which lead to the formation of cataclastic deformation bands. In granular material studies shear bands have been categorised as materials which display intense strain in particular areas (e.g. strain localisation) however the surrounding areas are unaffected by the strain (Ando 2013). Shear bands have been studied through a range of mechanical deformation tests.

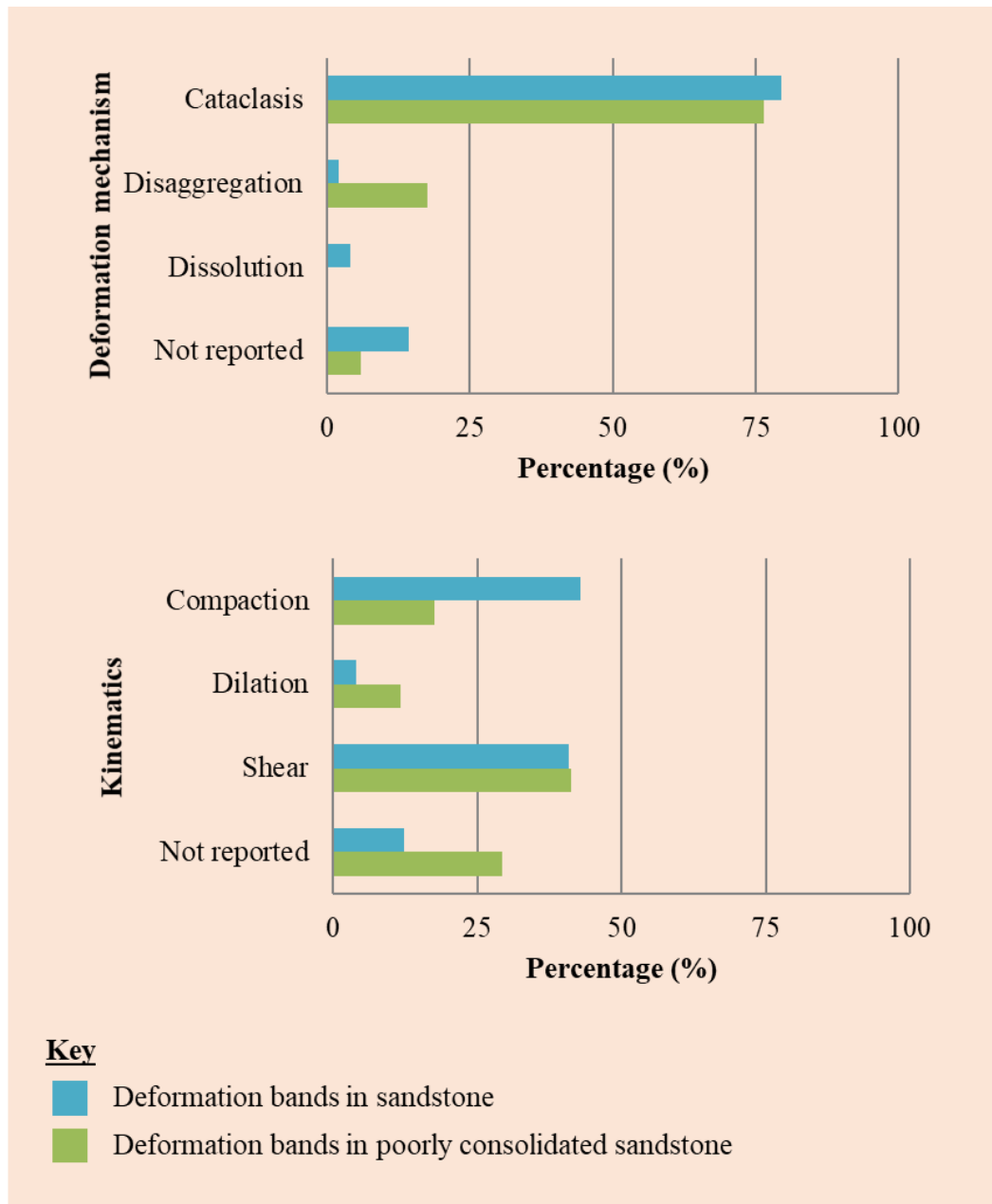


Figure 2.7: Deformation band properties summarised from published studies on sandstone and poorly consolidated sandstone (see Appendix 1 for master data set).

2.3.5.1 Mechanical deformation

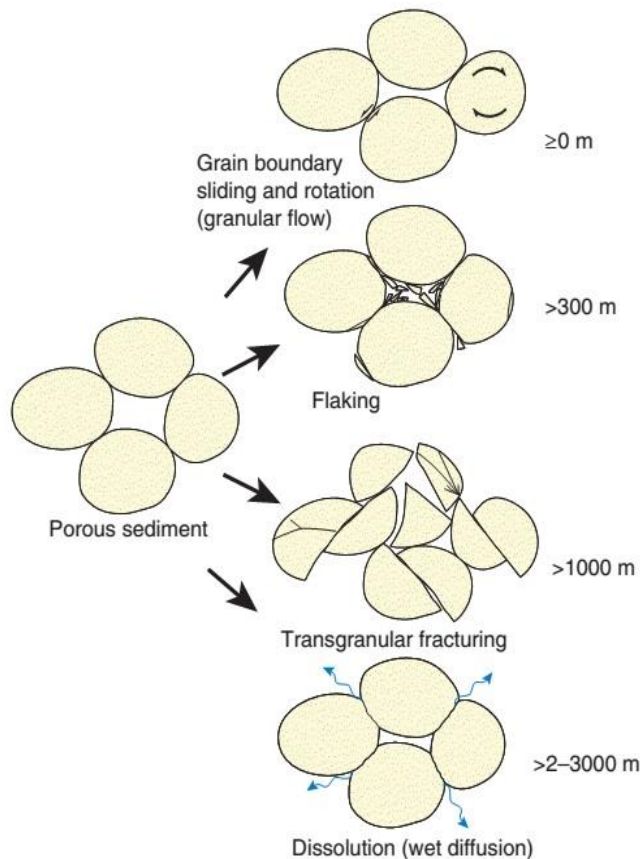


Figure 2.8: Types of grain fracture which can occur with estimated depths. From Fossen (2010).

deformation.

Uniaxial compressive strength (UCS)

Although there are no studies to our knowledge which show deformation bands forming in uniaxial compressive strength (UCS) test, UCS has been used to study the conditions which lead to grain breakage (Chuhan et al. 2002). Chuhan et al. (2002) suggests that grain breakage can begin at ~ 2 MPa (approximate equivalent depth of 78m) effective vertical stress however, the effects of grain breakage are more clearly defined in samples deformed at effective vertical stresses greater than 10 MPa (approximate equivalent depth of 392 m calculated using formula from Sharma (1997)).

One of the main areas of focus is the formation of deformation bands. Investigations into the formation of deformation bands (or shear bands) by means of mechanical testing have included sand box experiments (McClay and Ellis 1987), shear box, ring shear (Mandl et al. 1977; Agung et al. 2004; Torabi et al. 2007) and, the more popular, triaxial testing (Mair et al. 2000; Skurtveit et al. 2013; Alikarami et al. 2014). During all of the tests one of the main reference points to ascertain the depth at which deformation bands form is the level of grain fracturing (Figure 2.8) observed during

Shear box

The majority of shear box studies in literature have been used in geotechnical engineering to understand the load deformation characteristics and shear behaviour (maximum shear strength, ultimate/residual shear strength and failure envelope) of clays and soils (Roscoe 1970; Vangla and Latha Gali 2016; Yavari et al. 2016; Habibbeygi and Nikraz 2018). For example, the residual shear strength of soils is of particular interest for predicting the behaviour of landslides. A shear box works by forcing a shear plane to develop along a predefined surface. It is an inexpensive method to achieve accurate results in geotechnical tests. Across the shear box studies it is understood that a shearband forms in the material as the top plate of the shear box is pushed along a defined plane however it is challenging to remove and analyse an intact sample post-deformation from the shearbox without causing structural changes to the deformed sample.

Kaproth et al. (2010) found that during their single-direct shear test experiment on unlithified sandstone (tested at 0.5-1.85 MPa normal stress with a shear strain rate of 1×10^{-5} m/s) grain breakage took place at all tested normal stresses. Therefore highlighting that at slow strain rate conditions and low normal stress, grain breakage is possible in the subsurface.

Ring shear

Ring shear is able to give a better understanding of the structural changes which lead to shearing of a sample because it can create larger displacements than the shear box tests (Khidas and Jia 2012). Ring shear experiments (Clausen and Gabrielsen 2002; Agung et al. 2004; Sassa et al. 2004; Torabi et al. 2007; Cuisiat and Skurtveit 2010; Kimura et al. 2018) are growing in number across geosciences as a method to produce shear bands in the laboratory. Deformation of unconsolidated sands by ring shear has shown to display grain crushing and shear zone development (Agung et al. 2004; Cuisiat and Skurtveit 2010).

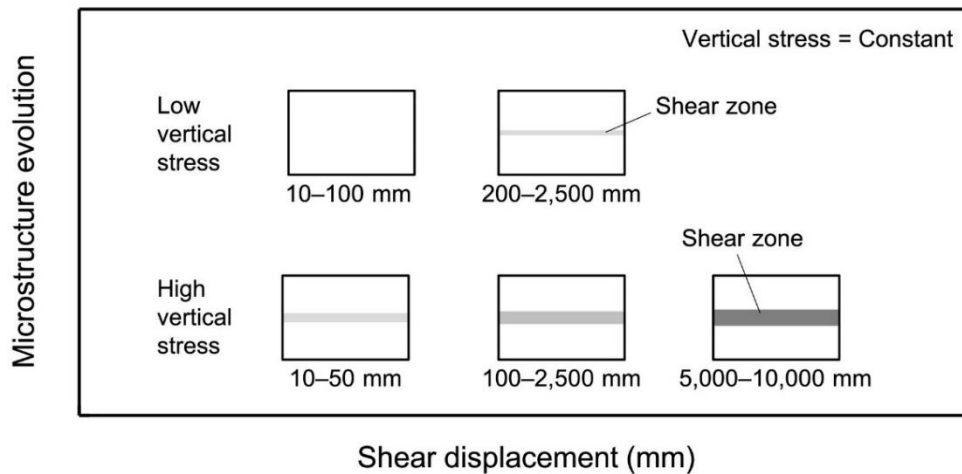


Figure 2.9: From Kimura et al. (2018) this figure shows the development of shear zones in sand (Tohoku silica sand No. 7) as displacement continues under high (e.g. 8 MPa) and low (e.g. 1 MPa) vertical stress from ring shear tests. This suggests that when a sample is subjected to low vertical stress and up to 100 mm displacement no shear band can be identified. As displacement continues the shear zone becomes wider and more developed.

The high pressure ring shear experiment by Torabi et al. (2007) demonstrates that sands with wide and poorly defined shear zones are more likely to form at lower stress levels (5 MPa) whereas shear zones in sands with clear, sharp boundaries are more likely to form in areas of higher stress (20 MPa). As depth increases the dominant grain breakage mechanism transitions from grain flaking to transgranular fracturing.

Meanwhile, Cuisiat and Skurtveit (2010), demonstrate that grain fracturing is observed from 10 MPa effective vertical stress (corresponding to approximately 500 m burial depth) in their high pressure ring shear experiments of clay smears.

Kimura et al. (2018) present a detailed study of the pore and grain sizes in sand shear zones created using ring shear (between 1-8 MPa effective vertical stress, with a shear rate of 2mm/min). Observations from Kimura et al. (2018) indicate that grain fracturing and ultimately shear zone development is dependent upon the total shear displacement (Figure 2.9) of a ring shear experiment. Therefore shear band formation

is unlikely to be observed at low vertical stresses with displacements less than 200 mm.

Across these experiments there is no consistency for the depth at which grain crushing can take place. However, it is worthwhile to note that for each shear box/ring shear experiment the results are only applicable to that individual soil/sand sample. In addition, Torabi et al. (2007), Cuisiat and Skurtveit (2010) and Kimura et al. (2018) do not account for cement (or poorly cemented sandstones) in their ring shear studies or materials which contain no cement phase.

With both shear box and ring shear experiments there are limited studies which track the movement of grains insitu as the shear tests take place. To the best of my knowledge I do not know of any studies which have successfully imaged grain movement of sandstones in a shear box using an X-CT. However, Tobler et al. (2018) were able to image the effects of shear on microbially induced calcite precipitation (MICP) sealed granite cores (of 37 mm diameter) by scanning sample pre and post deformation and using a plaster cast to hold the cylindrical sample in place in the square shearbox.

Triaxial

Triaxial testing to form compaction bands and shear bands has been widely used over the last 20 years (Wong et al. 1997; Mair 2002; Baud et al. 2004; Fortin et al. 2006; Louis et al. 2007; Tembe et al. 2008; Yang and Jiang 2010; Hall et al. 2010; Charalampidou et al. 2011; Cheung et al. 2012; Ando 2013; Ingraham et al. 2013; Ma and Haimson 2013; Heap et al. 2015). These studies have shown that deformation bands can form over a range (~0.1-550 MPa) of effective pressures.

Some of these studies describe evidence of grain crushing (Fortin et al. 2006; Charalampidou et al. 2011; Skurtveit et al. 2013). However, studies have also explored strand development (Mair et al. 2000) the impact of creep conditions (Heap et al. 2015) and the formation of deformation bands in unconsolidated sands (Ando 2013; Alikarami et al. 2014).

Skurtveit et al. (2013) used triaxial tests to identify that grain rearrangement is most significant in the deformation of high porosity sands under low stresses of 2 and 5

MPa hydrostatic loading pressures (hydrostatic loading pressures were used as the samples were frozen when they were mounted into the triaxial cell). However, when the stress is increased (15 MPa hydrostatic loading pressure) grain fracturing becomes the dominant deformation mechanism. Grain fracturing is most significant in coarser grained materials.

Mair et al. (2000) investigated the increase in the number of deformation band strands with increased axial strain under triaxial deformation. The study showed that at 34 MPa cataclastic deformation bands formed in consolidated sandstone.

Heap et al. (2015) investigate the formation of compaction bands due to creep. They show that compaction bands can form as a result of exposure to constant creep conditions. Under creep conditions compaction bands form at a lower differential stress (80 MPa) than constant strain experiments (100 MPa). Furthermore, the compaction band growth rate in sandstones is dependent upon the applied stress to the sample. Therefore as the strain rate increases the growth rate of compaction bands increase.

Ando (2013) carried out insitu triaxial testing of three sands (Hostun, Ottawa and Caicos ooids) inside the X-CT at Laboratoire 3SR to form shear bands. Samples were 22 x 11mm in size. Ando (2013) allows for the porosity changes during the formation of deformation bands to be measured and imaged in 3D. Furthermore, kinematic measurements can be performed on individual grains during deformation.

2.3.5.2 Sample size

Ando (2013) discuss that the size of the sample analysed does not matter to enable the formation of deformation band in sand by triaxial experiment. However, the lab studies carried out by Mair et al. (2000) find that deformation bands only form in sandstone samples of large enough dimensions (100 mm diameter with lengths ranging from 189.5-229 mm). Despite shear bands being well studied in granular materials the size of the samples being deformed are rarely larger than 40 mm in height and 20 mm diameter (Alikarami et al. 2014; Torabi et al. 2014; Heap et al. 2015). This therefore creates uncertainty as to whether deformation band formation in sand versus sandstone are sample size dependent.

2.3.5.3 Varying porosity

Understanding evolution in porosity and permeability of sandstones under confining pressures is important to understanding the formation and properties of cataclastic deformation bands.

UCS test studies have shown that the compressive strength of sandstones increase as porosity decreases (Palchik 1999; Lin et al. 2005; Weng et al. 2005, 2008). This therefore shows that the porosity present in a sandstone is key to the mechanical properties of the rock. However, as mentioned previously, to my knowledge no UCS studies have formed deformation bands.

Porosity and permeability evolution of triaxial experiments have shown that as porosity and grain size increases a sandstone becomes less brittle during deformation (Wong et al. 1997). Wong and Zhu (1999) show that in a triaxial rig at confining pressures less than 100 MPa sandstone will initially display evidence of dilatancy and a reduction in permeability followed by a period of compaction. This is associated with microcracking and the formation of a cataclastic shear band in the sandstone (Main et al. 2000). A porosity decrease of up to one order of magnitude can be seen inside deformation bands, in comparison to the host rock (Fossen et al. 2007). Furthermore, as the bulk sample permeability increases during the period of dilatancy the sample porosity will increase (Main et al. 2000).

This increase in porosity assists the formation of deformation bands. If porosity and grain size decreases it is believed the opportunity for the development of cataclastic deformation bands will decrease (Chuhan et al. 2003). This therefore suggests that porosity is a key variable in the formation of cataclastic deformation bands.

One method to reduce the porosity in sandstones is to fill the pores with cement (Scherer 1987; Selley and Sonnenberg 2015).

2.4 Cement in sandstones

During diagenesis cementing minerals are formed between grains. As sand is deposited (e.g. in a dune or beach environment) it will be buried under continuing sedimentation. As burial increases, the temperature and pressure increases, and the

sediment is exposed to groundwater of varying chemical composition. During this process of diagenesis unconsolidated sand becomes consolidated (or lithified) as the grains compact (mechanical compaction) and intergranular cement (chemical compaction) forms in the pore space between grains.

Cement can form as grain overgrowths and as bridges between grains. As the percentage of cement in a sandstone increases the porosity decreases. Cement which forms during diagenesis is called primary cement. Cement which has formed as a result of subsequent mechanical or chemical interactions is known as secondary cement. This work focuses on primary cement and does not take into consideration the impact of secondary cement on the consolidation level of sandstones.

Depending on the degree of consolidation sands and sandstones can be classified into unconsolidated, poorly consolidated or consolidated sandstone (Figure 2.10).

Unconsolidated, loose sand with no cement holding the grains together; poorly consolidated sand which can be broken easily by hand; consolidated, sandstone which remains intact and requires a hammer to break it. With increasing cement content the porosity decreases the sandstone becomes denser and as a result stronger.



Figure 2.10: Process of consolidation. In this classification there are two end members: unconsolidated and consolidated. However, there are a range of levels of consolidation which fit under the term ‘poorly consolidated’. This classification was created based on the fieldwork carried out during this thesis.

Whilst looking at poorly cemented sandstones it is important to consider that the deformation which is identified on the present day landscape may have developed

before lithification of the rock. This includes the formation of deformation bands as it is possible that they can form before and after lithification.

2.4.1 Types of cement

Two of the most common natural cements in sandstones are silica (e.g. quartz) and calcite (CaCO_3).

Silica cement

Silica cement takes the form of pressure solution, quartz overgrowths, microquartz, megaquartz, chalcedonic quartz and opaline silica (Tucker 2001).

One area which has not been widely discussed in literature, and is relevant to the diagenesis of sandstone, is the formation of quartz cement in shallowly buried sandstones (Milliken et al. 2005). Traditionally quartz cementation is particularly significant above 90°C (Fisher et al. 2003; Lander et al. 2008), or ~ 3 - 3.6 km burial depth (assuming a geothermal gradient between 25 - $30^\circ\text{C}/\text{km}$) (Ramm and Bjørlykke 1994). However, Philit et al. (2015) show that at shallow burial depths (<2 km) quartz cementation is possible by groundwater silicretes.

Calcite cement

The two main types of calcite cement are poikilotopic crystals and drusy calcite spar (Tucker 2001). Poikilotopic is when a single cement crystal encompasses many smaller crystals. Drusy calcite spar are equant crystals which fill the pore space between the grains (Tucker 2001).

2.4.2 Cement distribution

The distribution of cement varies at the grain scale and the outcrop scale. Cement distribution in the outcrop scale can be dependent on depositional environments, tectonic setting, pore throat distribution (no porosity, unconnected pores or connected pores) and the burial history (with particular focus on the flow of liquids through the outcrop) over time. In addition, the distribution of cement can also depend upon secondary elements such as weathering. Whereby acid rain/fluids, and strong winds can preferentially decay the cements that join the grains together. At the grain scale cement distribution can vary on how the cement sticks to the grains. For example, the cement may fill the complete pore space between the grains. However,

it can also coat the grains or form at the joins between grains. As the percentage of cement increase the available pore space decreases (Figure 2.11).

In some cases cement distribution is referred to by how the cement fills the pore space (e.g. intergranular vs intragranular cements) however, there are limited studies which consider the shape of the cement distribution across the sandstone body or where the cement grows around to the grains. Fonseca et al. (2013) show that if cement is distributed along an extended contact (e.g. along the a full grain side, instead of cement point contacts between grains) the formation of intra-granular cracking will be hindered between sand grains. This suggests that the distribution of cement around sand grains has a direct impact on the mechanisms which take place during sandstone deformation.

There is a growing community of studies which use X-CT to visualise grain, cement and porosity distribution in natural or synthetic sandstones (Cnudde et al. 2011; Ando 2013; Fonseca et al. 2013; Wennberg and Rennan 2017). However, the majority of studies which look at cement distribution primarily image cement by scanning electron microscopy (SEM) (Saidi et al. 2005; Gomez et al. 2017; Qian et al. 2018).

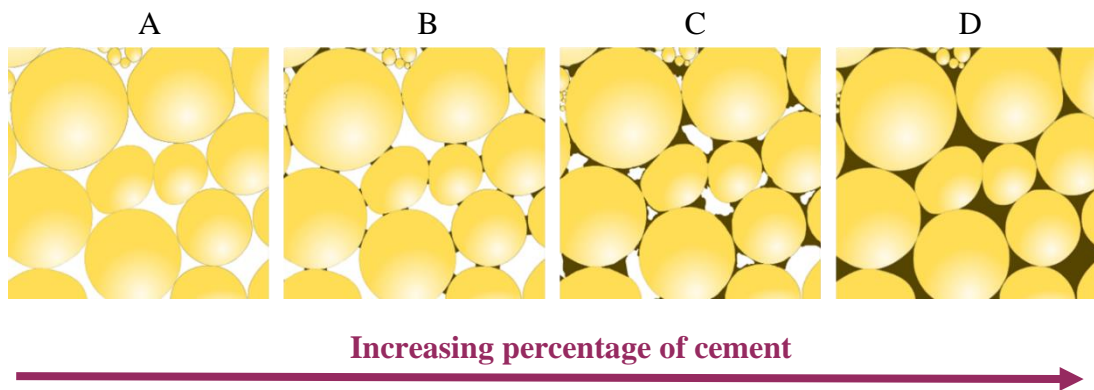


Figure 2.11: Cement distribution A) Grain supported packed sand with closed pore throats in 2D. B) Cement on grain to grain contacts holding the grains together. C) Primarily cement supported grains. Significant loss in pore space. D) All pore space filled with cement.

Calcite cement distribution

The geometry of first generation calcite cements can be described as isopachous (uniform thickness) or gravity and meniscus cement. Figure 2.12 displays examples of carbonate cement fabrics. The environment in which the unconsolidated material (e.g. sand) was present controls the geometry of the cement. Isopachous cements are indicative of precipitation in the phreatic zones where all the pores are filled with water. Gravity (stalactitic) and meniscus cement are indicative of vadose-zone precipitation (not saturated with water).

Other cements can be made of any mineral that has been deposited in pore space to form grain-to-grain contacts. This can include, and is not limited to, calcite, clay minerals (e.g. smectite), haemitite and gypsum. The presence of clay minerals in sandstone inhibit quartz cementation at greater burial depths. These sandstones are therefore more likely to maintain porosity during burial (Ramm and Bjørlykke 1994). The type of cement formed depends on the grain chemistry, groundwater chemistry, volume of fluids present and burial conditions.

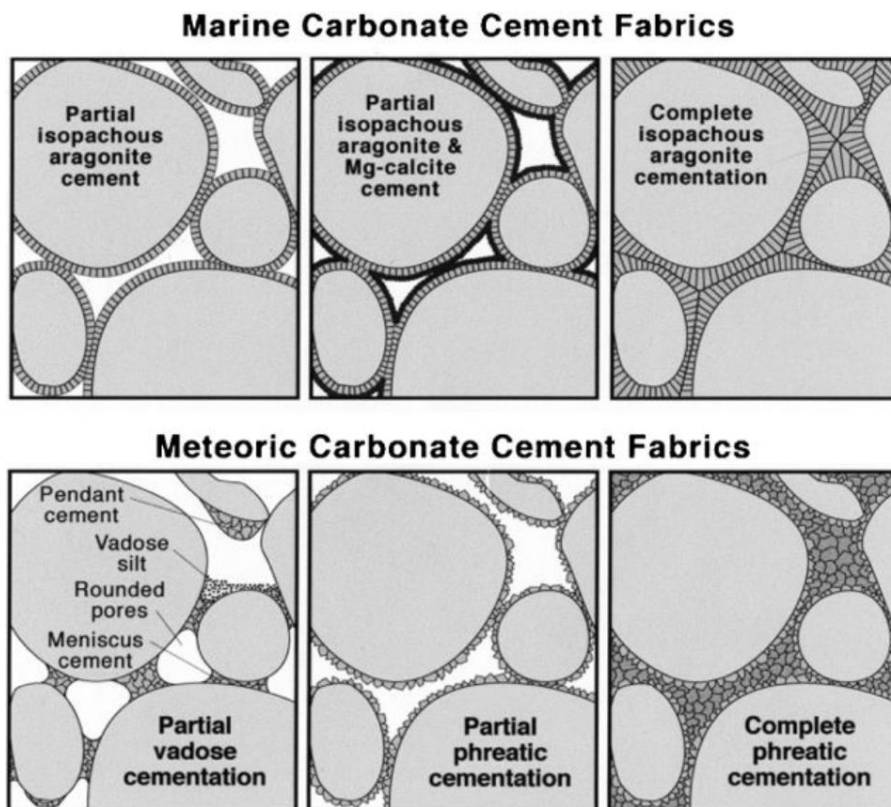


Figure 2.12: Isopachous (uniform thickness) and meniscus cement fabrics from Scholle and Ulmer-Scholle (1979).

Degree of cementation

One key aspect when examining work published on poorly consolidated sandstones is to understand the degree to which cementation has taken place. Studies published on deformation bands in sediments describe the level of cementation in a qualitative manner (Fonseca et al. 2013; Philit et al. 2015). However, the degree to which the sediments are cemented can vary across different units in the same outcrop (Fischer et al. 2013). Furthermore, Fonseca et al. (2013) shows the degree of cement present affects the failure mode of sandstones during triaxial deformation. Thus it is important to understand the degree of cementation quantitatively. The degree to which cementation occurs can depend upon numerous variables including the volume of cement containing fluids present, the external pressures, the available pore space and the environmental conditions during cementation. This thesis investigates how the level of cementation in poorly consolidated synthetic sandstones impacts its mechanical strength properties.

2.4.3 Cement textures

Previously cements textures have been studied and referred to as a crystalline form because traditionally all rocks, including clays, are crystalline (Pettijohn 1975). In the case of arkose sandstones cemented by calcite the term *crystalline aggregate* was previously used. However, due to the detrital nature of sandstones the term ‘clastic’ is applied (Pettijohn 1975).

A clastic texture is defined as grains and clasts cemented together (with no grain interlocking) (Pettijohn 1975). However, this definition does not differentiate between clastic textures which display different cement distributions (e.g. cement forming point contacts, cement coating grains, cement filling all available porosity). To my knowledge there are limited studies which explore the types of clastic texture and their distribution. Furthermore, unlike Folk (1959) and Dunham (1962) classifications for carbonate rocks there is no scheme which has been used as a reference to describe the distribution of cement in sandstones.

2.4.3.1 Recrystallisation textures

Recrystallisation textures can be formed in sedimentary rocks (including carbonates and calcium sulphate rocks) at normal pressure and temperatures (Pettijohn 1975).

For example, anhydrite can recrystallise to gypsum as it becomes hydrated. This thesis does not study cements undergoing recrystallisation. However, Chapter 6 shows the hydration and dehydration of calcium sulphate phases is relevant to the formation of gypsum and anhydrite recrystallisation textures.

2.4.4 Cement strength

Cement is the primary control in the mechanics of granular materials (Clough et al. 1981; Bruno and Nelson 1991) and when cement is deposited at grain to grain contacts it will increase the strength and stiffness of the material (David et al. 1998; Saidi et al. 2005). Furthermore, Al-Tahini et al. (2006) report a direct correlation between concentration of cement and the strength of sandstone.

ASTM D2488 Standard Practice for Description and Identification of Soils (Visual Manual Procedure) classifies coarse grained soils based on their reaction when finger pressure is applied (Table 2.2). In this study the level of cementation in the sandstone and synthetic sandstone samples is classified using this scheme.

Table 2.2: Description of the level of cementation in coarse soils by ASTM D2488 Standard Practice for Description and Identification of Soils (Visual Manual Procedure).

Description	Criteria
Weak	Crumbles or breaks with handling or little finger pressure
Moderate	Crumbles or breaks with considerable finger pressure
Strong	Will not crumble or break with finger pressure

To my knowledges there has been no published research which investigates the impact of cement strength on the formation of deformation bands in synthetic sandstones. Fossen et al. (2017) suggests that cement strength affects the degree of cataclasis in deformation bands. Whereby strong cements e.g. Silica (SiO_2) produce deformation bands with a higher degree of cataclasis than deformation bands cemented with carbonate (CaCO_3) or iron oxide (Fe_2O_3).

2.4.5 Cement, grain and porosity interactions

The interaction between grains and porosity has previously been studied due to their applications in aquifers and hydrocarbon reservoirs (Selley 1976). Sippel (1968) shows that as burial depth increases the grain contacts progress from 1) tangential contacts to 2) long contacts to 3) sutured contacts at depth. As a result, there is a decrease in porosity and increase in the number of contact points per grain. However, this research does not consider the distribution of cement around the grains.

Cementation and cataclastic (or compaction) deformation band formation both reduce the available pore space in a sandstone. Milliken et al. (2005) state that cementation is the main cause of porosity loss (as opposed to cataclasis) in studied sandstones. The importance of the relationship between cementation and cataclasis was highlighted by Philit et al. (2015) and Philit et al. (2018). In Philit et al. (2015) it is noted that cementation is increased in areas displaying higher degrees of cataclasis. This may be due to an increased number of 'fresh' nucleation sites in contact with mineral rich cementing fluids (Fisher and Knipe 1998; Lander et al. 2008; Williams et al. 2015). It is therefore possible that increased cementation in areas of cataclasis increases the strength of the deformation bands (Philit et al. 2018).

However, the timing of cementation is important in understanding the diagenetic history of the deformation band formation. The timing of cementation can be speculated based on the distribution of cement in the sandstone sample. In addition, it is possible that excess cementation can act as a barrier to cataclasis hence reducing the number of fragmented grains inside the deformation band (Milliken et al. 2005).

Throughout the background research, porosity (de Lima Rodrigues et al. 2015) and cementation are key variables in order to understand the formation of cataclastic deformation bands. For this reason these properties have been chosen for detailed investigation (distribution and volume) in this thesis. In this study I use X-CT to characterise the cement and porosity distribution in each samples (Chapter 5 and 7).

2.5 Sampling consolidated and poorly consolidated sandstones

Consolidated sandstone samples can be removed from outcrops using a hammer and chisel. Due to the friable nature of poorly consolidated sandstones they can prove

difficult to remove intact. Different methods have been tested to remove intact poorly consolidated sandstones from outcrop. Methods have included using epoxy in-situ (Lommatzsch et al. 2015), sampling by hand (Exner and Tschegg 2012) and cutting samples out using small core holders (Beke et al. 2019) (Figure 2.13). In this study poorly consolidated samples were cut out from the outcrop using a knife and wrapping the samples in bubble wrap/Duct tape. However, it remains difficult to remove poorly consolidated sandstones without grain rearrangement taking place.



Figure 2.13: Two methods for removing poorly consolidated sandstones. On the left hand side, the sample was cut out using a machete to avoid grain rearrangement, to be reduced in size once taken back to the laboratory. However, difficulty came in keeping the sample intact whilst transporting it. On the right hand side, a core tube was pushed into the sediment. This was an effective transportation method however the sand structure was disrupted as the core was pushed into the sediment.

2.6 Summary

- Deformation bands are a precursor to fault formation.
- Deformation bands in consolidated sandstone have been widely studied to date due to their presence in oil and gas reservoirs, across the world, and the fact that they change the mechanical and hydraulic properties of sandstones.

Chapter 2 - Literature review

- Most recently there have been an increasing number of fieldwork studies of deformation bands in poorly consolidated sandstones. This therefore has raised the question: at what stage during burial history do deformation bands form?
- Cataclastic deformation bands observed in poorly consolidated sandstone samples make it particularly difficult to believe that all deformation bands form post lithification during uplift. However, this then raises the question of how do you achieve grain crushing (cataclasis) at shallow burial depths?
- Field studies have focussed on characterising porosity and deformation band structure across each of the samples. In this thesis, three case studies are used to help pick apart the relationship between cementation and deformation band formation (Chapter 5).
- Based on studies of sandstones and sands, grain crushing of sand grains appears to take place at a range of normal stress stresses from 0.5 MPa depending on the size and composition of the grains being tested.
- To date lab experiments have focussed on the conditions at which grain crushing takes place in sandstones and sands. However, there are limited studies which investigate grain crushing in poorly cemented sandstones, or which investigate how the level of cement effects the grain crushing.
- Sand(stone)s have been deformed using ring shear and triaxial experiments to form deformation bands.
- Methods of imaging cement have previously relied on thin sections and SEM scans however; this has not given enough detail of the 3D cement structures. X-CT imaging provides a means in which 3D structures can be imaged and mapped out in 3D (Chapter 3).

Chapter 3 - X-ray Computed Microtomography

3.1 Rationale

This chapter begins with a literature review of X-ray computed tomography (X-CT), the X-CT methodology used in this study and concludes by presenting data on the impact of scan resolution on segmentation data analysis.

X-ray computed tomography (X-CT) allows for non-destructive view of solid objects and their internal structures. The X-CT is used to characterise the internal structures of objects both quantitatively and qualitatively. Terminology of X-CT studies varies across research groups and it can sometimes be referred to as micro-CT, x-ray tomography, XRCT, XMT, HRXCT and CMT (Wildenschild and Sheppard 2013).

3.2 Types of X-CT

There are three main types of X-CT: medical, synchrotron and laboratory. A medical X-CT spins the x-ray source and detector around a stationary object (or person). Medical X-CT scanners generally have a fan beam configuration (Figure 3.1).

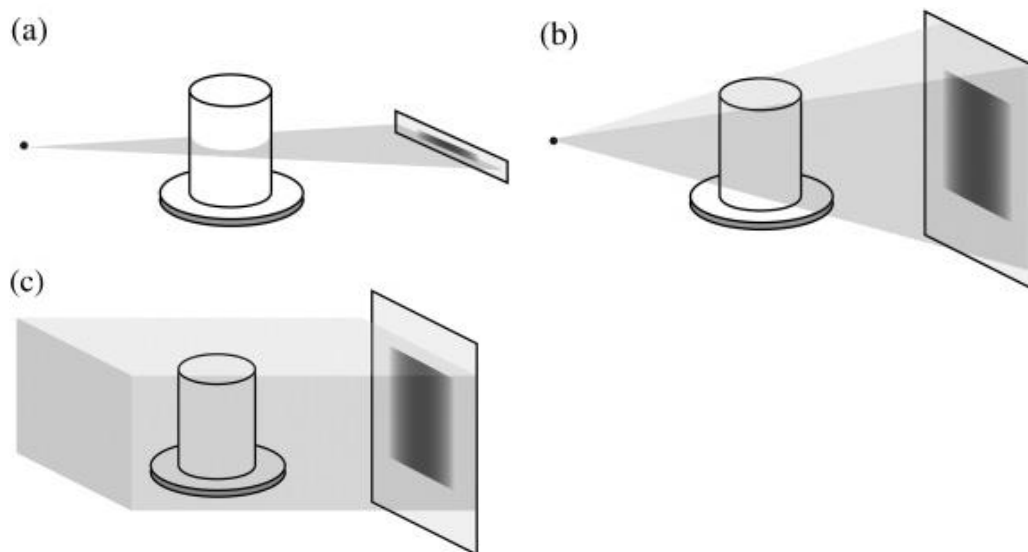


Figure 3.1: X-CT configurations a) Fan beam b) Cone beam c) Parallel beam from Landis and Keane (2010) (Landis and Keane 2010).

Fan beam uses a 1D detector to collect 2D slices of the scanned object. Medical X-CT scanners are fast and can produce resolutions of up to 70 μm (du Plessis et al. 2016). In both laboratory and synchrotron X-CT, the x-ray source and detector remain stationary and the object rotates on a stage. Synchrotron X-CT uses a large electron ring (Diamond Light Source UK, 562 m circumference) which produces white light (polychromatic) or monochromatic X-rays upon collision with a target. Slightly higher resolution is possible i.e. 700 nm (Coenen et al. 2004) compared to laboratory X-CT which produces image resolution in the range of 2-150 μm . In addition, synchrotron X-CT requires shorter scan times of a few seconds, reduces beam hardening, and improves the signal to noise ratio. However, synchrotron X-CT is only accessible via competitive biannual applications to the UK national facility, Diamond Light Source. In the case of a laboratory X-CT the x-ray beams form a cone shape around the object and can work in either transmission or reflection, whereas synchrotron X-CT x-ray beam runs parallel through the object to the detector (Figure 3.1).

3.3 How the X-CT works

The laboratory X-CT is set up with an x-ray source (or x-ray tube), a rotating sample stage and a detector (either an x-ray detector or scintillator). X-ray photons are fired at the sample, which absorbs and scatters photons (attenuation) and the remaining photons are collected at the detector. The amount of X-ray photons absorbed depends on the sample thickness, density, atomic number and incident beam energy. The captured photons are used to produce a 'projection' or radiograph. Each projection is defined for a particular angular position. By rotating the sample relative to the detector and X-ray source, a collection of projection images is produced. These images are reconstructed into a 3D volume using an appropriate algorithm.

Beer's Law is used to define the linear attenuation coefficient for each pixel of a homogeneous material:

$$\frac{I}{I_0} = \exp(-\mu x)$$

Where I_0 is the incident x-ray intensity, I is the remaining x-ray intensity after sample absorption, x is the sample thickness (length of X-ray path through the material), and μ is the linear attenuation coefficient (Kak and Slaney 2001; Ketcham and Carlson 2001; Cnudde and Boone 2013). However, this equation does not take into account any inhomogeneity in the sample. As the majority of studies are inhomogeneous samples therefore this equation is most relevant in defining the linear attenuation coefficient as follows:

$$I = I_0 \exp \left[- \sum_i \mu_i x_i \right]$$

Where a value for μ (μ_i) is calculated for each phase in the material and x_i is the phase thickness (Ketcham and Carlson 2001; Wildenschild and Sheppard 2013), although more commonly Beer's law is expressed in terms of the mass attenuation coefficient, which is μ/ρ for each phase and has units of cm^2/g .

3.4 X-CT Limitations

In the conventional cone beam geometry, the sample is positioned between the source and detector. This means that the resolution achievable is affected by the X-ray source spot size, detector resolution and sample to source distance. Resolution is mainly limited by the focal spot size (Cnudde and Boon, 2013) and is usually around c. 1 micron but the reconstructed projection data is discretized by the pixelated detector into a 3D matrix of volume elements called voxels. The main trade off in imaging is that smaller samples produce a smaller voxel size, which is desirable when looking at finer pored rocks and not insurmountable as it would be for cultural or archaeological samples. Artefacts arise when there are features present (ie. pores) which are smaller than the minimum voxel size. The interface between features has an average value of μ over the volume of the voxel and therefore the boundary between features with a different μ value will not be clearly seen, such as the matrix-pore interface. In order to achieve the best scan resolution, the size of the study sample must be decreased but by decreasing the size, the sample becomes less representative of the original outcrop.

3.4.1 Beam hardening and ring artefacts

Polychromaticity is produced in lab X-ray instruments by 'braking radiation' known as Bremsstrahlung which is caused by electron beam deceleration when it hits the target. When a polychromatic beam passes through an object the lower energy x-rays are more readily absorbed, leaving the beam spectrum with a greater number of higher energies. As the higher energies pass into the sample (from all directions) attenuation is greater around the edges than in the centre of the sample (Wildenschild and Sheppard 2013). Once a scanned sample is reconstructed this uneven attenuation distribution can be identified as a 'halo' like effect around the edges of the sample. Filters (e.g. copper, aluminium etc.) can be used at the time of scanning to remove low energy. Beam hardening can be reduced during image reconstruction stages. In this work, the beam hardening correction on PRO 3D software was used (© 2004-2016 Nikon Metrology) (Figure 3.2).

Ring artefacts are concentric rings visible in the sample. These are caused by irregularities in either source or detector. As with beam hardening the effects of ring artefacts can be reduced during the image reconstruction stages.

In general with all X-CT studies it is accepted that the larger the scan volume (or sample size), the larger the size of the artefacts which will be present (Atkin and Kovsky 2003).

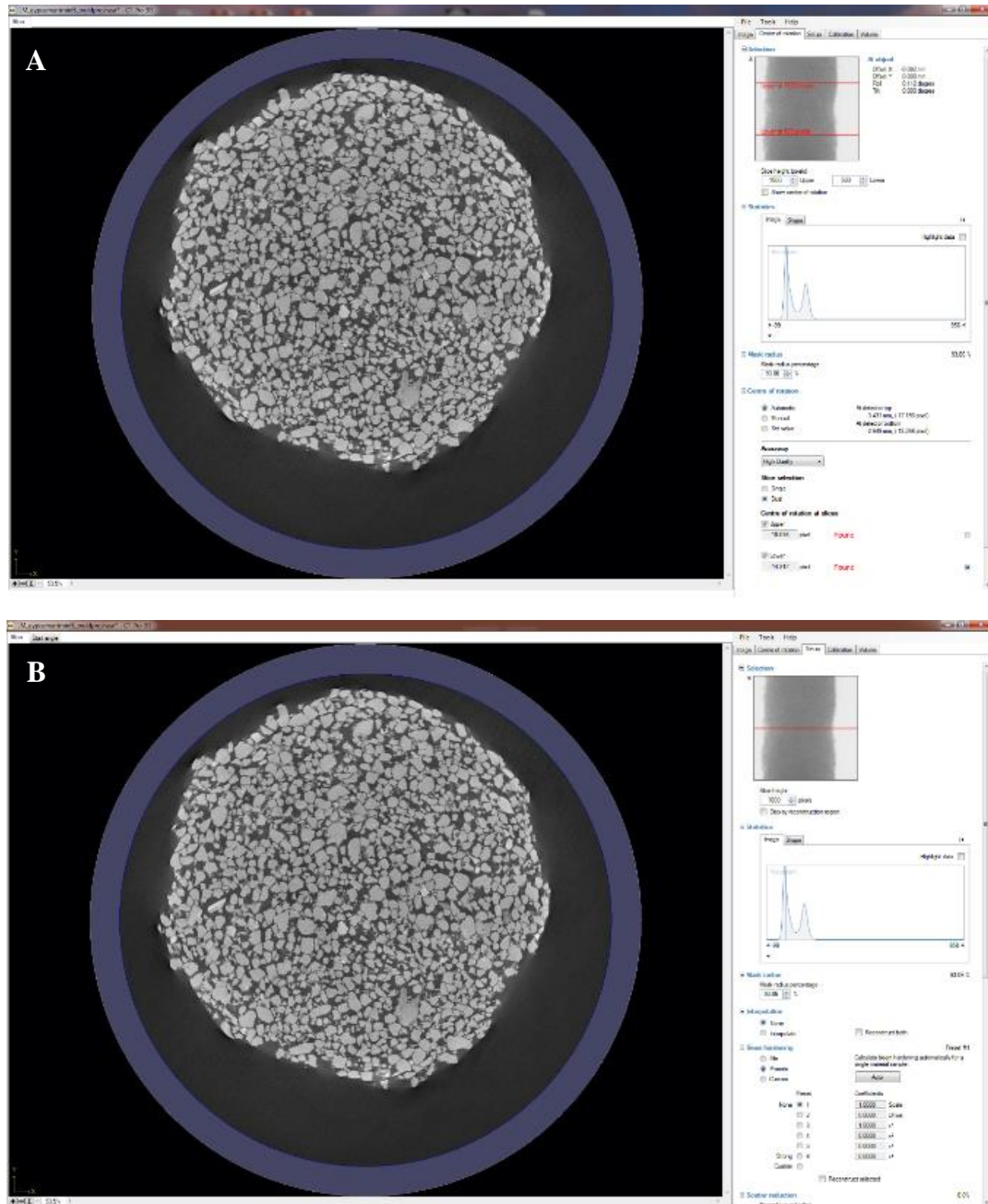


Figure 3.2: Images from PRO 3D software (© 2004- 2016 Nikon Metrology) reconstruction software A) Stage 1: finding the centre of rotation. During this stage lighter grey coloured grains are identified around the edge of the image. This is the halo effect. B) Stage 2: reducing the effects of beam hardening.

3.5 Use of X-CT in geological research

Due to its high quality imaging capabilities the X-CT has become widely used in various fields of research. Fields include medicine (Hendee 1979; du Plessis et al. 2016; Thompson et al. 2017), material science (Landis and Keane 2010; Adrien et al. 2016), geology (Cnudde and Boone 2013; Peng et al. 2014; Bendle et al. 2015; Griggs et al. 2015; Macente et al. 2017; Beaudoin et al. 2018) and geotechnics (Wang et al. 2011).

In geosciences the X-CT has been used to image reservoir cores (Wu et al. 2015), calculate petrophysical properties, fracture visualisation (Kobchenko et al. 2011) and analyse the texture of fossils (Warke 2017). In particular X-CT has been used on sandstone examples to investigate the porosity distribution (Bera et al. 2011; Bossennec et al. 2018), clay minerals present (Kareem et al. 2017), image deformation structures e.g. compaction bands (Louis et al. 2006) and deformation bands (Zambrano et al. 2017). In this work, laboratory X-CT was used to image the pore network and cement distribution through fieldwork and synthetic rock samples and calculate the porosity of the 3D sample.

Traditionally thin sections have been used to observe deformation bands however the use of the X-CT allows for deformation bands to be imaged non-destructively in 3D at the grain scale. This gives a more complete picture of the porosity and cement distribution across the sample. Previous X-CT studies of deformation bands are few but include (Antonellini et al. 1994; Charalampidou 2011; de Lima Rodrigues et al. 2015; Radzik et al. 2015; Fossen et al. 2017; Zambrano et al. 2017).

Rodrigues et al. (2015) focus on three samples of shear compaction band samples from Brazil. Initially the field samples were cut into cuboids (<20 mm in width) and scanned in the X-CT. From there data sub-volumes were segmented and cropped around selected areas of interest (e.g. deformation bands). The data sub-volumes were segmented into 3 phases: rock (e.g. siliceous material and quartz/feldspar clasts), pore space and dense minerals. Rodrigues et al. (2015) compares the total porosity, variation in porosity and pore connectivity from the host rock and inside the deformation bands. Rodrigues et al. (2015) describe an increase in the number of

isolated pores but a decrease in total porosity and connected pores inside the deformation band.

Radzik et al. (2015) used X-CT to perform microstructural analysis on Outer Carpathian sandstone deformation band samples (cores of 25 mm diameter and 38 mm height). Radzik et al. (2015) conducted X-CT scans using resolutions from 2.1 – 20 microns but were unable to give accurate porosity measurements as the pore size inside the deformation bands was smaller than the resolution of the X-CT.

Fossen et al. (2017) uses X-CT to calculate the porosity, pore connectivity and visualise the porosity distribution of deformation band (CSB, PCB and SECB) sub-volumes (~ 1 to 2 cm in length) from Utah and Nevada sandstones. The measurements show that there is an undoubtable reduction in porosity across all three types of deformation bands.

Zambrano et al. (2017) uses both synchrotron and laboratory X-CT to quantitatively calculate the porosity distribution and connectivity in carbonates from Sicily. Analysis was performed on several sub volume samples from across the scanned carbonate samples (approximately 30 x 5 x 5 mm in size) and conclude that in deformation bands porosity and pore connectivity are reduced in comparison to host rock.

The use of X-CT to quantitatively image deformation bands is still in early stages. X-CT is an expensive technology to use, however, it's ability to quickly image a sample in 3D and section a sample into 2D slices makes it a useful piece of equipment to understand the properties (both internally and externally) of a rock over a larger area than conventional SEM or optical microscopy.

The majority of studies to date have used singular sub-volumes in their studies to illustrate the porosity distribution and connectivity. However in order to achieve more robust data for these complex structures a more detailed statistical approach should be applied to the sub volume sampling technique. This could include multiple sub volume samples or an algorithm which automatically samples every $x \mu\text{m}$. In this thesis I implement two sampling techniques to better understand the distribution of cement and porosity across each of the samples.

3.6 X-CT at Strathclyde

Each sample was scanned using a Nikon XT H 320/225 X-CT (Figure 3.3). The X-CT uses a cone beam configuration (Figure 3.1B). After scanning the samples were reconstructed using PRO 3D software (© 2004- 2016 Nikon Metrology) and image analysis was carried out on Avizo[®] Software (v.9.0.1, ©FEI). The X-CT has a 225kV x-ray tube and a 2000 x 2000 pixel photodetector with a cell size of 0.2 x 0.2mm.

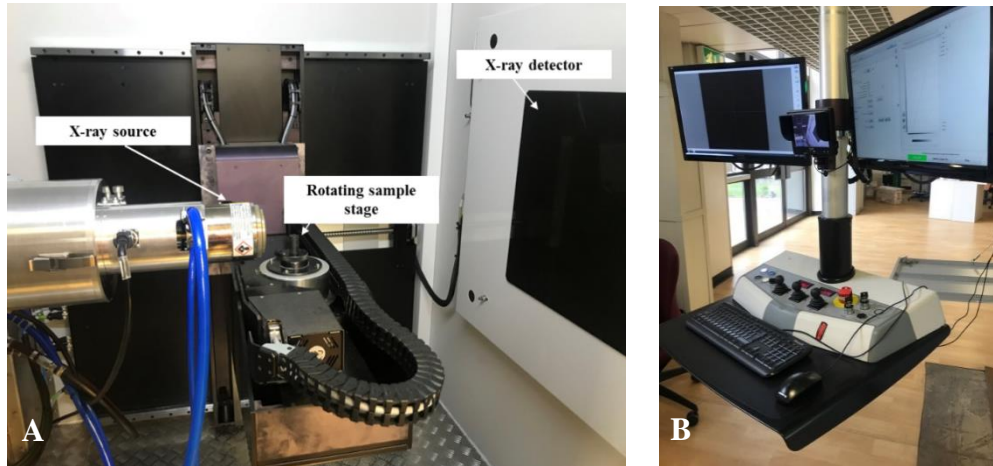


Figure 3.3: A) X-ray source, stage and detector setup inside the Nikon XT H 320/225. B) X-CT control station at the University of Strathclyde.

3.7 Use of X-CT in this study

X-CT was used throughout this study to image the sandstone samples collected from fieldwork and the synthetic sandstones made in the laboratory. Using these images samples were processed and segmented following the procedure in this chapter (Figure 3.4) to calculate the petrophysical parameters of the samples.

3.8 X-CT Process

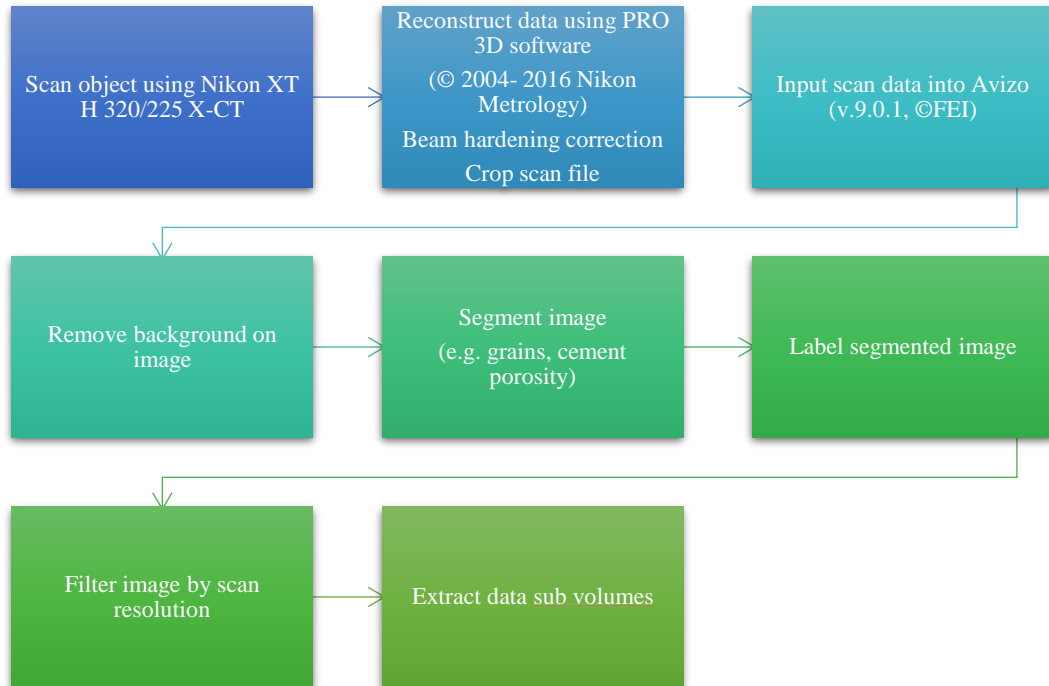


Figure 3.4: Flowchart for X-CT analysis using Avizo[®]. This process was applied to all sandstone samples.

3.8.1 Sample preparation for X-CT

Due to their friable nature the poorly cemented deformation band sandstones were impregnated for analysis using blue epoxy resin and then cut to size using a saw.

Synthetic samples were initially scanned prior to deformation but the resolution achieved ($\sim 20 \mu\text{m}$) was too low to adequately quantify the cement. To achieve a higher quality of resolution, and image the cement distribution, a smaller sample ($\sim 4 \text{ mm}^3$) of each cement strength was made for scanning in the X-CT. The smaller samples were made from cut offs from the original synthetic sample before they were trimmed to size.

3.8.2 Sampling for analysis

3.8.2.1 Deformation band sandstone samples

For each deformation band sample, physical volumes of less than $20 \times 10 \times 10 \text{ mm}$ (2000 mm^3) were scanned in the X-CT. From these scans a long sub volume ($6 \times 2 \times$

2 mm = 24 mm³) was selected for analysis and a comparison of cement and porosity across the deformation band was calculated (Figure 3.5). Along these long volumes 0.125 mm³ cubes were selected (5 inside the deformation band and 5 in the host sediment) to improve statistical significance and give a better understanding of the impact of sampling on both cement and porosity volumes and distribution.

Analysis was also carried out on 2D slices cutting through the sample so the percentage of cement and porosity could be measured in small increments through both the host rock and deformation band (Figure 3.5B). Therefore, allowing the identification of any patterns in cement or porosity in the transition from host rock to deformation band.

3.8.2.2 Synthetic sandstones

Synthetic rock samples analysis was carried out on data sub volumes of 1 mm³. For each synthetic sandstone sample a small (~16mm³) volume was cut off the top of the cylindrical samples (Chapter 7) before they were filed to length for mechanical testing (Chapter 8). This small ~16mm³ volume was scanned in the X-CT and one data sub volume (~1mm³) from each sample was cropped for compositional analysis (Chapter 7). Seven samples were analysed from the synthetic sandstones in total.

3.8.3 Image processing and analysis

For each sample 3,141 projections (standard settings for the laboratory X-CT scanner used) were collected with an exposure time of 1s. The individual scan conditions are listed in Appendix 2.

It has been proven that beam hardening can alter the porosity measurements from X-CT analysis particularly around the edges of scans (Romano et al. 2019). To reduce the impact of beam hardening on each of the samples, data sub-sampling was conducted away from the edge of the scan.

3.8.4 Background removal

The background is required to be removed when the voxels have the same grey values as the porosity in the object or when the object has a coating e.g. mould or membrane (Figure 3.6).

This was applicable to each of the synthetic samples. In order to remove the background from the image first the image must be converted to binary. The binary image is dilated by increasing the voxels which in turn reduce the volumes of void space present.

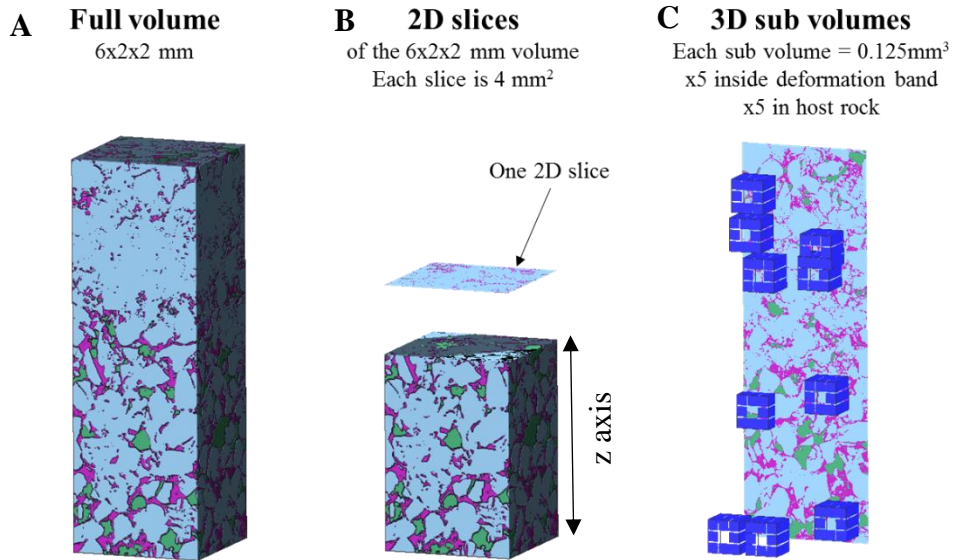


Figure 3.5: Three methods of sampling used to analyse the natural deformation band samples. A) Full volume. B) 2D slices. 3) 3D sub volumes.

A mask is then created which includes all particles and void space. After the mask is created it is then shrunk back to its original size (prior to dilation) using the erode function. The mask now forms a separate layer and can be applied to the original image. By applying it to the original image it gives all background features a grey value of 0 and the object has grey values between 1- 65000. This process of background removal was applicable to all sandstone samples and made it possible to analyse the samples without showing the mould or membrane.

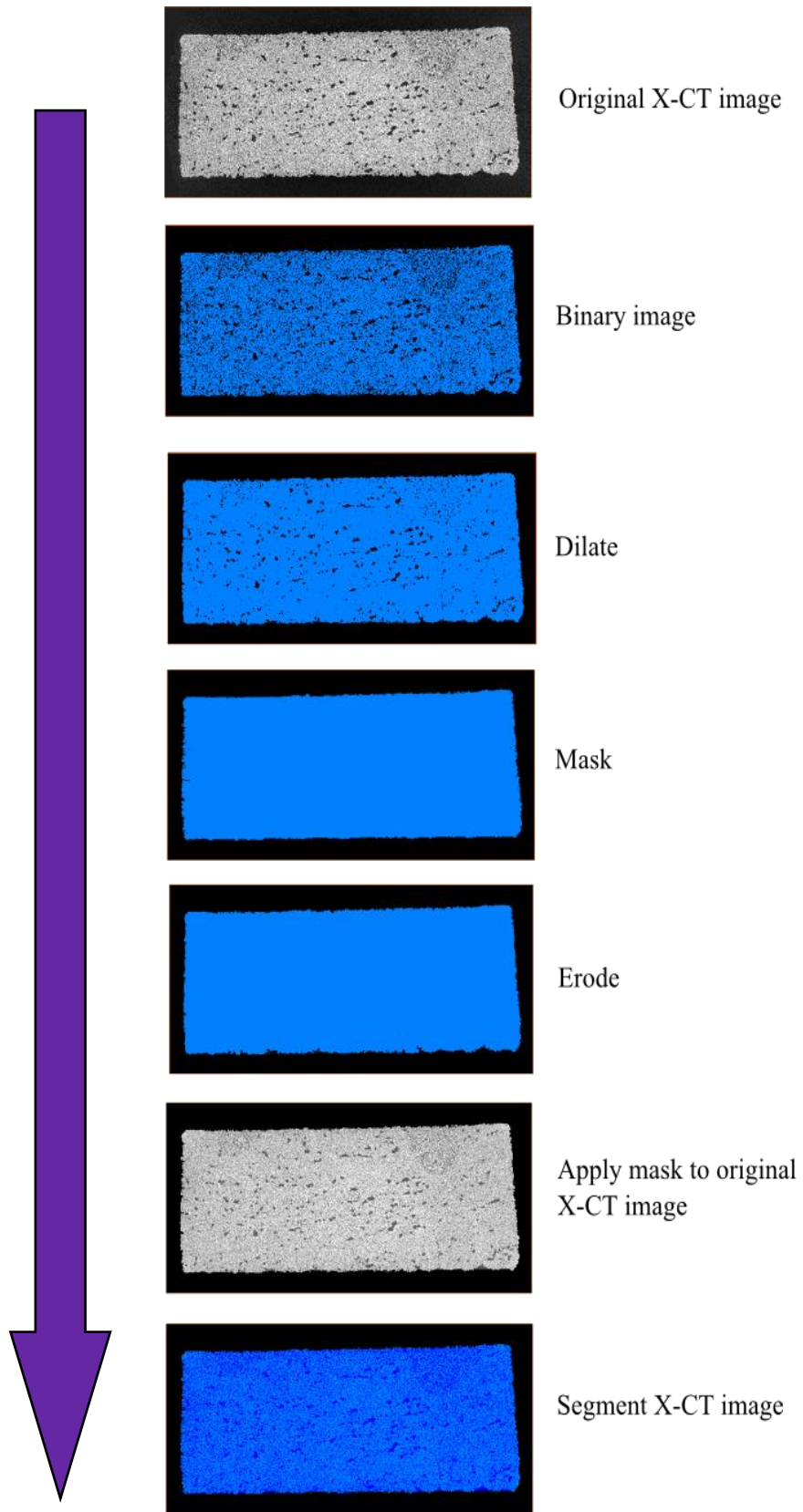


Figure 3.6: Object background removal during post processing of the X-CT scan. This is an example from a gypsum cemented synthetic sandstone sample.

3.8.5 Image segmentation

Image segmentation is used to separate the phases in an object based on their grey values. The grey values obtained from the X-CT arise from the linear attenuation coefficient contrast between phases present, including air. For example, the majority of sandstone studies are segmented based on two phases, particles (grains) and the voids between the grains (pore space, air). For the purpose of this study all of the samples were segmented to show three distinct phases; grains, cement and porosity in 2D and 3D (Figure 3.7). To enable segmentation each volume was manually thresholded by grey values to select the grains, cement and porosity. All quartz and feldspar grains were classified as grains. No distinction was made between grain mineralogy. From this volume segmentation the percentage of grains, cement and porosity was calculated by dividing the total volume of each phase from the volume of the selected area.

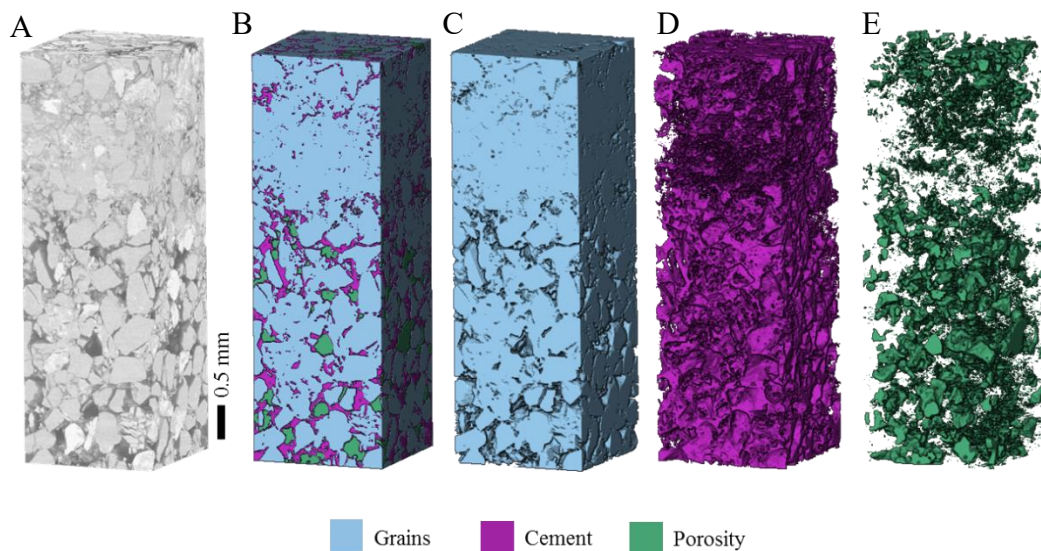


Figure 3.7: Image segmentation of sample HN11 to show three phases: grains, cement and porosity. A) Original grey rendered 3D image. B) 3D image with grains, cement and porosity highlighted. C) Grains selected only. D) Cement selected only. E) Porosity selected only.

The data from the segmentation of each sample is either used for 2D or 3D analysis.

3.8.5.1 Segmentation error

In order to estimate the maximum errors present in segmentation each deformation band sample was segmented into three phases (grains, cement and porosity) and from there each phase was numerically eroded or dilated by 1 voxel (Figure 3.8)

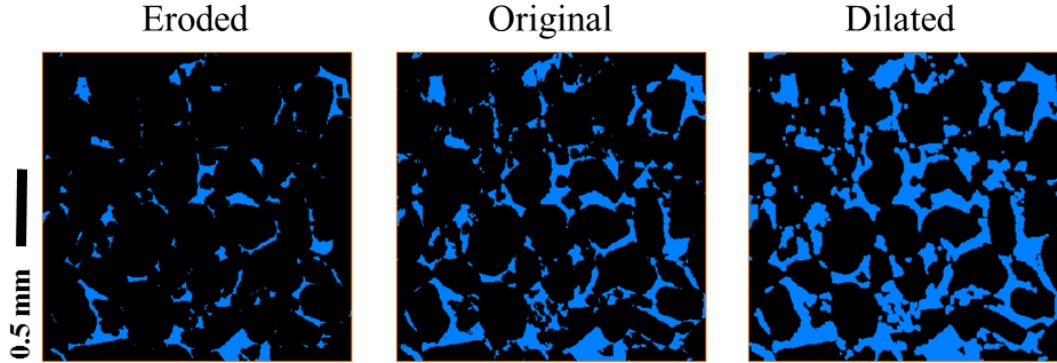


Figure 3.8: Impact of erosion and dilation by 1 voxel on porosity phase (blue) from sample AR01.

Understanding maximum errors is important as they affect the phase volume calculations (Figure 3.9) for each sample (Arns et al. 2002). Further details of this process are described in Fuisseis et al. (2012) and Macente et al. (2017). Overall this is a robust method for calculating the maximum errors present. However, the method can in some cases overestimate the errors. This is discussed further in Chapter 5.

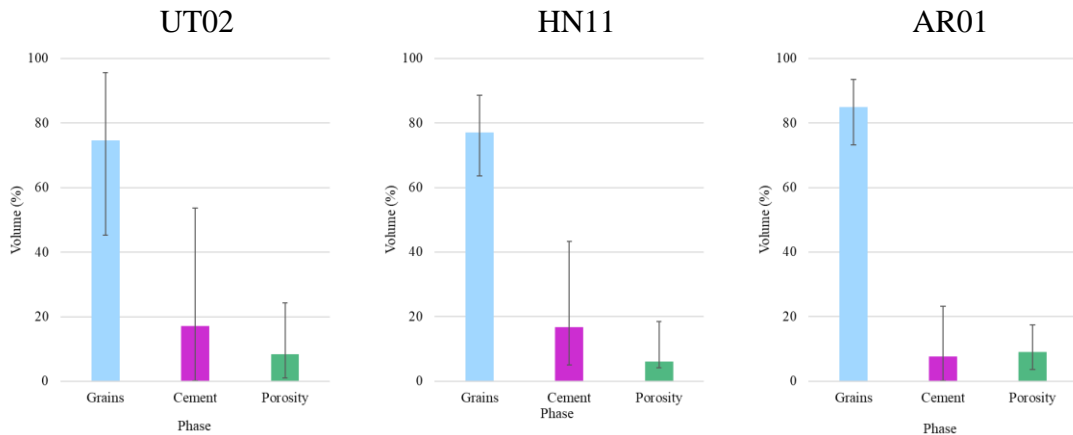


Figure 3.9: Volume fraction of each segmented phase for each of the full volume deformation band samples. The error bars on these graphs show the maximum possible error created due to segmentation of these samples.

3.8.5.2 Separating grains

In Avizo[®] the *Separate Objects* module (Figure 3.10) splits connected particles using water-shedding (Figure 3.11). This method works well to split grains from synthetic sandstones. However, for the natural sandstones, and in particular the deformation bands, the grains are touching and make it difficult to separate the grains. In some cases, there is evidence of grains being cut in half by a false straight line or a single colour being assigned to neighbouring grains. This therefore produces false readings of grain size distribution. Instead, image segmentation was used to calculate the percentage of grains, cement and porosity present in a given sample.

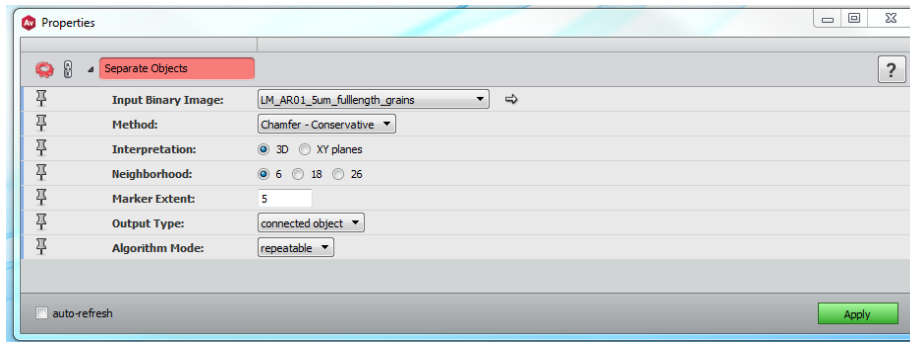


Figure 3.10: *Separate objects* module in Avizo[®].

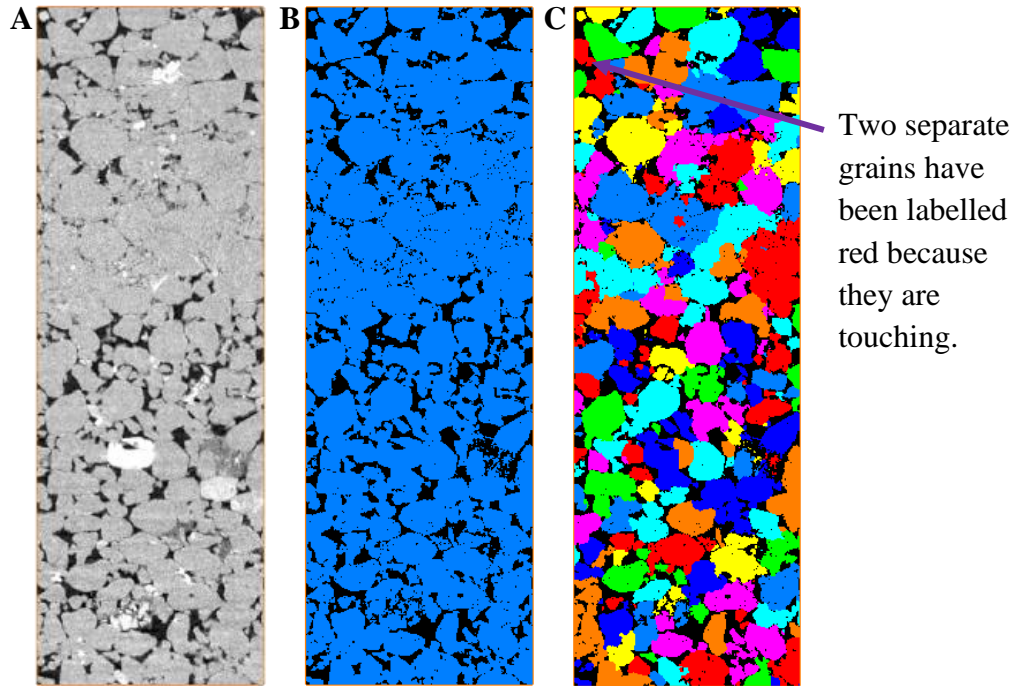


Figure 3.11: 3D *Separate objects* module applied to sample AR01 A) Original grey-scale image of sandstone with deformation band. B) Binary image of grains only after segmentation. C) Image post *Separate objects* using a 3D interpretation, a neighbourhood of 6, marker extent of 5, module in Avizo®. Here the module is unable to determine the individual grains inside the deformation band.

3.8.5.3 Labelling of segments

Cement and pore connectivity of the sample was determined using the *Labeling* function. By selecting *Labeling* each cement deposit or pore is given a number and a colour. If cement deposits or pores are connected, they will be given the same colour (Figure 3.12).

This can give a visual representation of the distribution and connectivity of pores and cement. In addition, *Labeling* will also calculate the volume of each pore or cement pod.

3.8.5.4 Filtering

Each sub volume was filtered based upon the limits of the scan resolution. Any pixels which were below the scan resolution were deleted from the data set (Figure 3.13) to enable the most accurate representation of data available.

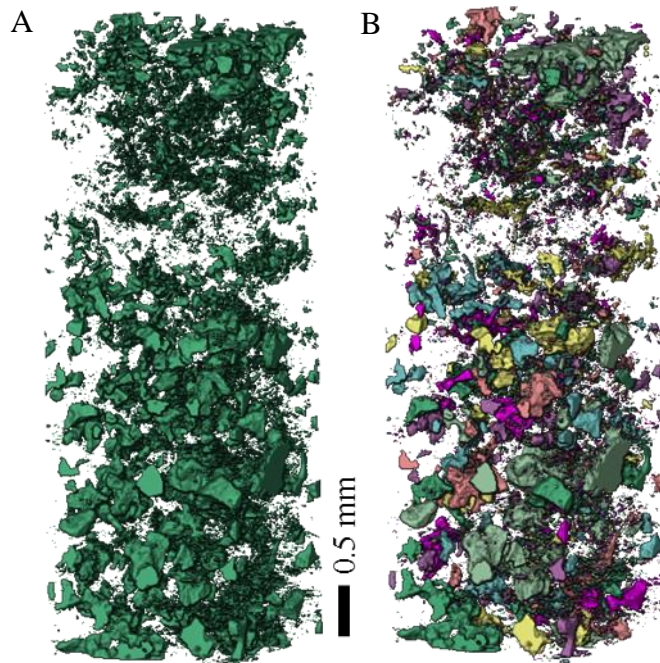


Figure 3.12: Labelling of porosity from sample HN11. A) All the pores from sample HN11. B) Here connected areas of porosity are given the same colour. This shows the pores are disconnected across the full sample.

3.8.6 Impact of resolution

To better understand and quantitatively determine the impact of X-CT scan resolution error on data from analysed images, sample HN11 was scanned three times using the X-CT at three different resolutions ($4\mu\text{m}$, $7\mu\text{m}$ and $10\mu\text{m}$). This data was used to help determine the uncertainty in measurements (e.g. percentage porosity and cement) conducted using the Nikon XT H 320/225. As highlighted by Radzik et al. (2015), sandstones with deformation bands require to be scanned with a higher resolution to accurately determine the porosity through the deformation bands. The raw 2D resolution slices and segmented slices for sample HN11 are shown in Figure 3.14.

Chapter 3 - X-ray Computed Microtomography

Each resolution was initially segmented in 2D to highlight the same features on each whilst taking into consideration the varying resolution. By repeating scans at different resolutions the grey value labels change (no scan is identical due to the gradual deterioration of the filament over time) therefore care must be taken when reselecting grey values for comparison across the resolutions. The visual method of segmentation used across the three resolutions has a clear impact on the phases present. For example, there is clearly more pixels labelled as cement (red) in the 10 μm resolution compared to the 4 μm resolution image.

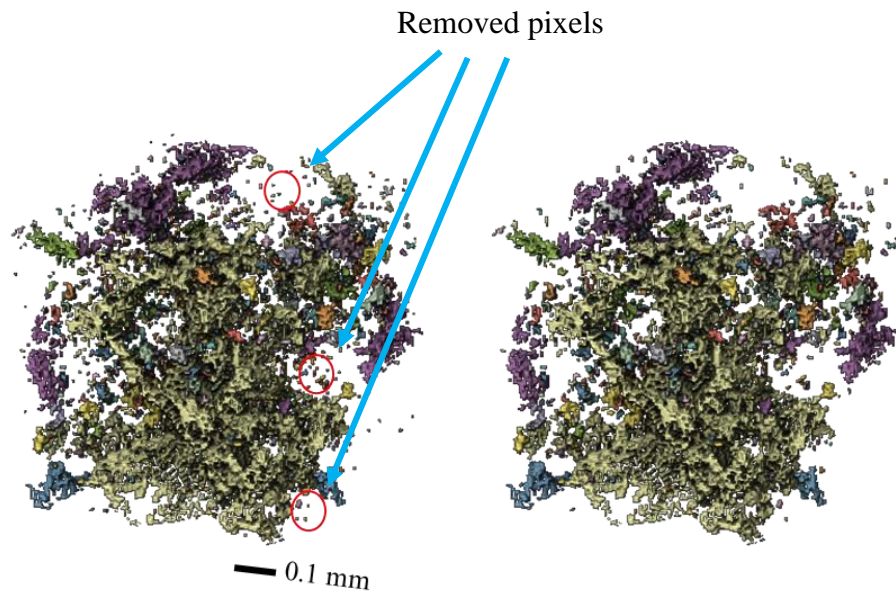


Figure 3.13: Sub volume sample from AR01 before (A) and after (B) resolution analysis filter applied.

From the segmented images, ten data sub-volumes of 0.5 x 0.5 x 0.5 mm were selected in the host sediment and inside the deformation band (5 data sub volumes in each respective zone). This work has demonstrated that there is a considerable difference between the porosity and cement values obtained for each scan resolution (Table 3.1). For each of these measurements it should be considered that they are based on the application of three different thresholds (one per scan) by one person. Thresholding is subjective to the user undertaking the threshold and it would be expected that a different user would acquire results which vary slightly from those in this study.

Table 3.1: Average volume percentage and standard error from five sub volumes of 0.5 mm³ inside the host rock and deformation band (DB).

Resolution (μm)	Inside DB			Outside DB		
	Grains%	Cement%	Porosity%	Grains%	Cement%	Porosity%
4	88.5 \pm 2.6	10.1 \pm 2.2	1.4 \pm 0.6	69.5 \pm 3.3	20.0 \pm 1.8	10.6 \pm 1.5
7	92.8 \pm 1.4	6.4 \pm 1.3	0.8 \pm 0.3	74.1 \pm 1.8	18.6 \pm 0.6	7.3 \pm 1.7
10	80.7 \pm 5.7	18.4 \pm 5.8	0.9 \pm 0.3	67.9 \pm 1.1	20.2 \pm 0.6	11.9 \pm 1.0

From the results the 7 μm resolution scan has the smallest overall standard error both inside and outside the deformation band. Meanwhile, the 10 μm scan has the greatest standard error for grains and cement inside the deformation bands. Inside the deformation bands there is an increase in the number of smaller grain fragments and smaller, isolated cement volumes. This along with the poorer resolution capabilities of the 10 μm scan are likely to account for the larger standard errors. The 4 μm resolution scan displays errors which fall between the errors from the 7 and 10 μm scans. From this work the percentage error in each of the measurements can be estimated based on the scan resolution.

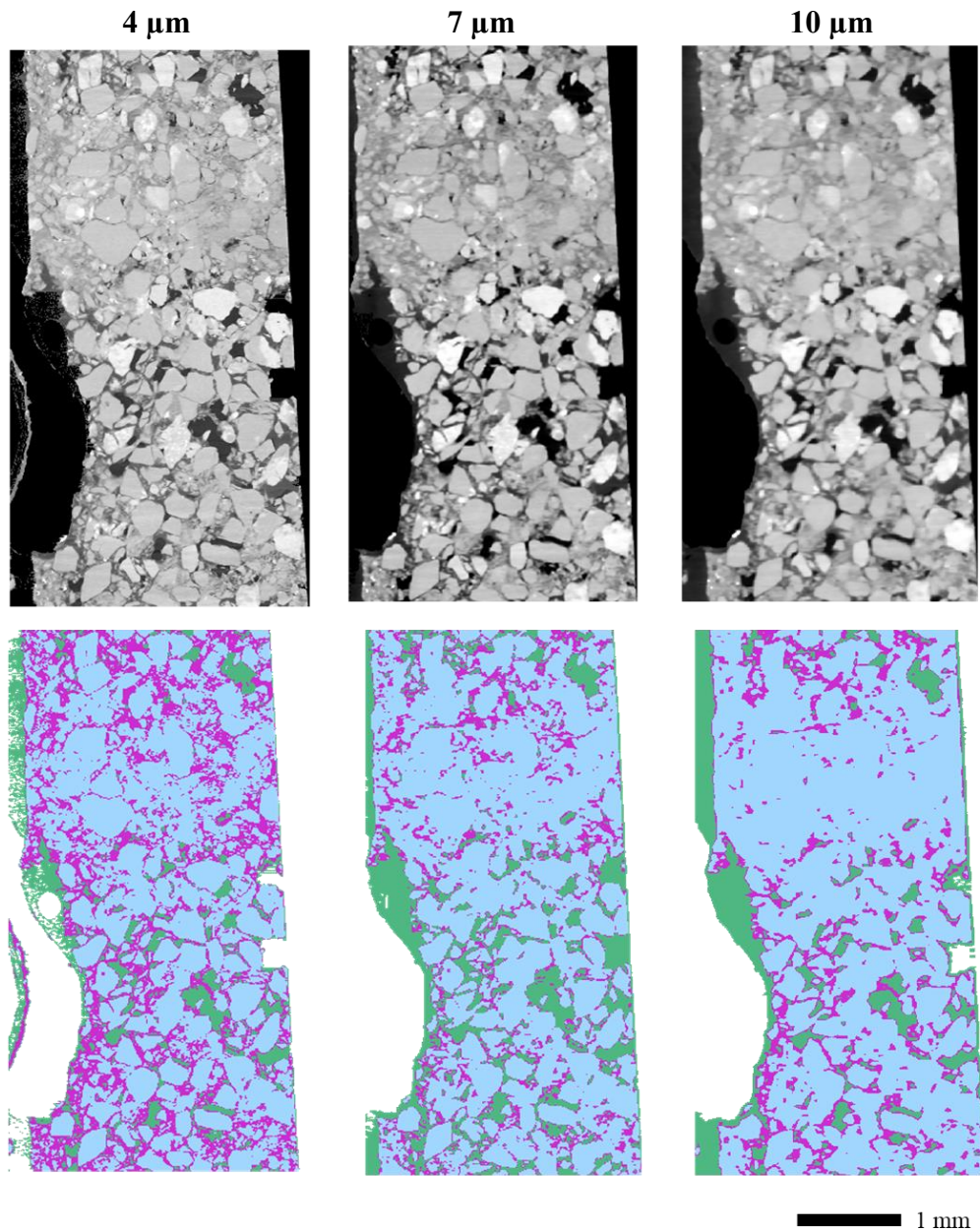


Figure 3.14: X-CT greyscale and segmented 2D slices from HN11 sample scanned at 4, 7 and 10µm resolution. As the resolution of the scan is increased the edges of the grains and cement become sharper and the contrast between grey values is improved.

3.9 Summary

- X-CT scanning is an effective non-destructive technique to map out 3D structures in all materials, including sandstones.

Chapter 3 - X-ray Computed Microtomography

- X-CT technique is still developing as a means to quantify deformation band properties at the micro scale.
- Currently most of the X-CT work focuses on individual samples at the micro scale. Methodology needs to be developed to show how X-CT can be used to systematically analyse large field areas (for examples see Chapter 4).
- It is possible with higher resolution X-CT or synchrotron X-CT that porosity and cement distributions can be more accurately calculated.
- Although the process to scan each of the samples and visualise them is quick, attention should be paid to potential limitations of the reconstruction process and resulting data interpretation.
- There is a large variation in calculated values of porosity and cement ($< \pm 30\%$) between X-CT scans at 4, 7 and 10 μm . Further work (e.g. mercury intrusion porosimetry tests) is required to determine which is the most accurate of these resolutions using a laboratory X-CT.

Chapter 4 Geological history of field sites

4.1 Rationale

In this chapter the geological history, site description and details of the deformation bands for each field locality are introduced. Samples of host rock and deformation bands from four sites have been selected as part of this study: Arran, Scotland (AR01); Pannonian basin, Northern Hungary (HN11); and Utah, USA (UT02). These sites cover a range of compositions, burial history, tectonic settings and cement properties (type, distribution etc.). Table 4.1 summarises the details of each site. The three examples allow us to investigate cement type, timing and distribution of cement.

Chapter 4 – Geological History

Table 4.1: Summary of field locations used in this study. Includes previous literature which studies this area and geological setting.

	1	2	3
Location	Great Britain	South Central Utah	Hungary
Field Area	Isle of Arran	Paradox Basin	Pannonian Basin
Fault(s)	Merkland Point Fault	Iron Wash Fault	Etes graben
Literature	(Underhill and Woodcock 1987; Bright 2006)	(Richey 2013; Heather-Cooley 2017)	(Petrik et al. 2014)
Sample number	AR01	UT02	HN11
Host lithology	Corrie sandstone	Earthy member, Entrada Sandstone	Eggenburgian Sandstone
Type of exposure	Shoreline	Canyon	Hillside
Grain size	Fine- medium grained	Fine grained	Fine- medium grained
Grain size range (μm)^a	57.88 -242.66	33.99 - 199.52	36.29 - 397.11
Sorting	Well sorted	Well sorted	Poorly sorted
Composition	Subarkosic	Sublitharenite	Arkosic
Mean host porosity (%)^b	15.25	13.74	7.17
Dominant cement type	Quartz	Quartz	Clays
Secondary cements	Hematite and clays	Hematite and calcite	N/A
Level of cementation	Well cemented	Well cemented	Poorly cemented
Depositional Environment	Aeolian	Shallow marine	Marine
Type of deformation band	Cataclastic	Cataclastic	Cataclastic

^a Grain size is defined here as the length along the longest grain axis.

^b Mean host porosity calculated from five X-CT subvolumes in the host rock. See Chapter 5 for full results.

4.2 Methods

4.2.1 Field data collection

All three sites have been the subject of previous studies. Data were collected on each site for geological history, burial history, mineralogy and deformation band identification (Underhill and Woodcock 1987; Richey 2013; Petrik et al. 2014; Heather-Cooley 2017). All three sites have been mapped to varying degrees, so field visits focussed on characterising the host rock lithologies and sample collection.

4.2.2 Microscopy

Thin sections of deformation bands and their host rocks were prepared in order to characterise the porosity, cement type and distribution, and grain shape and size. All thin section samples were analysed and photographed using the Nikon Eclipse LV100ND microscope with the DS-Ri2 camera in the Civil and Environmental Engineering Department at the University of Strathclyde.

4.2.3 X-ray diffraction

X-ray diffraction (XRD) analysis was carried out to characterise the chemical composition of the rock. XRD data were collected at the Advanced Materials Research Laboratory (AMRL), University of Strathclyde. Using the BRUKER D8 ADVANCE with DAVINCI, from 5 – 70 2θ with step size of 0.02 2θ and a count time of 1s at 40kV and 40 mA. For each of the samples the XRD results were classified using a Quartz, Feldspar, Lithics (QFL) composition diagram.

4.2.4 Grain size

Grain size is one of the key factors in determining deformation band formation (see Section 2.3.1). Grain size analysis was conducted to in order to compare the samples to each other and determine how grain size varies across the deformation band. For each of the following examples grain size analysis is produced using 2D microscopy. The longest grain axis and the shortest grain axis were measured on sandstone thin sections using the microscope software. A total of 50 grains were used for each selected area.

4.3 Utah

The site in Utah was chosen because it had been previously studied by Richey (2013) and Heather-Cooley (2017) and has been known to display cataclastic deformation bands.

4.3.1 Geological context of the Iron Wash fault zone

This area of Utah has a very well characterised geological history. Early mapping of the fault structures is available in Richey (2013). Sample UT02 was located in the main fault zone of the Iron Wash fault.

The field sites sit within the Paradox Basin on the Colorado Plateau of central Utah (Figures 4.1 Figure 4.2). The Paradox Basin consists of units from the Cambrian to Jurassic in age (Figure 4.3). Underneath the Paradox Basin lies Early Proterozoic metamorphic gneiss and schist. A sequence of terrestrial, fluvial and lacustrine sediments was deposited within the basin (Figure 4.3). The Colorado Plateau has been subjected to three main periods of regional tectonic deformation (Davis 1999). The first stage, a period of faulting and folding, took place as the North American plate converged with the Farallon plate during the Laramide Orogeny (90-50 Ma). The San Rafael Swell is a large NE-anticline formed during the Laramide Orogeny. The second stage of deformation took place in the Miocene (25-19 Ma). During this period plate convergence slowed, the angle of subduction was increased and igneous activity followed. Most recently they area has been subjected to faulting during the Basin and Range extension (~15 Ma - present) (Davis 1999).

Deformation bands in Utah's Jurassic Navajo and Entrada formations are well exposed and have therefore been the subject of many detailed studies on their development and growth. Studies looked at deformation band petrophysics (Aydin 1978; Fossen 2010; Fossen and Rotevatn 2012), mechanics of deformation band formation (Skurtveit et al. 2013), general field observations (Mollema and Antonellini 1996) and the deformation band formation in relation to the fault damage zone (Shipton and Cowie 2001).

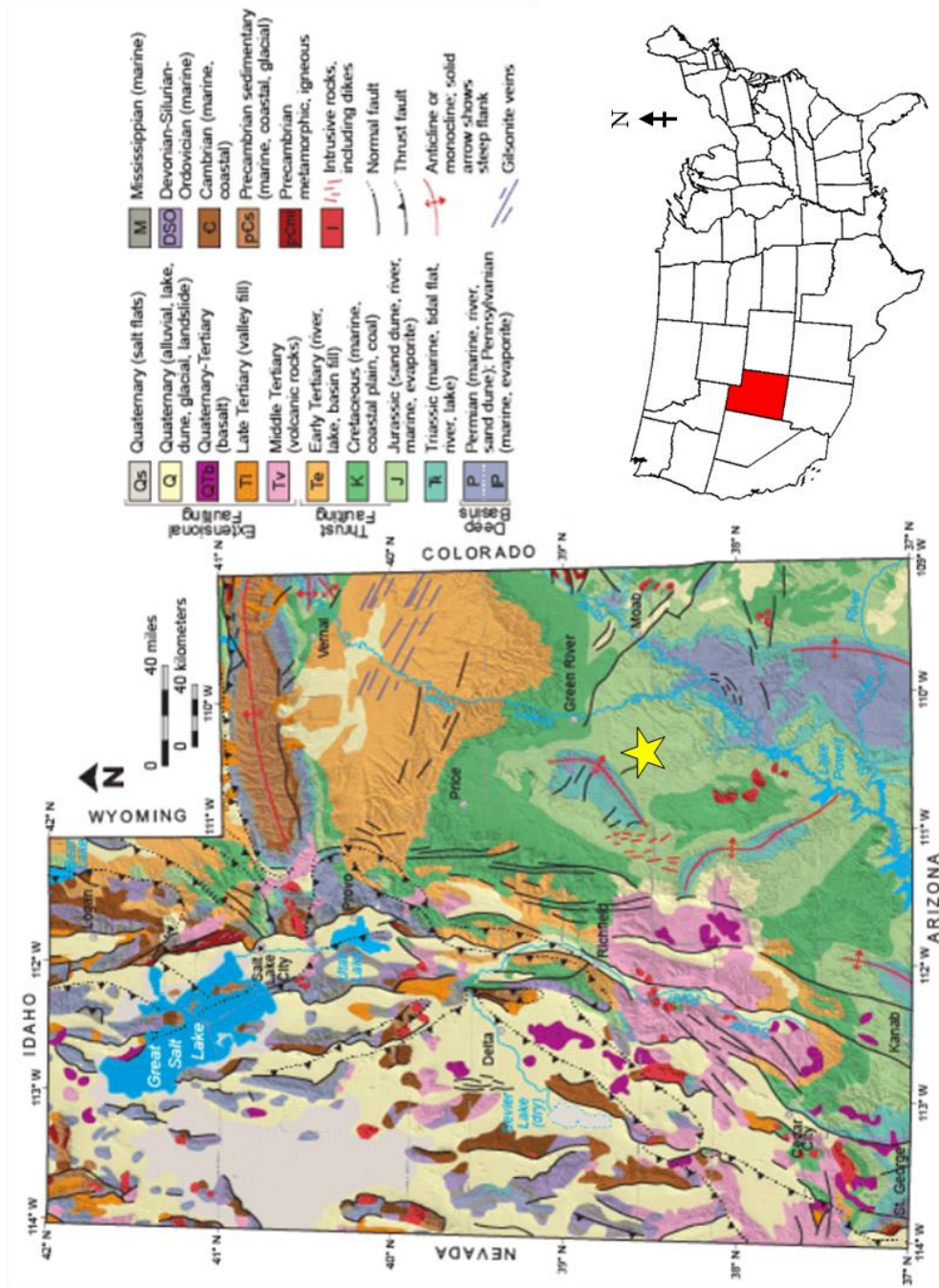


Figure 4.1: Simplified geological map of Utah. A star marks Iron Wash fault field location. The yellow star indicates the position of the field study area.

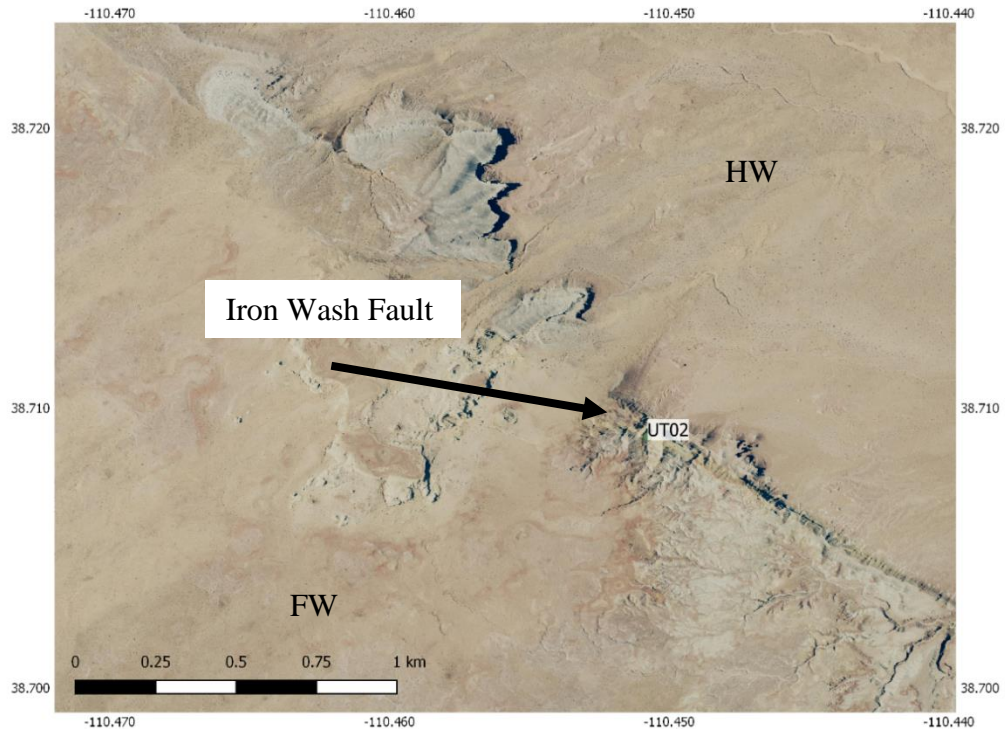


Figure 4.2: Location map of field area UT02 along the Iron Wash Fault zone. FW= Footwall, HW= Hanging wall. Image from Google Earth (2018).

Iron Wash Fault field site is located in the North west edge of the Paradox Basin (Figure 4.1), to the east of the San Rafael Swell, in central Utah (Lat 38°41'40'' N, Long -110°27'16'' W) (Richey 2013; Heather-Cooley 2017).

The unit studied in this thesis is the Entrada formation which is mid-Jurassic (Figure 4.3) in age (~140-180 Ma). In particular the field site focuses on the Earthy member which is approximately 31m thick in the field area (Heather-Cooley 2017). Estimations suggest a maximum sediment burial depth of 3km in areas south of Green River (Heather-Cooley 2017).

Chapter 4 – Geological History











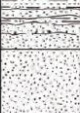



Age	Formation	Symbol	Approx.Thickness (m/ft)	Lithology	Permeability		
Jurassic	Late	Morrison Fm.	Jm	99/~325		LOW	
	Middle	Summerville Fm.	Js	66/~215		LOW	
		Curtis Fm.	Jct	55/~180		LOW	
		Entrada Ss.	Slickrock Mbr.	Jes	30/~100		MODERATE
			Earthy Mbr.	Jee	40/~130		LOW
		Slickrock Mbr.	Jes	60/~200		HIGH	
		Carmel Fm.	Upper	Jcu	35/~115		LOW
			Lower	Jcl	30/~100		LOW HIGH
	Page Ss.	Jp	3/~10				
	Early	Navajo Ss.	Jn	120/~390		VERY HIGH	
		Kayenta Fm.	Jk	48/~155		LOW- MODERATE	
		Wingate Ss.	Jw	63/~205		MODERATE	
Triassic		Chinle Fm.	TRc	73/~240		LOW	
	Moenkopi Fm.	TRm	152/~500		LOW		

Figure 4.3: Stratigraphy of Utah study area from Richey (2013). This thesis focuses on deformation bands from the Entrada formation.

4.3.2 Iron Wash field site

Sample UT02 is taken from the centre of the Iron Wash Fault zone (Heather-Cooley 2017). The host sediment from UT02 is the Entrada Earthy member (Jee) sandstone, it is sublitharenite in composition but it has been strongly altered by fault-related fluid flow (Figure 4.4). The porosity of the host rock from Brush valley UT02 sample is approximately 10.8 - 19.0%. The level of cementation in UT02 can be classified as strong (see Table 2.2).

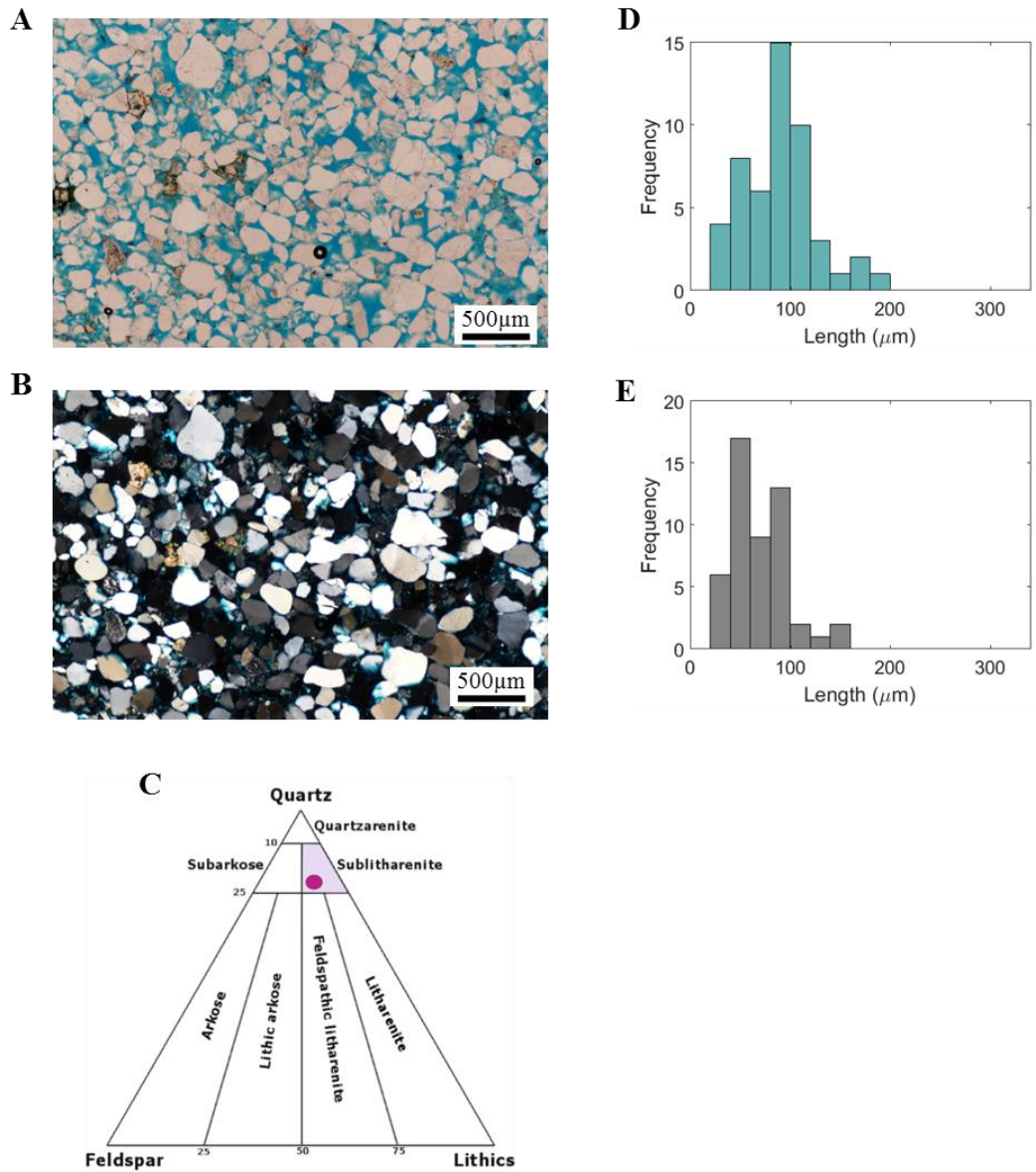


Figure 4.4: Sample UT02 host rock analysis. A) PPL thin section of host sediment which shows the grains are well sorted and subrounded in shape. B) XPL thin section of host sediment. C) QFL diagram shows the sample to be sublitharenite in composition. D) Grain size distribution along the longest axis shows the predominant grain length to be 80-100 μm. E) Grain size distribution along the shortest axis shows the predominant shortest axis to be 40-60μm.

4.4 Hungary

The site in Hungary was chosen because of its clear tectonic history, excellent exposure and good level of cementation in the sandstone (the sandstone could be sampled without the sample failing).

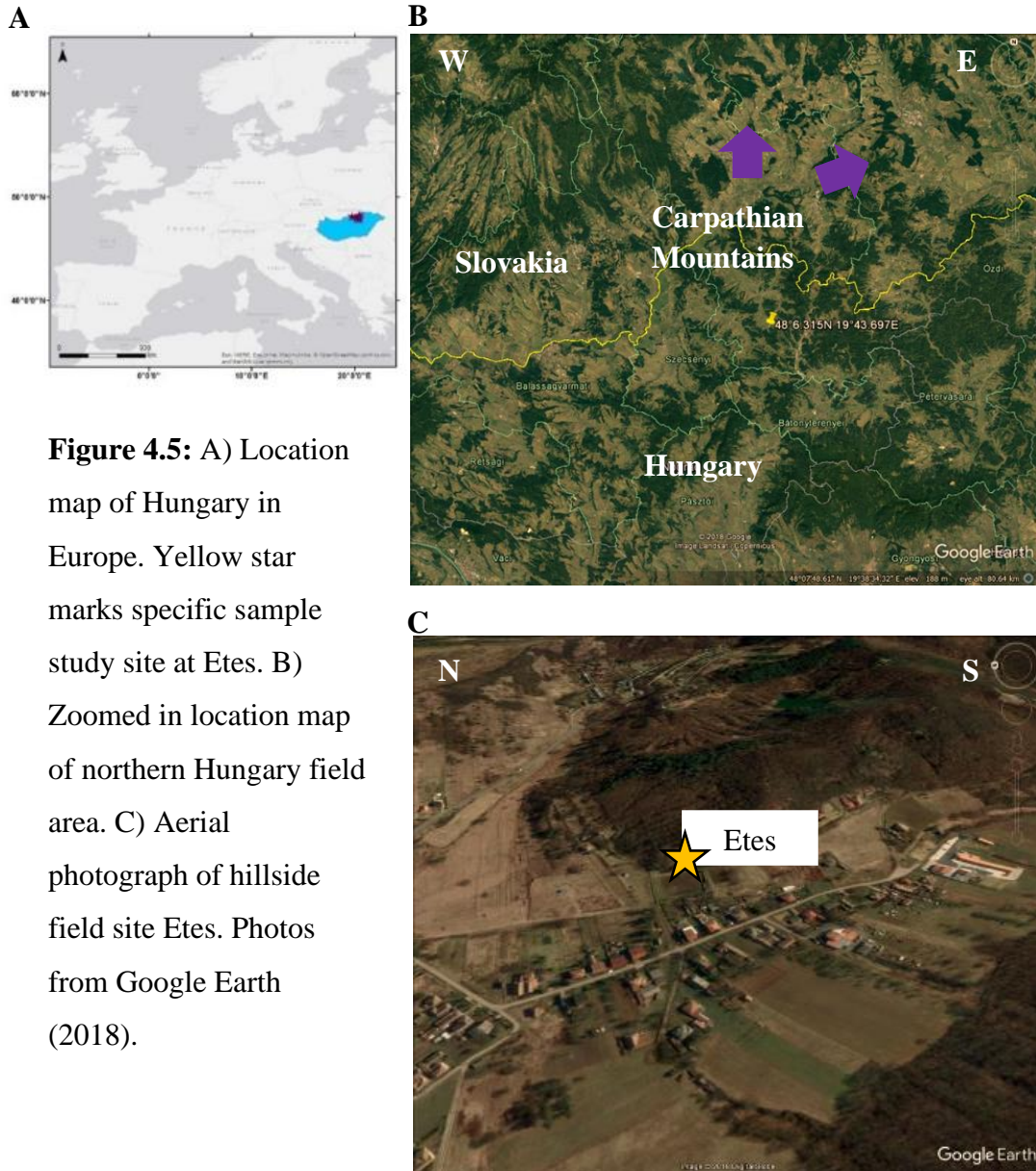


Figure 4.5: A) Location map of Hungary in Europe. Yellow star marks specific sample study site at Etes. B) Zoomed in location map of northern Hungary field area. C) Aerial photograph of hillside field site Etes. Photos from Google Earth (2018).

4.4.1 Geological history of The Pannonian Basin

The Pannonian Basin is a complex extensional basin which formed during the Miocene (Royden et al. 1983; Horváth et al. 2015; Balázs et al. 2016; Lukács et al. 2018). The basin extends for approximately 600 x 500km and is bordered by the Carpathian Mountains (Figure 4.5) to the north and east; the southern and Eastern Alps on the West and the Southern Carpathian (Dinaric Alps) to the south (Dolton, 2006). Following the Miocene extension phase a period of subsidence, syn-rift deformation and volcanic activity took place approximately 18.2 Ma. Rifting then occurred between 11.6 and 9 Ma, lasting until the late Miocene (Dombrádi et al. 2010; Petrik et al. 2016; Lukács et al. 2018). For a full description of the deformation events during the formation of the Pannonian Basin please see Petrik et al. (2014).

Due to the extensional tectonics the geothermal gradient in Hungary is higher than average at 5-6°C/100m. Therefore during burial the sediments were exposed to elevated temperature conditions.

The Pannonian Basin demonstrates a wide array of deformation bands types (Petrik et al. 2014). These include dilation bands, disaggregation bands and cataclastic bands (of varying cataclastic intensity). It is believed that deformation band formation is synchronous with the Miocene rifting phase.

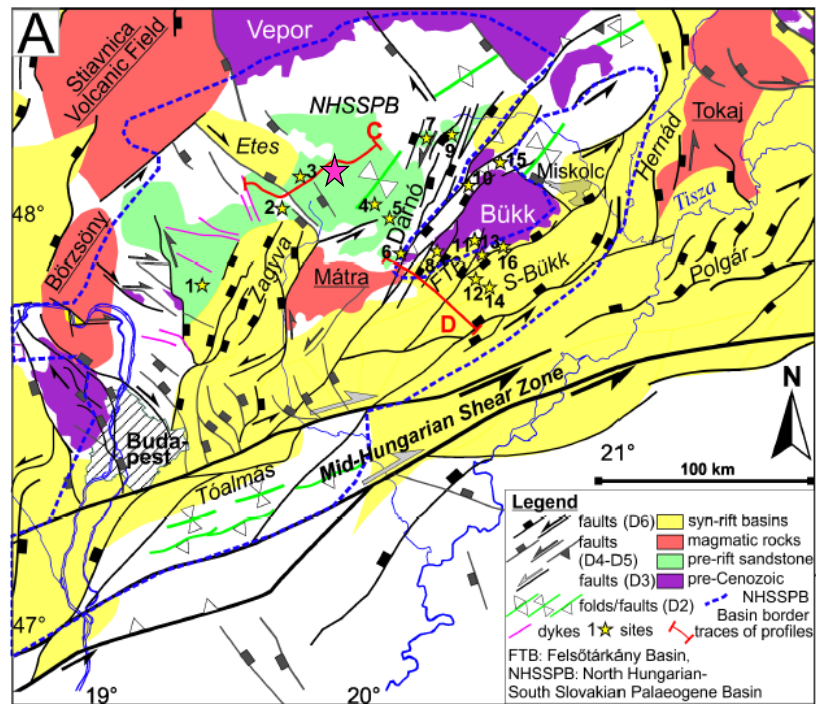


Figure 4.6: Geological map of Hungary field area. Etes field site is marked with a pink star. The site is from the SE corner of the Etes graben in pre-rift sediments. From Beke et al. (2019).

4.4.2 Etes field site

In this study we focus on pre-rift sediments to the SE of the Etes graben (Figure 4.6) which were deposited between 21 – 19 Ma (Beke et al., 2019) during the Eggenburgian stage (Figure 4.7). The Etes graben is formed syn-rift.

The host rock for HN11 is the Pétervására Formation sandstone (**Error! Reference source not found.**). The Pétervására Formation is a poorly consolidated sandstone which is solid to touch however it breaks easily to form a sand when force is applied. It therefore makes it an ideal example of poorly consolidated sandstone.

The Pétervására Formation is an arkosic, fine-medium grained, poorly sorted sandstone with angular-subangular grains (Figure 4.9). The mean grain size is 197.35 μm and it ranges from 36.29 to 397.11 μm (Figure 4.9D). Clay forms at point contacts between the grains (Figure 4.9A) to create a ‘cement’ like bond.

At the outcrop there is evidence of conjugate deformation bands with some deformation bands protruding from the outcrop. However, the bands are much softer

Chapter 4 – Geological History

than the band in Utah and the maximum height these bands protrude to is 20-30 cm. The level of cementation in sample HN11 can be classified as moderate (see Table 2.2).

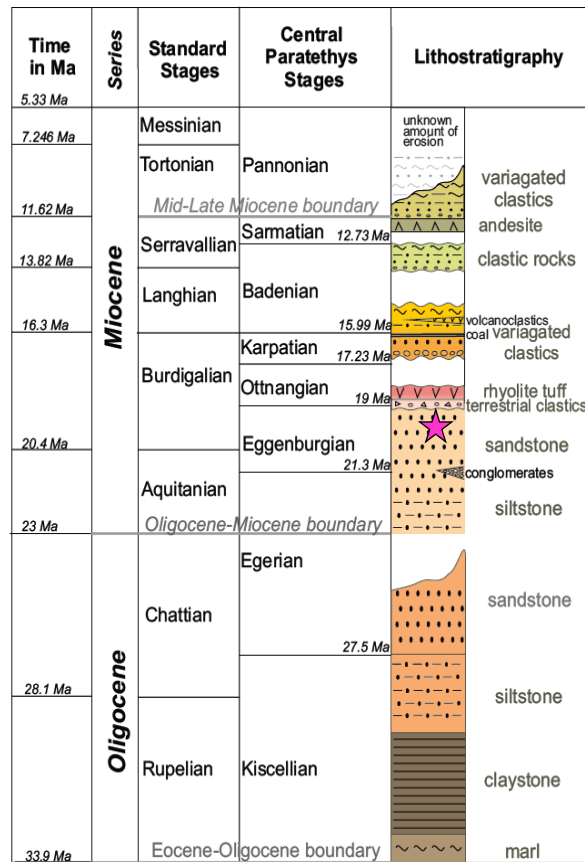


Figure 4.7: Lithostratigraphic column of Hungary. Field site Etes was deposited during the Eggenburgian stage (it is marked with a pink star). Adapted from Petrik et al. (2014).

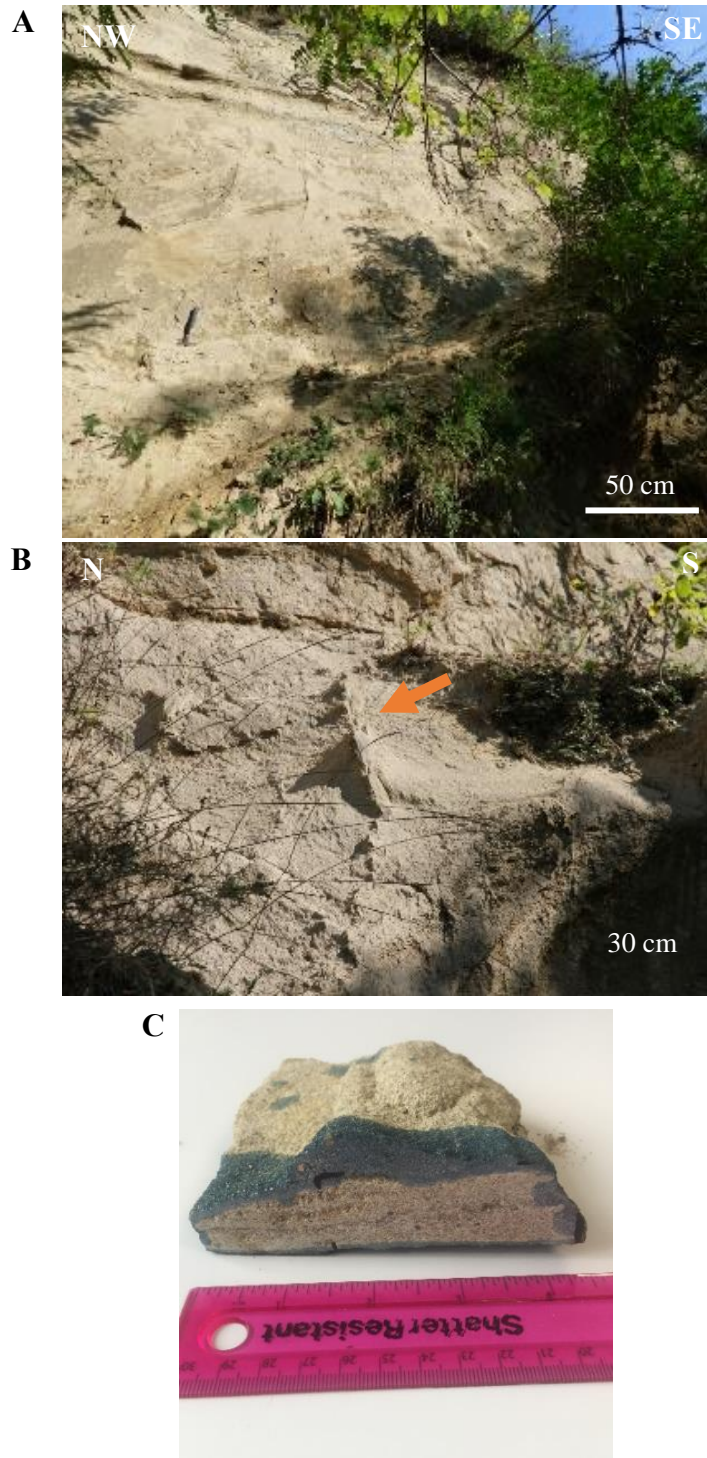


Figure 4.8: Summary of field site and sample from Etes, Hungary. A) Overview of outcrop with conjugate deformation bands present. B) Sample from protruding deformation band. C) Deformation band sample cut open across deformation bands.

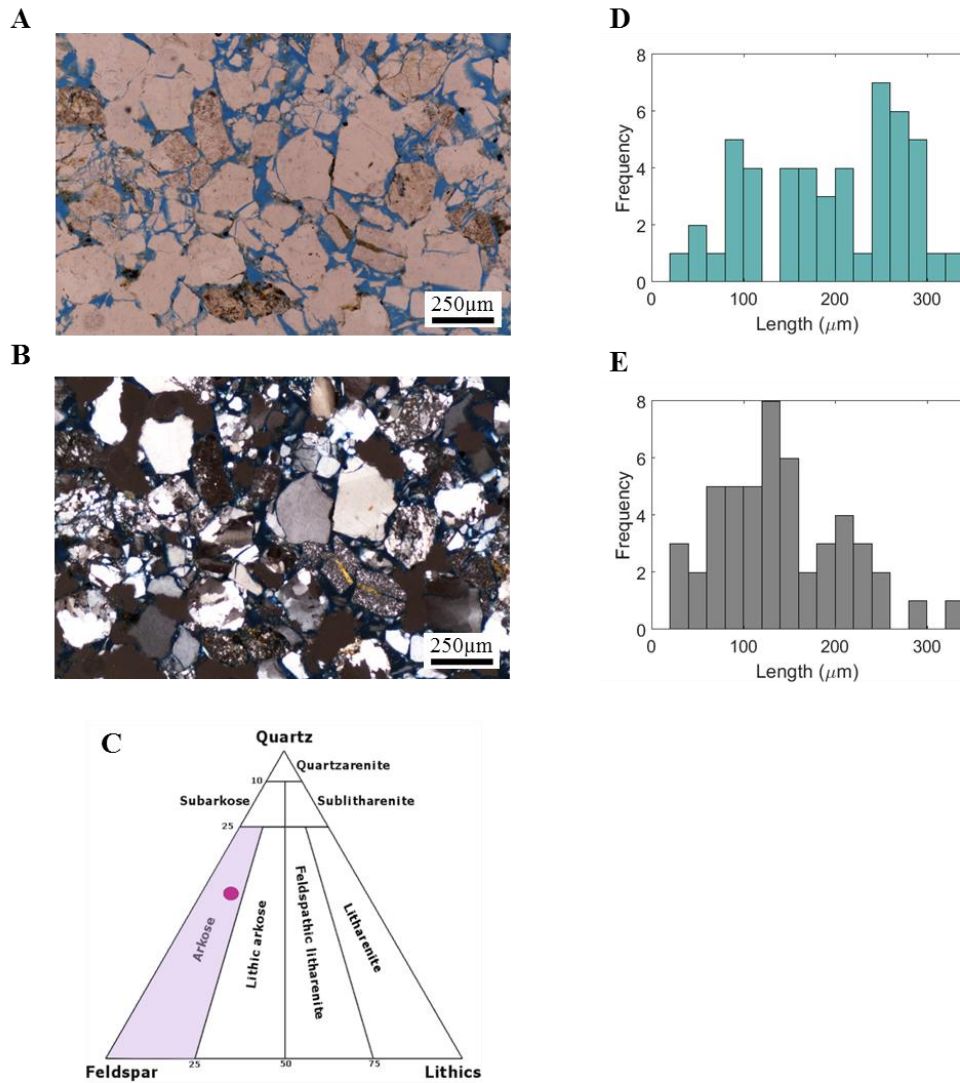


Figure 4.8: Sample HN11 host rock analysis A) PPL thin section of host sediment. The grains are poorly sorted and subangular-angular in shape. B) XPL thin section of host sediment. C) QFL diagram shows the sample to be arkose in composition. D) Grain size distribution along the longest axis shows the predominant longest axis to be 240-260 μm in length. E) Grain size distribution along the shortest axis shows the predominant shortest axis to be 120-140 μm in length.

4.5 Scotland

A field survey was carried out on the island of Arran (Scotland) to analyse the relationship between and collect samples of deformation bands previously studied here by Underhill and Woodcock (1987) and Bright (2006).

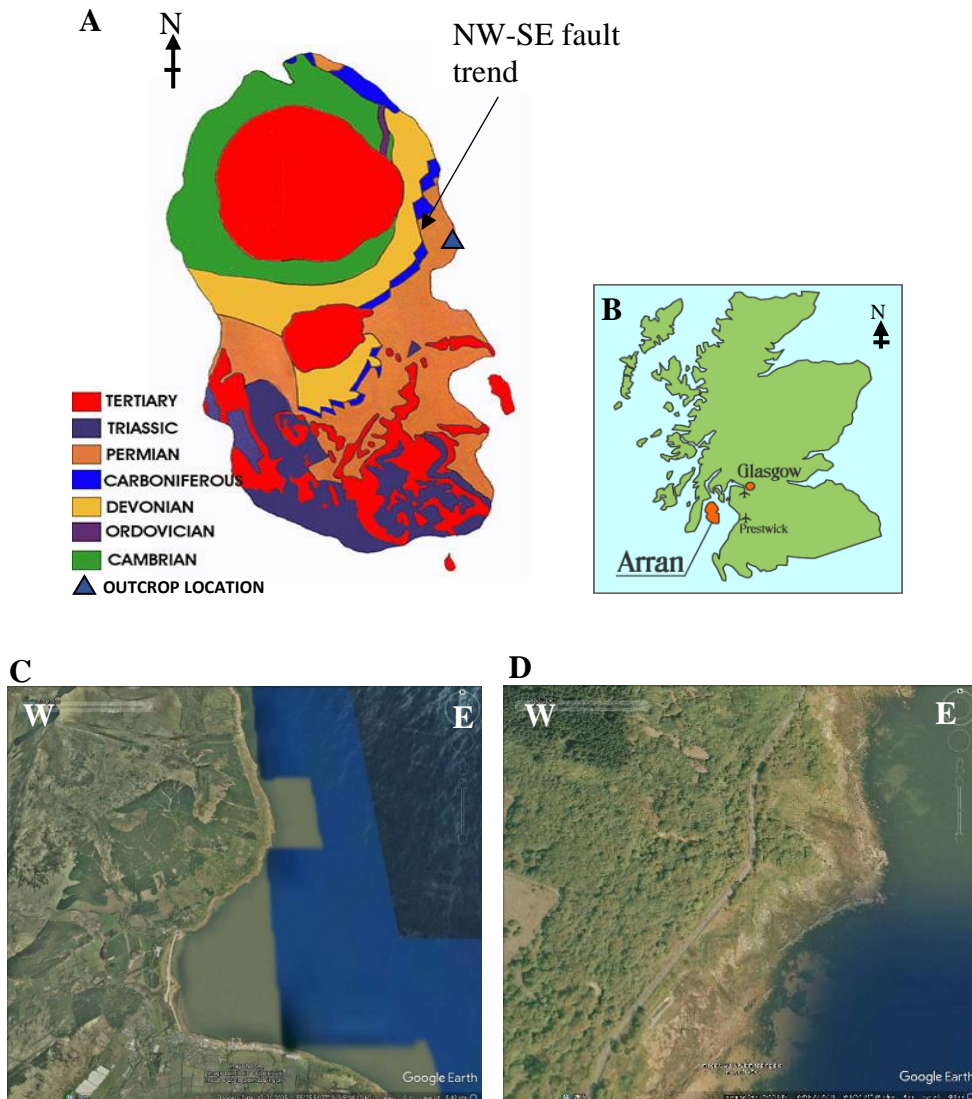


Figure 4.9: A) Simplified geological map of Arran with highlighted outcrop location (from Arran Museums 2015). B) Map of Scotland with location of Arran shown. C) East coast of Arran at Merkland Point. D) Zoomed location of coastal outcrop. Images from Google Earth (2018).

4.5.1 Geological Context of the Arran site

The geology on Arran dates back to the Cambrian (~541- 485.4 Ma) at which time sediment was deposited in the form of grewackes and shales. Since then Arran has had a history of metamorphism (Cambrian), volcanics (Ordovician), folding (Silurian), further extended period of sedimentation (Devonian – Cretaceous in age), dykes and intrusions (Tertiary) and most recently glacial erosion (Quaternary). The main focus of this study is the sediments which were deposited from the Devonian – Cretaceous period and their interaction with the Tertiary volcanics. The samples we collected from the Corrie Sandstone Stewartry Group were formed in an aeolian environment (Clemmensen and Abrahamsen 1983; McKeever 1992) and are Permian in age (271-299 Ma).

Arran is dominated by NW-SE trending extensional fault system on the east coast of the island (Figure 4.10). Fault formation is thought to have taken place synchronous with sedimentation during basin development in the Permian (Woodcock and Underhill 1987). However, it is also probable that the faults were reactivated during granitic intrusion during the Tertiary period (Underhill and Woodcock 1987), in which case during fault formation the overburden would have been between 1-2 km (Woodcock and Underhill 1987).

4.5.2 Arran field site

The outcrop study is situated on the east coast of Arran at Merkland Point (Figure 4.10). At Merkland Point there is a network of deformation bands which form in the damage zone to two faults. There are also two basaltic dykes (23-66 Ma) which run NW-SE.

The host rock sandstone for AR01 is a subarkosic, predominantly medium grained, well sorted sandstone with subrounded grains. The grains are cemented together with quartz via pressure solution. The dominant grain length is 240-260 μm (Figure 4.11). The level of cementation in AR01 can be classified as strong (see Table 2.2).

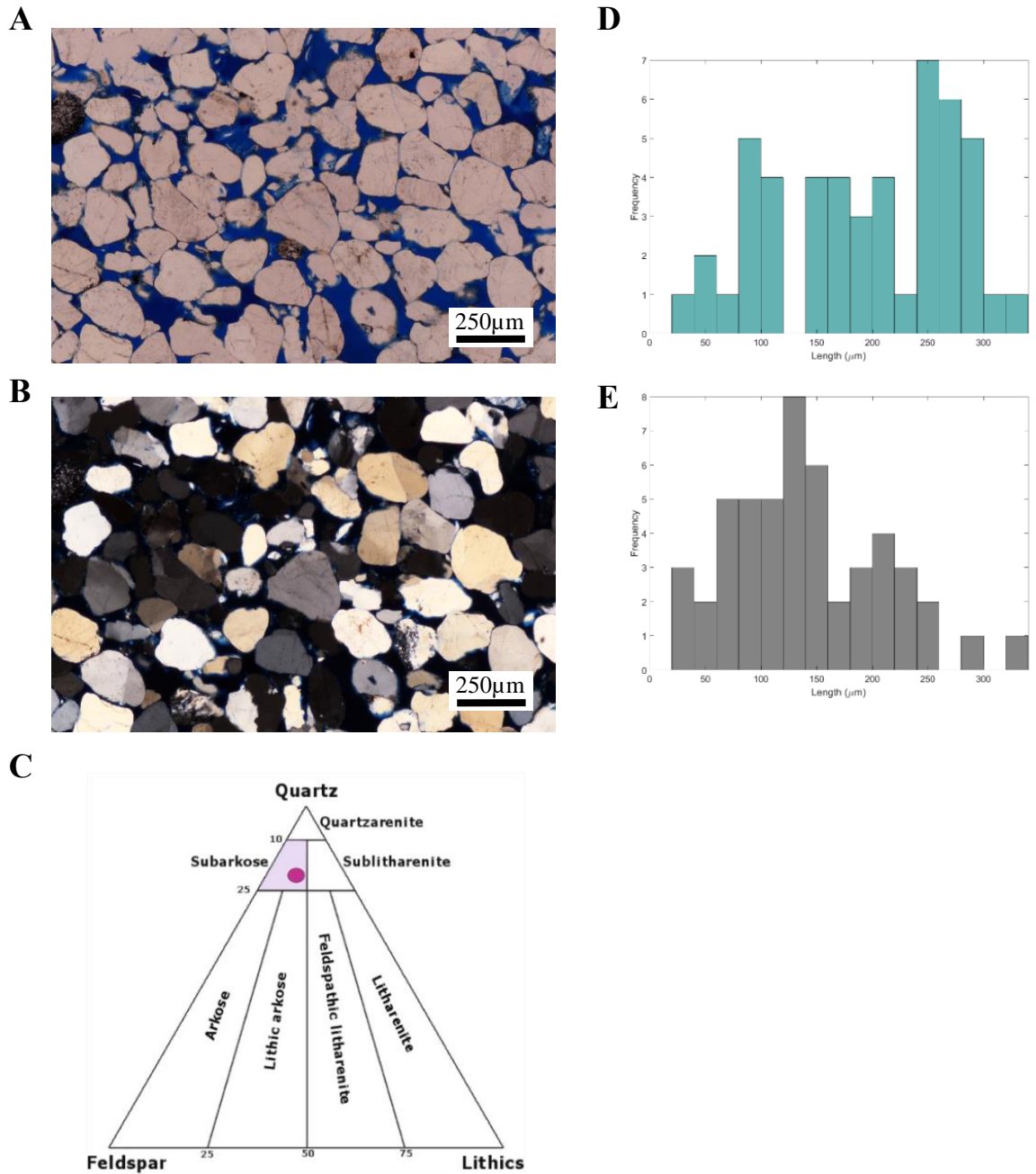


Figure 4.10: Sample AR01 host rock analysis. A) PPL thin section of host sediment. B) XPL thin section of host sediment. C) QFL diagram shows that the sample is subarkosic in composition. D) Grain size distribution along the longest axis. The dominant grain length is 240-260 μm. E) Grain size distribution along the shortest axis where the dominant short axis grain length is 120-140 μm.

4.6 Summary

The geological histories of Crow's Nest Fault, Etes and Arran are all quite different. Arran has the largest grain size (240-260 μm) from all the sample localities. Etes has the highest clay percentage across all of the deformation band samples. The main difference between UT02 and AR01 host sediments is the grain size and depositional environment.

Chapter 5 – Cement and porosity variation across deformation bands

5.1 Rationale

In this chapter I examine the petrophysics of sandstones, and the deformation bands that they contain, to look at the range of textures and cement distributions formed within real deformation bands. In addition, this chapter develops a quick and qualitative method to analyse the geometry and textures of the deformation bands using X-ray computed tomography (X-CT).

In the following sections I will describe and analyse each of the deformation bands in turn using thin sections and both 2D and 3D X-CT scans. The descriptions will include analysis of size, distribution and connectivity of the grains, cement and pores in each sample. For the grain size analyses long and short axes of 50 grains per sample were measured using point counting

Each of the cataclastic deformation bands are semi-quantified by the level of cataclasis present in each band using the scheme defined by Beke et al. (2019) (see Section 2.3.2).

Understanding the effect that the percentage of cement in a host rock has on the mechanical properties of the host and the resulting evolution of deformation bands requires unpicking the relative timing of the cement phase from the deformation band formation. For all three samples in this chapter I investigate if the *Segmentation* application in Avizo® v.9.0.1 can be used to adequately pick the cement phase and therefore the connected volumes of cement and pores. The connected volume of pores is crucial to understand the permeability.

The results from this chapter allow for a comparison of both X-CT 2D and 3D analysis techniques to determine which is most suitable for deformation band analysis.

5.1.1 Data sampling

The X-CT analysis is based on three different data sets. The first of these is full volume (Figure 5.1A) which includes data from both the deformation band and host rock. The second data set is from 2D slices (Figure 5.1B). This data set consists of 2D slices (4mm^2) along the z axis of each sample. The third data set is 3D sub volumes (Figure 5.1C). Each of the 3D sub volumes is 0.125mm^3 (0.5mm on each side). Five of the sub volumes for each site are from inside the deformation band and the other five sub volumes are from the host rock.

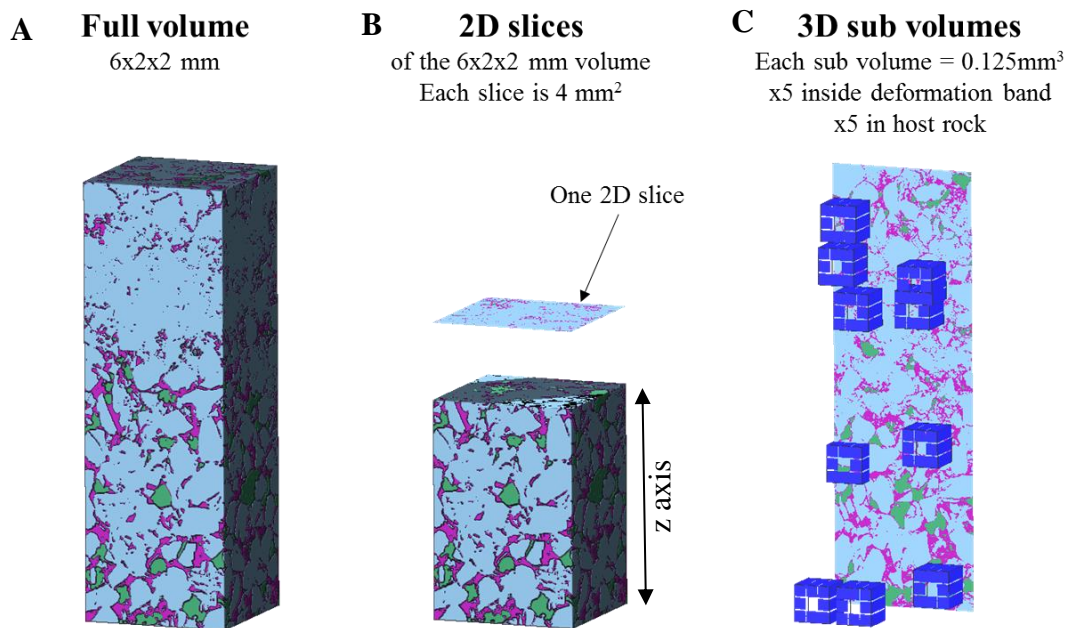


Figure 5.1: Three methods used to sample data in this chapter. A) Full volume. B) 2D slices. C) 3D sub volumes.

5.2 Deformation bands from Iron Wash Fault, Utah

As described in Chapter 4 the main field site is at the Iron Wash Fault, Utah. Previous fieldwork (Heather-Cooley 2017) has shown that there are several generations of deformation bands present. In this section I focus solely on the cataclastic deformation bands found at the Iron Wash Fault.

5.2.1 Outcrop

The deformation bands cut the bleached Earthy member (Jee) of the Entrada sandstone (Figure 5.2). The bedding in this outcrop dips less than 30° to the North and North-West. There are two clear sets of deformation bands in the Earthy member: the first runs subparallel to the fault zone with a shallow dip (<30°) to the south-east; the second are high angle deformation bands (70-88°) which run almost perpendicular to bedding. The deformation bands are predominantly <1cm thick, tightly packed together (less than 10cm spacing between bands) and form an anastomosing pattern as they protrude from the host sandstone in the hanging wall of the Iron Wash Fault.

5.2.2 Thin section analysis

Sample UT02 is an example of a cataclastic deformation band. In thin section a zone of host lithology and a large (6.5mm in length) deformation band zone can be identified (Figure 5.3). The deformation band zone can be further split into an area of intense cataclasis where no pore space is visible (the main deformation band) and an intermediate zone whereby pore space and fractures can be identified.

A summary of the grain length distributions along both long and short axes for fifty grains from each zone is shown in Figure 5.4. The host rock displays evidence of spalling and transgranular fracture and has a mean grain length along the long and short axis of 82.6 μm and 57.3 μm respectively. The predominant longest grain axis in the deformation band and intermediate zone is 20-40 and 40-60 μm respectively. In the intermediate zone there is an overall decrease in average grain size in comparison to the host zone. The mean grain length along the long and short axis is 64.6 μm and 50.4 μm respectively.

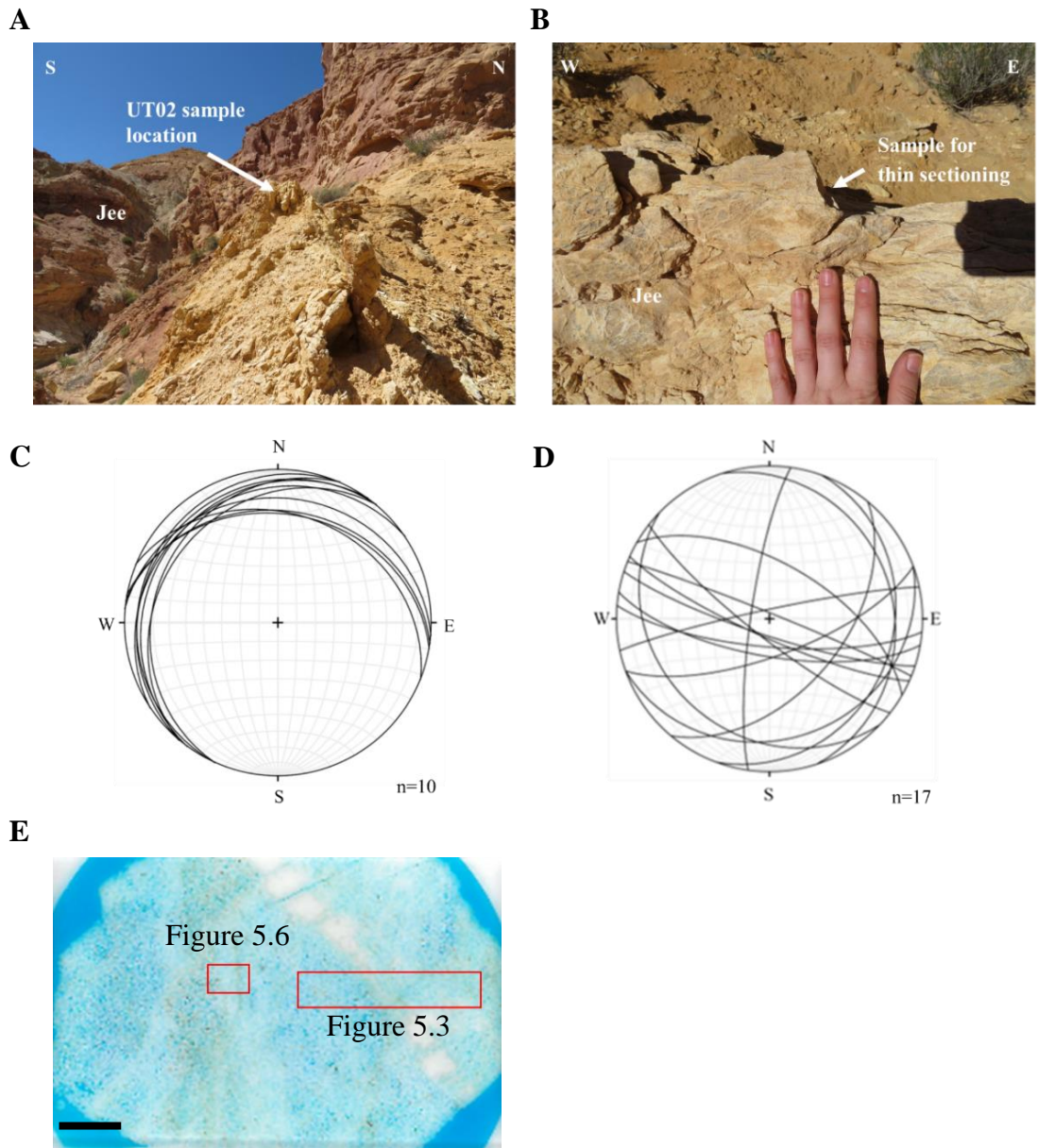


Figure 5.2: UT02 deformation bands from the field. A) Sample location from inside the Iron Wash Fault zone. Here we see the Entrada Earthy member which has been bleached in the foreground. B) Location of sample for thin sectioning. C) Lambert equal area stereonet projection of bedding in the Entrada Earthy member. D) Lambert equal area stereonet projection of deformation band strike and dip measurements. E) Photograph of thin section slide for sample UT02 with locations of thin sections marked. Scale bar is 5 mm.

Jee = Entrada Sst. Earthy Member (See stratigraphic table in Figure 4.3).

Chapter 5 - Deformation bands

In the zone of cataclasis the mean long and short axes are 50.9 μm and 38.9 μm . This represents a mean reduction in grain size of 38.4 and 22.8% respectively. From the variation in the size of the quartz grains present inside the deformation band this can be subcategorised as an advanced cataclastic deformation band using the Beke et al. (2019) classification (Chapter 2). From the observations in this section, it is possible that the deformation band has been subjected to localised secondary calcite cementation.

While not a focus of this study it is worth noting that the bands are associated with iron oxides in coatings and patches, and dots of oil (Heather-Cooley 2017). In Figure 5.3 an orange rim coats the edges of the cataclastic zone, and is likely to be hematite: within this hematite rim calcite (Figure 5.5) can be seen and the porosity is lower (as highlighted by the blue dye). There is also evidence of black opaque dots (Figure 5.6) which are concentrated inside the deformation band. Heather-Cooley (2017) used observations of these geochemical changes to constrain the burial history of the site.

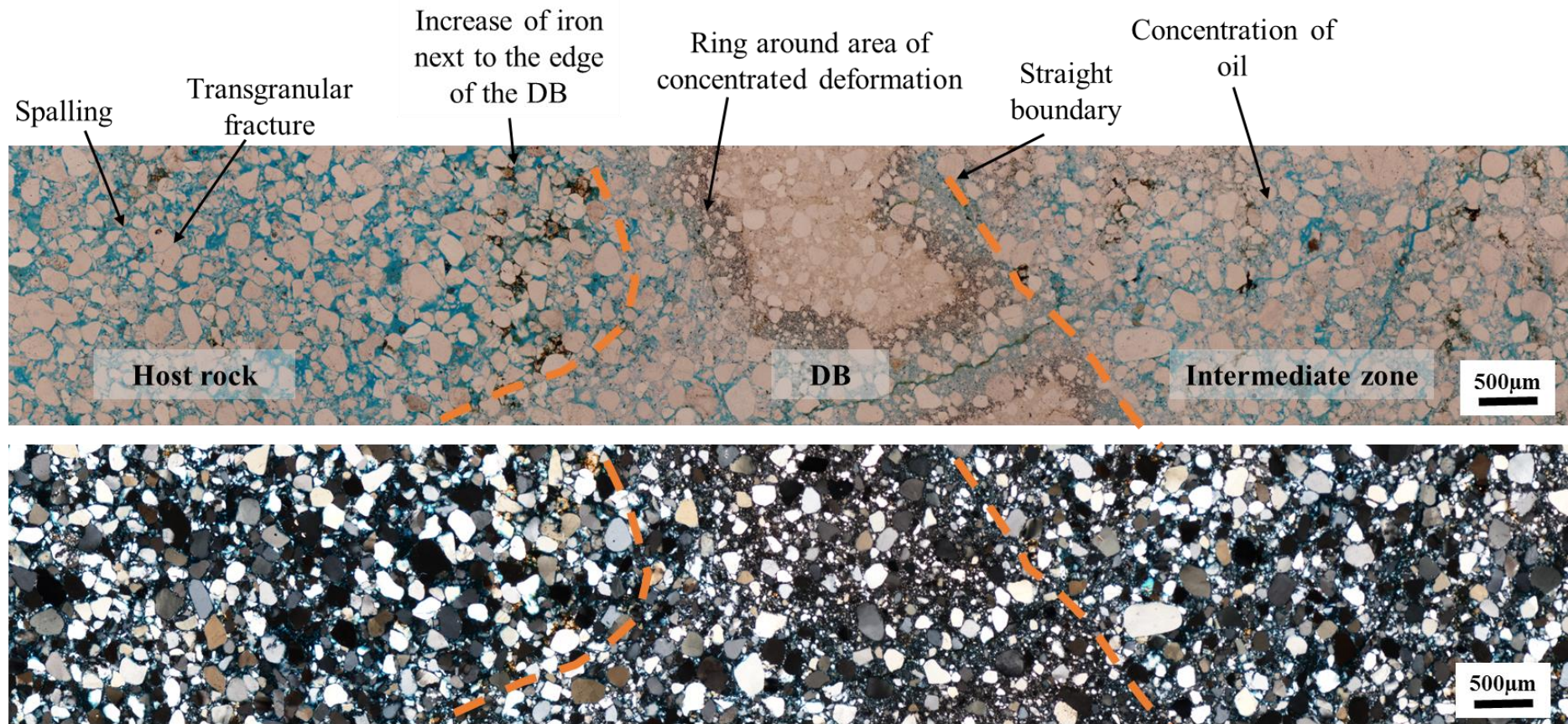


Figure 5.3: Thin section of sample UT02 deformation band zone (PPL and XPL). The deformation band (DB) has quite a clear cut off with the host rock on the left-hand side.

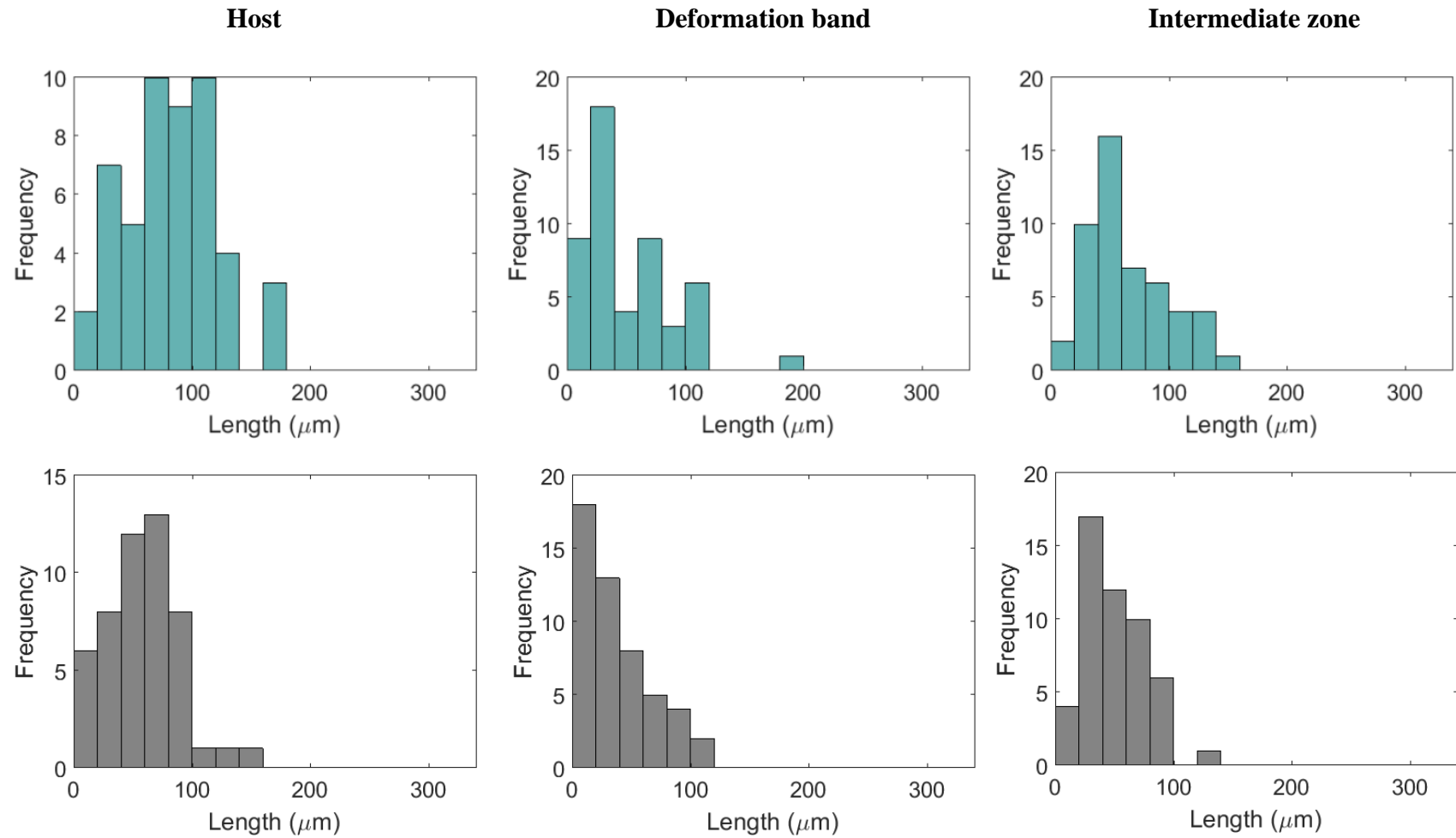


Figure 5.4: Sample UT02 grain length distributions along the long (blue graphs) and short axis (grey graphs) in each of the three areas described in Figure 5.2; host, deformation band and intermediate zone. Fifty grains were measured for each area in sample UT02.

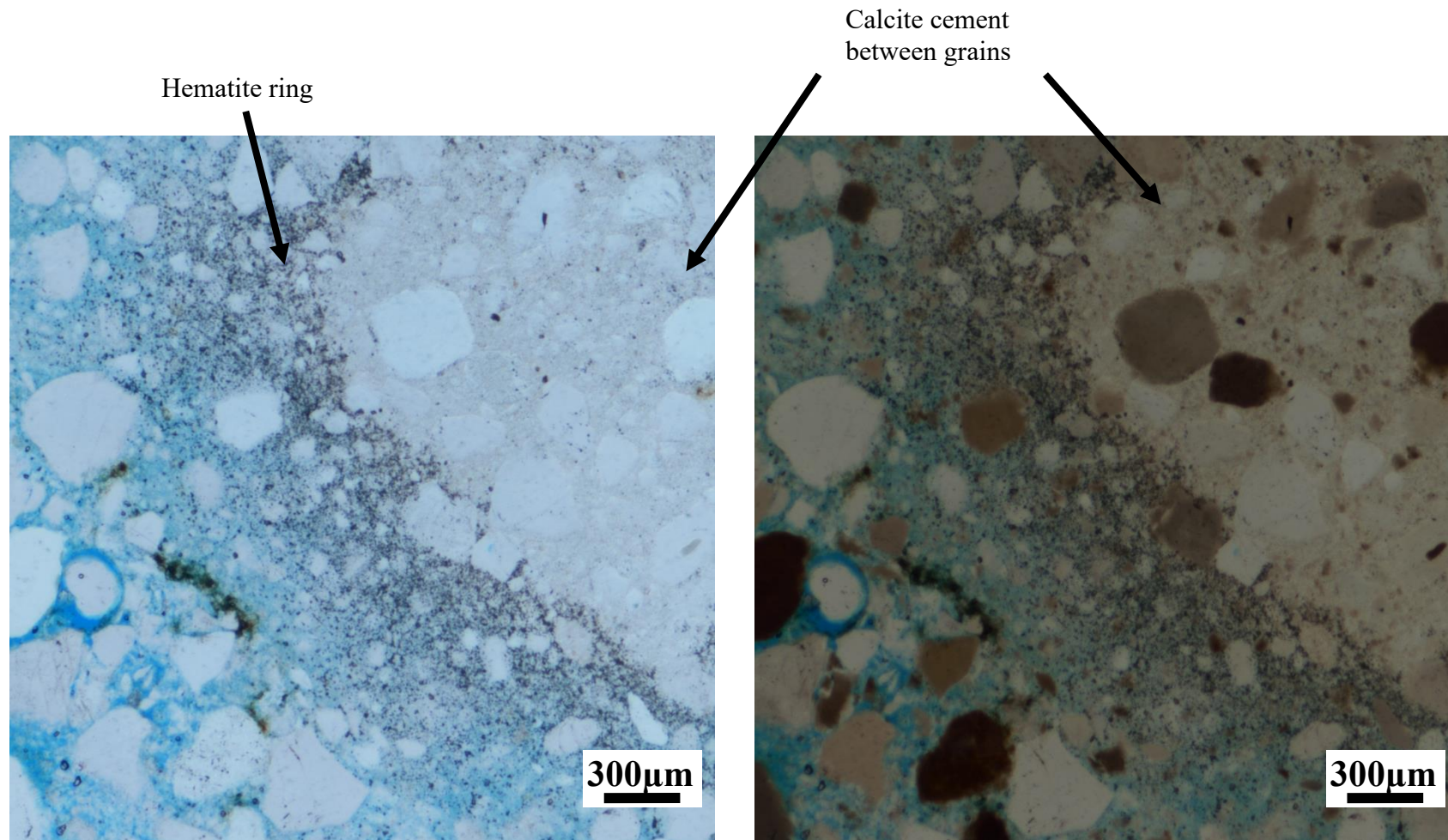


Figure 5.5: Zoomed PPL and XPL images of UT02 with focus on hematite ring and calcite cement inside deformation band between grains.

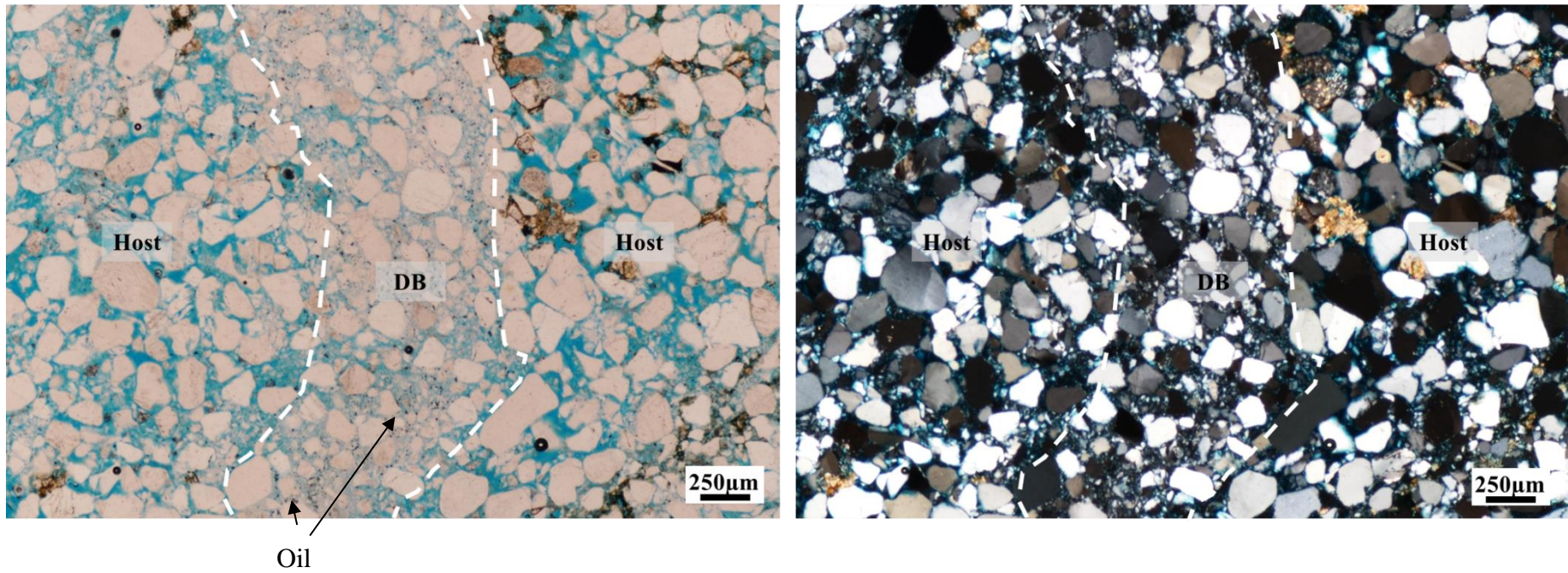


Figure 5.6: Zoomed in image of UT02 and focus on dots of oil (<25µm in diameter). The oil is concentrated inside the zone of most intense cataclasis.

5.2.3 Avizo® analysis

A sub-sample (21 x 11 x 17 mm) of UT02 was scanned in the X-CT at a resolution of 5.7 μm (Appendix 2.). Figure 5.7 displays the three phases of Avizo® segmentation. UT02 is predominantly quartz cemented with secondary calcite and hematite cementation (Figure 5.5). Because the grains and first cement phase consist of quartz, I am unable to segment the first cement phase due to the overlap in grey values (see Section 5.5.4). Instead the secondary calcite and hematite cementation phases are segmented.

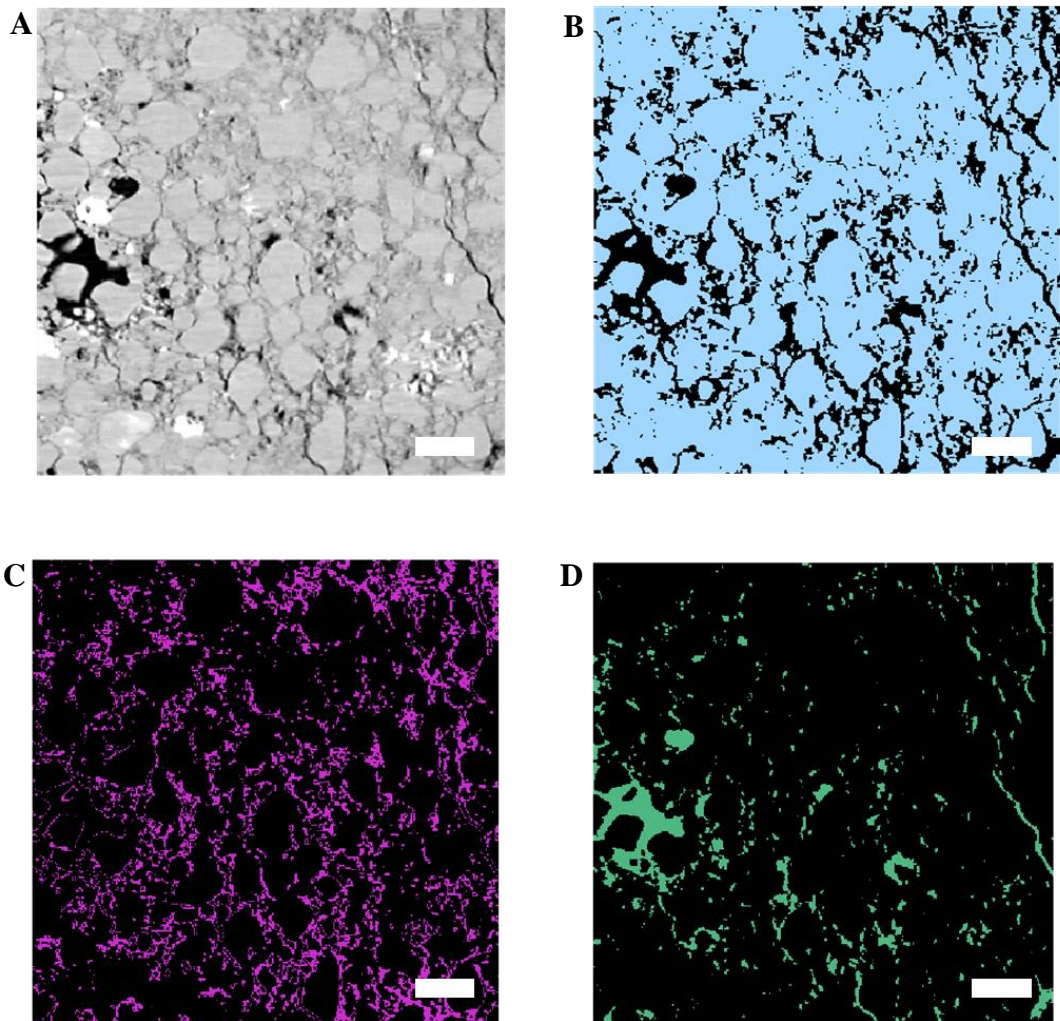


Figure 5.7: UT02 segmented slices showing: A) original grey image, B) Grains phase, C) Cement phase and D) Pores phase. 0.25mm scale bar.

Figure 5.8 shows the results of segmentation of successive slices through sample UT02. The 3D volume is segmented using the methodology outlined in Chapter 3, and the values for percentage open pores, cement and grains are calculated for each of the 1046 slices through the sample.

Figure 5.9 shows the segmented phases in 3D present in the long (6 x 2 x 2 mm) data subsample.

By comparing both these figures host rock (H1 and H2) and three deformation band sections (labelled DB1, DB2 and DB3 respectively) are separated into five zones (Figure 5.9). DB1 is the widest of the deformation bands (up 1.5mm wide) in the sample and displays the greatest level of cataclasis. DB 2 is a narrower deformation band up to 1mm wide, while DB3 is the narrowest with a thickness of up to 0.75mm in this section.

Figure 5.10 shows the cement (Fig 5.10A) and porosity (Fig 5.10 B) connectivity. If individual cement pockets or pores are connected, then they are labelled with the same colour. These range from tiny, isolated pockets of cement, to large interconnected bodies filling, or partially filling, many hundreds of pore spaces.

5.2.3.1 Grain and cement distribution

Analysis of 2D slices of the scanned sample shows there is an overall decrease (from 95.25-49.73%) in the percentage grains present across this sample. Table 5.1 displays the segmentation results of the 2D slices from each of the labelled zones. DB 1 has the largest percentage of grains present across the sample. This percentage is then followed by DB 2 and DB 3 respectively.

Table 5.1: Average percentage of grains, cement and porosity for each zone (defined by the 2D slice numbers – see Figure 5.6) in UT02. DB = deformation band zone, H = host rock zone.

Zone	Z slice number	Grains (%)	Cement (%)	Porosity (%)
H 1	0-78	79.80	14.07	6.13
DB 1	79-306	87.76	9.80	2.44
DB 2	439-628	77.98	17.81	4.21
H 2	629-837	62.84	18.71	18.45
DB 3	838-1004	66.08	24.77	9.16

The percentage of cement inside the deformation bands ranges from 4.29–28.63 %. The average percentage of cement increases from DB 1 to DB 3. DB1 is the zone with the lowest percentage of cement. The 2D slices show that, as expected, the percentage of grains is inversely correlated with the percentage of cement and pores. DB 3 seems anomalous. While the zone is clearly formed from a deformation band, it has a combined porosity and cement phase of 35%, higher than the host rock, and yet is clearly not a dilation band. From Figure 5.8 a small fracture running vertically through the sample is connected to a zone of dilation. From Heather-Cooley (2017) fracturing in this area has taken place after deformation band formation.

In the 3D Avizo® segmentation the definition of the individual grains is lost significantly through D1, D2 and D3 (Figure 5.9B). Inside the deformation bands the grains appear as one mass due to the low-resolution, whereas in the host rock individual grains can be resolved.

Table 5.2: Percentage of grains, cement and porosity from UT02 0.125mm³ sub volumes inside the deformation band and the host rock.

0.125 mm ³ sub volumes	Deformation band			Host		
	Grains (%)	Cement (%)	Porosity (%)	Grains (%)	Cement (%)	Porosity (%)
1	95.24	4.30	0.46	70.18	11.47	18.35
2	91.70	7.78	0.52	74.75	13.78	11.46
3	77.51	19.74	2.74	58.32	18.51	23.17
4	76.99	21.19	1.81	66.05	17.68	16.27
5	80.10	17.66	2.24	66.26	15.69	18.05
Average	84.31	14.13	1.56	67.11	15.43	17.46

The 3D cement phase is shown in Figure 5.9C. Figure 5.10A shows that the cement is connected throughout the host rock, and across DB 2 and 3. However, the cement is disconnected across DB1.

The average percentage cement from the five 3D sub volumes is lower across the deformation bands than in the host rock (Table 5.2).

For each of the five 3D 0.125mm³ sub volumes histograms of the volumes of connected cement bodies in the deformation band (Figure 5.11) and host rock (Figure 5.12) are displayed. The linked cement volumes in the host rock range from 3.80×10^{-7} - 2.34×10^{-2} mm³ with a median of 7.60×10^{-7} mm³. Whereas the linked cement volumes in the deformation band range from 3.80×10^{-7} - 2.71×10^{-2} mm³ with a median of 1.14×10^{-6} mm³. This shows that the host rock has the largest range and median values of linked cement volumes. Cataclasis has reduced the size of the cement bodies inside the deformation bands.

5.2.3.2 Distribution of pore space

In the 2D slices the porosity is lowest in DB 1 (2.44%) and then gradually increase in DB 2 (4.21%) and 3 (9.16%) respectively (Table 5.1). This suggests that the level of cataclasis experienced across the three deformation bands is unequal. It is interesting

that between three bands in the same sample the characteristics of the deformation band can vary significantly.

Meanwhile, the porosity in zones H1 and H2 is host rock porosity was calculated at 6.13% and 18.45% respectively. This difference of 12.32% between the two host rock zones is quite significant and suggests that H1 is inside a zone of deformation. Most of the pores in the host rock above D1 are disconnected.

In Figure 5.10B the porosity is unconnected across DB1. Across DB2 there are areas of connected porosity, and across DB3 it appears that the porosity is predominantly connected. This suggests that across narrower deformation bands porosity may be connected. However, in larger deformation bands (~1.5mm wide) porosity is less likely to be connected across the deformation band.

The average porosity from the five 3D sub volumes is lower across the deformation bands than in the host rock (Table 5.2).

For each of the five 3D 0.125mm³ sub volumes histograms of the volumes of connected pores in the deformation band (Figure 5.13) and host rock (Figure 5.14) are displayed. The pore volumes in the host rock range from 1.90×10^{-7} - 2.97×10^{-2} mm³ with a median of 9.50×10^{-7} mm³. Meanwhile in the deformation band they range from 3.80×10^{-7} - 4.26×10^{-4} mm³ with a median of 1.33×10^{-6} mm³. The pore volumes inside the host rock have a larger range of values, but a smaller median.

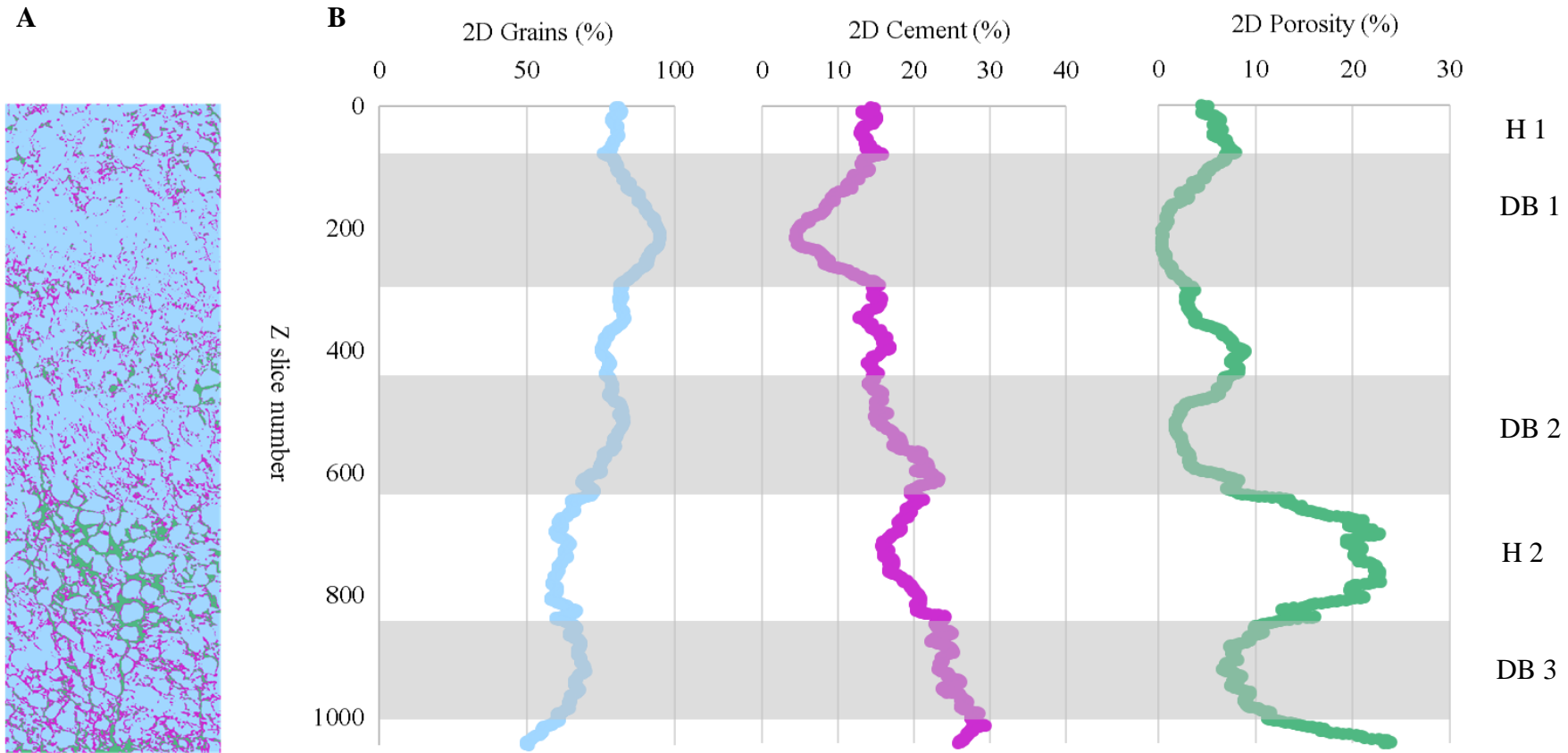


Figure 5.8: A) 2D vertical slice through a 6x2x2mm sub-sample of UT02: grain (blue), cement (purple) and porosity (green) percentage. B) Corresponding values of percentage grains, cement and porosity percentage for each horizontal slice along the z axis of the subsample. Three deformation band zones have been highlighted in grey. Here there is an overall increase in percentage grains and decrease in percentage cement as z slice number increases. At each deformation band there is a decrease in porosity. However, the amount by which the porosity decreases varies for each deformation band.

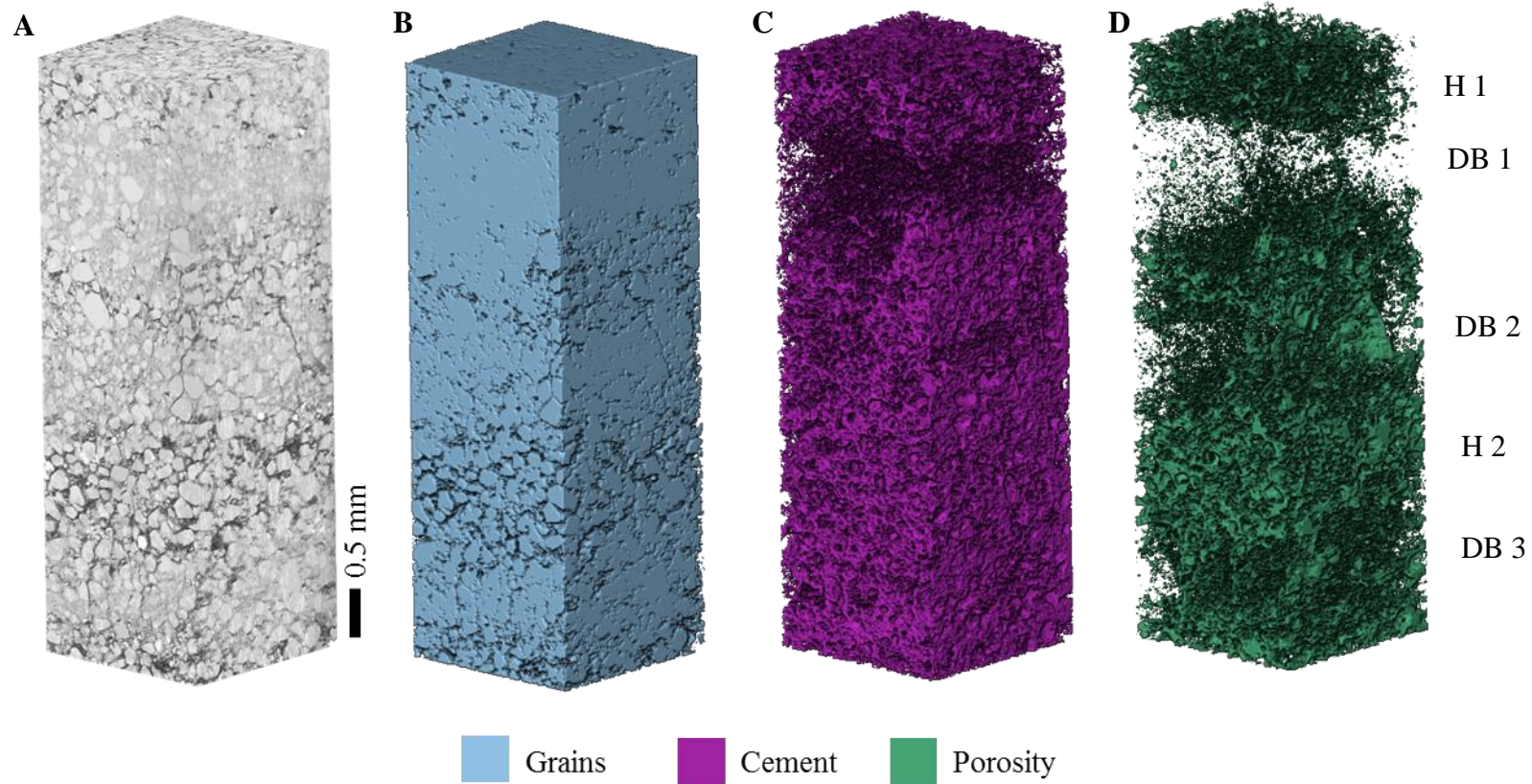


Figure 5.9: Sample UT02 full volume segmented in Avizo® A) Original grey scale 3D image. B) Grains segmented image. The grains segment is 74.54% of the total volume. Almost all the grains are in contact with each other inside the deformation band. C) Cement segmented image. The cement segment is 17.11% of the total volume. D) Porosity segmented image. The porosity segment is 8.35% of the total volume.

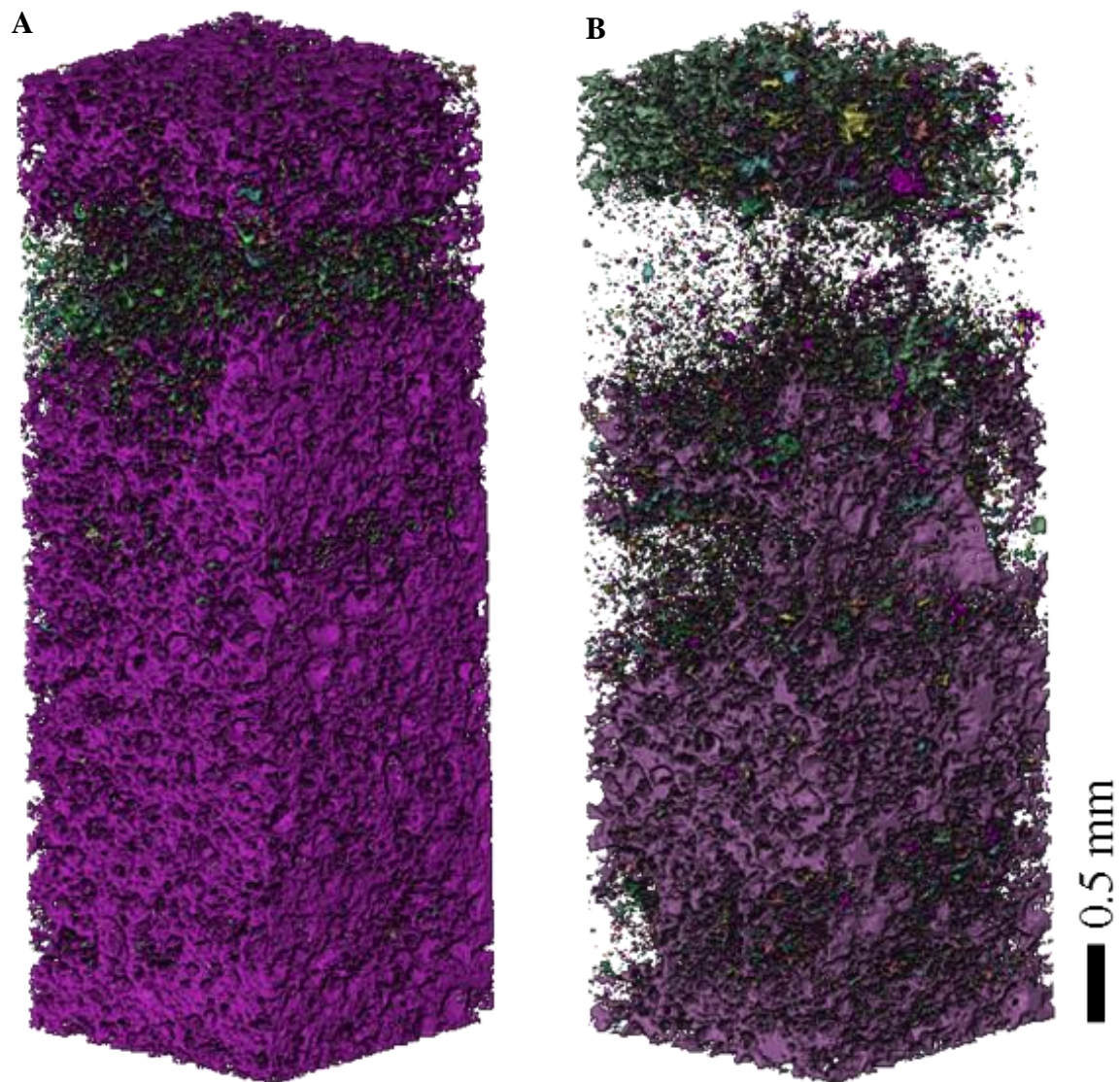


Figure 5.10: Cement and porosity connectivity UT02. Pores that are connected are coloured in a single colour. A) Connected cement. Most of the cement in the host rock is connected. B) Connected porosity. Porosity is connected in the host sandstone however, in the deformation band and the pores are isolated.

Chapter 5 - Deformation bands

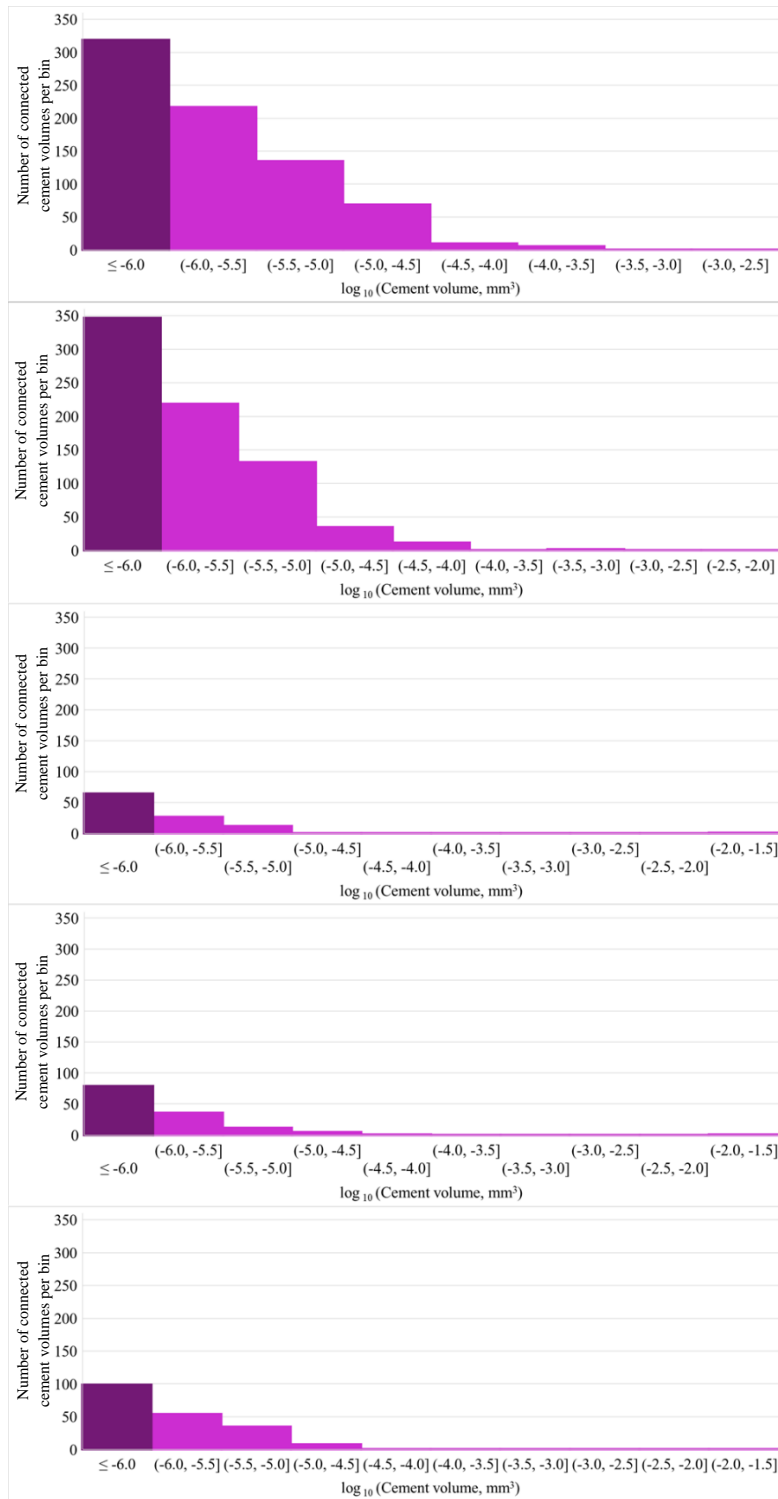


Figure 5.11: Histogram showing the number of connected cement volumes from five 0.125mm³ sub volumes in the UT02 deformation bands. The bin width is 0.5. The column on the left is an overflow bin for all cement volumes less than 0.000001 mm³. The largest connected cement volume was 0.027 mm³.

Chapter 5 - Deformation bands

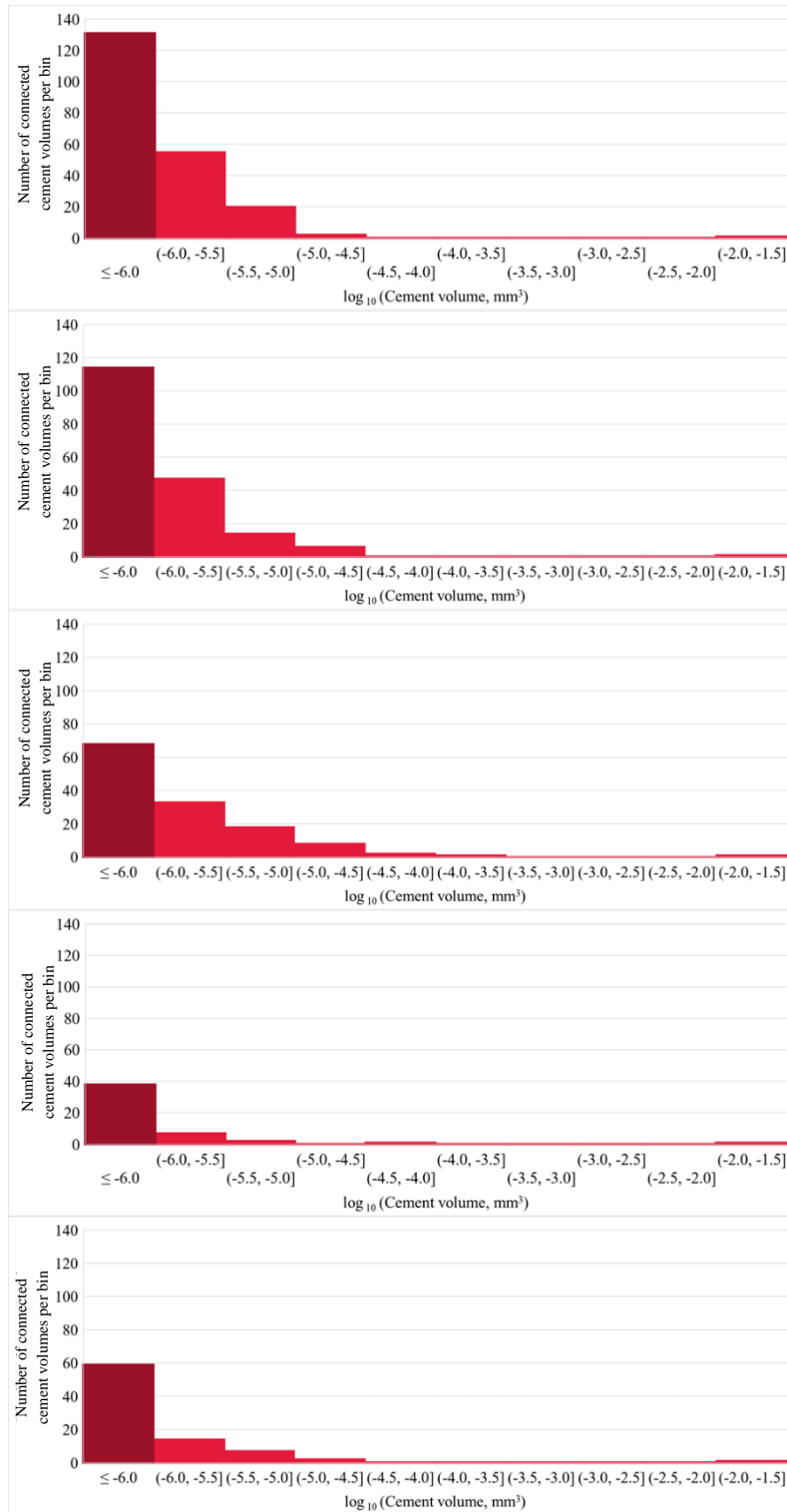


Figure 5.12:
Histogram showing the number of connected cement volumes from five 0.125 mm^3 sub volumes in the UT02 host rock. The bin width is 0.5. The column on the left is an overflow bin for all cement volumes less than 0.0000001 mm^3 . The largest connected cement volume was 0.023 mm^3 .

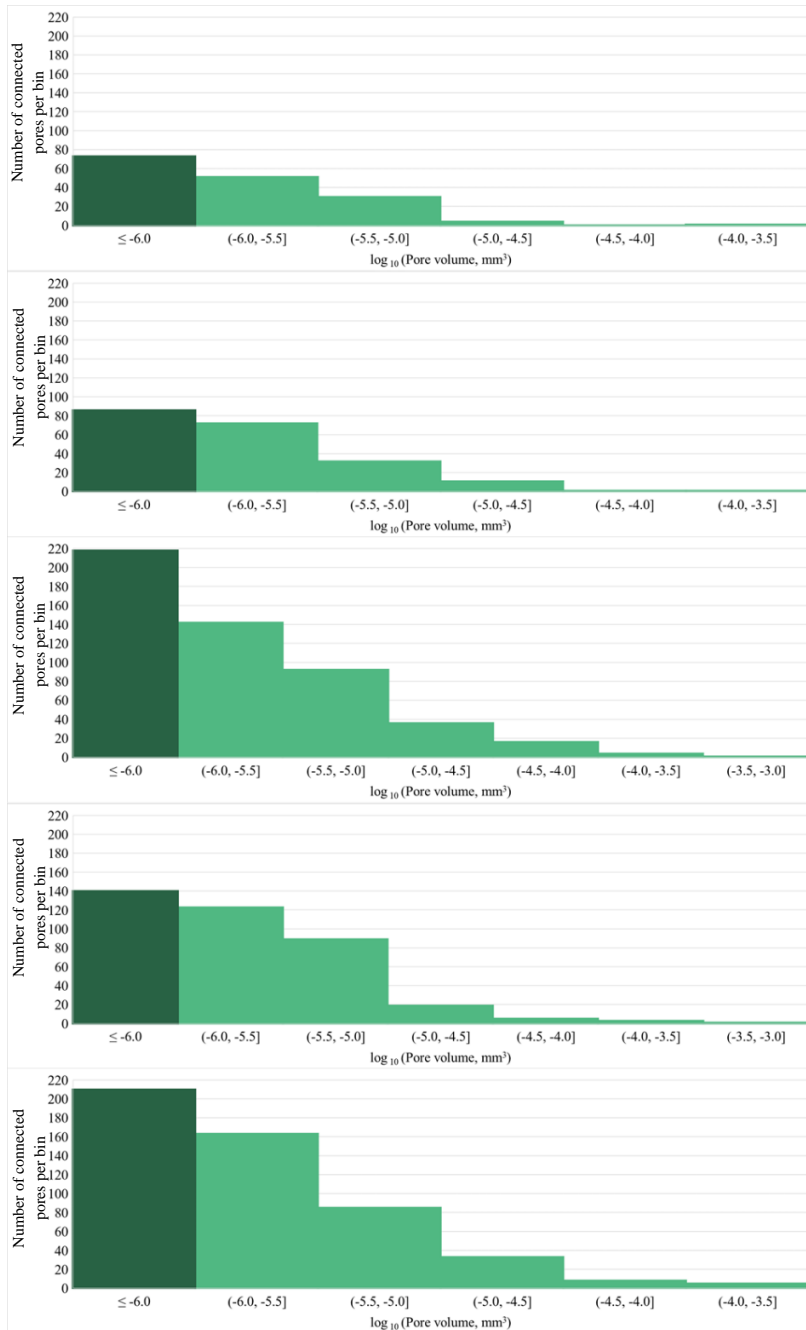


Figure 5.13: Histogram showing the number of connected pore volumes from five 0.125 mm³ sub volumes in the UT02 deformation bands. The bin width is 0.5. The column on the left is an overflow bin for all pore volumes less than 0.0000001 mm³. The largest connected pore volume was 0.00043 mm³.

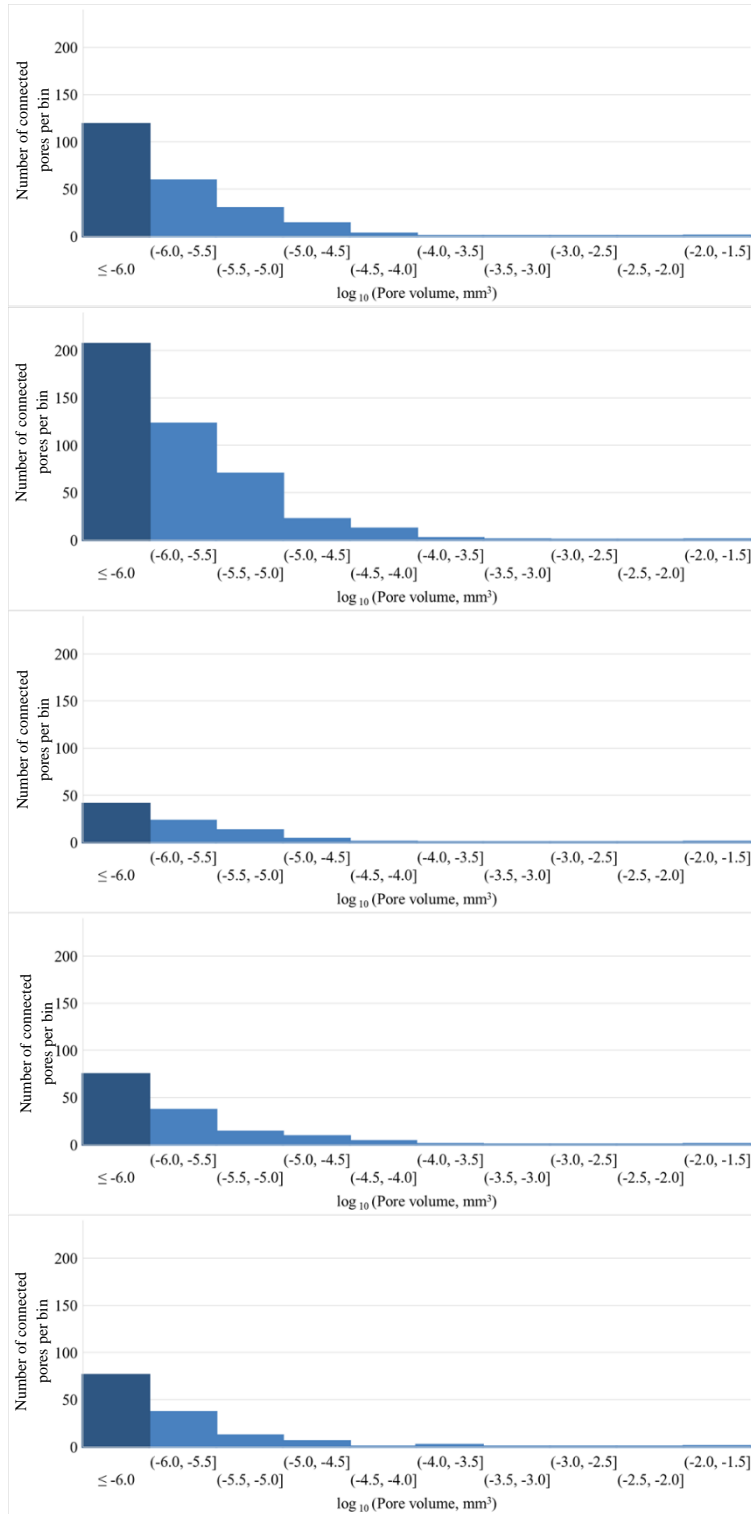


Figure 5.14: Histogram showing the number of connected pore volumes from five 0.125 mm³ sub volumes in the UT02 host rock. The bin width is 0.5. The column on the left is an overflow bin for all pore volumes less than 0.000001 mm³. The largest connected pore volume was 0.03 mm³.

5.3 Deformation bands in Etes

This section presents examples of deformation bands from the Etes field site in the Pannonian basin. The deformation bands are thought to have formed here during the Miocene (Beke et al. 2019).

5.3.1 Outcrop

The deformation bands at Etes are singular, less than 3cm wide, with the occasional conjugate set and are widely spread out across the 20m field site (Figure 5.15). Due to surrounding vegetation and construction it is difficult to determine the full extent of the deformation bands. The bedding around sample HN11 strikes NW-SE, parallel to the Etes graben.

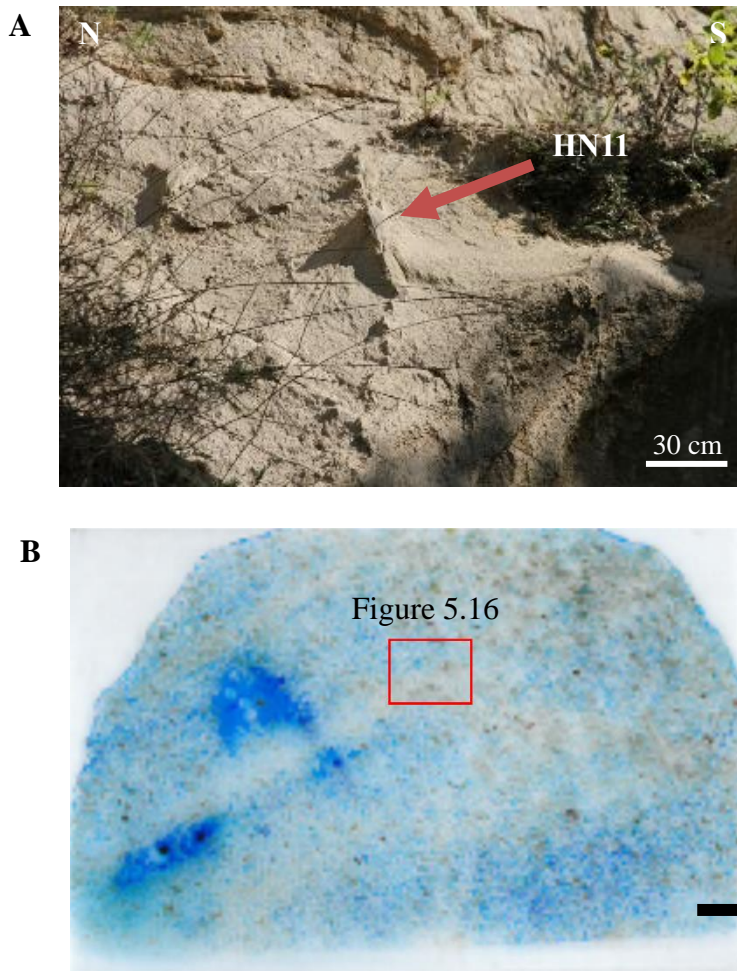


Figure 5.15: Summary of field site and sample from Etes, Hungary. A) Overview of outcrop with conjugate deformation bands present. B) Photograph of thin section slide for sample HN11 with locations of thin section marked. Scale bar is 5 mm.

5.3.2 Thin section analysis

Sample HN11 is a cataclastic deformation band which runs perpendicular to the Etes graben. One deformation band (approximately 3 mm wide) is visible in thin section (Figure 5.16). The grains are poorly cemented in the host rock by clays. Despite the limited cementation the sandstone is strong enough to be handled and subsampled without crumbling. In the quartz grains of the host rock transgranular fracture is most common and there is evidence of grain spalling. The mean grain length along the long and short axis is 197.4 μm and 140.2 μm respectively.

Inside the deformation band there is a shift to smaller grain length distributions along both the long and short axis (Figure 5.17). In the zone of cataclasis the mean long and short axes are 73.9 μm and 49.0 μm . This represents a mean reduction in grain size of 62.6 and 65.0% along the respective long and short axes. Due to the reduction in pore space and range of grain size present inside the deformation band HN11 can be subcategorised as an advanced cataclastic deformation band using the Beke et al. (2019) classification (see Chapter 2).

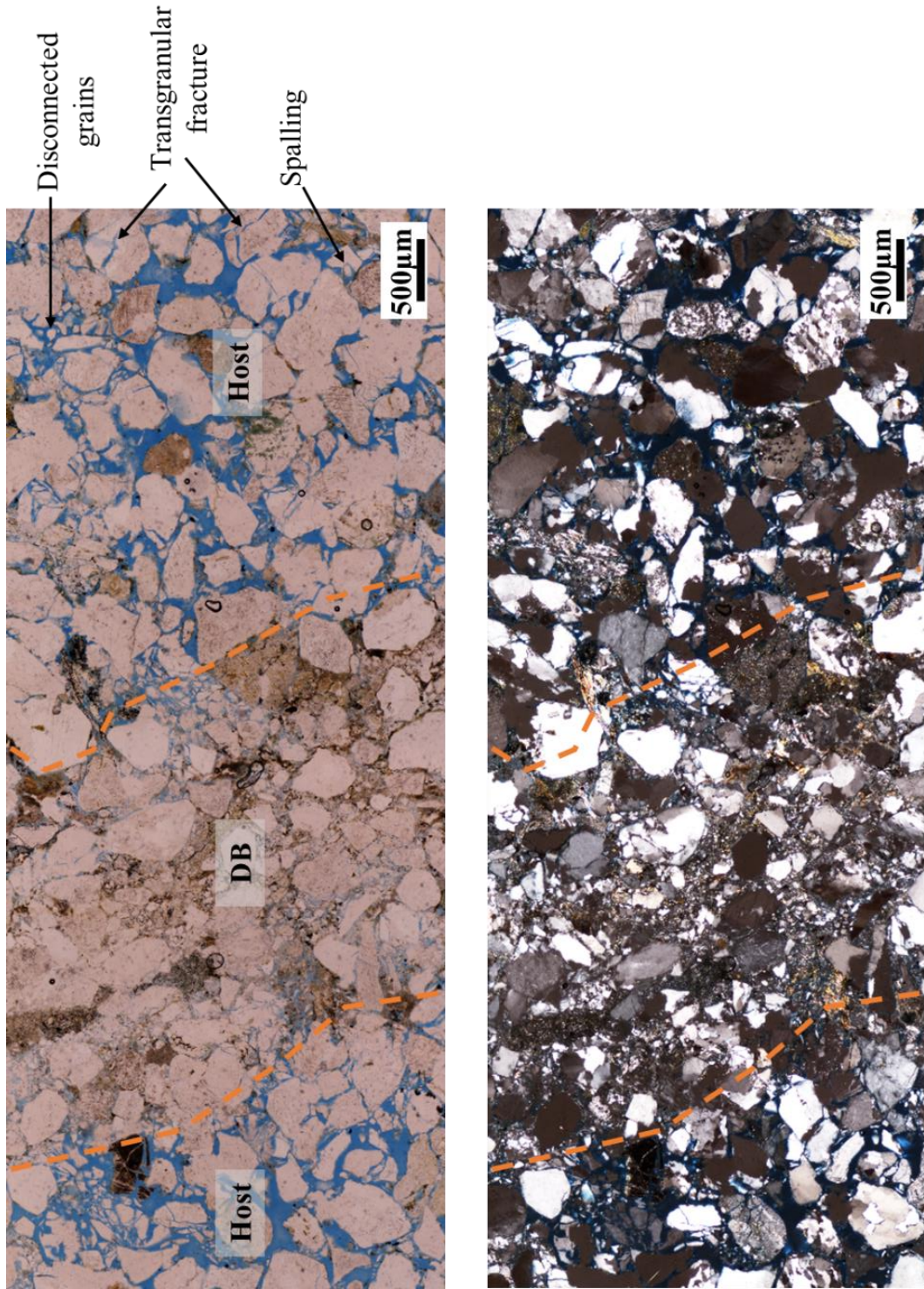


Figure 5.16: Thin section of deformation band in PPL and XPL of HN11

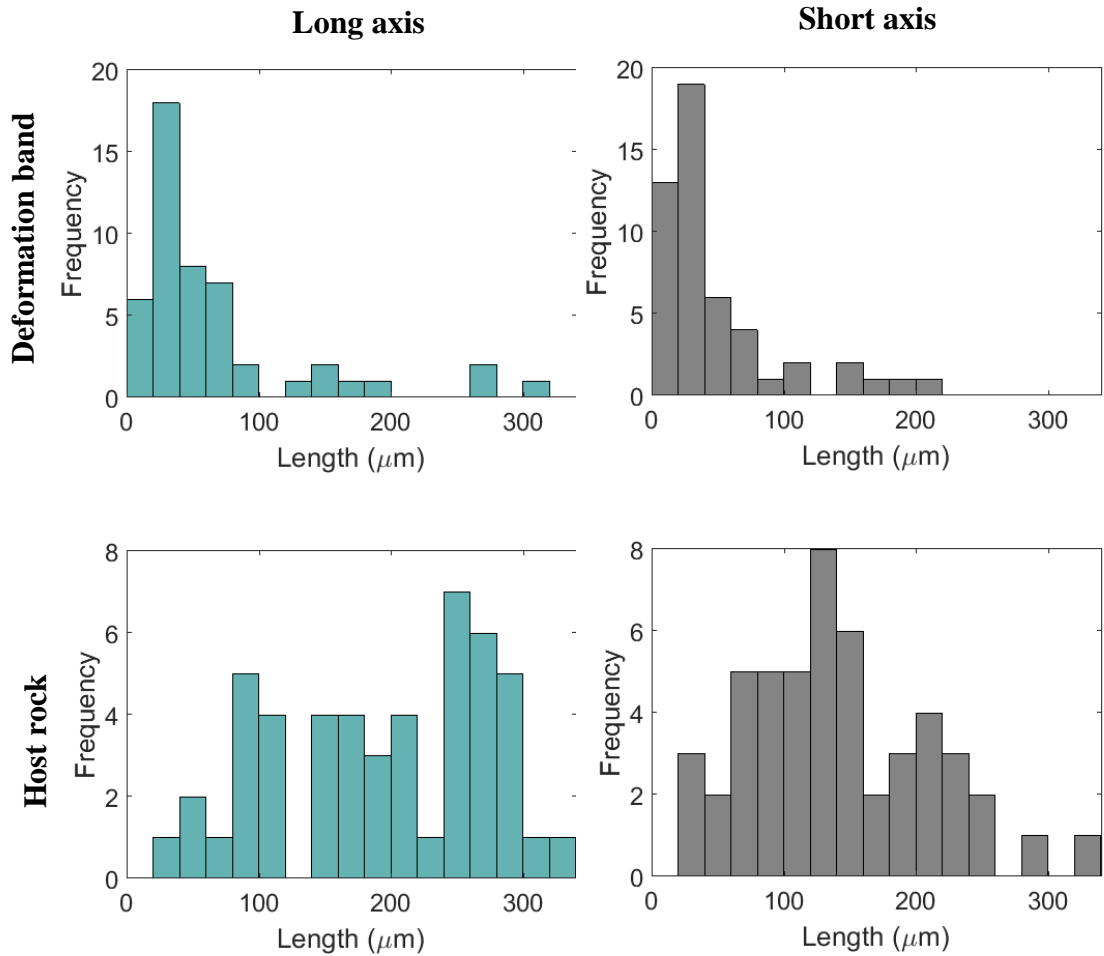


Figure 5.17: Sample HN11 grain length distributions along the long (blue graphs) and short axis (grey graphs) of fifty grains in both the host rock and the deformation band (see Figure 5.16).

5.3.3 Avizo® analysis

A long cubeoid sample of Sample HN11 was scanned in the X-CT at a resolution of 4.35 μm (Appendix 2). As before the 3D volume is segmented using the methodology outlined in Chapter 3. Figure 5.18 displays the three phases from Avizo® sectioning.

Figure 5.32 shows the results of segmentation of successive slices through sample HN11. The 3D volume is segmented using the methodology outlined in Chapter 3, and the values for percentage open pores, cement and grains are calculated for each of the 1248 slices through the sample.

Figure 5.20 shows the segmented phases in 3D present in the long (6 x 2 x2 mm) data subsample. By comparing both these figures the host rock (H1) and the deformation band (DB1) zone is identified. DB1 is approximately 2-2.5mm wide.

Figure 5.21 shows the cement (Fig 5.21 A) and porosity (Fig 5.21 B) connectivity. As before, if the cement pockets or pores are connected, then they are labelled with the same colour.

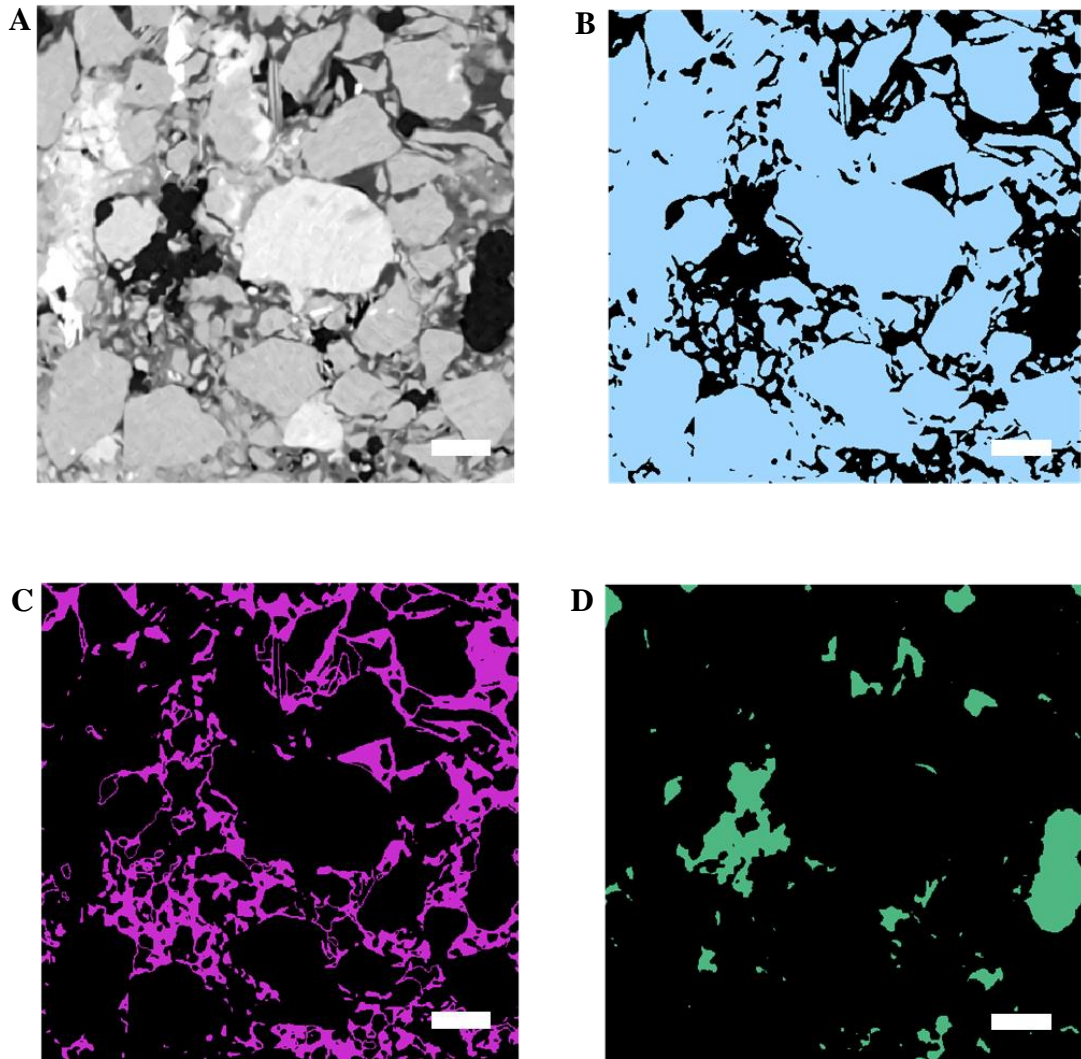


Figure 5.18: Three phases of HN11 segmented. A) original grey image, B) Grains phase, C) Cement phase and D) Pores phase. 0.25mm scale bar.

5.3.3.1 Grain and cement distribution

Analysis of 2D slices of HN11 shows the percentage of grains across the sample vary from 81.13% at the top of the sample to 67.19 % at the base (Figure 5.19). Table 5.3 displays the average segmentation results of the 2D slices from each of the labelled zones. There is a clear increase (18.20%) in the percentage of grains present inside DB1 in comparison to H1. This is due to cataclasis which is likely to have decreased cement and porosity inside DB1. The percentage of grains present inside DB 1 ranges from 64.27-90.79%.

Table 5.3 shows a reduction (36.36%) in the percentage of cement inside DB1 in comparison to H1. The percentage of cement inside DB1 ranges from 8.32 -24.41 %. As with samples UT02 the percentage of grains present is inversely correlated with the percentage of cement and pores.

In the 3D Avizo® segmentation the definition of the individual grains is lost inside the deformation band (Figure 5.20 B). Instead the grains appear as one mass in the deformation band, whereas in the host rock individual grains can be resolved.

The 3D cement phase is shown in Figure 5.20 C. Figure 5.21 shows the cement is connected throughout the host rock and across the deformation band. However, the cement becomes disconnected in some areas inside the deformation band.

The average percentage cement from the five 3D sub volumes is lower across the deformation band than in the host rock (Table 5.4). This is due to grain crushing taking place inside the deformation band.

Table 5.3: Average percentage of grains, cement and porosity for each 2D slices zone in HN11. DB = deformation band zone, H = host rock zone.

Zone	Z slice number	Grains (%)	Cement (%)	Porosity (%)
DB1	0 - 461	85.60	12.34	2.06
H1	461-1248	72.42	19.39	8.19

For each of the five 3D 0.125mm³ sub volumes histograms of the volumes of connected cement bodies in the deformation band (Figure 5.22) and host rock (Figure 5.23) are displayed. The linked cement volumes in the host rock range from 8.25x10⁻⁸ – 3.62x10⁻² mm³ with a median of 4.95x10⁻⁷ mm³. Whereas the linked cement volumes in the deformation band range from 8.25x10⁻⁸ – 2.13x10⁻² mm³ with a median of 5.77x10⁻⁷ mm³. This shows that the deformation band has the largest range and median of linked cement volumes.

5.3.3.2 Distribution of pore space

In the 2D slices the porosity present ranges from 0.60-17.34%. The average porosity inside DB 1 is 2.06%. Meanwhile the average host rock porosity is 8.19%.

In the 3D Avizo® connectivity image (Figure 5.21B) most of the pores in the sample are disconnected and there is a noticeable reduction in the pore size inside DB 1. This is confirmed with results from the 3D sub volumes where the porosity in the host rock has a calculated average 10.55% and the deformation band has an average porosity of 1.4% (Table 5.4).

Table 5.4: Percentage of grains, cement and porosity from HN11 0.125mm³ sub volumes inside the deformation band and the host rock.

0.125 mm ³ sub volumes	Deformation band			Host		
	Grains (%)	Cement (%)	Porosity (%)	Grains (%)	Cement (%)	Porosity (%)
1	80.88	14.96	4.17	73.38	17.34	9.28
2	93.13	6.49	0.38	68.68	21.47	9.85
3	94.30	4.97	0.72	72.58	17.69	9.73
4	92.51	7.09	0.41	76.91	16.07	7.02
5	81.74	16.95	1.31	55.80	27.33	16.87
Average	88.51	10.09	1.40	69.47	19.98	10.55

Chapter 5 - Deformation bands

For each of the five 3D 0.125mm^3 sub volumes histograms of the volumes of connected pores in the deformation band (Figure 5.24) and host rock (Figure 5.25) are displayed. The linked pores in the host rock range from 8.25×10^{-8} – 2.12×10^{-2} mm^3 with a median of 4.95×10^{-7} mm^3 . Whereas the linked cement volumes in the deformation band range from 8.25×10^{-8} – 4.26×10^{-3} mm^3 with a median of 5.77×10^{-7} mm^3 . This shows that the host rock has the largest range but the smallest median of linked pores volumes. A possible reason for this is the poor image resolution inside the deformation bands.

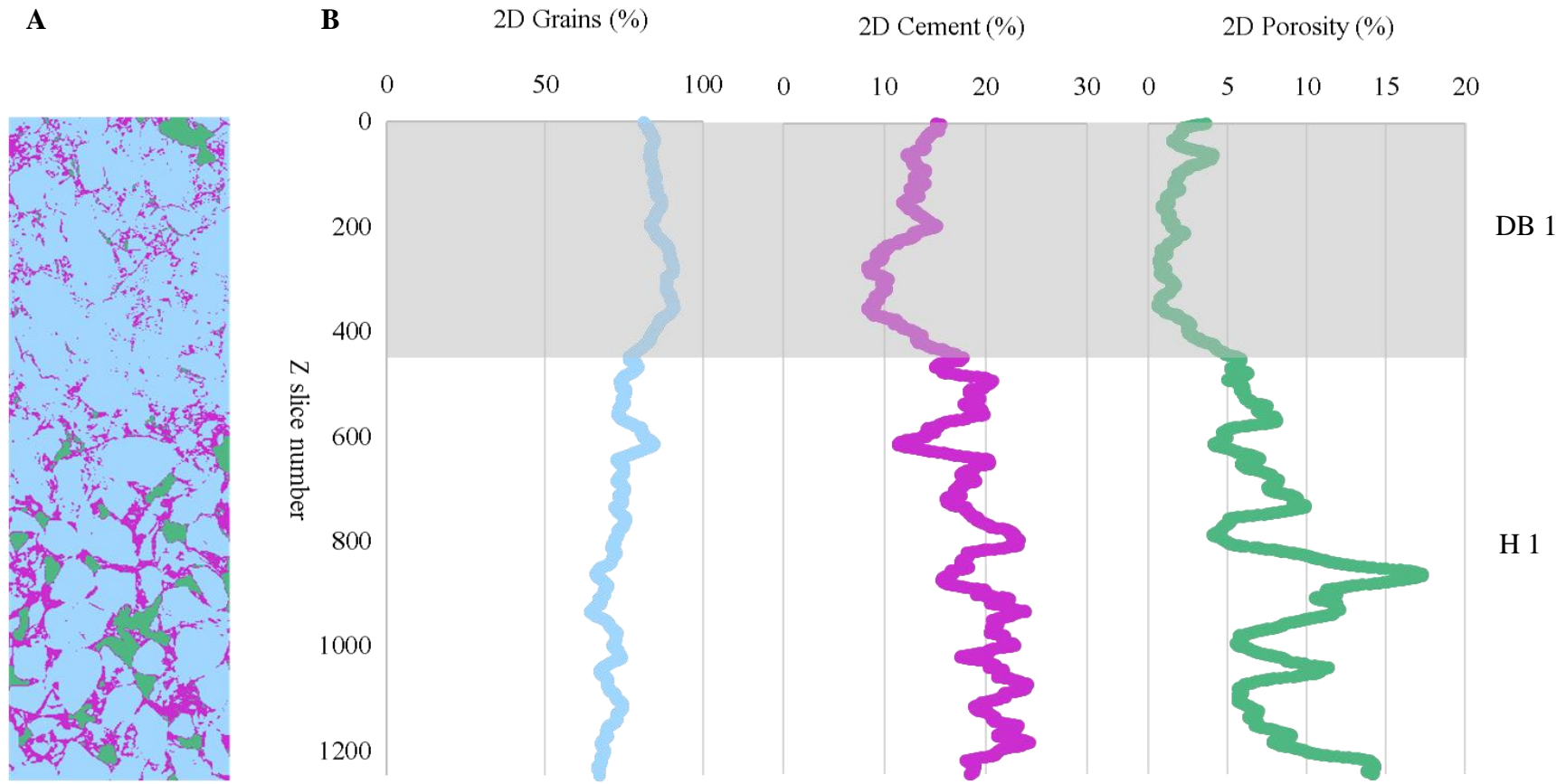


Figure 5.19: A) 2D vertical slice through a 6x2x2mm sub-sample of HN11: grain (blue), cement (purple) and porosity (green) percentage. B) Corresponding values of percentage grains, cement and porosity percentage for each horizontal slice along the z axis of the subsample. The location of the deformation band is highlighted in grey. There is an overall increase in the average number of grains present inside DB 1. The average cement is lower inside DB 1 (12.34%) than in H1 (19.39%).

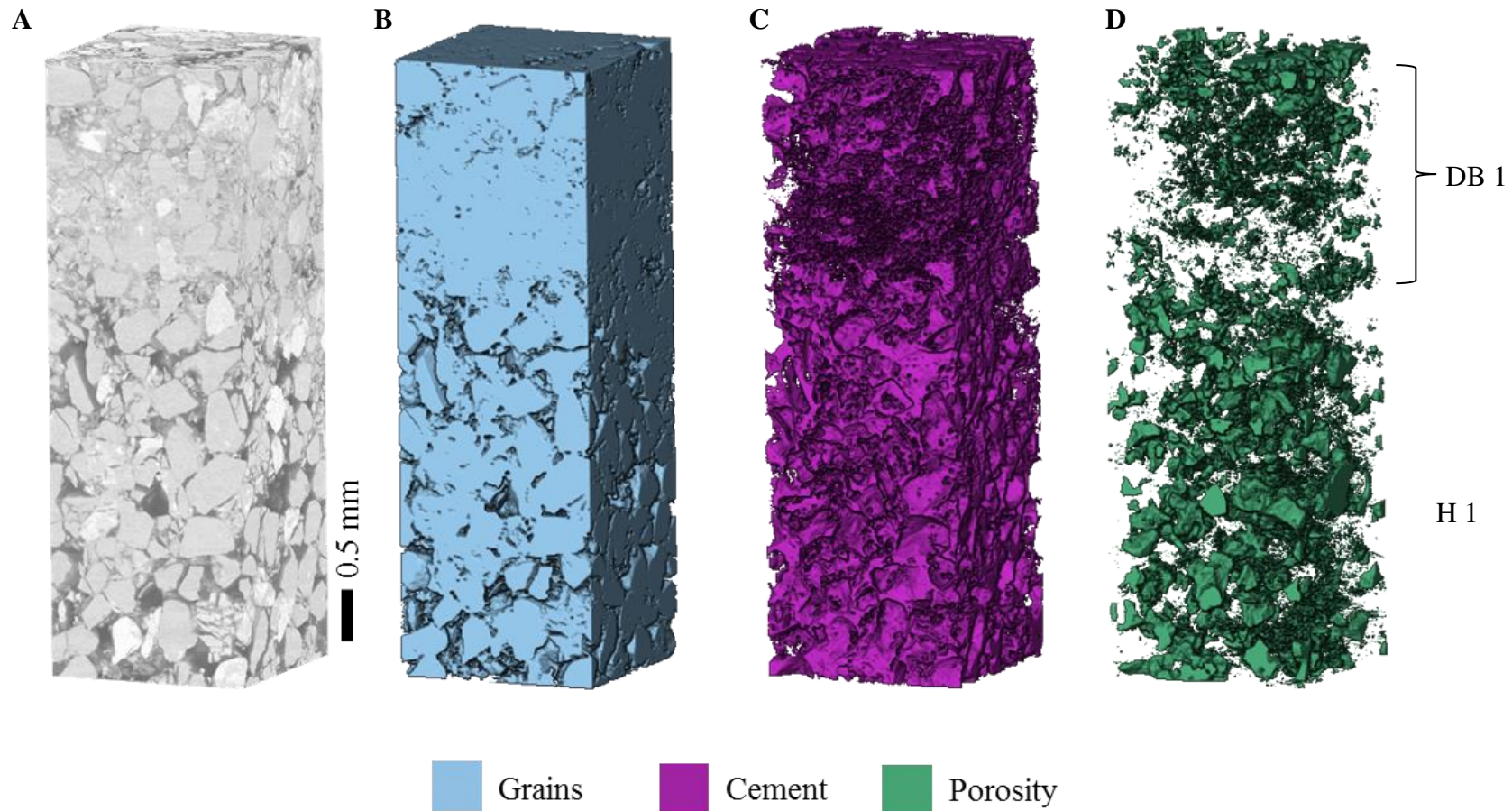
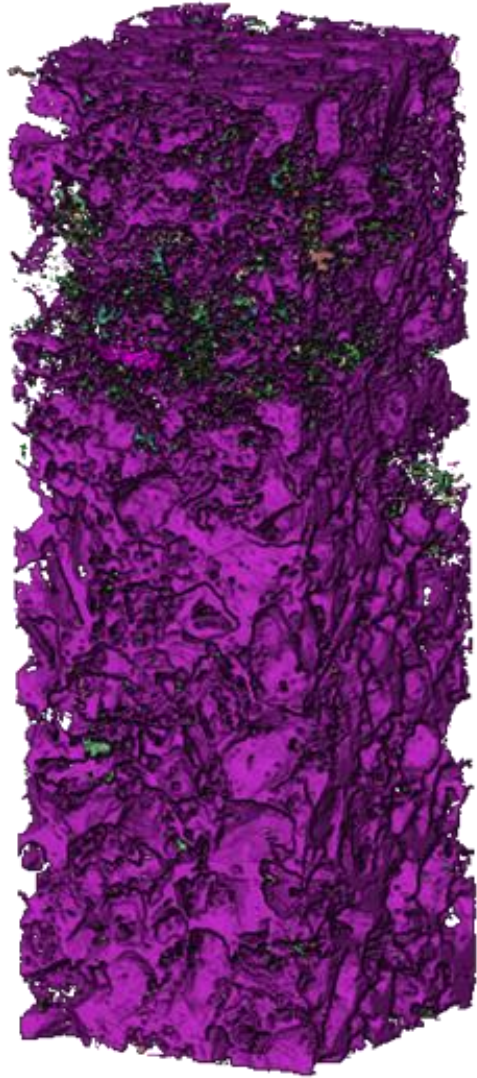
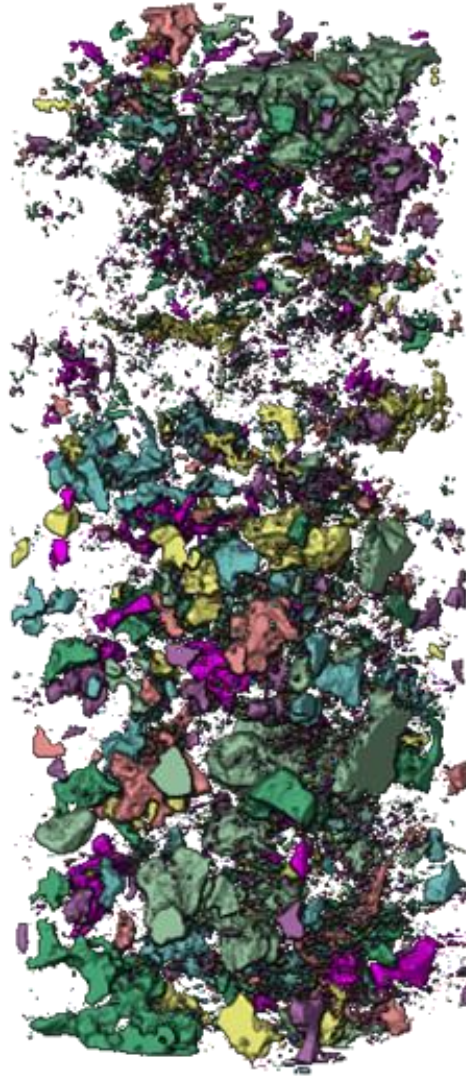


Figure 5.20: Sample HN11 full volume segmented in Avizo[®]. A) Original grey scale 3D image. B) Grains segmented image. The grains segment is 77.07% of the total volume. C) Cement segmented image. The cement segment is 16.79% of the total volume. D) Porosity segmented image. The porosity segment is 6.15% of the total volume.

A



B



0.5 mm

Figure 5.21: Cement and porosity connectivity A) Connected cement. The cement in the host rock is connected but is disconnected by the deformation band. B) Connected porosity. Porosity is predominantly unconnected across the whole sample.

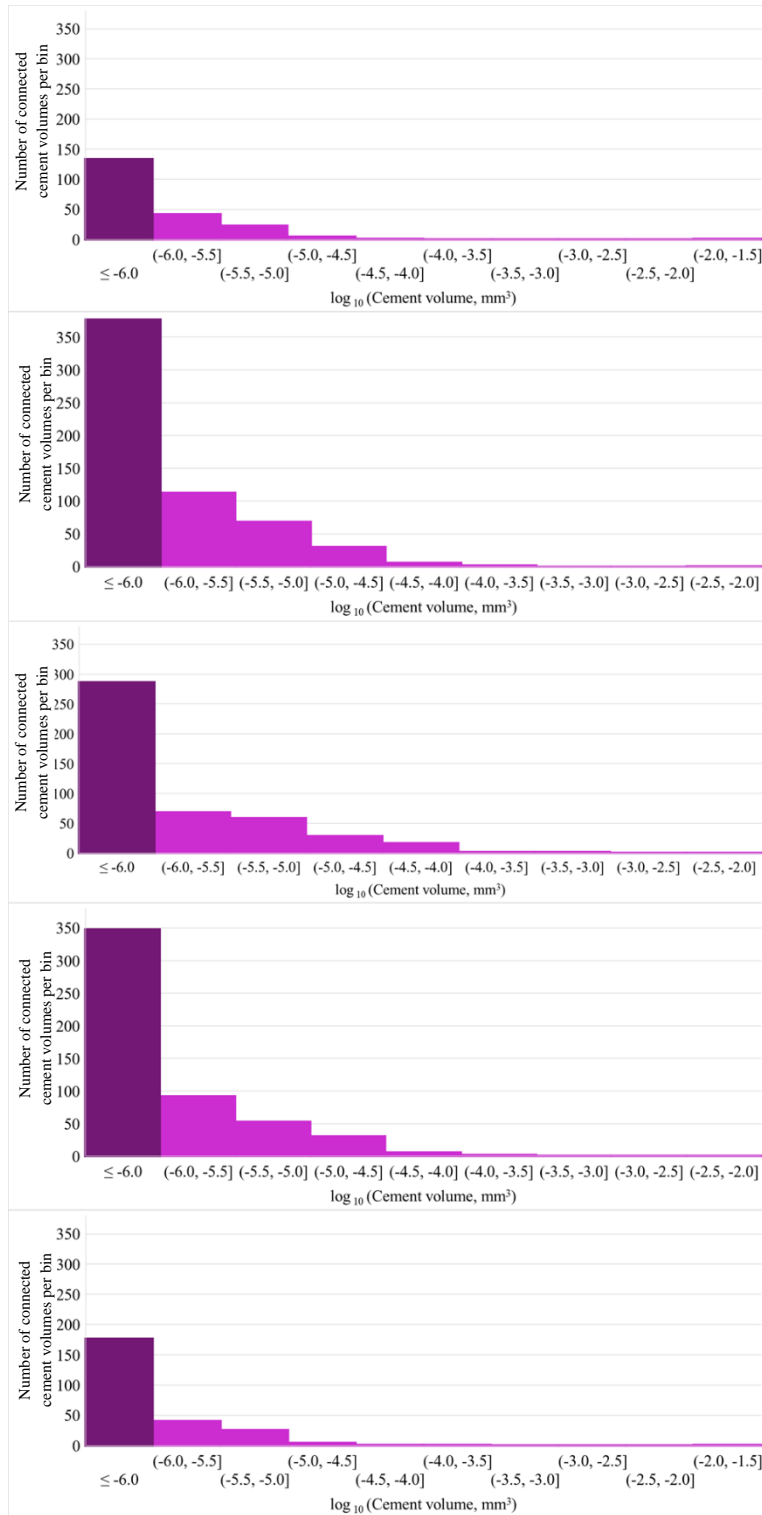


Figure 5.22: Histogram showing the number of connected cement volumes from five 0.125mm³ sub volumes in the HN11 deformation bands. The bin width is 0.5. The column on the left is an overflow bin for all cement volumes less than 0.000001 mm³. The largest connected cement volume was 0.021 mm³.

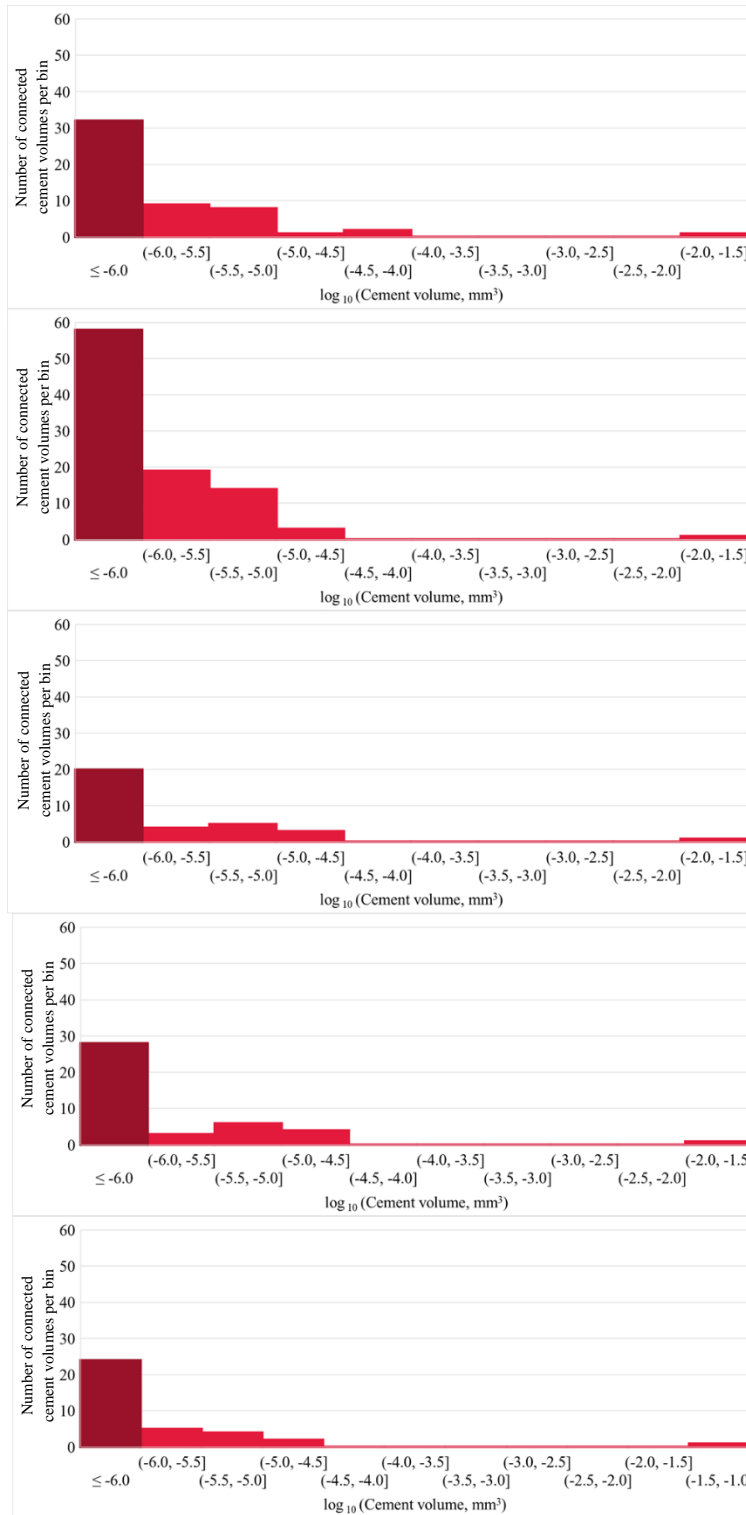


Figure 5.23: Histogram showing the number of connected cement volumes from five 0.125mm³ sub volumes in the HN11 host rock. The bin width is 0.5. The column on the left is an overflow bin for all cement volumes less than 0.000001 mm³. The largest connected cement volume was 0.036 mm³.

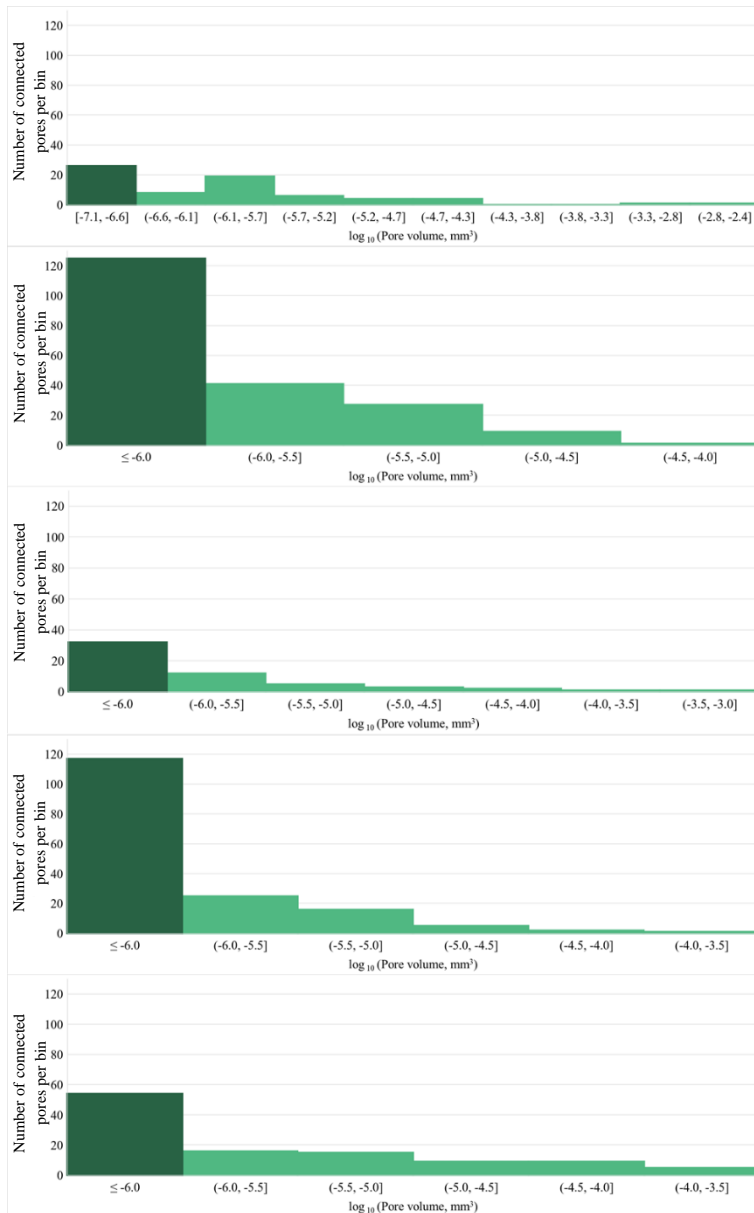


Figure 5.24: Histogram showing the number of connected pore volumes from five 0.125 mm³ sub volumes in the HN11 deformation bands. The bin width is 0.5. The column on the left is an overflow bin for all pore volumes less than 0.0000001 mm³. The largest connected pore volume was 0.0043 mm³.

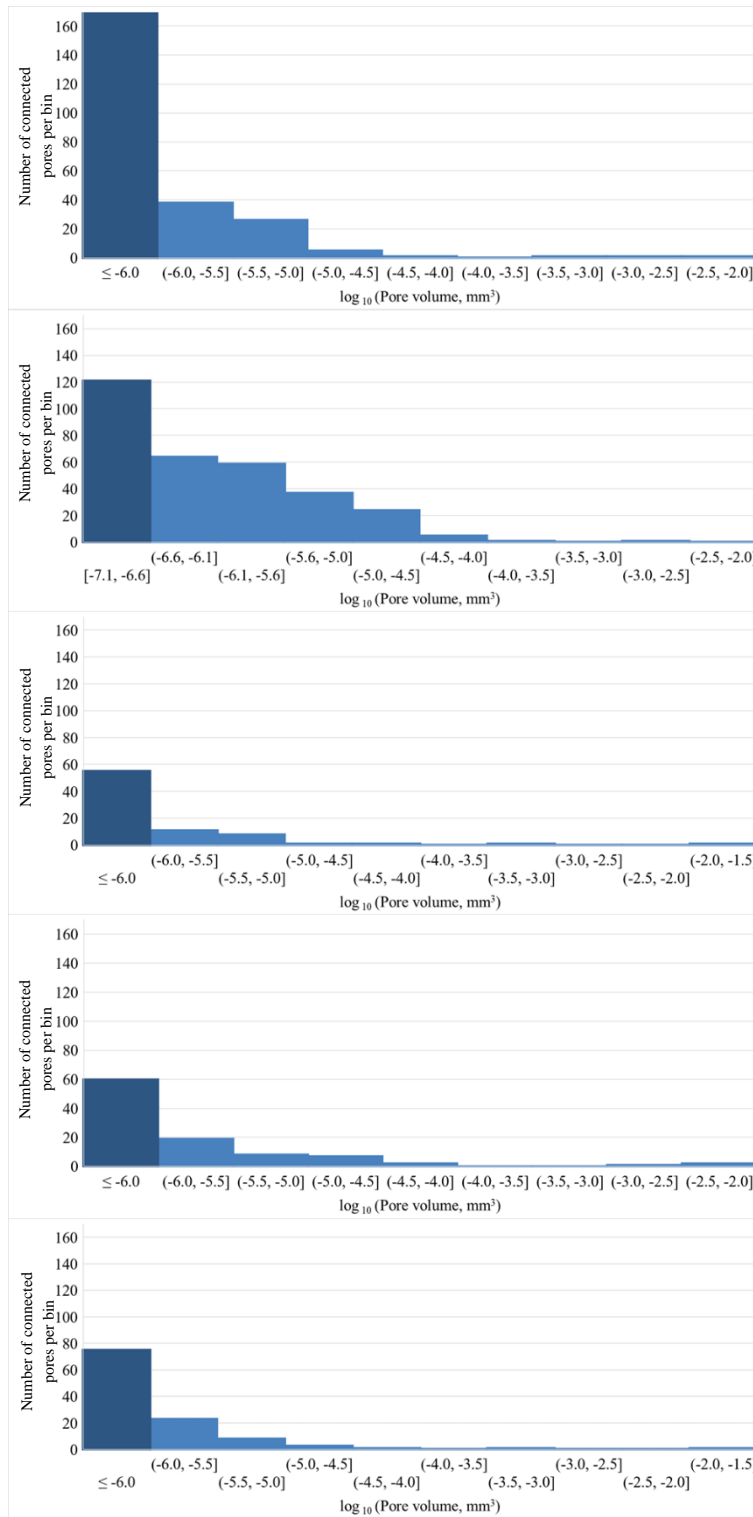


Figure 5.25: Histogram showing the number of connected pore volumes from five 0.125 mm³ sub volumes in the HN11 host rock. The bin width is 0.5. The column on the left is an overflow bin for all pore volumes less than 0.000001 mm³. The largest connected pore volume was 0.021 mm³.

5.4 Deformation bands in Arran

Previous deformation band fieldwork at Merkland Point is described by Bright (2006). The structure of these deformation bands replicates those found in the Entrada and Navajo formations in Utah (Aydin & Johnson 1978). In the deformation bands we see evidence of step over structures (Figure 5.26A) and lozenge shape zones of accumulated strain (Figure 5.26B).

The cataclastic deformation bands at Merkland Point can be split into two based upon visual inspection. The first of these are 0.7 cm wide by 10's of metres long, individual, N-S trending sub parallel bands. These offset < 10 cm wide deformation band zones (Figure 5.26C). The offsets displayed are a maximum of 20 cm. The second set of deformation bands are less than 1 cm in width and display evidence of lozenge shapes (Figure 5.26 B).

5.4.1 Outcrop

In Figure 5.26 there is evidence of the wider deformation bands offsetting the single bands. This therefore suggests that the narrow deformation bands were formed first, and the wider deformation band was formed during a second phase of deformation. A possible explanation for both the width of these deformation bands and the timing is that the older, narrower deformation bands were formed first at deeper depths in the earth where confining pressures are higher and therefore restricted the width of the deformed grain zone. If this was the case the wider deformation bands formed subsequent to this, at lower confining pressures and crosscut the initial phase of narrow deformation bands.

5.4.2 Thin section analysis

Sample AR01 is an example of a cataclastic deformation band which runs perpendicular to the basaltic dykes and fault trend in the area. The wider deformation band is ~1.3cm wide and offsets a narrower 0.4 cm wide deformation band. The majority of the grains are in contact with another grain. The most common form of grain breakage in this thin section is transgranular fracture of the quartz grains. As with the other deformation examples there is also evidence of grain spalling.

In Figure 5.28 the deformation band has been split into 5 areas; DB1, Intermediate zone, DB2 Section 1, DB2 Section 2 and Host rock. A summary of the grain length

distributions along both long and short axis for fifty grains from each zone is show in Figure 5.29.

The host rock section is approximately 2.5mm wide and has an average grain size along the long and short axis of 143.3 and 103.4 μm .

DB1 is approximately 2 mm wide and consists of a partial view of a wider cataclastic deformation band and the average grain size along the long and short axis is 52.0 and 39.7 μm . This represents a mean reduction in grain size of 63.7 and 61.6% along the respective long and short axes. DB1 can be subcategorised as an advanced cataclastic deformation band (Beke et al. 2019) due to the significant reduction in grain size and pore space in comparison to the host rock.

The intermediate zone is 1.75 mm wide and an average grain length of 88.7 μm . DB 2 is approximately 2.5mm wide and is a cataclastic deformation band. DB 2 has been split up into two sections due to an area of increased porosity down the middle of the band.

To give the most accurate analysis of the deformation band the two sides of the deformation band were studied separately and called Section 1 and 2 respectively.

The mean grain length of DB2 Section 1 and Section 2 is 61.9 and 43.1 μm respectively. This represents a mean reduction in grain size of 56.8 and 58.3% along the respective long and short axes. Both sections in D2 can be subcategorised as an advanced cataclastic deformation band (Beke et al. 2019) due to the significant reduction in grain size and pore space.

The results from the grain length analysis show that there is a significant decrease across the both the deformation bands and the intermediate zones in comparison to the host rock. This therefore confirms the existence of the so-called intermediate zones whereby the grain lengths do not align with either those in the deformation band or in the host rock.

Underhill and Woodcock (1987) describe the composition of sandstone samples from nearby locations in Arran to contain Fe oxide and clay. Under the microscope it is

Chapter 5 - Deformation bands

clear to see the Fe oxide coating the quartz grains and forming wedge features between the grains (Figure 5.30). Therefore, Sample AR01 is a grain supported sandstone consisting primarily of quartz grains with Fe oxide grain coatings and clay between grains.

Chapter 5 - Deformation bands



Figure 5.26: Photos of deformation bands on Arran. A) < 1 cm wide deformation bands creating step structure. B) Within the thin (< 1 cm wide) deformation bands are thickened sections which create lozenge shapes- looks like a shear indicator/slip surface C) > 10 cm wide deformation zones. Evidence of a crosscutting relationship between narrow and wider deformation band. D) Anastomosing deformation bands.

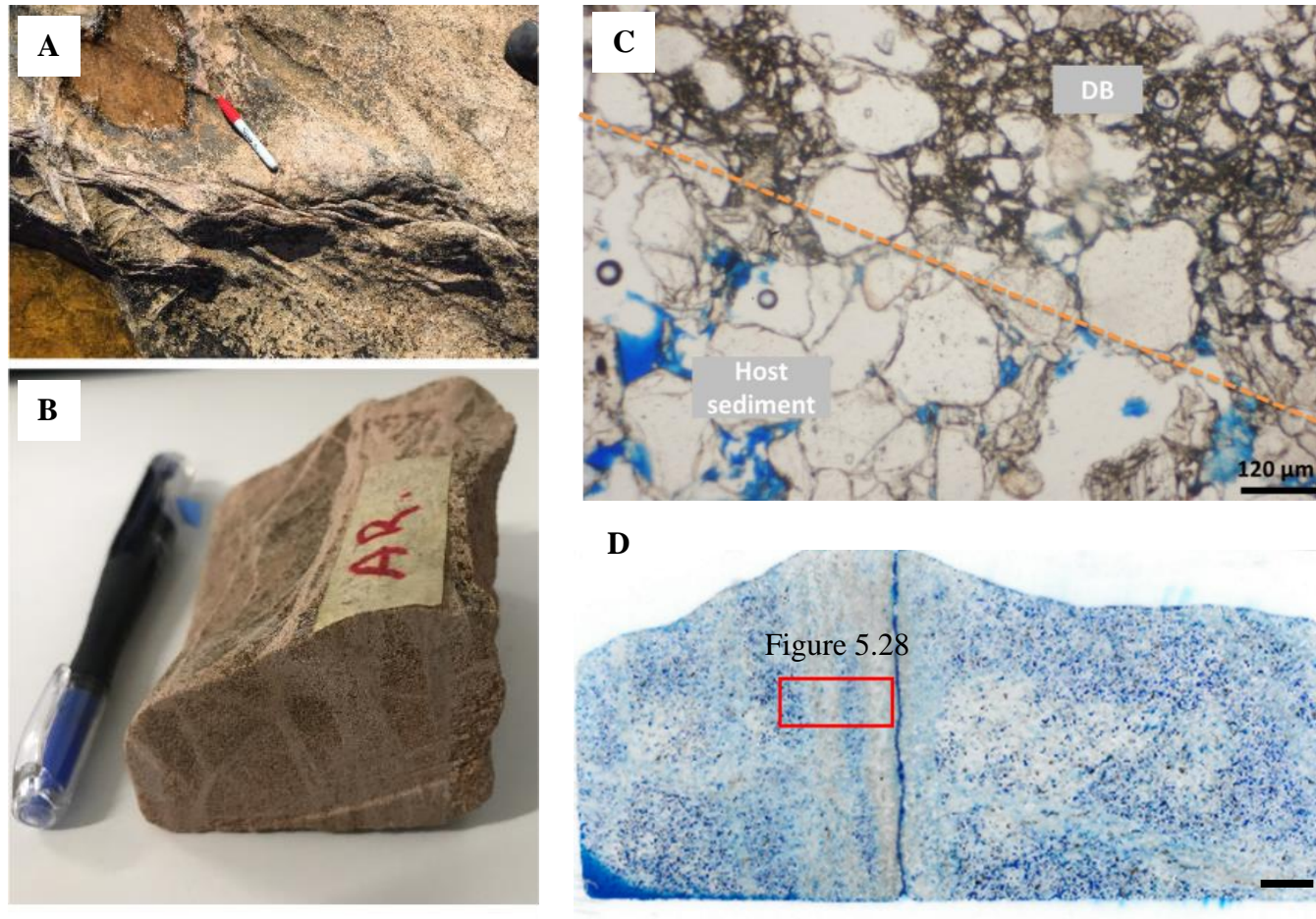


Figure 5.27: Arran deformation band sample AR01. A) Field sample site. B) Sample for thin sectioning. C) Thin section displaying contact (dashed orange line) between deformation band and host sediment. D) Photograph of thin section slide for sample AR01 with locations of thin section marked. Scale bar is 5 mm.

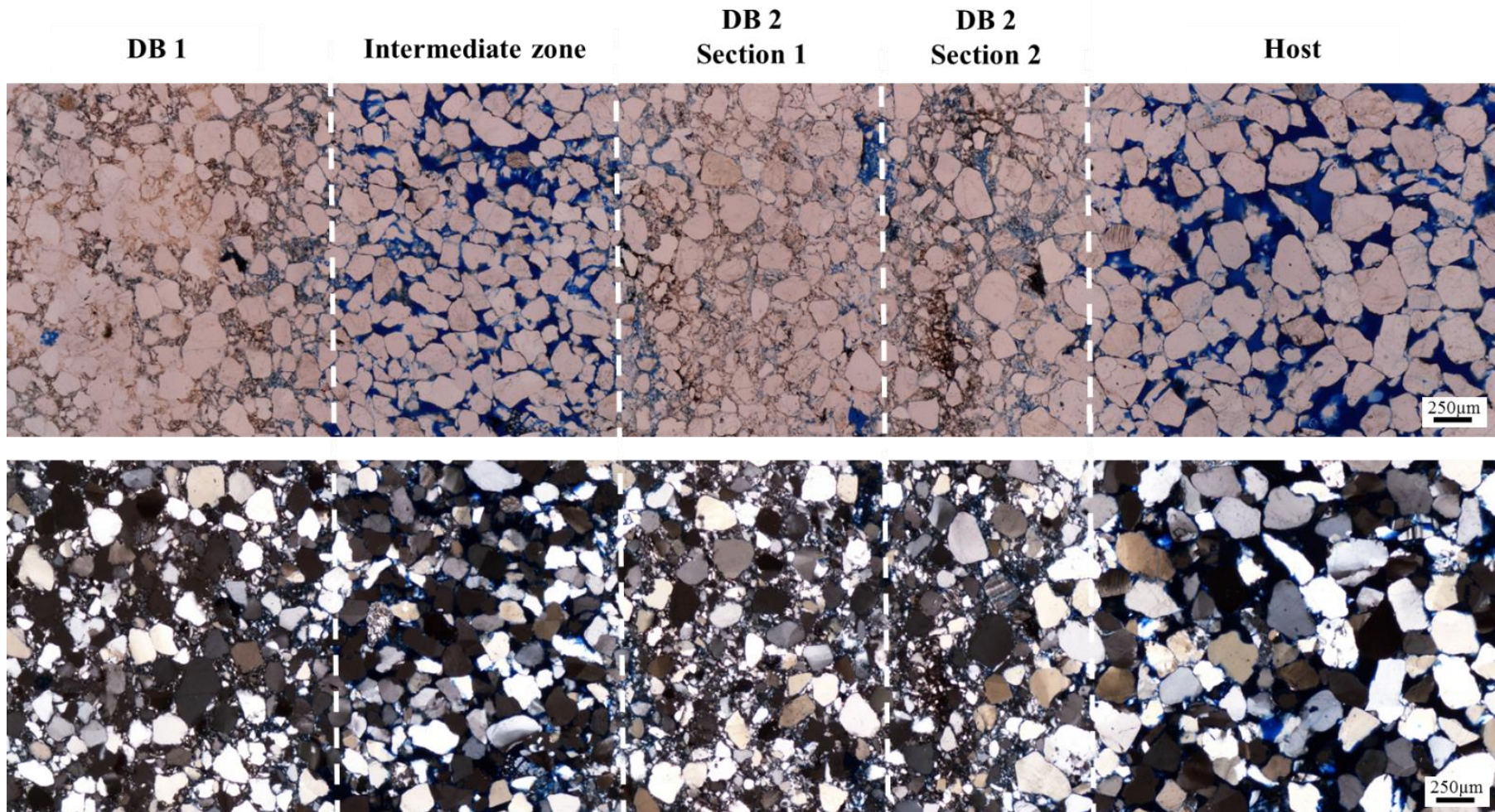


Figure 5.28: AR01 thin section in PPL and XPL. The thin section has been split up into five sections to reflect changes in grain size (see Figure 5.29).

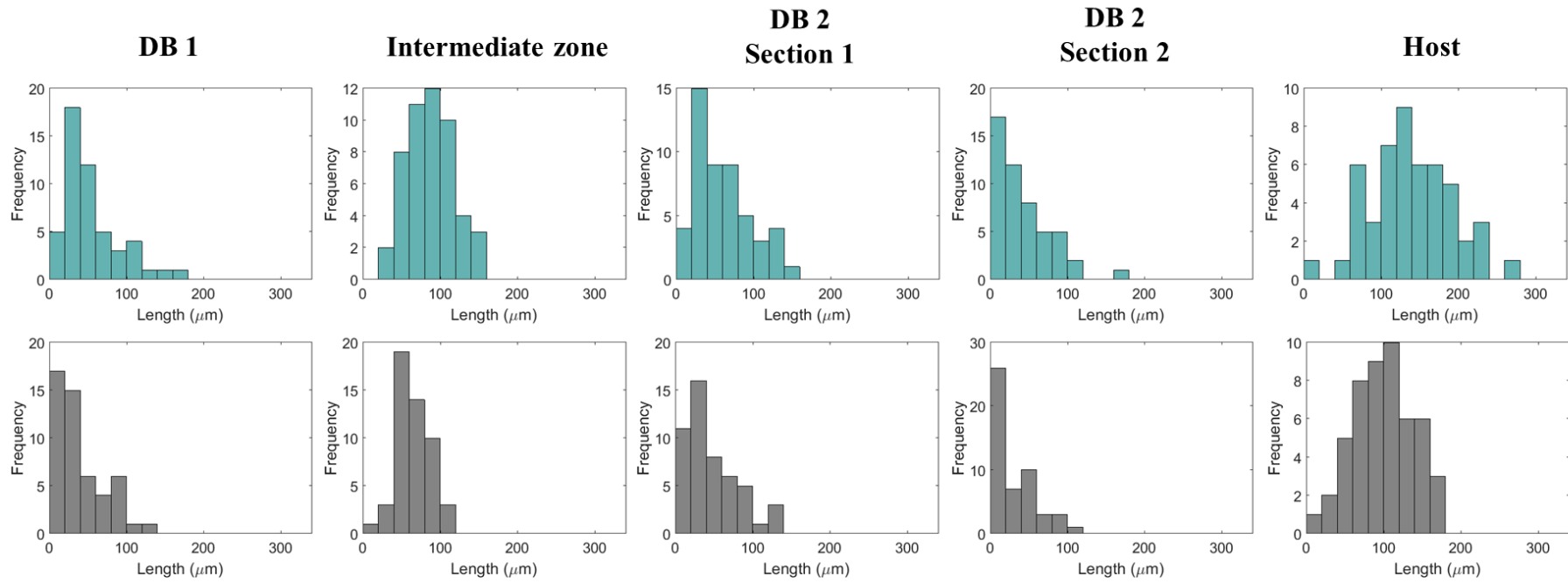


Figure 5.29: Sample AR01 grain length distributions along the long (blue graphs) and short axis (grey graphs) of fifty grains in each of the five areas shown in Figure 5.27.

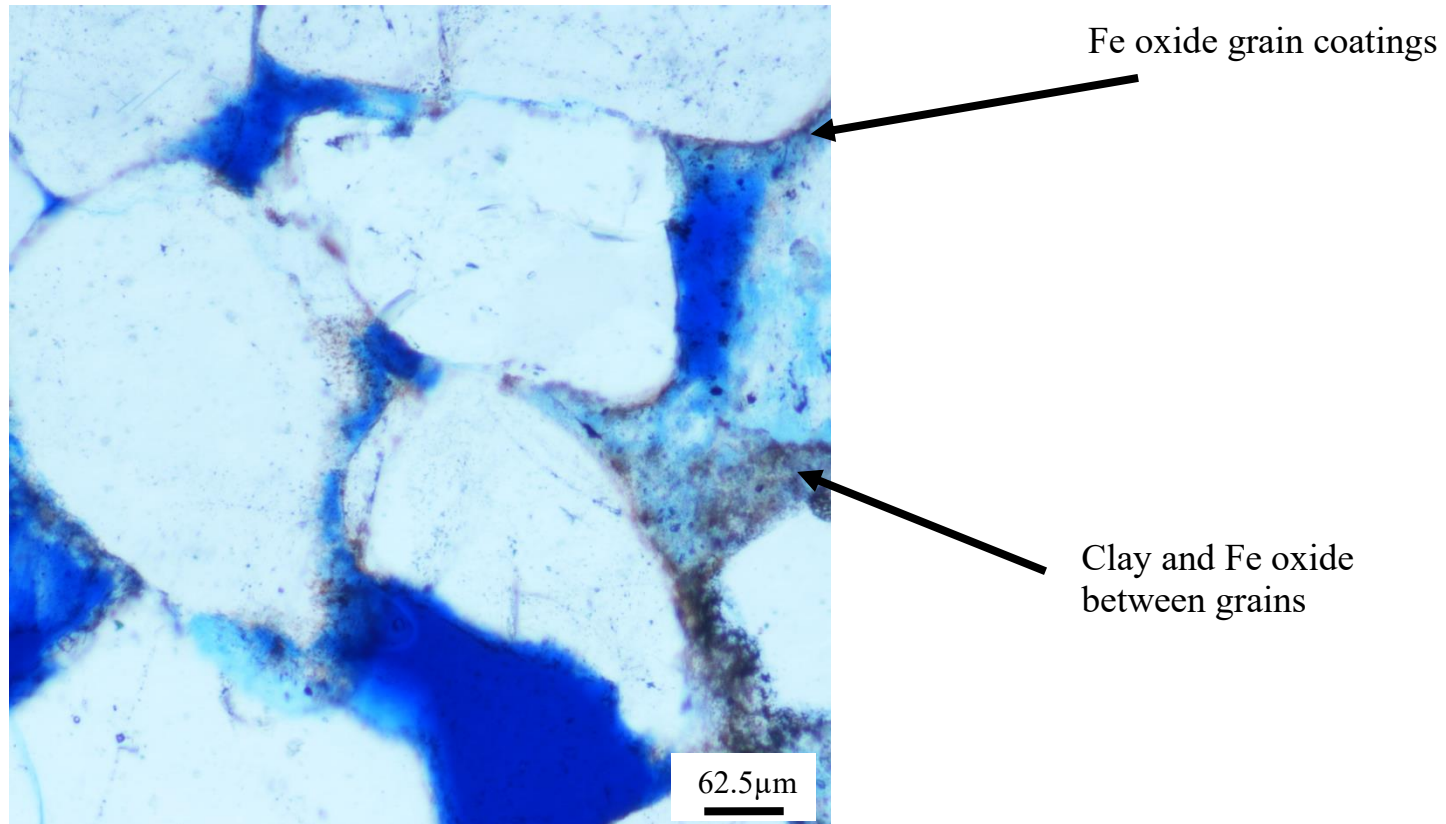


Figure 5.30: Fe oxide and clay coating grains of sample AR01.

5.4.3 Avizo® analysis

A long cuboid sample of Sample AR01 was scanned in the X-CT at a resolution of 5.41 μm (Appendix 2). Figure 5.31 displays the three phases from Avizo® sectioning.

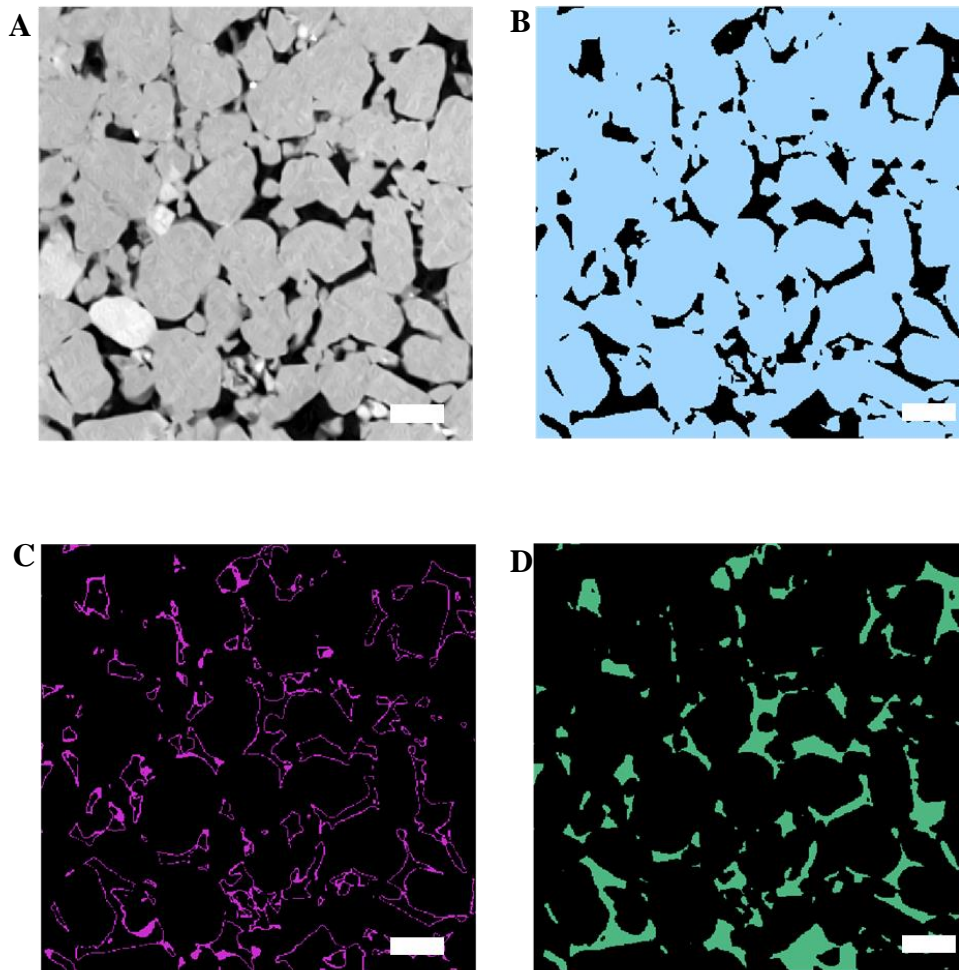


Figure 5.31: Three phases from AR01 segmentation A) original grey image, B) Grains phase, C) Cement phase and D) Pores phase. 0.25mm scale bar.

The 3D volume is segmented using the methodology outlined in Chapter 3, and the values for percentage open pores, cement and grains are calculated for each of the 1111 slices through the sample. Figure 5.32 shows the results of segmentation of successive slices through sample AR01.

Figure 5.33 displays each of the 3D segmented phases present in the long (6 x 2 x 2 mm) data subsample. From these segmented phases the distribution of cement and pore space in relation to the deformation band can be analysed.

By comparing both figures the host rock zones (H1 and H2) and the deformation band section (DB1) is identified (Figure 5.32). DB1 is approximately 2 mm wide and displays evidence of cataclasis.

Figure 5.34 shows the cement (Fig 5.34 A) and porosity (Fig 5.34 B) connectivity. As before if individual cement pockets or pores are connected, then they are labelled with the same colour.

5.4.3.1 Grain and cement distribution

Analysis of 2D slices of AR01 shows the percentage of grains across the sample vary from 81.47% at the top of the sample to 82.26 % at the base. Table 5.5 displays the average segmentation results of the 2D slices from each of the labelled zones. There is a slight increase (11.62%) in the percentage of grains present inside DB1 in comparison to H1. The percentage of grains present inside DB 1 ranges from 77.85-95.50%. This increase in percentage of grains and decrease of cement in the deformation band is similar to other localities in this study.

Table 5.5 shows a 27.16% reduction in the percentage of cement inside DB1 in comparison to H1. The percentage of cement inside DB1 ranges from 2.92 - 9.03 %. As with sample UT02, the percentage of grains present is inversely correlated with the percentage of cement and pores.

In the 3D Avizo® segmentation the definition of the individual grains is reduced inside the deformation band (Figure 5.33B) due to cataclasis taking place and poor resolution of the broken grains. In the host rock individual grains can be resolved.

The 3D cement phase is shown in Figure 5.33C. Figure 5.34 shows the cement is connected throughout the host rock and connects across the deformation band. However, the cement becomes disconnected inside the deformation band where smaller volumes of connected cement are identified.

Table 5.5: Average percentage of grains, cement and porosity for each 2D slices zone in AR01. DB = deformation band zone, H = host rock zone.

Zone	Z slice number	Grains (%)	Cement (%)	Porosity (%)
H 1	0 - 70	80.45	6.96	12.58
DB 1	71 - 543	89.80	5.07	5.14
H 2	544 -1111	81.41	6.70	11.89

For each of the five 3D 0.125mm³ sub volumes histograms of the volumes of connected cement bodies in the deformation band (Figure 5.35) and host rock (Figure 5.36) are displayed. The linked cement volumes in the host rock range from 3.16×10^{-7} - 1.55×10^{-2} mm³ with a median of 7.90×10^{-7} mm³. Whereas the linked cement volumes in the deformation band range from 3.16×10^{-7} – 6.55×10^{-3} mm³ with a median of 1.11×10^{-6} mm³. This shows that the host rock has the largest range but the smallest median of linked cement volumes.

5.4.3.2 Distribution of pore space

In the 2D slices the porosity is lowest in DB1 with an average of 5.14 % (Table 5.5). Meanwhile, the average porosity in zones H1 and H2 is host rock porosity was calculated at 12.58% and 11.89% respectively. This difference of 0.69% between the two host rock zones is very small and suggests the porosity across the host rock is consistent.

Table 5.6: Percentage of grains, cement and porosity from AR01 0.125mm³ sub volumes inside the deformation band and the host rock.

0.125 mm ³ sub volumes	Deformation band			Host		
	Grains (%)	Cement (%)	Porosity (%)	Grains (%)	Cement (%)	Porosity (%)
1	93.28	4.20	2.51	79.69	6.67	13.64
2	91.78	5.16	3.06	80.53	5.71	13.76
3	93.15	4.65	2.20	78.32	8.32	13.37
4	94.07	4.20	1.73	70.84	12.24	16.92
5	97.37	2.11	0.51	82.47	5.08	12.46
Average	93.93	4.06	2.00	78.37	7.60	14.03

In the 3D segmentation (Figure 5.34B) the porosity is split into three areas: above the deformation band, inside the deformation band and below the deformation band. The pores in H1 zone, above the deformation band (light purple), are connected. This is then followed by the DB1 which is filled with predominantly unconnected pores. The final pore zone (H2) is at the base of the deformation band (green zone). Although the porosity inside H2 is connected the zone remains unconnected from H1. This therefore makes AR01 unlike the other examples of cataclastic deformation bands because the porosity is not connected across the deformation band.

The average porosity from the five 3D sub volumes is lower across the deformation bands (an average porosity of 2.00%) than in the host rock (an average porosity of 14.03%) (Table 5.6).

Chapter 5 - Deformation bands

For each of the five 3D 0.125mm³ sub volumes histograms of the volumes of connected pores in the deformation band (Figure 5.37) and host rock (Figure 5.38) are displayed. The linked pores in the host rock range from 3.16×10^{-7} – 2.15×10^{-2} mm³ with a median of 9.48×10^{-7} mm³. Whereas the linked cement volumes in the deformation band range from 3.16×10^{-7} – 1.63×10^{-3} mm³ with a median of 1.26×10^{-6} mm³. This shows that the host rock has the largest range but the smallest median of linked pores volumes.

In order to sense check the X-CT porosity results a sample (~ 3 x 3 x 10 cm in size) of AR01 was tested using vacuum saturation. The sample was a mixture of deformation bands and host rock. After measuring the initial dry mass of the sample, it was saturated in a vacuum chamber with deionised H₂O. The volume was determined by immersing the sample in de-aired water and the porosity was calculated. The results showed that sample AR01 had 22% porosity. This is double the result obtained from the X-CT analysis which showed the sample to have 9.06% porosity (Figure 5.33). One possible reason for this difference is that the sample measured by vacuum saturation was not the same as the sample scanned in the X-CT. For an accurate comparison the same sample should be used for vacuum saturation and X-CT analysis.

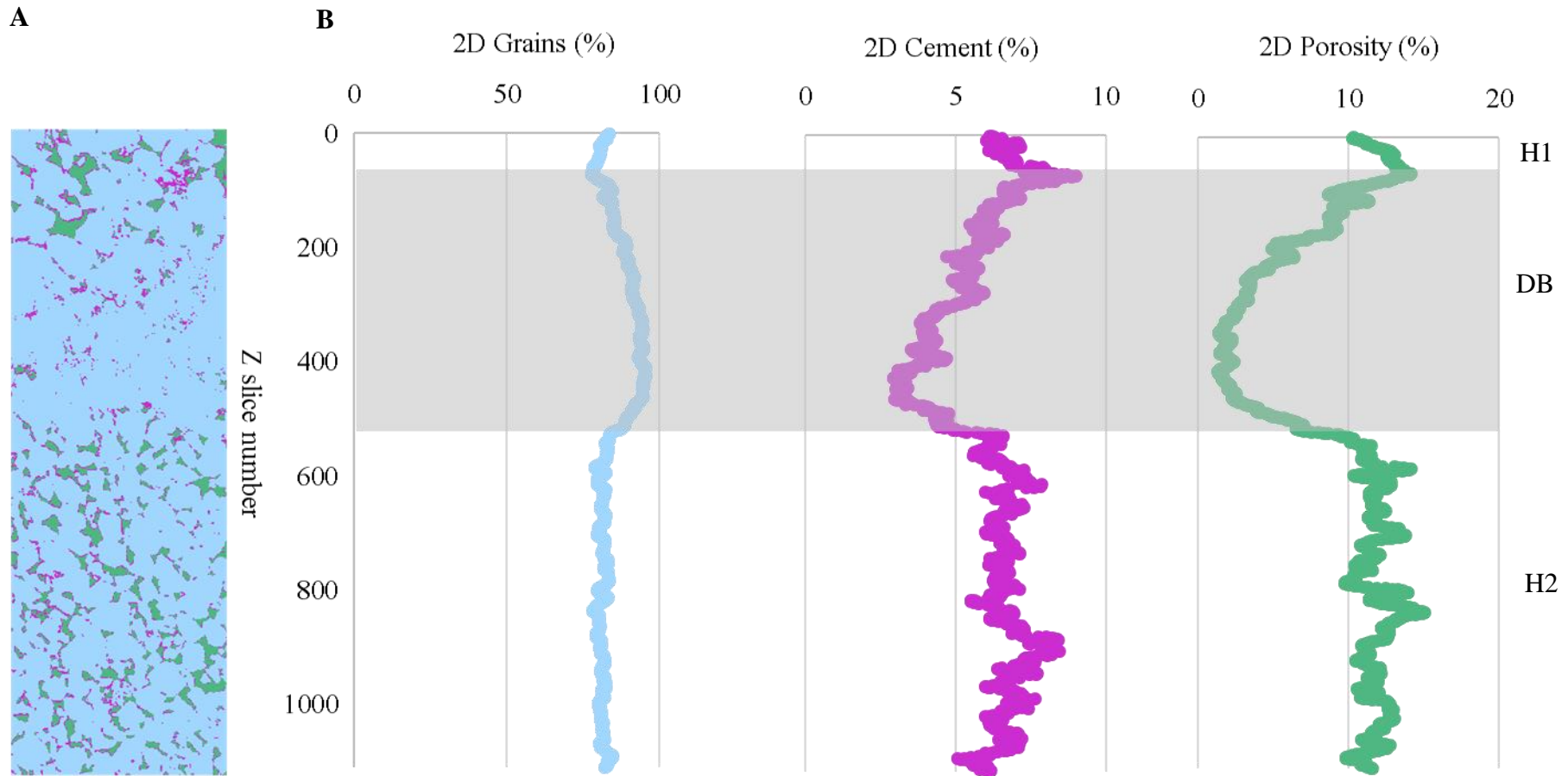


Figure 5.32: A) 2D vertical slice through a 6x2x2mm sub-sample of AR01: grain (blue), cement (purple) and porosity (green) percentage. B) Corresponding values of percentage grains, cement and porosity percentage for each horizontal slice along the z axis of the subsample. Deformation band is highlighted in grey. A sudden drop in percentage cement towards the base of the deformation band in comparison to the top. This is mirrored by a 9% increase in the percentage grains present inside the deformation band.

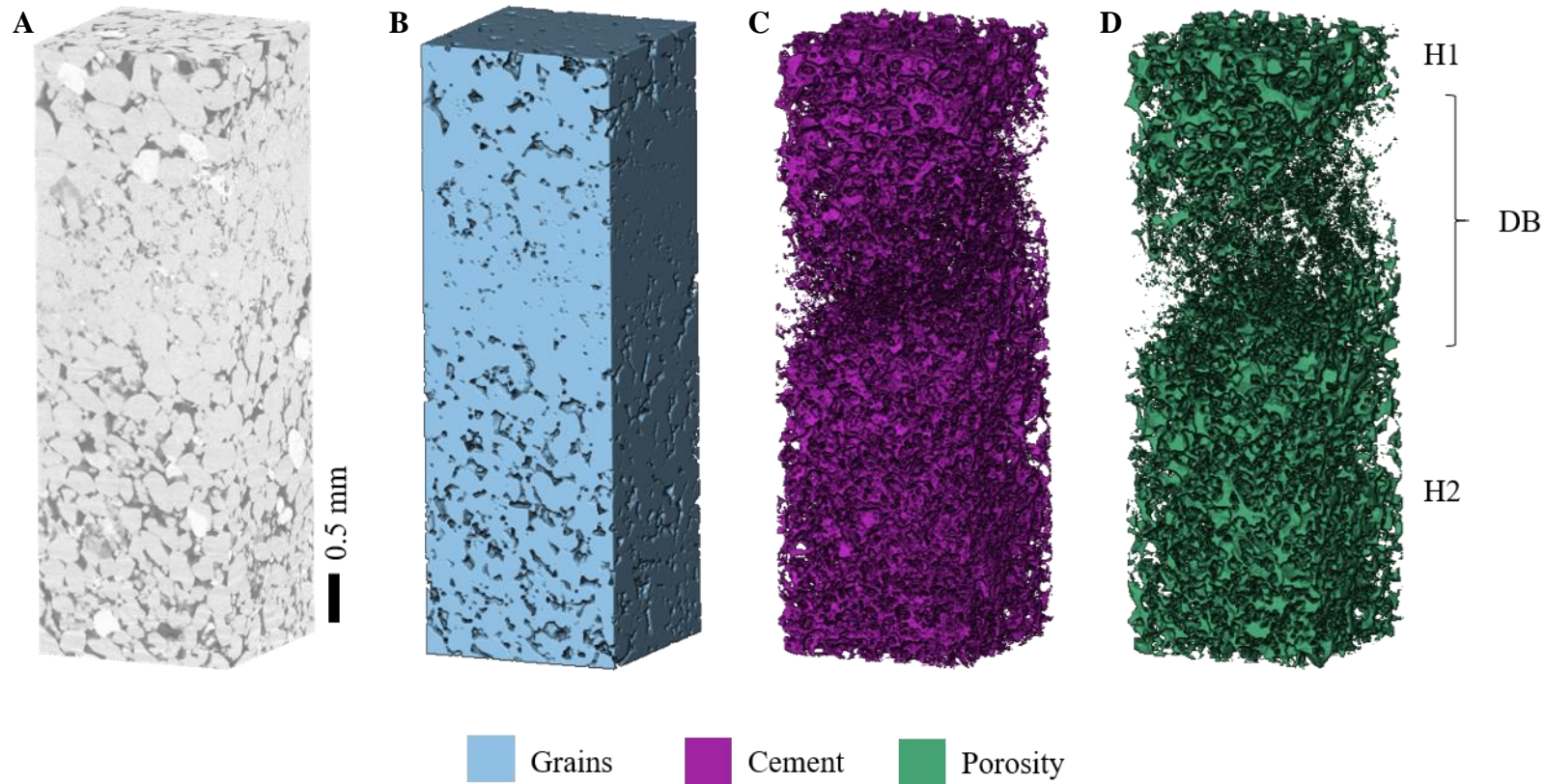


Figure 5.33: Sample AR01 full volume segmented in Avizo[®]. A) Original grey scale 3D image. B) Grains segmented image. The grains segment is 84.91% of the total volume. No isolated grains are present. C) Cement segmented image. The cement segment is 7.67% of the total volume. D) Porosity segmented image. The porosity segment is 9.06% of the total volume.

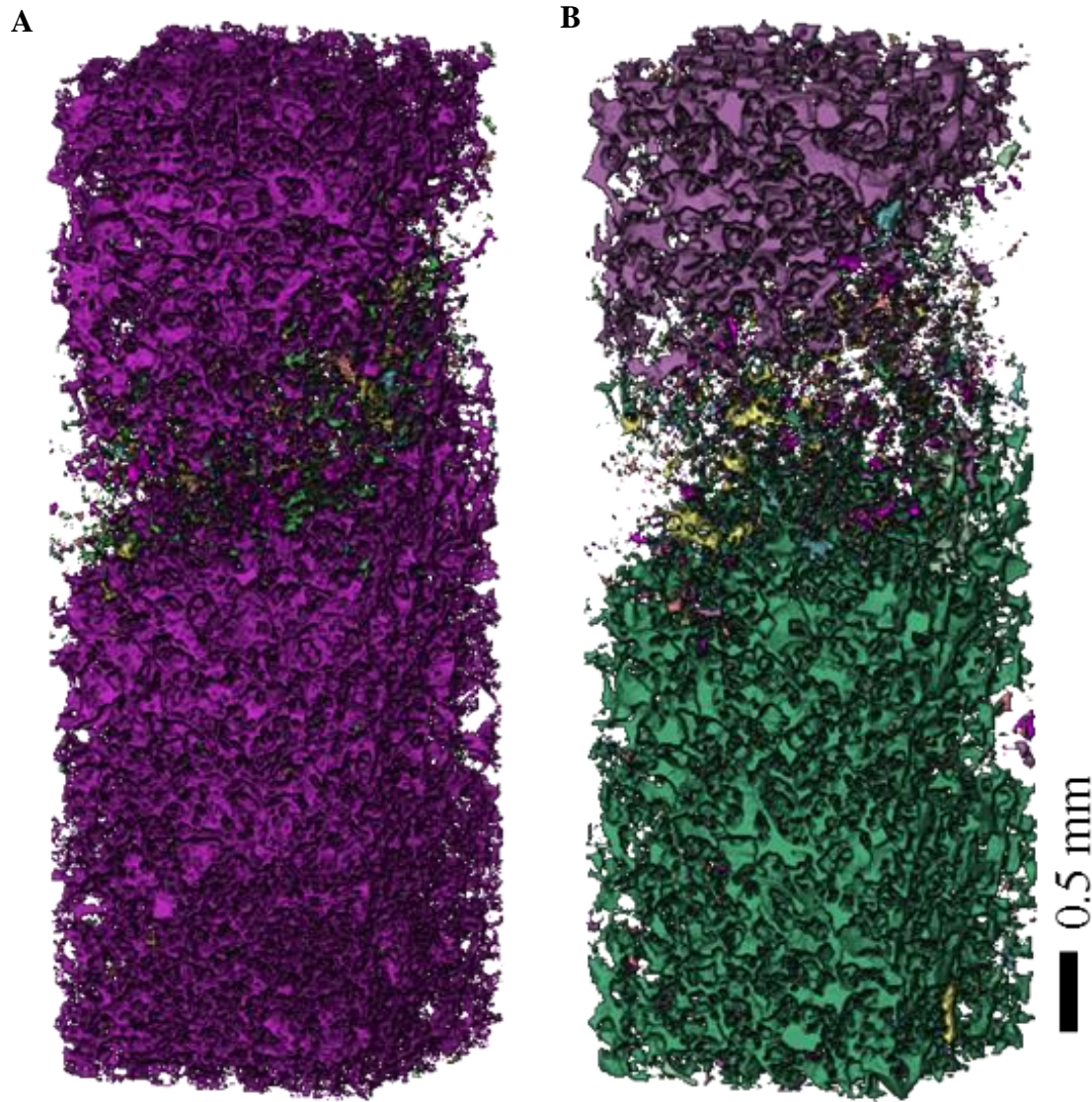


Figure 5.34: Cement and porosity connectivity across sample AR01
A) Connected cement. The cement is connected across DB1, therefore connecting H1 and H2. Inside the deformation band most of the cement is connected (green colour) however, the size of the connected cement pockets is smaller than those in the host rock. B) Connected porosity. Porosity is connected in H1 and H2 however, it is disconnected inside DB1. Inside DB1 there is a decrease in the size of the connected pores. The pores in H1 and H2 do not connect across the deformation band.

Chapter 5 - Deformation bands

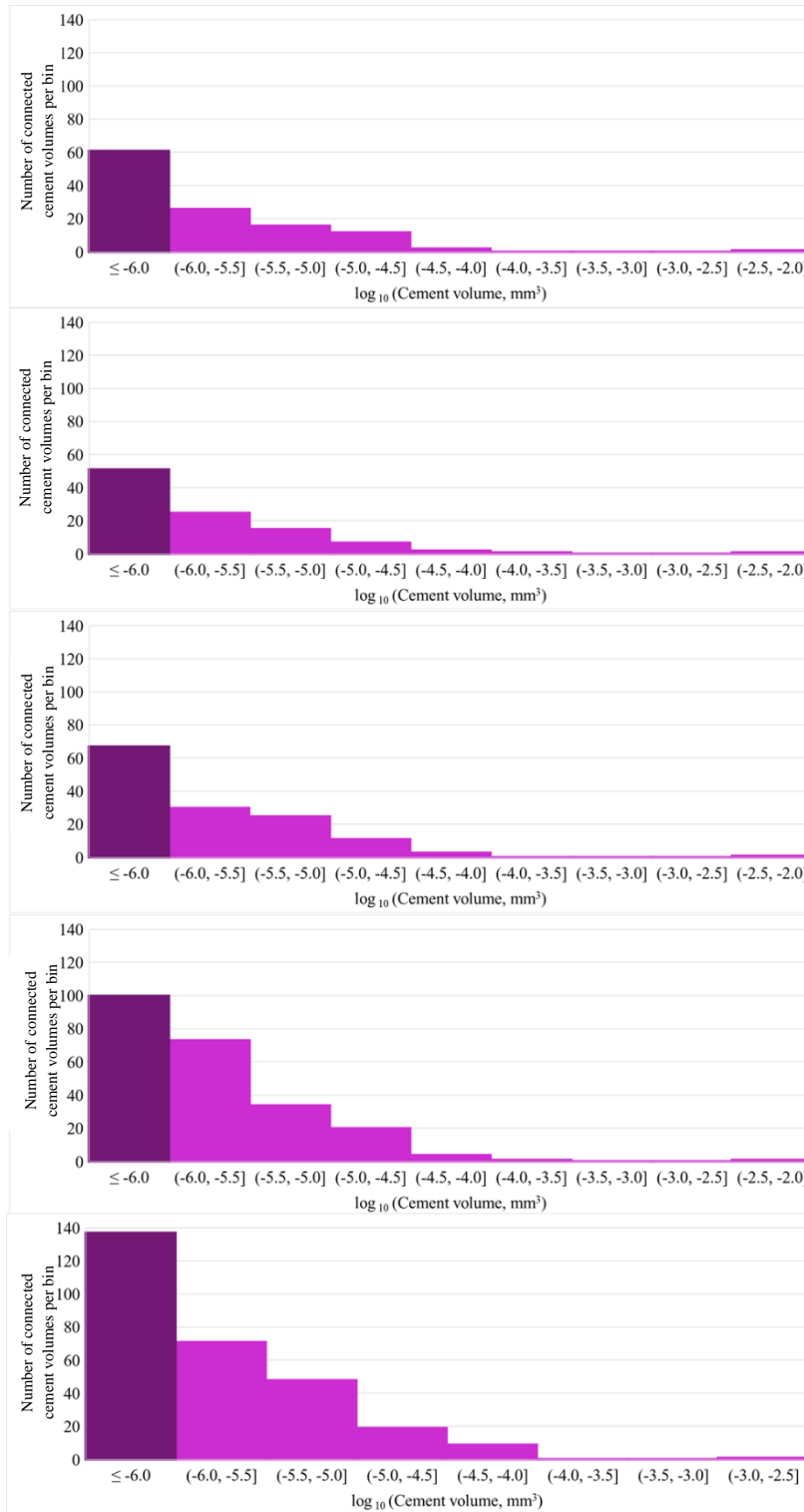


Figure 5.35: Histogram showing the number of connected cement volumes from five 0.125mm^3 sub volumes in the AR01 deformation bands. The bin width is 0.5. The column on the left is an overflow bin for all cement volumes less than 0.000001mm^3 . The largest connected cement volume was 0.0066mm^3 .

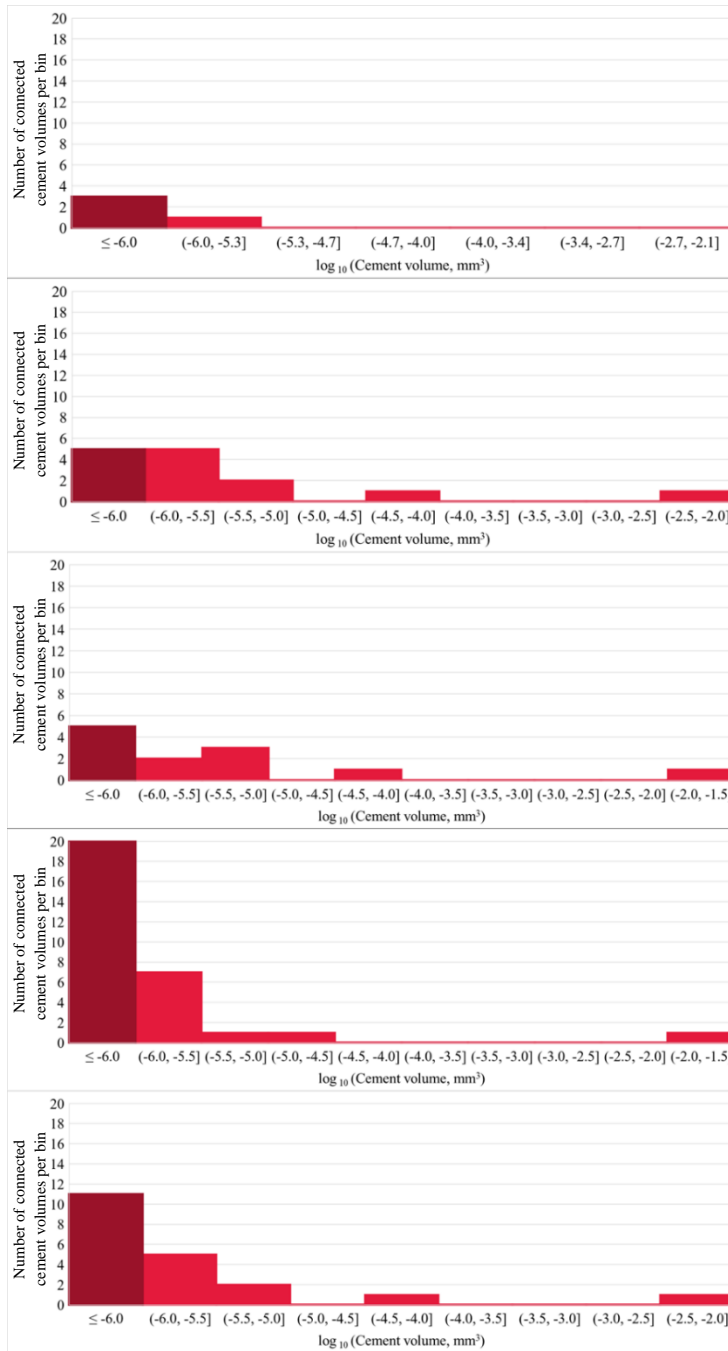


Figure 5.36: Histogram showing the number of connected cement volumes from five 0.125mm³ sub volumes in the HN11 host rock. The bin width is 0.5. The column on the left is an overflow bin for all cement volumes less than 0.000001 mm³. The largest connected cement volume was 0.016 mm³.

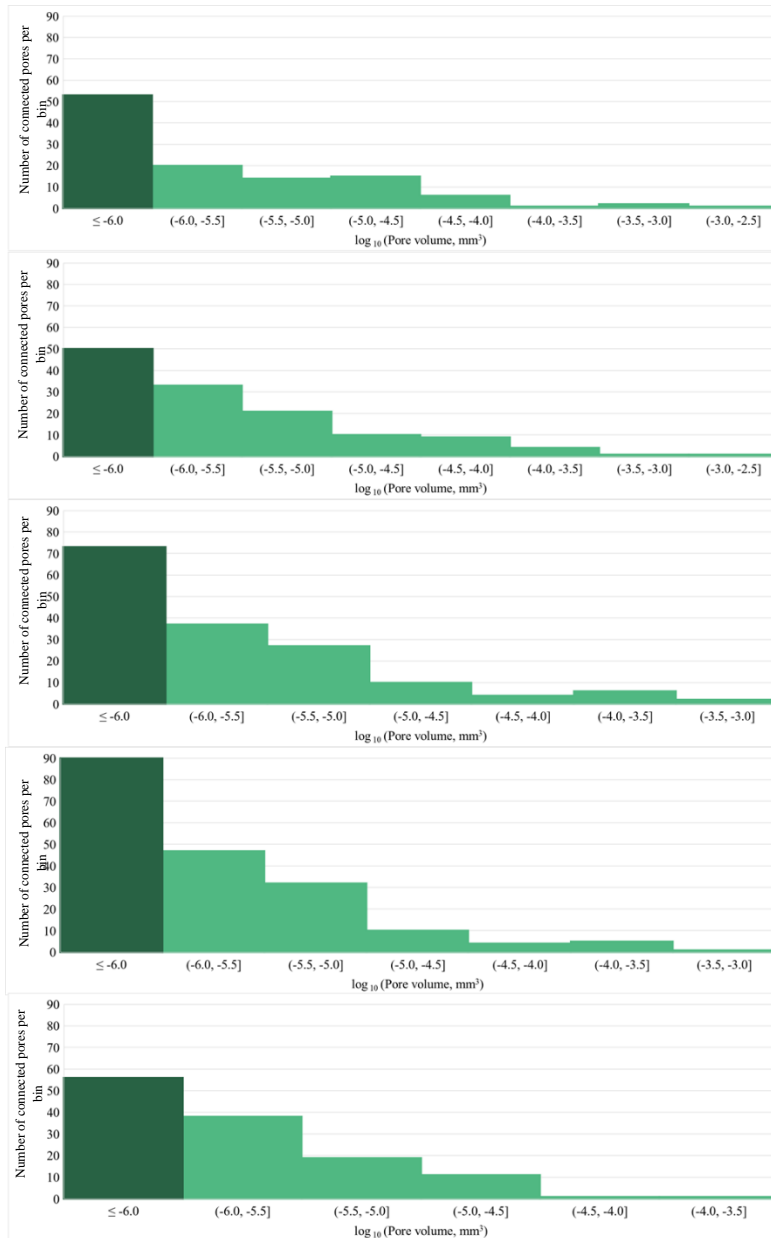


Figure 5.37: Histogram showing the number of connected pore volumes from five 0.125 mm^3 sub volumes in the AR01 deformation bands. The bin width is 0.5. The column on the left is an overflow bin for all pore volumes less than 0.0000001 mm^3 . The largest connected pore volume was 0.0016 mm^3 .

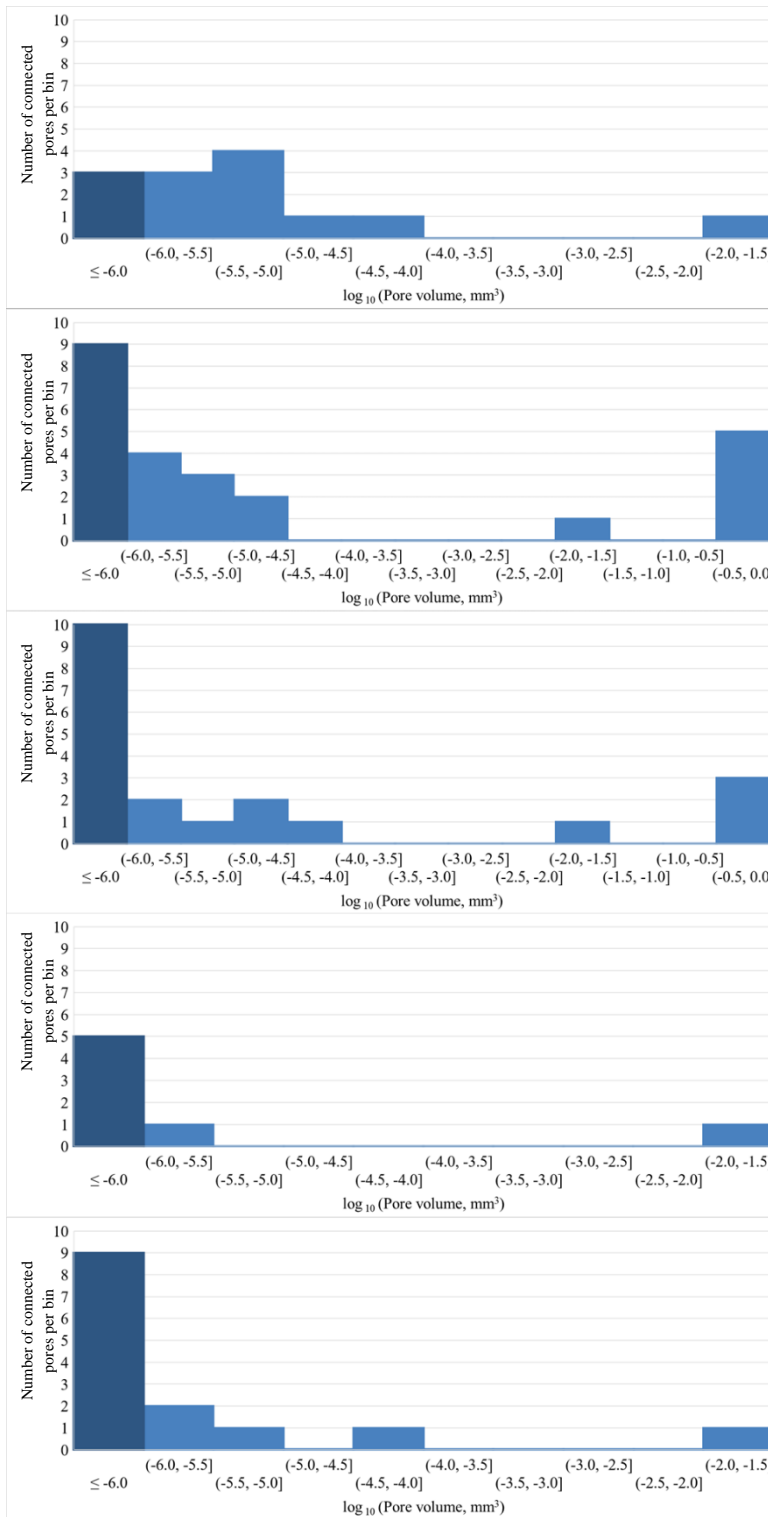


Figure 5.38: Histogram showing the number of connected pore volumes from five 0.125 mm³ sub volumes in the AR01 host rock. The bin width is 0.5. The column on the left is an overflow bin for all pore volumes less than 0.000001 mm³. The largest connected pore volume was 0.022 mm³.

5.5 Discussion

5.5.1 Full sample analysis

A summary of the percentage of grains, cement and porosity across the three 6 x 2 x 2 mm samples with calculated error bars is shown in Figure 5.39. These full samples contain both host rock and deformation bands, so although Figure 5.39 gives an overview to the composition of each sample it is not possible to separate the impact of the deformation band. Ideally the volumes would be cropped into areas that contained only host rock and areas that only contained deformation bands. However, the boundaries between the bands and host rock are irregular and diffuse so this is not straightforward in three dimensions.

The error bars are calculated based on a one-pixel dilation and erosion (based on the technique used by Fousseis et al. (2012); see Section 3.8.5 for details). This method of calculation results in a very large error, and in the smaller volume phases, can be larger than the calculated volume for that phase (e.g. cement in HN11). This is in part because the cement occurs in small pores or along grain boundaries (a maximum of one pixel wide), so in some instances dilating by one pixel can double the apparent volume of an area of cement. It is therefore recommended that this technique is not used for disseminated phases, and that it may be more appropriate to estimate error by thresholding and segmenting the image multiple times. From optical microscope observations, the deformation bands have smaller grains and less cement that is disseminated in smaller patches. Therefore, the errors calculated with the dilation and erosion method would be higher in the deformation bands.

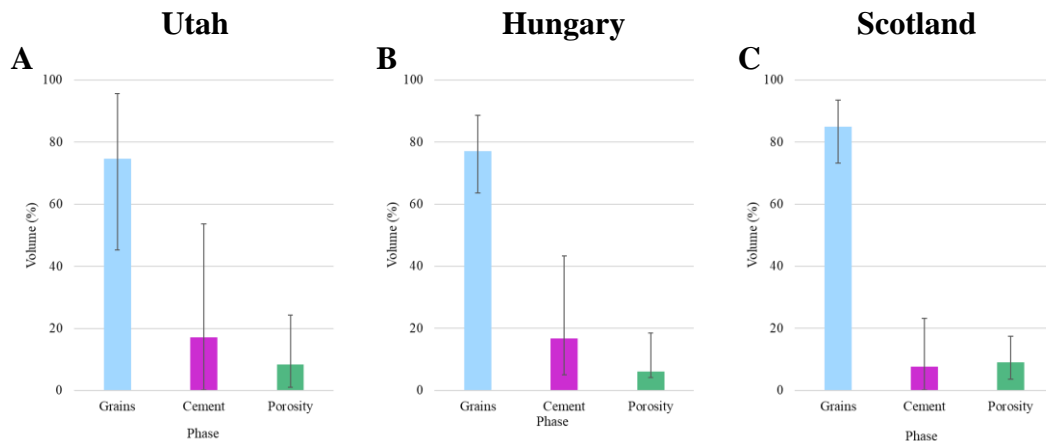


Figure 5.39: *Volume fraction* of each segmented phase for all deformation band samples (6 x 2 x 2 mm) A) UT02 B) HN11 C) AR01 from erosion and dilation calculations (see Chapter 3).

5.5.2 2D Slice analysis

One way to try and extract distinct properties for the deformation bands and host rock is to examine the calculated petrophysical properties from all the possible 2D slices through the 3D sample. This requires that the deformation bands cross the sample at right angles to the long axis.

Overall this method was very successful at determining the location of the deformation bands. It was also good at finding subtle variations inside the deformation bands and transitions from the host rock to the deformation band. For example, when the technique is applied in AR01 (Figure 5.32) it shows a gradual decrease in cement and porosity going into the deformation band from the top of the sample. However, at the base of the deformation band the boundary between the deformation band and host rock is more abrupt.

Another benefit of this method is that the background variability in the host rock can be identified. By comparing the maximum and minimum values of grains, cement and porosity in the host rock it is possible that the background variability could be used as an approximation for the segmentation error. For example, in the combined host rock of sample AR01 the percentage of cement has an average of 6.83% and ranges from 5.07-8.71%. This range could be classified as the measurement error.

One possible suggestion to improve this technique is to repeat the 2D slices on larger and smaller sample volumes. By carrying out these repeats trends across the larger sample can be identified. The smaller sample volumes would also allow finer variations to be picked up and tracked along the sample. However, this repetitive technique would be time consuming.

5.5.3 Sub-volume analysis

There has been long discussion about the difficulty of capturing 3D properties from 2D images. To investigate this, I undertook sub-volume analysis.

Sub-volume should be larger than the 'REV', and ideally contain several grains. The number of repeats is a function of the background spatial variability. From the 2D slice analysis it appears that the background spatial variability in phase density is relatively low in the host rock (Section 5.5.2). In the deformation bands the fact that there are trends across a band may mean that the number of sub-volumes to characterise the band is higher.

3D sub volume analysis is a less robust method of sub sampling the data and is reliant on the representative elementary volumes (REV). If the sample size or REV is too small in comparison to the sample size the phase percentage results may oscillate. One possible improvement to this system would be to write a code which automatically segments and separates each deformation band sample into REV's suitable for the size of the sample. This code would allow for an increase in the number of 3D sub volumes so the full sample could be analysed. By altering the code REV size comparisons can be made. Furthermore, the criteria for the REV code can be altered to reflect the internal micro-structure of the deformation band. This type of code would take time to write and was beyond the scope of this thesis however, once written it could be applied to any deformation band.

5.5.4 Cement and Porosity Calculations

One of the main issues with using X-CT to undertake cement analysis is that it is reliant on a density contrast between the grains and the cement phases. Both samples UT02 and AR01 are primarily made of quartz grains and are quartz cemented. This therefore makes it almost impossible to segment the two phases. Instead I focussed

on segmenting their secondary cement phases (e.g. hematite and calcite in UT02; hematite and clays in AR01).

Sample HN11 has a higher percentage of feldspar than the other two host rocks (Chapter 4) and is primarily cemented by clays. This therefore made it easier to segment the primary cementation phase. However, the attenuation value for quartz and clays can overlap at given X-ray energies. The energy that each sample was scanned at was optimized to give the best image. Figure 5.40 shows that there is a clear separation between quartz (grains + cement) and hematite however the difference between quartz and the other cementing phases (illite, kaolinite, calcite) is smaller, and this is more problematic at the higher scanning energies for these three samples. Therefore, it is recommended that scanning is undertaken at the lowest possible X-ray energy while still maintaining image quality.

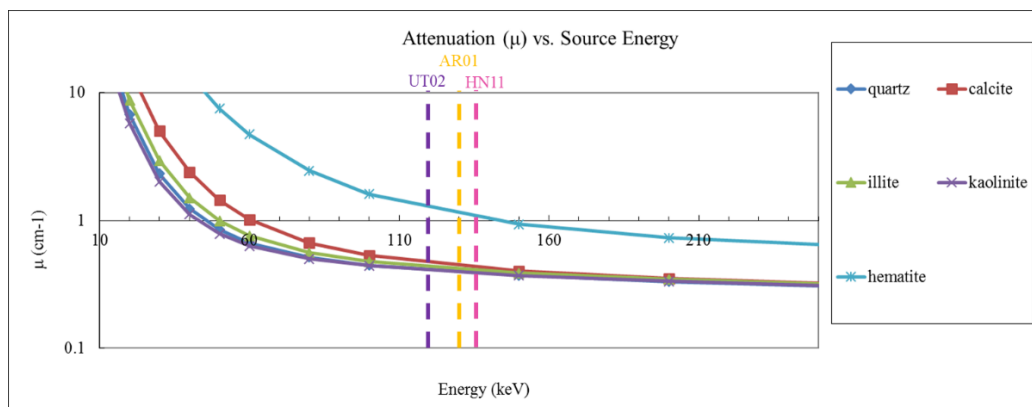


Figure 5.40: X-ray linear attenuation coefficient calculated for each listed mineral using MuCalc (Hanna and Ketcham 2017). The three deformation band samples and the energy which each sample was scanned at is highlighted.

In the 2D Avizo® slice analysis there is a reduction in the percentage of cement and porosity inside the deformation band for all three samples. HN11 has the lowest porosity (2.1%) inside the deformation band compared to the other samples. AR01 has the lowest percentage of cement (5.1%) and second highest porosity inside the deformation band compared to the other samples. The highest porosity is in Utah DB3, which may have been affected by later fracturing.

One sample of interest is UT02 which displays evidence of three deformation bands in the scanned sample. As noted in Section 5.2.3 the properties of the deformation bands change going down the sample (Figure 5.8).

This reduction in the percentage of cement and porosity inside the deformation band can also be seen across the 3D sub volumes. HN11 has the lowest porosity (1.4%) inside the deformation band compared to the other samples. AR01 has the lowest percentage (4%) of cement inside the deformation band compared to the other samples.

Despite the differences in absolute numbers from the 2D slice analysis and the 3D sub volume analysis the overall trends are the same. For example, HN11 has the lowest porosity and AR01 has the lowest percentage of cement inside the deformation bands across both techniques.

The 2D slice analysis has proven to be the most successful technique at visualising and quantifying the changes in the percentage of grains, cement and porosity across the deformation bands. It can also be used to help identify deformation bands in areas where they are not as clear to identify by eye. This will be particularly important in bands with lower degrees of cataclasis.

A summary of the 2D slice analysis and 3D sub volume analysis is shown in Figure 5.41. The range of values presented in this figure allows for comparison of results between both analysis techniques. The overall trend shows that regardless of analysis technique used or the width of the deformation bands, there is an overall decrease in the percentage of cement and pores present inside the deformation band. The range of values calculated from both techniques are very similar implying that both techniques are robust.

5.5.5 Connectivity of cement and porosity

For each of the samples, the cement phase is connected within the host rock. For samples HN11, AR01 and the top deformation band in UT02 the cement is fragmented inside the deformation band. Interestingly although the cement is not connected inside these deformation bands it connects the host rock on each side of the deformation band. This therefore suggests that there are traces of cement which

Chapter 5 - Deformation bands

are connected all the way through the sample. It could be interpreted from these results that the cement formed first and then the deformation band formed.

The exception to this is the two lower deformation bands in UT02. Here the cement becomes increasingly more connected across DB2 and DB3. This proves that over a small distance (<4 mm) the properties of deformation bands can change, and it should not be assumed that all deformation bands in one sample are identical. The first possible explanation is that the cement could not pass through the first wider deformation band (DB1). A second explanation is that the timing of cementation and deformation band formation varied across sample UT02. However, this would need further research and a larger data set to understand if this is a possibility.

Unlike cement connectivity the porosity connectivity is different for each sample.

In UT02 the porosity is disconnected across DB1 however, it remains connected across DB2 and DB3. Furthermore, the host rock above DB1 is disconnected from the other host rock.

HN11 has completely unconnected pores across the host rock and the deformation band. This suggests that the grains and cement combined are all in contact with each other.

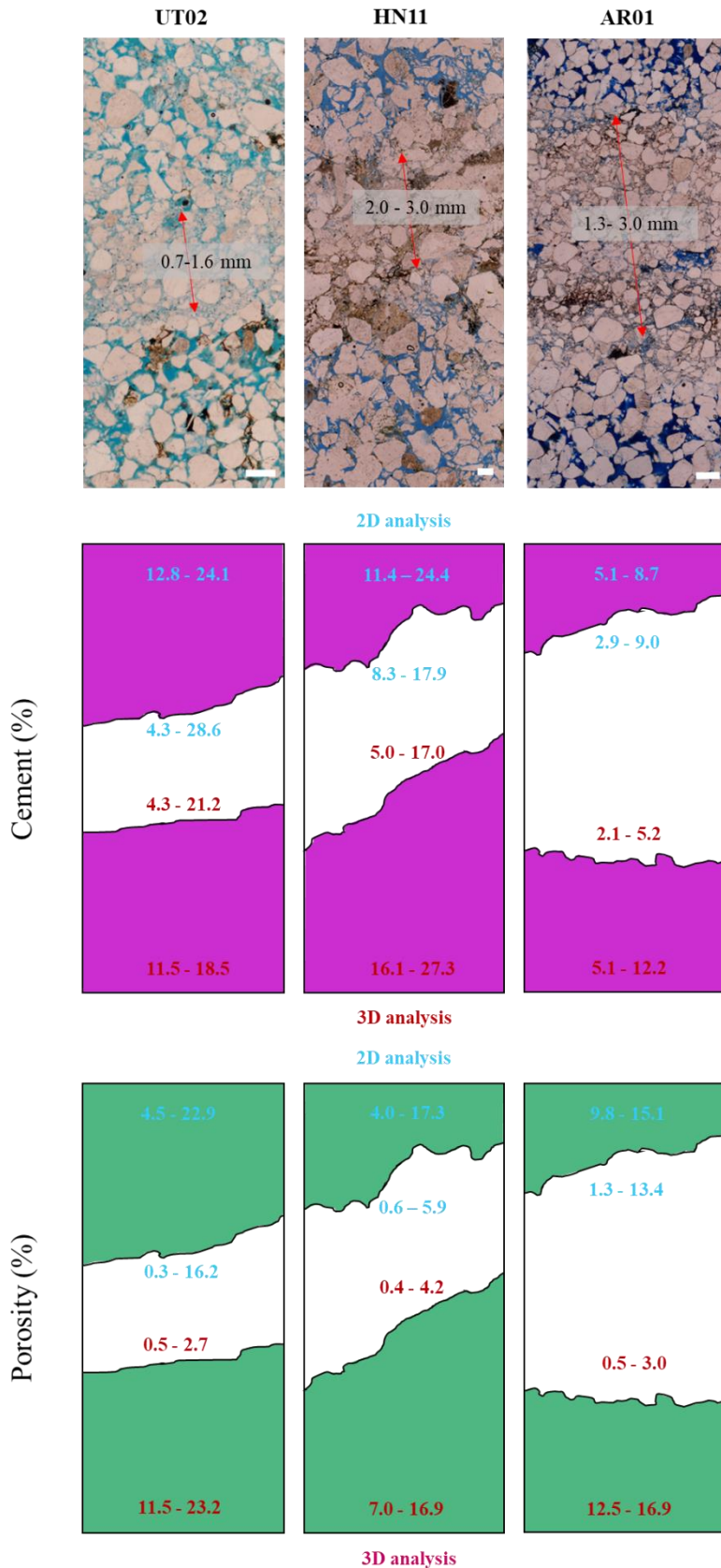


Figure 5.41: Schematic summary of deformation bands. The scale bar on the deformation band images is 250 μm .

This shows the variation in cement and porosity phases across 2D slice and 3D sub volume analysis.

The values at the top of each schematic refer to the 2D slice analysis ranges. Meanwhile, the values at the base of each schematic refer to the 3D sub volume analysis ranges.

Meanwhile, sample AR01 pores are connected above and below, but not across the deformation band.

From the results in this study it can be said that across wider deformation bands (> 1mm wide) the host rock porosity is likely to be disconnected. If the deformation band is < 1mm wide the porosity in the host rock is likely to be connected across the deformation band. Therefore, deformation band width effects the pore connectivity.

5.5.6 Impact of cement on the mechanical deformation

The initial hypothesis of this thesis was to test if the cement distribution effects the mechanical deformation of the deformation bands. Due to time pressures of this PhD this initial hypothesis is now out-with the scope of this PhD. By using the methodology outlined in this chapter it would be possible for a future PhD student to continue this work and test the initial hypothesis.

To achieve the aims of the original hypothesis testing a minimum of twenty samples would be required with three repeats of each sample. This sample size would begin to account for the variables (mineralogy, grain shape, width of deformation band etc.) present in the deformation bands.

In Chapter 8 the mechanical influence of different cement types on sandstone is investigated.

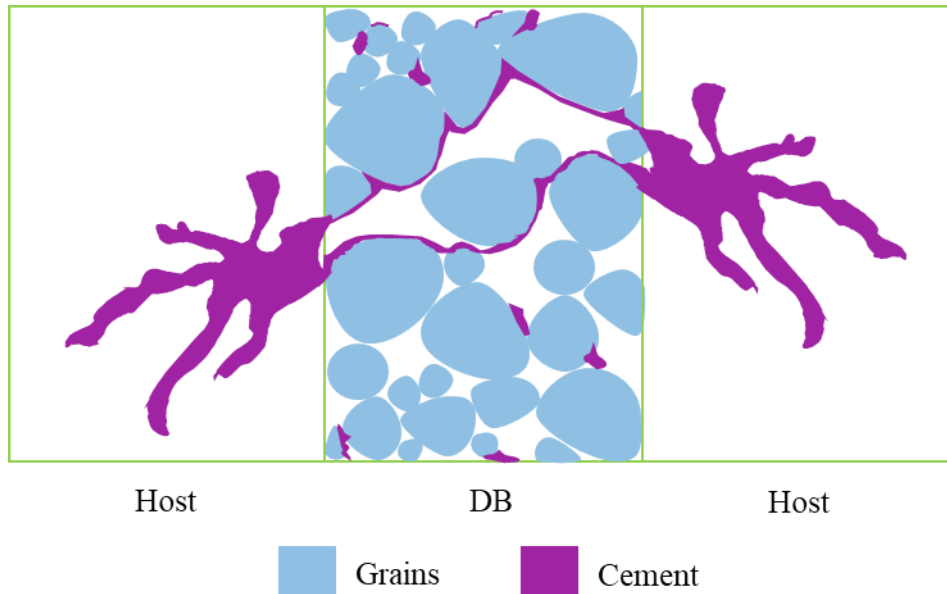


Figure 5.42: Schematic of cement connectivity through deformation bands. Here cement is connected in both the host zones and a fine trace of cement connects the host zones through the deformation band.

5.6 Summary

- 2D thin section analysis is useful to gauge an overall understanding of the grain shapes and composition of deformation band samples.
- 3D X-CT images give a good visual representation of the complexity of deformation bands on a micro scale.
- X-CT analysis can be used to calculate the percentage of phases (e.g. grains, cement and porosity) present in sandstones and across structural features such as deformation bands.
- Two methods of X-CT analysis can be used to analyse the distribution of the phases present across deformation bands. These are 2D slice and 3D sub volume analysis.
- The 2D slices are an excellent means of analysis for displaying overall trends in the segmented X-CT scanned sections. With the format used in this chapter

Chapter 5 - Deformation bands

the 2D slice analysis accounts for more localised variability than the 3D sub volume analysis.

- Despite the different analysis techniques, the range of values (the percentage of grains, cement and porosity present) produced by the two techniques are very similar.
- For each of the samples (UT02, HN11 and AR01) there is an overall reduction in the percentage of both cement and porosity inside the deformation band.
- The cement is connected through the samples and across the deformation bands.
- The majority of porosity is connected in the host rock but disconnected inside the deformation band for samples UT02 and AR01. However, sample HN11 shows disconnected porosity across the full sample.
- The disconnected porosity across sample HN11 is possibly due to the distribution of the clay cement. Due to the shape of the cement around the grains individual pores become isolated in the sandstone.

Recommendations for future practice:

- Scan at the lowest possible X-ray energy to facilitate separation of cement phases.
- Develop an algorithm which automatically subsamples the full deformation band sample for analysis.
- Consider other methods of calculating the error due to segmentation with Avizo®.

Chapter 6 - Calcium sulphate phases

6.1 Rationale

This chapter provides a greater insight into the chemistry behind the gypsum cemented sandstones (Chapter 7) and images the physical growth of the gypsum crystals over time to help better understand growth that occurs between sand grains in the cemented sandstones.

It is important to understand the physical growth of the gypsum crystals and the transitions of the calcium sulphate phases when investigating the properties of gypsum cemented sandstone at the micro-scale and when considering the geomechanical applications of gypsum cemented sandstone e.g. at depth or in lower latitude environments, where temperatures are elevated.

The literature surrounding calcium sulphate phases is large and it combines fundamental properties (i.e. crystal structure and growth rate) with more applied studies, but which are predominantly focused on the construction and biomedical fields. Construction, in this context, relates to the production of plaster of Paris or the addition of gypsum to Portland cement to prevent flash setting. However, there are limited studies which focus on the comparison of the hydration and dehydration of calcium sulphate over industrial calcination temperatures (120 - 180°C) or gypsum crystal growth from bassanite dissolution, which is the mechanism used in this work to form synthetic sandstones.

By applying an integrated, quantitative approach, this chapter aims to improve the understanding of calcium sulphate kinetics during dehydration and subsequent hydration through the application of Thermogravimetric analysis/ Differential scanning calorimetry (TGA/DSC), synchrotron x-ray diffraction (XRD) and petrographical studies. This chapter shows the co-existence of calcium sulphate phases during the dehydration of gypsum and quantitatively demonstrates that dehydrating calcium sulphate to a given calcining temperature will affect the gypsum crystal form and growth rate. The implication is that calcining will affect setting times, and ultimately, mechanical properties.

6.2 Review of calcium sulphate literature

Calcium sulphate minerals are widely studied and used across industry, medicine, materials science and geosciences. However, the fundamental calcium sulphate mineral transitions remain poorly understood. Early research focused on measuring solubility to identify the three main phases of calcium sulphate, largely before X-ray diffraction was an established laboratory technique (Partridge and White 1929; Hill 1937; Bock 1961). Subsequent research has tried to identify the sequence of calcium sulphate phase formation, the presence of intermediate bassanite forms and the temperature of bassanite and γ -anhydrite transition during dehydration (Putnis et al. 1990; Bezou et al. 1995; Strydom et al. 1995; Chang et al. 1999; Vaniman et al. 2008; Ballirano and Melis 2009; Jacques et al. 2009; Weiss and Bräu 2009; Berthold et al. 2011; Lou et al. 2011). Meanwhile studies on the hydration of calcium sulphate forms have focussed on the precipitation pathway of gypsum as it is formed from the hydration of bassanite (Jones, 2012; Saha et al. 2012; Van Driessche et al. 2012; Wang et al. 2012; Stawski et al. 2016) but none of these studies have worked with pre-produced bassanite crystals as the initial material.

Calcium sulphate can occur in three mineral phases; dihydrate (gypsum), hemihydrate (bassanite) and the anhydrous phase (anhydrite). Each phase is chemically defined by the number of moles of water present in its chemical structure and can be formed either in the laboratory or the natural environment (Wirsching 2000). As calcium sulphate minerals undergo hydration or dehydration, they can transform from one mineral phase to the next. In nature, calcium sulphate deposits form as a result of sea water precipitation and is of interest to geologists as they can be used as a paleothermometer. Natural gypsum can be calcined for the manufacture of Plaster of Paris in the construction industry and medical industries to make plasterboard and casts, respectively. When plaster of Paris powder is hydrated it re-precipitates as gypsum. As it does so it hardens and can be used for casts or moulds.

This work presents multi-scale analysis of the dehydration and subsequent hydration of calcium sulphate powder. In doing so it identifies coexisting hydrate phases and shows for the first time the effect of calcining temperatures on gypsum crystal

formation. The results highlight the importance of choosing the best gypsum calcining temperature for the industrial or medical application required.

6.2.1 Calcium Sulphate Mineralogy and Formation

Gypsum ($\text{CaSO}_4 \cdot 2\text{H}_2\text{O}$) is the stable form of calcium sulphate at room temperature, it has a monoclinic crystal structure and can be found in four crystal habits; alabaster, massive, satin spar and selenite (Harrison 2012). Gypsum has also, albeit rarely, been identified as forming spherulites (Shtukenberg et al. 2012) or stellates (Rendel et al. 2018).

Gypsum remains thermodynamically stable up to $\sim 42^\circ\text{C}$, has a solubility of 0.24g/100ml at 20°C and can form by the hydration of bassanite or indirectly by the hydration of anhydrite but in both cases hydration is via the solution phase (Wirsching 2000).

Bassanite, or hemihydrate is formed from the dehydration of gypsum (transforming from solid gypsum or via gypsum precipitation in an aqueous solution) or re-hydration of anhydrite and it has a solubility of 0.65g/100ml at 20°C . It forms in two thermodynamically different morphological states α -bassanite and β -bassanite (Kelley *et al.* 1941). β -bassanite is produced by dry heating gypsum from $45- 200^\circ\text{C}$ (Wirsching 2000; Singh and Middendorf 2007; Christensen et al. 2008; Hildyard et al. 2011) e.g. in an oven or in a vacuum (Hildyard et al. 2011) and is assumed to be the product formed here.

Anhydrite is formed when all the water of hydration is removed. The forms of anhydrite are: hexagonal γ -anhydrite (γ -anhydrite or anhydrite III); orthorhombic anhydrite (β -anhydrite or anhydrite II); and a high temperature anhydrite (α -anhydrite or anhydrite I) which is stable above $\sim 1214^\circ\text{C}$ (Newman 1941; Freyer and Voigt 2003).

6.2.2 Calcium Sulphate in the construction industry

Gypsum is a common construction material which has been used since the 17th century (Hernigou 2016). It is used in the construction industry to manufacture plasterboards, partition panels, ceiling tiles and fibre boards due to its fire-retardant properties (Wirsching 2000) and is commonly known as Plaster of Paris or stucco.

Chapter 6 - Calcium sulphate phases

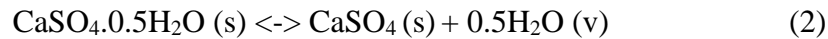
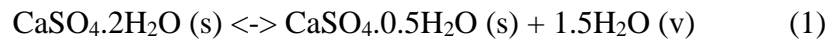
Plaster of Paris is formed by dehydrating (or ‘calcining’) gypsum, heating it to between 100-180°C to form bassanite (Wirsching 2000; Weiss and Bräu 2009; Tydlitát et al. 2011). The recommended temperature which gypsum should be heated to form Plaster of Paris varies depending on purpose the plaster is used for, the type of gypsum used (e.g. is it natural or synthetically produced), operators’ production guidelines and what is most economically viable for the operator (Cunningham et al. 1952). For use as plasterboard, the plaster of Paris is hydrated by mixing the powder with water (and other additives), reversing the dehydration process to form gypsum crystals. Additives such as citric acids and phosphonates are added during bassanite hydration to slow down the gypsum precipitation rate and limit growth on the (111) crystal faces (McCartney and Alexander 1958; Tadros and Mayes 1979; Lioliou et al. 2006). The strength of Plaster of Paris is dependent on the temperature and humidity at which it is set, the time left to set undisturbed and the crystal strength. As plaster of Paris paste is setting it forms a network of interconnected gypsum crystals with inter-crystalline porosity. Research into plaster of Paris formation has primarily focused on the most efficient methods to form synthetic bassanite. Packter (1974) and Amathieu and Boistelle (1988) previously studied the size and number of gypsum crystals. Finot et al. (1999) studied the adhesiveness of gypsum faces to each other and their impact as the gluing agent in plaster. They discovered that gypsum crystals preferentially adhere by van der Waals forces and ionic correlation forces on the (-101) and (120) faces respectively. For plaster formation, crystal size, growth rate, crystal grouping, gypsum purity, moisture content and the use of additives, all play an important role in determining the final plaster properties, such as compressive strength. However, few studies since Cunningham et al. 1952 image the growth of gypsum crystals (Lewry and Williamson 1994; Dumazer et al. 2009; Saha et al. 2012; Adrien et al. 2016) and analyse what the implications are for the calcining temperature to form plaster of Paris.

Lewry and Williamson (1994) characterises α - and β - forms of basanite. Dumazer et al. (2009) models the parameters which affect the gypsum morphology and gypsum growth dynamics during gypsum formation from a suspension of basanite grains in aqueous solution. Saha et al. (2012) images the formation of acicular gypsum from a supersaturated solution of basanite by using time-resolved cryogenic transmission

electron microscopy. Adrien et al. (2016) uses X-ray computed tomography (X-CT) to image the dissolution of bassanite and formation of gypsum in 3D.

6.2.3 Dehydration pathway

The gypsum - bassanite – anhydrite dehydration reactions are:



When water is added to bassanite, it dissolves and precipitates as gypsum. This is the reaction which takes place as plaster of Paris sets. The exothermic reaction which takes place when bassanite reacts with water is:



Reported transition temperatures for the calcium sulphate system are not consistent between published studies in the literature (Singh and Middendorf 2007; Jacques et al. 2009; Gazdič et al. 2013). A range of variables impact the final product formed by dehydrating gypsum, such as humidity, pressure and time in the kiln. For example, an opensample environment produces different results from a sealed sample environment (Table 6.1).

Table 6.1: Jacques et al. (2009) uses a standard heating rate of (10K/min) shows how the temperatures transition (°C) during the dehydration of gypsum is affected by different sample environments (e.g. sealed, not sealed). Here the sealed environment increases the transition temperatures. Table from Jacques et al. (2009)

Event/ Capillary environment	Open+N ₂	Open	Sealed	Sealed + H ₂ O
50% gypsum 50% hemihydrate	149	151.5	162.5	166
Inception of major structural change in hemihydrate	180	177	208	242
Formation of γ -anhydrite	200	184	216	251
50% γ -anhydrite 50% anhydrite	360	375	330	291

During industrial processes, focus is put on the setting time of plaster of Paris. The setting time is controlled by three variables; these are the solubility of bassanite, the number of nuclei that form and the rate of crystal growth.

There are three outstanding research questions over the calcium sulphate dehydration pathway. Firstly, it is not yet clear if there is a direct precipitation pathway from gypsum to γ -anhydrite (Sarma et al. 1998; Carbone et al. 2008) or a multistage pathway which transitions from gypsum to bassanite to γ -anhydrite (Abriel et al. 1990; Chang et al. 1999; Ballirano and Melis 2009). Prasad (2005) showed that γ -anhydrite can form during gypsum dehydration. Most recently Lou et al. (2011) have proven that the pathway taken during dehydration is dependent upon temperature and relative humidity. Furthermore, Lou *et al.* (2011) suggests that if gypsum is dehydrated in a humid environment all three phases of calcium sulphate may be present at a given state temperature. Therefore, before the gypsum to bassanite transformation is complete the transformation of bassanite to soluble anhydrite can begin. It is worthwhile noting that as relative humidity is increased there is a decrease in the rate of dehydration (Robertson and Bish 2007).

Secondly, there is uncertainty over the temperature at which the bassanite to γ -anhydrite phase transition occurs (Jacques et al. 2009; Berthold et al. 2011) or even if it occurs at all (Berthold et al, 2011), which is investigated in this chapter.

Finally, there remains a question over the presence of intermediate bassanite forms, known as sub-hydrates, during dehydration of gypsum (Putnis et al. 1990; Bezou et al. 1995; Strydom et al. 1995; Vaniman et al. 2008; Weiss and Bräu 2009). Across the majority of studies, the transformation between the calcium sulphate forms is described as a one-stage transition, with no intermediate forms (when $\text{CaSO}_4 \cdot x\text{H}_2\text{O}$, $x \neq 0.5$) present. Putnis et al. (1990) state there is no evidence for intermediates states of bassanite and more recently Weiss & Brau (2009) state that a bassanite with composition $\text{CaSO}_4 \cdot x\text{H}_2\text{O}$ where $x > 0.5$ is unlikely to exist. However, the presence of intermediate bassanite ($x > 0.5$) forms have been identified by Abriel (1983), Bushuev et al. (1983), Bezou et al. (1995) and Vaniman et al. (2008). Both studies by Abriel (1983) and Bushuev et al. (1983) are criticised by Lager et al. (1984) who states that the bassanite structure does not support the additional water content (when $\text{CaSO}_4 \cdot x\text{H}_2\text{O}$, $x = 0.8$ and 0.67 respectively). While a later synchrotron XRD and neutron powder diffraction study by Bezou et al. (1995) describe the presence of a sub-hydrate with $x = 0.6$.

6.2.4 Hydration pathways

Several kinetic models have been proposed to describe the formation of gypsum crystals from hydrated bassanite (Figure 6.1). These models are either based on nucleation-controlled crystal growth fitted with the Avrami equation (Hand 1994), the crystal's solubility (Schiller 1962) or the rate of hydration (Ridge 1964). Despite the Avrami equation being the best overall fit, none of the models fit gypsum crystal growth completely and do not take into consideration the dissolution of the starting mineral phase (in this case, bassanite) or the effect that dissolution rate has on limiting gypsum crystal growth rate (Singh and Middendorf 2007).

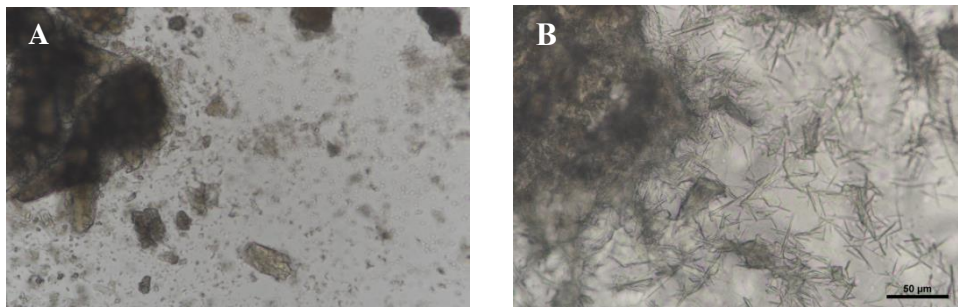


Figure 6.1: Formation of gypsum crystals from hydrated bassanite. A) Optical microscope image of 140°C bassanite. B) Gypsum growth from hydrated 140°C bassanite. Same scale for both images.

More recently simulation models have been used to analyse gypsum crystal growth and its implications for plaster of Paris on both the micro and mesoscale (Dumazer et al. 2009; Joiret et al. 2014). Dumazer et al. (2009) find as the number of nuclei present per bassanite grain increase, the slower the induction time and as a result the smaller the needle length. Whereas Joiret et al. (2014) developed a Monte Carlo simulation model for the kinetics of gypsum crystal growth which enables predictive modelling of additives to plaster of Paris.

The most recent research investigates the precipitation pathway of gypsum crystals at the nanoscale. Here focus is on the initial stages of crystal growth to understand the pathway of gypsum crystal formation. Van Driessche et al. (2012) and Singh & Middendorf (2007) describe the precipitation of gypsum from solution to occur via nano-bassanite. Meanwhile Saha et al. (2012) and Wang et al. (2012) describe the growth of gypsum as a multistep pathway via an amorphous phase and bassanite.

Recently a synchrotron scattering experiment study by Stawski et al. (2016) indicates a four stage gypsum nucleation and growth pathway which begins after only 30 seconds from a super saturated gypsum solution. The four stages are: stage 1 sees the formation of primary species (<3 nm in size); stage 2 shows the primary species grouping together and beginning to show similar alignment; in stage 3 the species begin to join together; and stage 4 is when the aggregates of primary species grow.

To the best of my knowledge there are no studies that consider the impact of calcination temperature on the growth of gypsum crystals.

6.3 Characterisation of materials/Experimental methods

6.3.1 Sample preparation

β -bassanite was prepared by heating gypsum powder overnight at five different bassanite forming temperatures (120, 140, 160, 180 and 200°C). Using powdered samples achieves more complete, faster transformations due to the small particle size/greater surface area. Furthermore, powders are most commonly used in industrial and medical applications. By dry heating the samples bassanite phase formation is restricted to β -bassanite. Calcined samples were used to imitate the conditions under which calcination takes place, thereby investigating the impact of calcination temperature (hydration state) on the formation of gypsum crystals (Figure 6.1).

6.3.2 Thermogravimetric analysis/ Differential scanning calorimetry (TGA/ DSC)

TGA/DSC analysis was carried out on certified grade gypsum powder (99% Fisher Scientific) using the NETSZCH STA 449 F1 Jupiter® over the temperature range of 25-500°C in a nitrogen atmosphere. A platinum pan of diameter 6.8mm and a 1mm hole was used. The dehydration behaviour of gypsum, heated at a rate of 0.1, 0.5, 1, 5, 10, 15, 20°C min⁻¹ with a gas flow of 20 mL min⁻¹ is displayed in Figure 6.7. Sample masses used were 22.0-26.1 mg. TGA/ DSC was used to measure the in-situ water lost as gypsum undergoes direct heating. TGA can be used to identify the solid phase and their variation in composition as temperature is increased.

Heating rate has a significant effect on dehydration kinetics and so heating rates varying from 0.1 – 20°C per minute were chosen for investigation.

6.3.3 Synchrotron XRD analysis

Synchrotron XRD data was used to study the impact of pre-heat temperature on the crystal structure. In-situ XRD measurements were carried out over two sessions at the UK synchrotron Diamond Light Source, using a 2D monochromatic high-energy beam (54.715 keV and $\lambda=0.2266 \text{ \AA}$ (session 1) or 0.23345 Å and 53.111 keV (session 2) on the Joint Engineering, Environmental and Processing (I12-JEEP) beamline. The X-ray beam size was 0.3 x 0.3 mm². X-ray diffraction images were collected in transmission geometry with a large area 2D detector (Pixium RF4343; Thales). The exposure time for collection of a single diffraction image was 240 seconds. The precise energy calibration was determined by measuring a CeO₂ standard (NIST Standard Reference Material 674b) at five standard-to-detector distances with the relative difference of 100 mm between two detector positions following the approach of Hart et al. (2013). A standard sample was then measured again to calibrate the absolute sample-to-detector distance, the orthogonality of the detector with respect to the incoming beam, and the position of the beam centre on the detector. 2D patterns were radially integrated in Q-space to obtain intensity curves, I(Q), using DAWN software. A gypsum standard was run at room temperature plus four gypsum samples which had been calcined to 40°C, 105°C, 200°C and 500°C respectively for 16 hours each (session 1) and 40°C, 105°C, 200°C, 300°C, 400°C, and 500°C (session 2). Samples were contained in 0.5 mm diameter capillaries and sealed. XRD pattern analysis and Rietveld refinement was carried out using TOPAS (Bruker 2009) by Dr. Andrea Hamilton and Dr. Pieter Bots. Crystallographic information files used in the refinement are given in Table 6.2.

Table 6.2: Crystallographic information files used in the analysis and Rietveld refinement of the gypsum XRD results.

Phase	ICSD reference	ICSD cell parameters
Gypsum	15982	C2/c; a=10.47Å, b=15.15Å, c=6.5Å, β =151.55, Z=4
Hemihydrate (bassanite)	92947	I2; a=12.0317Å, b=6.9272Å, c=12.6711Å, β =90.27, Z=12.
γ -Anhydrite	86316	P6 ₂ 22; a=b=6.998Å, c=6.3303Å, Z=3
Anhydrite	16382	Amma; a=7.006Å, b=6.998Å, c=6.245Å, z=4

6.3.4 Crystal growth analysis

The stages of gypsum crystal growth from hydrated β -bassanite were observed using image analysis of optical photomicrographs.

Early stage β -bassanite hydration studies were carried out using a Nikon Eclipse LV100ND optical microscope and DS-Ri2 camera to explore the industrial calcinating temperatures.

To image the calcium sulphate hydration reaction at room temperature 4×10^{-4} g of β -bassanite powder was distributed and taped to a glass slide. Once fixed in place 10 μ l of deionised water was added to the slide to create a saturated solution. Each of the microscope images were maintained at the same magnification to allow for accurate area analysis. No grain size analysis was carried out as optical resolution prohibits effective quantification of crystal growth in 3D. The focus of this study is the growth of gypsum crystals and for simplicity the dissolution of bassanite is ignored. A micrograph of the gypsum crystals during growth was taken every 2 minutes, over a period of 1 hour.

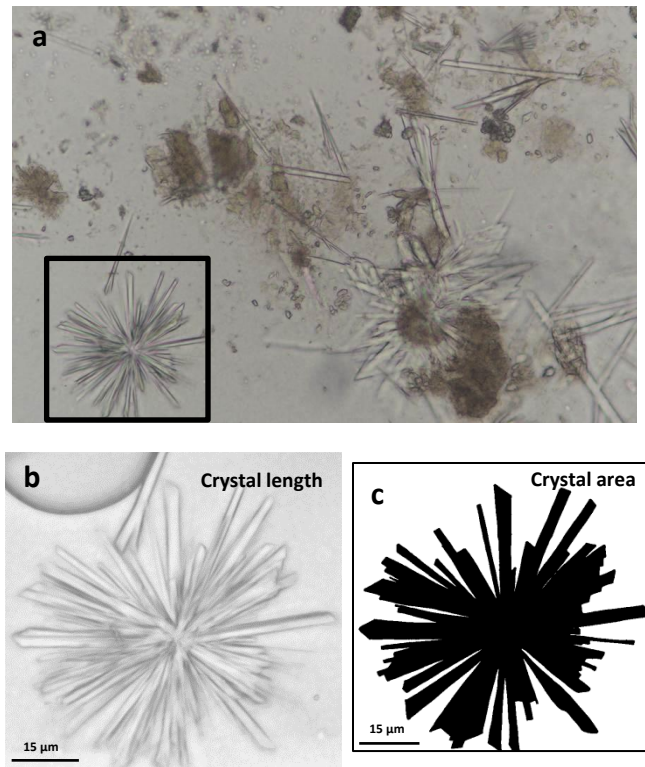


Figure 6.2: Gypsum calcinated at 160°C to form β -bassanite and subsequently hydrated to show gypsum needle growth. (a) Original micrograph with selection of 1000 x 1000 pixel area. (b) Zoomed grey-scale image. (c) Binary black and white image of the gypsum crystal is used to calculate the crystal growth over time as a percentage. The black pixels occupy 39.7% of the total image area.

Images stopped being taken at 60 minutes as at that time the growth of gypsum had significantly decreased and the visible change in crystal shape/size was limited. Crystal growth was measured across the length of individual crystallites along the long axis and the total area of crystals using ImageJ.

a) Length

The length of 50 gypsum crystals per micrograph was measured using Nikon software (NIS Elements BR Version 4.5) and the mean crystal length for each microscope image was calculated.

b) Area

In order to characterise both the changes in length and width of the gypsum crystals, the area of crystal growth was calculated using a three-step process.

Chapter 6 - Calcium sulphate phases

From each microscope section a smaller area of 1000 x 1000 pixels was used to analyse the area of gypsum crystal growth over time (Figure 6.2).

Due to both reflected light and shadow effects on the microscope slides standard filtering and thresholding of grey-values in ImageJ was not possible. All images were loaded and edited into binary images using the graphic editing software Inkscape. Here black pixels represent the newly grown crystals and the white pixels represent the background/pore space. The new binary image was compared with the original image to ensure there were no artefacts present as a result of the processing technique. The black pixels were counted and the percentage of black to white pixels (total crystal area) was calculated using ImageJ.

6.4 Results and discussion

6.4.1 The dehydration of calcium sulphate

The starting material used for session 1 was reagent grade gypsum (Sigma Aldrich, Fisher Scientific) but it was observed after session 1 that the gypsum used contained 13% bassanite, as analysed from the XRD patterns. New gypsum was purchased (Fisher Scientific), XRD analysis confirms it contained 2 wt% bassanite and this was used for session 2 samples.

Low temperature samples: no pre-heating and 40°C:

Enough bassanite was present in the session 1 samples to allow both phases to be refined, the quantity of bassanite is 13 wt% (no heating) and 19 wt% (40°C) but analysis was carried out on separate samples which could reflect variation in the source gypsum. Refinement shows the unit cell volume is reduced from 1058.8512 Å³ to 1057.8524 Å³ (0.09 %) in the 40°C sample compared to the unheated one and the main change in cell parameters is the c-axis reduction in the heated sample. The structure of bassanite has channels where water molecules are located which is situated along the c-axis (Figure 6.3). Water can be removed from these channels without significant structural re-ordering. It is possible that the observed reduction in bassanite cell volume and c-axis is a real effect from heating and if so, it would be the first-time water loss from gentle heating has been reported. Considering gypsum, the variation in unit cell between the two samples is significantly less than bassanite.

A slight increase in cell volume by 0.003% (494.722 \AA^3 at room temperature to 494.738 \AA^3 at 40°C) is observed but this is 30 times less than alteration to the bassanite cell, which suggests the effect is real, although the conclusion is tentative.

The second session samples, made from a new bottle of gypsum, have very little bassanite (c. 2 wt%) in both samples, and the quantity is too small to accurately refine the bassanite structure. Gypsum cell volume increases between the unheated and heated sample, as before, this time by 0.05%.

Heating to 105°C :

In both samples (sessions 1 and 2) heated to 105°C , no gypsum is present (Figure's 6.4 and 6.5). This is in line with the literature and TGA/DSC results, which show that gypsum converts to bassanite at 94°C at the lowest heating rate used (0.1 K/min). After conversion to bassanite, γ -anhydrite can start to form straight away (Jacques et al., 2009). Berthold et al. (2011) report they are unconvinced that γ -anhydrite forms at all. Their explanation is that bassanite loses water from the zeolite-like channels along the c-axis but without undergoing structural re-arrangement from monoclinic to hexagonal (ICSD 86316, γ -anhydrite). Both Jacques et al. (2009) and Berthold et al. (2011) used *in situ* XRD with the same heating rate (10 K/min) and the similar data collection rates but Jacques et al. (2009) used synchrotron XRD and more sophisticated crystallographic analyses. Uncertainty over the existence of γ -anhydrite arises from the similarity of the powder patterns for both phases and its instability at ambient conditions. Jacques et al. (2009) show that the bassanite unit cell expands on heating, but oxygen atoms linked to water in the channels reduce occupancy at c. 235°C showing water loss from bassanite without structural re-arrangement. They see structural re-arrangement occur at c. 252°C when the unit cell volume jumps up (but c-axis length sharply reduces) due to water loss from bassanite and then re-organisation into the higher symmetry hexagonal cell. The samples presented here were heated differently to both Jacques et al. (2009) and Berthold et al. (2011): isothermally for 16 hours and then cooled in a desiccator. Therefore, the transition temperatures would not be expected to be the same as those presented by Jacques et al. (2009) and Berthold et al. (2011). The patterns were refined as either a) gypsum, b) bassanite, c) γ -anhydrite, d) bassanite + γ -anhydrite, e) bassanite + β -anhydrite, f)

Chapter 6 - Calcium sulphate phases

γ -anhydrite + β -anhydrite or γ β -anhydrite with Rwp (goodness of fit) values used to choose the most appropriate scenario. Results are presented in Table 6.3. From visual inspection of Figure 6.5, highlighted as the region where the two phases, bassanite and γ -anhydrite, show the clearest divergence from each other, the samples appear to be bassanite. Refinement (Table 6.3) of the session 1 sample produces the best Rwp for 100% bassanite while the refinement for the session 2 sample produces the best Rwp for a mix of bassanite (77%) and γ -anhydrite (23%). The reflections for the session 2 sample are slightly shifted towards the γ -anhydrite positions, which is possibly why refining the pattern with both phases produces a better goodness of fit (Rwp=2.74 compared to 4.25). A tentative alternative is that the sample is slightly dehydrated bassanite.

Heating to 200°C

For both samples (session 1 and session 2) the best fit is to bassanite only although bassanite + γ -anhydrite also produces a good Rwp value for the first session sample, but the calculated quantity of γ -anhydrite is very low (3.4% with 96.6% bassanite). In both cases, the 200°C sample shows continual ‘shift’ of the highlighted reflections (Figure 6.6) towards the γ -anhydrite but without transforming into γ -anhydrite, as all patterns for either session at 105°C and 200°C cannot be refined as pure γ -anhydrite.

Heating to 300°C:

Only one sample was heated to 300°C (session 2). The sample contained β -anhydrite and was refined as β -anhydrite + bassanite or β -anhydrite+ γ -anhydrite. The lowest Rwp was achieved by refining as β -anhydrite (71%) and bassanite (29%).

Heating to 400°C and 500°C:

The sample is pure β -anhydrite for both samples analysed.

Both samples were heated for 16 hours in an open (unhydrated) atmosphere, cooled in a desiccator and sealed in glass capillary tubes prior to analysis. It’s clear that under these conditions, gypsum does not reform and the sample remains bassanite or

Chapter 6 - Calcium sulphate phases

bassanite and β -anhydrite, depending on calcining temperature. There is some indication that γ -anhydrite remained in the room temperature sample (105°C, session 2 sample) and while γ -anhydrite is unstable at room temperature in the presence of moisture, as it quickly converts to bassanite, the samples were cooled over desiccant. No sample was purely γ -anhydrite and it is possible that the 105°C sample was slightly dehydrated bassanite rather than γ -anhydrite.

Table 6.3: Rietveld refinement results using TOPAS. Where the Rwp values were very similar, the simplest solution was chosen (highlighted in bold).

Sample	Gypsum	Bassanite	Bassanite + γ - anhydrite	γ -anhydrite	Bassanite + β - anhydrite	γ - anhydrite + β - anhydrite	β - anhydrite
Unheated (session 1)	a	10.4903	12.0185				
	b	15.1999	6.9354				
	c	6.5228	12.7033				
	β	157.5974	90.1476				
	V	494.7220	1058.8512				
	Rwp	9.459					
Unheated (session 2)	a	10.4949	12.0211				
	b	15.2063	6.9147				
	c	6.5255	12.6964				
	β	151.5936	90.1828				
	V	495.4172	1053.6793				
	Rwp	6.672					
40°C (session 1)	a	10.4909	12.0267				
	b	15.1991	6.9343				
	c	6.5231	12.6846				
	β	151.598	90.188				
	V	494.738	1057.8524				
	Rwp	9.102					
40°C (session 2)	a	10.4997	11.9834				
	b	15.2073	6.9528				
	c	6.527	12.65734				
	β	151.6053	90.2553				
	V	95.6782	1054.5783				
	Rwp	7.93					
105°C (session 1)	a		12.037	12.0368			Refinement poor
	b		6.9343	0.9341			
	c		12.6666	12.6663			

Chapter 6 - Calcium sulphate phases

	β	90.2679	90.2682		
	V	1057.2489	1057.1732		
	Rwp	4.089	4.082	10.763	
105°C (session 2)	a	12.0728	12.6543	Refinement poor	
	b	0.9265	6.9273		
	c	12.6456	12.6417		
	β	90.1508	90.1255		
	V	1057.4471	1055.628		
	Rwp	4.254	2.738	8.159	
200°C (session 1)	a	12.0686	12.6706	Refinement poor	
	b	6.9306	6.9308		
	c	12.644	12.6453		
	β	90.1142	90.1028		
	V	1057.5767	1057.8887		
	Rwp	4.883	4.653	8.737	
200°C (session 2)	a	12.0499	12.0503	Refinement poor	
	b	6.9321	6.9318		
	c	12.6834	12.6833		
	β	90.2481	90.2439		
	V	1059.446	1059.4252		
	Rwp	3.922	3.12	28	
300°C (session 2)	a			12.1017	7.0006
	b			6.9349	6.9922
	c			12.6170	6.2554
	β			90.295	
	V			1058.8605	306.2
	Rwp			2.546	3.84
400°C (session 2)	a				6.9996
	b				6.9918
	c				6.2437
	V				305.5657
	Rwp				2.654
500°C (session 2)	a				6.9998
	b				6.9924
	c				6.2441
	V				305.6205
	Rwp				2.685

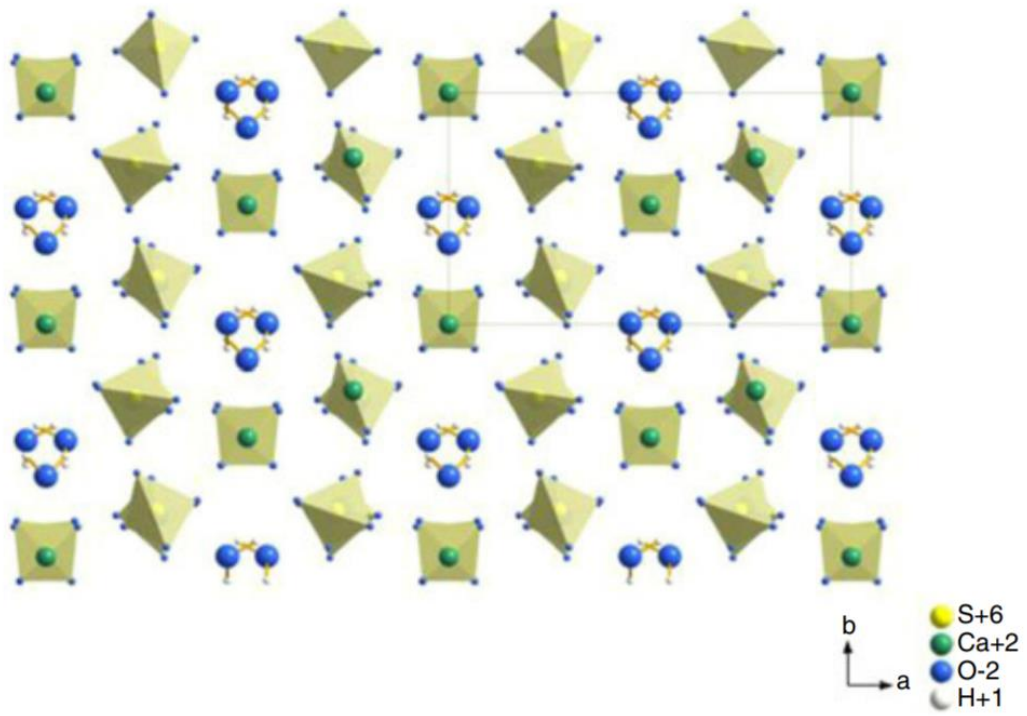


Figure 6.3: Bassanite displaying channel structure. From Berthold et al. (2011).

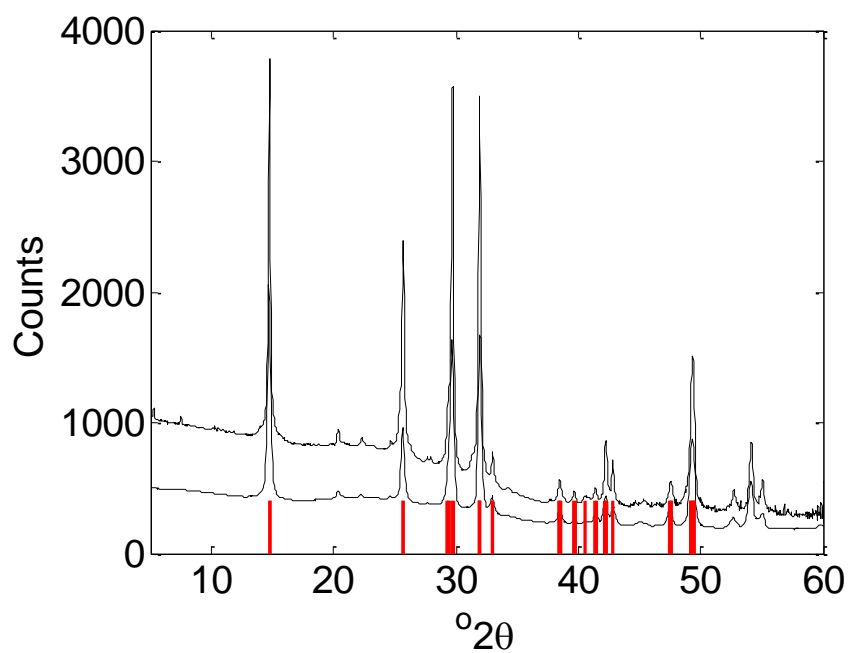


Figure 6.4: Synchrotron XRD pattern of gypsum heated to 105°C. Top pattern is from the second session, bottom pattern is from the first session. Bassanite (ICSD collection code 92947) reflection positions are marked in red.

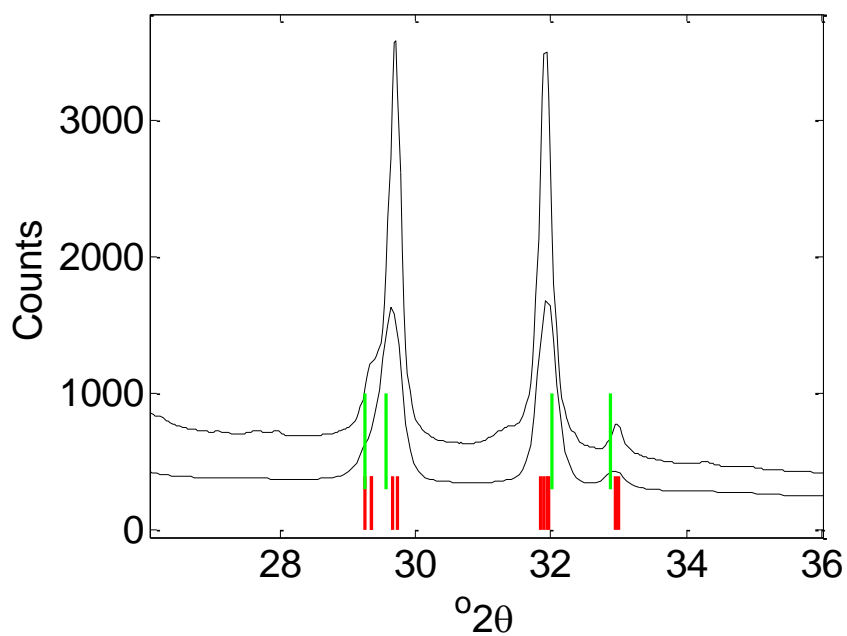


Figure 6.5: A magnified version of Figure 6.4, showing γ -anhydrite (ICSD collection code 86316) reflection positions marked in green.

105 and 200 °C, session 1

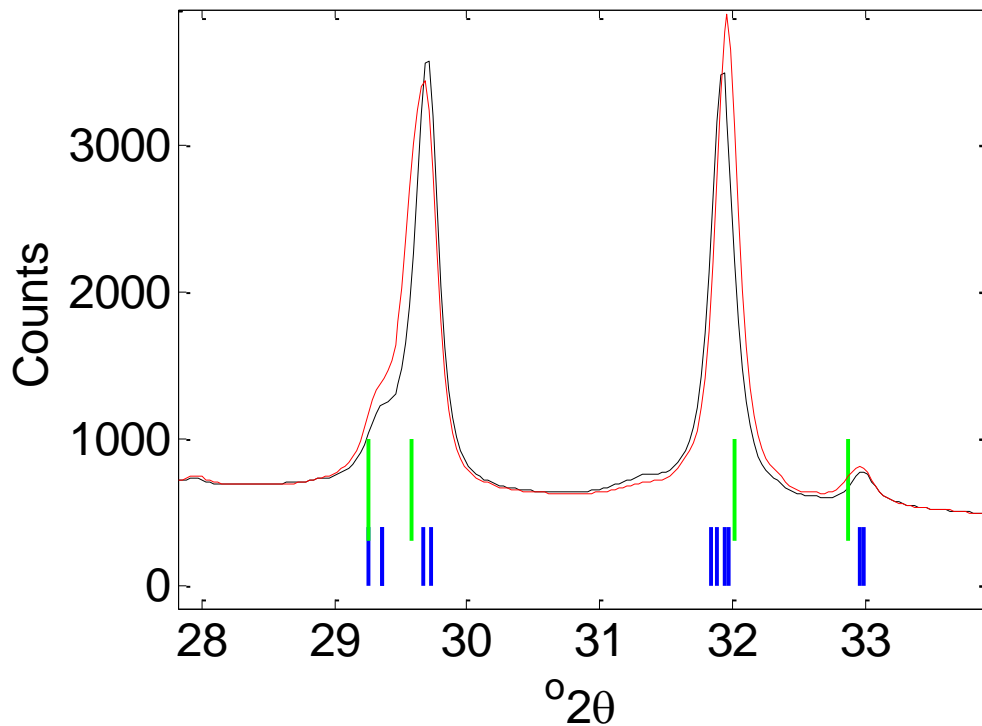


Figure 6.6: XRD pattern of calcium sulphate samples from session 1. Black is 105°C, red is 200°C, blue stickplot is bassanite, green is gamma-anhydrite. It's clear that the 200°C sample is shifted towards the gamma anhydrite reflections compared to the 105°C samples.

6.4.1.1 TGA

The bassanite temperature of formation varies with heating rate (Figure 6.7), as one would generally expect, but the temperature of formation doubles over the heating rate range explored: 0.1 – 20 K/min as shown in Table 6.4. Jacques et al (2009) and Lou et al. (2011) both show using TGA (Lou et al. 2011) and XRD (Jacques et al. 2009), that water vapour pressure affects the transition temperature. Here a pin hole lid is used to produce an autogenous P_{H_2O} which is similar to the sealed tube with excess moisture used by Jacques et al. (2009), who see gypsum-bassanite transition at 162.5°C (heating rate = 10K/min) and matches well with the value presented here for 10K/min. As shown in Figure 6.8, the expected mass loss for bassanite formation (dashed horizontal line at fractional mass=0.843) is reached but the subsequent mass loss for complete dehydration to anhydrite is not reached within the temperature

Chapter 6 - Calcium sulphate phases

range explored (up to 500°C) which was chosen in line with the synchrotron XRD data. Compared with other studies of gypsum dehydration under autogenous conditions (sealed crucible with a pin hole lid), it is unusual that full dehydration is not reached and worthy of further study. One explanation is that as the vapour pressure of water is increased, the bassanite structure is stabilised to higher temperatures and variations might be present between publications using different sealed crucibles. A set of three experiments was carried out at 5K/min to test instrument reproducibility.

Table 6.4: TGA gypsum- bassanite transition temperatures with heating rate.

Heating rate (K/min)	Temperature of bassanite formation (°C)
0.1	94
0.5	114
5	149
10	162
20	180

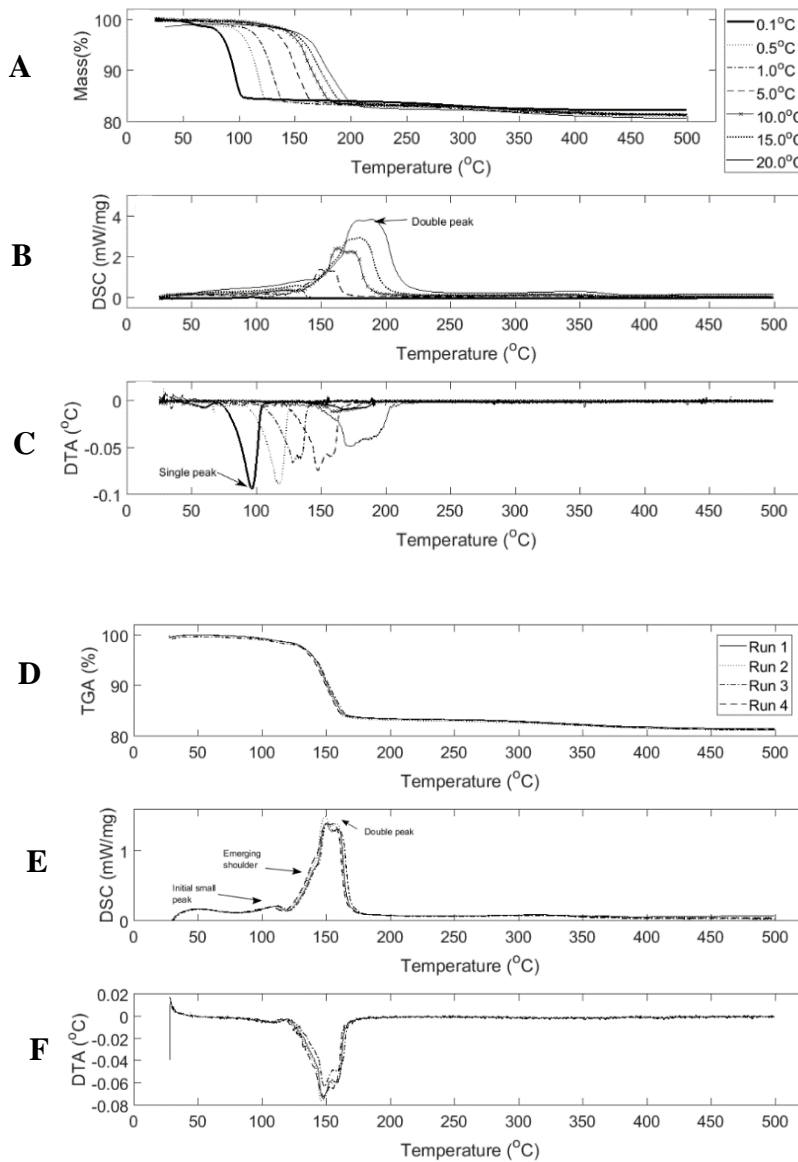


Figure 6.7: Thermogravimetric analysis of gypsum powder. A-C) Gypsum TGA (A), DSC (B) and DTA (C) results when heated from ambient temperature to 500°C at 0.1, 0.5, 1, 5, 10, 15, 20°C/min. Legend values are all in °C/min. E-F) Gypsum TGA (D), DSC (E) and DTA (F) curves for gypsum heated from ambient temperature to 500°C at 5°C/min with repeats. All tests were run in a nitrogen atmosphere with a purge rate of 50 mL/min. At heating rates of 0.1-10°C/min DTA results highlight the two stages of gypsum dehydration by the double peak. However, heating rates of 15 and 20°C/min show a single peak thus ‘skip’ over the second peak. The double peak can be interpreted as the two stages of gypsum dehydration (Equations 1 & 2).

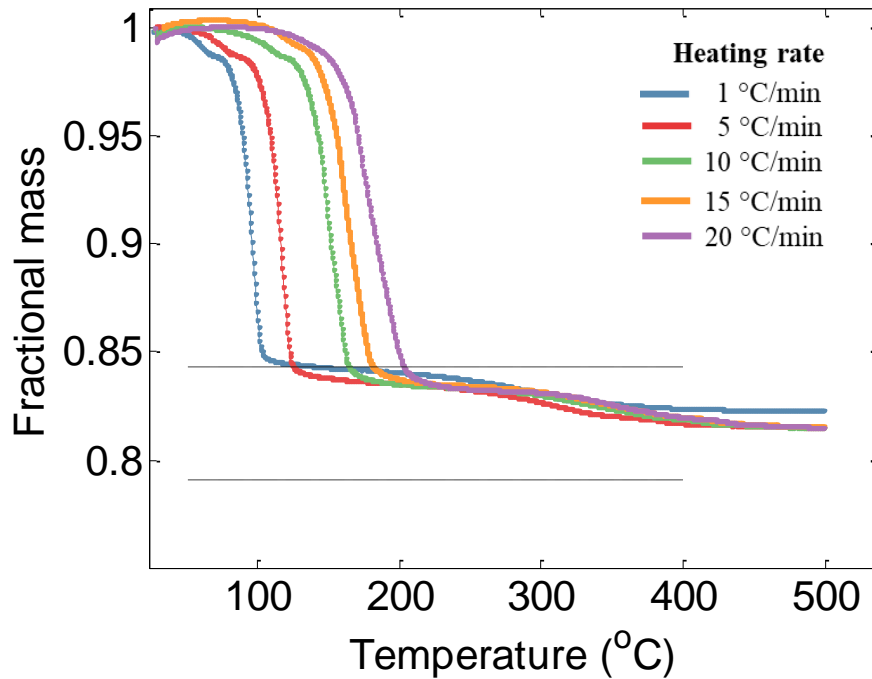


Figure 6.8: TGA analysis where the horizontal dashed lines at 0.8430 and 0.7907 show the theoretical fractional mass content of bassanite and anhydrite. Under the conditions of the experiment, the sample does not fully dehydrate to anhydrite.

Dehydration began at 60°C and continued until approximately 130°C where there was a sharp 14% mass decrease until 175°C. At the end of the experiment a total mass loss of $18.7\% \pm 0.5\%$ is observed. This is equivalent to losing 89% of molecular water, which leaves 11% molecular water, again showing complete dehydration was not reached.

The reaction enthalpy for the dehydration of gypsum to bassanite was between 372-400 J g⁻¹. Dehydration reaches completion between 105-200°C. A mass loss of 0.2% is observed between room temperature and 95°C, and a total mass loss of 15-16% between 95-170°C.

6.4.1.2 DSC

Lou et al. (2011) show that using a sealed crucible produces a double decomposition peak which corresponds to the dehydration of gypsum to bassanite and bassanite to γ -anhydrite while they state a single endothermic peak corresponds to a one step

dehydration of gypsum to γ -anhydrite. A similar feature at higher heating rates can be identified (Figure 6.7E) and is mirrored in the DTA results (Figure 6.7F). As the peaks overlap, the two dehydration processes are occurring simultaneously, which indicates that in a high P_{H_2O} pressure environment three main calcium sulphate phases (gypsum, bassanite and γ -anhydrite) can co-exist. However, it should be noted that thermal techniques cannot distinguish water free bassanite from γ -anhydrite and therefore the second peak could also correspond to water leaving the crystallographic channels of bassanite (Figure 6.3). As TGA shows, pure water free bassanite (or γ -anhydrite) is not obtained, therefore there is some water still trapped within the bassanite channels which is very slowly lost in this autogenous system, even at 500°C. At the lower heating rates, it is likely that the 2 endothermic peaks overlap more completely and therefore cannot be meaningfully deconvolved.

6.4.2 The hydration of calcium sulphate: gypsum growth and kinetics

Spherulite is a term given to radially polycrystalline aggregates with an outer spherical envelope (Shtukenberg et al. 2012). Such a form can only result from the successive branching of a nucleus. It must be non-crystallographic branching, also known as small angle branching and therefore the branches cannot be crystallographically related – such as dendritic growth observed in snowflakes or the fractal like forms of diffusion limited aggregates. High crystallographic driving force is a precondition of spherulitic growth which produces the exaggerated aspect ratio (long thin needles). The morphology observed (note, only the ball shaped aggregates) is tentatively described as open spherulites, also called spiky spherulites by Shtukenberg et al. (2012). The driving force for crystallisation from solution is supersaturation: where $\Delta\mu$ is the change in chemical potential, R is the universal gas constant ($8.314 \text{ J K}^{-1}\text{mol}^{-1}$), T is absolute temperature in Kelvin. IAP is the ion activity product and K_{sp} is the solubility product. For stoichiometric solutions this simplifies to concentration (C , molality) divided by the concentration at saturation (C_{eq} , molality). v is the number of ions in the neutral complex. Shtukenberg et al. (2012) say that $\Delta\mu/RTv$ has to be $> \sim 0.6$ for spherulitic growth to be likely. Using solubility values from Krumbalz (2018) for bassanite and gypsum, the calculated value of $\Delta\mu/RTv$ is 1.43. Assuming the needles produced are not crystallographically related (single crystal diffraction is required to confirm this) then

Chapter 6 - Calcium sulphate phases

this is one of the few reports of gypsum spherulites. From the microscope and X-CT images of the gypsum cemented sandstones in Chapter 7 partial spherulites appear to be present around the sand grains. Shtukenberg et al. (2012) say the growth regime is defined by the product (see equation 3 below) where D is the diffusion coefficient of the ion ($9.285 \times 10^{-10} \text{ m}^2/\text{s}$) from Samson et al. (2003). δ_D is the thickness of the diffusion boundary layer which is often equal to the radius of the growing crystal (average gypsum radius at 60 minutes ranges from 4.34-31.55 μm - see Figure 6.9). β is the kinetic coefficient (growth rate). By using a growth rate of $3 \times 10^{-8} \text{ m/s}$ a value of 0.01 is achieved (this is a dimensionless value). When the value is less than 1 then growth is interface controlled. When it is greater than 1 then it is diffusion controlled. Therefore, growth of the gypsum crystal is interface controlled.

Equation 1
$$\frac{\Delta\mu}{RT} = \ln \left(\frac{IAP}{K_{sp}} \right)$$

Equation 2
$$\frac{\Delta\mu}{RTv} = \ln \left(\frac{C}{C_{eq}} \right)$$

Equation 3
$$\frac{\beta\delta_D}{D}$$

a) Crystal Length

Gypsum crystal growth is observed in samples calcined at all temperatures (Figures 6.9 and 6.10). Gypsum crystals grew up to 116.74 μm over the period of 60 minutes (growth rate of $3 \times 10^{-8} \text{ m/s}$). Crystal length varied from 0.56 to 63.1 μm . Here there are two key observations. The first is the greatest crystal length is seen with a calcination temperature of 160°C. Secondly, the rate of crystal growth is fastest at a calcination temperature of 160°C. For each crystal calcination temperature and time period 50 crystal length measurements were carried out.

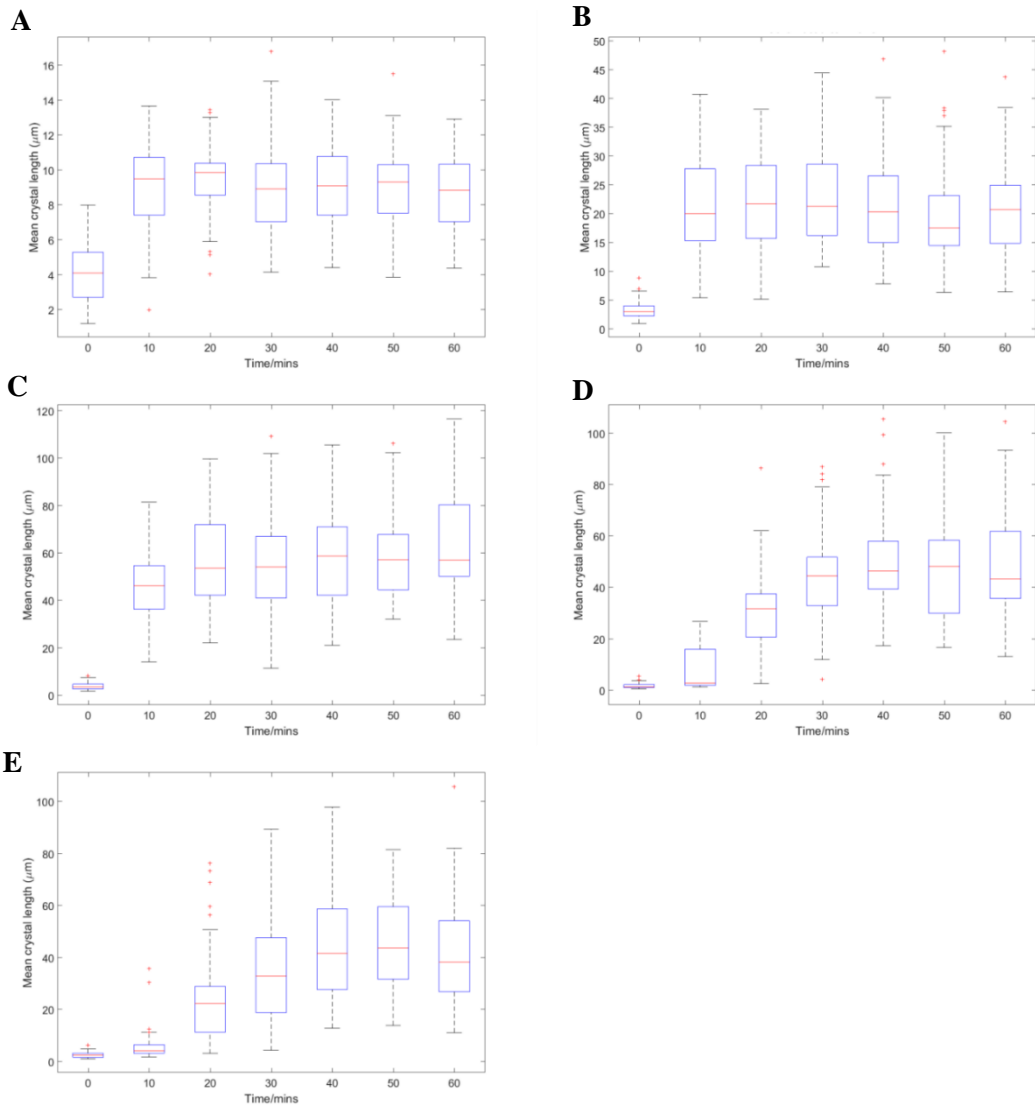


Figure 6.9: Average crystal lengths for each calcination temperature after set time periods (10, 20, 30 mins. etc.). (A) 120° calcination temperature. (B) 140° calcination temperature. (C) 160° calcination temperature. (D) 180° calcination temperature. (E) 200° calcination temperature. The calcination temperature which shows the fastest initial growth rate and the longest crystals is 160°C. For each calcination temperature and time period 50 crystal lengths were measured.

b) Crystal Area

Figure 6.10 shows the binary images of the growth of gypsum from hydrated bassanite with the total crystal areas plotted in Figure 6.11. For each sample three

Chapter 6 - Calcium sulphate phases

steps during crystal growth are identified. These are crystal initiation, acceleratory period and the completion of hydration. For samples with a greater calcination temperature, the time at which gypsum crystal growth initiated was later. For samples calcined to 120°C and 140°C the initiation period takes places before the first measurement at 2 minutes. In the results only the acceleratory period (120°C = 2-4 minutes, 140°C = 2-24 minutes) and the completion of hydration (120°C = after 4 minutes, 140°C = after 24 minutes) can be identified. For samples calcined to 160, 180 and 200°C all three stages can be identified (initiations = 0 - 4 mins, 0-12 mins, 0 - 12 mins respectively); acceleratory period = 4 – 18 mins, 12-40 mins, 12 - 50 mins respectively; completion of hydration = after 18, 40 and 50 minutes respectively). The time for which each of the steps lasts for is dependent on the calcination temperature chosen. The sample calcined to 140°C displays the largest percentage crystal area of all samples tested (66%), whereas samples with calcination temperatures of 160°C, 180°C and 200°C display a final 2D crystal area between 53-57%.

1

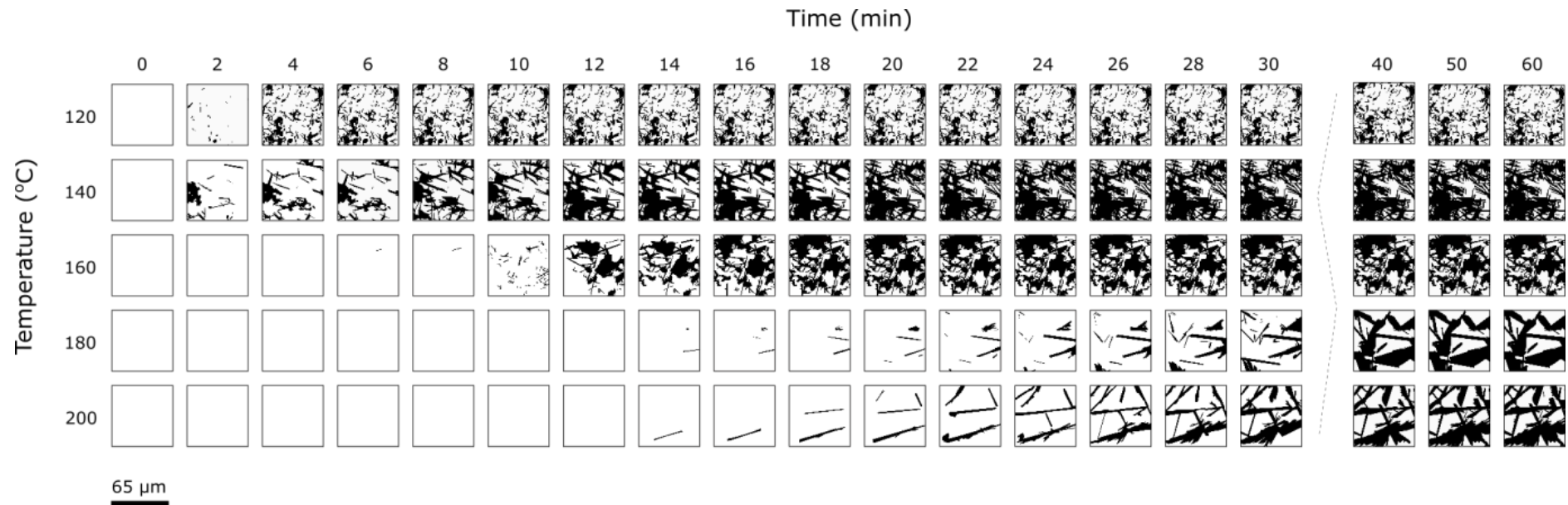


Figure 6.10: Binary images demonstrating how calcination temperatures (120, 140, 160, 180 and 200°C) impacts the rate and size of gypsum crystal growth. Image analysis was used to calculate the percentage of black (crystal) and white (background/pore space) pixels for each calcination temperature hydrated over a 60-minute period. Each image is 1000 x 1000px in size.

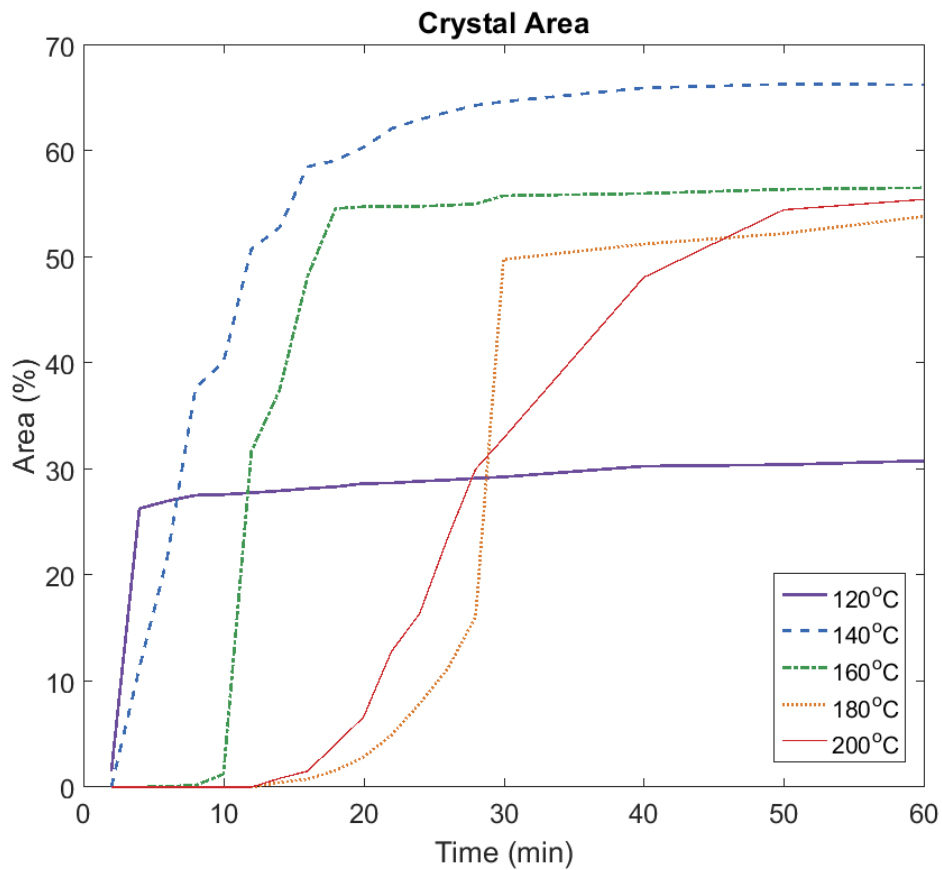


Figure 6.11: For each calcination temperature three steps of gypsum crystal growth were identified: initiation, acceleratory period and completion of hydration.

6.5 Summary

The results of this chapter were used to understand gypsum formation from bassanite for use in creating synthetic sandstone samples. Results are as follows:

- Calcium sulphate hydrates coexist during the dehydration of gypsum. This was proven using both hard synchrotron XRD and TGA analysis.
- Detailed image analysis shows that varied calcination temperatures (120-200°C) directly impact the rate of crystal growth and the size of the gypsum crystals which are formed during hydration.

The research contributes to the expanding work on calcium sulphate system kinetics however, in doing so, emphasises the complexities of dehydration and hydration in

Chapter 6 - Calcium sulphate phases

the calcium sulphate system. Notably the results indicate the importance of choosing the best calcination temperature to suit the application.

Recommendations:

- Further work should look at the implications of crystal length on the mechanical properties of plaster of Paris and how the crystal length can affect the choice of additive.
- Carry out single crystal diffraction to confirm if the gypsum needles produced are crystallographically related.

Chapter 7 - Making synthetic sandstones

7.1 Rationale

There are an increasing number of studies which focus on deformation bands in poorly consolidated sandstones (Chapter 2). Shipton et al. (2017) speculate the importance of understanding the conditions which lead to the formation of deformation bands in shallow subsurface conditions. Understanding deformation in natural rocks is complex because of multiple interacting parameters such as mineralogy, distribution of cement, composition and grain size. By using synthetic sandstones, the structure of natural sandstones can be imitated, and the system simplified by controlling the parameters (e.g. mineralogy, grain size, grain shape, density).

In this chapter I used two different cementing phases to recreate sandstone in the laboratory: gypsum and microbially induced calcite precipitation (MICP). The synthetic sandstones are formed in the shape of cylinders and cuboids (Table 7.1). I explore the creation of synthetic sandstones of variable strengths using gypsum and MICP as cementing agents. Then using microscopy and X-CT analysis I investigate the distribution and connectivity of sand grains, cement and pores in these samples. In order to fully compare these synthetic sandstones to naturally formed sandstones it is important to explore the mechanical properties of the sandstones. The mechanical properties of these synthetically cemented sandstones are discussed in Chapter 8.

Table 7.1: Gypsum and MICP synthetic samples were created in the following shapes in preparation for mechanical testing (Chapter 8).

Shape of sample	Deformation method
Cylinder	Uniaxial compression strength (UCS) and triaxial testing
Cuboid	Shear box testing

7.2 Literature review: synthetic sandstones

Synthetic sandstones have been previously made using various materials as cement to bind the grains together.

Cement phases have included resin (Almossawi 1988), Portland cement (Acar and El-Tahir 1986; Chang and Woods 1993; Saidi et al. 2005; Asaei and Moosavi 2013), epoxy glue (Rathore et al. 1995), lime (Chang and Woods 1993), silica-glass (David et al. 1998), sodium silicate solution under pressure (Holt et al. 1993), silica gel (Brok et al. 1997), MICP (DeJong et al. 2006; Anbu et al. 2016), calcium carbonate (Molenaar and Venmans 1993) and gypsum (Ismail et al. 2002; Mohsin and Airey 2005; DeJong et al. 2006).

7.2.1 Gypsum cemented sandstones

Gypsum cemented sandstones have been created by dry mixing sand and bassanite powder together by weight %, compressing it in a cylinder mould, and saturating the sample in a triaxial rig or under confining pressure for a period of time (Huang and Airey 1991; Ismail et al. 2002; Mohsin and Airey 2005; DeJong et al. 2006).

Gypsum was chosen as a cement type because of its short curing time (less than 1 month). Confining pressure is applied during cementation to encourage formation of a grain supported matrix. Table 7.2 lists the confining pressures used to form synthetic gypsum sandstones in previous studies.

It should be noted that the starting phase in the work presented in this thesis is bassanite, not gypsum (see Chapter 6). It is the dissolution of bassanite that allows the less soluble phase, gypsum, to form.

Table 7.2: Confining pressures used to form synthetic gypsum sandstone from previous gypsum studies.

Study	Confining pressure (kPa)
Huang and Airey (1998)	30
Ismail et al. (2002)	200-800
Mohsin and Airey (2005)	300
DeJong et al. (2006)	100 and 50

Chapter 7 - Making synthetic sandstones

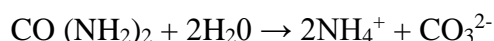
Ismail et al. (2002) and DeJong et al (2006) use SEM to image the gypsum crystals around the sand grains. However, none of the other studies of artificially gypsum cemented sandstones have explored the 3D distribution of gypsum cement across the sample. It is likely that the gypsum crystals start forming when bassanite dissolves (Chapter 6). This could lead to reduced permeability around the water injection area or gypsum could accumulate at the base of the sample as the bassanite crystals are finer ($< 2\mu\text{m}$ in length when initially forming) than the pores. Ismail et al. (2002) note that the gypsum crystals tend to form predominantly along the flat surfaces of the sand grain.

7.2.2 MICP cemented sandstones

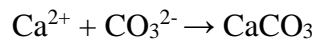
Microbially induced calcite precipitation (MICP) is a microbiological method that has previously been studied as an alternative to grout (Whiffin 2004; Mitchell and Santamarina 2005), a method to reduce soil erosion (Li et al. 2018), to seal fractures in applications such as carbon capture, and nuclear waste storage reservoirs (MacLachlan 2017; Minto et al. 2017), and improve slope stability (Salifu et al. 2016; Khaleghi and Rowshanzamir 2019) and enhancing oil recovery through plugging of pores (Nemati et al. 2005)

MICP produces calcite by the hydrolysis of urea between grains of sand. MICP is used as a sandstone cement in this study because of the short time required to prepare the samples (2 weeks), the ease with which the MICP feed can be produced and because calcite is often found as a cement in natural sandstones.

Different types of microorganism that have been previously used in MICP studies these include *Sporosarcina pasteurii* (MacLachlan 2017) and enzyme induced carbonate precipitation (EICP) (Hamdan and Kavazanjian 2016). This thesis uses *Sporosarcina pasteurii* bacteria. Calcium carbonate is produced at grain contacts to cement the loose sand grains together. The bacteria (*Sporosarcina pasteurii*) hydrolyses urea to produce ammonia (NH_4^+) and as a result precipitates calcium carbonate (CaCO_3) on the bacteria sites.



Precipitation of calcium carbonate:



Previous studies have shown the strength of the MICP cemented sandstone can be dependent upon, but is not limited to, the following factors: concentration of urea-calcium chloride solutions (the feed) (Al Qabany et al. 2012), number of feeds (Yu et al 2018), sand grain size (Terzis and Laloui 2018) and environmental conditions (Mortensen et al. 2011).

Studies using MICP to strengthen fine grained soils (DeJong et al. 2006; Whiffin et al. 2007; van Paassen et al. 2010) have focussed on using SEM analysis to image the growth of the MICP between sand grains. Most recently Terzis and Laloui (2018) have used x-ray computed tomography (XCT) to study the distribution, orientation, and bonding of MICP with the sand grains. Terzis and Laloui (2018) segmented an X-CT scan to identify the grains and cement phases of six MICP cemented samples; three fine and three medium grained sands. Although Terzis and Laloui (2018) focus on grain size and the length of calcite crystals, their volumetric calcite results can be used as a comparison for the synthetic samples made in this chapter (see Section 7.3.2). In addition, the results of Terzis and Laloui (2018) is used for comparison of the mechanical properties of synthetic sandstones in Chapter 8.

7.2.1.1 Feeding cycles

Different feeding techniques, including single/multipoint/parallel injection (Whiffin et al. 2007; Al Qabany et al. 2012; Tobler et al. 2012; Cuthbert et al. 2013; Bernardi et al. 2014; El Mountassir et al. 2014; Minto et al. 2016), premixing method (Zhao et al. 2014) or percolation under gravity (Cheng and Cord-Ruwisch 2012; Achal et al. 2015) in saturated or unsaturated sand samples, have been used to implement bacterial and CaCO_3 solutions across the literature (Mujah et al. 2017). It has been suggested that the lower the saturation level (i.e. a lower content of water in the sand sample), the more likely calcite will concentrate at inter-particle contact points therefore increasing the overall strength of the synthetic sandstone (El Mountassir et al. 2018). The preferred feeding technique across the literature is the injection method (Mujah et al. 2017). Regardless of feeding technique, it is accepted that as the number of feeding cycles is increased the strength of the previously

unconsolidated sands increases (Whiffin et al. 2007; van Paassen et al. 2010) and with an increased number of feeds a more even distribution of calcite between grains can be seen (Minto et al. 2017).

For this study all MICP feeding cycles were carried out by percolation under gravity. Percolation under gravity is the cheapest feeding technique. Cheng and Cord-Ruwisch (2012) demonstrated flow by means of percolation down the full length of a 1 m sand column. Percolation is therefore a suitable technique for the experiments in this thesis.

7.2.1.2 MICP cement distribution

MICP calcite has the ability to clog pores between grains, reducing the porosity and therefore the permeability of a sandstone. Tobler et al. (2012) demonstrated that sand treated with MICP can have up to 90-95% permeability reduction. This can cause issue at the feeding end of the sample. As the bacterial solutions are fed into the sample the pores become clogged restricting flow of the remaining solution through the sample. As a result of the cement distribution, an MICP cement gradient is formed, with the majority of cement concentrated around the feeding zone. Gomez et al. (2014), calculate calcite content by dissolving calcite with hydrochloric acid and then measuring the pressure produced by carbon dioxide gas in a test chamber. Gomez et al. (2014) shows that for each of the sample's the mass of calcite present decreases from the injection point across the length (139.7 mm) of the sample cylinder by approximately 1.5-5%. The total mass percentage of calcite present at the injection point across all the samples produced by Gomez et al. (2014) ranges from 5.5-10.5%. Distribution of bacteria has been indirectly calculated by measuring ammonium concentrations in experiment effluent using a process similar to the Nessler method (Harkes et al. 2010). By measuring the calcite content with a U-tube manometer Whiffin et al. (2007) shows that in a sample of 5 m in length calcite content tends to decrease away from the injection point from approximately 87 to 5 kg/m³.

The distribution has been visualised by X-CT studies of 15mm length samples (Terzis and Laloui 2018). Meanwhile, Minto et al. (2017) use X-CT analysis to

measure the porosity distribution in a core (50.8 mm in diameter and 100 mm long) and miniature core (13.5mm diameter) of a MICP cemented sample.

7.3 Synthetic sandstone procedure

7.3.1 Sand

The sand used in this study was from Alloa quarry, Scotland. It is arkosic in composition subrounded-subangular grains with a mean grain length of 118.7 μ m (Figure 7.1). The longest grain axis and the shortest grain axis were measured on 50 sand grains using the microscope.

Cylindrical samples were made by tamping damp sand into large cylinders (100mm length x 38mm dia.).

Cuboid samples were made by tamping damp sand into cuboid moulds (60mm length x 60mm depth x 30mm height). The cuboid moulds were made from wood wrapped in Duct Tape. Both the gypsum and MICP cemented samples were sanded to remove any uneven surfaces and fit inside the shear box (59 x 59 x 20 mm). Ideally shear box samples are formed *in situ* in the shear rig. However, due to the volume of samples and the length of time to cure (14 days for MICP samples and 28 days for gypsum samples) each sample was made externally to the shear box and then fitted into place for testing. Cylindrical samples were sanded at both ends to level them off.

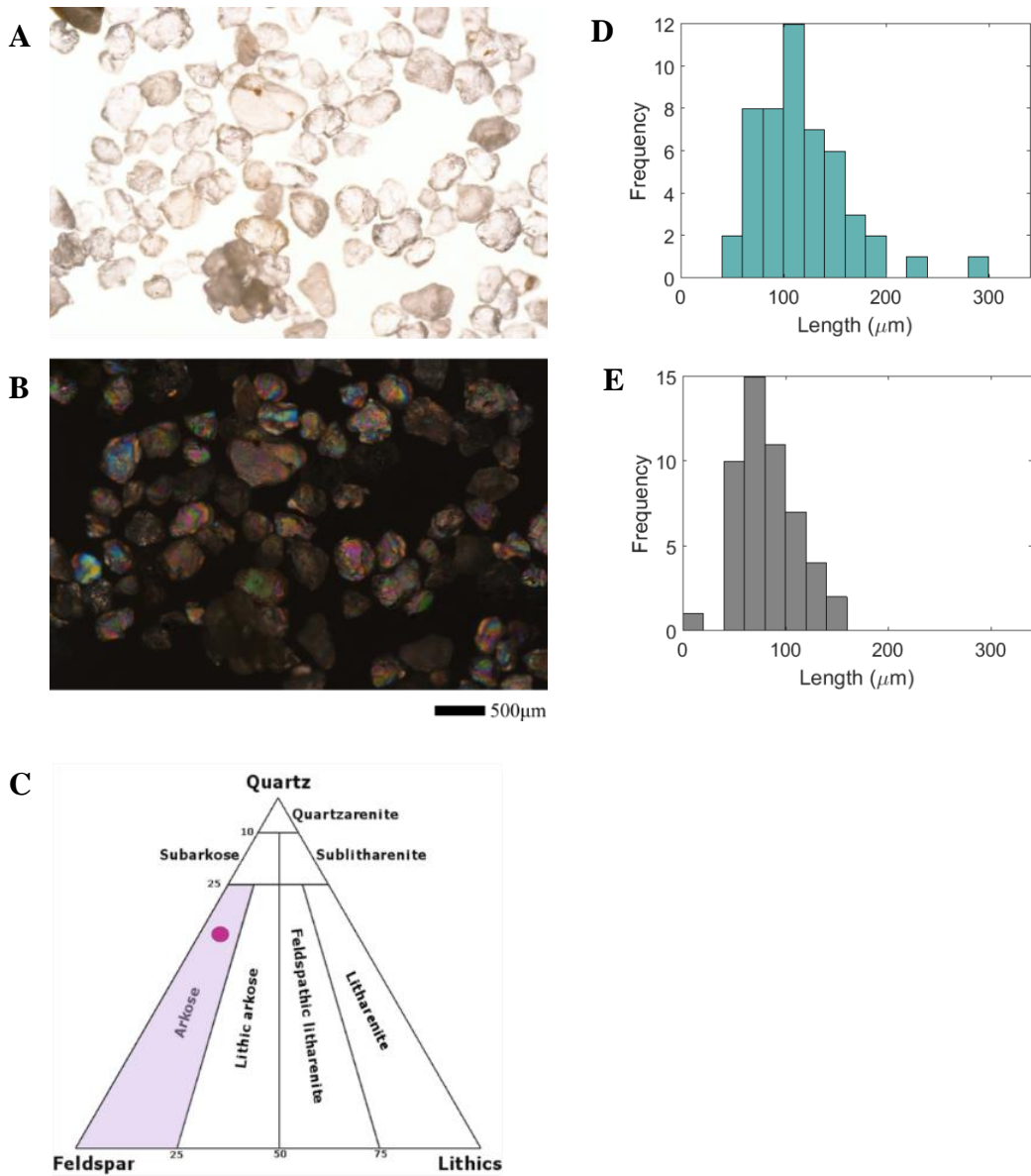


Figure 7.1: Microscope image in (A) plane polarised light and (B) cross polarised light of sand from Alloa Quarry. (C) QFL diagram of sand shows it is arkosic in composition. (D) Grain size distribution along the longest axis shows the predominant grain length to be 100-120 µm. (E) Grain size distribution along the shortest axis shows the predominant shortest axis to be 60-80µm.

7.3.2 Cementation of the synthetic sandstones

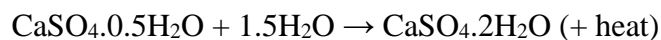
7.3.2.1 Gypsum

This study builds upon the methodology of DeJong et al. (2006), but uses bassanite powder (created by calcining gypsum powder) instead of gypsum powder. The method used to make gypsum cemented sandstones in this chapter uses a longer curing time, and a higher curing temperature (40°C) than DeJong et al. (2006).

Gypsum powder was heated in an oven to 105°C for 16 hours to form β -bassanite. 105°C was selected as the gypsum calcining temperature because the XRD analysis in Chapter 6 has shown that all gypsum is converted at 105°C to bassanite without formation of beta-anhydrite or significant formation of gamma-anhydrite.

When β -bassanite is mixed with water it becomes hydrated, dissolves, with a solubility in water of 0.30g per 100ml of water at 25°C, and precipitates as gypsum. Gypsum remains thermodynamically stable up to ~42°C therefore was stable during the curing conditions used (40°C).

Gypsum can form by the dissolution of bassanite (Wirsching 2000):



In Chapter 6 it was demonstrated that gypsum crystal growth is visible as early as two minutes after bassanite is in contact with water. This gives a limited time frame before gypsum crystal growth begins.

7.3.2.1.1 Gypsum feeding procedure

Due to the fine nature of the gypsum powder, dry pluviation was not able to be carried out.

To account for this, the respective dry volumes of sand (with initial density of sand ranging from 0.98 to 2.15 g/cm³) and β -bassanite were weighed to a constant mass, mixed and packed into moulds (cylinders and cuboids). 40 ml of deionised water was injected onto the sample surface and allowed to filter through the sample. A mass was added to the top of the samples to create a confining pressure of 1.36 kPa (cuboid) or 1.38 kPa (cylinder). The sample was then placed inside the oven at 40°C for 28 days until the sample has reached a constant mass. In order to determine the

Chapter 7 - Making synthetic sandstones

constant mass each sample was taken out of the oven and weighed every day. Figure 7.2 shows a schematic of the feeding procedure for both the cuboid and cylinder samples.

Chapter 7 - Making synthetic sandstones

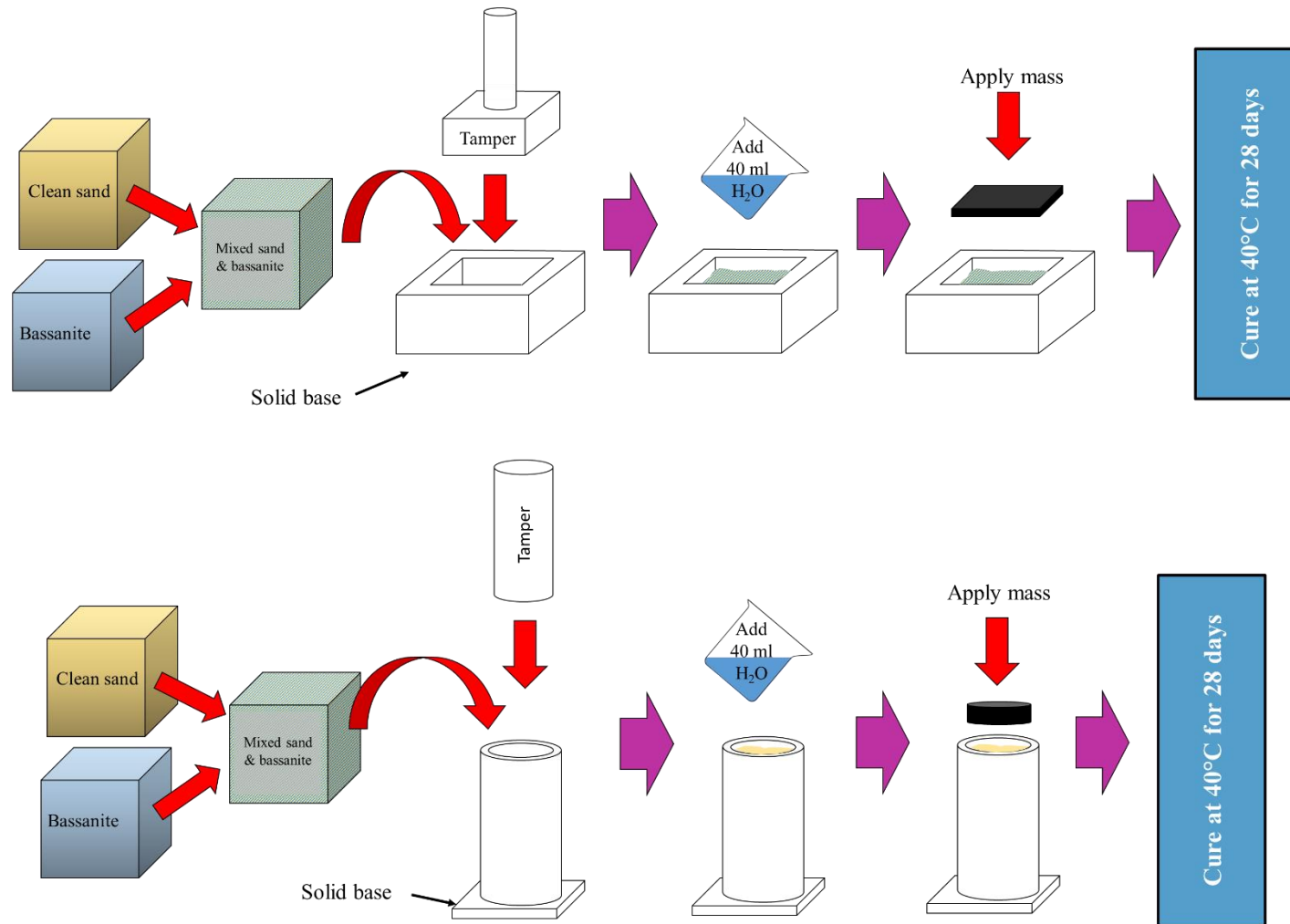


Figure 7.2: Schematic of gypsum cemented sandstone sample preparation in cuboid and cylinder moulds.

Chapter 7 - Making synthetic sandstones

Figure 7.3 shows an example of a finished gypsum cemented sandstone cuboid and cylinder. The solid density of the gypsum-cemented sandstones ranged from 1.82 to 2.63 g/cm³ with calculated porosities ranging from 6.64 to 46.61%. The measured porosities for comparison are given in the following section. The actual mass of gypsum produced from the bassanite hydration is shown in Table 7.3 and 7.4.

The confining pressure used to form these gypsum-cemented sandstones (1.36 kPa for the cuboid samples and 1.38 kPa for the cylinder samples) is lower compared with the confining pressures used by the studies in which ranged from 30 kPa to 800 kPa (Table 7.2).

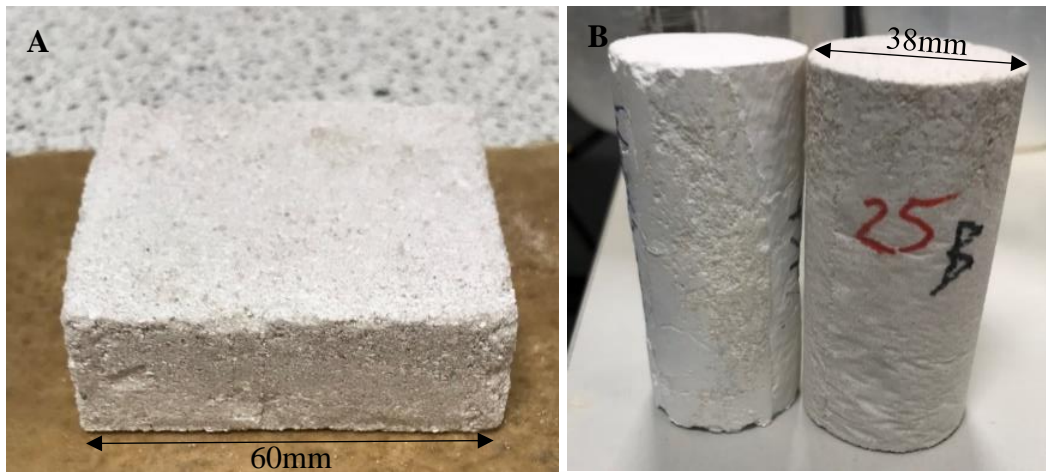


Figure 7.3: Photographs of gypsum cemented sandstone samples (A) Cuboid sample (60mm length x 60mm depth x 20mm height) cured in the oven at 40°C for 28 days. Sample Gyp20AC (B) Cylinder samples (90mm length x 38mm diameter) cured in the oven at 40°C for 28 days.

Table 7.3: Summary of all cylindrical gypsum cemented sandstones and their properties. The percentage of cement and porosity are calculated using the crystallographic density of quartz (2.65 g/cm^3) and gypsum (2.316 g/cm^3). These samples were tested by uniaxial compression (UCS) and triaxial testing: results presented in Chapter 8.

	Sample group replica samples	Initial mass of bassanite (g)	Mass of gypsum formed (g)	Sample volume (cm^3)	Bulk density (g/cm^3)	Cement (%)	Porosity (%)	Sample prepared for
1	G10A	15	17.79	84.07	1.82	8.11	30.40	UCS
2	G10B	15	17.79	94.44	1.62	7.21	38.04	UCS
3	G10D	15	17.79	77.43	1.97	8.80	24.42	Triaxial
4	G15A	22.5	26.69	90.32	1.71	11.40	34.14	UCS
5	G15B	22.5	26.69	92.52	1.67	11.13	35.71	UCS
6	G15C	22.5	26.69	89.87	1.72	11.46	33.82	Triaxial
7	G15D	22.5	26.69	88.25	1.75	11.67	32.60	Triaxial
8	G20A	30	35.58	94.53	1.65	14.63	36.04	UCS
9	G20B	30	35.58	94.22	1.65	14.68	35.84	UCS
10	G20C	30	35.58	94.15	1.65	14.69	35.79	Triaxial
11	G20D	30	35.58	98.59	1.58	14.02	38.68	Triaxial
12	G20E	30	35.58	100.40	1.55	13.77	39.79	Triaxial
13	G25A	37.5	44.48	97.22	1.61	17.90	36.81	UCS
14	G25B	37.5	44.48	96.48	1.63	18.04	36.33	UCS
15	G25C	37.5	44.48	101.52	1.11	24.08	40.79	Triaxial
16	G25D	37.5	44.48	96.27	1.17	25.39	35.78	Triaxial
17	G25E	37.5	44.48	91.71	1.23	26.65	32.59	Triaxial

Table 7.4: Summary of all cuboid gypsum cemented sandstones and their properties. The percentage of cement and porosity are calculated. The crystallographic density of quartz is 2.65 g/cm^3 . These samples were sheared in the shear box: results presented in Chapter 8.

Sample group replica samples	Initial mass of bassanite (g)	Mass of gypsum formed (g)	Sample volume (cm^3)	Bulk density (g/cm^3)	Cement (%)	Porosity (%)
GS1	6	7.12	57.06	2.12	4.74	19.30
GS2	6	7.12	57.19	2.12	4.73	19.49
GS3	6	7.12	60.22	2.01	4.49	23.54
GS4	12	14.23	58.77	2.08	9.28	20.34
GS5	12	14.23	54.97	2.22	9.92	14.84
GS6	12	14.23	51.85	2.36	10.51	9.72
GS7	12	14.23	55.24	2.21	9.87	15.26
GS8	12	14.23	50.14	2.44	10.87	6.64
GS9	28	33.21	86.58	1.68	14.90	34.83
GS10	28	33.21	82.40	1.76	15.66	31.53
GS11	28	33.21	91.17	1.59	14.16	38.11
GS12	28	33.21	88.69	1.64	14.55	36.38
GS13	28	33.21	88.15	1.65	14.64	35.99
GS14	28	33.21	94.56	1.54	13.65	40.33
GS15	35	41.52	90.07	1.63	18.04	36.34
GS16	35	41.52	97.35	1.51	16.69	41.10
GS17	35	41.52	107.39	1.36	15.13	46.61
GS18	35	41.52	99.93	1.47	16.26	42.62
GS19	35	41.52	92.78	1.58	17.51	38.20

Chapter 7 - Making synthetic sandstones

GS20	35	41.52	106.85	1.37	15.20	46.34
GS21	24	28.47	72.90	1.71	15.17	33.66
GS22	24	28.47	73.96	1.68	14.96	34.60
GS23	30	35.58	68.43	1.84	20.35	28.18
GS24	30	35.58	70.25	1.79	19.82	30.05
GS25	30	35.58	71.12	1.77	19.58	30.90
GS26	18	21.35	74.86	1.65	11.00	36.43
GS27	18	21.35	76.53	1.61	10.76	37.82
GS28	18	21.35	73.49	1.68	11.21	35.25
GS29	24	28.47	74.61	1.67	14.83	35.18

7.3.2.1.2 Distribution of gypsum cement and porosity

In this section I investigate the distribution of gypsum cement in the synthetic sandstones using microscopy and X-CT analysis.

The gypsum samples' cement and pore distributions were studied in 2D using optical microscopy (Table 7.3 and 7.4). Thin sections were made from gypsum-cemented samples which had 10, 15, 20 and 25% wt% bassanite mixed with the sand. Samples with 5 wt% basanite were not thin sectioned due to their friable nature.

Microscopy shows gypsum crystals coating the quartz grains. In thin section, needle shaped crystals and concentrations of gypsum (opaque blobs) can be identified on top of and surrounding the grains. Due to the size of the gypsum crystals it can be difficult to identify their extent from the sandstone porosity in thin section (Figure 7.4).

Four $\sim 4\text{mm}^3$ sub volumes (one from 10%, 15%, 20% and 25% samples) were scanned in the X-CT (see Table 7.5 for a list of the scanned samples), segmented by phase (grains, cement and porosity). Then the data, rather than the physical sample,

Chapter 7 - Making synthetic sandstones

was subsampled in cubes of size 1mm^3 . In 2D X-CT images, the gypsum cement needles can also be observed connecting the sand grains (Figure 7.5).

Initially these samples were segmented using Avizo (a basic intensity thresholding system). However, whilst carrying out segmentation of the gypsum cemented sandstones using Avizo it was discovered that the cement and pore value analysis did not replicate the calculated values (see Table 7.3 and 7.4). I interpreted the reason for this to be due to the overlapping grey values between the sand grains and gypsum crystals (Figure 7.6). Avizo segmentation is reliant on a contrast between the grey values in order to pick out individual phases. When very little contrast is available, or the grey values inside the two different phases overlap accurate segmentation cannot be carried out. All four of the gypsum cemented sandstone samples were scanned at energies of 150 keV. At 150 keV the attenuation values of quartz (sand grains) and gypsum are 0.372 and 0.348cm^{-1} respectively (Figure 7.6). This produces a difference in attenuation of 0.024 cm^{-1} . It is clear from the scanned samples that this is not enough of a contrast to allow each of the phases to be accurately segmented.

To try to improve the segmentation of gypsum and grains I tested the same X-CT scans with Trainable Weka Segmentation (Weka) (Frank et al. 2016). Weka segmentation uses machine learning algorithms to recognise features (e.g. shape, roughness and internal porosity) to produce segmented images (Frank et al. 2016).

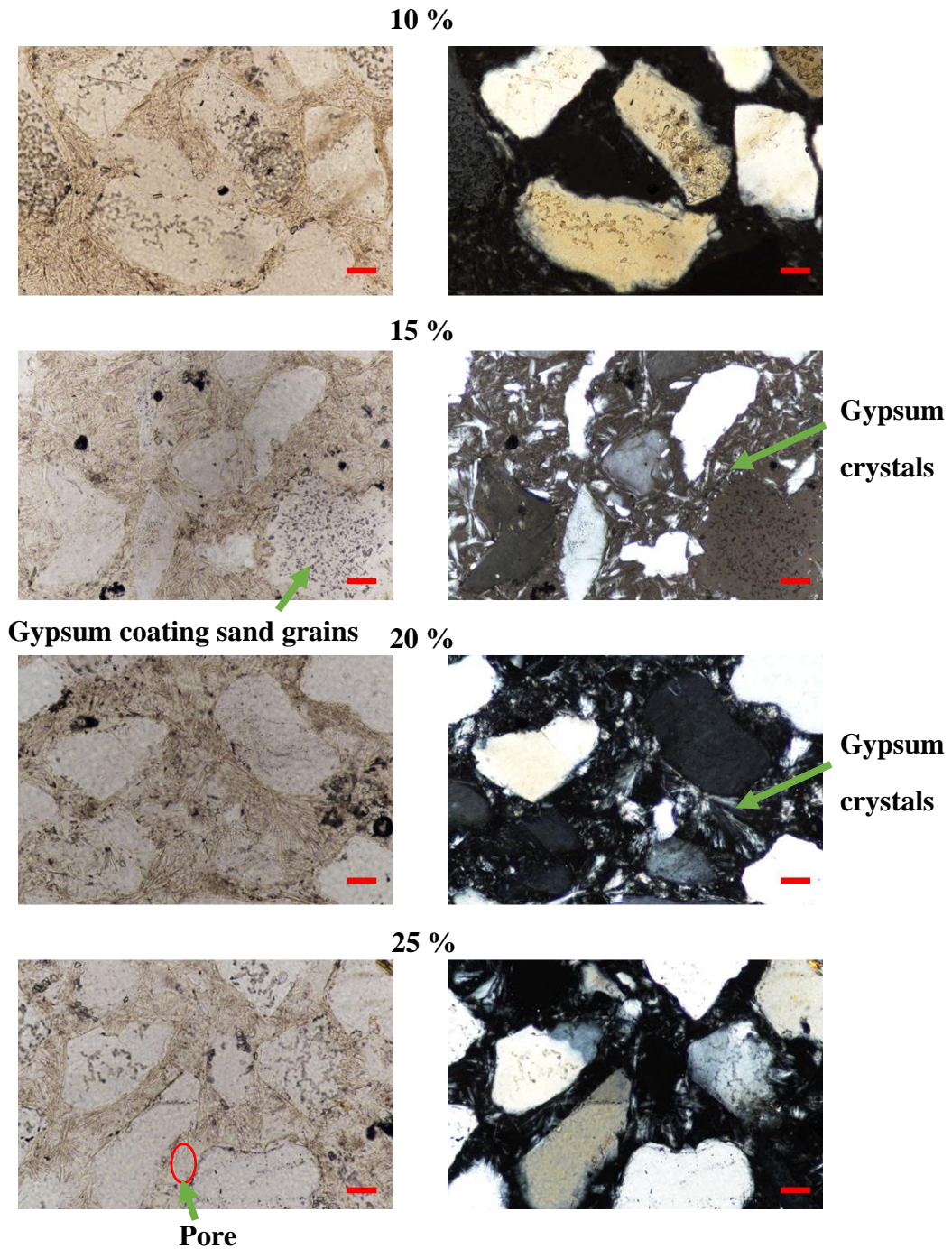


Figure 7.4: Gypsum cemented (10, 15, 20 and 25 wt % bassanite added) sandstone PPL and XPL microscope images. Red scale bar is 50 μ m. When viewed in thin section it is difficult to identify porosity.

For the purposes of this chapter three classes were determined; grains, cement and porosity. I trained the algorithm by selecting individual pixels which belonged to each class. For the majority of pixels, the Weka algorithm was able to reliably pick out the difference between the gypsum crystals and the quartz grains.

Chapter 7 - Making synthetic sandstones

The Weka segmentation produced probability maps which demonstrate the likelihood that each individual pixel belongs to a particular class. The probability of each pixel is displayed in a grey scale, where white is ~100% and black is ~0% probable. The probability maps for Gyp 10 are shown in Figure 7.7. The grains probability map shows the algorithm is successful in picking out the individual grains. The cement probability map shows the algorithm is successful in selecting the large gypsum crystals. However, some of the grey pixels that outline the sand grains were selected as part of the cement class. From thin section observations, it is unlikely that these grey pixels belong to the cement class. Instead it is possible that they belong to either the grains or porosity class. Finally, the porosity probability map is able to identify the large pores clearly. However, it become less certain of pores between gypsum crystals: reflected by the grey probability shades.

Although Weka segmentation is not perfect (Figure 7.8), for the gypsum-cemented sandstones the cement and pore results produced are within error (Figure 7.17) of the values calculated based on the chemistry and sample preparation (Table 7.5).

The error bars in Figure 7.17 are calculated by eroding and dilating each image by one pixel (for further details see Chapter 3). Of note here are the cement error bars. As with the sandstone samples (Chapter 5) the cement in some areas is one pixel wide. Therefore, by eroding or dilating the cement pixels, the volume of cement present will either double or be eroded away completely.

Table 7.5 shows that the difference between the calculated and measured for both the percentage of cement and porosity present is 6% or less. This is therefore within the range of error shown in Figure 7.17.

Chapter 7 - Making synthetic sandstones

Table 7.5: Summary of gypsum cemented samples scanned in X-CT for micro analysis. This table allows for a direct comparison between the measured (Weka segmentation) and calculated cement and porosity values (from the density and volume of each sample).

Sample name	Sample composition (%)	Chemistry calculated cement (%)	Weka segmentation measured cement (%)	Difference in cement (%)	Chemistry calculated porosity (%)	Weka segmentation measured porosity (%)	Difference in porosity (%)
10B	10	7.21	13.00	5.79	38.04	36.23	1.81
15B	15	11.13	11.19	0.06	35.71	32.43	3.28
20B	20	14.68	18.83	4.15	35.84	30.84	5.00
25B	25	18.04	22.50	4.46	36.33	32.88	3.46

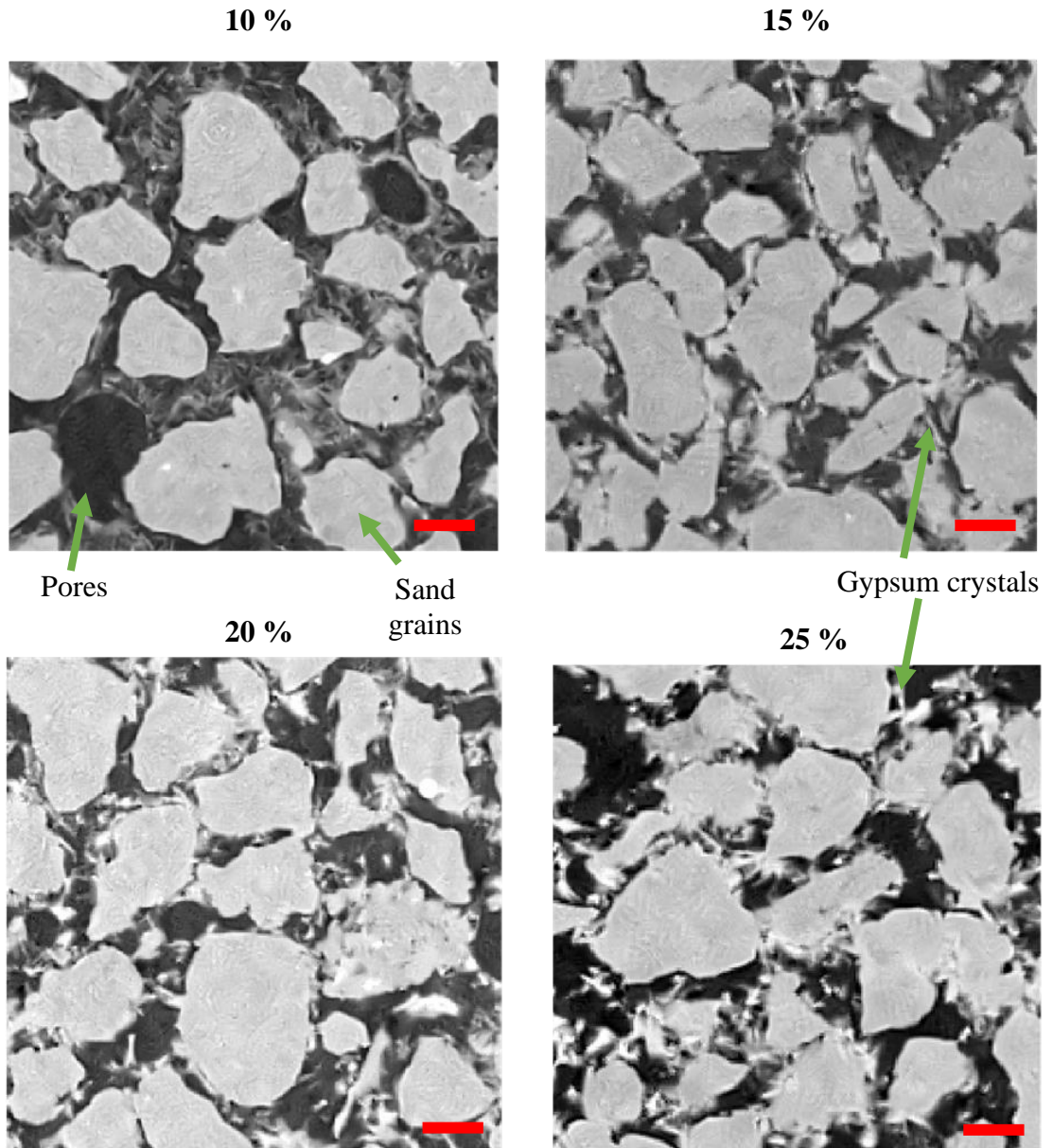


Figure 7.5: 2D X-CT slices of the four gypsum cemented samples. The gypsum crystals can be easily identified due to their needle like shape. However, the grey values of the gypsum crystals overlap with the grey values of the sand grains. The red scale bar equals 125 μ m.

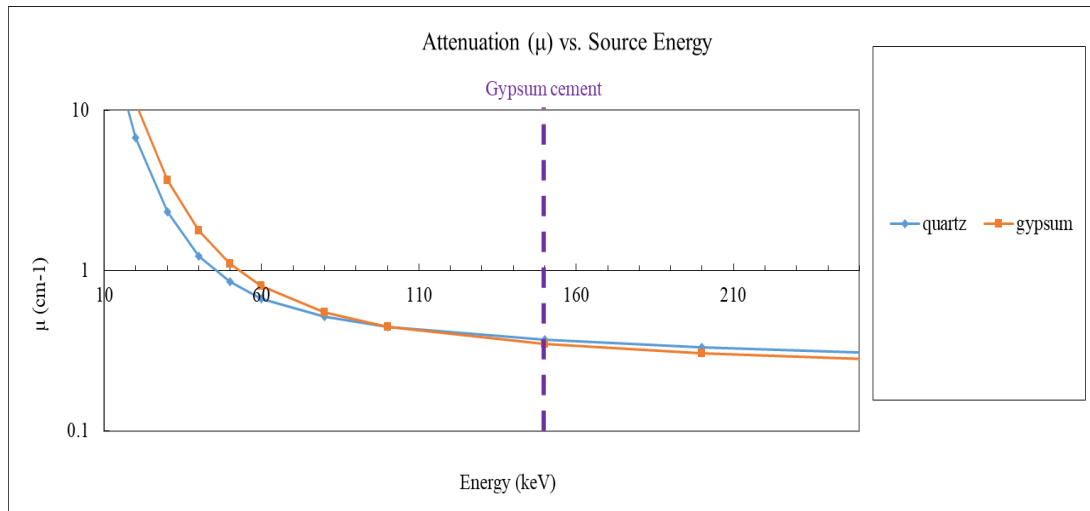


Figure 7.6: X-ray linear attenuation coefficient calculated for quartz and gypsum using MuCalc (Hanna and Ketcham 2017). The four scanned gypsum cemented samples are highlighted. At lower energies (<60 keV) there is a clear separation between quartz and gypsum (0.135 cm⁻¹). However, at 150keV the difference between the two minerals is reduced to 0.024 cm⁻¹. The greater the difference between the attenuation values of two minerals at a given energy, the clearer the phase segmentation. The small difference in attenuation between quartz and gypsum accounts for the overlapping grey values.

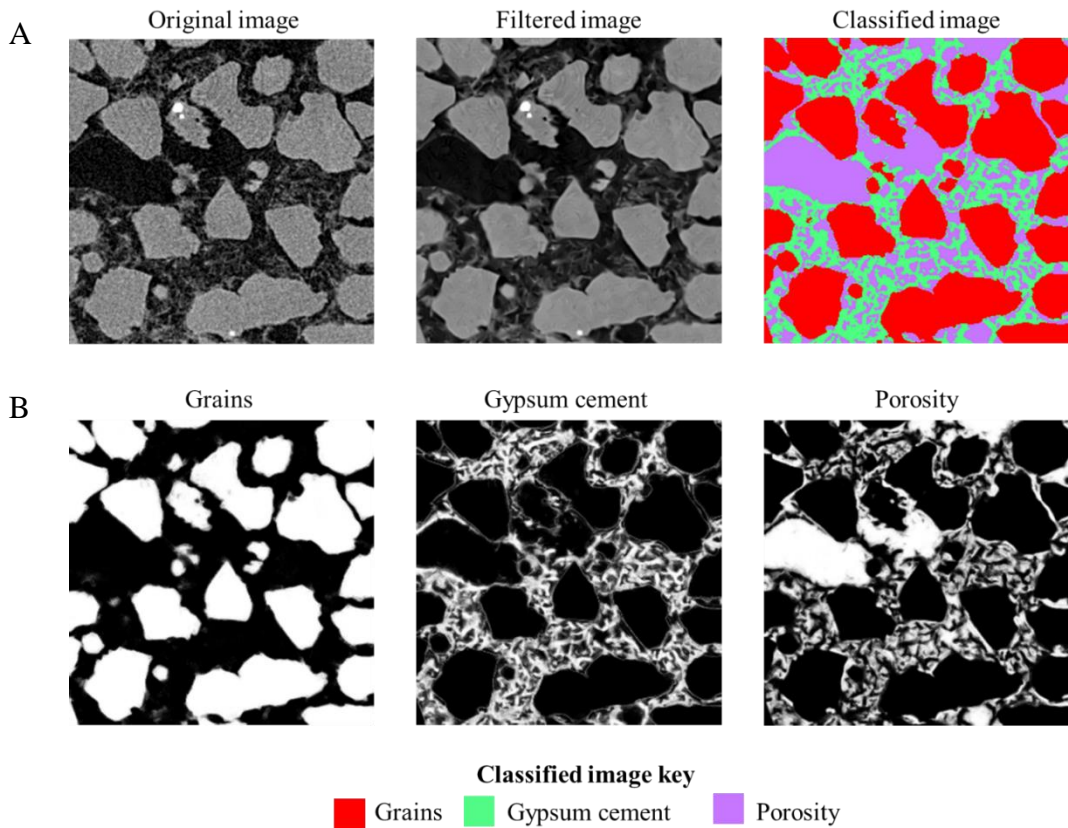


Figure 7.7: Weka probability maps for gypsum sample 10B, slice 71. Each box is 1mm^2 in size. A) Compares the classified image to the original and filtered images. B) Shows the probability maps for the three identified classes; grains, cement and porosity.

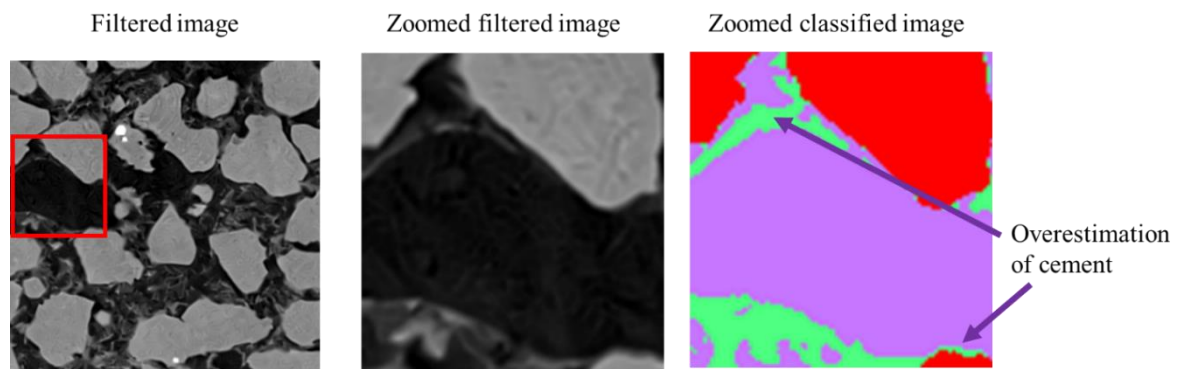


Figure 7.8: Analysis of WEKA segmentation on sample 10B. Filtered image is 1mm^2 in size. When sections are magnified overestimations in the cement phases can be identified.

7.3.2.1.3 Gypsum X-CT Results

Figures 7.9-7.16 visually demonstrate the relationship between grains, cement and porosity for each of the gypsum cemented samples. Figure 7.17 summarises the volume percentage of each phase; grains, cement and porosity, for the four gypsum cemented sandstone samples.

10% sample

Figure 7.9 shows the 3D segmented phases present in the 1mm^3 sub volume from sample 10B. The grains (blue) are clearly defined and only a few grain to grain contacts can be seen inside the sample. This suggests that the sample is matrix supported. Figure 7.10 shows the cement (Fig 7.10A) and porosity (Fig 7.10B) connectivity: if the cement pockets or pores are connected, then they are labelled with the same colour. Figure 7.10A shows that 98.2% of the cement is connected throughout the sample. Any cement volumes which are not connected to the main body are less than 0.13mm^3 in volume. Figure 7.10B shows 99.9% of the pores are connected throughout the sample. Any pores which are not connected to the main body are less than 0.36mm^3 in volume.

15% sample

Figure 7.11 shows the segmented phases in 3D present in the 1mm^3 sub volume from sample 15B. As with the Sample 10B, sample 15B is matrix supported. Figure 7.12 shows the cement (Fig 7.12A) and porosity (Fig 7.12B) connectivity. As before if the cement pockets or pores are connected, then they are labelled with the same colour. Figure 7.12A shows 97.5% of cement (pale pink colour) is connected throughout the sample. Any cement volumes which are not connected to the main body are less than 0.041mm^3 in volume. Figure 7.12B shows 99.9% of the pores (green) are connected throughout the sample. Any pores which are not connected to the main body are less than 0.12mm^3 in volume.

20% sample

Figure 7.13 shows the segmented phases in 3D present in the 1mm^3 sub volume from sample 20B. As with the previous samples sample 20B is matrix supported. Figure

Chapter 7 - Making synthetic sandstones

7.14 shows the cement (Fig 7.14 A) and porosity (Fig 7.14 B) connectivity. As before if the cement pockets or pores are connected, then they are labelled with the same colour. Figure 7.14A (purple) shows 99.2% of the cement is connected throughout the sample. Figure 7.14B shows 99.7% of the pores (green) are connected throughout the sample. Any pores which are not connected to the main body are less than 0.24 mm^3 in volume.

25% sample

Figure 7.15 shows the segmented phases in 3D present in the 1 mm^3 sub volume from sample 25B. As with the previous samples 25B is matrix supported. Figure 7.16 shows the cement (Fig 7.16 A) and porosity (Fig 7.16 B) connectivity. As before if the cement pockets or pores are connected, then they are labelled with the same colour. Figure 7.16 A shows that 99.7% of the cement (purple) is connected throughout the sample. Any cement volumes which are not connected to the main body are less than 0.08 mm^3 in volume. Figure 7.16 B shows 99.9% of the pores are connected throughout the sample. Any pores which are not connected to the main body are less than 0.12 mm^3 in volume.

For each of the four samples listed above histograms of the volumes of connected cement bodies and pores are shown in Figure 7.18.

Figure 7.17 shows an overall increase (13.0 – 22.5%) in the percentage of cement and a slight decrease (36.2 – 32.9%) in the percentage of pores present, as the weight percentage of basanite increases (10-25%)

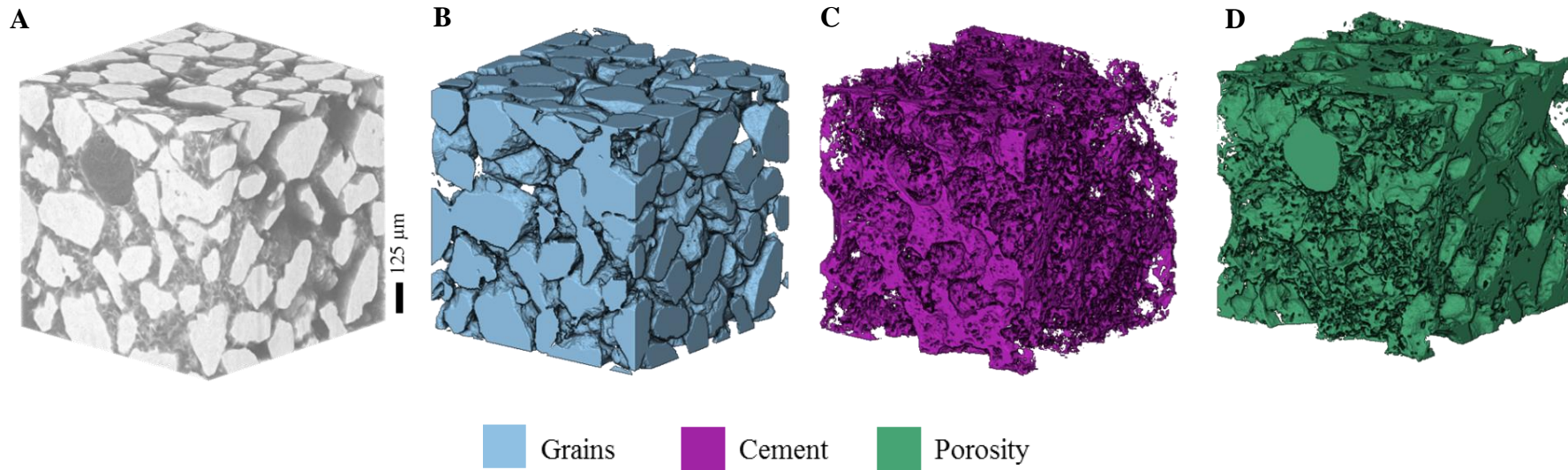


Figure 7.9: X-CT segmented 3D images of a 1mm³ data sub volume from sample 10B. This sample was made with 10wt% bassanite added A) Original grey scale 3D image. B) Grains segmented image. Analysis using Avizo finds the grains segment is 50.8% of the total volume. Here we can see limited grain-grain contacts. This therefore suggests that the grains are matrix supported C) Cement segmented image. The cement segment is 13.0% of the total volume. D) Porosity segmented image. The porosity segment is 36.2% of the total volume.

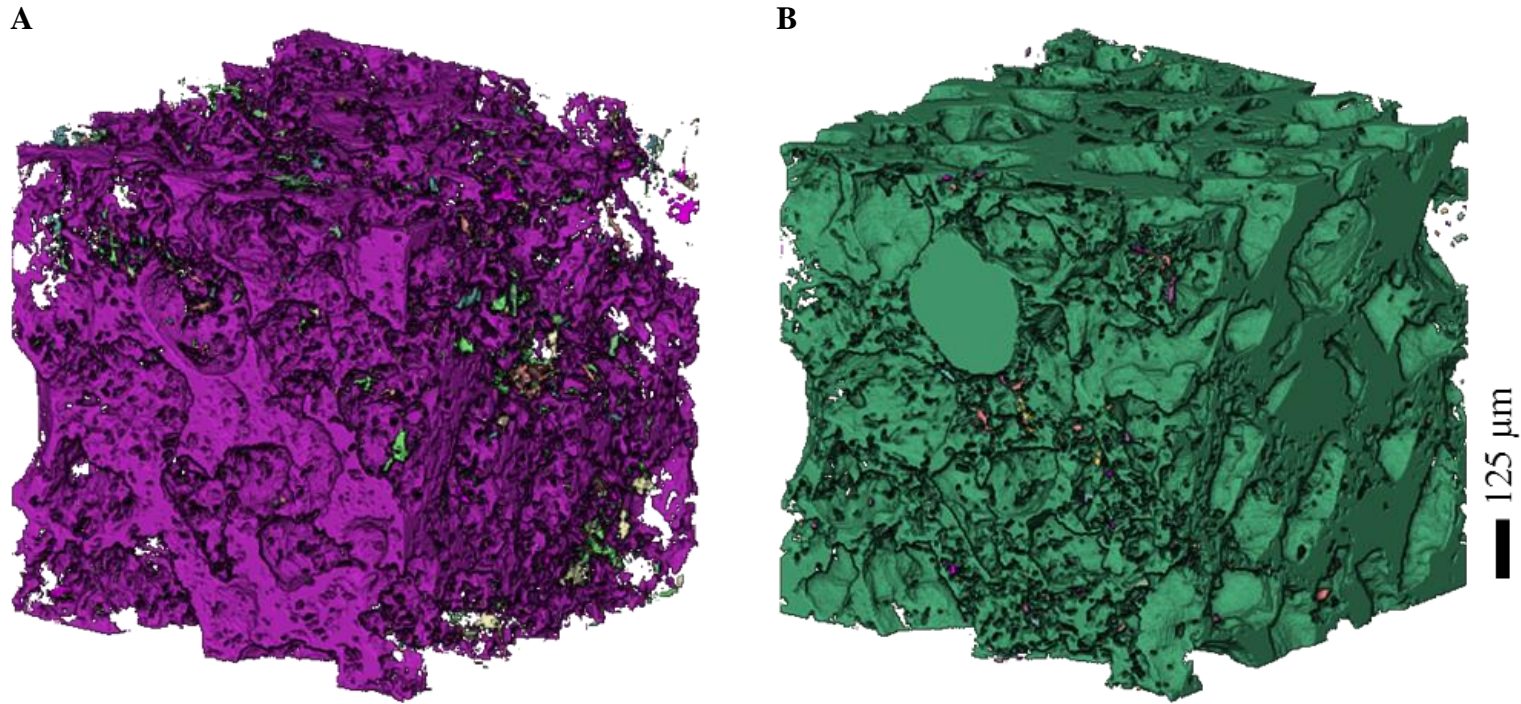


Figure 7.10: Sample 10B (10% wt) cement and porosity connectivity. Cement or pores which are connected are coloured in a single colour. A) Connected cement. The majority of the cement is connected however there are small pockets of disconnected cement inside the pores and around the grains. B) Connected porosity. Almost all of the porosity is connected

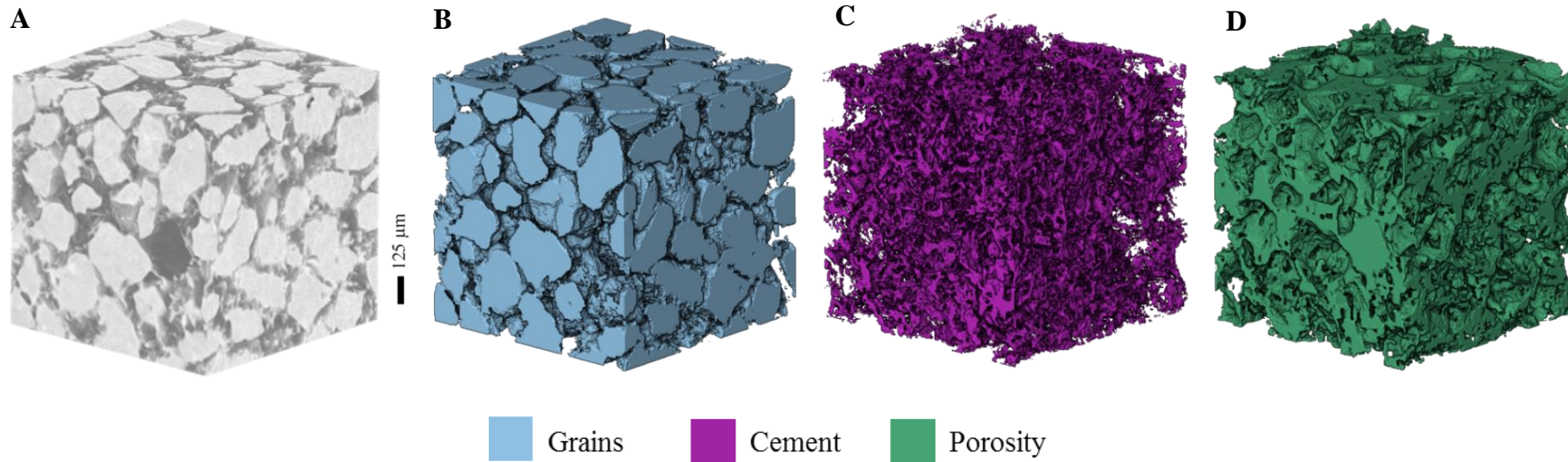


Figure 7.11: X-CT segmented 3D images of a 1mm³ data sub volume from sample 15B. This sample was made with 15wt% bassanite added. A) Original grey scale 3D image. B) Grains segmented image. The grains segment equals 56.4% of the total volume. Here we can see limited grain-grain contacts. This therefore suggests that the grains are matrix supported. C) Cement segmented image. The cement segment is 11.2% of the total volume. D) Porosity segmented image. The porosity segment is 32.4% of the total volume.

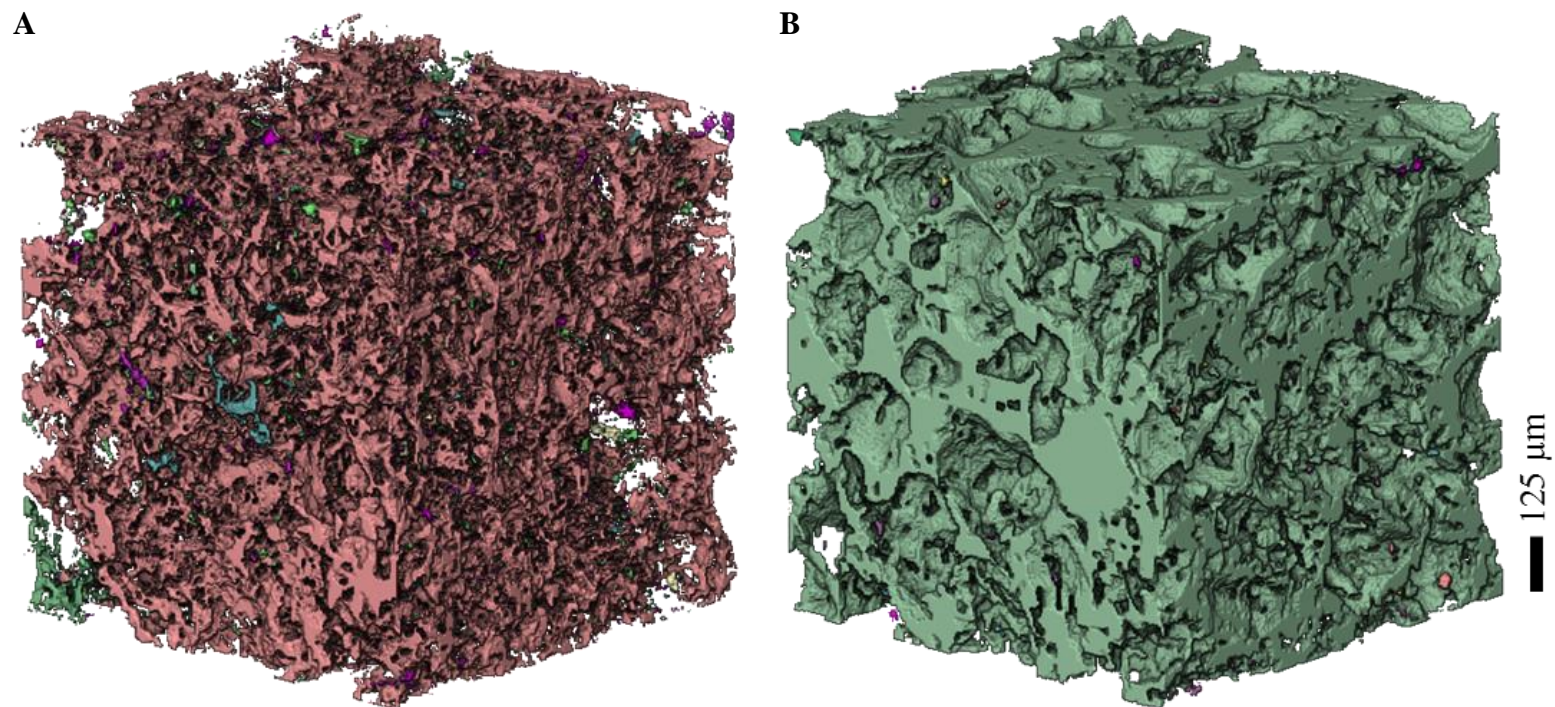


Figure 7.12: Sample 15B (15% wt) cement and porosity connectivity. Cement or pores which are connected are coloured in a single colour. A) Connected cement. The majority of the cement is connected however there are small pockets of disconnected cement inside the pores and around the grains. B) Connected porosity. Almost all the porosity is connected

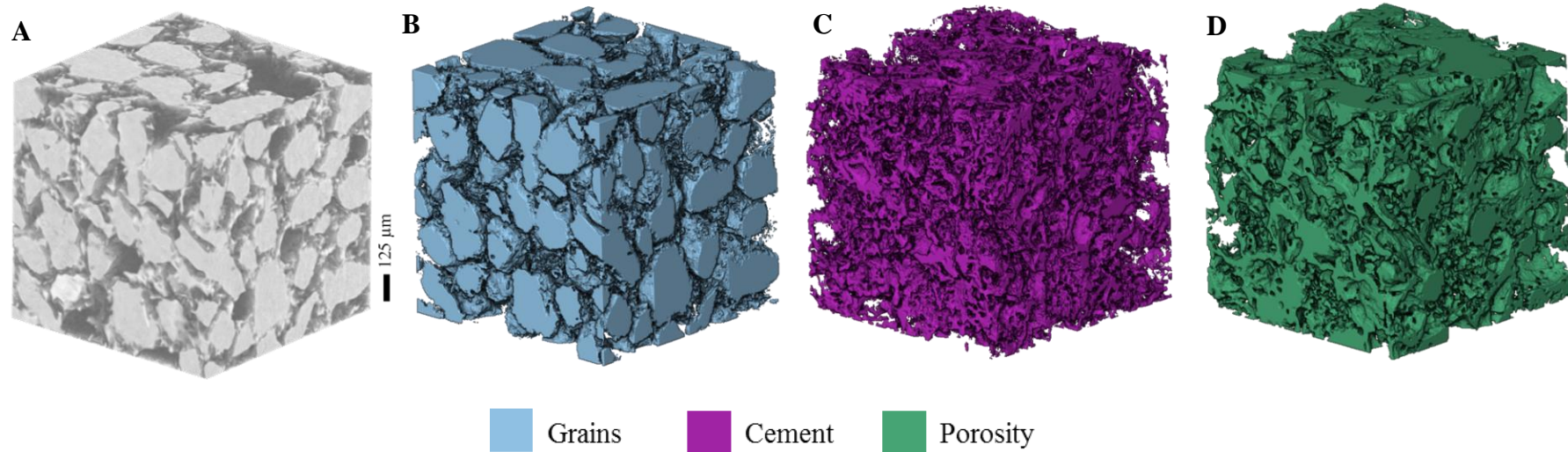


Figure 7.13: X-CT segmented 3D images of a 1mm^3 data sub volume from sample 20B. This sample was made with 20wt% bassanite added. A) Original grey scale 3D image. B) Grains segmented image. The grains segment equals 50.3% of the total volume. Here we can see limited grain-grain contacts. This therefore suggests that the grains are matrix supported. C) Cement segmented image. The cement segment is 18.8% of the total volume. D) Porosity segmented image. The porosity segment is 30.8% of the total volume.

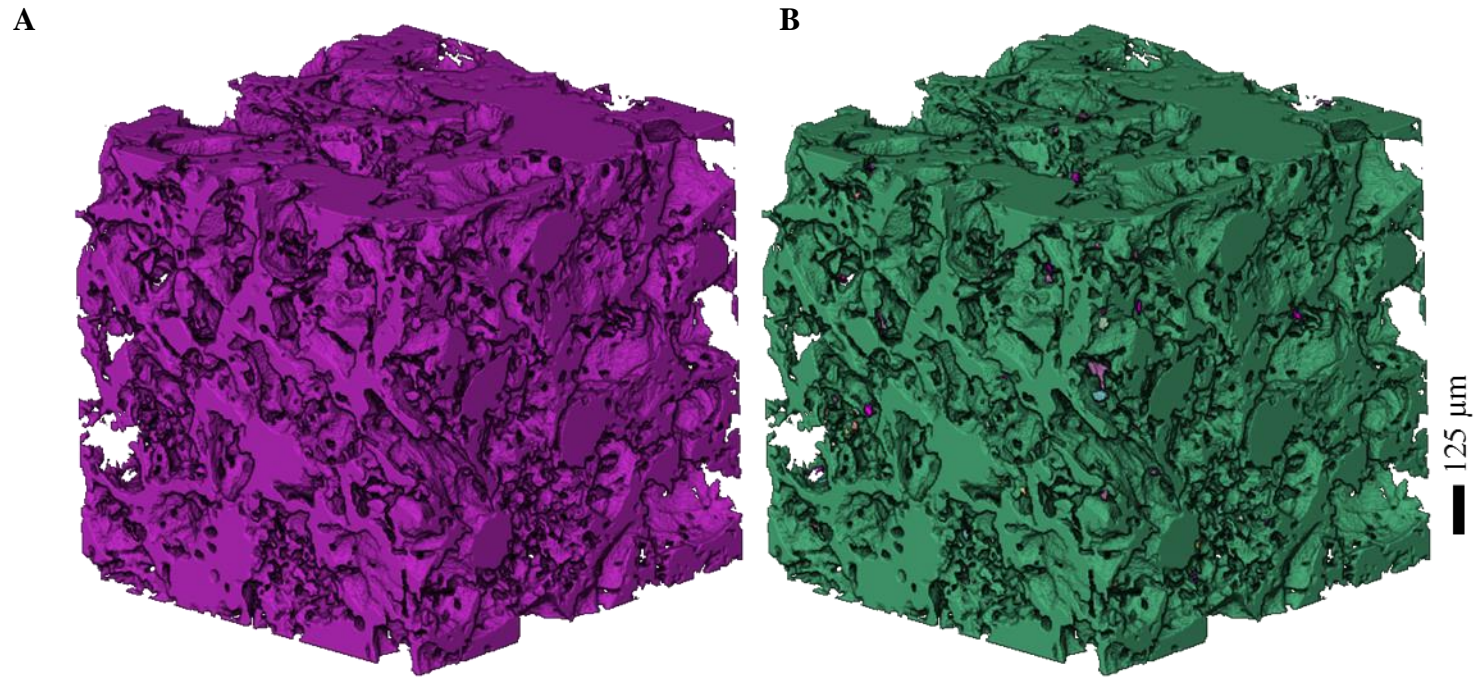


Figure 7.14: Sample 20B (20% wt) cement and porosity connectivity. Cement or pores which are connected are coloured in a single colour. A) Connected cement. All the cement is connected. B) Connected porosity. Almost all the porosity is connected.

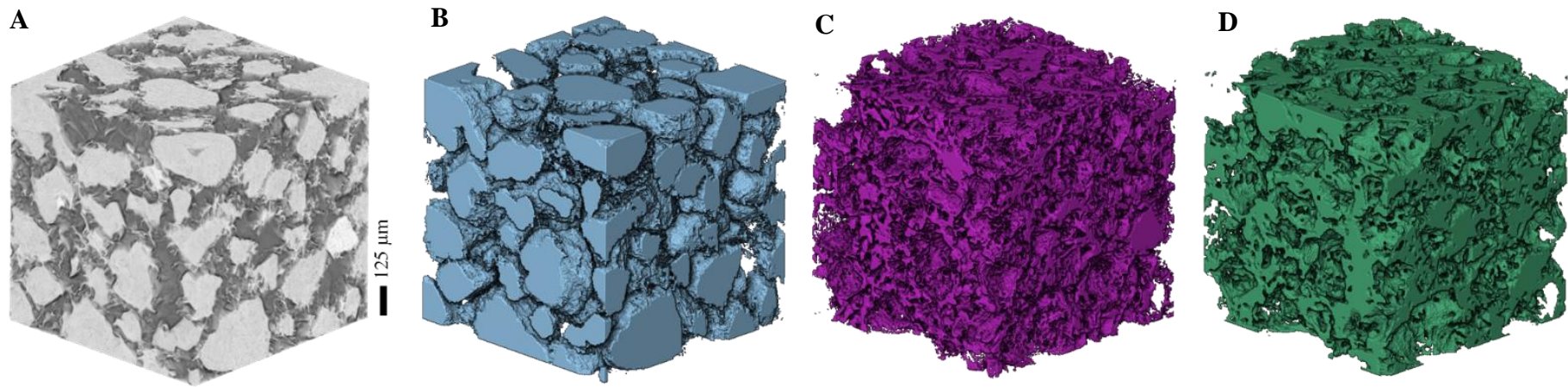


Figure 7.15: X-CT segmented 3D images of a 1mm³ data sub volume from sample 25B. This sample was made with 25wt% bassanite added. A) Original grey scale 3D image. B) Grains segmented image. The grains segment equals 44.6% of the total volume. Here we can see limited grain-grain contacts. This therefore suggests that the grains are matrix supported C) Cement segmented image. The cement segment is 22.5% of the total volume. D) Porosity segmented image. The porosity segment is 32.9% of the total volume.

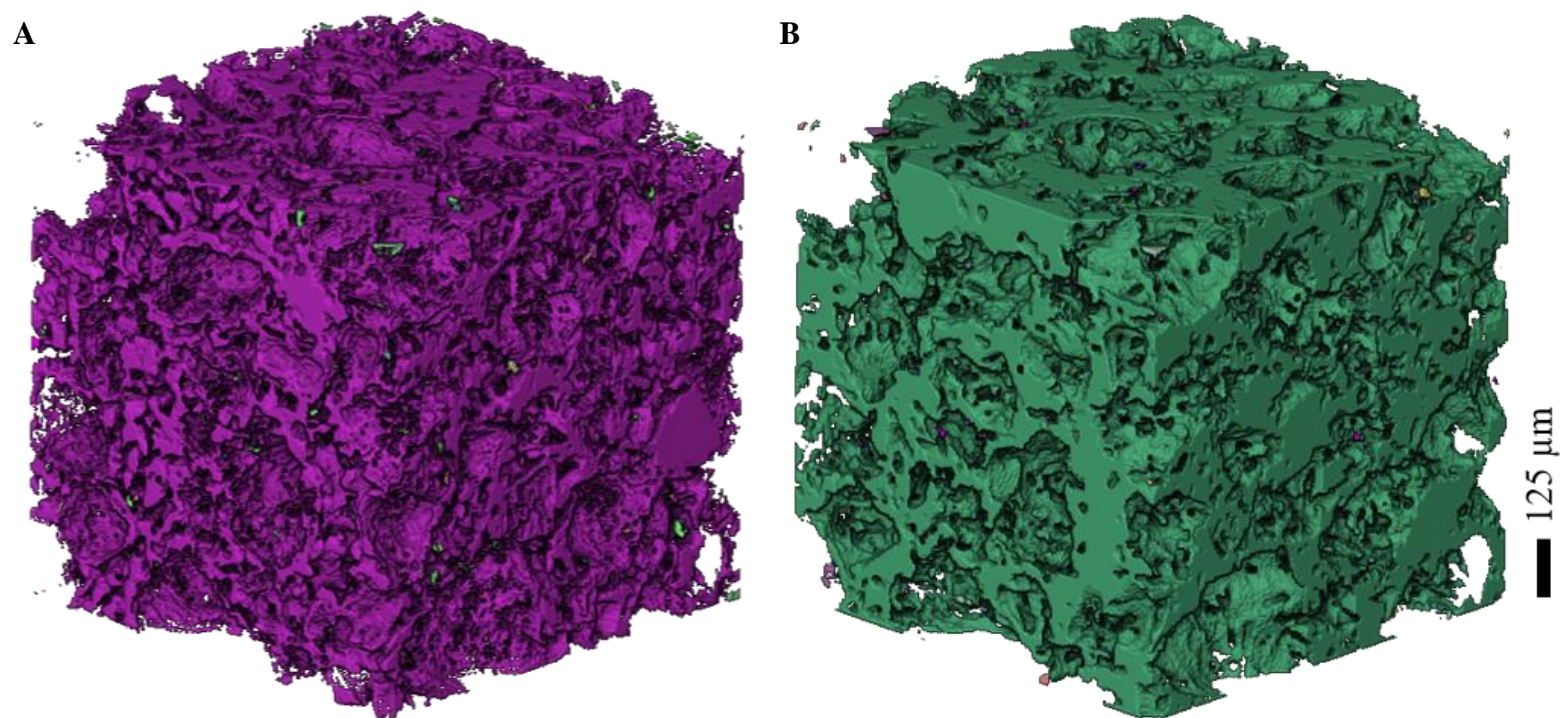


Figure 7.16: Sample 25B (25% wt) cement and porosity connectivity. Cement or pores which are connected are coloured in a single colour. A) Connected cement. Almost all the cement is connected. B) Connected porosity. Almost all the porosity is connected.

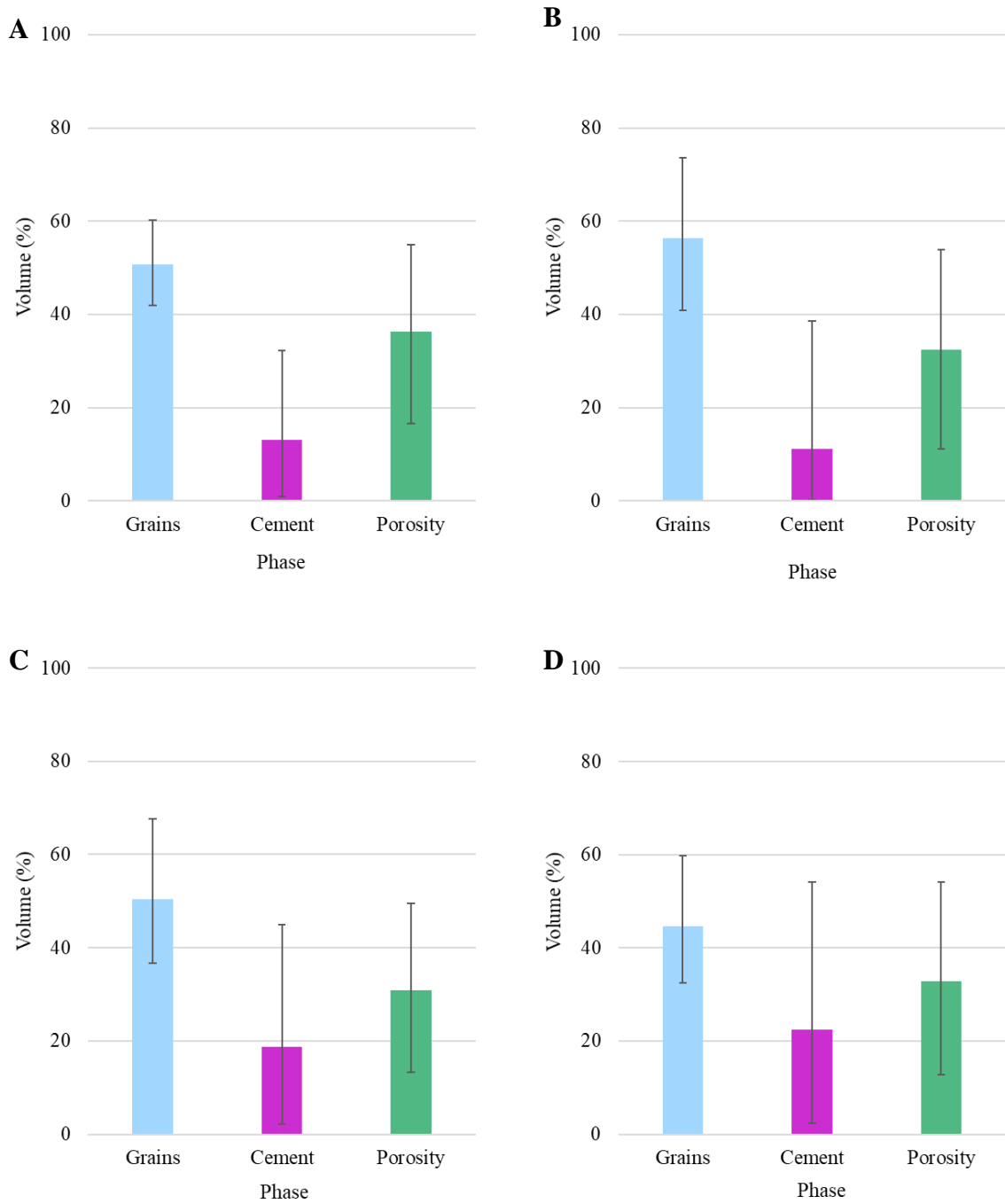


Figure 7.17: Volume of each segmented phases for all four gypsum cemented samples A) 10% B) 15% C) 20% D) 25% from erosion and dilation calculations (see Chapter 3).

Chapter 7 - Making synthetic sandstones

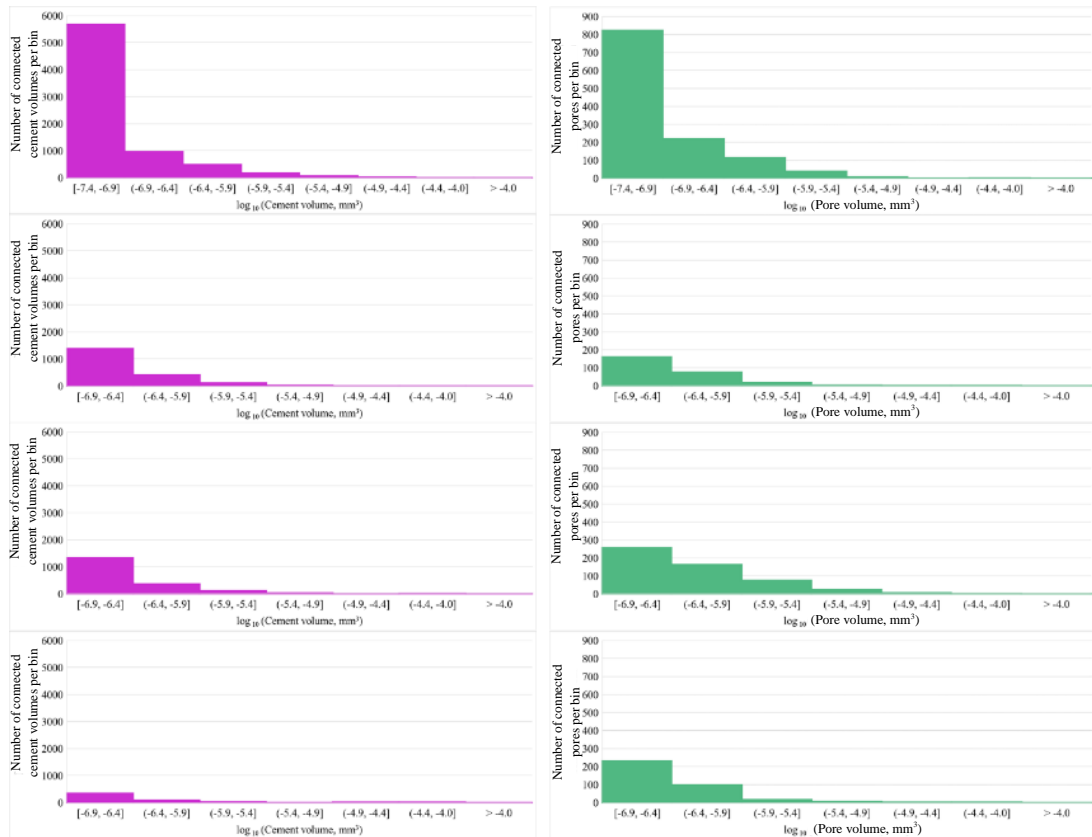


Figure 7.18: Histogram showing the number of connected cement and pore volumes from each of the four gypsum cemented 1 mm^3 samples. The bin width is 0.5. The column on the right is an overflow bin for all cement and pore volumes more than 0.018 mm^3 .

There are several varying factors (e.g. distribution due to mixing, leaching, clumping) when using gypsum to cement sand. However, because the method by which the gypsum is made is a closed system (e.g. basanite is not able to flow out of the set up) the percentage of gypsum formed in the sample can be readily calculated. The comparison between the calculated and measured cement and porosity demonstrates that the Weka segmentation using machine learning has proved to be a successful method to calculate the percentage of grains, cement and porosity present in a gypsum cemented sample.

Across each of the samples most of the cement and pores are connected. This implies the samples are predominantly cement supported and the samples have good permeability.

7.3.2.2 MICP

7.3.2.2.1 Solution preparation

To form MICP cemented sandstones two solutions are required; the bacterial solution and the cementing solution.

The bacterial solution of 37 g/L Brain Heart Infusion (BHI) broth and 20 g/L urea concentration were prepared and inoculated with *Sporosarcina pasteurii* following the outline of Minto et al. (2016). The ureolytic activity is the rate at which *Sporosarcina pasteurii* hydrolyses urea and is referred to as K_{urea} (mM urea/min/OD₆₀₀) (El Mountassir et al. 2018). In order to determine the ureolytic activity K_{urea} conductivity was measured for each bacterial solution every minute over the course of six minutes and then the ureolytic activity was calculated following the procedure of Minto et al. (2016). A measure of ureolytic activity is useful in this study to understand the ureolysis potential of each bacterial solution and to explain CaCO₃ precipitation variations in the samples formed. The optical density (OD) of a 1 ml sample from each mixed solution was measured at a wavelength of 600nm. The K_{urea} results are shown in Table 7.6. Across the four batches the OD varied slightly from 0.09-0.16. This was due to differences in the amount of bacteria used during broth inoculation. The K_{urea} measurements are shown in Appendix 3. The cementing solution comprised 1.4 M urea and 1.4 M CaCl₂. Once prepared the bacteria solutions were kept for up to 7 days whilst they were used to feed the sand samples.

Table 7.6: Optical density (OD) and specific ureolytic activity results for each diluted bacterial solution used to make the MICP cemented synthetic sandstones.

Batch ID	Date tested	OD ₆₀₀ (of diluted)	Specific Ureolytic Activity [mM urea/min/OD]
BS3	24/01/2018	0.16	2.31
BS4	12/02/2018	0.16	2.05
BS5	19/03/2018	0.16	2.74
BS6	23/10/2018	0.09	2.48

Table 7.7: Summary of all MICP cemented cylinders and their properties. See Chapter 8 for a description of the cylinders deformation by uniaxial compression testing (UCS).

Sample group replica	MICP feed (ml)	Sample volume (cm ³)	Initial mass of sand (g)	Sample prepared for	K_{urea} batch ID
C1	200	96.10	183.80	UCS	BS5
C2	200	96.54	188.29	UCS	BS5
C3	160	94.73	165.74	UCS	BS5
C4	200	96.65	191.56	UCS	BS5
C5	160	94.29	190.66	UCS	BS5
C6	120	98.23	195.52	UCS	BS5
C7	160	101.54	215.54	UCS	BS5
C8	120	96.68	196.91	UCS	BS5
C9	120	98.69	200.70	UCS	BS5

Table 7.8: Summary of all MICP cemented cuboids and their properties prior to deformation (see Chapter 8)

Sample group replica samples	MICP feed (ml)	Sample volume (cm ³)	Initial mass of sand (g)	K_{urea} batch ID
L1	120	117.67	181.9	BS3
L2	120	104.86	182.86	BS4
L3	120	111.07	182.71	BS4
L4	120	115.05	182.16	BS6
L5	120	119.62	182.91	BS6
L6	120	120.03	183.24	BS6
L7	120	118.62	183.74	BS6
M1	160	115.15	183.68	BS3
M2	160	113.07	183.15	BS3
M3	160	117.22	182.91	BS4
M4	160	103.55	182.47	BS6
M5	160	133.34	184.21	BS6
M6	160	120.71	183.2	BS6
M7	160	104.00	183.65	BS6
H1	200	116.98	182.25	BS3
H2	200	116.93	181.69	BS4

Chapter 7 - Making synthetic sandstones

H3	200	115.96	182.45	BS4
H4	200	120.25	182.11	BS6
H5	200	135.00	183.21	BS6
H6	200	119.69	183.55	BS6
H7	200	121.64	183.45	BS6

7.3.2.2.2 MICP feeding procedure

The strengths of the MICP samples were varied by the total volume of bacterial and cementing solution fed to each sand. The feeding of each sample consisted of two phases both of which were by percolation under gravity. The first was the bacterial solution and the second was the cementing solution. Figure 7.19 schematically illustrates how both the cylinder and cuboid samples were made. All sand samples in this study were initially fed with 40 ml of bacterial solution to allow the bacteria to attach themselves to the sand grains. This was then followed one hour later with 40 ml of cementing solution. Each 40 ml feed took approximately 30 minutes to complete. This produced an approximate flow rate of the feed being applied to the top of the sample of 1.33 mm min^{-1} based on the amount of time for solution to exit the sample. Between feeds the cylinder and cuboid samples were compressed under a 0.5 and 0.16 kg mass respectively (pressure = 1.36 and 1.38 kPa) to encourage formation of a grain supported matrix. This feeding procedure was then repeated 8 hours later until the total feed volume was reached for each sample. The bacterial and cementing solutions were fed (by syringe) evenly across the exposed surface of each sand sample leaving the solutions to percolate through each sample due to gravity. Once the total volume of feed was reached (120, 160 and 200ml) feeding was stopped. At this point the masses were removed from the samples. They were flushed with 200 ml of deionised water to remove any residual salt produced during the precipitation of calcite and dried at room temperature until they reached constant mass. After this the samples were sanded and deformed (see Chapter 8). Figure 7.20 shows examples of finished MICP cemented sandstones.

Chapter 7 - Making synthetic sandstones

Due to the method for making each of the samples and their fragile nature grains can be lost from around the edges. This directly impacts how the volume of calcite present in the sample is calculated.

Chapter 7 - Making synthetic sandstones

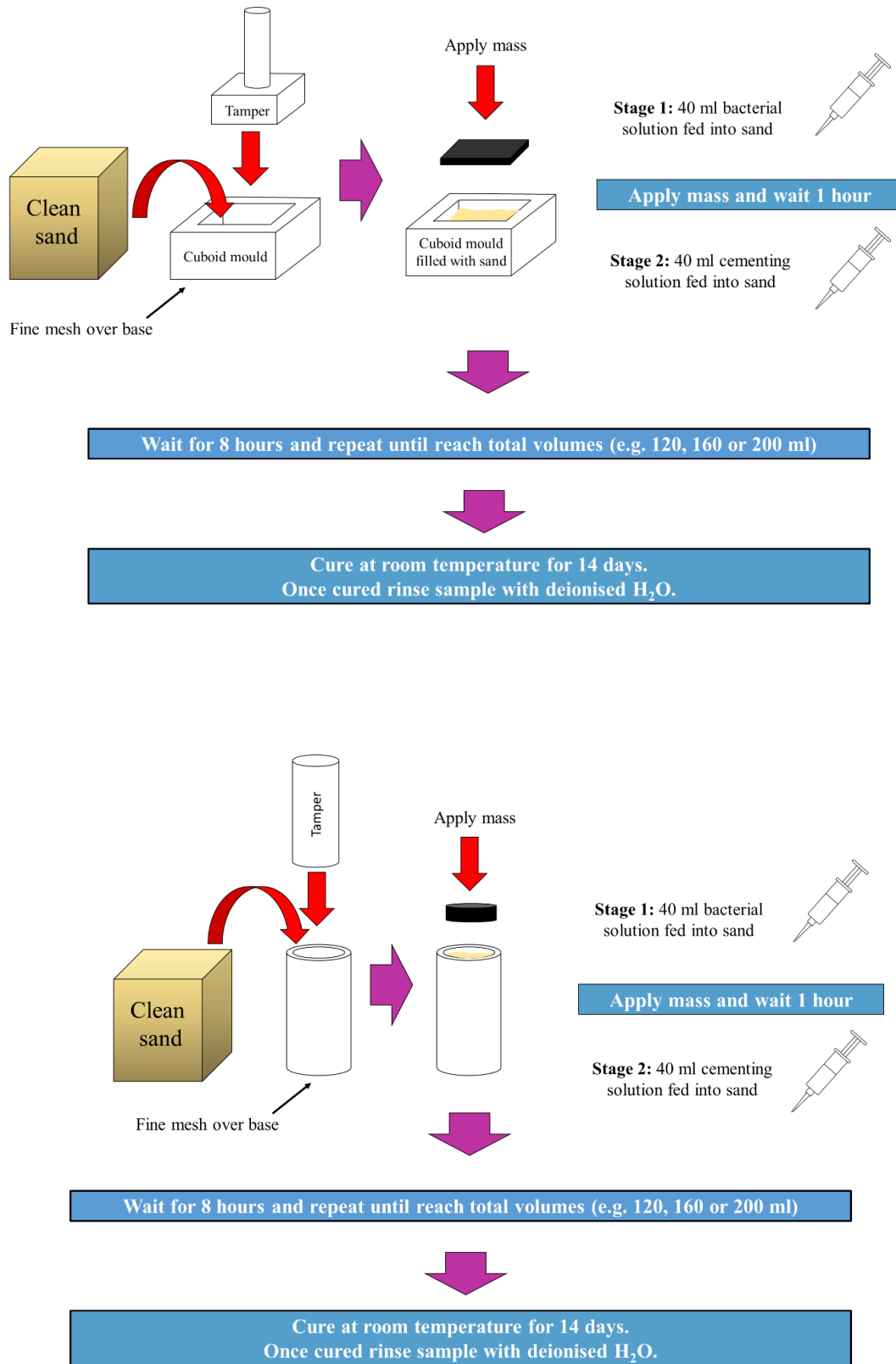


Figure 7.19: Schematic of MICP cemented sandstone sample preparation in cuboid and cylinder moulds.

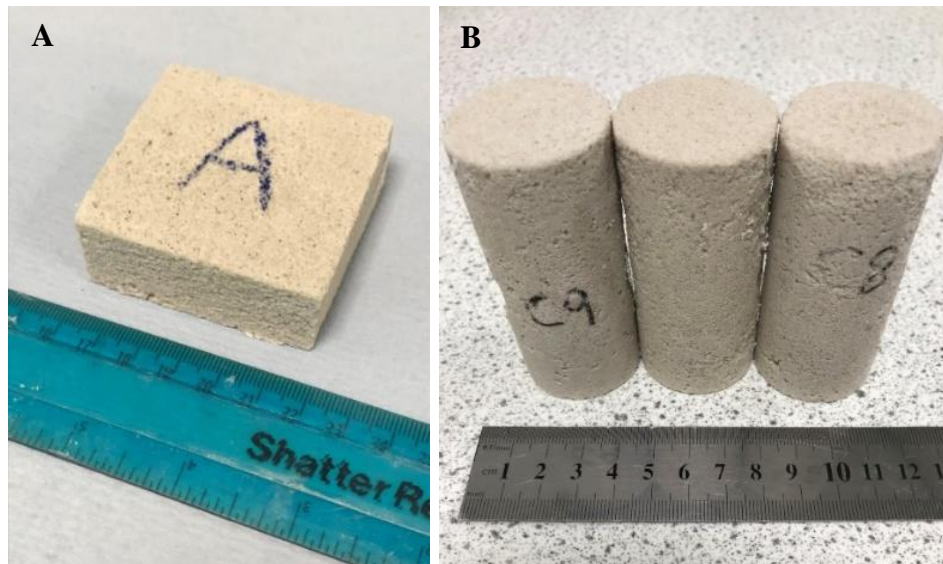


Figure 7.20: Photographs of MICP cemented sandstone samples. A) Sample A ($59 \times 59 \times 20 \text{ mm}^3$) was fed with 200ml of bacterial solution and CaCl_2 . B) Samples C8, C6 and C9 were each fed with 120ml of bacterial solution and CaCl_2 .

7.3.2.2.3 Measuring CaCO_3 content of the MICP samples

The total calcium carbonate precipitate content was measured by following the acid-soluble weight loss method (Chaney et al. 1982). Eight cylindrical MICP samples (C1-C5 and C7-C9) were sub sampled (approx. 15 mm in height and 38 mm in diameter) to enable the CaCO_3 content to be tested. Figure 7.21 shows the sub sample volume. These samples were then used as a proxy to determine a rough index of the carbonate content (or cement percentage) in each of the MICP cemented samples. This method dissolves the calcite in the MICP samples by saturating the sample in hydrochloric acid ($\text{HCl} \sim 4\%$ concentration). After being saturated the samples were rinsed and reweighed after treatment. The difference in mass between the acid treated samples and their original mass gives the mass of calcium carbonate present in each sample (Table 7.9)

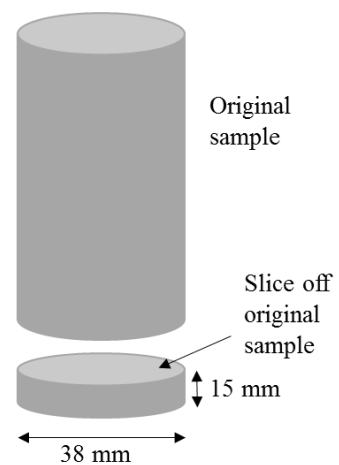


Figure 7.21: Sub sample for measuring CaCO_3 content of MICP samples.

Chapter 7 - Making synthetic sandstones

From the mass of calcite the average calcite (wt%) of each sample can be calculated. The MICP cemented sandstones range in bulk density from 1.51 -1.93 g/cm³ with porosities ranging from 27.4-42.5% based on X-CT analysis. The average percentage calcite present in each sample ranges from 8.56- 13.47%. This is very similar to the volumetric calcite range for a fine grained sandstone (100-200 μm) given by Terzis and Laloui (2018). Terzis and Laloui (2018) calculate the volumetric calcite to range from 9-13% using X-CT analysis on their MICP cemented sandstones. Due to the time constraints of this PhD only the cylinder samples were analysed.

If the average calcite percentages calculated in Table 7.8 are applied to the full cylinder MICP samples then the number of times the original pore volume was filled by solution can be calculated (Table 7.10). This is an alternative way to quantify the volume of feed (ml) in term of the sample size.

Chapter 7 - Making synthetic sandstones

Table 7.9: Measured calcite content of sampled sub slice from the cylindrical MICP cemented sandstone core.

Sample number	Feed volume (ml)	Mass of calcite present (g)	Average Calcite (wt%)	Porosity (%)	Average Porosity (%)	Calcite (%)	Average calcite (%)	Grains (%)	Average grains (%)
C1	200	5.77	6.01	34.11	38.47	13.42	13.47	52.47	48.06
C2		6.09		38.15		13.58		48.27	
C4		6.17		43.14		13.42		43.44	
C3	160	6.36	4.79	32.52	32.58	14.08	12.00	53.40	55.43
C5		5.79		29.10		12.90		57.99	
C7		3.80		36.11		9.01		54.88	
C8	120	3.89	3.48	27.40	34.92	10.16	8.56	62.44	56.51
C9		3.08		42.45		6.97		50.58	

Table 7.10: Average total number of times pores were filled by bacterial and cementing solutions for each MICP cylinder sample.

Sample	Volume (cm ³)	Feed (ml)	Sample volume (cm ³)	Pore volume (cm ³)	Calcite volume (cm ³)	Original pore volume before cementation (cm ³)	Number of times pore volume is filled with solution	Average
C1	96.10	200	96.10	32.78	12.90	45.68	4.38	4.01
C2	96.54		96.54	36.83	13.11	49.94	4.00	
C4	96.65		96.65	41.69	12.97	54.66	3.66	
C3	94.73	160	94.73	30.81	13.34	44.14	3.62	3.72
C5	94.29		94.29	27.44	12.16	39.60	4.04	
C7	101.54		101.54	36.67	9.15	45.82	3.49	
C8	96.68	120	96.68	26.49	9.82	36.31	3.30	2.88
C9	98.69		98.69	41.90	6.88	48.77	2.46	

Chapter 7 - Making synthetic sandstones

The porosity of each MICP cylinder sample was measured using vacuum saturation. After measuring the initial dry mass each sample was saturated in a vacuum chamber with deionised H₂O. The samples remained here until a fully saturated condition was achieved. The volume was determined by immersing each sample in de-aired water and the porosity of each sample was calculated.

7.3.2.2.4 Cement distribution in MICP samples

The MICP samples' porosity and cement distribution were studied using the microscope and the X-CT. Thin sections have been impregnated with blue resin to highlight connected porosity. Figure 7.31 displays plane polarised light (PPL) thin sections and the corresponding cross polarised light (XPL) images for each of the MICP feed volumes. It is almost impossible to identify any calcite from the PPL thin sections alone. The calcite is more clearly seen in XPL thin sections where it can be identified by its high order interference colours.

The 120 sample displays balls of calcite ranging from 15-40 µm in diameter (Figure 7.22). The smaller calcite crystals of 15 µm diameter tend to be located on the 'exposed' (e.g. not located on grain to grain contacts) grain edges.

160 ml sample displays evidence of multiple calcite balls (~50 µm in diameter) growing around the grain (Figure 7.22). This is the one main example of so many 'exposed' calcite crystals identified throughout the MICP cemented sandstone thin sections.

The 200ml sample displays balls of calcite up to 60 µm in diameter (Figure 7.22). Generally, the calcite balls in the 200ml sample are more evenly distributed in the thin section in comparison to the 160ml sample.

The balls of calcite are generally larger as the volume of feed is increased and most closely resemble the granular calcite studied in Ismail et al. (2002). In thin section there is no evidence of calcite coating the sand grains like those displayed in DeJong et al. (2006). Like the gypsum cemented samples the sand grains appear to be floating, with limited grain-grain contacts, and at these contacts calcite forms bridges between the grains.

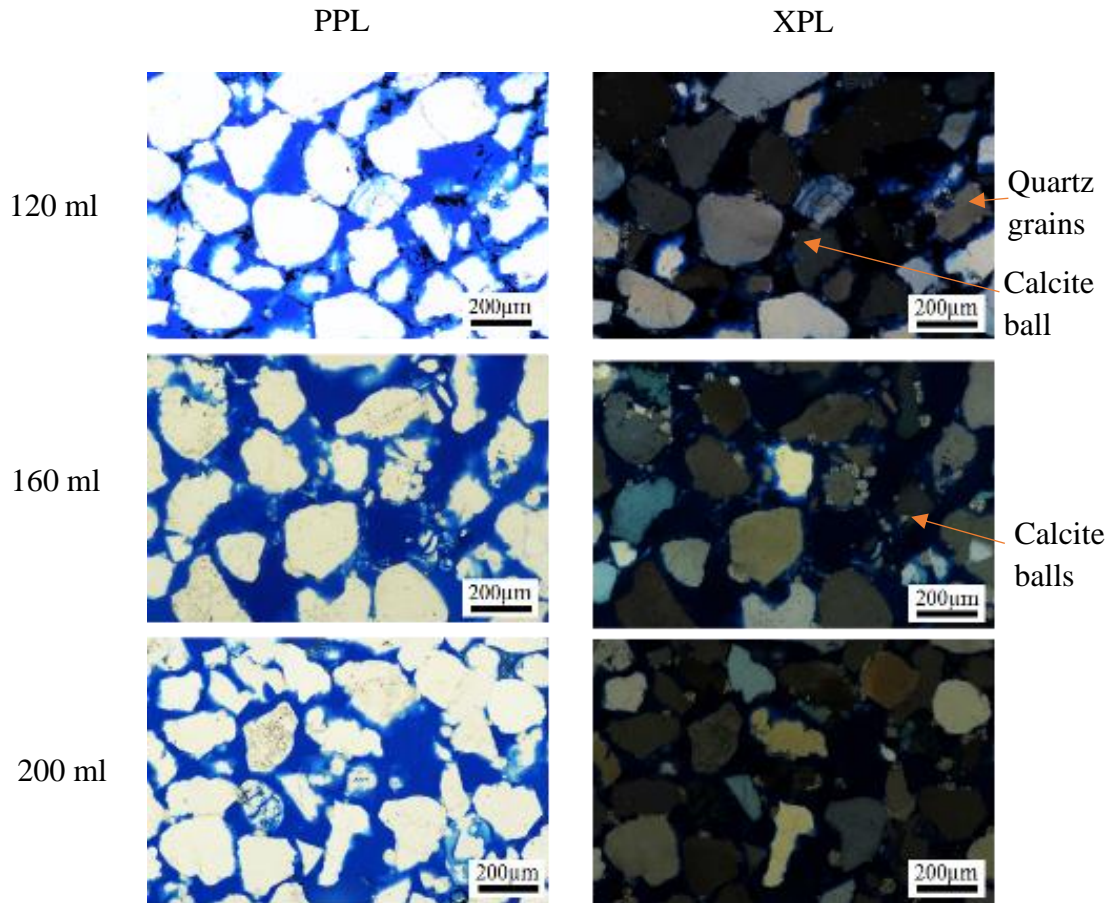


Figure 7.22: MICP cemented thin sections in plane polarised light (PPL) and cross polarised light (XPL). Due to their pale, high order interference colours the balls of calcite can be more readily identified in XPL light. At 120ml feed less calcite balls can be identified than at higher volumes of feed.

After scanning each $\sim 4\text{mm}^3$ sample in the X-CT a 1mm^3 sub volume was taken from each of the samples for analysis. The 1mm^3 sub volumes were used to investigate the impact of increasing the number of feeds (total volume of solution) and to show the distribution of the calcite cement through the sand grains.

Chapter 7 - Making synthetic sandstones

Primarily the MICP cement can be identified as small calcite balls (<100 μ m in diameter) connecting the grains with some evidence of MICP creating a fine halo on the grain surfaces (Figure 7.23). Although the physical shape of the cement does not replicate those of naturally formed cements in sandstones the location of the cement between grain to grain contacts is comparable to those seen in naturally cemented sandstones. The attenuation coefficient of the calcite balls is more clearly defined from the sand grains (Figure 7.24) than the gypsum crystals (Figure 7.6). This therefore leads to clearer segmentation of the calcite from the sand grains.

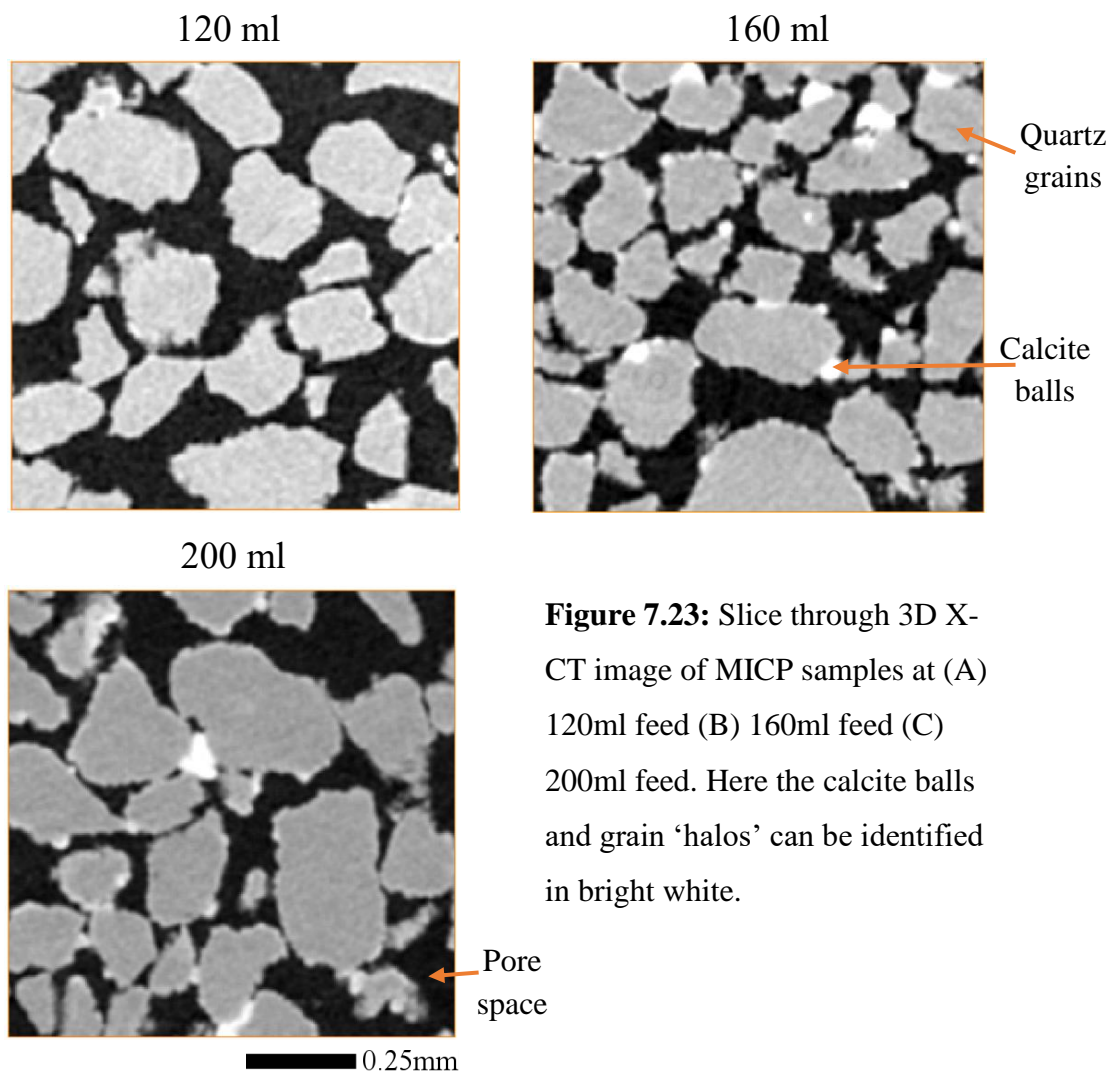


Figure 7.23: Slice through 3D X-CT image of MICP samples at (A) 120ml feed (B) 160ml feed (C) 200ml feed. Here the calcite balls and grain ‘halos’ can be identified in bright white.

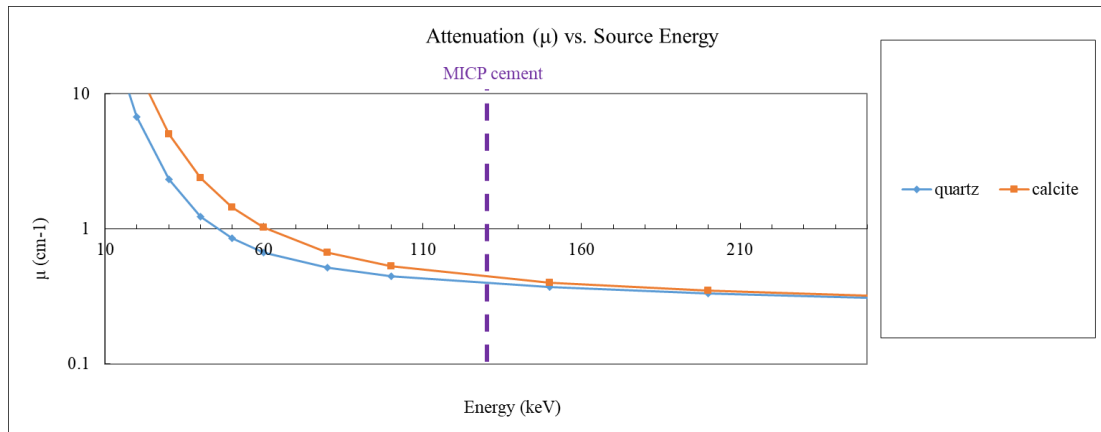


Figure 7.24: X-ray linear attenuation coefficient calculated for quartz and calcite using MuCalc (Hanna and Ketcham 2017). The energy of the scanned MICP samples is highlighted (purple dashed line). At lower energies there is a clear separation between quartz and calcite (e.g. at 60 keV the difference is 0.353 cm^{-1}). However, at 130keV the difference between the two minerals is reduced to $\sim 0.085 \text{ cm}^{-1}$. The greater the difference between the attenuation values of two minerals at a given energy, the clearer the phase segmentation.

On analysis of the thin sections and X-CT images the calcite balls appear to grow largest in sand grain alcoves or where one grain is ‘sheltered’ by another (e.g. at grain to grain contacts). This therefore suggests either a) the bacteria from the initial bacterial solution prefers to attach itself to areas of sand grains which are more ‘sheltered’, or b) the bacteria deposited by the bacterial solution is washed away by the secondary cementing solution (and following feeds). Therefore, the bacteria which remain attached are those which were more sheltered from the following flow feeds.

Based on the thin sections and the X-CT slices presented in this chapter it is likely that when the sand grains were deposited and compacted they preserved a high level of porosity (ranging from 30-50%). Therefore, as the calcite forms on the sand grains the calcite balls must grow in order to come into contact with the neighbouring sand grain. Once the calcite has formed a bridge between the two sand grains it then begins to grow to fill the corridor-like space between the sand grains to create bridges. This suggests that improvements must be made with the initial packing of sandstone grains to ensure that the grains are in contact with each other.

Chapter 7 - Making synthetic sandstones

Figures 7.26-7.31 visually demonstrate the relationship between grains, cement and porosity for each of the MICP samples. Figure 7.31 summarises the volume percentage of each phase; grains, cement and porosity, for the four gypsum cemented sandstone samples.

Figure 7.31 shows an overall increase (2.3 – 17.0%) in the percentage of cement and a decrease (39.8 – 31.9 %) in the percentage of pores present, as the number of feeds increases (120, 160, 200 ml).

120ml sample

Figure 7.25 shows the segmented phases in 3D present in the 1mm^3 sub volume. Figure 7.26 shows the cement (Fig 7.31A) and porosity (Fig 7.31B) connectivity. As with the gypsum cemented sandstones, if the cement volumes or pores are connected, then they are labelled with the same colour. Figure 7.26A shows the cement is disconnected throughout the sample. The largest cement volume is approximately $2.4 \times 10^{-3} \text{mm}^3$. Figure 7.26B shows almost all of the pores are connected throughout the sample. Any pores which are not connected to the main body are less than $2.65 \times 10^{-5} \text{mm}^3$ in volume.

160ml sample

Figure 7.27 shows the segmented phases in 3D present in the 1mm^3 sub volume. Figure 7.28 shows the cement (Fig 7.33A) and porosity (Fig 7.33B) connectivity. As before if the cement volumes or pores are connected, then they are labelled with the same colour. Figure 7.28A shows a large volume ($\sim 4.8 \times 10^{-2} \text{mm}^3$) of connected cement however, the remaining volume is disconnected. Figure 7.28B shows almost all of the pores are connected throughout the sample. Any pores which are not connected to the main body are less than $1.7 \times 10^{-5} \text{mm}^3$ in volume.

200ml sample

Figure 7.29 shows the segmented phases in 3D present in the 1mm^3 sub volume. Figure 7.30 shows the cement (Fig 7.35A) and porosity (Fig 7.35B) connectivity. As before if the cement volumes or pores are connected, then they are labelled with the same colour. Figure 7.30A shows a large volume ($\sim 1.6 \times 10^{-1} \text{mm}^3$) of connected

Chapter 7 - Making synthetic sandstones

cement however, the remaining volume is disconnected. Figure 7.30B shows almost all of the pores are connected throughout the sample. Any pores which are not connected to the main body are less than $1.1 \times 10^{-5} \text{ mm}^3$ in volume.

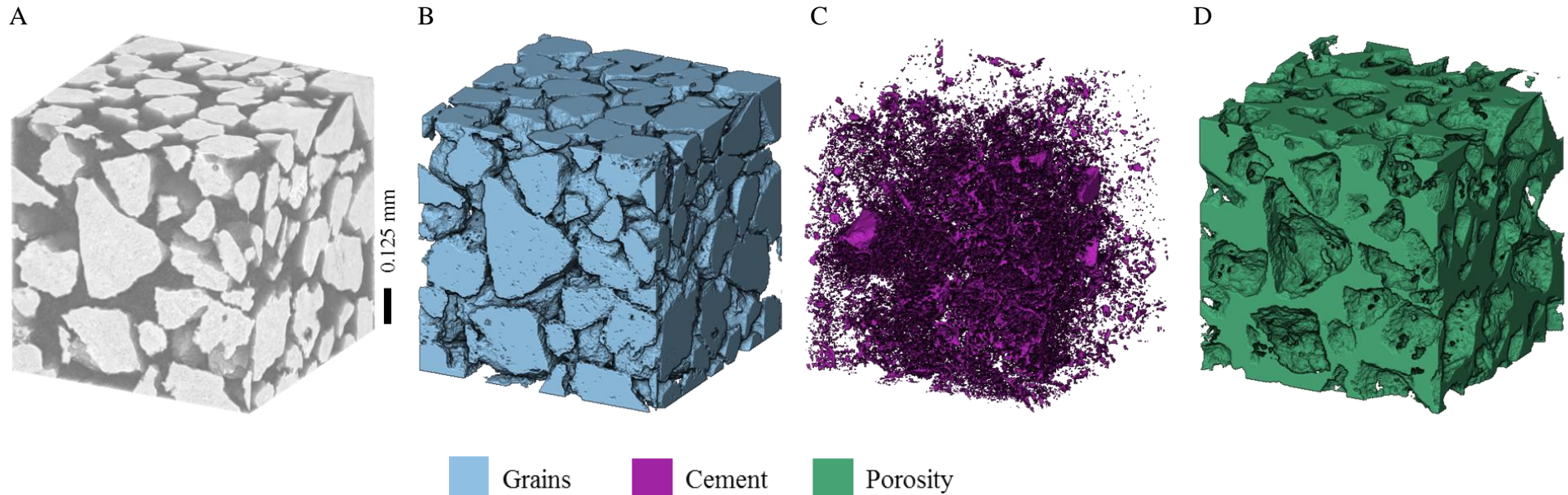


Figure 7.25: X-CT segmented 3D images of a 1mm^3 data sub volume from MICP cemented sample L7 (120ml). This sample was fed with 120ml of bacterial and cementing solution. A) Original grey scale 3D image. B) Grains segmented image. The grains segment is 57.9% of the total volume. Here we can see some grain-grain contacts, however the majority of grains are connected by cement. C) Cement segmented image. The cement segment is 2.3% of the total volume. From the shapes of the cement it appears to coat the sand grain. D) Porosity segmented image. The porosity segment is 39.8% of the total volume.

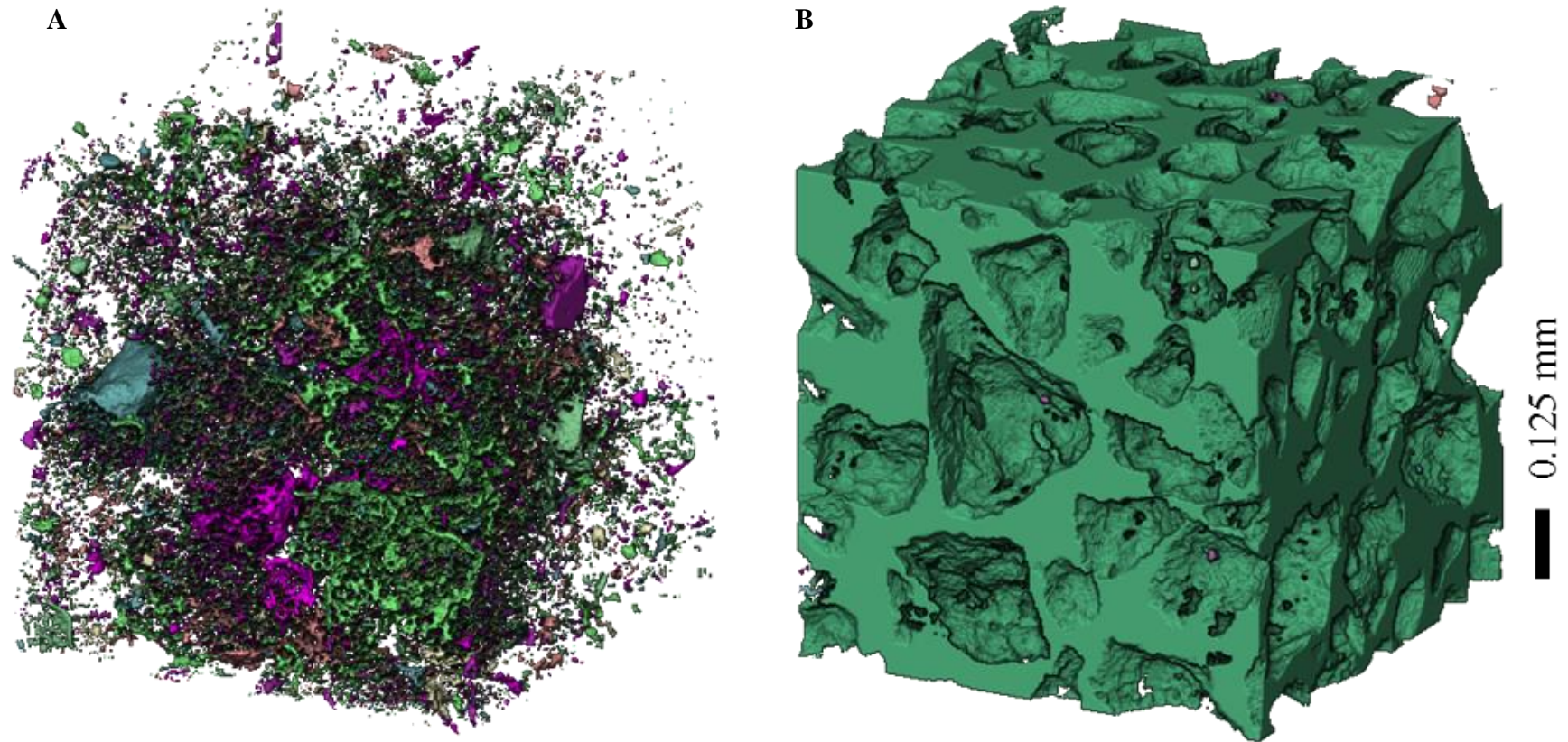


Figure 7.26: Sample L7 (120 ml) cement and porosity connectivity. Cement or pores which are connected are coloured in a single colour. A) Connected cement. The cement is disconnected across the sample. The largest volume of connected cement is 10% of the total cement volume. B) Connected porosity. 99.9% of the porosity is connected.

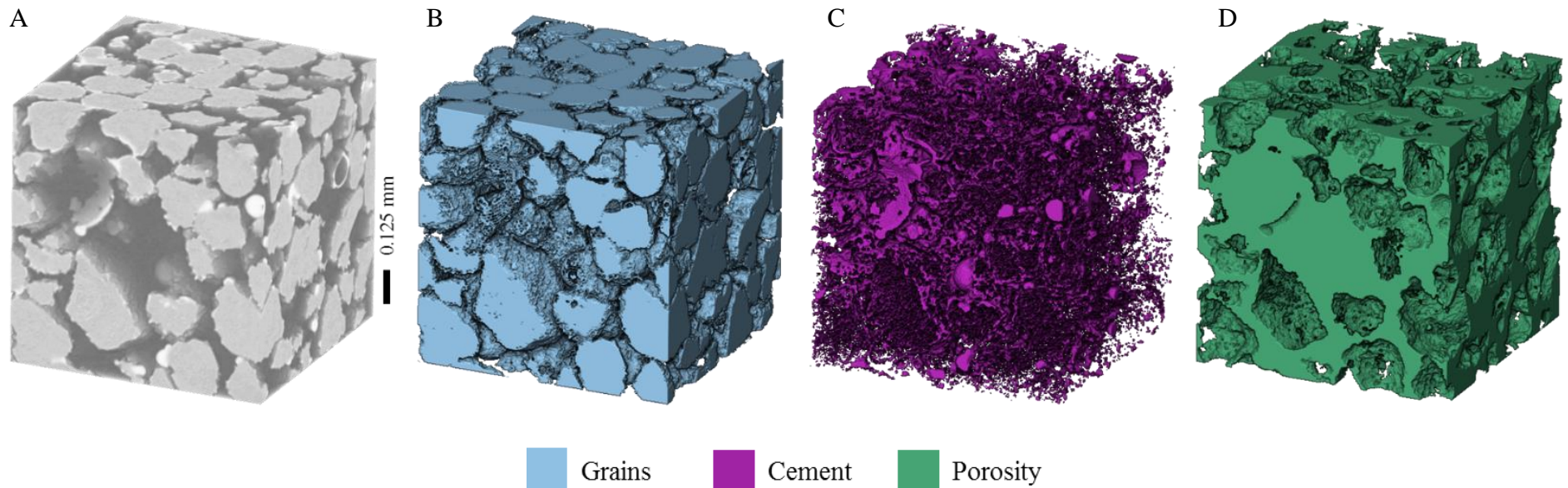


Figure 7.27: X-CT segmented 3D images of a 1mm^3 data sub volume from MICP cemented sample M7 (160ml). This sample was fed with 160ml of bacterial and cementing solution. A) Original grey scale 3D image. B) Grains segmented image. The grains segment is 55.0% of the total volume. Here we can see some grain-grain contacts, however the majority of grains are connected by cement. C) Cement segmented image. The cement segment is 7.1% of the total volume. D) Porosity segmented image. The porosity segment is 37.9% of the total volume.

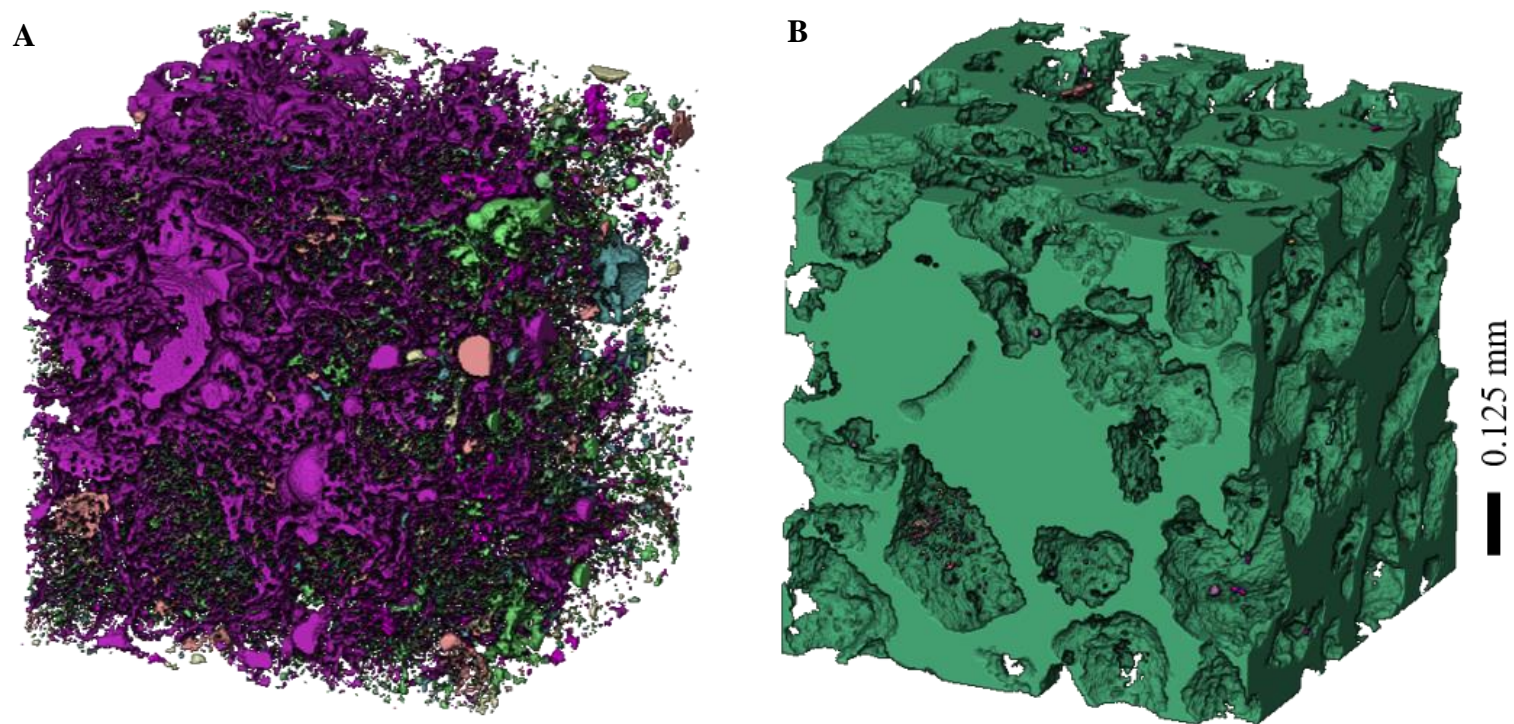


Figure 7.28: Sample M7 (160 ml) cement and porosity connectivity. Cement or pores which are connected are coloured in a single colour. A) Connected cement. Approximately 69% of the cement is connected (purple colour). The remaining 31% is pockets of disconnected cement. B) Connected porosity. 99.9% of the porosity is connected.

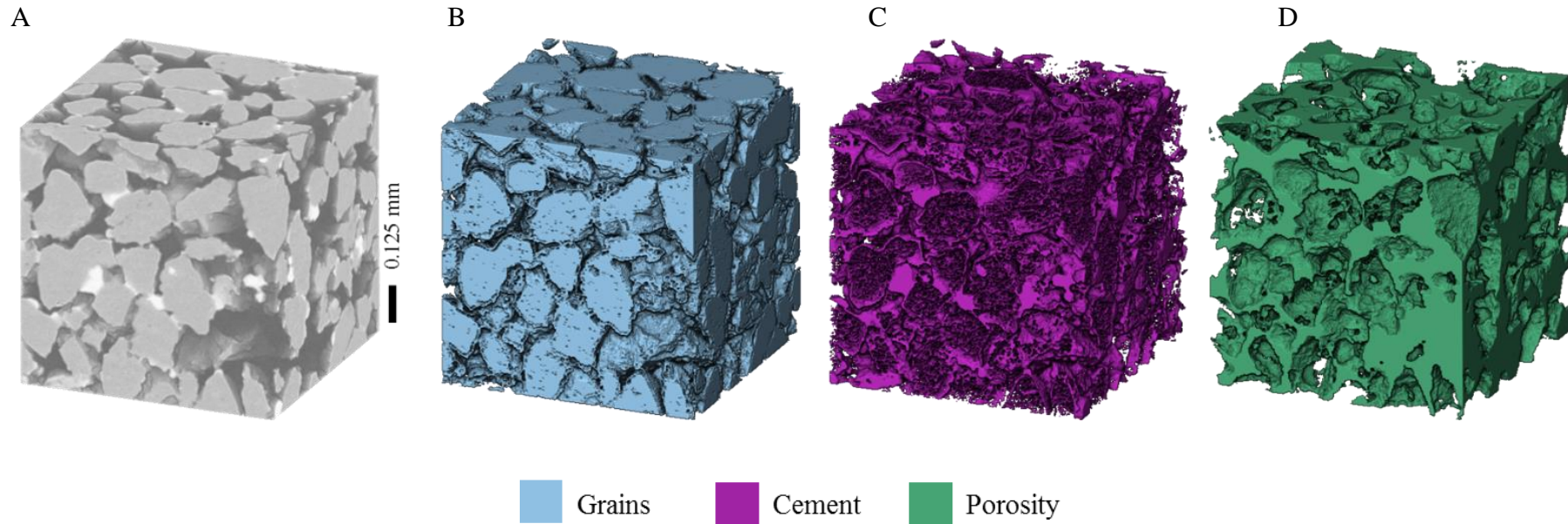


Figure 7.29: X-CT segmented 3D images of a 1mm^3 data sub volume from MICP cemented sample H6 (200ml). This sample was fed with 200ml of bacterial and cementing solution. A) Original grey scale 3D image. B) Segmented image of all three phases. C) Grains segmented image. The grains segment is 52.5% of the total volume. Here we can see some grain-grain contacts; however the majority of grains are connected by cement. D) Cement segmented image. The cement segment is 17.0% of the total volume. E) Porosity segmented image. The porosity segment is 31.5% of the total volume.

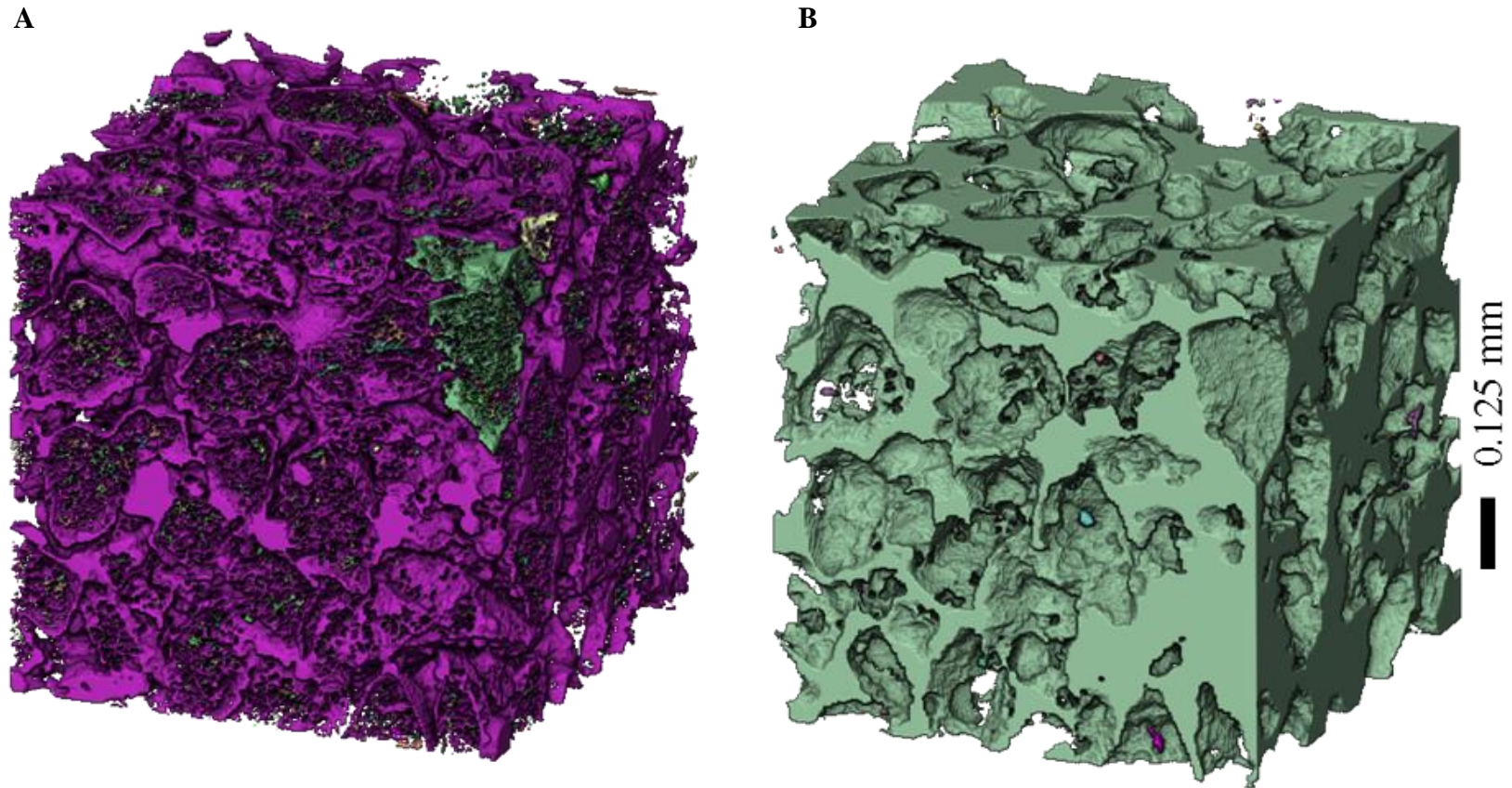


Figure 7.30: Sample H6 (200 ml) cement and porosity connectivity. Cement or pores which are connected are coloured in a single colour. A) Connected cement. Approximately 95% of the cement is connected (purple colour). The remaining 5% is pockets of disconnected cement. B) Connected porosity. 99.9% of the porosity is connected.

Chapter 7 - Making synthetic sandstones

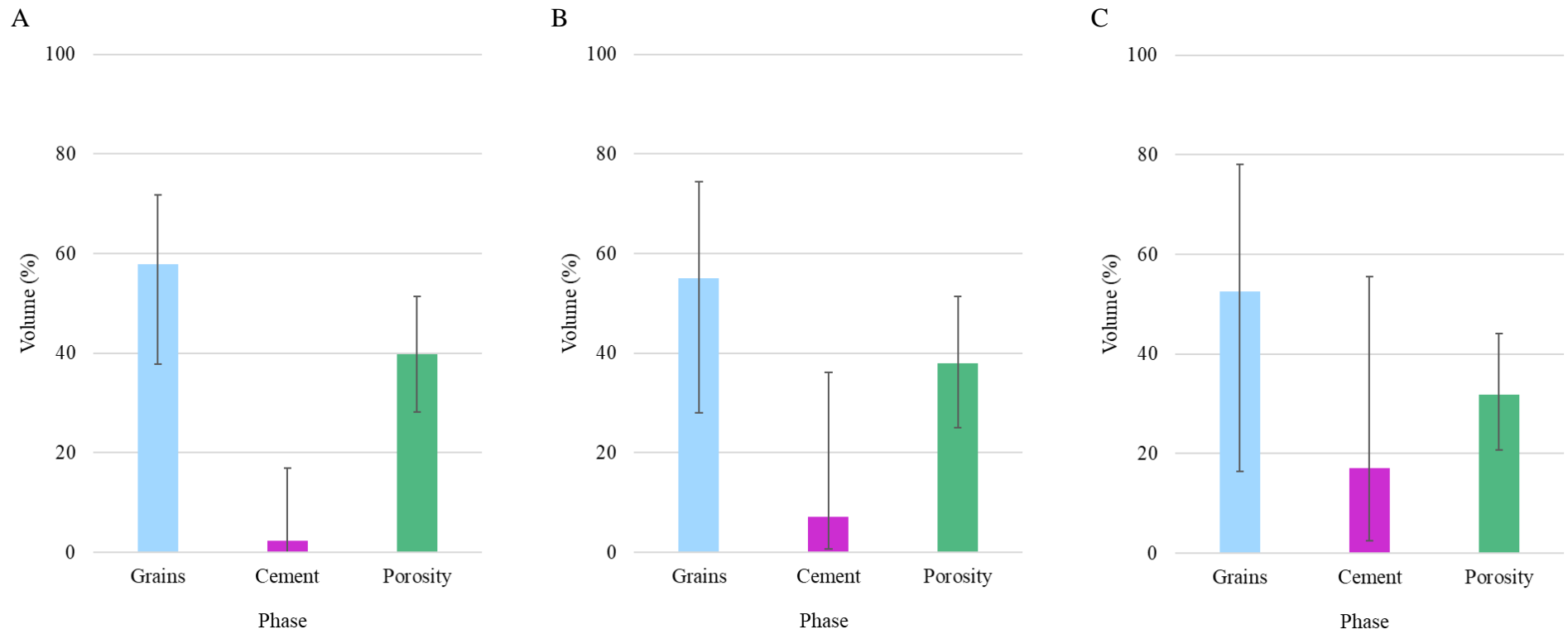


Figure 7.31: Summary of phases (grains, cement and porosity) present in the MICP cemented sub volumes. A) 120 ml B) 160 ml C) 200ml.

Chapter 7 - Making synthetic sandstones

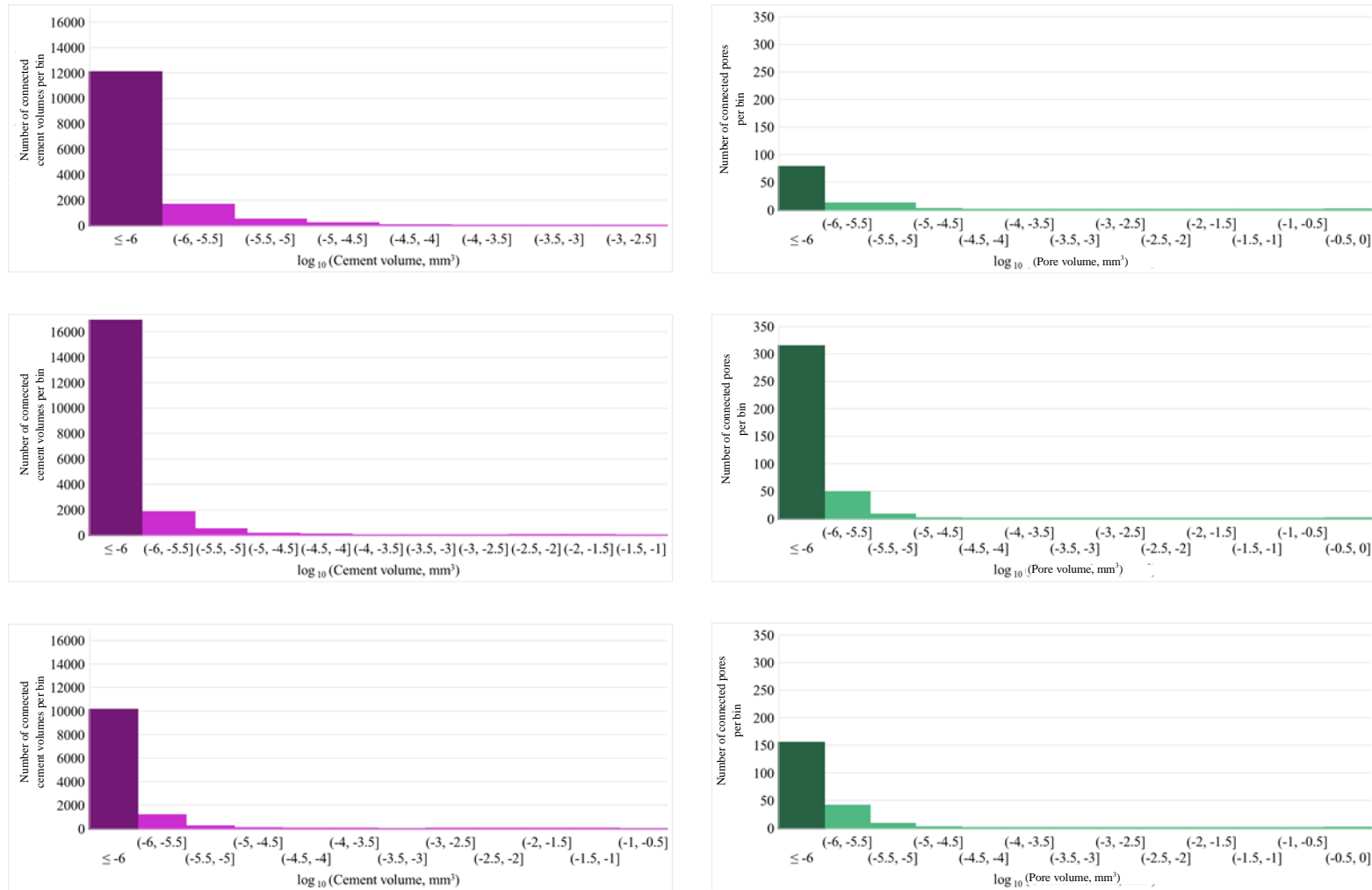


Figure 7.32: Histogram showing the number of connect cement (purple) and pore(green) volumes for the 1mm^3 MICP samples 120, 160 and 200ml. The bin width is 0.5. The column on the left (shaded column) is an overflow bin for all cement and pore volumes less than 0.000001 mm^3 .

Figure 7.31 summarises the percentage of grains, cement and porosity present for each of the MICP samples shown in Figures 7.25-30. From this figure there is an overall increase in the percentage of cement (from 2.3- 17.0%) and decrease in the percentage of pores (39.8- 31.5%) as the volume of feed increases.

The cement does attach itself to the edges of the grains however the spread of the cement around the grains is thin and irregular. Unlike the gypsum cemented sandstones the cement in the MICP cemented sandstones can be unconnected, confirming that the cement has an irregular distribution around the sand grains. Across all three samples the pores are connected this therefore suggests that the permeability of these samples is high.

One main factor which needs to be considered to further improve the method outlined in this chapter for forming MICP cemented sandstones is the physical set up of the experiment. Due to the ‘flush through’ mechanism to feed the sandstones there is no way to determine accurately the mass of calcite which has been produced. Back calculating the calcite present through treatment with HCl gives only an approximation. One possible solution is to create a closed system similar to Harkes et al. (2010) whereby the effluent produced as a result of the procedure can be collected and measured.

Table 7.11: List of MICP samples scanned in X-CT for micro analysis. Here the ‘measured’ results are from Avizo/machine learning. The ‘calculated’ results are the average results from the cylinder sub volumes (See Table 7.9). The vacuum saturation results are also displayed.

Sample name	Feed (ml)	Estimated calculated cement (%)	Measured cement (%)	Estimate calculated porosity (%)	X-CT Measured porosity (%)	Vacuum saturation porosity (%)
L7	120	8.56	2.34	34.92	39.77	46.06
M7	160	12.00	7.05	32.58	37.90	38.31

H6	200	13.47	17.00	38.47	31.86	36.30
----	-----	-------	-------	-------	-------	-------

Table 7.11 compares the calculated values from Section 7.3.2.2.3 to the Avizo measurements for the percentage of cement and porosity in each of the three 1mm³ sub volume samples (L7, M7 and H6). Here it can be seen that as the number of feeds increase, the percentage of calculated and measured cement increases and the measured porosity decreases. The porosity measurements from the vacuum saturation test are also displayed in Table 7.11. Like the porosity results from the X-CT, the vacuum saturation results show that the porosity of the samples decrease as the volume of calcite increases. The difference between the X-CT measurements and the vacuum saturation tests ranges from 5-11%. However, the calculated porosity trend is not as well-defined.

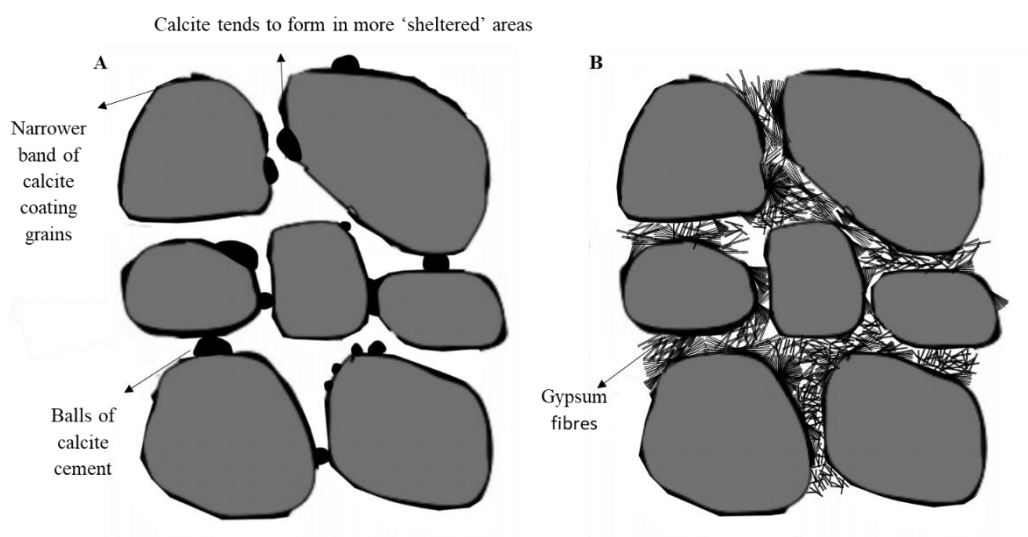


Figure 7.33: Schematic diagram of cement growth between grains. Each of these diagrams have been modified from Cheng et al. (2013). Schematics have been created based on thin section and X-CT samples from this study. A) Calcite (MICP) cemented sandstone. This schematic illustrates a narrower calcite grain coating and rounded calcite links between quartz grains. B) Gypsum cemented sandstone. Here the gypsum crystals have grown in the pores around the sand grains.

Figure 7.33 schematically compares the distribution of calcite (from MICP) to gypsum cement observed in this chapter (Figure 7.33B). The observations from this chapter show the

calcite to form in balls and in very thin, uneven, grain coatings. The calcite balls are more likely to be located in more ‘sheltered’ areas where the grain to grain distance is smallest. This builds on the schematic by Cheng et al. (2013) which focuses on the distribution of the cementation solution prior to calcite formation.

Figure 7.33B shows a schematic of the gypsum cemented sandstone. Here the gypsum needles appear to have to random orientations and almost all the cement is in contact.

7.4 Discussion

7.4.1 Naturally formed sandstones

One of the criteria of this chapter was to form sandstones which replicate both the physical and mechanical properties of naturally formed sandstones.

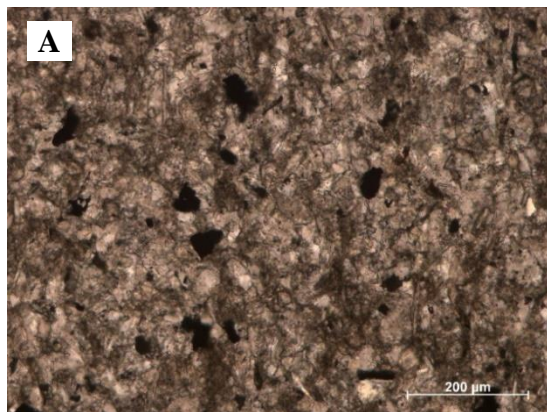
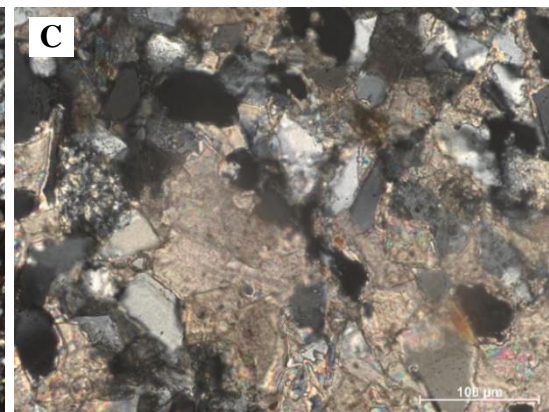


Figure 7.34: Example of calcite cemented Devonian aged Caithness Flagstone in PPL (A) and XPL (B and C). Here the grains are in contact and the calcite fills the pore space. Image from Andrea Hamilton.



In naturally formed calcite cemented sandstone such as the Caithness flagstone (Figure 7.34) the sandstone is primarily grain-supported with calcite cement filling the available pore space. The gypsum-cemented sandstones formed in this chapter have a similar cement distribution however they are cement supported sandstones with no visible grain to grain contacts. Meanwhile, under visual inspection the MICP cemented sandstones show some (estimated 8% of all grains) examples of grain to grain contacts they do not replicate the

cement distribution seen in Figure 7.34, instead the cement forms balls which act as grain-bridging cements. Both the gypsum and MICP synthetic sandstones are matrix supported sandstones.

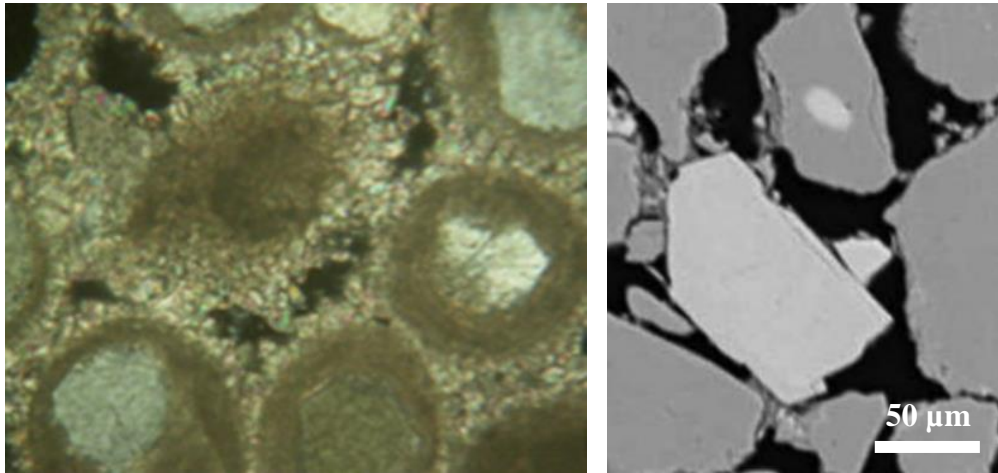


Figure 7.35: Thin sections for comparison with gypsum cement. A) Beachrock from Mauz et al. (2015). No scale is provided. B) An example of clay cemented sand grains from Wooldridge et al. (2018).

In the naturally calcite cemented sandstone from Caithness no porosity can be identified in thin section. From previous analysis the porosity of Caithness Flagstone was measured by vacuum saturation to be ~2% (Hamilton 2005). The lowest porosity value from the Avizo sub volumes of the MICP cemented sandstone samples is 31.5% (See Figure 7.30). This therefore shows the properties of MICP cemented sandstone samples are not similar to the properties of Caithness sandstone. However, this is only one example of naturally formed calcite cemented sandstone.

The gypsum textures formed here are most comparable to bladed aragonite beach rock displayed in Mauz et al. (2015). However, to my knowledge there are limited cements in sandstone which resemble the gypsum cement in this chapter (see further discussion in Chapter 9). However, the shape of the prominent gypsum bridges identified in the X-CT sections (Figure 7.5) is most similar to the types of cement structures which can be identified in clay cemented sandstones (Figure 7.35). However, this resemblance is not perfect.

7.4.2 Mineral segmentation

The type of cement used to form the synthetic sandstones has direct implications for the segmentation of the grains and cement in each of the samples. Accurate Avizo segmentation could not be completed in the gypsum-cemented samples due to the similarity in attenuation values between quartz and gypsum. When scanning a sample containing gypsum cement, a lower scanning energy (<60 keV) is recommended in order to see a contrast in attenuation values. Although this will reduce the image resolution of the scans.

The attenuation contrast between quartz and calcite is larger than the difference between quartz and gypsum. As a result, the sand grains and calcite cement could straightforwardly be segmented using Avizo.

Further work is required to further explore the benefits of one cementing technique over the other. Table 7.12 summarises the pros and cons of using each cementing method.

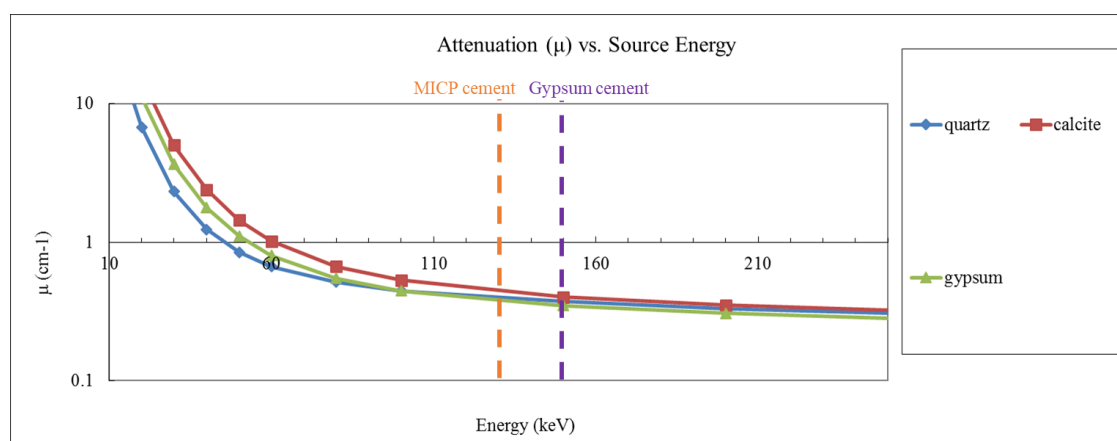


Figure 7.36: X-ray linear attenuation coefficient calculated for quartz, gypsum and calcite using MuCalc (Hanna and Ketcham 2017). The three scanned MICP samples are highlighted. At lower energies there is a clear separation between quartz and calcite. However, 130keV the difference between the two minerals is reduced. The greater the difference between the attenuation values of two minerals at a given energy, the clearer the phase segmentation.

Table 7.12: Pros and cons of gypsum vs MICP cement.

<u>Gypsum</u>		<u>MICP</u>	
Pros	Cons	Pros	Cons
Closed precipitation system- can calculate the volume of gypsum present and porosity in the sample	Segmentation is complex	Fast curing time	Requires more work to calculate MICP present in each sample
Can form in nature	Difficult to identify in thin section	Fast segmentation	Does not form in nature
	Distribution does not replicate gypsum-cemented sandstones in nature		Distribution of cement does not replicate calcite formed in nature
	Gypsum powder is often sold with impurities.		

7.4.3 Sampling technique

The method used in this chapter to calculate the percentage of grains, cement and porosity is a simplified version of the method shown in Chapter 5.

Due to time constraints this chapter only seven of the seventy-seven samples produced in this chapter were analysed. Here it is assumed that the one chosen sample from each synthetic sandstone is representative of all the samples. Furthermore, the analysis does not take into consideration the potential for any spatial variation of the three phases across each of the samples (e.g. potentially due to restricted flow).

In order to fully analyse these samples in the future it would be best to scan a minimum of three sub volumes from each of the samples (top, middle and base of the sample). This would enable a greater understanding of the variation of cement and porosity across the sample.

Ideally, as mentioned in Chapter 5, an automated algorithm which could sub sample each sample in multiple ways would work best to build an accurate picture of the phases inside each sample.

7.5 Summary

- X-CT can be used to image the internal structure of synthetic sandstones.
- Both gypsum and MICP can be used to cement grains of sand together in less than four and two weeks respectively.
- 20 and 25% gypsum cemented samples are the most robust of the gypsum cemented sandstones due to their higher percentage of cement present. These are tested further in Chapter 8.
- The gypsum samples show an overall increase in the percentage of cement and decrease in the percentage of pores present as the wt% of basanite increases (10-25%).
- The distribution of cement in the gypsum synthetic sandstones fills the pores between grains therefore is most like the distribution found in naturally formed sandstone (e.g. Caithness Flagstone).
- MICP creates balls of calcite between the sand grains. This does not replicate the distribution of cement in naturally formed sandstones.
- The density contrast between the calcite, produced by MICP, and quartz grains allowing calcite cement to be readily identified on X-CT scans.
- In order to truly compare a synthetically cemented sandstone to a naturally cemented sand all formation factors must be replicated (e.g. depositional environment, composition etc.).

Chapter 7 - Making synthetic sandstones

Recommendations:

- Use geophysical methods, such as shear wave velocity, to unobtrusively understand the approximate MICP cementation level throughout each sample.
- For future production of synthetic sandstones make the sandstones in a chamber where:
 - A continual load can be applied to each sample.
 - Effluent can be gathered and measured.

Chapter 8 - Mechanical deformation

8.1 Rationale

The aim of this chapter is to use mechanical deformation techniques to experimentally recreate the deformation setting in which deformation bands may form naturally in the subsurface. Synthetic samples are deformed in order to reduce the number of variables present in comparison to real sandstone. By simplifying the sandstone samples the impact of the deformation on the three phases (grains, cement and porosity) can be better understood.

It has been shown that MICP treatment improves the strength and stiffness of the sands (Khaleghi and Rowshanzamir 2019). As discussed in Chapter 7, MICP treatment can also decrease the permeability of a sand sample. This chapter investigates the mechanical properties to characterise of the synthetically cemented sandstones and the impact of varying the percentage of cement present in each sample.

In this chapter the shear box, uniaxial rig and triaxial rig (on gypsum cemented samples only) are used to measure the shear and compressive strength of the synthetic sandstones which have been cemented with gypsum and microbial induced calcite precipitation (MICP).

Previous studies have shown that deformation bands can form when real sandstone cores are triaxially deformed. In this chapter the gypsum cemented samples are triaxially deformed, under similar deformation conditions as the real sandstone samples, to understand if deformation bands can form in these synthetic samples. No MICP samples were triaxially deformed due to the cost and time available to run additional samples on the triaxial rig. Gypsum samples were tested over MICP cemented samples because the distribution of cement in gypsum cemented samples is most similar to real rocks. See Chapter 9 for full comparison.

In the sections which follow each of the test apparatus, results and analysis are listed in turn.

8.2 Direct Shear box test

Direct shear test is conventionally used to measure the shear strength of soils, or weakly cemented materials. The shear box tests are a quick method to determine the maximum shear strength of the synthetic sandstones however there are limitations in using a shear box. With the direct shear box the maximum displacement is limited to one length of the box. The failure plane is always horizontal and forced along the joint between the upper and lower box. However, due to heterogeneities in the sample the area between the upper and lower box may not be the weakest area of the sample. There is a non-uniform distribution of stresses along the shear plane. As the top of the shear box slides past the fixed shear box base, there is a decrease in the contact surface area between the two halves, therefore causing an uncertainty in the measurements of both shear and normal stresses.

The samples are held in a metal box consisting of two halves (Figure 8.1). The bottom half is fixed in place and the top half is attached to a motor which drives the top half forward at a fixed rate (e.g. 0.5 mm/min). Metal spacing plates can be placed at the base and the top of the sample. A vertical force is applied to the top of the sample. For the purpose of this thesis this load is used to create the confining pressure during shearing. As the top half of the shear box moves the force required to create the movement (shear the sample) and the total displacement along the x and y axis is recorded. The shear box is used to measure the shear strength parameters maximum and ultimate shear stress.

Schematic stress-strain curve results from shear box testing are shown in Figure 8.2. Here examples of stereotypical shear stress curves are given for brittle (sudden failure experienced) and non-brittle (gradual failure, or creep) of materials.

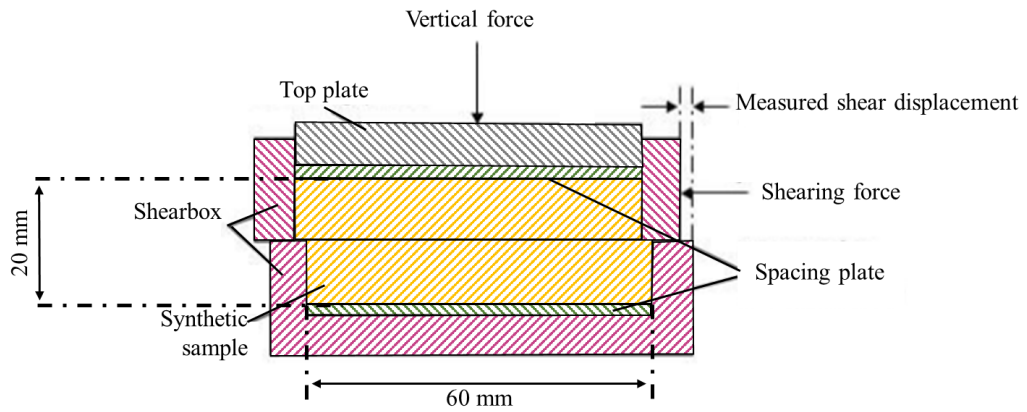


Figure 8.1: Schematic cross section of shear box set up. Modified from Knappett & Craig (2012).

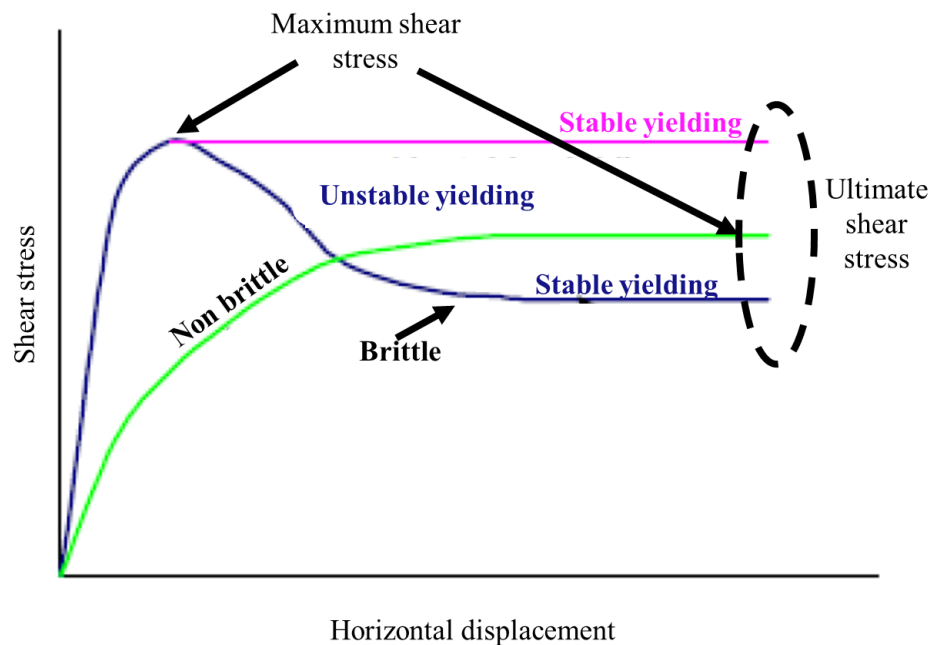


Figure 8.2: Schematic stress-strain curves from shear box tests. The blue curve highlights the expected shear response for brittle materials or dense coarse grained sands. The green curve shows a non-brittle material or loose sand response with stable yielding. Edited from Osano (2012).

8.2.1 Test apparatus

The direct shear box used was from the University of Strathclyde's Geotechnics Laboratory (Figure 8.3).

Chapter 8 - Mechanical deformation

Samples were prepared to sample size of 60 mm height x 60 mm width x 20 mm depth. Two shear box set ups were used to improve the chance of shear band evolution. In the first set up the lower half of the shear box was fixed in place and the upper half of the shear box was placed directly on top. This configuration was used for dry sand samples. For the second configuration the lower half was fixed into place and the upper half of the shear box was lifted off the lower half using steel balls of 2 mm diameter. The balls were held in place with petroleum jelly. The second configuration was used for all synthetic sandstone samples. Two Linear Variable Differential Transformers (LVDT's) monitored the vertical thickness change as the sample was loaded and sheared, and the horizontal displacement as shearing took place. Spacer plates were used to prop the sample, so it was central to the shear plane. A lever arm loading system applied a vertical load with a 10:1 beam ratio.

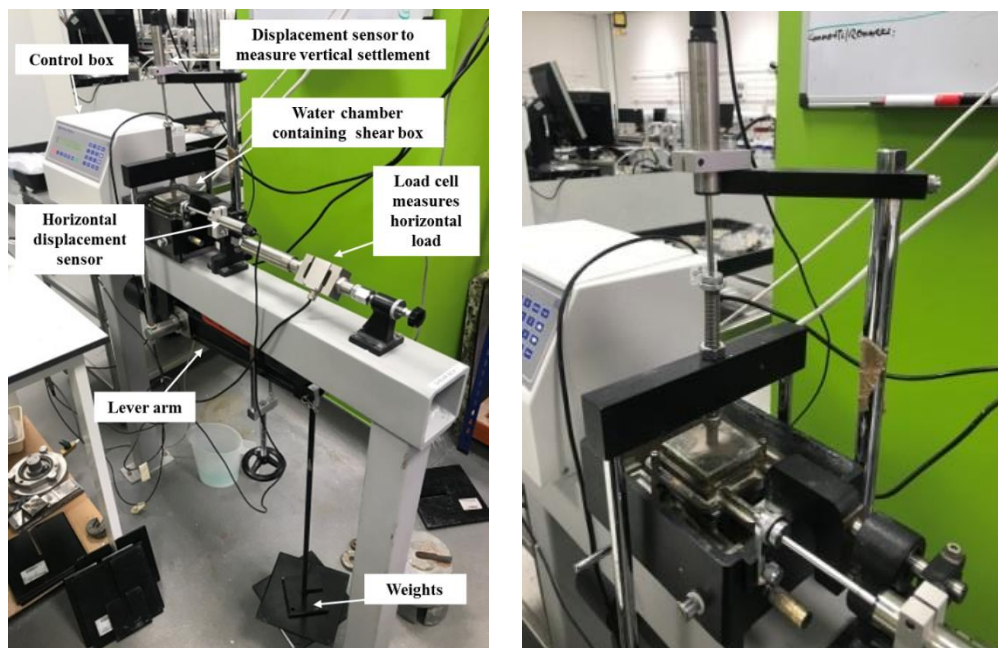


Figure 8.3: Shear box set up at the University of Strathclyde. 60mm square shear box set up including horizontal and vertical LVDT's.

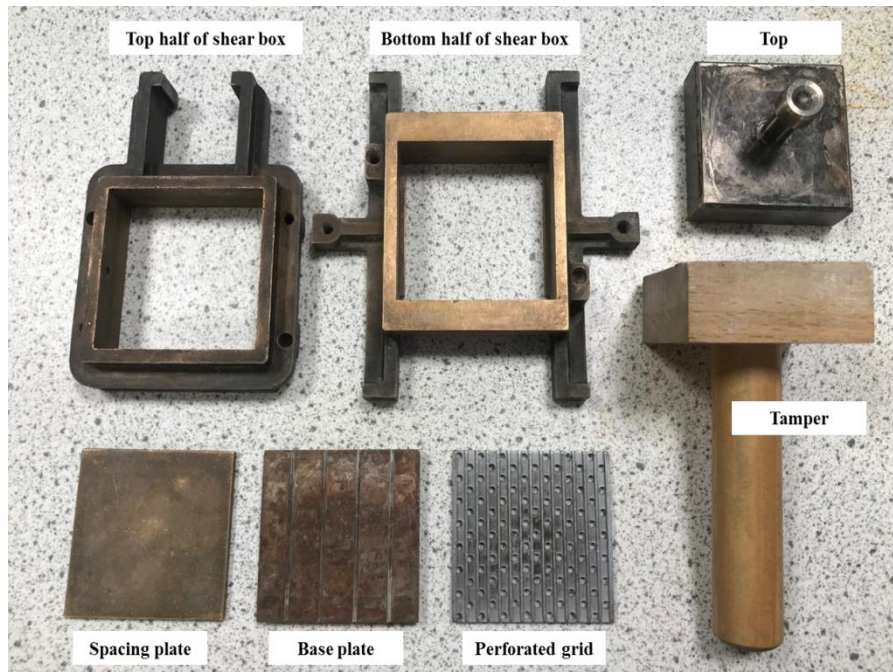


Figure 8.4: Components of the direct shear box. The internal dimensions of the shear box were 60mm width x 60mm depth x 40 mm height.

8.2.2 Shear box procedure

The direct shear box tests were carried out in unsaturated conditions. Once placed into the shear box body each sample was initially loaded (or ‘consolidated’) with a vertical load. See Table 8.1 for load mass to normal stress conversions. The majority of samples had 95.38 kPa normal stress applied. After consolidation the samples were sheared at a constant shear rate of 0.5mm/min until they reached a maximum of 6 mm horizontal displacement. Three repeat tests were made for each sand and synthetic sandstone.

To test the effect of normal stress on shear stress additional shear tests, at equivalent normal stresses of 27.25 and 163.50 kPa, were performed on some of the gypsum and MICP synthetic samples.

Table 8.1: Vertical mass applied to shear box and calculated equivalent normal stress. These conversions can be applied to all of Chapter 8.

Vertical mass (kg)	Equivalent normal stress (kPa)	Approximate depth underground if sand (m) ^a	Approximate depth underground if sandstone (m) ^b
1	27.25	1.60	1.07
3.5	95.38	5.61	3.74
6	163.50	9.62	6.42

^a Using sand density from Craig (2004)

^b Using sandstone density from Sharma (1997)

8.2.3 Previous shear box studies on MICP cemented sands

Table 8.2 summarises the published results from previous shear box experiments on MICP samples. Generally, as normal stress increases, the maximum and ultimate shear stresses will increase.

These results will be used in the discussion later in this section.

Table 8.2: Summary of maximum and ultimate shear stress results from previous MICP shear box test.

Literature	Normal stress (kPa)	Maximum shear stress (kPa)	Ultimate shear stress (kPa)
Khaleghi & Rowshanzamir 2019	50	190	75
Khaleghi & Rowshanzamir 2019	100	225	107
Khaleghi & Rowshanzamir 2019	150	288	150
Chou et al. 2011	11	8	8
Chou et al. 2011	21	16.5	16.5
Chou et al. 2011	31	25	25
Golmohamadi et al. 2016	55	153	N/A
Golmohamadi et al. 2016	55	168	N/A
Golmohamadi et al. 2016	55	174	N/A

Golmohamadi et al. 2016	55	190	N/A
Golmohamadi et al. 2016	111	195	N/A
Golmohamadi et al. 2016	111	203	N/A
Golmohamadi et al. 2016	111	206	N/A
Golmohamadi et al. 2016	111	212	N/A
Golmohamadi et al. 2016	222	278	N/A
Golmohamadi et al. 2016	222	270	N/A
Golmohamadi et al. 2016	222	268	N/A
Golmohamadi et al. 2016	222	260	N/A
Canakci et al. 2015	13.6	21.5	20
Canakci et al. 2015	20.4	30	30
Canakci et al. 2015	27.2	38	38
Feng & Montoya 2015	100	800	350

8.2.4 Shear box results

For each of the experiments the maximum and ultimate shear stress is noted (see Figure 8.2 for location of maximum and ultimate shear stress). These parameters give the shear strength of the soil.

The shear stress versus horizontal displacement is plotted for comparison between the type of cement, volume of cement and normal stress.

Whilst analysing the shear stress results it became clear that there was an artefact present amongst almost all the synthetic sandstone samples (Figure 8.5). Up to 0.509 mm displacement along the x-axis was observed before any observed displacement in the y axis. This suggests that up until 0.509 mm displacement the sample is not in contact with the shearing plates. The main reason for this is that because the samples are made prior to placing them in the shear box they may be shorter than the shear box sample holder (60mm in length).

One possible means to overcome this is to make the samples within the sample holders prior to deformation. However, this requires a more complex experimental set up.

To correct for this artefact each samples' x-axis is adjusted (see Figure 8.5C).

Chapter 8 - Mechanical deformation

Another feature which is seen in the shear stress results are data ‘drop off’ points (Figure 8.6). These ‘drop off’ points are caused by stick slip of the sand grains along the sliding surface of the sample. The drop-off points do not seem to have an impact on the maximum or ultimate shear stress results as the shear stress continues to increase after the drop off points.

Overall the shear stress curves are quite irregular. This is unusual for shear box test results. One possible explanation for this irregularity is that the surface of the sample is not completely flat at the ends. Therefore, as the top shear plate moves edges of the sample are being chipped off.

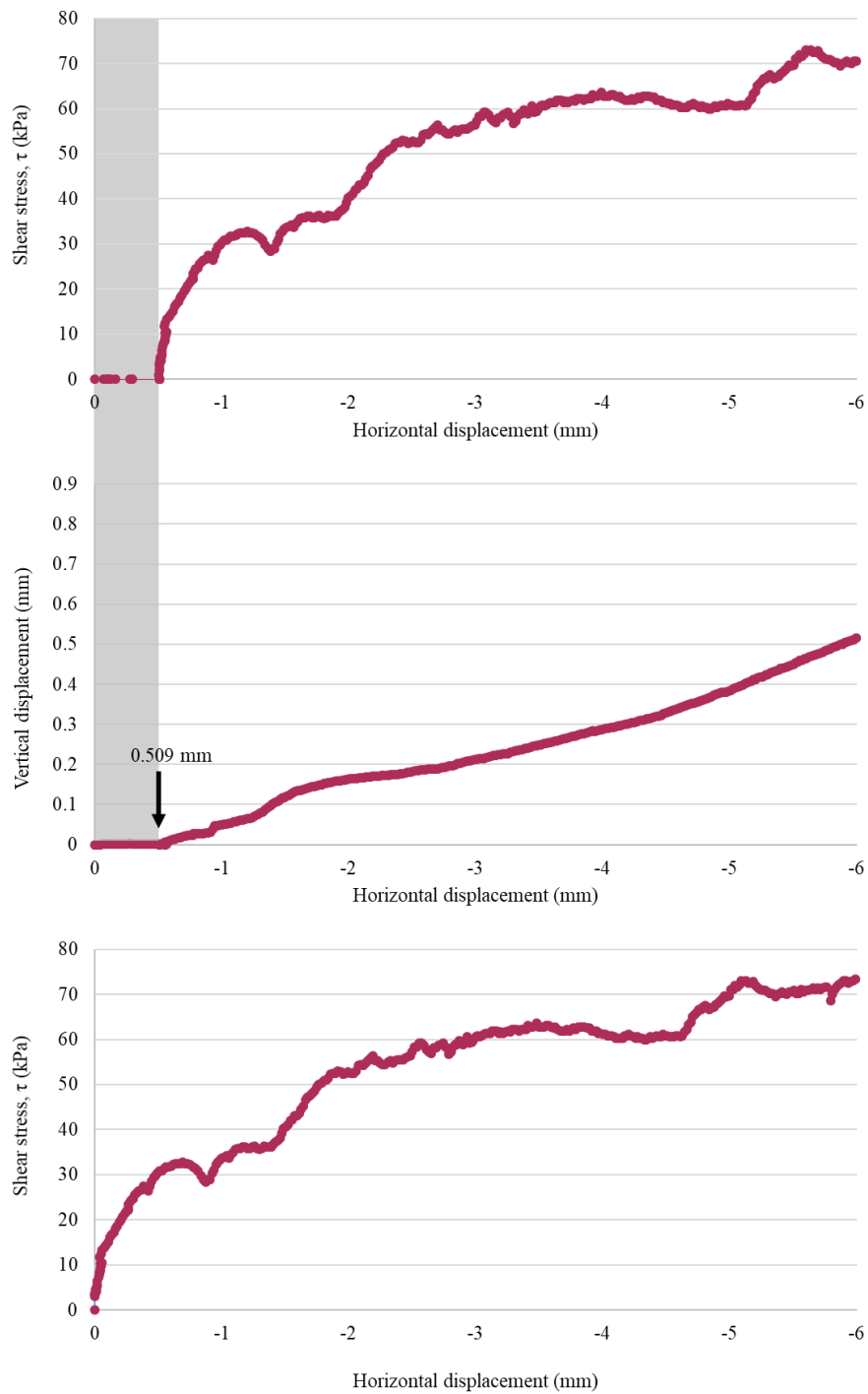


Figure 8.5: Artefacts of shear box tests. A) Original shear stress versus horizontal shear displacement at 95.38 kPa normal stress result for Sample L5 (120 ml). B) Analysis of the horizontal vs vertical displacement shows that no vertical displacement takes place until 0.509 mm horizontal displacement (see area highlighted in grey). This is an artefact seen in each experiment. C) Graph with corrected horizontal displacement axis.

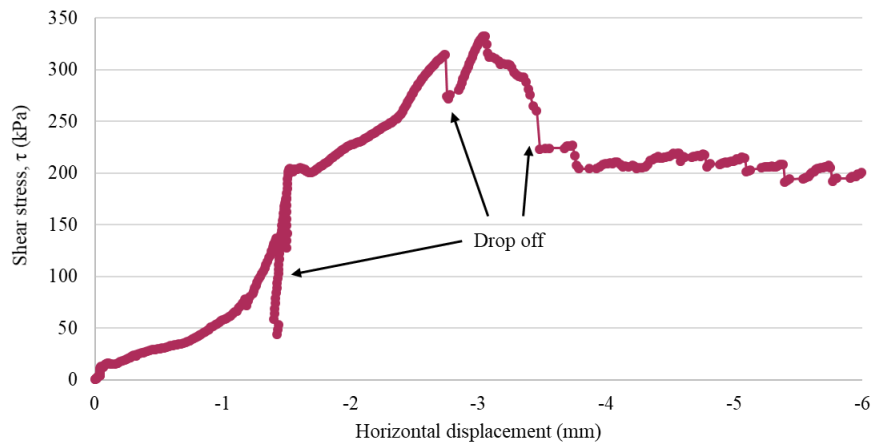


Figure 8.6: Artefacts from sample M5 (160 ml). Drop off points formed due to stick slip of the sand grains during shearing

8.2.4.1 Untreated sands

To enable the impact of the synthetic sandstones to be assessed, clean Alloa sand was initially tested in the shear box at a normal stress of 95.38 kPa. The Alloa sand was the starting material for the synthetic sandstones. For details of how the Alloa sand was made into the synthetic sandstones see Chapter 7.

The sands were cleaned and then sieved directly into the shear box. A tamper (Figure 8.4) was then applied to the sample to pack the sand grains closer together. Figure 8.7 shows shear stress versus horizontal displacement graphs for the three repeated sand samples. The three repeats show the maximum shear stress ranging from 77.78-91.39 kPa, with the ultimate shear stresses ranging from 63.89-64.44 kPa.

The shape of the three curves indicate a dense sand response. However, the shear stress in Sand 3 increases much faster over a shorter horizontal displacement. The dilation and contraction of the shear tests are analysed by plotting the vertical displacement against the horizontal displacement (Figure 8.8). Here Sands 1 and 2 display evidence of initial contraction followed by dilatancy during shearing. Meanwhile, Sand 3 displays a contractional behaviour throughout shearing. This therefore suggests that the sand grains were not as tightly packed as they were for Sands 1 and 2. It is likely that the sharp increase in shear stress observed in Sand 3 is

Chapter 8 - Mechanical deformation

due to heterogeneities inside the sample. It is possible at the initiation of shearing Sand 3 was more densely packed than in the remainder of the sample.

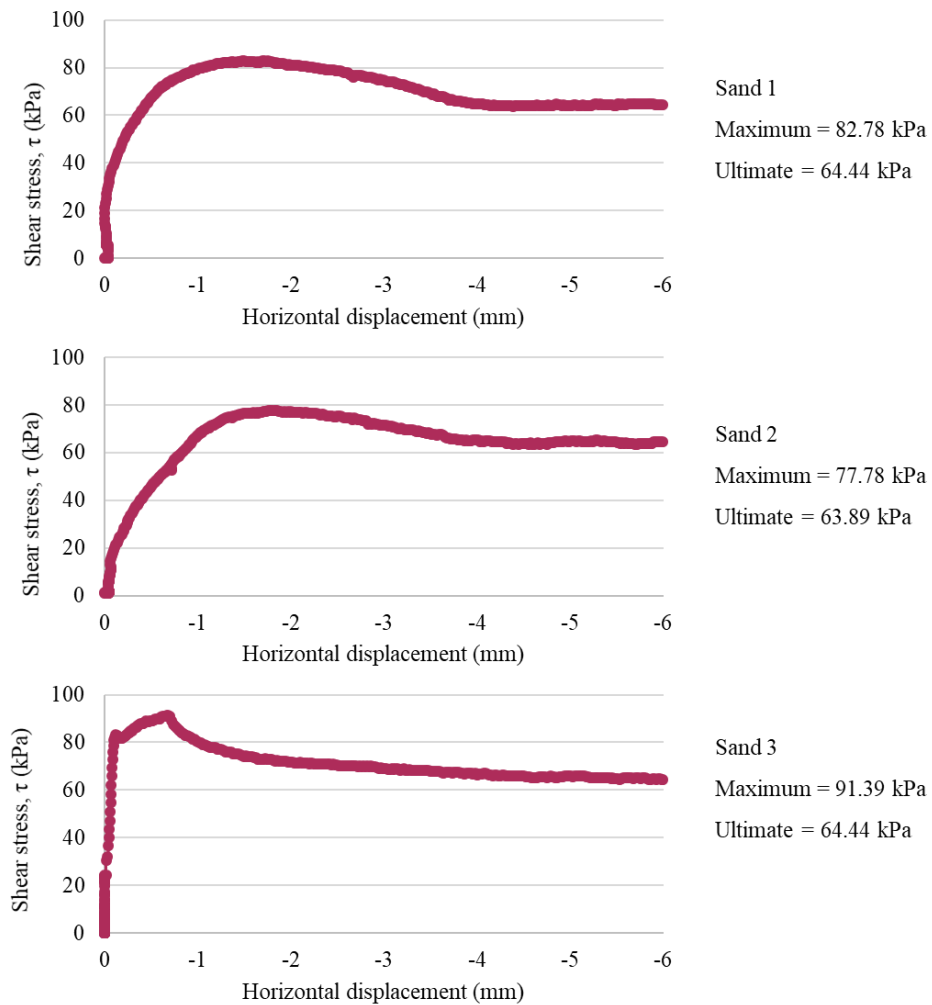


Figure 8.7: Repeatability test showing the response of untreated sand samples to shearing. Shear stress versus horizontal displacement under normal stress of 95.38 kPa. The graphs for Sand 1 and 2 reflect a stereotypical dense sand shear response. Meanwhile, Sand 3 has an unusually fast increase in shear stress with horizontal displacement.

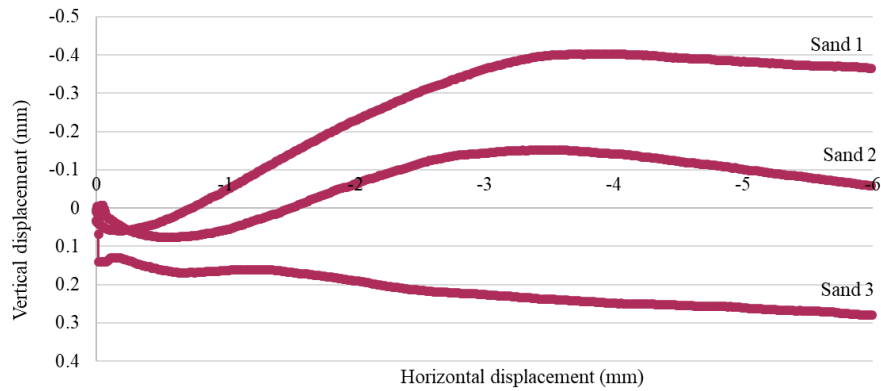


Figure 8.8: Vertical vs horizontal displacement of the three sheared sand samples. Here Sands 1 and 2 are dilating as horizontal displacement is increasing. Meanwhile Sand 3 behaves differently and shows mainly contractional behaviour.

8.2.4.2 Gypsum cemented sandstones

8.2.4.2.1 Gypsum cemented sandstone shear tests

10, 15, 20 and 25% gypsum cemented sandstones were sheared at 27.25, 95.38 and 163.50 kPa normal stress (Table 8.3). The shear stress versus horizontal displacement along the x-axis is plotted for each gypsum shear experiment at 95.38 kPa in Figure 8.9. The shear stress results for the 20 and 25% gypsum cemented sandstones at 27.25 kPa and 163.50 kPa are shown in Figure 8.10.

Table 8.3: Summary of all sheared gypsum cemented sandstones and the normal load conditions at which they were sheared.

Sample group replica samples	Sample composition (%)	Mass applied (kg)	Normal load (kPa)
GS4	10	3.5	95.38
GS5	10	3.5	95.38
GS6	10	3.5	95.38
GS26	15	3.5	95.38
GS27	15	3.5	95.38
GS28	15	3.5	95.38
GS9	20	1	27.25
GS10	20	6	163.50
GS11	20	1	27.25
GS12	20	6	163.50
GS13	20	6	163.50
GS14	20	3.5	95.38
GS21	20	3.5	95.38
GS22	20	1	27.25
GS29	20	3.5	95.38
GS15	25	6	163.50
GS16	25	1	27.25
GS17	25	1	27.25
GS18	25	6	163.50
GS19	25	1	27.25
GS20	25	6	163.50
GS23	25	3.5	95.38
GS24	25	3.5	95.38
GS25	25	3.5	95.38

Chapter 8 - Mechanical deformation

At 95.38 kPa there was an overall increase in the maximum shear stress from 10 to 25% gypsum cement content. However, the variation in shear stress is dependent on the individual samples.

The shape of each of the graphs can be compared to the schematic curves outlined in Figure 8.2. The following text describes the graphs shown in Figure 8.9 and Figure 8.10.

10% Gypsum cement

Sample GS4 (repeat 1) shows an initial brittle response which then becomes stable at higher shear stress.

Sample GS5 (repeat 2) most closely resembles the brittle response. However, between 1 and 2.75 mm horizontal displacement the shear strength appears to stabilise.

Sample GS6 (repeat 3) resembles a non-brittle shear stress curve. One possible reason for this is that the cement had little impact on the strength of the sample and instead behaved more like a loose unconsolidated sand. This is further confirmed by the low maximum (65.28 kPa) and ultimate (63.06 kPa) shear strength observed. The maximum shear strength is lower than the shear strength observed in unconsolidated sands (Figure 8.7).

15% Gypsum cement

Sample GS26 (repeat 1) has a shear stress response closest to a loose sand response. However, the peak and ultimate shear stress are almost equal.

Sample GS27 (repeat 2) shows a predominantly loose sand shear stress response.

Sample GS28 (repeat 3) shows a loose sand response to shearing.

20% Gypsum cement

Sample GS29 (repeat 1) resembles a loose sand shear stress response. As a result, the peak and ultimate shear stress are almost the same value.

Chapter 8 - Mechanical deformation

Sample GS14 (repeat 2) shows a brittle response to shearing with a short unstable yielding period.

Sample GS21 (repeat 3) shows a brittle response to shearing. Of particular interest in the period from 0 to 1.5 mm horizontal displacement. It is therefore possible that this is an artefact of the shear box.

25% Gypsum cement

Sample GS23 (repeat 1) shows a brittle response to shearing. However, unlike the other samples the shear stress increases again after peak shear stress.

Sample GS24 (repeat 2) shows a brittle response to shearing. However, there is little evidence of stable yielding.

Sample GS25 (repeat 3) shows a brittle response to shearing. However, there is little evidence of stable yielding.

To summarise, Figure 8.9 shows that 10 and 15% cemented samples are more likely to display loose sand shear responses. This suggests that the cement phase in each of these is likely to crumble. Meanwhile samples with 20 and 25% cement are more likely to display brittle behaviour characteristic of densely packed sand.

A description from each of the shear stress results from 27.25 and 163.50 kPa (Figure 8.10) confining pressure are listed below.

20% at 27.25 kPa

Sample GS9 (repeat 1) shows an overall non brittle response to shearing with stick slip observed at 3.7 mm displacement.

Sample GS22 (repeat 2) shows a non-brittle response to shearing. At 6 mm displacement the shear strength continues to increase.

Sample GS11 (repeat 3) resembles a loose sand shear stress response. As a result, the peak and ultimate shear stress are almost the same value.

25% at 27.25 kPa

Sample GS19 (repeat 1) shows a brittle response to shearing.

Sample GS16 (repeat 2) shows a brittle response to shearing with a yielding period.

Sample GS17 (repeat 3) most closely resembles a brittle shear stress response. Of noted interest is the angular nature of the curve. This is possibly due to multiple stick slip events.

20% at 163.50 kPa

Sample GS12 (repeat 1) most closely resembles a non-brittle response to shearing.

Sample GS13 (repeat 2) shows a non-brittle response to shearing.

Sample GS10 (repeat 3) shows an overall non brittle response to shearing.

Regardless of the non-brittle responses the overall shear strength remains high at an average of 194.17 kPa across the three samples. A possible explanation for each of these samples showing non brittle shear behaviour is that the normal load placed on each sample has crushed some of the cement between the grains.

25% at 163.50 kPa

Sample GS15 (repeat 1) shows a brittle response to shearing with an unstable yielding period where the shear stress appears to steadily increase.

Sample GS18 (repeat 2) shows a brittle response to shearing with a stable yielding period.

Sample GS20 (repeat 3) resembles a loose sand shear stress response. As a result, the peak and ultimate shear stress are almost the same value. As with sample GS17, the shear response is more angular. This is most likely due to stick slip occurring in the sample.

Chapter 8 - Mechanical deformation

Figure 8.11 plots the maximum and ultimate shear stress for each sample and allows for a better understanding of the spread of data and a comparison between the samples with different percentages of gypsum cement.

Overall there is a general increase in both maximum and ultimate shear stress as the normal load increases. The maximum shear stress tends to increase as the percentage of gypsum present increases. However, this trend varies depending on individual samples.

In order to determine if there is a trend with increasing percentage of gypsum present in the gypsum cemented sandstone samples, a greater number of samples should be tested.

Chapter 8 - Mechanical deformation

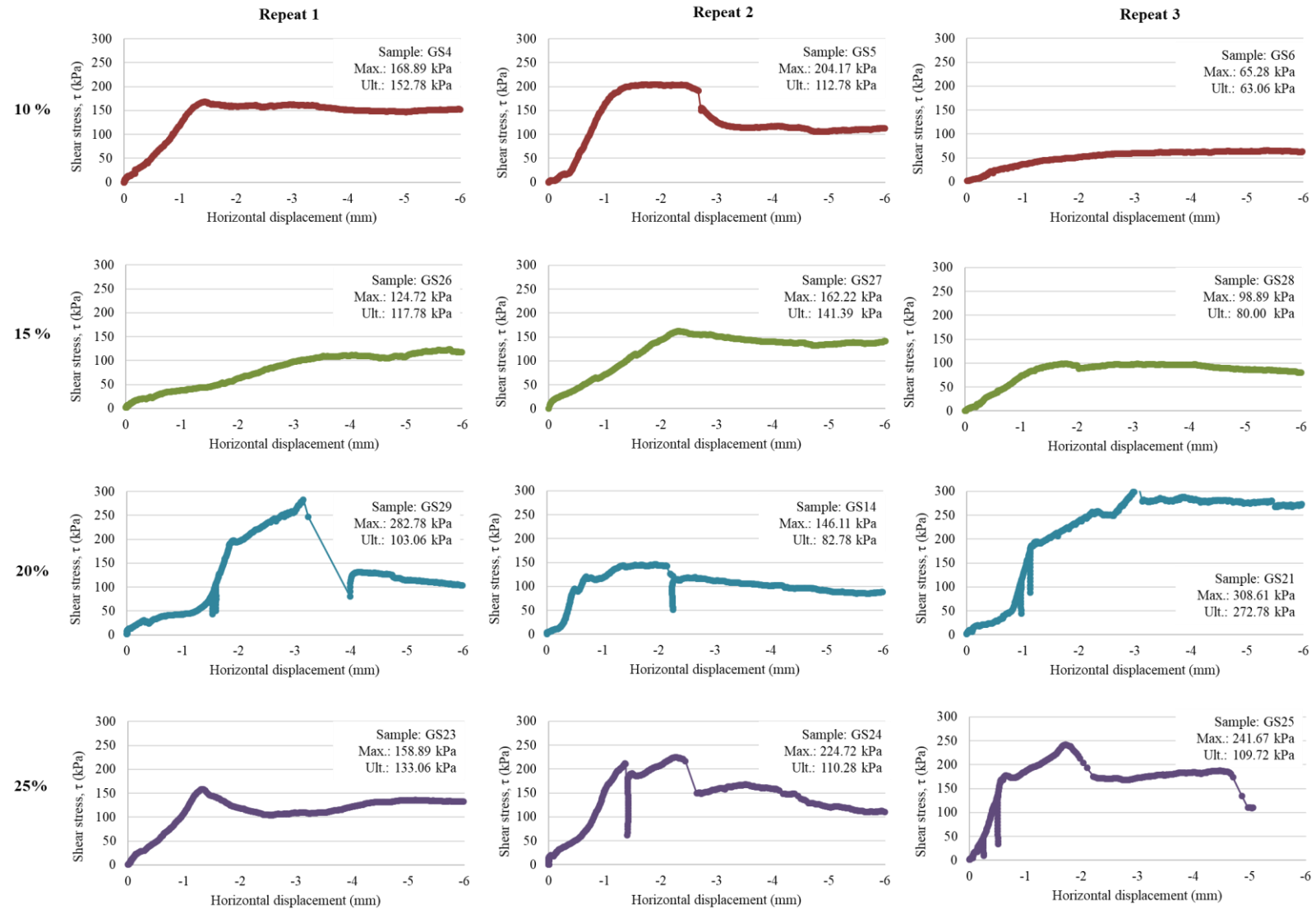


Figure 8.9: Shear stress vs horizontal displacement for gypsum cemented sandstones (10, 15, 20 and 25%) deformed at 95.38 kPa normal load.

Chapter 8 - Mechanical deformation

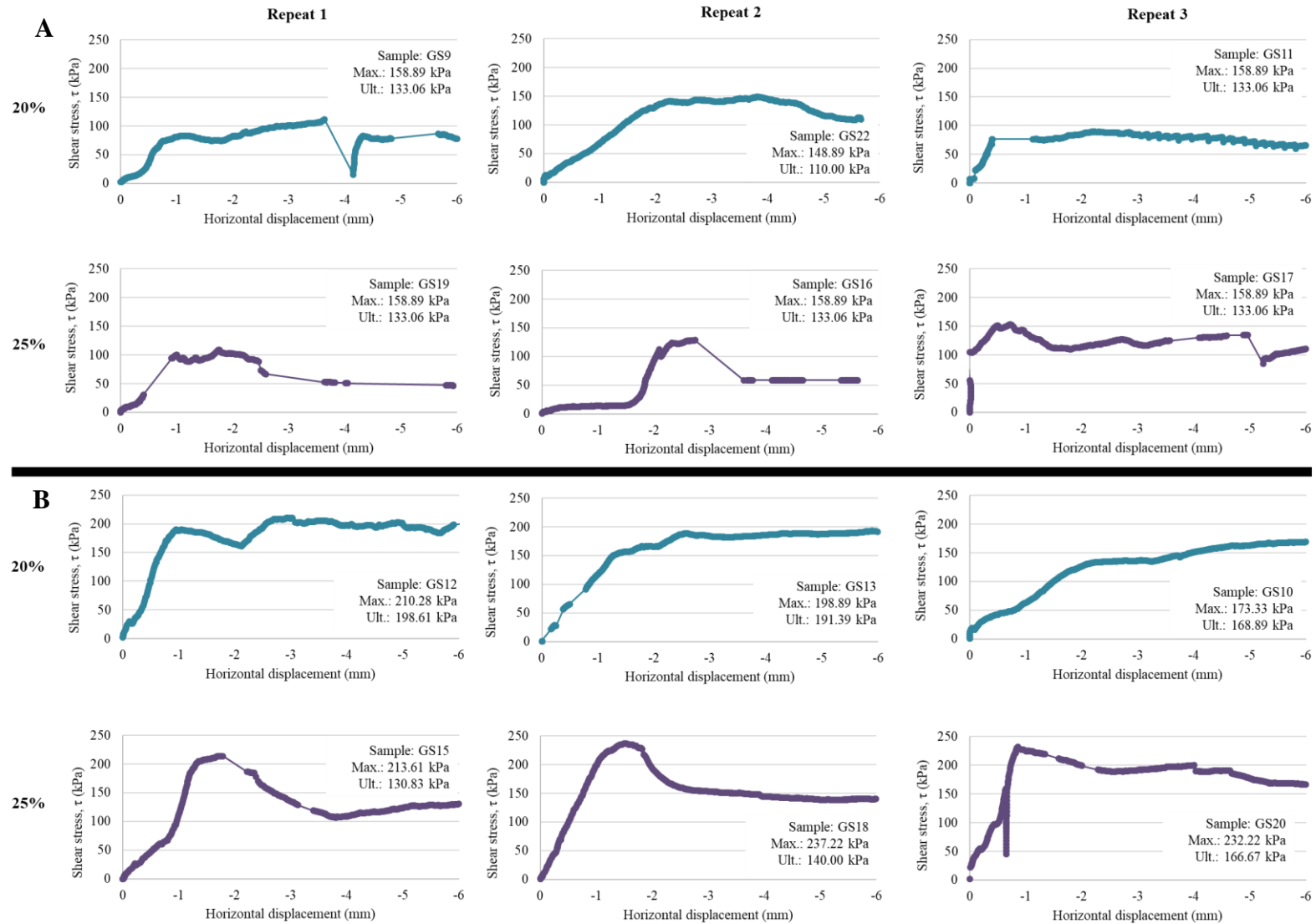


Figure 8.10: Shear stress vs horizontal displacement for gypsum cemented sandstones with 20% and 25% gypsum cement at A) 27.25 kPa and B) 163.50 kPa normal load.

Chapter 8 - Mechanical deformation

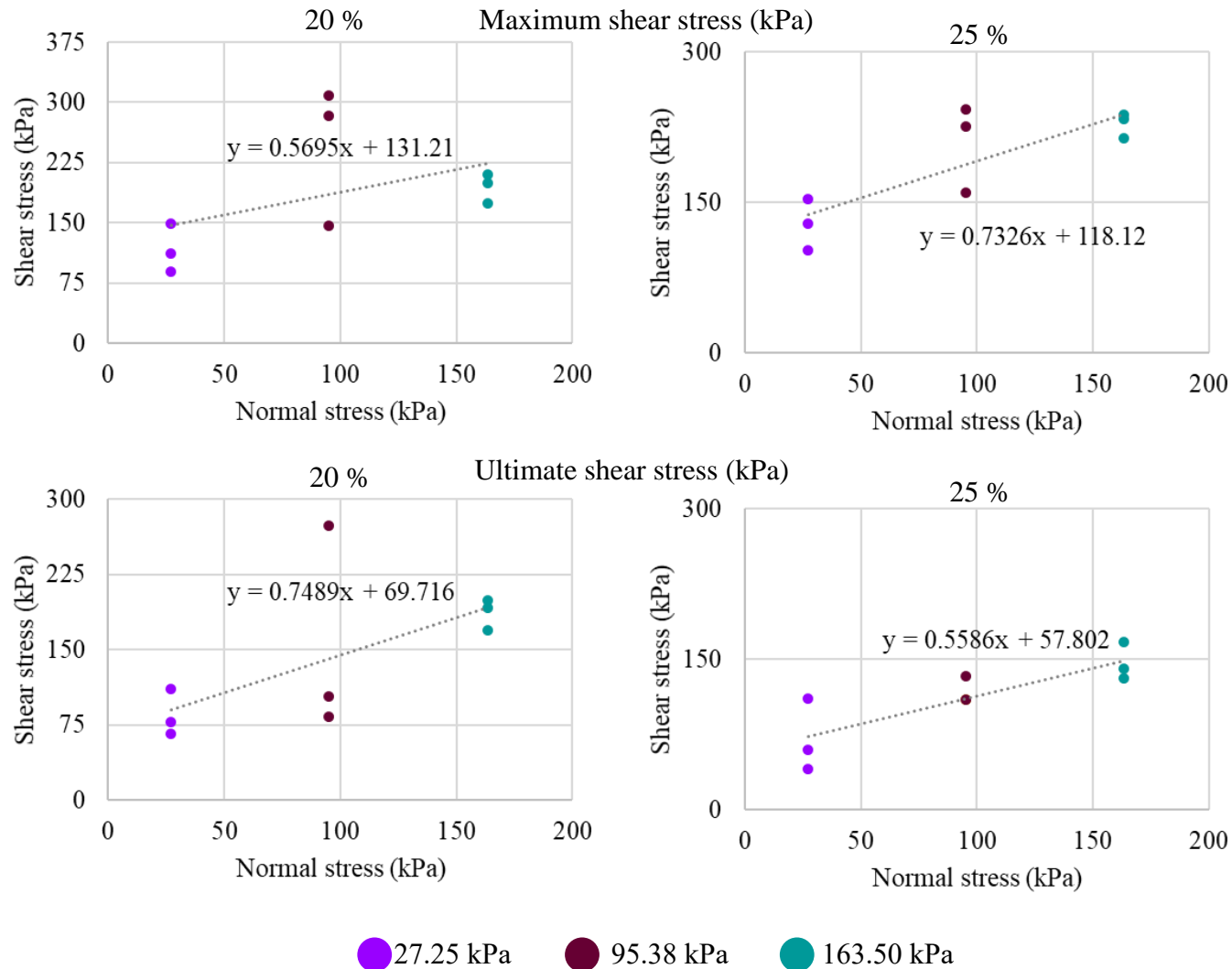


Figure 8.11: 20 and 25% gypsum cement sandstones maximum and ultimate shear stress plotted against the normal applied stress. Here the overall trend shows that shear stress increases as normal stress increases.

8.2.4.2.2 Gypsum shear test

In order to investigate the influence of the sand grains on the gypsum cemented samples a 100% gypsum cuboid sample (GypA) was shear tested.

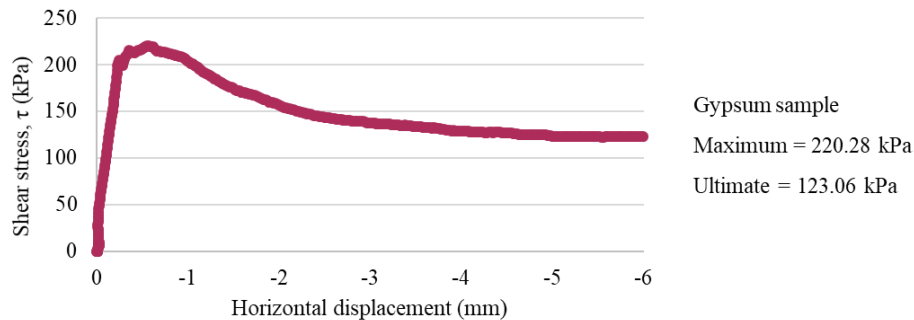


Figure 8.12: Shear stress vs horizontal displacement for 100% gypsum shear box sample (GypA).

The gypsum sample was prepared by packing 150g basanite powder into the cuboid mould (see Section 7.3) and then hydrating with 40 ml of deionised H₂O. The sample was placed in the oven at 40°C to cure for 28 days (as following the gypsum cemented sandstone procedure). No mass was placed on top of the sample due to its fluid nature when wet. It is unlikely that any residual basanite remains because at 40°C only gypsum is stable (Chapter 6).

After curing, the gypsum sample was sheared at 95.38 kPa normal stress. Figure 8.12 plots shear stress versus horizontal displacement for the sheared sample.

The untreated sands (sand without gypsum) have a maximum shear stress which ranges from 77.78-91.39 kPa and an ultimate shear stress which ranges from 63.89-64.44 kPa. The maximum shear stress of the gypsum cemented samples ranges from 65.28-308.61 kPa, and the ultimate shear stress ranges from 63.06-272.78 kPa. This indicates that the presence of gypsum cement increases the shear strength of the gypsum cemented sandstones.

The gypsum sample shows a maximum and ultimate shear stress of 220.28 kPa and 123.06 kPa respectively. These shear stress values are comparable to the synthetic gypsum cemented sandstones. Therefore, suggesting that the presence of the sand

grains has little effect on the shear stress, instead shear stress is controlled by the gypsum cement.

8.2.4.3 MICP cemented sandstones

8.2.4.3.1 MICP cemented sandstone shear tests

All sheared MICP cemented sandstones are listed in Table 8.4. As with the gypsum cemented sandstone the samples were sheared at 27.25, 95.38 and 163.50 kPa normal stress using masses of 1, 3.5 and 6 kg respectively. The majority of the samples were sheared at 95.38 kPa (Figure 8.13). The shear stress results for each of these samples shows that as the number of MICP feeds is increased, the maximum and ultimate shear stress increases (Figure 8.13).

The shear stress results for the MICP cemented sandstones at 27.25 kPa and 163.50 kPa are shown in Figure 8.14.

Table 8.4: Summary of all sheared MICP cemented sandstones and the normal load conditions at which they were sheared.

Sample group replica samples	MICP feed (ml)	Mass applied (kg)	Normal load (kPa)
L1	120	1	27.25
L2	120	1	27.25
L3	120	6	163.50
L4	120	6	163.50
L5	120	3.5	95.38
L6	120	3.5	95.38
L7	120	3.5	95.38
M1	160	6	163.50
M2	160	6	163.50
M3	160	1	27.25
M4	160	1	27.25
M5	160	3.5	95.38
M6	160	3.5	95.38
M7	160	3.5	95.38
H1	200	1	27.25
H2	200	1	27.25
H3	200	6	163.50
H4	200	6	163.50
H5	200	3.5	95.38
H6	200	3.5	95.38
H7	200	3.5	95.38

Chapter 8 - Mechanical deformation

At 95.38 kPa there was an overall increase in the maximum shear stress from 120 to 200ml MICP feed. However, the variation in shear stress is dependent on the individual samples.

The following section describes each of the shear stress graphs in turn for normal loads of 95.38, 27.25 and 163.50 kPa (Figures 8.13 and 8.14).

120 ml MICP cement

Sample L5 (Repeat 1) shows a non-brittle response. Where the maximum shear stress is almost equal to the ultimate shear stress.

Sample L6 (Repeat 2) most closely resembles a non-brittle response. However, a peak can be identified at approximately 2 mm displacement.

Sample L7 (Repeat 3) resembles a non-brittle shear stress curve. As with Sample L5 the maximum shear stress is almost equal to the ultimate shear stress.

160ml MICP cement

Sample M7 (Repeat 1) has a shear stress response closest to a brittle response. The overall shape is similar to Sample L6. However, in this case the peak displayed at 1.8 mm displacement is the maximum shear stress.

Sample M6 (Repeat 2) displays a brittle response. The maximum shear stress occurs at approximately 1.8 mm displacement.

Sample M5 (Repeat 3) displays a brittle response. The maximum shear stress occurs at approximately 1.5 mm displacement.

200ml MICP cement

Sample H5 (Repeat 1) shows a brittle response to shearing. With stick slip at 1.3 mm displacement and again at 2.8 mm displacement. During what should be the yielding phase the curve displays multiple stick slips. It is possible that the irregular composition of the calcite cement around the grains is causing resistance as shearing takes place therefore creating the observed stick slip.

Chapter 8 - Mechanical deformation

Sample H6 (Repeat 2) shows a brittle response to shearing. With stick slip at 1.5 mm displacement and again at 2.8 mm displacement.

Sample H7 (Repeat 3) shows a brittle response to shearing with an unstable yielding until 4.5 mm displacement.

Across all of these samples it is clear there is a plateau before shearing begins. It is possible that this plateau shape is an artefact of the shear box or is caused due to the irregular sample shape.

MICP samples at 27.25 kPa

120 ml

Sample L1 (repeat 1) shows a brittle response to shearing with a peak at 1.8mm displacement. There is a slight increase in shear strength during yielding.

Sample L2 (repeat 2) shows a brittle response to shearing however it displays an extended period of unstable yielding after the maximum shear stress at 2mm displacement.

160 ml

Sample M3 (repeat 1) shows a brittle response to shearing with maximum shear stress at 1.3 mm displacement.

Sample M4 (repeat 2) displays an overall brittle response to shearing. Two stick slips can be determined at approximately 2 mm and 3.1 mm displacement.

200 ml

Sample H1 (repeat 1) shows a brittle response to shearing and unstable yielding.

Sample H2 (repeat 2) shows an overall brittle response to shearing. However, the peak shear stress does not occur until 4.5 mm displacement. This is then followed by unstable yielding.

MICP samples at 163.50 kPa

120 ml

Sample L3 (repeat 1) shows a brittle response to shearing with two visible shear stress peaks at 1.3 and 2.3 mm displacement.

Sample L4 (repeat 2) shows a brittle response to shearing and maximum shear stress at 1.1 mm displacement.

160 ml

Sample M1 (repeat 1) does not clearly show either a brittle or non-brittle response to shearing. Sample M1 displays three peaks and a stable yielding after 4.2 mm displacement. Overall the shear strength increase as shearing continues.

Sample M2 (repeat 2) most closely resembles a non-brittle shear response. This suggests that at the given normal stress the calcite bonds have begun to break between the sand grains.

200 ml

Sample H3 (repeat 1) shows a brittle response to shearing with an overall stable yielding phase.

Sample H4 (repeat 2) shows an overall brittle response to shearing. However, the peak shear stress does not occur until 4.5 mm displacement.

Figure 8.15 plots the maximum and ultimate shear stress for each sample and allows for a better understanding of the spread of data and a comparison between the samples with increasing cement content (Table 8.5).

The shape of each of the graphs can be compared to the schematic curves outlined in Figure 8.2.

8.2.4.3.2 Visual deformation

Figure 8.16 displays photographs of MICP shear box samples before and after shearing at 95.38 kPa normal stress. As expected from the shear strength results the

Chapter 8 - Mechanical deformation

120 ml feed (3.48 wt% calcite) samples are the weakest of all three feeds. Here samples display evidence of crumbling at the edges and splitting in half down the middle, perpendicular to the direction of shear.

From the three 160 ml feed (4.79 wt% calcite) results on display here it is clear that although the bulk of the sample is stronger than the 120ml feed, the sample still displays evidence of crumbling at the edges and has the ability to crumble completely (sample M7).

The 200 ml feed (6.01 wt% calcite) results are in bulk stronger than the previous (120 and 160 ml) feed samples. However, as before the samples are still subject to crumbling at the edges and complete sample deformation. Sample H5 shows the beginnings of shear plane development. However, due to either the heterogeneous nature of the sample or possible preformed fractures inside the sample the shear plane dips as it progresses, to produce two uneven sides.

The deformation displayed by each sample cannot be generalised by the weight percentage of calcite present. Instead it is clear the heterogeneous nature (possibly due to the uneven distribution of cement and/or grain packing) of the synthetic sandstones controls the way in which the rocks will deform.

Table 8.5: Feed volume (ml) and corresponding average calcite content (wt%) per sample. Reproduced from Table 7.9.

Feed volume (ml)	Average calcite (wt%)
120	3.48
160	4.79
200	6.01

Chapter 8 - Mechanical deformation

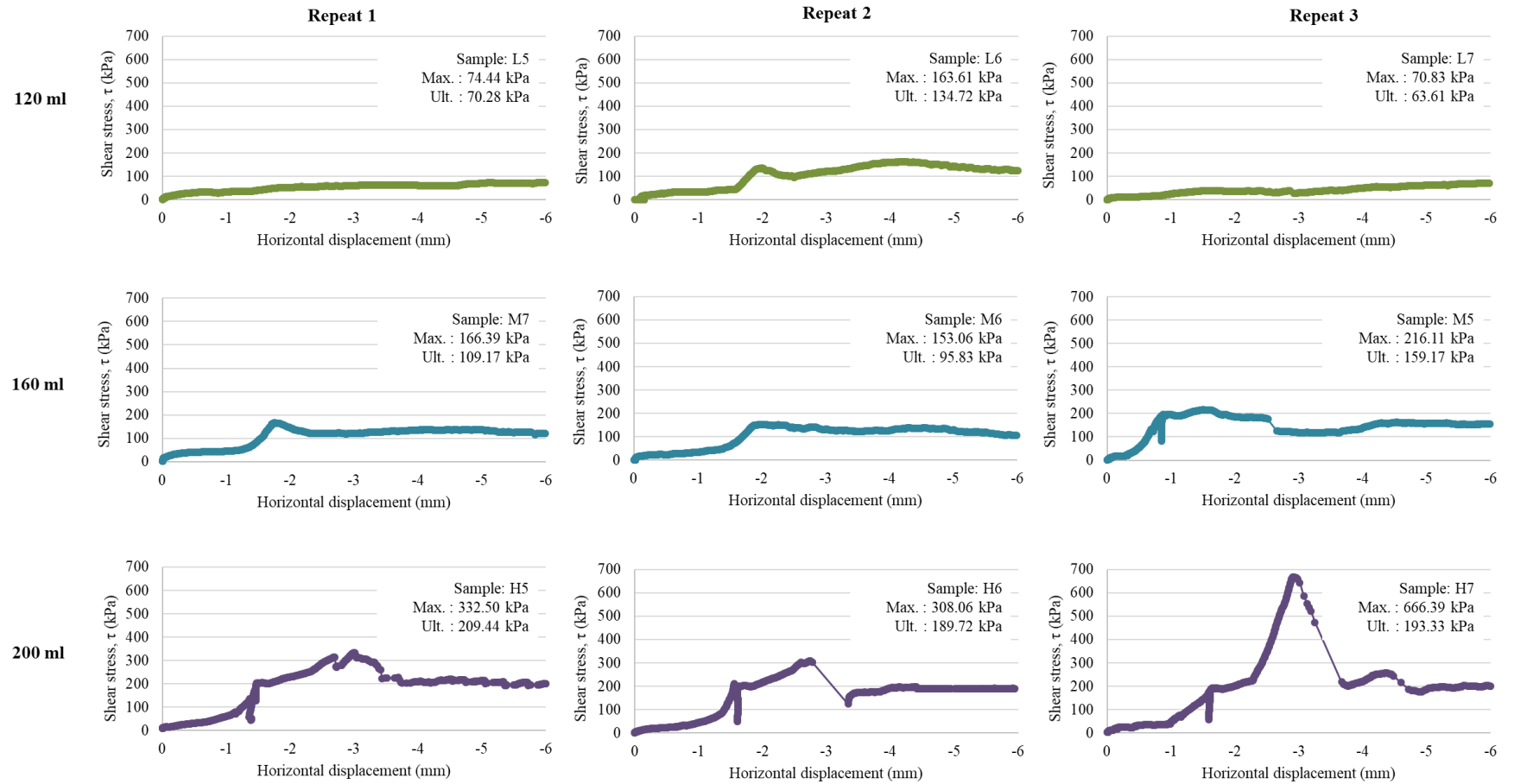


Figure 8.13: Shear stress vs horizontal displacement for MICP cemented sandstones shear results of all samples at normal stresses of 95.38 kPa.

Chapter 8 - Mechanical deformation

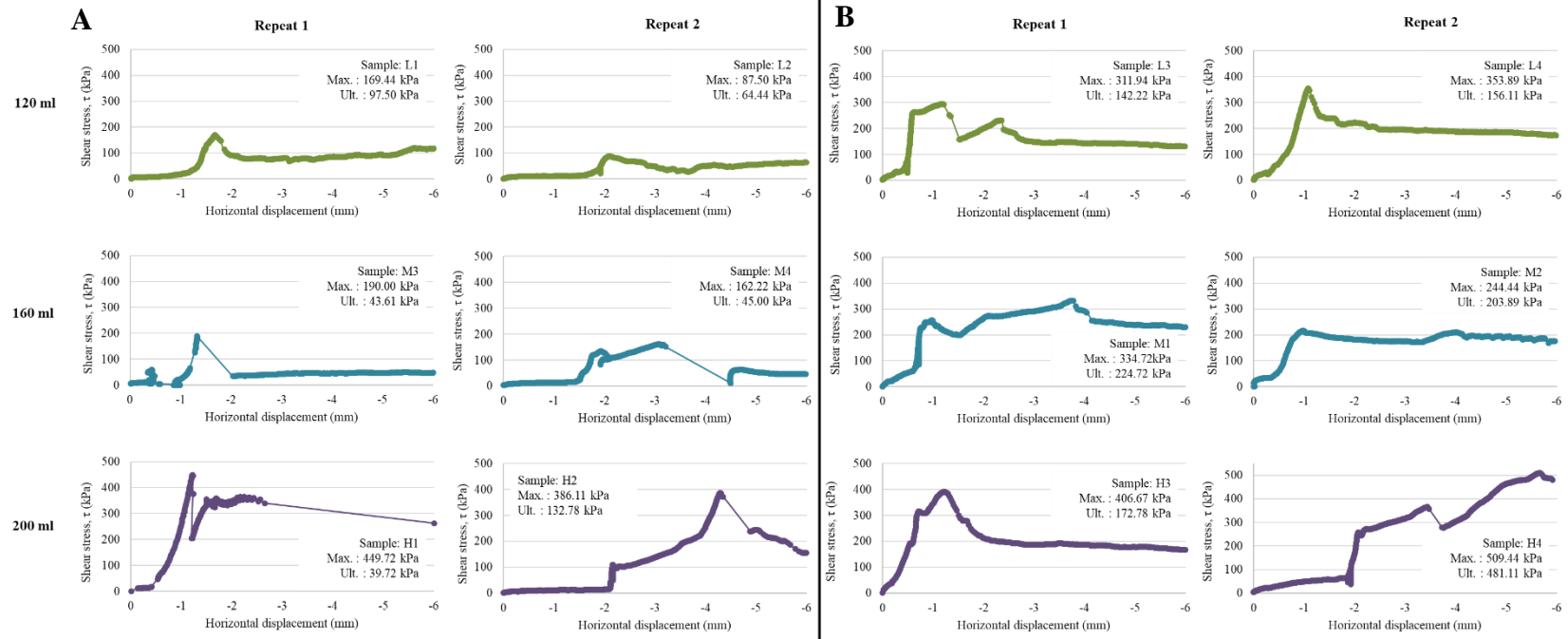


Figure 8.14: Shear stress vs horizontal displacement for MICP cemented sandstones shear results of all samples at normal stresses of A) 27.25 kPa and B) 163.50 kPa.

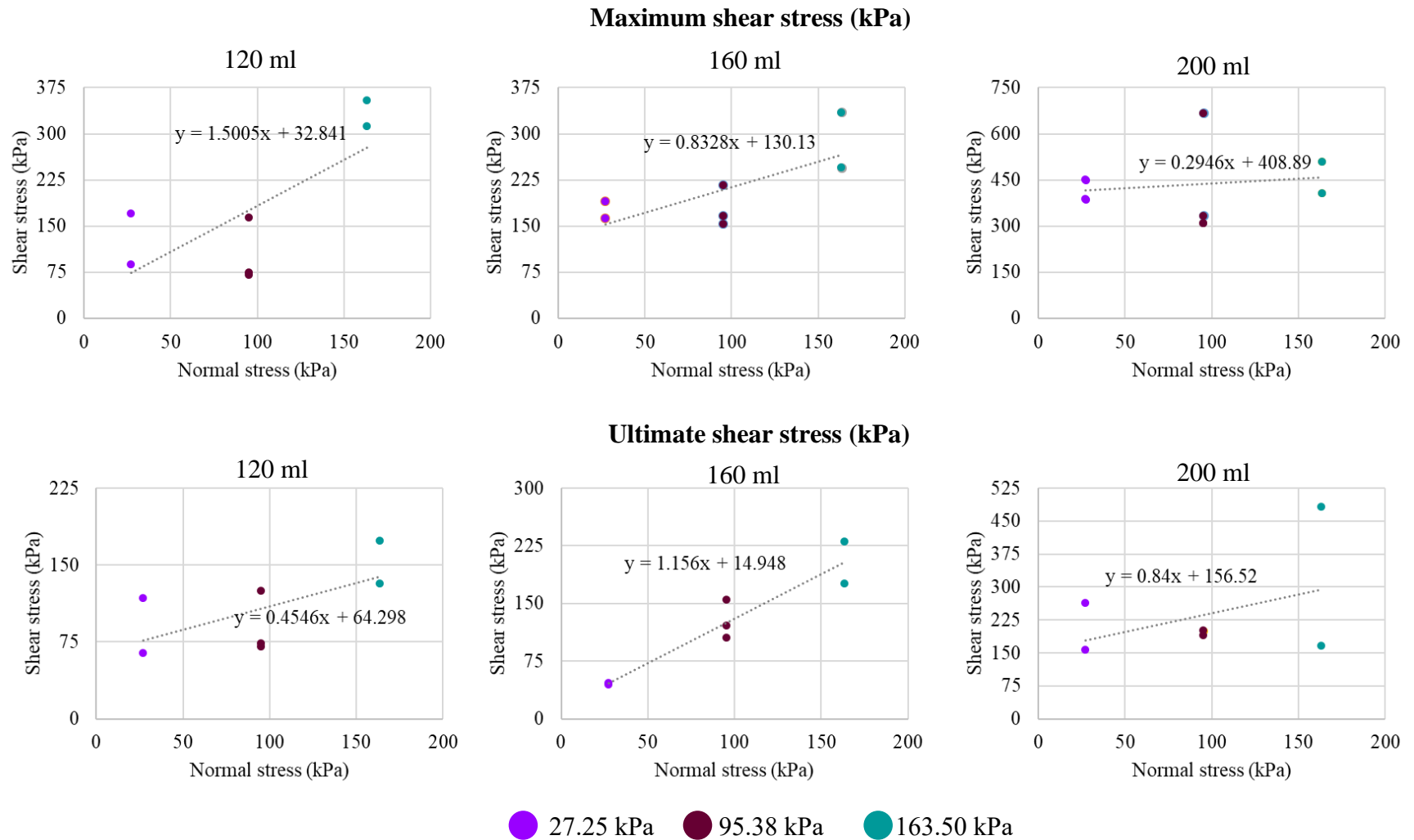


Figure 8.15: Maximum and ultimate shear stress of MICP shear samples (120, 160 and 200 ml) at normal stresses of 27.25, 95.38 and 163.50 kPa. With increasing cement both maximum shear stress and ultimate shear stress increase.

Chapter 8 - Mechanical deformation

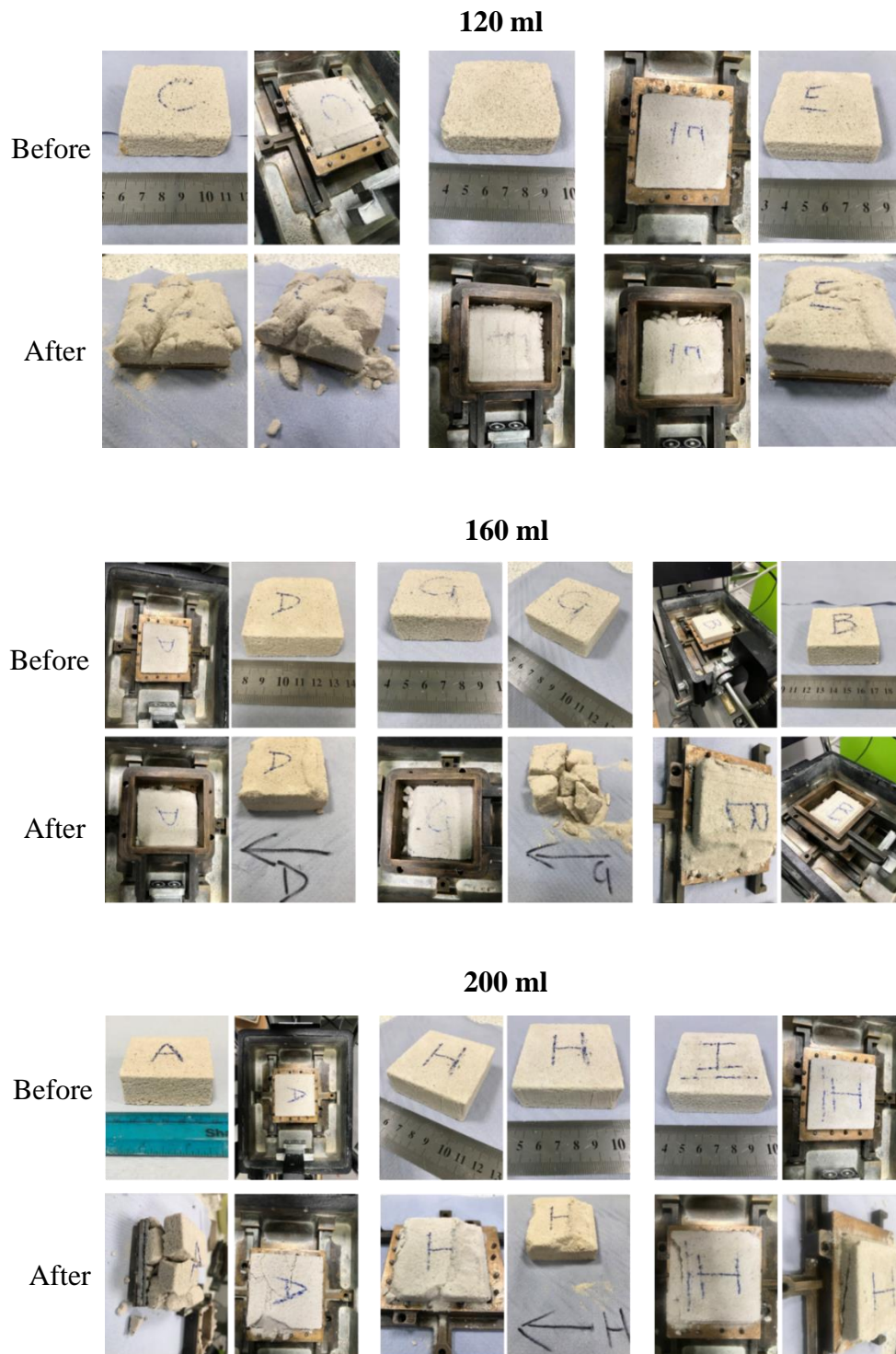


Figure 8.16: Images of MICP 120ml, 160ml and 200 ml feed samples before and after deformation.

8.2.4.3.3 Grain analysis

Thin sections were taken of the MICP cemented samples after deformation by shear box testing to determine the impact of the test at the grain scale.

The 120 ml feed (Figure 8.17) displays evidence of fracture in the calcite balls which cement the grains together. However, there are no fractures visible in the sand grains. Because the deformation is in the cement its most likely that the deformation took place after shearing.

Meanwhile, the 160 ml (Figure 8.18) and 200 ml (Figure 8.19) display evidence of grain spalling and fracture in the sand grains. However, there is no evidence of fracture in the calcite cement from the thin section images. Furthermore, the timing of the deformed grains cannot be accurately placed.

One possible reason for the fractured calcite balls is that the 120 ml samples display a lower weight percentage of calcite cement than 160 and 200ml samples. This analysis confirms that the strength of the rock increases as the weight percentage of calcite cement increases.

Chapter 8 - Mechanical deformation

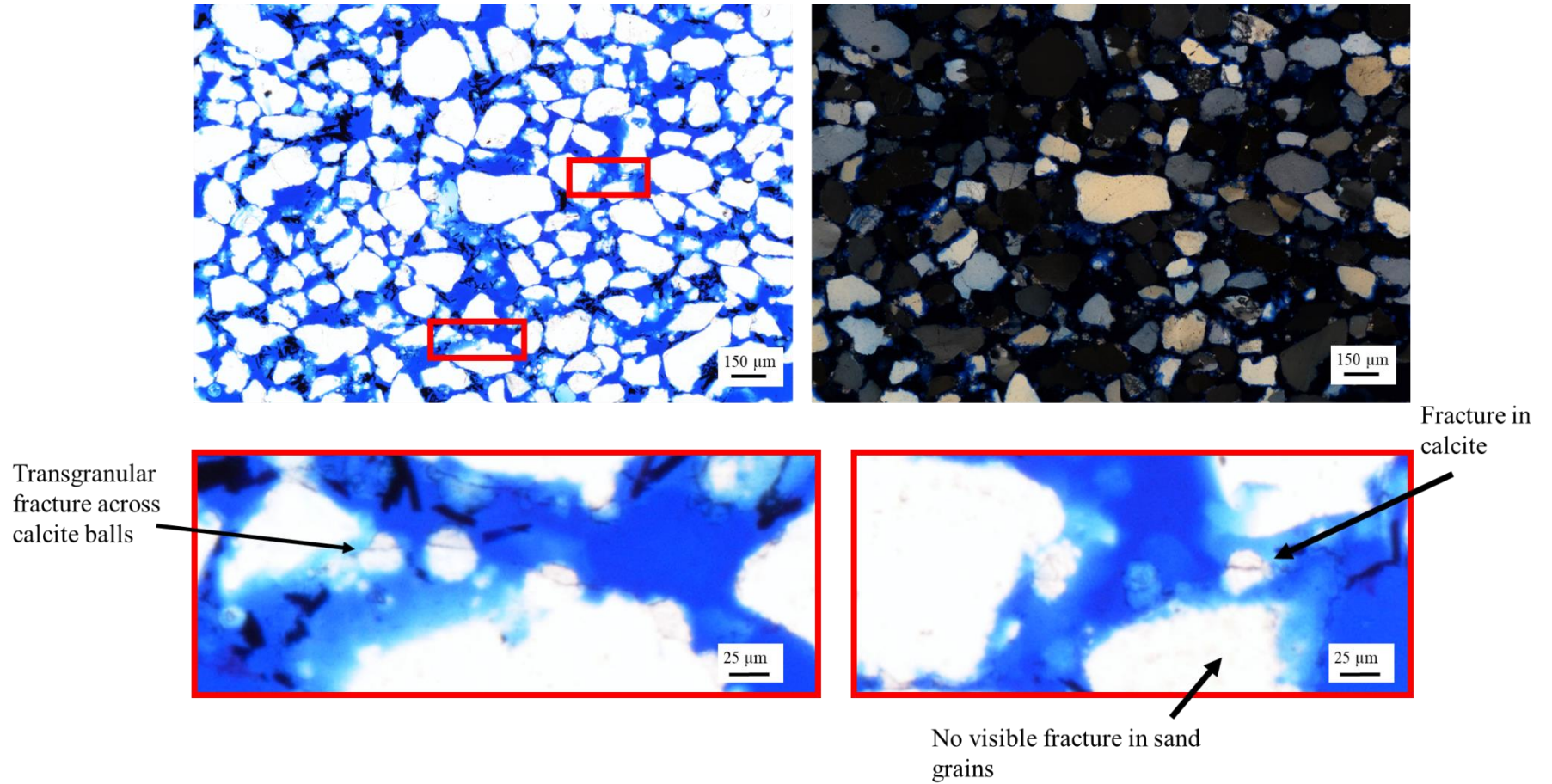


Figure 8.17: Thin section evidence from MICP 120 ml sample of fractured calcite cement after shearing. Shearing took place at 95.38 kPa. Here fractures across the calcite cement balls can be seen. However, there is no visible evidence of fracture in the sand grains.

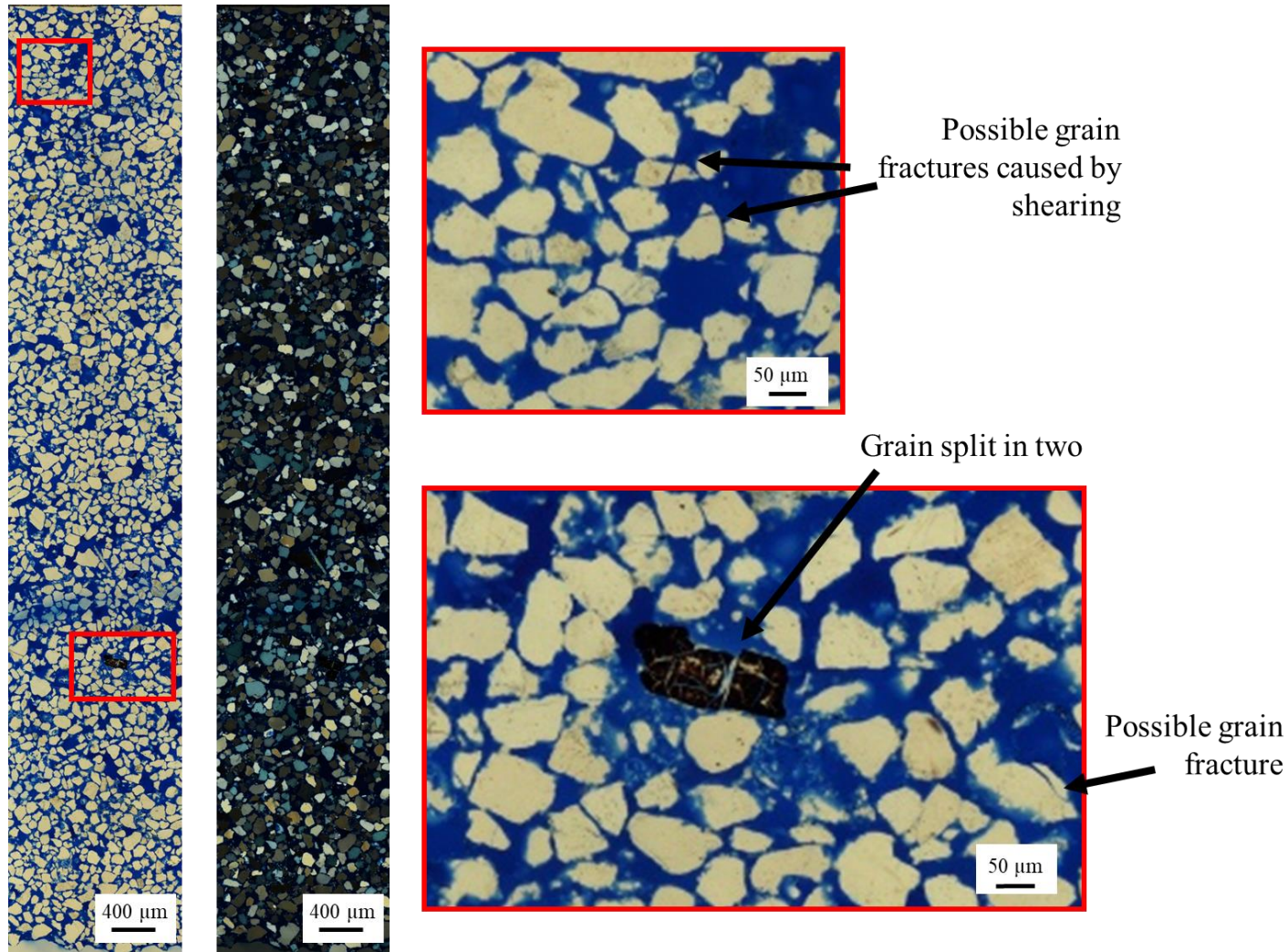
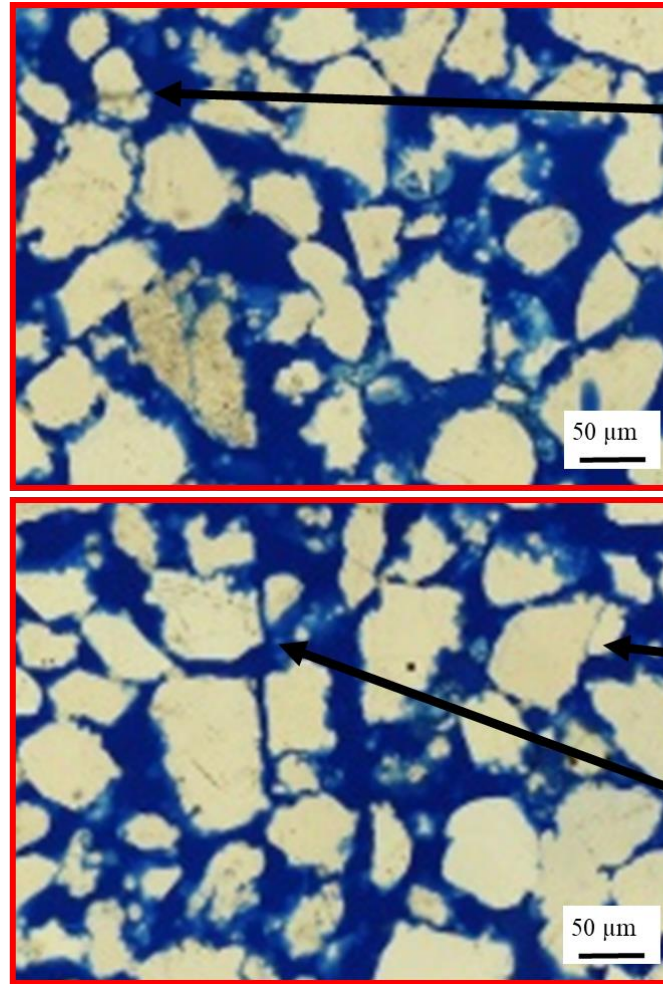
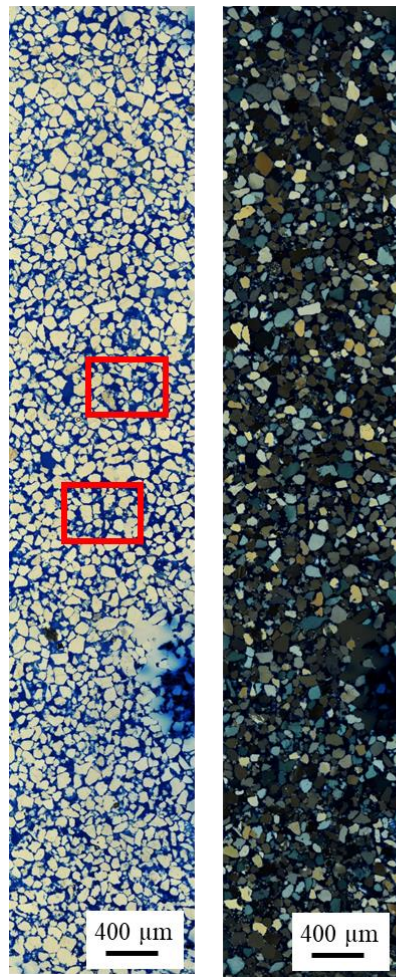


Figure 8.18: Thin section evidence of fractured grains after shearing the 160 ml feed MICP synthetic sandstone. Shearing took place at 95.38 kPa. Here some fractures in the sand grains can be seen. However, there is no evidence of the calcite cement fracturing. As a result, it is difficult to determine if the grain fracturing took place before or after shearing.



Grain fracture

Possible grain fracture caused by shearing

Unusually straight grain fracture pattern across two grains

Figure 8.19: Thin section evidence of fractured grains after shearing the 200 ml MICP synthetic sandstone. Shearing took place at 95.38 kPa. Here some fractures in the sand grains can be seen. However, there is no evidence of the calcite cement fracturing. As a result, it is difficult to determine if the grain fracturing took place before or after shearing. Of particular interest here are the two grain fractures which appear almost aligned with each other.

8.2.3.3.4 Comparison to other MICP shear box studies

The maximum and ultimate shear stress results from previous MICP shear box studies (Table 8.2) are compared to the MICP cemented synthetic sandstone sample results from this thesis in Figure 8.20 and 8.21.

By comparing these graphs and Tables 8.2 and 8.5 it is clear that the range of maximum and ultimate shear stresses is larger in this study than in previous literature. This suggests the method used in Chapter 7 to produce the 200ml feed samples produces stronger MICP cemented sandstone samples than in previous studies. The higher strength is possibly due to the large percentage of calcite present in each of the samples. From Chapter 7 the average weight percentage of calcite present in samples ranged from 3.48-6.01%. Of all the studies described below only Canakci et al. (2015) and Feng and Montoya (2015) list the percentage of calcite present in their synthetic sandstone samples.

Results from Chou et al. (2011) and Canakci et al. (2015) show little variability. Canakci et al. (2015) have synthetic sandstone samples with 15-19% calcite present, this is approximately three times higher than the range of calcite cement present in this study. Khaleghi and Rowshanzamir (2019)'s results show a general increase in shear stress as normal stress is increased. Meanwhile, Golmohamadi et al. (2016) shows the largest number of shear box measurements. The maximum shear stress results from this thesis fit best with the results from Khaleghi and Rowshanzamir (2019) and Golmohamadi et al. (2016). The 200 ml feed samples are the exception to this. The 200 ml samples maximum and ultimate shear stress is generally x2 times greater than the shear stress of the previous studies and the 120 and 160ml feed. The only exception to this is the result produced by Feng and Montoya (2015). Feng and Montoya (2015)'s sample had approximately 4.3% cement and at a normal stress of 100 kPa produced a maximum stress of 800 kPa. The maximum shear stress is approximately four times larger than the majority of the results. However, this result is based on only one sample. As seen from the MICP shear box results in this chapter the shear stress can vary considerably due to heterogeneities in the synthetic sandstones.

Chapter 8 - Mechanical deformation

The main thing which all these studies lack is repeat tests. In order to better constrain the maximum and ultimate shear stress of MICP cemented sandstones more samples are required. Furthermore, due to the large number of variables in MICP cementation each sample must be better characterised before deformation to allow for accurate comparison to be made between the samples.

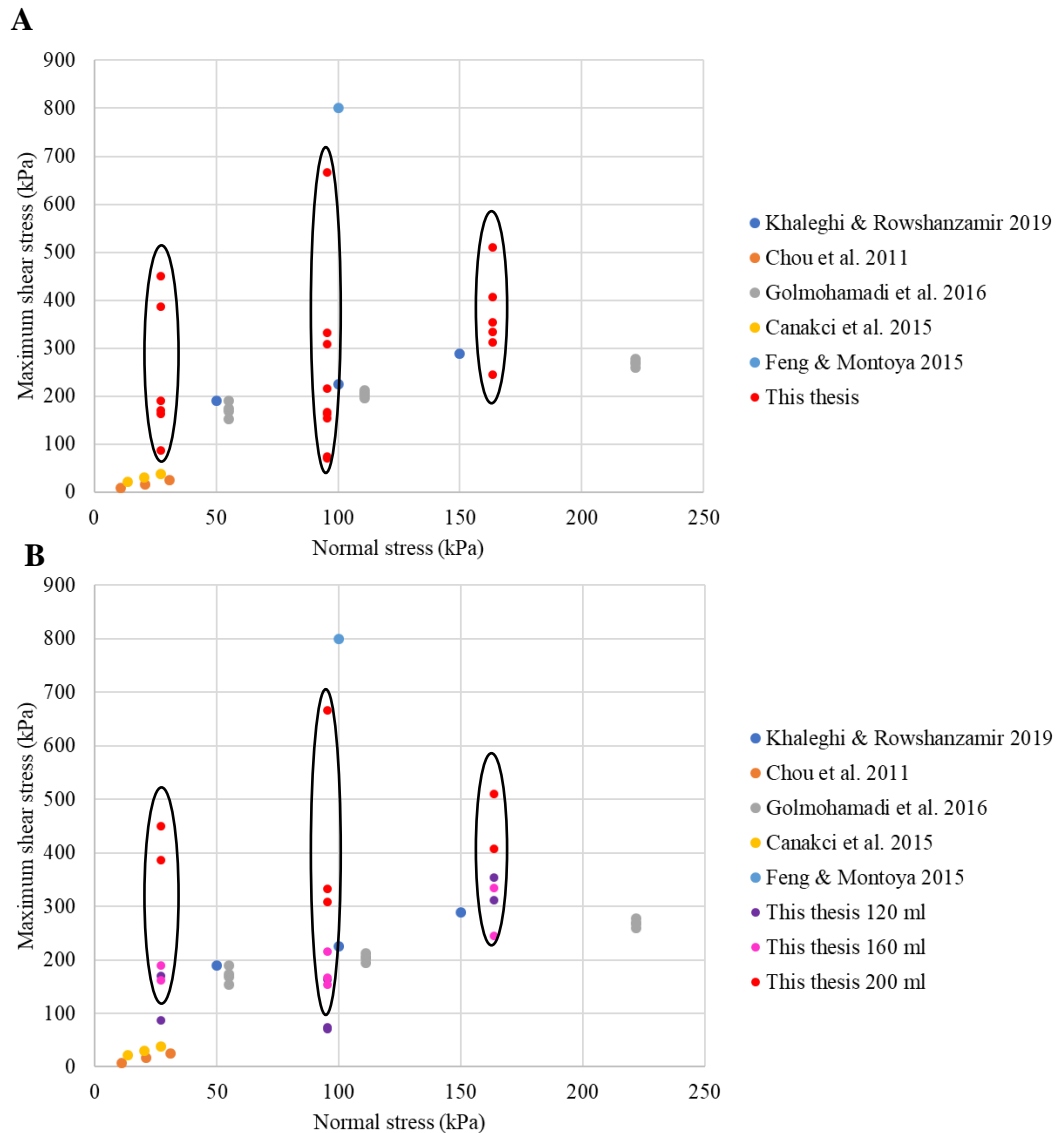


Figure 8.20: Comparison of maximum shear strength results vs normal stress of the MICP cemented sandstone results in this study and those listed in Table 8.2. A) Compares the combined results from this thesis. B) Separates the results from this thesis into the MICP feed volumes.

Chapter 8 - Mechanical deformation

This would allow for clearer investigations on how the impact of increasing the weight percentage of calcite cement present affects the shear stress of each sample.

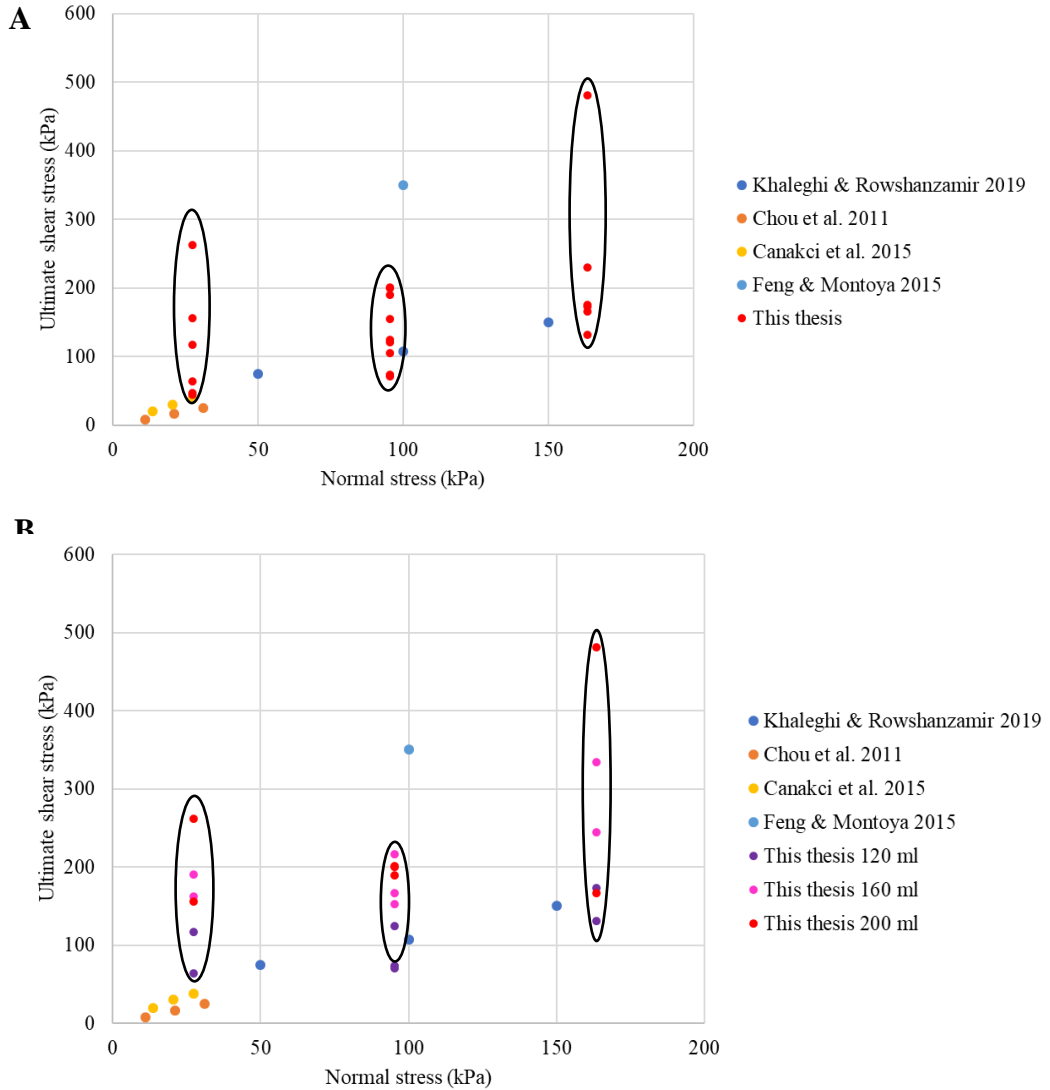


Figure 8.21: Comparison of the ultimate shear stress vs normal stress of the MICP cemented sandstone results in this study and those listed in Table 8.2. A) Compares the combined results from this thesis. B) Separates the results from this thesis into the feed volumes. Golmohamadi et al. (2016) do not display ultimate shear stress data.

Table 8.6: Range of average maximum shear stress for each applied normal stress during all of the MICP samples tested in this chapter.

Normal stress (kPa)	Range of average maximum shear stresss (kPa)
27.25	128.47 - 417.92
95.38	102.96 - 435.65
163.50	289.58 - 458.06

8.2.5 Shear box summary

- Table 8.7 summarises the average maximum and ultimate shear stress across each sample category. Both gypsum and MICP cemented sandstones have higher maximum and ultimate shear stress than unconsolidated sand. This therefore shows that adding synthetic cement does improve the shear strength of unconsolidated sand.
- Both the maximum and ultimate shear stress increases as the weight percentage of calcite cement increases. Overall the maximum and ultimate shear stress is largest in the 200 ml MICP cemented sandstones (Figure 8.15).
- For the gypsum cemented sands an overall increase in maximum and ultimate shear stress can be identified at 95.38 kPa (Table 8.7). However, the trend is not as clear in the gypsum cemented samples in comparison to the MICP cemented samples, and it varies depending on individual samples.
- The 100% gypsum cuboid has a maximum and ultimate shear stress comparable to gypsum cemented synthetic sandstones. This suggests that the shear strength of the gypsum cemented sandstones is primarily controlled by the gypsum cement.

Chapter 8 - Mechanical deformation

Table 8.7: Average maximum and ultimate shear stress per sample group.

Material	Sample(s)	Cement	Normal stress (kPa)	Maximum stress (kPa)	Ultimate stress (kPa)	
Unconsolidated sand	Sand 1, 2, 3	N/A	95.38	83.98	64.26	
Gypsum	GypA	% 100	95.38	220.28	123.06	
Gypsum cemented sand	GS 4, 5 6 GS 26, 27, 28 GS 29, 14, 21 GS 23, 24, 25	% 10	95.38	146.11	109.54	
		15	95.38	128.61	113.06	
		20	95.38	245.83	152.87	
		25	95.38	208.43	117.69	
	GS 9, 22, 11 GS 19, 16, 17	20	27.25	116.57	84.26	
		25	27.25	127.87	69.72	
	GS 12, 13, 10 GS 15, 18, 20	20	163.50	194.17	186.30	
		25	163.50	227.69	145.83	
	MICP cemented sandstones	L 5, 6, 7 M 7, 6, 5 H 5, 6, 7	ml 120	95.38	102.96	89.35
			160	95.38	178.52	126.76
200			95.38	435.65	196.94	
L1 & L2 M3 & M4 H1 & H2		120	27.25	128.47	90.42	
		160	27.25	176.11	45.28	
		200	27.25	417.92	209.17	
L3 & L4 M1 & M2 H3 & H4		120	163.50	332.92	152.36	
		160	163.50	289.58	202.78	
		200	163.50	458.06	323.61	

8.3 Uniaxial compression strength tests

Uniaxial compression strength (UCS) is one of the most commonly used methods in geotechnics to test the strength of rocks (Kuhinek 2011). UCS tests are used to explore the response of each synthetic sample to loading and to calculate its compressive strength. UCS testing was carried out at the University of Strathclyde's Geotechnics Laboratory (Figure 8.22).

The sample was loaded into the UCS rig and end platens were placed at the top and base of the sample to disperse the load equally on the sample. During testing the load is gradually increased over time and the results are recorded until sample failure occurs. To calculate the UCS the load was divided by the surface area of the sample.

Each sample was tested at room temperature using the UCS test in accordance with ASTM Standard D7012 – 14e1 (2017), with a confining pressure of $\sigma_3=0$ and a constant axial strain rate of 1mm/min.

The top three sources of errors/uncertainties with UCS testing are sample heterogeneity, the pressure applied and the measurements of sample diameter ($\sim \pm 0.025$ mm). The error created due to sample heterogeneity is unable to be measured. For the purposes of this chapter the standard error has been used to analyse the total errors present.

Figure 8.23 compares a typical brittle and ductile uniaxial response. As a rock is uniaxially deformed the process undergone by the rock can be summarised in four stages: (i) pore closure, (ii) elastic deformation, (iii) crack growth, and (iv) post



Figure 8.22: Uniaxial compression testing rig at the university of Strathclyde's Geotechnics Laboratory

failure softening. These stages are further outlined in Saxena et al. (2018). Also, of interest is the analysis of the pore deformation as axial strain and stress increases (Figure 8.23B).

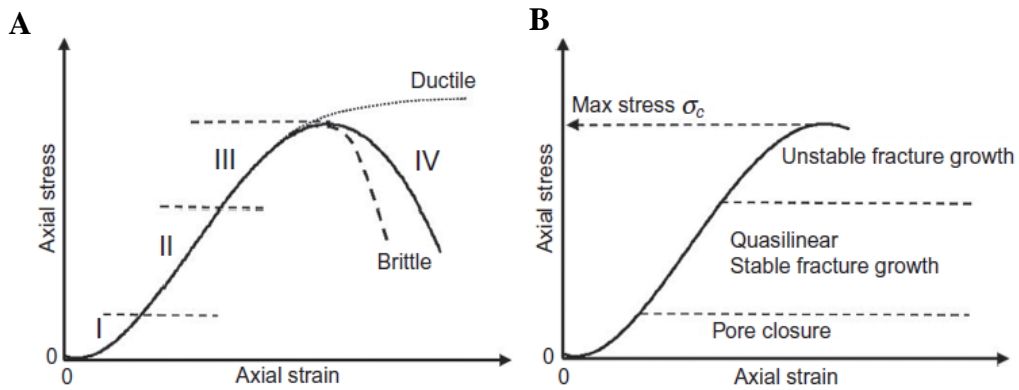


Figure 8.23: A typical uniaxial compression strength (UCS) test deformation curve from Saxena et al. (2018). A) Stress-strain profile (I) pore closure, (II) stable fracture growth, (III) unstable fracture growth, (IV) post failure. B) Illustrates the pore deformation as axial strain is increased.

There are many different modes of sample failure that can occur as a result of uniaxial compression conditions. Some of these modes of failure are sketched in Figure 8.24. These modes of failure will be used later to describe the deformation observed in the uniaxial tests.

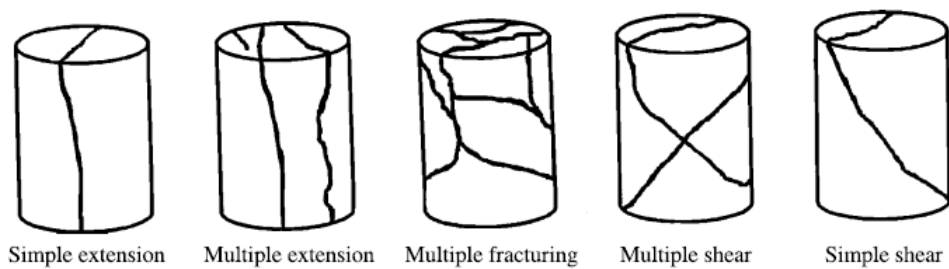


Figure 8.24: Uniaxial compression testing modes of sample failure from Szwedzicki (2007).

A list of typical intact rock compressive strengths is given in Table 8.8. This table is used to characterise the compressive strength of each sample later in this chapter (Section 8.3.1.4).

Table 8.8: Typical range of unconfined compressive strength of intact rocks. Edited from Zhang (2017).

General Description	Rocks	Unconfined Compressive Strength, σ_c^a (MPa)
Carbonate rocks with well-developed crystal cleavage	Dolostone	33-310
	Limestone	24-290
Lithified argillaceous rock	Argillite	29-145
	Claystone	1 - 8
	Siltstone	10-117
	Shale	7-35
	Slate	145-207
Arenaceous rocks with strong crystals and poor cleavage	Conglomerate	33-221
	Sandstone	67-172
^a Range of unconfined compressive strength reported by various investigators.		

8.3.1 Gypsum cemented sandstone results

Eight gypsum cemented sandstone samples (two of each 10, 15, 20 and 25% cement content/volume) were tested to compare the impact of cement volume on the compressive strength of the synthetic samples. Chapter 7 describes how the samples were made.

8.3.1.1 Mechanical analysis

Figure 8.25 shows the responses for each of the UCS tested gypsum cemented sandstone samples. The UCS values for the gypsum cemented samples ranged from 139.20 to 2340.67 kPa.

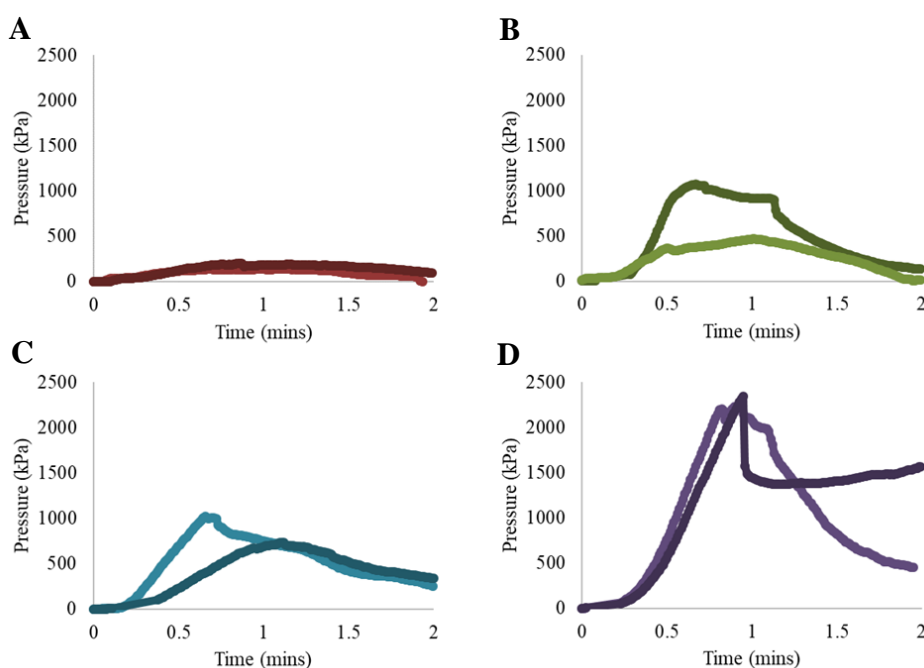


Figure 8.25: UCS graphs for gypsum cemented synthetic sandstones A) 10%, B) 15%, C) 20% and D) 25%.

Figure 8.26 plots the gypsum content against the maximum UCS and sample porosity. Figure 8.26A shows that as the percentage of gypsum present in a sample increases, the UCS increases. Samples with 25% wt gypsum are the strongest samples and display compressive strengths greater than 1300 kPa. Standard error is greatest for the 15% gypsum cement sandstones. Figure 8.26B plots the calculated sample porosity against the gypsum content. Here the porosity standard error is

greatest for the 10% gypsum cement sandstones and generally decreases as the percentage of cement increases.

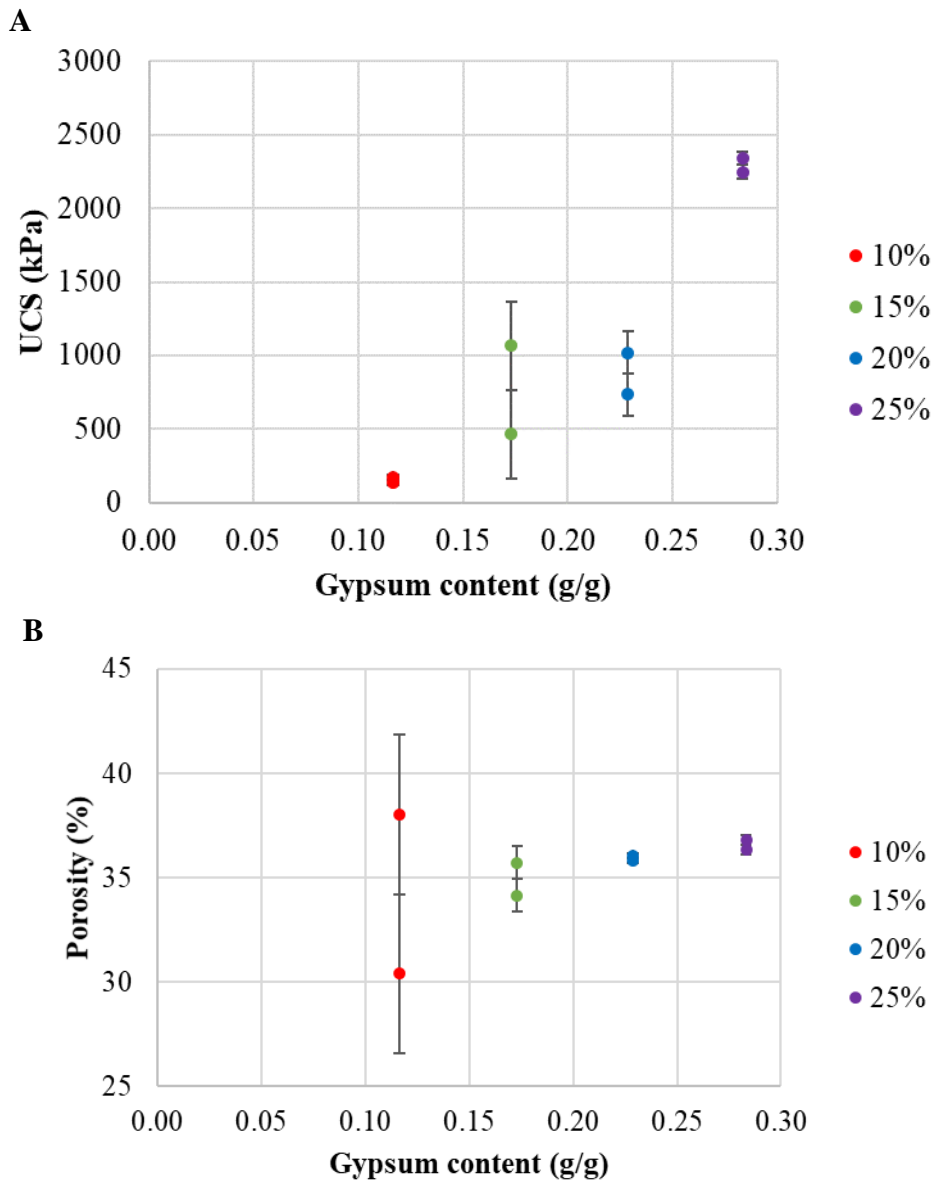


Figure 8.26: UCS and porosity vs gypsum content for each of the gypsum cemented sandstone samples. A) Gypsum content versus the maximum pressure for each gypsum cemented synthetic sandstone during UCS with standard error bars. B) The porosity of each sample plotted against the gypsum content with standard error bars.

8.3.1.2 Grain analysis

Thin sections were taken of the gypsum cemented samples after deformation by UCS testing to determine the impact of the test at the grain scale. In Figure 8.27 there is evidence of transgranular fracture in the quartz grains of 10% and 25% cement samples. As with the transgranular fracture observed in the shear box results the timing of the fracturing is unclear. It is most likely that the fracturing of the quartz grains occurred due to UCS. However, it is also possible that the grains fractured during packing of the sands, whilst the synthetic sandstones were being made. One potential method of determining timing of grain fracture is the location of the gypsum cement. If there is gypsum cement between the fractured grain pieces, it is likely that grain fracture has taken place prior to cementation. From visual inspection of the gypsum cement (Figure 8.27) it is difficult to determine if there is any gypsum which has formed between the fractured grains.

From thin section it is difficult to determine the impact of the UCS testing on the cement because thin section is a 2D insight which only takes into consideration a small sub-sample size. One possible improvement would be to X-CT scan the sample prior to and after deformation to allow the deformation of the grains to be analysed in 3D.

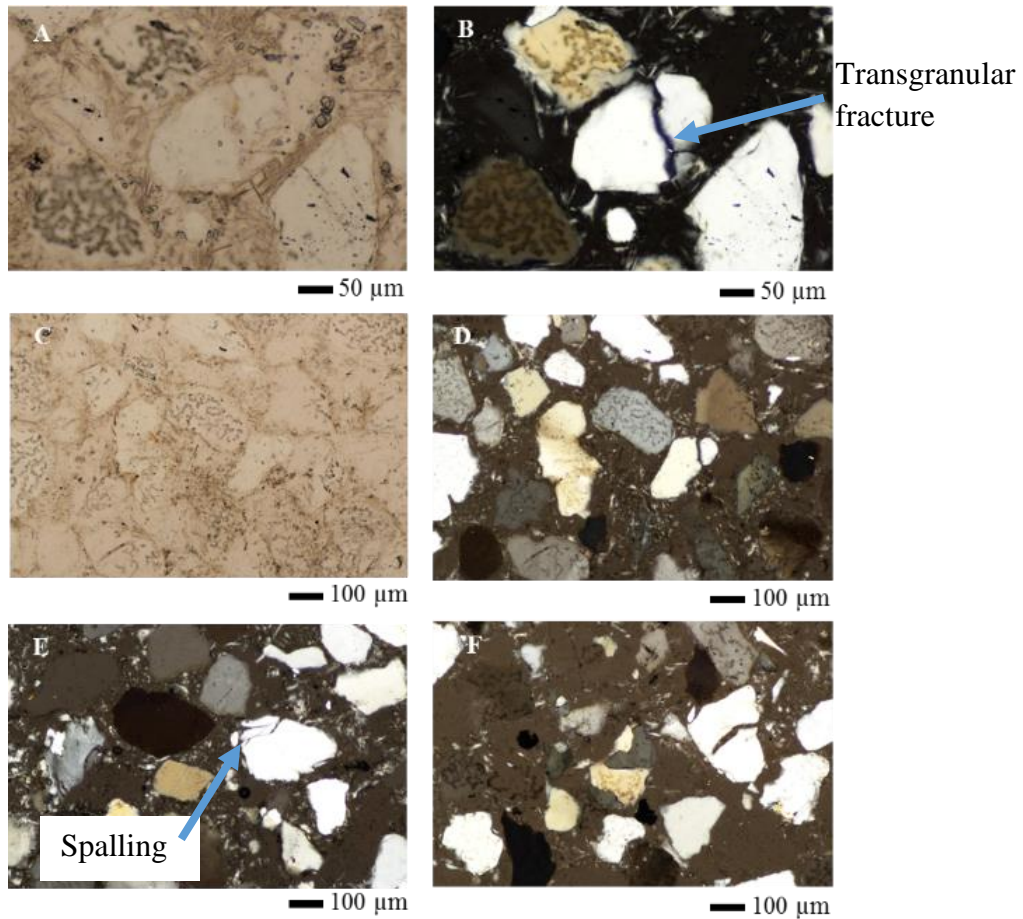


Figure 8.27: Thin section evidence of transgranular fracture and grain spalling of gypsum cemented sandstones during uniaxial compaction testing. A) PPL image of 10% gypsum cemented sandstone. B) XPL image of 10% gypsum cemented sandstone with transgranular fracture. C) PPL image of 25% gypsum cemented sandstone. D) XPL image of 25% gypsum cemented sandstone with evidence of transgranular fracture. E) XPL image of 20% gypsum cemented sandstone with evidence of grain spalling. F) XPL image of 25% gypsum cemented sandstone with evidence of transgranular fracture.

8.3.1.3 Gypsum UCS test

In order to investigate the influence of the sand grains on the gypsum cemented samples a 100% gypsum cylinder sample was UCS tested (Figure 8.28).

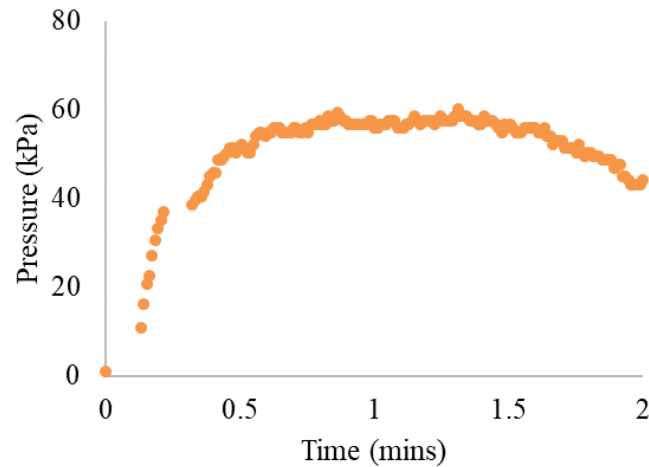


Figure 8.28: UCS test result for 100% gypsum cylinder sample.

The maximum UCS of the 100% gypsum sample is 60.34 kPa (Table 8.9). This is considerably lower than the gypsum cemented sandstones (Figure 8.25). As a result, this suggests that the compressive strength of the gypsum cemented sandstones is primarily controlled by the sand grains present in each sample.

Table 8.9: Summary of each gypsum cemented sandstone sample deformed by UCS. All samples were deformed at a strain rate of 1mm/min.

	Sample group replica samples	Bassanite (%)	Maximum UCS test result (kPa)	Average UCS for each Gypsum sample group (kPa)
1	G10A	10	139.20	157.22
2	G10B	10	175.24	
3	G15A	15	1068.64	768.075
4	G15B	15	467.51	
5	G20A	20	1019.98	877.76
6	G20B	20	735.54	
7	G25A	25	2247.54	2294.11
8	G25B	25	2340.67	
10	GYPA	100	60.34	N/A

8.3.1.4 Comparison of UCS to other rocks

The average UCS results from the gypsum cemented sandstones (Table 8.9) are 0.2-3.4% of the sandstone UCS values (Table 8.8). The UCS of the 25% gypsum cemented samples are most comparable to claystone. The UCS of gypsum cemented sandstones is not comparable to sandstones. This is because the gypsum cemented sandstones created in this thesis are poorly consolidated.

8.3.2 MICP cemented sandstone results

8.3.2.1 Mechanical analysis

Figure 8.29 shows the responses for each of the UCS tested MICP cemented sandstone samples. The UCS values for the MICP cemented samples ranged from 444.56 to 2407.72 kPa (Table 8.10). The average UCS increases as the weight percentage of calcite increases.

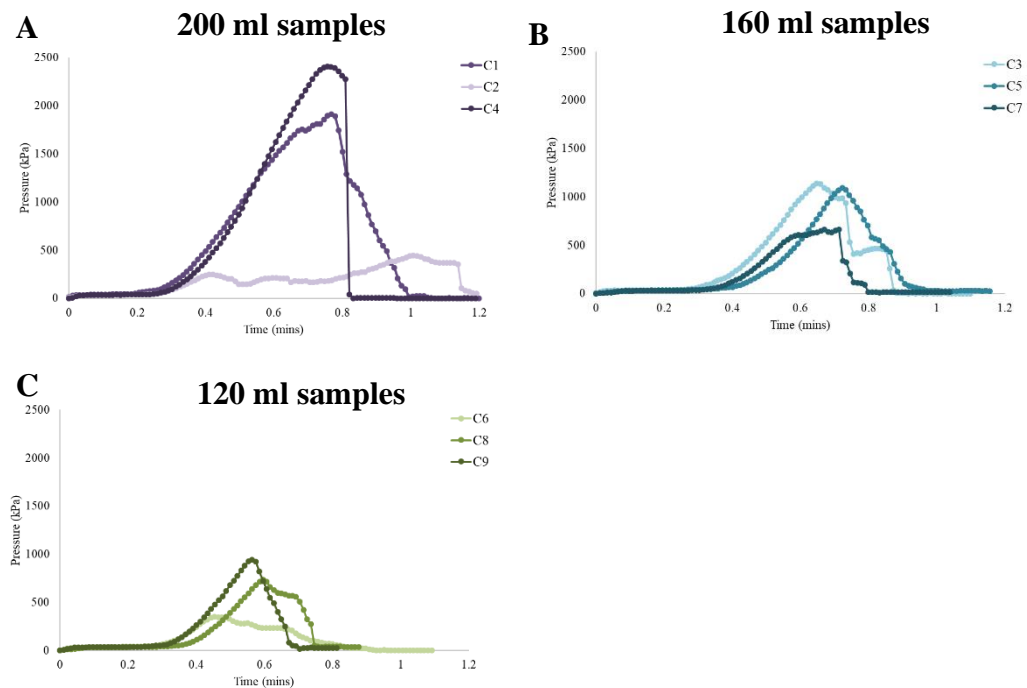


Figure 8.29: Uniaxial compression strength test results showing variation of stress over time for 120, 160 and 200ml MICP samples. Three replicas are tested for each MICP feed: 200 ml (samples C1, C2 and C4), 160 ml (samples C3, C5 and C7) and 120 ml (samples C6, C8 and C9). See Table 8.5 for feed to calcite (wt%) conversion.

Table 8.10: Summary of each MICP sample deformed by UCS. All samples were deformed at a strain rate of 1mm/min.

Sample group replica	MICP feed (ml)	Maximum UCS test result (kPa)	Average UCS for each MICP feed (kPa)
C1	200	1913.62	1588.63
C2	200	444.56	
C4	200	2407.72	
C3	160	1137.51	963.69
C5	160	1090.79	
C7	160	662.77	
C6	120	349.36	674.97
C8	120	732.72	
C9	120	942.84	

Figure 8.30 displays photos of the samples before and after deformation. By comparing the failure of each sample (Figure 8.30) with the modes of failure outlined by Szwedzicki 2007 and by Yan et al. (2019) it appears each of the samples display evidence of a failure surface, with shear-slip features (Figure 8.24). However, the failure surface appears to be offset on the top of the samples. A possible reason for this is that top and base of the samples were not perfectly smooth (despite having been sanded down) and therefore the pressure during deformation was unevenly distributed.

Figure 8.31 plots the calcite content against the maximum UCS and sample porosity. Figure 8.31A shows that as the weight percentage of calcite present in a sample

Chapter 8 - Mechanical deformation

increases, the UCS increases. Samples with 200ml feed are overall the strongest however they also have the greatest range and standard error. Figure 8.31B plots the calculated (by using the solid density) sample porosity against the calcite content. The porosity across the samples does not directly correlate to the feed volume, here the standard error is greatest for the 160 ml MICP sandstones.

The 200ml MICP samples have the lowest porosity, it therefore suggests that as sample porosity increases the sample has a higher UCS.

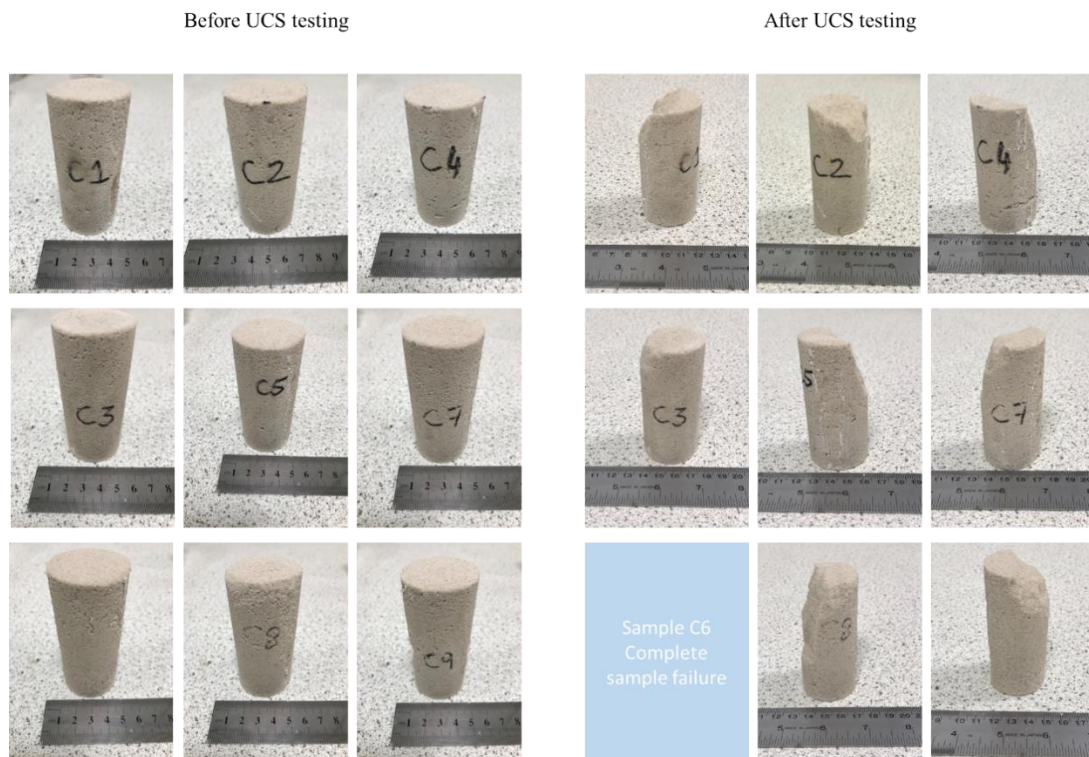


Figure 8.30: Photos of MICP samples before and after UCS deformation.

The majority of the MICP samples show evidence of failure surface development with shear-slip features.

8.3.2.2 Comparison to other MICP UCS studies

Previous MICP UCS tests have measured strengths ranging from 0.014 – 18560 kPa (El Mountassir et al. 2018). The particle size ($D_{50} = 0.113$ mm) of the sands used in this study is most comparable to those in van Paassen et al. (2010) and the fine grained sands in Terzis and Laloui (2018).

When plotted along with all previous UCS data gathered by El Mountassir et al. (2018) the UCS results from the MICP cemented sandstones in this thesis plot most closely to van Paassen et al. (2010). However, van Paassen et al. (2010) is the only UCS experiment whereby the method of formation was carried out at large field scale (8m x 5.6m x 2.5m). The study by van Paassen et al. (2010) is relevant because if MICP is used as a means of stabilising soils it is likely that the outcrops will be large (more than 1 m²). Therefore, the MICP process needs to be adequately tested in similar large field scale environments before being applied in nature (e.g. to resolve slope stabilisation issues).

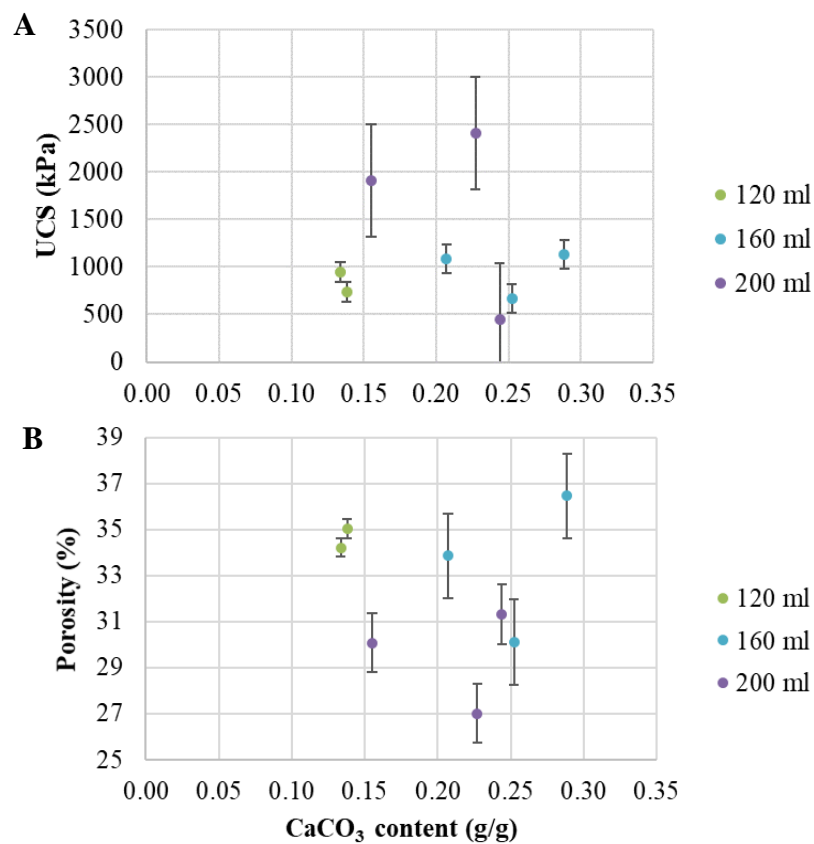


Figure 8.31: A) CaCO₃ content versus the maximum pressure for each MICP cemented synthetic sandstone during UCS with standard error bars. B) The porosity of each sample plotted against the CaCO₃ content with standard error bars.

The review by El Mountassir et al. (2018) gathers data from multiple MICP UCS studies (including van Paassen et al. 2010; Qabany and Soga 2013; Terzis and Laloui 2018). El Mountassir et al. (2018) describe Terzis and Laloui (2018) and van Paassen et al. (2010) as outliers to the bulk data results. The results from Terzis and Laloui (2018) suggest that a larger grain size increases the UCS. Meanwhile, van Paassen et al. (2010) investigates the properties of MICP single injection at field scale.

Figure 8.32 shows the results from the samples in this thesis and compares them to the results presented in El Mountassir et al. (2018) and Mahawish et al. (2018). For the purposes of this thesis focus is primarily put on the outliers plotted in Figure 8.32. The UCS values from this thesis are in line with the bulk of the data however, the CaCO₃ content is significantly higher than the majority of samples. The CaCO₃ content puts these samples more in line with the results by van Paassen (2010).

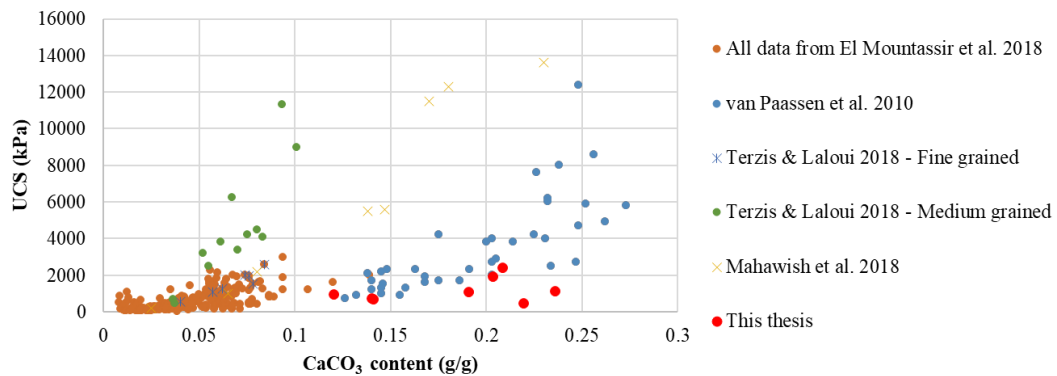


Figure 8.32: CaCO₃ content and unconfined compressive strength of MICP cemented sandstone samples from van Paassen et al. (2010), El Mountassir et al. (2018), Mahawish et al. (2018), Terzis & Laloui (2018) and this thesis. All samples from this thesis are shown in red.

However, the UCS values are generally lower than van Paassen et al. (2010)'s. One possible explanation for this is that the average urease activity is lower in the results from this thesis (2.4 mM/min) than van Paassen et al. (2010).

A comparison, of some of the variables, between van Paassen et al. (2010), Mahawish et al. (2018), Terzis and Laloui (2018), Mahawish et al. (2018) and this study are outlined in Table 8.11.

One variable which is different between this study and the other studies present in Table 8.11 is the level of saturation when the sand was initially cemented. Terzis and Laloui (2019) highlight that in partially saturated conditions (e.g. those experienced in this thesis) the menisci from the solutions tend to form around grain to grain contacts. Therefore, increasing the UCS of each synthetic sandstone.

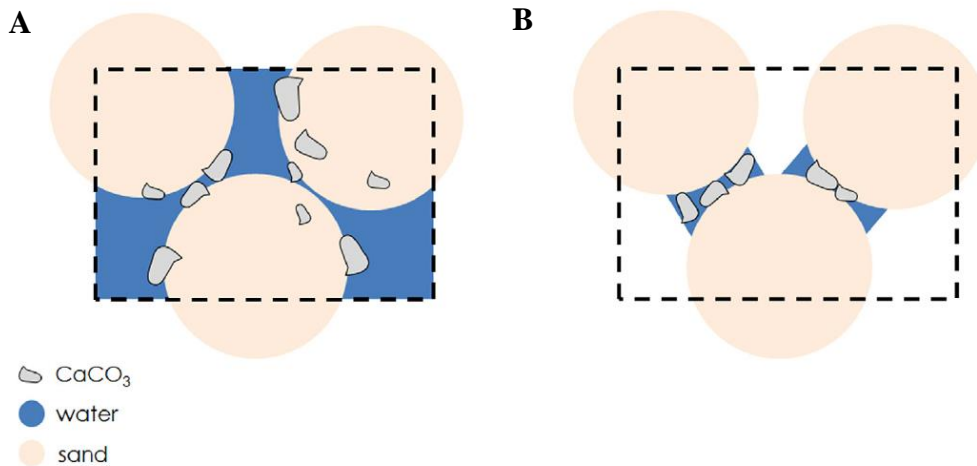


Figure 8.33: Schematic representation of the impact of saturation on the location of calcite growth. A) Shows distribution of calcite under saturated conditions. B) Shows the distribution of calcite under partial saturation. Image from Terzis and Laloui (2019).

The comparison made in this section only looks at eight variables (Table 8.11). Many other variables (including temperature, cementing treatment procedure, the length of time the bacterial and cementing liquids are exposed to the sample, pH of the cementing solution) should be compared to determine what controls the UCS of these synthetic sandstones.

From the results plotted in Figure 8.32 and the summarised variables (Table 8.11) it could be hypothesised that increased urease activity and grain size will produce increased UCS results. However, the results from these ‘outlier’ studies are widespread and highlight the range of CaCO₃ content used in MICP cemented sandstone studies. More tests with samples showing higher CaCO₃ content would be required to analyse the relationship between the percentage of calcite cement precipitated and UCS.

8.3.3 UCS summary

- The average uniaxial compressive strength (UCS) increases as the weight percentage of gypsum cement present increases in gypsum cemented sandstones.
- Gypsum cemented sandstones produce higher UCS results than samples made of 100% gypsum. This suggests that the presence of quartz grains increases the UCS.
- Sand grains may become fractured in synthetic sandstones due to UCS testing. However, in order to test this, analysis should be conducted in synthetic sandstones in which the cement is visible with microscopy.
- The average UCS increases as the weight percentage of calcite increases in MICP cemented sandstones.
- Under UCS conditions the MICP synthetic sandstones display evidence of a failure surface, with the potential to develop a shear plane if load is distributed evenly across the top of the sample.

Table 8.11: Comparison of some variables in selected MICP UCS studies.

Variable	Van Paassen et al. (2010)	Terzis & Laloui 2018 - Fine grained	Terzis & Laloui 2018 - Medium grained	Mahawish et al. 2018	This thesis
Saturation	Fully saturated	Fully saturated	Fully saturated	Fully saturated	Partial saturation
Injection sequence	Single	Multiple cycles	Multiple cycles	Multiple cycles	Multiple cycles
Sand size	D ₅₀ = 0.166 mm	D ₅₀ = 0.19mm	D ₅₀ = 0.39mm	D ₅₀ = 1.60 mm	D ₅₀ = 0.113 mm
Sample scale	Large scale ~ 100m ³	Core ^a	Core ^a	Core - 51 mm dia. x 102 mm length	Core - 38mm dia. x 100mm length
Mean porosity	41.10%	35.9-41.5%	40.8-47.1%	26-40% ^b	35%
Ca concentration	1 M	1M	1M	1M	1.4 M
Urea concentration	1 M	1M	1M	1M	1.4 M
Urease activity	18.33 mM/min	1.73 mM/min	1.73 mM/min	19.38–21.45 mM/min	2.40 mM/min ^c

^a Information from accompanying paper Terzis et al. (2016).

^b Range of porosity achieved depended on number of treatment cycles.

^c Average ureolytic activity from four samples. For full results see Table 7.6.

8.4 Triaxial testing

The initial aim of this section was to deform synthetic sandstones using triaxial testing and create deformation bands in the samples. By doing this it was hoped the cement and porosity properties before and after deformation could be monitored using X-CT. However, as can be seen in Chapter 7, it became clear that gypsum and MICP were not suitable materials to reflect the cementation in natural quartz/calcite/gypsum cemented sandstones due to the textures formed (instead the gypsum bridges most closely resembled clay cemented sandstones).

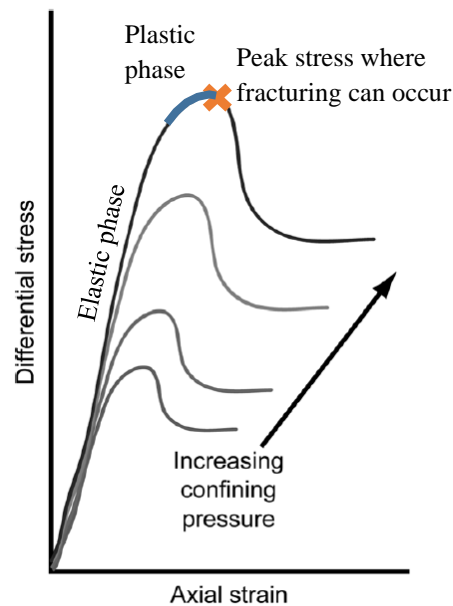


Figure 8.34: Triaxial schematic response modified from Dewhurst et al. (2011) shows that differential stress increases with increased confining pressure.

Regardless, this section has become insightful into the triaxial properties of gypsum cemented rocks and adds to the data collected earlier in this chapter from shear box and uniaxial experiments. Triaxial deformation was carried out on the gypsum cemented sandstones in order to test the response of gypsum cement to triaxial loading, thus determining the impact of gypsum concentration as a cementing agent on the strength of the synthetic sandstones under confined conditions.

Figure 8.34 displays a schematic triaxial response whereby differential stress increases as confining pressure increases. The curve shows a similar response to previous sandstone triaxial tests shown in Mair et al. (2000).

Although deformation bands were not formed during this study, the surrounding literature is included for context and analysis of the data. Due to time and financial constraints only a selected number of gypsum cemented sandstones were tested in this chapter.

8.4.1 Choosing the most relevant deformation conditions

Previous studies have formed deformation bands in sandstone cores during triaxial testing (Wong et al. 1997; Mair 2002; Ngwenya et al. 2003; Ando 2013; Skurtveit et al. 2013; Alikarami et al. 2014; Heap et al. 2015; Ma and Haimson 2016). To determine the parameters used to form deformation bands in the triaxial rig the confining pressures, shear rates and the type of deformation bands formed in previous studies are summarised (Table 8.12). For comparison with the results from the field (Chapter 5), the applied stress in each test was used to calculate equivalent depth of formation in the Earth. From the results displayed in Table 8.12 it appears that no cataclastic deformation bands have been formed during experiments with confining pressures less than 6497 PSI (equivalent to approximately 1758m depth). 1 psi equals approximately 6.89 kPa.

Table 8.12 shows that dilation bands can form between 1960-6005 psi (~13.5-41.4 MPa) at strain rates of 5×10^{-6} . Meanwhile compaction bands can form at higher confining pressures between 7950-21760 psi (~ 54.8-150.0 MPa) at strain rates of 5×10^{-5} or 5×10^{-6} . Finally, shear bands form in the widest range of confining pressures (14.50- 21755.66 psi) with strain rates ranging from 7.5×10^{-3} to 5×10^{-6} . These results suggest that confining pressure has an impact on the formation of different types of deformation band.

It is possible that the wide range of shear band forming confining pressures is due to a misuse in terminology. Across the literature on grain breakage in triaxial deformation, the terminology varies due to the interdisciplinary nature of these studies. This therefore makes it challenging to compare studies, and more complex to identify which type of deformation bands have been formed during deformation.

Chapter 8 - Mechanical deformation

Laboratory triaxial experiments were performed under 27.58 MPa confining pressure to investigate the stress-strain characteristics of gypsum cement. The tests were carried out using synthetic sandstones with gypsum cement varying from 10-25% of the total sample mass. In addition to these samples a 'standard' sandstone sample and a sample made of 100% gypsum were analysed. This allowed for a comparison to be made between samples. See Chapter 7 for the formation of the gypsum cemented sandstones. The method described in Section 8.2.4.2 was repeated to form the 100% gypsum cylinder.

Chapter 8 - Mechanical deformation

Table 8.12: Summary of previous triaxial studies and determination of which type of deformation band has been formed.

Reference	Sample	Approximate burial depth (m) ^a	psi (pound-force per square inch).	Strain rate (s ⁻¹)	Type of band formed
Ando 2013	Caicos	3.92	14.50	8x10 ⁻⁶ - 7.5x10 ⁻³	Shear
Ando 2013	Ottawa	11.77	43.51	8x10 ⁻⁶ - 7.5x10 ⁻³	Shear
Alikarami et al. 2014	Hostun and Ottawa sands	39.25	145.04	3.5x10 ⁻⁷	Cataclastic
Wong et al. 1997	Adamswiller sandstone	196.23	725.19	5x10 ⁻⁵	Shear
Ando 2013	H	274.73	1015.26	8x10 ⁻⁶ - 7.5x10 ⁻³	Shear
Ma and Haimson 2016	Bentheim sdst (high porosity = 24%)	313.97	1160.30	5x 10 ⁻⁶	Shear
Heap et al. 2015	Bleurswiller sdst	392.46	1450.38	5x10 ⁻⁵	Single shear
Ma and Haimson 2016	Coconino sdst (medium porosity = 17.5%)	392.46	1450.38	5x 10 ⁻⁶	Single shear
Mair 2002	Locharbriggs sandstone	529.83	1958.01	5x10 ⁻⁶	Dilation
Ma and Haimson 2016	Bentheim sdst (high porosity = 24%)	588.70	2175.57	5x 10 ⁻⁶	Shear
Ngwenya et al. 2003	Clashach sandstone	608.32	2248.08	5x10 ⁻⁶	Dilation
Ma and Haimson 2016	Coconino sdst (medium porosity = 17.5%)	784.93	2900.75	5x 10 ⁻⁶	Single shear
Wong et al. 1997	Adamswiller sandstone	784.93	2900.75	5x10 ⁻⁵	Shear
Ngwenya et al. 2003	Clashach sandstone	812.40	3002.28	5x10 ⁻⁶	Dilation
Mair 2002	Locharbriggs sandstone	1071.43	3959.53	5x10 ⁻⁶	Dilation
Ma and Haimson 2016	Bentheim sdst (high porosity = 24%)	1177.39	4351.13	5x 10 ⁻⁶	Shear
Skurtveit et al. 2013	Uchaux sands	1569.86	5801.51	1x10 ⁻⁶	Cataclastic
Wong et al. 1997	Adamswiller sandstone	1569.86	5801.51	5x10 ⁻⁵	Shear

Chapter 8 - Mechanical deformation

Mair 2002	Locharbriggs sandstone	1624.80	6004.56	5x10 ⁻⁶	Dilation
Ngwenya et al. 2003	Clashach sandstone	1758.24	6497.69	5x10 ⁻⁶	Cataclastic
Ma and Haimson 2016	Coconino sdst (medium porosity = 17.5%)	1962.32	7251.89	5x 10 ⁻⁶	Single shear
Mair 2002	Locharbriggs sandstone	2150.71	7948.07	5x10 ⁻⁶	Compaction
Ma and Haimson 2016	Bentheim sdst (high porosity = 24%)	2354.79	8702.26	5x 10 ⁻⁶	Shear
Wong et al. 1997	Adamswiller sandstone	2354.79	8702.26	5x10 ⁻⁵	Cataclastic
Mair 2000	Locharbriggs sandstone	2705.95	10000.00	5x 10 ⁻⁶	Cataclastic
Heap et al. 2015	Bleurswiller sdst	3139.72	11603.02	5x10 ⁻⁵	Compaction
Ma and Haimson 2016	Coconino sdst (medium porosity = 17.5%)	3139.72	11603.02	5x 10 ⁻⁶	Shear
Ma and Haimson 2016	Bentheim sdst (high porosity = 24%)	3139.72	11603.02	5x 10 ⁻⁶	Shear
Ma and Haimson 2016	Coconino sdst (medium porosity = 17.5%)	3924.65	14503.77	5x 10 ⁻⁶	Shear
Wong et al. 1997	Adamswiller sandstone	3924.65	14503.77	5x10 ⁻⁵	Cataclastic
Ma and Haimson 2016	Coconino sdst (medium porosity = 17.5%)	4709.58	17404.53	5x 10 ⁻⁶	Shear
Ma and Haimson 2016	Bentheim sdst (high porosity = 24%)	4709.58	17404.53	5x 10 ⁻⁶	Shear-enhanced compaction band
Ma and Haimson 2016	Coconino sdst (medium porosity = 17.5%)	5886.97	21755.66	5x 10 ⁻⁶	Shear
Ma and Haimson 2016	Bentheim sdst (high porosity = 24%)	5886.97	21755.66	5x 10 ⁻⁶	Pure compaction
Wong et al. 1997	Adamswiller sandstone	5886.97	21755.66	5x10 ⁻⁵	Cataclastic

^a calculated using sandstone density of 2600 g/cm³ (Sharma 1997).

8.4.2 Triaxial sample preparation and test procedure

Triaxial tests were carried out at the University of Edinburgh's Geosciences department (Figure 8.35). Once formed the samples were carefully transported to Edinburgh for testing by wrapping the samples in bubble wrap and carrying them in person. Prior to testing samples were smoothed off using sandpaper to between 75-90mm in length. After smoothing the samples were fitted with heat shrink sleeves (Figure 8.36) to keep poorly consolidated rock together inside the rig.

For each sample, oil confining pressure of 1000, 4000 and 8000 psi were used. Strain rates used were either $1 \times 10^{-5} \text{ s}^{-1}$ or $7 \times 10^{-5} \text{ s}^{-1}$. The fastest strain rate which the triaxial rig could achieve was $7 \times 10^{-5} \text{ s}^{-1}$. No pore fluid was present. Experiments were carried out at ambient temperature and were stroke controlled. End caps were used to increase the overall height of the sample and create a better fit inside the rig. The axial stress is maintained using the pump system. The offset was measured by two LVDTs to find the average displacement. Figure 8.37 illustrates the mechanics behind the triaxial rig at the University of Edinburgh. Table 8.13 summarises the conditions for each triaxial test.

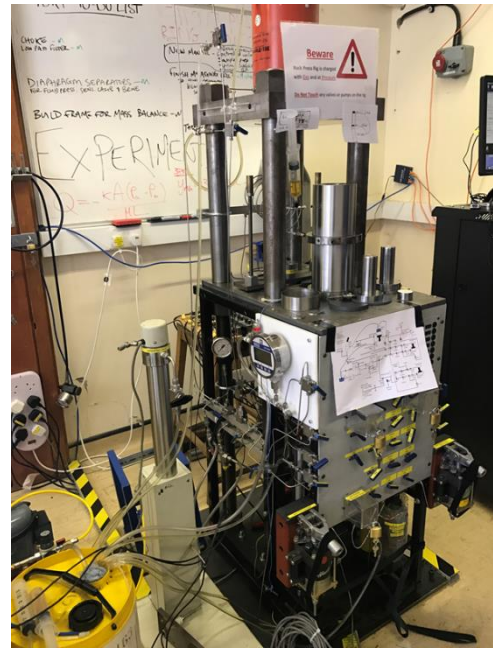


Figure 8.35: Triaxial rig set up at the University of Edinburgh.

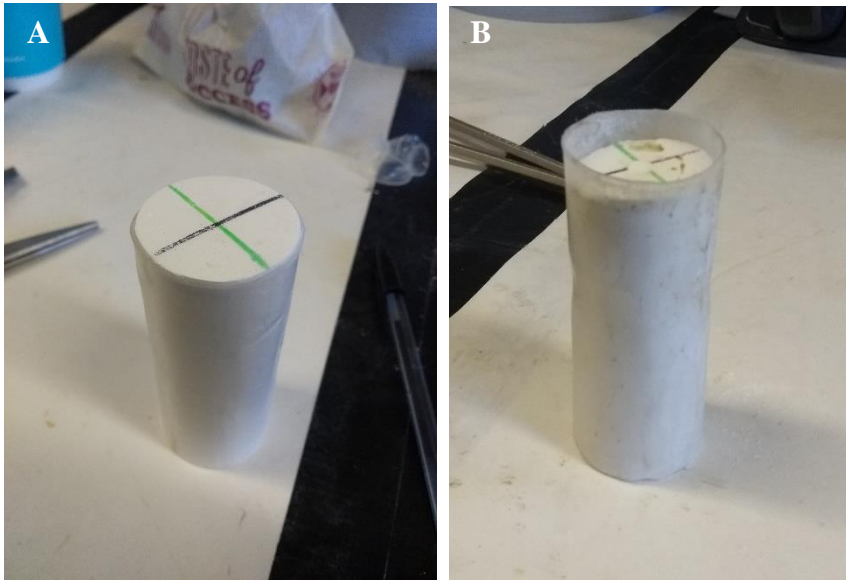


Figure 8.36: 100% gypsum triaxial sample fitted with a heat shrink sleeve (A) before, and (B) after deformation

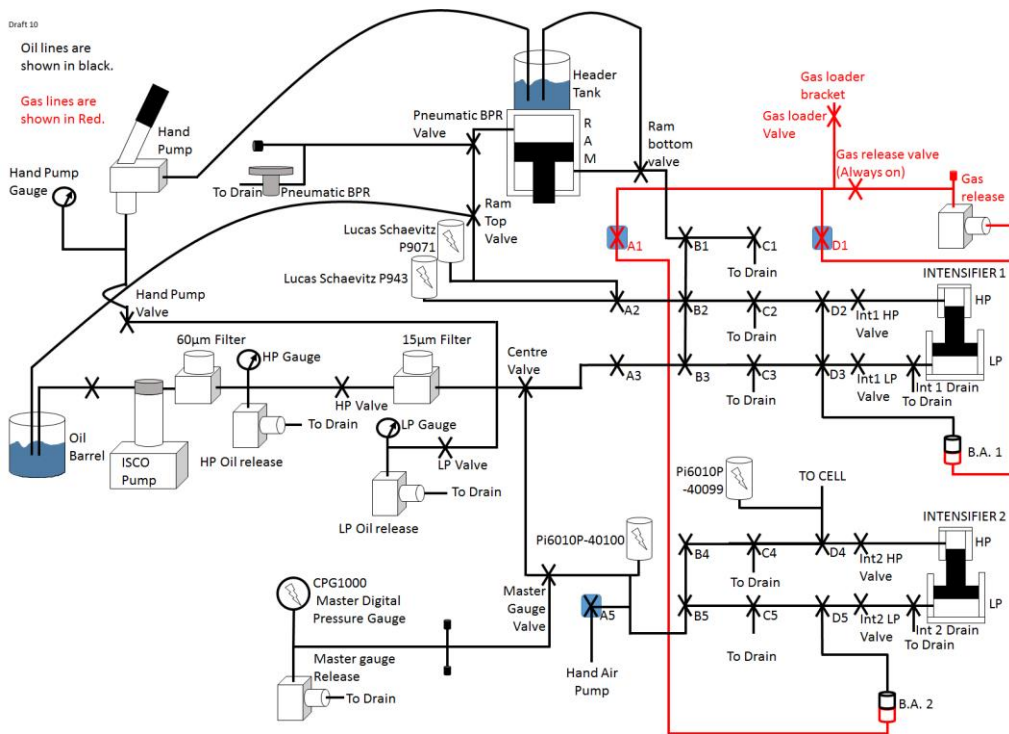


Figure 8.37: Triaxial rig plumbing diagram built by Iain Butler and Michael Flynn, Geosciences Department, University of Edinburgh, figure courtesy of Iain Butler.

Chapter 8 - Mechanical deformation

Table 8.13: Summary of samples (gypsum cemented sandstones, sandstone and 100% gypsum sample) tested by triaxial deformation. Total displacement for each gypsum cemented sandstone was 8mm. Both strain rates were kept at a constant during each experiment.

Sample	Cement (%)	psi used	Strain rate	Initial sample length (mm)	Final sample length (mm)	Difference in length (mm)	Notes
15C	15	4000	7×10^{-5}	74.4	71.92	2.48	
15D	15	4000	7×10^{-5}	77.14	69.71	7.43	No sleeve used
20C	20	1000	7×10^{-5}	83.17	78.14	5.03	
20D	20	4000	1×10^{-5}	80.12	77.56	2.56	
20E	20	8000	7×10^{-5}	79.52	76.84	2.68	
25C	25	1000	7×10^{-5}	82.04	79.52	2.52	
25D	25	4000	1×10^{-5}	85.29	82.87	2.42	
25E	25	8000	7×10^{-5}	85.63	84.63	1.00	
Sandstone	N/A	4000	7×10^{-5}	91.71	91.20	0.51	
Gypsum	100%	4000	7×10^{-5}	96.70	90.32	6.38	

8.4.3 Triaxial results

There is no evidence of shear failure in the gypsum cemented and 100% gypsum sample. Instead each of the gypsum cemented sandstones and 100% gypsum sample were compressed inside the jacket. The only evidence of shear failure is from the sandstone sample which was run to act as a comparison between classical triaxial failure and the failure observed by the gypsum cemented sandstones.

No grain breakage was noted to the naked eye. Instead plastic deformation was observed with release fractures forming perpendicular to the loading direction, whilst the samples remained in the jacket.

Table 8.13 lists each of the samples and their lengths before and after triaxial deformation. The total compression experienced for each sample was approximately 8mm according to the LVDT response. However, the height of the sample once it is removed from the rig does not reflect this change. Instead it appears that the gypsum cemented synthetic sandstones have ‘bounced’ back and increased in length once unloaded. However, the new sample length remains shorter than the original length. Neither the sandstone nor the 100% gypsum sample behave in the same way as the gypsum cemented synthetic rocks. This therefore suggests that the samples behave plastically. Further work on this to understand the reasons that this ‘bounce’ back took place is out with the scope of this thesis. It is possible that if a lower confining pressure was used instead of 27.57 MPa no ‘bounce’ back would take place.

Regardless of the plastic behaviour the overall cohesion remained across each sample (the sample could be removed from the triaxial rig in one piece) and they were not subjected to complete crumbling.

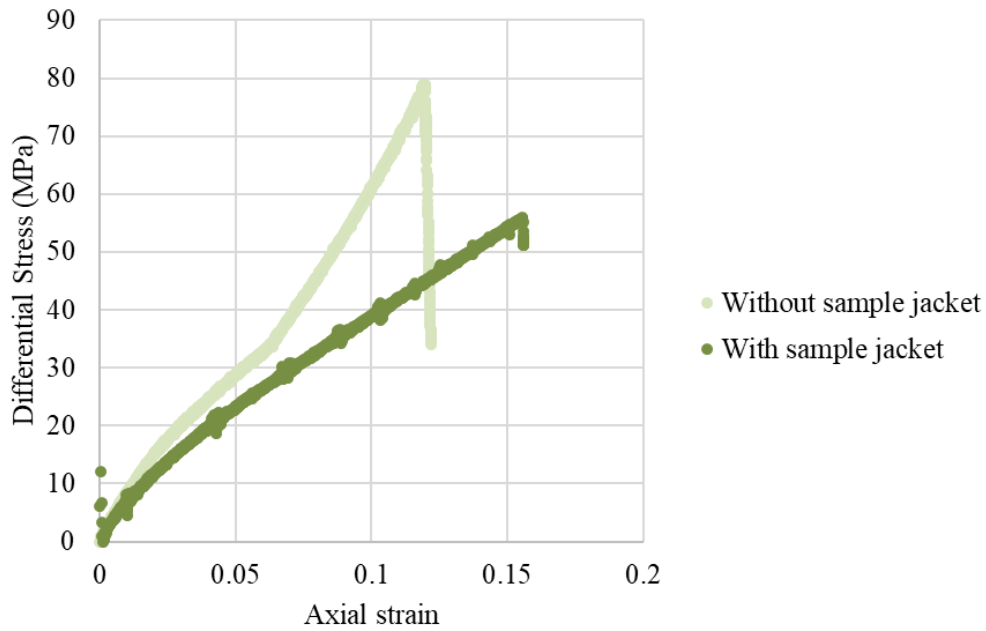


Figure 8.38: Triaxial results showing the comparison of 15% gypsum samples with and without a sleeve at 4000 psi. This shows without the sample sleeve the differential stress increases at a higher rate than the sample with a jacket.

Peak shear stress was not reached during deformation of the gypsum cemented sandstone or 100% gypsum experiments. Instead each sample behaved in a plastic manner and did not seem to reach plastic phase or fracturing. Recording was stopped before the triaxial rig stroke ran out.

Two 15% gypsum cemented sandstone samples were tested at 4000 psi (27.57 MPa) confining pressure to understand if the sample sleeve had an impact on the triaxial response. From the response the sleeve does impact the triaxial response (Figure 8.38). Therefore, it is possible that with no sleeve, failure is more likely to occur.

Figure 8.39 shows the axial strain versus the differential stress for each of the 20 and 25% gypsum cemented sandstones. Figure 8.40 compares the results from all the gypsum cemented sandstone samples at 1000, 4000 and 8000 psi. Here the increasing percentage of gypsum cement volume appears to have no effect on the differential stress profile as each sample is deformed. However, as no peak

Chapter 8 - Mechanical deformation

differential stress was reached it is impossible to say if this trend would have continued during sample deformation.

Figure 8.41 compares the gypsum cemented sandstone samples to the 100% gypsum and natural sandstone sample.

Figure 8.41A displays the differential stress response for the 100% gypsum cemented sample tested at 4000 PSI confining pressure. When deformed at 4000 PSI the gypsum cemented sandstone is stronger than the 100% sandstone sample (Figure 8.41C). Furthermore, the 100% gypsum sample provides a similar differential stress response as the gypsum cemented sandstones deformed at 1000 PSI.

Figure 8.41B shows the differential stress response for the natural sandstone sample tested at 4000 PSI confining pressure. The sample has a peak differential stress of 360 MPa at an axial strain of 0.023. From this response the gypsum cemented sandstones do not behave like naturally formed sandstone (Figure 8.41C).

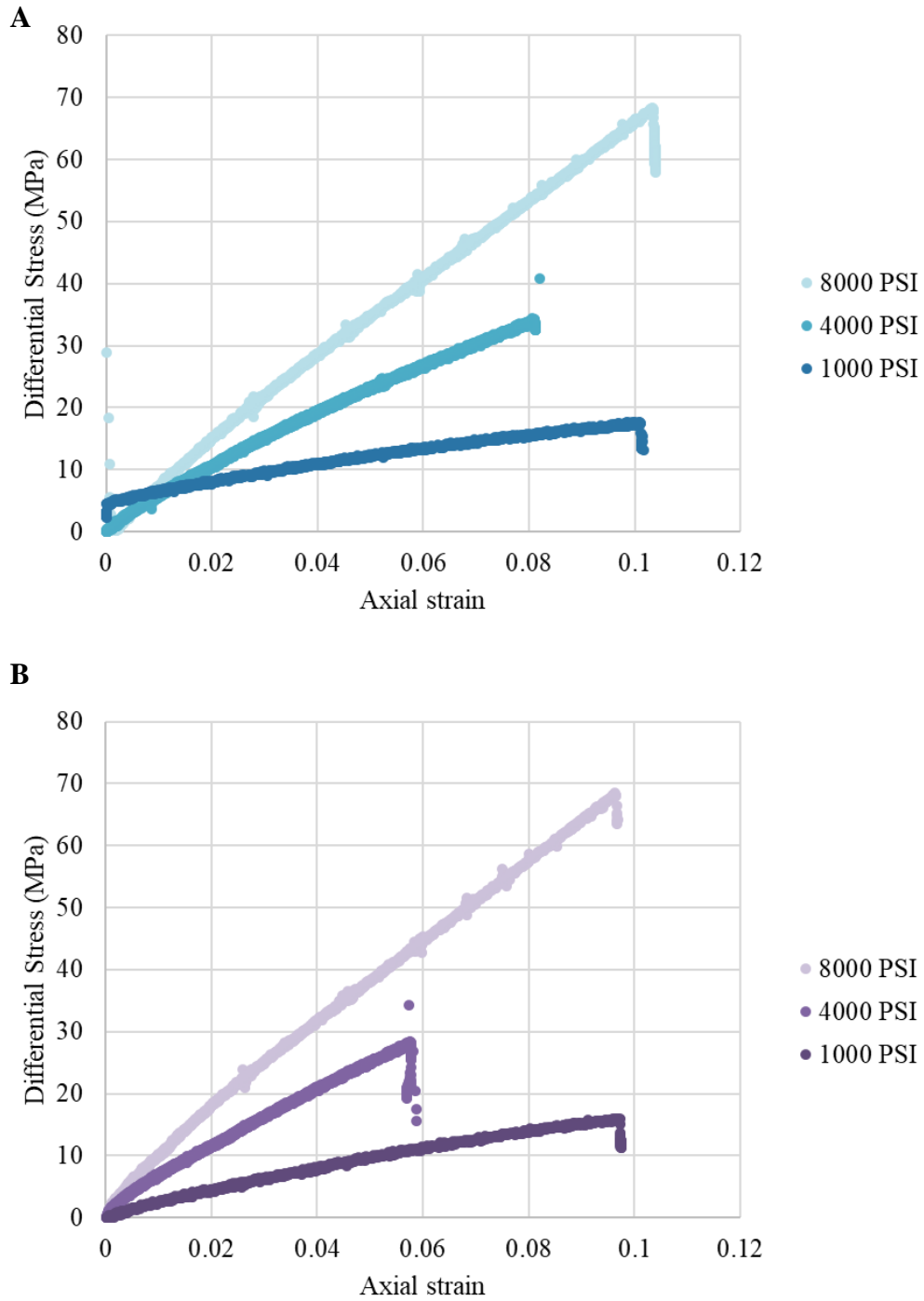


Figure 8.39: Triaxial deformation results of A) 20 and B) 25% gypsum cemented sandstones. Tested at a strain rate of 7×10^{-5} (1000 and 8000 psi samples) and 1×10^{-5} (4000 psi samples). Each experiment was stopped before the triaxial stroke ran out.

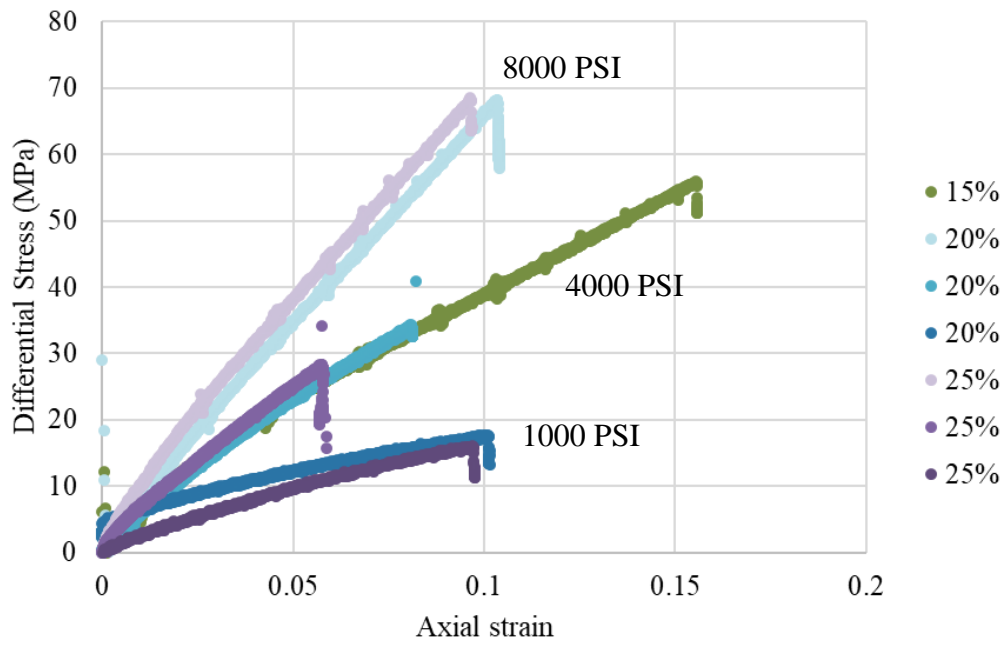


Figure 8.40: Summary of triaxial results for gypsum cemented sandstones. Regardless of percentage of gypsum cement present in the synthetic samples the differential stress response is similar for each confining pressure. This suggests confining pressure controls the differential stress observed.

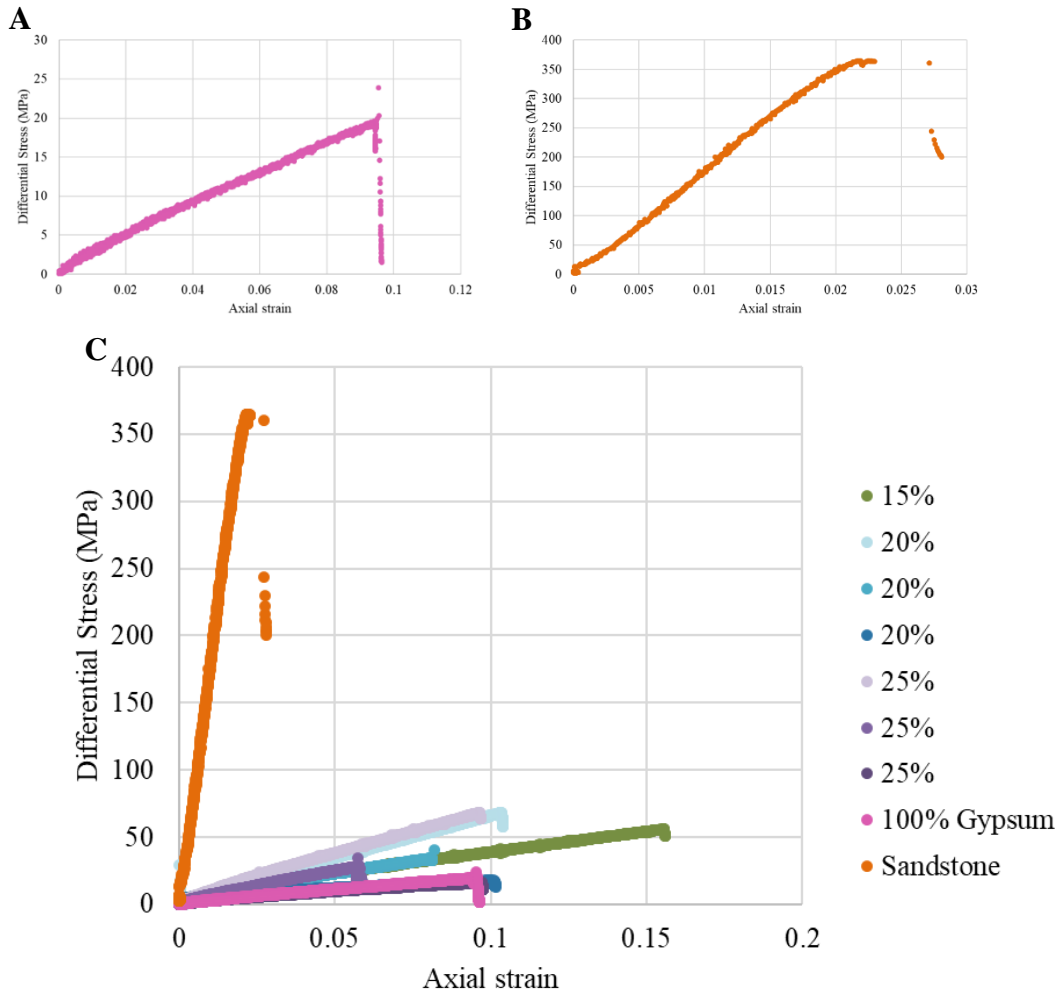


Figure 8.41: Triaxial results from A) 100% gypsum sample. B) Shows a typical sandstone sample. C) Comparison between all samples.

8.4.4 Triaxial deformation summary

- Following recommendations by Wong et al. (1997), it would be advisable to repeat these experiments with measurements of porosity change and acoustic emission during loading to enable accurate determination of stress and deformation parameters.

- It would be worthwhile to repeat and increase the number of (minimum 5 repeats of each) these experiments using the MICP cemented sandstones. The repeats would take into consideration any heterogeneity across the samples. When repeating

experiments do so on a rig which can accommodate a larger stroke value to allow the experiments to continue for longer.

- One way of measuring porosity change over time would be in an X-CT scanner. However, to enable this to be tested effectively insitu deformation whilst scanning would have to be carried out. This would require a smaller sample size (< 2 cm in height).

8.5. Comparison between cement and deformation techniques

The initial aim of this chapter was to gain a better understanding of the mechanics at the grain scale which lead to cataclastic deformation band formation in shallow burial depths with respect to the quantity of cementing phase. As deformation bands were not formed in these synthetic samples, this chapter has focused on their mechanical response (shear box, UCS, triaxial deformation).

8.5.1 Effect of cement

From this chapter it can be summarised that the distribution and mineralogy of cement directly impact the mechanics of the synthetic sandstones. Table 8.14 summarises the average results from both the shear box and UCS tests for gypsum and MICP cemented synthetic sandstones. The triaxial results for the synthetic sandstones are not included in this table as a maximum stress was not reached during the triaxial tests. The pink arrow highlights the overall trend which shows that as the cement content in each synthetic sample increases so does the shear and compressive strength of each sample. The MICP cemented sandstones have a larger range in shear strength than the gypsum cemented sandstones. These results reflect that the shear modulus is higher for calcite (30.3 GPa) than for gypsum (16 GPa) (Henderson and Henderson 2009). Meanwhile, the gypsum cemented sandstones have a larger range in compressive strengths than the MICP cemented sandstones. This therefore suggests that cement type should be considered depending on the application of the synthetic sandstone.

Table 8.15 describes the impact of increasing the volume of cement on each method of mechanical deformation (including triaxial deformation).

Table 8.14: Summary of average results from shear box and UCS tests on the synthetic sandstones. Pink arrows highlight overall trends. For both the shear box and UCS experiments show that as the cement content increases the average shear and confining stress increases.

			Experimental technique			
			Shear box (kPa)	UCS (kPa)		
			Average maximum shear stress at 95.38 kPa normal stress	Average UCS		
Sand			83.98	-		
Cement type	Gypsum	10 %	146.11	↓	157.22	↓
		15 %	128.61		768.075	
		20 %	245.83		877.76	
		25 %	208.43		2294.11	
	MICP	120 ml	102.96	↓	674.97	↓
		160 ml	178.52		963.69	
		200 ml	435.65		1588.63	

Table 8.15: Summary describing the effects of increasing gypsum and MICP cement volume on the mechanical deformation of synthetic sandstones.

Experimental technique	↑Gypsum	↑MICP
Shear box	Shows overall increase in shear strength as cement volume increases. However, the trend it is not clearly defined.	Shear strength increases as cement volume increases.
UCS	Compressive strength increases as cement volume increases.	Shows an overall increase in compressive strength as the CaCO ₃ content increases. However, the trend is not clearly defined.
Triaxial	No variation in differential stress response with increasing gypsum content. Instead the differential stress of the samples is controlled by the confining pressure.	N/A

8.5.2 Comparison of deformation techniques

Although cheap to run in comparison to the other deformation techniques the shear box has drawbacks. One main drawback of the shear box experiments is that it is difficult to analyse and compare each sample before and after deformation.

One possible solution to this is reducing the sample size so that it can be imaged using X-CT before and after deformation. However, there is a chance that the sample is unrecoverable once deformed e.g. the cement bonds have broken therefore no

structure can be seen. A method of achieving this would be to use plaster of Paris to hold the small sample (less than the size of the shear box) in place. Tobler et al. (2018) have used a similar method on less porous rocks. However, due to the high porosity of the synthetic sandstones this method would not work. Instead after the plaster was set in the shear box a hole (to match the size of the sample) would need to be drilled into both the top and base plate. Although this method overcomes the error created by the large 60x60x20mm samples and allows for the samples to be analysed before and after deformation in the X-CT, this method has the potential to create new errors due to misalignment of the sample in the drilled hole.

An alternative is to use X-CT to image the shear box in situ therefore undertaking 4D analysis. The shear box used in this study had sides made of thick metal which would make it impenetrable to x-rays. However, if the shear box was reconstructed using a thick plastic the sample could be deformed in-situ in the X-CT. Other points which would have to be taken into consideration is the positioning of the sample. For example, it is preferable to have the sample positioned for imaging so that it is standing upright rather than lying flat. Another point worth considering is the shear box sample cuboid size is 60 x 60 x 20 mm. This is a large sample size to scan in a laboratory X-CT and because of this the resolution is limited. Instead it would be beneficial to decrease the size of the shear box and sample size as to improve the scan resolution. Previous experiments have used transparent ring shear boxes and digital video camera systems to monitor grain movement during displacement (Fukuoka et al. 2007) therefore using the X-CT would be building on the technology used in these studies.

For future work with the triaxial rig I would recommend testing the MICP cemented sandstones for a better understanding of the impact of cement (balls vs needle network) on grain supported sandstones.

8.6 Summary

- As the volume of calcite is increased the strength of the synthetic sandstones is increased.
- As the weight percentage of gypsum cement is increased from 12-26% in the gypsum cemented sandstones there is an overall increase in the strength of each sample when tested in the shear box and by UCS (Figure 8.26).
- By forming the shear box samples outside of the test apparatus, small gaps (<1mm) form around the inside of the box. This therefore must be taken into consideration when interpreting the shear results.
- The maximum and ultimate shear stresses are higher for MICP than gypsum cemented sandstones.

Recommendations

- Form the synthetic sandstones in situ in the shear box. This will improve the fit of the sample inside the shear box.
- Create a plastic version of the shear box which could be placed inside the X-CT to monitor deformation over time and therefore the movement of sand grains, and possible development of a shear plane can be traced.
- A minimum of five repeat samples should be deformed for each mechanical deformation method.
- Develop a method to analyse the cement and grains before and after shearing to determine the impact of deformation at the micro-scale.

Chapter 9 Discussion, Conclusions and Future work

9.1 Discussion

The original aim of this thesis was to investigate the impact of cementation on deformation band formation by exploring the types of cement, cement chemistry, cement strength and the location of cement across both natural and synthetic sandstones. Due to the time restraints of this PhD deformation bands were unable to be formed in the synthetic sandstones. This altered the aim of the PhD to focus instead on developing a methodology for deformation band petrophysical analysis using X-CT, developing a method to form synthetic sandstones, comparing the properties of different types of cement used to form sandstone, investigating the chemistry behind gypsum cement and investigating the mechanical properties of the synthetic sandstones formed using the two cement types.

This chapter synthesises the results from this thesis.

9.1.1 Cement distribution and mineralogy is important for mechanics and hydraulics

The distribution and mineralogy of cement is important for both the mechanics and hydraulics of clastic rocks. To my knowledge there are no known classifications of cement distribution and strength in sandstones comparable to Folk (1959) and Dunham (1962) classifications. I speculate that this is due to the overlap in work between sedimentology and geomechanics.

Sedimentologists predominantly focus on the grains when analysing a sandstone. This includes the grain size, shape, composition and sorting. Work on cement primarily focusses on how cement fills the pores (therefore restricting fluid flow), looking for cement structures which indicate way up (e.g. geopetal structures) and 2D cement distribution in carbonates. However, to the best of my knowledge there appears to be little work which analyses the distribution of cement in 3D. Laubach et al. (2004b, 2004a) focusses on the distribution of cement in fractures to help identify the location of open fractures. However, the distribution of cement in fractures has a

different structure to the cement between sand grains, and, as a result, has a different impact on the mechanics and hydraulics of the rock.

Meanwhile, geomechanics focus on the overall macroscopic rock properties, e.g. rock strength, to determine if the rock being tested would be suitable for the required application e.g. a tunnel to be drilled in it. Within geomechanics Ismail et al. (2002), DeJong et al. (2006) and Terzis and Laloui (2018) have investigated the distribution of cement and its impact on the mechanics. However, these studies do not consider how the properties of the cements compared to natural sandstones.

The distribution of cement is of increased importance when analysing poorly cemented sandstones. The strength of a rock is likely to be controlled by the strength and distribution of cement (Figure 9.1). This in turn impacts the mechanics of the rock. This thesis has explored the distribution of cement across several samples of high porosity sandstone and synthetic sandstone, and characterised the impact of the strength of cement on the synthetic sandstones.

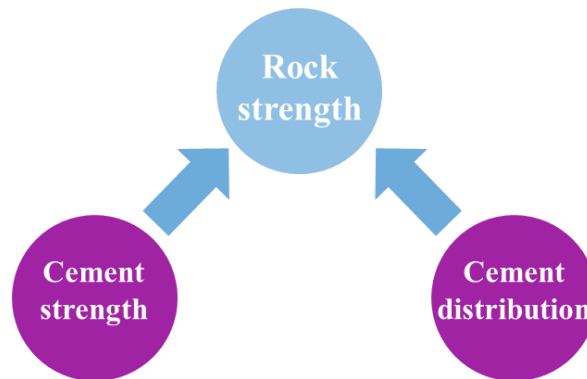


Figure 9.1: The strength of a rock is affected by cement in two ways. The first is the cement strength and the second is the distribution of cement.

Artificial sandstones do not have the same cementing processes as natural sandstone. Natural sandstones undergo a long period of consolidation (sometimes over millions of years) and can be subjected to multiple phases and volumes of fluid flow which produce diagenesis of the rock (chemical changes by which cements can precipitate from mineral rich fluids or localised dissolution), elevated temperature and pressure conditions, and structural changes which can alter the strength and the distribution of cement in the sandstone.

Chapter 9 – Discussion, conclusions and future work

The artificial sandstones produced in this thesis were formed over periods of up to four weeks. During this time the samples were subjected to between 1.36-1.38 kPa and between 1 and 5 phases of fluid flow of constant composition: gypsum cemented samples were subject to 1 phase, meanwhile MICP cemented samples were subject to between 3-5 phases. The confining pressure used to form the samples equates to approximately 6 cm burial depth (using sandstone density values from Sharma (1997)) and is significantly less than 127.5 MPa at 5km burial depth. Therefore, the confining pressure applied in the formation of the samples is not comparable to those found applied in nature. Furthermore, the fluid flow history with which the synthetic rocks are treated is oversimplified compared to what rocks may experience below the subsurface. Despite these differences, a clear variation in cement shear and compressive strength can be seen in the synthetic sandstones. This variation can only be amplified with increasing confining pressure and type/volume of fluid flow as this adds an extra layer of complexity to each sandstone.

This thesis has shown that cements can increase the strength and decrease the porosity of synthetic rock. Therefore, the distribution of cement does affect the mechanics of the sandstone

Figure 9.2 is a schematic displaying some of the cement types and distributions from silica, carbonate and clay cemented rocks. The figure is divided into the types of natural cement present (e.g. silica, carbonate and clay), the distribution of carbonate cement and refers to a simplified version of the Folk (1959) limestone classification.

The three types of silica cement are pressure solution, microcrystalline and overgrowths. Pressure solution is created due to the dissolution of minerals at grain to grain contacts. Here the cement is disconnected, the porosity and permeability are high, and the rock strength is increased. In addition, the shear and compaction strength are high. Microcrystalline quartz can form a cement by coating the sand grain. Microcrystalline quartz is overall unconnected therefore it preserves the porosity of sandstones (French et al. 2012). Silica overgrowths form in crystallographic continuity with host grain. The overgrowths are likely to be well connected however, they decrease the porosity of the sandstone (Lander and Walderhaug 1999).

Chapter 9 – Discussion, conclusions and future work

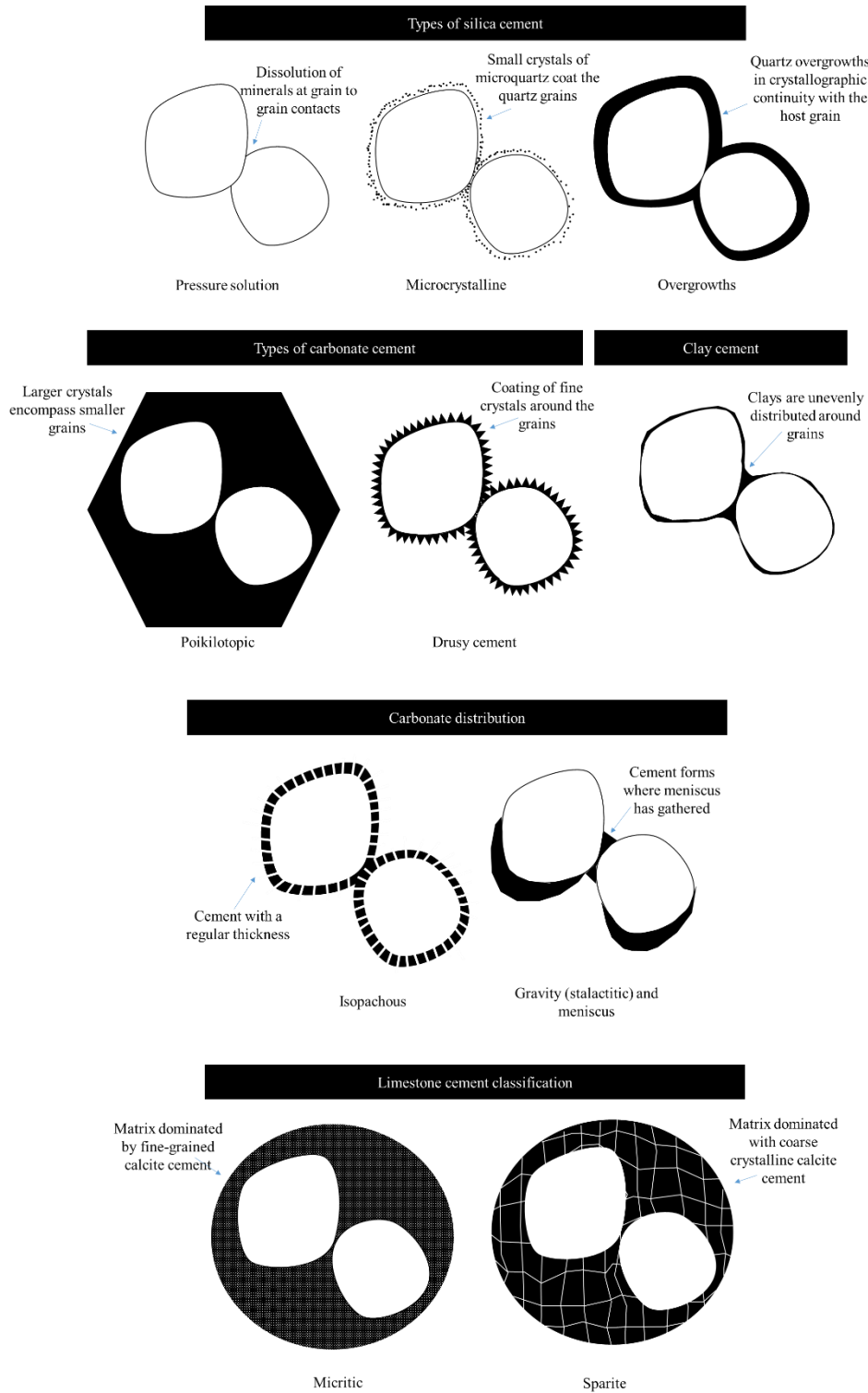


Figure 9.2: Schematic displaying some of the cement types and distributions from silica, carbonate and clay cemented rocks. This figure is for comparison with the natural and synthetic sandstones (Figure 9.4).

Chapter 9 – Discussion, conclusions and future work

The types of calcite cement are poikilotopic and drusy cement (originally mentioned in Section 2.4.1). For samples displaying poikilotopic cement, the cement is connected. However, the porosity and permeability are low. It is likely that the strength of these carbonates is dependent upon the cement strength. For samples displaying drusy cement, the cement is likely to be connected. However, in comparison to the poikilotopic cement higher porosity would be expected. The permeability is likely to be dependent on the interlocking 3D nature of the drusy cement.

A schematic of clay cement is also illustrated. In nature clay cement is known to form bridges between grains and the clay cement geometry mirrors that of meniscus cement (Figure 9.2).

The two types of carbonate distribution are isopachous, and gravity (stalactitic) and meniscus. The level of cementation (e.g. partial or complete) directly impacts the connectivity of the cement (see Figure 2.11). Carbonate cements which are partially cemented will have cement which is less connected than carbonate cements which are completely cemented. For further details on these cement distributions see Section 2.4.1.

The final schematic displayed in Figure 9.2 is the simplified version of the Folk (1959) limestone classification. In both a micrite and sparite the cement is connected, and porosity and permeability are low.

Figure 9.3 displays the Dunham (1962) carbonate classification. Dunham classes were defined by the supporting fabric of the original sediment (e.g. grain or matrix supported), the percentage of mud and grains, and the sediments bound state at the time of deposition. The classification is used later in this section for comparison with the synthetic sandstones.

Figure 9.4 illustrates the cement distribution in both the natural and synthetic sandstones from this thesis. It is clear from Chapter 5 that the natural sandstones are grain supported.

Chapter 9 – Discussion, conclusions and future work

Sample AR01 shows evidence of pressure solution primarily cementing the sandstone together, with secondary hematite and clay cement (not shown in schematic). From the thin sections the hematite cement appears to form bridges between grains. Sample UT02 shows evidence of grain overgrowths as the primary cement. Hematite and calcite (not shown in schematic) are visible as the secondary cement. Sample HN11 shows evidence of grains touching and of clays cementing the grains together. Furthermore, the clay cement has an irregular distribution around the sand grains.

The cement distribution of the MICP and gypsum synthetically cemented sandstones are described in Chapter 7. Both methods of cementing synthetic sandstones produce matrix (cement) supported sandstones.

The MICP cement preferentially nucleates in ball like shapes. These cement balls act as the main point of contact cementing the sand grains together. Meanwhile, the gypsum cement forms a network of needle like crystals (with evidence of partial spherulites) which grow around the grains. From the X-CT results in Chapter 7 both cement types maintain high porosity and good permeability (porosity connectivity) regardless of the percentage of cement present.





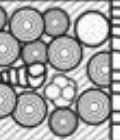

Depositional Texture Recognizable					Depositional Texture Not Recognizable (Subdivide according to classifications designed to bear on physical texture or diagenesis.)
Original Components Not Bound Together During Deposition			Grain-supported	Original components were bound together during deposition, as shown by intergrown skeletal matter, lamination contrary to gravity, or sediment-floored cavities that are roofed over by organic or questionably organic matter and are too large to be interstices.	
Contains mud (particles of clay and fine silt size, less than 20 microns)		Grain-supported			
Mud-supported	Grain-supported		Less than 10 percent mud		
Less than 10 percent grains	More than 10 percent grains	More than 10 percent mud			
Mudstone	Wackestone	Packstone	Grainstone	Boundstone	Crystalline Carbonate
					

Figure 9.3: Dunham classification of carbonate rocks (Dunham 1962). The synthetic sandstones produced in this study most closely resemble a wackestone or a packstone. The synthetic sandstones are cement supported with more than 10% grains present and between 7-27% cement.

Chapter 9 – Discussion, conclusions and future work

When comparing the synthetic sandstones (Figure 9.4) produced in this thesis to the natural sandstone cements (Figure 9.2) I believe that the gypsum cement more accurately reflects the even distribution of cement present in natural sandstones in comparison to MICP cement. As can be seen from Figure 9.2 natural cement tends not to form ‘ball’ like shapes (as seen in the MICP cemented sandstones) in nature. Future work would look at creating a method which might cause the bacteria to create an even coating around the sand grains. This would increase the points of contact and as a result could lead to increased strength of the sandstone.

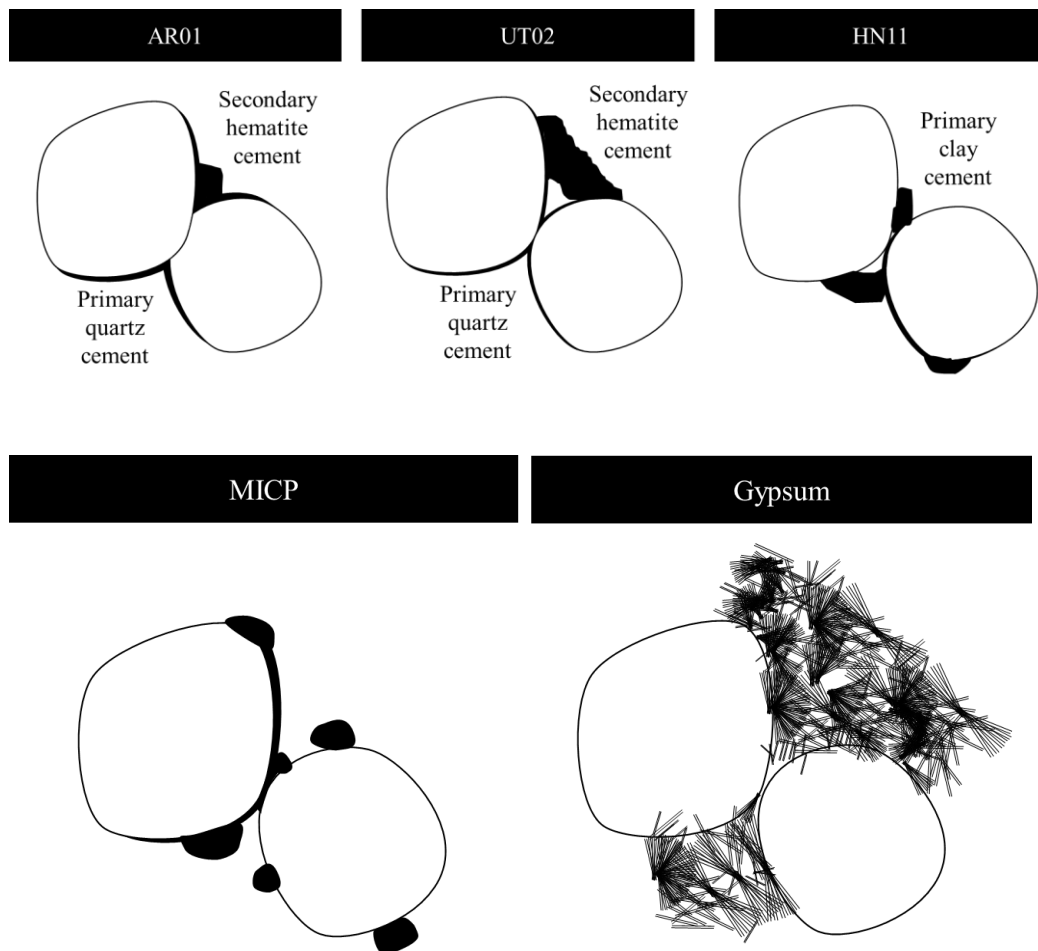


Figure 9.4: Schematic of the cement distribution observed in the natural and synthetic sandstones.

Each of the synthetic sandstones formed in this thesis contain more than 10% grains, are cement supported and are made from between 7-27% cement. In the absence of a silica sandstone classification scheme, I believe that the Dunham (1962)

classification of wackestone and packstone carbonates most closely resemble the cement distribution of the synthetic sandstones.

9.1.2 Timing of cementation in natural rocks

Timing of cement deposition is important as it helps to determine the diagenetic history of the sandstones. However, the timing of cement deposition in natural samples can be difficult to constrain. Table 9.1 summarises the properties of each of the deformation band samples.

For each sample the number of deformation periods is different. HN11 experiences one main deformation period meanwhile, in UT02 there are three deformation band forming periods (Chapter 3). Between the initial sediment deposition and these periods of deformation, the cement timing is poorly constrained. For the cements studied in this thesis I cannot be sure if the cement formed before or after deformation band formation. If the cements formed before deformation band formation their impact on reducing porosity in cataclastic structures will be relevant to band formation. Cementation tends to strengthen sandstone it is therefore likely that a larger force would be required to break the combination of grains and cement in sandstone bodies and form cataclastic deformation bands. Furthermore, as shown from the UCS studies (Chapter 8), increased cementation will reduce the likelihood of compaction taking place particularly at shallow depths.

In future studies of cement at other sites good data is required in order to better constrain the cement timing, the burial history and timing of fluid flow.

It is not possible to replicate the cementation process in the laboratory due to the length of time cementation takes in nature. However, it is possible to replicate the temperature and pressure in which cementation takes place. Table 9.1 highlights how variable each sandstone is. It is therefore recommended to build on the method from this thesis by creating further simplified synthetic sandstones.

Table 9.1: Summary of each field site with focus on the periods of potential deformation band formation, cement type, and porosity.

		1	2	3
Location		Great Britain	South Central Utah	Hungary
Field Area		Isle of Arran	Paradox Basin	Pannonian Basin
Age of sediments		299-271 Ma	180-140 Ma	21-19 Ma
Number of deformation band stages		2	3	1
Potential timing of DB formation	Stage 1	299-271 Ma	90-50 Ma (Laramide Orogeny)	21-19 Ma
	Stage 2	66-2.6 Ma	25-19 Ma	N/A
	Stage 3	N/A	15 Ma - present (Basin and Range formation)	N/A
Sample number		AR01	UT02	HN11
Mean host porosity (%)^a		14.03	17.46	10.55
Mean DB porosity (%)^b		2.00	1.56	1.40
Dominant cement type		Quartz	Quartz	Clays
Secondary cements		Hematite and clays	Hematite and calcite	N/A
Mean host cement (%)^a		7.60	15.43	19.98
Mean DB cement (%)^b		4.06	14.13	10.09
Level of cementation		Well cemented	Well cemented	Poorly cemented
Type of deformation band		Cataclastic	Cataclastic	Cataclastic

^a Mean host cement and porosity calculated from five X-CT sub-volumes in the host rock. See Chapter 5 for full results.

^b Mean DB cement porosity calculated from five X-CT sub-volumes in the DB.

9.1.3 Comparing synthetic rocks to real rocks

It is clear from the results of this thesis that synthetic rocks can be manufactured to reproduce the cement volume and distribution comparable to those seen in natural sandstones. This section compares the sub-volume grain, cement and porosity results

from the synthetically formed sandstones to those from the deformation band samples, analyses the mechanics and discusses the use and implications for synthetic sandstones.

9.1.3.1 Phase analysis

Across both natural and synthetic sandstones three phases (grains, cement and porosity) are segmented from the X-CT data for comparison. Table 9.2 summarises the percentage of phases present in each sample.

In the natural sandstones there is a larger percentage of grains (lower porosity) than in the synthetic sandstone samples. The porosity is approximately 4x higher in synthetic sandstones than natural sandstones. One explanation for this is that the sandstones were formed at higher confining pressures, therefore the grains were forced closer together than they were in the laboratory (more grains are packed into the same volume than in the synthetic sandstones). As mentioned previously it is likely the naturally formed sandstones were subjected to higher confining pressures. It is these higher confining pressures which are likely to have squeezed the grains together and therefore reduced the available pore space. As a result, neither of the synthetic sandstone samples replicate the pore distribution found in natural sandstones. Furthermore, in the case of UT02 and AR01 the grain phase segmented from the X-CT data will include the quartz cement. This will produce an inaccurate grain percentage.

The percentage of cement present was lowest in the MICP cemented sandstones. The percentage of cement in the gypsum cemented sandstones and natural sandstones is comparable. Although there are differences between their physical appearance and their distribution around the grains, the gypsum cemented sandstones most closely replicate the cement volumes found in the naturally formed sandstones analysed in Chapter 5.

The high initial porosity in the synthetic sandstones and the high confining pressure during triaxial testing could be used to explain why the gypsum samples displayed plastic deformation behaviour, never reached peak stress or formed deformation bands in the triaxial experiments.

The porosity connectivity is comparable in samples UT02, AR01 and the gypsum/MICP cemented sandstones. However, in sample HN11 the porosity is disconnected. A possible reason for this is because the sample is cemented with clay. Due to the nature of clay distribution between grain to grain contacts it is possible that the clay is isolating the pores (Figure 9.2).

One main issue with the porosity measurements achieved with this study is the majority have been calculated not measured. It would be recommended for future work that the porosity of all these samples is measured to enable the calculated results to be verified. Possible methods of measuring pore space in rocks include mercury intrusion porosimetry (MIP), gas adsorption and nuclear magnetic resonance (NMR).

9.1.3.2 Phase distribution

Cementing processes affects the cement distribution. Figure 9.5 visually summarises the cement distribution and connectivity across all natural and synthetic sandstones. In the host rock of the natural sandstones the cement is connected. The gypsum cemented sandstones show that almost all cement is connected, meanwhile the MICP cemented sandstones show variable levels of cement connectivity. This confirms the observations from Chapter 7 that the gypsum cement distribution is most similar to natural sandstones (excluding deformation bands) in comparison to the MICP cemented sandstones.

In addition, the connectivity of the cement in the gypsum cemented sandstone replicates the connectivity of the cement in all natural samples UT02, HN11 and AR01 (Table 9.3). However, considering the cementing phase imaged in UT02 and AR01 is a secondary cement (e.g. not quartz) it is possible that the synthetic samples do not replicate the primary phase.

The burial history will be more complex in real rocks. This impacts the type and distribution of cement present. As a result of compaction and cementation the initial porosity of natural sandstones before cementation will be much lower than in synthetic sandstones. With increased burial depth the type of deformation band

Chapter 9 – Discussion, conclusions and future work

formed can change from disaggregation to cataclastic (Section 2.3.2). However, there are lots of other factors (including mineralogy, lithification, confining pressure, grain size and shape) which control deformation band formation.

Overall, there are a lack of studies which show repeat formation and analysis of synthetically cemented sandstones. The results from this study have shown that even in a simplified system it remains difficult to accurately constrain all variables.

Table 9.2: Summary of grain, cement and porosity phases from X-CT analysis of naturally formed sandstones, gypsum cemented sandstones, and MICP cemented sandstones.

	Sample	Grains (%)	Cement (%)	Porosity (%)
Sandstone	UT02	74.54	17.11	8.35
	HN11	77.07	16.79	6.15
	AR01	84.91	7.67	9.06
Gypsum	10	50.8	13	36.2
	15	56.4	11.2	32.4
	20	50.3	18.8	30.8
	25	44.6	22.5	32.9
MICP	120	57.9	2.3	39.8
	160	55	7.1	37.9
	200	52.5	17	31.5

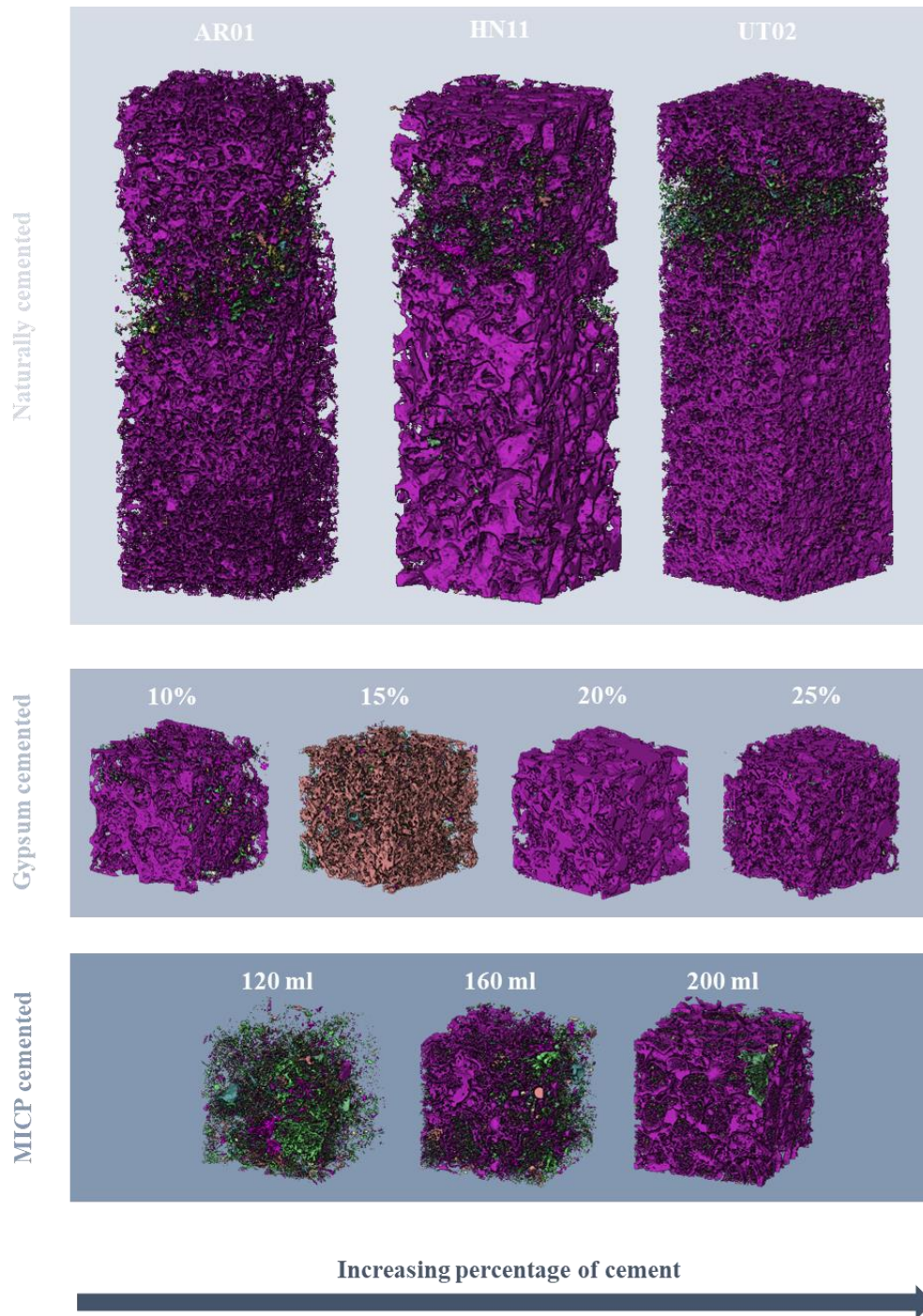


Figure 9.5: Summary diagram of 3D analysis showing the location of cement in real and synthetic rocks from this thesis.

Table 9.3: Summary of cement and porosity connectivity for natural sandstone, gypsum and MICP cemented synthetic sandstones.

Sample	Cementing material analysed	Cement	Porosity
UT02	Haematite and calcite	Majority connected	Majority connected in host rock Disconnected inside DB
HN11	Clay	Connected	Disconnected
AR01	Haematite and clays	Majority connected	Connected in host rock Disconnected inside DB
Gypsum cemented sandstones	Gypsum	Connected	Connected
MICP cemented sandstones	Calcite	Disconnected	Connected

9.1.3.3 Mechanics of real and synthetic rocks

From the research in this thesis it is clear that the synthetic rocks have sensible mechanics (they produce similar results from previous synthetic sandstone shear box and UCS tests- see Chapter 8). Although the synthetic sandstones are not as strong as natural sandstones, the MICP and gypsum cement increase the strength of the unconsolidated sands.

Figure 9.6 plots the maximum and ultimate shear stress for all synthetic sandstone shear experiments. For all samples, as normal stress increases the maximum and

Chapter 9 – Discussion, conclusions and future work

ultimate shear stress also increase. For the MICP cemented sandstones the shear stress increases as the weight percentage of calcite present increases. However, for the gypsum cemented sandstones this trend is not as clear. There appears to be very little difference between the shear stress of a sandstone cemented with 20 and 25% gypsum.

Figure 9.7 is reproduced from Chapter 8. Here the cement content of each of the MICP and gypsum cemented samples are plotted against their UCS and respective porosities. The gypsum cemented sandstones show that as gypsum content increases so does UCS. The MICP cemented sandstones do not show as clear a trend. Instead they have been grouped into approximate zones (grey dashed circles). The zones show the 160 and 200 ml feeds overlapping.

Figure 9.8 is the results of the triaxial testing on the gypsum cemented sandstones (reproduced from Chapter 8). For each of these tests the differential stress increases as the confining pressure increases regardless of the percentage of cement present in each sample.

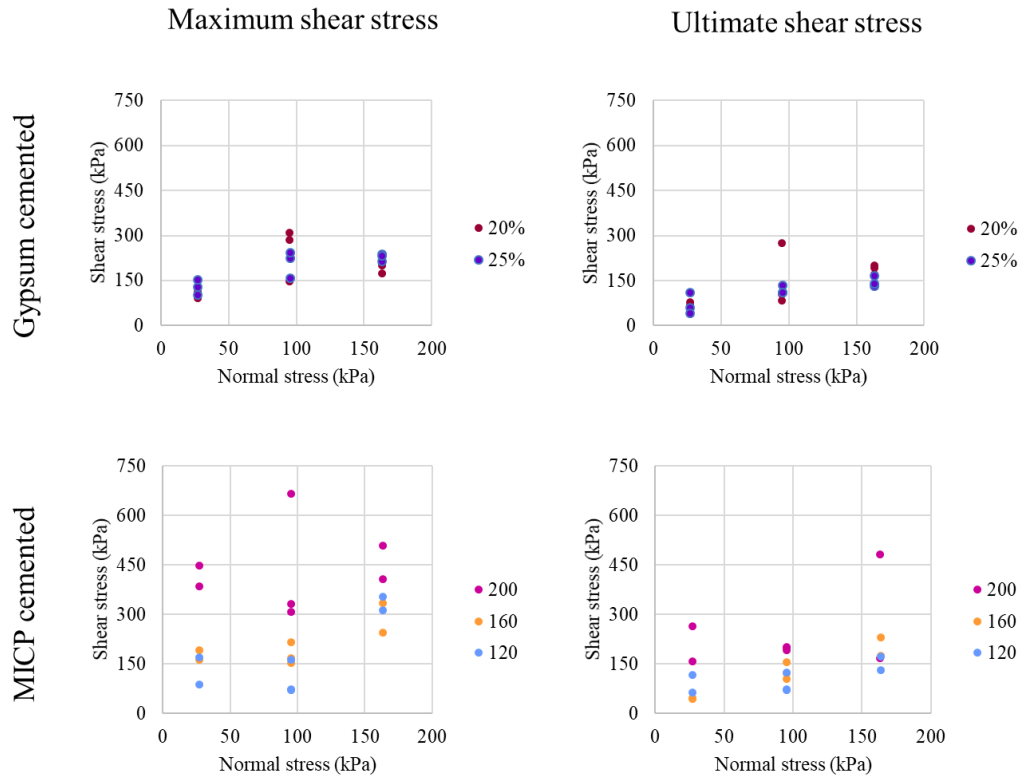


Figure 9.6: Summary of maximum and ultimate shear stress results for gypsum and MICP cemented sandstones. Each plotted dot represents a synthetic sandstone sample. On the top row the maximum and ultimate shear stress results are plotted for gypsum cemented sandstones (20 and 25% volume cement). On the bottom row the maximum and ultimate shear stress results are plotted for the MICP cemented sandstones (120, 160 and 200ml feed).

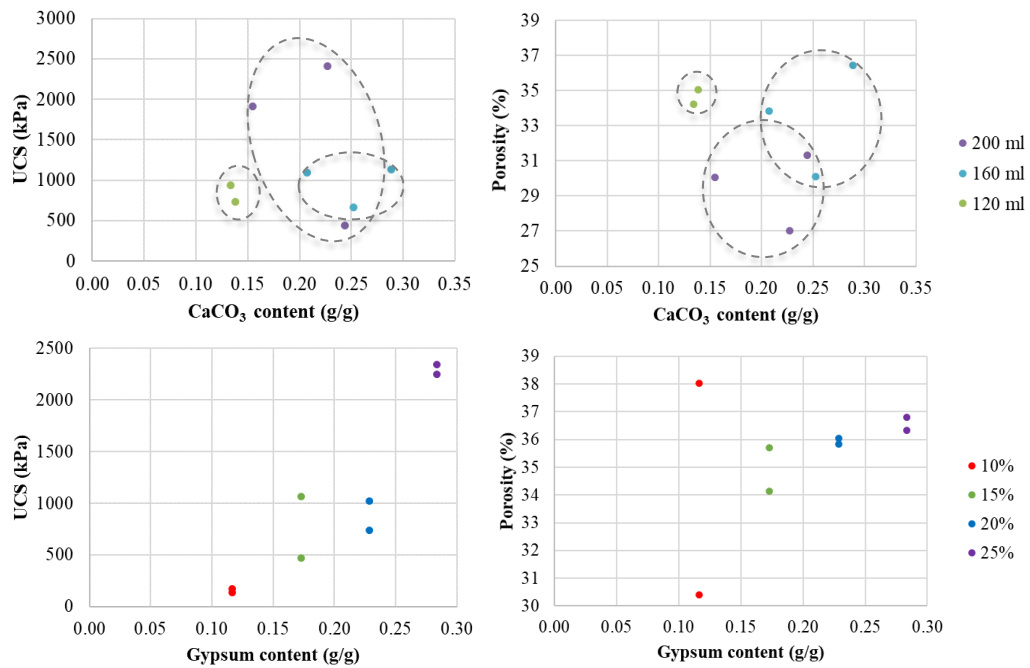


Figure 9.7: UCS and porosity (%) measurements from both MICP and gypsum cemented sandstones. Each plotted dot represents a synthetic sandstone sample.

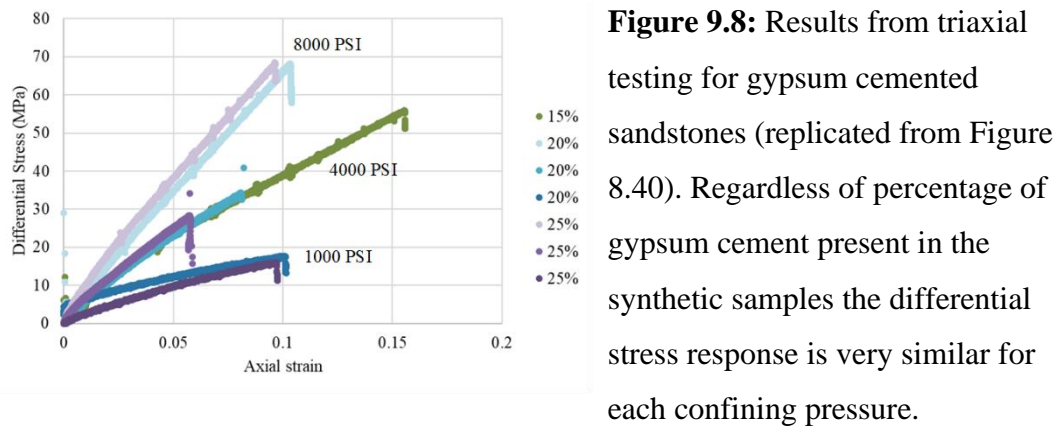


Figure 9.8: Results from triaxial testing for gypsum cemented sandstones (replicated from Figure 8.40). Regardless of percentage of gypsum cement present in the synthetic samples the differential stress response is very similar for each confining pressure.

For each of the geomechanical tests performed in this thesis (Chapter 8) the MICP cemented synthetic sandstones are both stronger and more permeable than gypsum cemented samples. The strength reflects calcite’s mineral properties (Table 9.4). Table 9.4 shows that calcite has a higher shear modulus and Mohs hardness than gypsum. Both the MICP and gypsum cemented sandstone show excellent porosity connectivity (Chapter 8). However, it is possible that the crystal network created by the gypsum cement will reduce the overall permeability of the sandstones in

comparison to the MICP cemented sandstones. The difference in permeability could alter the use of the synthetic sandstones.

Table 9.4: Moduli of selected minerals used in this study. Data compiled from Katahara (1996); Stretton et al. (1997); Henderson and Henderson (2009); Plachý et al. (2011); Brantut et al. (2012); Zhang (2017) .

Mineral	Density ρ (g cm⁻³)	Mohs hardness	Shear modulus μ (GPa)	Poisson's ratio σ
Quartz	2.65	7	44.7	0.07
Gypsum	2.32	2	16	0.25-0.35
Calcite	2.71	3	30.3	0.31
Feldspar (plagioclase - albite)	2.63	6	25.6	0.35
Feldspar (orthoclase)	2.57	6	27.3	-
Haematite	5.24	5	95	-
Kaolinite	2.52	2	31.8	0.26
Illite	2.79	1	31.7	0.248

Interestingly, the trend for the gypsum cemented samples shows that as the cement content increases so does the UCS and shear strength increase (Table 9.5). However, during triaxial experimentation there is no difference between the strength of samples. This is likely to be due to the confining pressure exerted during the triaxial deformation, suggesting at higher confining pressures, varying the percentage of cement present has no impact on the strength of the sandstone.

There is no doubt that the distribution of cement affects the mechanical properties of the resulting rock. However, with the small number of samples studied it is not a statistically significant pool of data to test this theory on. With the increasing number of studies on poorly consolidated sandstones and studies that use X-CT as a method to characterise the samples it would be beneficial for the deformation band community to record the impact of cement (and other variables) in future work.

Table 9.5: Summary describing the effects of increasing cement volume on the mechanical deformation of synthetic sandstones. Reproduced from Chapter 8.

Experimental technique	↑Gypsum	↑MICP
Shear box	Shows overall increase in shear strength as cement volume increases. However, the trend it is not clearly defined.	Shear strength increases as cement volume increases.
UCS	Compressive strength increases as cement volume increases.	Shows an overall increase in compressive strength as the CaCO ₃ content increases. However, the trend is not clearly defined.
Triaxial	No variation in differential stress. Instead the differential stress of the samples is controlled by the confining pressure.	N/A

9.1.3.4 Use of synthetic rocks

As discussed in Chapter 2 cements are being increasingly used to reduce soil erosion (Li et al. 2018), seal fractures (MacLachlan 2017; Minto et al. 2017) and improve slope stability (Salifu et al. 2016; Khaleghi and Rowshanzamir 2019). The majority of synthetic sandstone applications use MICP as a cementing agent. As demonstrated in Chapter 8 MICP cemented sandstones produce stronger rocks than gypsum cemented sandstones. Although the gypsum cemented sandstones display a cement volume and distribution most similar to natural rocks, the shear strength of the MICP cemented samples are more in line with natural sandstones. Because of this further work should look at characterising the size and dimension of the calcite balls created

by MICP cementation in relation to the urease activity and volume of feed applied to the samples. By improving the distribution of the cement around the sand grains there would be an increase in the number of contact points between grains, and this in turn would lead to a stronger synthetic sandstone. Developing MICP cementation methods with a range of strengths would enable MICP to be ‘tailor-made’ for a range of cementation applications (e.g. slope stability or fracture sealing).

9.1.3.5 Implications for synthetic sandstones

There is an increasing body of research in geotechnics aimed at cementing materials in situ to make them stronger. This thesis does not consider how the cementing techniques could be upscaled or the durability of the synthetic sandstones they produce, rather it focuses on how the microscale of the cement production can be characterised. However, there are some preliminary conclusions that can be drawn from this work that are relevant to considering how the methods can be upscaled and then their durability over time. For example, I speculate that gypsum cement would be better at stabilising sand grains in seismically active environments than MICP cement. This is because of the plastic response recorded during the triaxial deformation of the gypsum cemented sandstones.

Results from this thesis shows that the concentration of cement affects the shear strength of the MICP samples the most (Figure 9.6). In Figure 9.6 the MICP feeds display a wider range of shear stresses. The compressive strength of the gypsum samples is affected more by the concentration of cement than the MICP samples due to the composition and distribution of the cement present. Meanwhile, the triaxial experiments are completely unaffected by the percentage of cement present in each gypsum sample. It would therefore be interesting to test a MICP cemented sandstone in the triaxial rig to see if this result achieved is the same as the gypsum samples.

However, this thesis only looks at two methods of cementing sand, and it is worthwhile considering that there are other methods of cementing sandstones (e.g. colloidal silica) which are also currently being researched.

9.1.4 Heterogeneity

Across this thesis it has been important to consider the impact of sample heterogeneity. In order to overcome the issue of heterogeneities, ideally lots of well-characterised samples are required. However, it is difficult to reproduce identical synthetic sandstones in the laboratory using the procedures outlined in this thesis.

Natural deformation bands are heterogenous along-strike at the mm-scale. The host sandstones are also heterogenous. However, along-strike heterogeneity in the bands can occur even when there is no obvious visible sedimentological heterogeneity. One hypothesis might be that the variation in grain, cement properties and distribution produce heterogeneity in the bands. This is proven by Torabi and Fossen (2009) who show that porosity can vary by up to 18% in a deformation band.

Artificial sandstones do have heterogeneity in grain scale properties similar to real sandstones: for example, the localised variation in cement and porosity. Therefore, the mechanical properties of the artificial sandstones do depend on their heterogeneity.

The results from the mechanical testing are shown in Table 9.5. This mechanical results summary shows that although there is an overall trend that the shear and compressive strength of the synthetic sandstone increases as the percentage of cement increases, this is variable for each technique. It is possible that other variables (e.g. confining pressure) have a greater impact on the strength of the samples.

This shows that regardless of the attempt made to simplify the sandstones, localised variations in the synthetic sandstones can have a large impact on the properties of the sandstones. Therefore, the mechanical properties of real sandstone should be expected to be a function of the small-scale variability in properties, therefore producing variability in deformation band properties.

9.1.4.1 Synthetic rocks are realistic and controllable

Chapter 6 investigates the kinetics of the calcium sulphate phases. This chapter formed as a side project which complimented and gave a background to the chemistry of the gypsum cement. The chapter shows that gypsum cementation (mineral phase and solubility) is highly temperature dependent. At temperatures

Chapter 9 – Discussion, conclusions and future work

above ~40°C gypsum becomes unstable and above ~105°C basanite becomes unstable. This therefore means if gypsum is being used to create synthetic sandstones the calcium sulphate phase can change depending on the temperature it is formed at. For example, in lower latitudes and at depth, temperatures of 40°C are not improbable. Therefore, until the chemistry of gypsum as a grain cement have been characterised further it would not be recommended to use this as a cement in arid or deep environments.

Chapter 6 also gives an insight into the growth of the gypsum after hydrating basanite. Here the original calcination temperature seems to control the size of the gypsum crystals formed. Furthermore, how the gypsum crystals attach to the sand grains is not quite clear. It appears that the gypsum crystals form networks of crystals in the pore spaces between the sand grains. It is this network which holds the sand grains in place and defines the strength of the sandstone.

9.1.4.2 Characterisation of samples

X-CT analysis has played a large role in the analysis carried out in this thesis. In this section I look at the impact of imaging, resolution and developing methodology.

9.1.4.2.1 Imaging

X-CT/Avizo[®] analysis segments an image based on the density of the minerals present. For both the Utah and Arran samples the grains and cement were made of silica (quartz) making it challenging to accurately segment the cement and grains for these samples: there is a chance that the grey scale values overlap between the quartz grains and quartz cement. This thesis focussed instead on the secondary cements (haematite, clays and calcite) in both Utah and Arran samples. However, as quartz is the most common sandstone cementing phase a method of analysis to differentiate the two types of quartz (grains vs cement) would be required for future studies.

It is possible that quartz cements (authigenic quartz) could be differentiated from the quartz grains by their shape. It is therefore possible that the application of Weka algorithm (as seen applied to gypsum cemented sandstones in Chapter 6) could be trained to see the difference in shape between the quartz grains and the quartz

cement. However, this may become complicated in deformation band zones where the quartz grains have been broken up and no longer resemble ‘grain-like’ shape.

A second option is that quartz grains and overgrowths can be differentiated using scanning electron microscopy-cathodoluminescence (SEM-CL) (Milliken et al. 2005; Goldstein and Rossi 2007; French 2012). It is therefore possible that SM-CL analysis of the samples could allow for 2D area calculations of the percentage of quartz grains vs authigenic quartz present in each sample. This is not as robust a method as 3D analysis however, it would provide an approximation for further work. Furthermore, it is possible that by quantitatively analysing the percentage of intergranular quartz present that the burial depths can be estimated (Milliken et al. 2005).

Grain size distribution was carried out using 2D analysis. This is a 2D slice through a 3D object. Although microscopy is accepted as a cost-effective technique in measuring grain size other methods for measuring grain size distribution can be used. These include sieving, electron microscopy, sediment suspension and grain imaging. For future studies an Avizo[®] code to separate grains via labelling inside the deformation bands would be useful (see section 3.8.5). This would allow the longest grain axis to be measured using X-CT scans in 3D.

9.4.2.2 Resolution

Across this thesis the most complex sections to scan and analyse have been the finer details (e.g. the gypsum cement and the cataclastic deformation bands). The resolution of each X-CT scan is directly linked to the scanned sample size. The main causes of error are the sample size and the segmentation of the sample phases (e.g. grains, cement and porosity). These sources of error could be reduced if the resolution of each scan was improved.

One method of achieving better resolution would be to image the samples in a synchrotron X-CT. The maximum sample size of experimental synchrotron work is 4 x 4 x 30mm (Zambrano et al., 2017). This is a larger volume than the samples scanned in this thesis.

It may be easiest to characterise deformation bands if they are physically separated from the host rock prior to analysis, decreasing the sample size to improve the scan

resolution. However, by separating the bands from the host rock the transition zone between the host rock and deformation band is lost. I believe that there remains a lot more work to be done in understanding the properties of this transition zone. This may help to understand the mechanical evolution of deformation bands in more detail.

However, a balance should be found between imaging the bands and displaying a representative elementary volume (REV) of the outcrop features. The initial reason deformation bands have come to the forefront is due to their potential to act as a baffle or barrier on large sandstone reservoirs (Edwards et al. 1993; Ogilvie and Glover 2001), the possibility that they could be formed due to seismic events (Cashman et al., 2007) and therefore their presence could be inferred as an indicator of previous seismic events (Shipton et al. 2017).

Despite their small width dimensions, deformation bands can be 10's of metres long (Fossen et al. 2007; Tembe et al. 2008). It is therefore important that whilst analysing and understanding the mechanisms that are taking place on the sub cm scale are important (for overall understanding and for numerical modelling), it is also important that the results can be upscaled to full outcrops.

9.4.2.3 Developing methodology

Throughout the X-CT work in this thesis it has become clear that current X-CT studies lack a constrained methodology for analysing multiple samples. Two of the area which a methodology could be applied to is segmentation and sub-volume analysis.

In this thesis, initial segmentation is manual (e.g. selecting the pixels for each phase) and is therefore user dependent. It is possible that one interpretation of how the sample should be segmented will differ depending on the individual's preferences (Andrews et al. 2019). This can also account for error between segmented samples and therefore a variation in cement and porosity values. As described in Chapter 3, segmentation takes place by assigning a label to each pixel based on the pixel's grey scale value. Ideally a method (or automated program) should be developed which can accurately segment samples by taking into consideration the individual scan

parameters, the larger shapes of the phases in the sample and the individual pixels. Therefore, picking out phase shapes and density. This would therefore improve the segmentation process by speeding it up and allowing more samples to be analysed in a shorter period. For example image analysis such as those used in Kilian et al. (2011).

The majority of studies to date have used singular sub-volumes in their studies to illustrate the porosity distribution and connectivity in rocks (Zambrano et al. 2017). A more detailed statistical approach should be applied to the sub-volume sampling technique to produce more robust data. This could include multiple sub-volume samples or an algorithm which automatically samples every $x \mu\text{m}$.

9.2 Conclusions and Future work

- *The location of cement effects the cement connectivity.*

Sample HN11 display clay cemented and it is as a result of the disconnected structure of the clay cement (see Figure 9.2) that isolated pores are created. Furthermore, the type of cement in the synthetic sandstones controls the cement distribution e.g. the MICP cement forms in unconnected balls, whereas the gypsum cement forms a connected crystal network. Future work would look at investigating the impact of a wider range of cements on sandstone.

- *Cement distribution controls the permeability of the sandstones.*

The connectivity of the cements is controlled by the cement distribution, which in turn controls the permeability of the sandstones. In the case of the synthetic sandstones the permeability of the sample could determine the use of the synthetic sandstone in the future and what their potential applications may be (e.g. grout, reducing porosity of a sandstone).

Synthetic sandstones can be made from both gypsum and MICP cement. Although their properties and distribution can be comparable to real sandstone the structure of the cements do not imitate the structures of real cement.

Future work would look at investigating the effect of flushing more than one cementing fluid through a sand and map the interaction between the two cements.

This could begin to create the multiphase cements which can be seen in natural sandstones and might result in consistently stringer or less easy to weather synthetic sandstones.

- ***The strength of sands are improved when cemented with either gypsum or MICP.***

There is no doubt from the mechanical tests in Chapter 8 that the strength of the sands are improved when cemented with gypsum or MICP. However, the methods in which they were tested could have been improved by reducing the number of errors created due to sample shape or size, and by increasing the number of repeats.

There are limited studies which display the micro-structures of deformation in unconsolidated materials as deformation takes place. The majority of studies are used to compare the end members of deformation but not the stages between.

Furthermore, there is limited field evidence which shows the micro-structures of deformation in unconsolidated materials (at least at the time of deformation).

Therefore, 4D X-CT experiments are ideal for analysing deformation within these sediments as they are forming in the lab.

- ***Grain crushing can take place during shear box and UCS testing of synthetically cemented sandstones.***

The confining pressures used during shear box tests equalled up to ~9.62 m depth.

This therefore suggests that weakly cemented sandstones can undergo grain crushing at shallow burial depths. By imaging synthetic samples before and after deformation using the X-CT it will be possible to analyse the grains fracture patterns in 3D.

- ***In order to try and form deformation bands in the laboratory there are several factors which should be investigated. These include the porosity of the sample, the distribution of the cement between the grains, the confining pressures used and the strain rate of the experiment.***

This thesis was unsuccessful in forming deformation bands in the laboratory.

However, I speculate that deformation band formation may be possible by investigating the variables listed above.

- X-CT analysis can be used to approximate the percentage of phases present in natural or synthetic sandstones.

In this thesis segmentation is carried out on the sandstone samples by grouping all cementing phases together. Developing this methodology going forward there should be a way to isolate the types and phases of cement present in each sandstone sample. In order to update this methodology numerous sandstones of varying compositions and periods of cementation would need to be analysed. This would be a lengthy process and would consist of a database which multiple scientists could input their results.

References

- Abriel, W., Reisdorf, K., and Pannetier, J. (1990) Dehydration reactions of gypsum: A neutron and X-ray diffraction study. *Journal of Solid State Chemistry*, 85, 23–30.
- Acar, Y.B., and El-Tahir, E.A. (1986) Low Strain Dynamic Properties of Artificially Cemented Sand. *Journal of Geotechnical Engineering*, 112, 1001–1015.
- Achal, V., Mukherjee, A., Kumari, D., and Zhang, Q. (2015) Biomineralization for sustainable construction – A review of processes and applications. *Earth-Science Reviews*, 148, 1–17.
- Adrien, J., Meille, S., Tadier, S., Maire, E., and Sasaki, L. (2016) In-situ X-ray tomographic monitoring of gypsum plaster setting. *Cement and Concrete Research*, 82, 107–116.
- Agung, M.W., Sassa, K., Fukuoka, H., and Wang, G. (2004) Evolution of Shear-Zone Structure in Undrained Ring-Shear Tests. *Landslides*, 1.
- Al Qabany, A., Soga, K., and Santamarina, C. (2012) Factors Affecting Efficiency of Microbially Induced Calcite Precipitation. *Journal of Geotechnical and Geoenvironmental Engineering*, 138, 992–1001.
- Alikarami, R., Andò, E., Gkiousas-Kapnisis, M., Torabi, A., and Viggiani, G. (2014) Strain localisation and grain breakage in sand under shearing at high mean stress: insights from in situ X-ray tomography. *Acta Geotechnica*, 10, 15–30.
- Almossawi, H.I.H. (1988) Physical Properties of Synthetic Sandstone Rocks1. *Geophysical Prospecting*, 36, 689–699.
- Alshibli, K.A., and Alramahi, B.A. (2006) Microscopic Evaluation of Strain Distribution in Granular Materials during Shear. *Journal of Geotechnical and Geoenvironmental Engineering*, 132, 80–91.
- Alshibli, K.A., and Sture, S. (2000) Shear Band Formation in Plane Strain Experiments of Sand. *Journal of Geotechnical and Geoenvironmental Engineering*, 126, 495–503.
- Al-Tahini, A.M., Sondergeld, C.H., and Rai, C.S. (2006) The effect of cementation on the mechanical properties of sandstones. *SPE Reservoir Evaluation and Engineering*, 9, 308–316.

References

- Amathieu, L., and Boistelle, R. (1988) Crystallization kinetics of gypsum from dense suspension of hemihydrate in water. *Journal of Crystal Growth*, 88, 183–192.
- Anbu, P., Kang, C.-H., Shin, Y.-J., and So, J.-S. (2016) Formations of calcium carbonate minerals by bacteria and its multiple applications. *SpringerPlus*, 5, 250.
- Ando, E. (2013) Experimental investigation of microstructural changes in deforming granular media using x-ray tomography. *Université Grenoble Alpes*.
- Andò, E., Viggiani, G., Hall, S.A., and Desrues, J. (2015) Experimental micro-mechanics of granular media studied by x-ray tomography: recent results and challenges. *Géotechnique Letters*.
- Andrews, B., Roberts, J., Shipton, Z., Bigi, S., Chiara Tartarello, M., and Johnson, G. (2019) How do we see fractures? Quantifying subjective bias in fracture data collection. *Solid Earth*, 10, 487–516.
- Antonellini, M., Aydin, A., Pollard, D.D., and D’Onfro, P. (1994) Petrophysical study of faults in sandstone using petrographic image analysis and X-ray computerized tomography. *Pure and Applied Geophysics PAGEOPH*, 143, 181–201.
- Arns, C.H., Knackstedt, M.A., Pinczewski, W.V., and Garboczi, E.J. (2002) Computation of linear elastic properties from microtomographic images: Methodology and agreement between theory and experiment. *Geophysics*, 67, 1396–1405.
- Asaei, H., and Moosavi, M. (2013) Experimental measurement of compressibility coefficients of synthetic sandstone in hydrostatic conditions. *Journal of Geophysics and Engineering*, 10.
- ASTM Standard D7012 – 14e1 (2017) Standard Test Methods for Compressive Strength and Elastic Moduli of Intact Rock Core Specimens under Varying States of Stress and, 1–9 p. West Conshohocken, PA.
- Atkin, S.&, and Kovscek, A.R. (2003) Computed tomography in petroleum engineering research. In *Applications of X-ray Computed Tomography in the Geosciences* pp. 23–38.
- Aydin, A. (1978) Small faults formed as deformation bands in sandstone. *Pure and Applied Geophysics PAGEOPH*, 116, 913–930.
- Aydin, A., and Johnson, A.M. (1978) Development of faults as zones of deformation bands and as slip surfaces in sandstone. *Pure and Applied Geophysics PAGEOPH*, 116, 931–942.

References

- Aydin, A., Borja, R.I., and Eichhubl, P. (2006) Geological and mathematical framework for failure modes in granular rock. *Journal of Structural Geology*, 28, 83–98.
- Balázs, A., Matenco, L., Magyar, I., Horváth, F., and Cloetingh, S. (2016) The link between tectonics and sedimentation in back-arc basins: New genetic constraints from the analysis of the Pannonian Basin. *Tectonics*, 35, 1526–1559.
- Ballas, G., Soliva, R., Sizun, J.P., Benedicto, A., Cavailhes, T., and Raynaud, S. (2012) The importance of the degree of cataclasis in shear bands for fluid flow in porous sandstone Provence, France. *AAPG Bulletin*, 96, 2167–2186.
- Ballas, G., Soliva, R., Sizun, J.P., Fossen, H., Benedicto, A., and Skurtveit, E. (2013) Shear-enhanced compaction bands formed at shallow burial conditions; implications for fluid flow (Provence, France). *Journal of Structural Geology*, 47, 3–15.
- Ballirano, P., and Melis, E. (2009) Thermal behaviour and kinetics of dehydration of gypsum in air from in situ real-time laboratory parallel-beam X-ray powder diffraction. *Physics and Chemistry of Minerals*, 36, 391–402.
- Balsamo, F., and Storti, F. (2010a) Grain size and permeability evolution of soft-sediment extensional sub-seismic and seismic fault zones in high-porosity sediments from the Croton basin, southern Apennines, Italy. *Marine and Petroleum Geology*, 27, 822–837.
- Balsamo, F., and Storti, F. (2010b) Size-dependent comminution, tectonic mixing, and sealing behavior of a “structurally oversimplified” fault zone in poorly lithified sands: Evidence for a coseismic rupture? *Geological Society of America Bulletin*, 123, 601–619.
- Baud, P., Klein, E., and Wong, T. (2004) Compaction localization in porous sandstones: spatial evolution of damage and acoustic emission activity. *Journal of Structural Geology*, 26, 603–624.
- Beaudoin, N., Hamilton, A., Koehn, D., Shipton, Z.K., and Kelka, U. (2018) Reaction-induced porosity fingering: Replacement dynamic and porosity evolution in the KBr-KCl system. *Geochimica et Cosmochimica Acta*, 232, 163–180.
- Beke, B., Fodor, L., Millar, L., and Petrik, A. (2019) Deformation band formation as a function of progressive burial: Depth calibration and mechanism change in the Pannonian Basin (Hungary). *Marine and Petroleum Geology*, 105, 1–16.

References

- Bendle, J.M., Palmer, A.P., and Carr, S.J. (2015) A comparison of micro-CT and thin section analysis of Lateglacial glaciolacustrine varves from Glen Roy, Scotland. *Quaternary Science Reviews*, 114, 61–77.
- Bera, B., Mitra, S.K., and Vick, D. (2011) Understanding the micro structure of Berea Sandstone by the simultaneous use of micro-computed tomography (micro-CT) and focused ion beam-scanning electron microscopy (FIB-SEM). *Micron* (Oxford, England : 1993), 42, 412–8.
- Bernardi, D., DeJong, J.T., Montoya, B.M., and Martinez, B.C. (2014) Bio-bricks: Biologically cemented sandstone bricks. *Construction and Building Materials*, 55, 462–469.
- Berthold, C., Presser, V., Huber, N., and Nickel, K.G. (2011) 1 + 1 = 3: Coupling μ -XRD2 and DTA New insights in temperature-dependent phase transitions. *Journal of Thermal Analysis and Calorimetry*, 103, 917–923.
- Bezou, C., Nonat, A., Mutin, J.-C., Christensen, A.N., and Lehmann, M.S. (1995) Investigation of the Crystal Structure of γ -CaSO₄, CaSO₄ · 0.5 H₂O, and CaSO₄ · 0.6 H₂O by Powder Diffraction Methods. *Journal of Solid State Chemistry*, 117, 165–176.
- Bock, E. (1961) On the solubility of anhydrous calcium sulphate and of gypsum in concentrated solutions of sodium chloride at 25 °C, 30 °C, 40 °C, and 50 °C. *Canadian Journal of Chemistry*, 39, 1746–1751.
- Borja, R.I., Song, X., Rechenmacher, A.L., Abedi, S., and Wu, W. (2013) Shear band in sand with spatially varying density. *Journal of the Mechanics and Physics of Solids*, 61, 219–234.
- Bossennec, C., Géraud, Y., Moretti, I., Mattioni, L., and Stemmelen, D. (2018) Pore network properties of sandstones in a fault damage zone. *Journal of Structural Geology*, 110, 24–44.
- Brantut, N., Schubnel, A., David, E.C., Héripré, E., Guéguen, Y., and Dimanov, A. (2012) Dehydration-induced damage and deformation in gypsum and implications for subduction zone processes. *Journal of Geophysical Research: Solid Earth*, 117.
- Bright, A. (2006) Deformation Band Fault Core: Character, Evolution and Influence on Bulk Fluid Flow. University of Dublin.
- Brok, S. den, David, C., and Bernabé, Y. (1997) Preparation of synthetic sandstones with variable cementation for studying the physical properties of granular rocks. *Comptes Rendus de l'Académie des Sciences - Series IIA - Earth and Planetary Science*, 325, 487–492.

References

- Bruno, M.S., and Nelson, R.B. (1991) Microstructural analysis of the inelastic behavior of sedimentary rock. *Mechanics of Materials*, 12, 95–118.
- Busch, B., Hilgers, C., Gronen, L., and Adelman, D. (2017) Cementation and structural diagenesis of fluvio-aeolian Rotliegend sandstones, northern England. *Journal of the Geological Society*, 174, 855–868.
- Canakci, H., Sidik, W., and Halil Kilic, I. (2015) Effect of bacterial calcium carbonate precipitation on compressibility and shear strength of organic soil. *Soils and Foundations*, 55, 1211–1221.
- Carbone, M., Ballirano, P., and Caminiti, R. (2008) Kinetics of gypsum dehydration at reduced pressure: an energy dispersive X-ray diffraction study. *European Journal of Mineralogy*, 20, 621–627.
- Cashman, S., and Cashman, K. (2000) Cataclasis and deformation-band formation in unconsolidated marine terrace sand, Humboldt County, California. *Geology*, 28, 111–114.
- Cavailhes, T., Soliva, R., Benedicto, A., Loggia, D., and Schultz, Richard Wibberley, C. (2009) Are cataclastic shear bands fluid barriers or capillarity conduits? Insight from the analysis of redox fronts in porous sandstones from Provence, France. In *European Association of Geoscientists and Engineers: Fault and Top Seal conference*. Montpellier.
- Chaney, R.C., Slonim, S.M., and Slonim, S.S. (1982) Determination of Calcium Carbonate Content in Soils. *Geotechnical Properties, Behavior, and Performance of Calcareous Soils*, ASTM STP 7, 3–15.
- Chang, B.T., and Woods, R.D. (1993) Effect of particle contact bond on shear modulus. *J. Geotech. Eng.*, 118, 1216–1233.
- Chang, H., Jane Huang, P., and Hou, S.C. (1999) Application of thermo-Raman spectroscopy to study dehydration of $\text{CaSO}_4 \cdot 2\text{H}_2\text{O}$ and $\text{CaSO}_4 \cdot 0.5\text{H}_2\text{O}$. *Materials Chemistry and Physics*, 58, 12–19.
- Charalampidou, E.M. (2011) Experimental study of localised deformation in porous sandstones.
- SCharalampidou, E.-M., Hall, S.A., Stanchits, S., Lewis, H., and Viggiani, G. (2011) Characterization of shear and compaction bands in a porous sandstone deformed under triaxial compression. *Tectonophysics*, 503, 8–17.
- Cheng, L., and Cord-Ruwisch, R. (2012) In situ soil cementation with ureolytic bacteria by surface percolation. *Ecological Engineering*, 42, 64–72.

References

- Cheung, C.S.N., Baud, P., and Wong, T. (2012) Effect of grain size distribution on the development of compaction localization in porous sandstone. *Geophysical Research Letters*, 39, n/a-n/a.
- Chou, C.-W., Seagren, E.A., Aydilek, A.H., and Lai, M. (2011) Biocalcification of Sand through Ureolysis. *Journal of Geotechnical and Geoenvironmental Engineering*, 137, 1179–1189.
- Christensen, A.N., Olesen, M., Cerenius, Y., and Jensen, T.R. (2008) Formation and Transformation of Five Different Phases in the $\text{CaSO}_4 \cdot \text{H}_2\text{O}$ System: Crystal Structure of the Subhydrate $\beta\text{-CaSO}_4 \cdot 0.5\text{H}_2\text{O}$ and Soluble Anhydrite CaSO_4 . *Chemistry of Materials*, 20, 2124–2132.
- Chuhan, F.A., Kjeldstad, A., Bjørlykke, K., and Høeg, K. (2002) Porosity loss in sand by grain crushing—experimental evidence and relevance to reservoir quality. *Marine and Petroleum Geology*, 19, 39–53.
- Chuhan, F.A., Kjeldstad, A., Bjørlykke, K., and Høeg, K. (2003) Experimental compression of loose sands: relevance to porosity reduction during burial in sedimentary basins. *Canadian Geotechnical Journal*, 40, 995–1011.
- Clausen, J.A., and Gabrielsen, R.H. (2002) Parameters that control the development of clay smear at low stress states: an experimental study using ring-shear apparatus. *Journal of Structural Geology*, 24, 1569–1586.
- Clemmensen, L.B., and Abrahamsen, K. (1983) Aeolian stratification and facies association in desert sediments, Arran basin (Permian), Scotland. *Sedimentology*, 30, 311–339.
- Clough, G.W., Sitar, N., and Bachus, R.C. (1981) Cemented Sands under Static Loading. *Journal of the Geotechnical Engineering Division*, 107, 799–817.
- Cnudde, V., and Boone, M.N. (2013) High-resolution X-ray computed tomography in geosciences: A review of the current technology and applications. *Earth-Science Reviews*, 123, 1–17.
- Cnudde, V., Boone, M., Dewanckele, J., Dierick, M., Van Hoorebeke, L., and Jacobs, P. (2011) 3D characterization of sandstone by means of X-ray computed tomography. *Geosphere*, 7, 54–61.
- Coenen, J., Tchouparova, E., Jing, X., Exploration, S.I., and Production, B. V (2004) Measurement Parameters and Resolution Aspects of Micro X-Ray Tomography for Advanced Core Analysis. *Society*, 1–14.
- Craig, R.F. (2004) *Craig's Soil Mechanics*, 7th ed., 447 p. Taylor and Francis Group, London and New York.

References

- Cuisiat, F., and Skurtveit, E. (2010) An experimental investigation of the development and permeability of clay smears along faults in uncemented sediments. *Journal of Structural Geology*, 32, 1850–1863.
- Cunningham, W.A., Dunham, R.M., and Antes, L.L. (1952) Hydration of Gypsum Plaster. *Industrial & Engineering Chemistry*, 44, 2402–2408.
- Cuthbert, M.O., McMillan, L.A., Handley-Sidhu, S., Riley, M.S., Tobler, D.J., and Phoenix, V.R. (2013) A Field and Modeling Study of Fractured Rock Permeability Reduction Using Microbially Induced Calcite Precipitation. *Environmental Science & Technology*, 47, 13637–13643.
- David, C., Menéndez, B., and Bernabé, Y. (1998) The mechanical behaviour of synthetic sandstone with varying brittle cement content. *International Journal of Rock Mechanics and Mining Sciences*, 35, 759–770.
- Davis, G.H. (1999) Structural Geology of the Colorado Plateau Region of Southern Utah, with Special Emphasis on Deformation Bands. Special Paper 342: Structural Geology of the Colorado Plateau Region of Southern Utah, with Special Emphasis on Deformation Bands, 1–157.
- de Lima Rodrigues, M.C.N., Trzaskos, B., and Lopes, A.P. (2015) Influence of deformation bands on sandstone porosity: A case study using three-dimensional microtomography. *Journal of Structural Geology*, 72, 96–110.
- DeJong, J.T., Fritzsche, M.B., and Nüsslein, K. (2006) Microbially Induced Cementation to Control Sand Response to Undrained Shear. *Journal of Geotechnical and Geoenvironmental Engineering*, 132, 1381–1392.
- Desrues, J., and Viggiani, G. (2004) Strain localization in sand: An overview of the experimental results obtained in Grenoble using stereophotogrammetry. *International Journal for Numerical and Analytical Methods in Geomechanics*, 28, 279–321.
- Dewhurst, D.N., Siggins, A.F., Sarout, J., Raven, M.D., and Nordgård-Bolås, H.M. (2011) Geomechanical and ultrasonic characterization of a Norwegian Sea shale. *Geophysics*, 76, WA101–WA111.
- Dombrádi, E., Sokoutis, D., Bada, G., Cloetingh, S., and Horváth, F. (2010) Modelling recent deformation of the Pannonian lithosphere: Lithospheric folding and tectonic topography. *Tectonophysics*, 484, 103–118.
- Du Bernard, X., Eichhubl, P., and Aydin, A. (2002) Dilation bands: A new form of localized failure in granular media. *Geophysical Research Letters*, 29, 2176.

References

- du Plessis, A., le Roux, S.G., and Guelpa, A. (2016) Comparison of medical and industrial X-ray computed tomography for non-destructive testing. *Case Studies in Nondestructive Testing and Evaluation*, 6, 17–25.
- Dumazer, G., Narayan, V., Smith, A., and Lemarchand, A. (2009) Modeling Gypsum Crystallization on a Submicrometric Scale. *The Journal of Physical Chemistry C*, 113, 1189–1195.
- Dunham, R.J. (1962) Classification of carbonate rocks according to depositional texture. In *Classification of carbonate rocks: American Association of Petroleum Geologists Memoir* pp. 108–121.
- Edwards, H.E., Becker, A.D., and Howell, J.A. (1993) Compartmentalization of an aeolian sandstone by structural heterogeneities: Permo-Triassic Hopeman Sandstone, Moray Firth, Scotland. *Geological Society, London, Special Publications*, 73, 339–365.
- Eichhubl, P., Hooker, J.N., and Laubach, S.E. (2010) Pure and shear-enhanced compaction bands in Aztec Sandstone. *Journal of Structural Geology*, 32, 1873–1886.
- El Mountassir, G. El, Lunn, R.J., Moir, H., and Maclachlan, E. (2014) Hydrodynamic coupling in microbially mediated fracture mineralization: Formation of self-organized groundwater flow channels. *Water Resources Research*, 50, 1–16.
- El Mountassir, G., Minto, J.M., van Paassen, L.A., Salifu, E., and Lunn, R.J. (2018) Applications of Microbial Processes in Geotechnical Engineering. *Advances in Applied Microbiology*, 104, 39–91.
- Exner, U., and Tschegg, C. (2012) Preferential cataclastic grain size reduction of feldspar in deformation bands in poorly consolidated arkosic sands. *Journal of Structural Geology*, 43, 63–72.
- Fagereng, Å., and Toy, V.G. (2011) Geology of the earthquake source: an introduction. *Geological Society, London, Special Publications*, 359, 1–16.
- Feng, K., and Montoya, B.M. (2015) Drained Shear Strength of MICP Sand at Varying Cementation Levels. *Ifcee*, 2242–2251.
- Finot, E., Lesniewska, E., Mutin, J.-C., and Goudonnet, J.-P. (1999) Investigations of Surface Forces between Gypsum Microcrystals in Air Using Atomic Force Microscopy. *Langmuir*, 16, 4237–4244.
- Fischer, C., Waldmann, S., and von Eynatten, H. (2013) Spatial variation in quartz cement type and concentration: An example from the Heidelberg

References

- formation (Teufelsmauer outcrops), Upper Cretaceous Subhercynian Basin, Germany. *Sedimentary Geology*, 291, 48–61.
- Fisher, Q.J., and Knipe, R.J. (1998) Fault sealing processes in siliciclastic sediments. Geological Society, London, Special Publications, 147, 117–134.
- Fisher, Q.J., Casey, M., Harris, S.D., and Knipe, R.J. (2003) Fluid-flow properties of faults in sandstone: The importance of temperature history. *Geology*, 31, 965.
- Folk, R.L. (1959) Practical petrographic classification of limestones. *American Association of Petroleum Geologists Bulletin*, 43, 1–38.
- Fonseca, J., Bésuelle, P., and Viggiani, G. (2013) Micromechanisms of inelastic deformation in sandstones: an insight using x-ray micro-tomography. *Géotechnique Letters*, 3, 78–83.
- Fortin, J., Stanchits, S., Dresen, G., and Guéguen, Y. (2006) Acoustic emission and velocities associated with the formation of compaction bands in sandstone. *Journal of Geophysical Research*, 111, B10203.
- Fossen, H., Schultz, R.A., Shipton, Z.K., and Mair, K. (2007) Deformation bands in sandstone: a review. *Journal of the Geological Society*, 164, 755–769.
- Fossen, H. (2010) Deformation bands formed during soft-sediment deformation: Observations from SE Utah. *Marine and Petroleum Geology*, 27, 215–222.
- Fossen, H., Schultz, R.A., and Torabi, A. (2011) Conditions and implications for compaction band formation in the Navajo Sandstone, Utah. *Journal of Structural Geology*, 33, 1477–1490.
- Fossen, H., and Rotevatn, A. (2012) Characterization of deformation bands associated with normal and reverse stress states in the Navajo Sandstone, Utah: Discussion. *AAPG Bulletin*, 96, 869–876.
- Fossen, H., Zuluaga, L.F., Ballas, G., Soliva, R., and Rotevatn, A. (2015) Contractional deformation of porous sandstone: Insights from the Aztec Sandstone, SE Nevada, USA. *Journal of Structural Geology*, 74, 172–184.
- Fossen, H., Soliva, R., Ballas, G., Trzaskos, B., Cavalcante, C., and Schultz, R.A. (2017) A review of deformation bands in reservoir sandstones: geometries, mechanisms and distribution. Geological Society, London, Special Publications, 459, SP459.4.
- Frank, E., Hall, M.A., and Witten, I.H. (2016) The WEKA Workbench. In *Online Appendix for “Data Mining: Practical Machine Learning Tools and Techniques”* pp. 553–571. Morgan Kaufmann.

References

- French, M. (2012) Quartz growth: understanding porosity-preserving microcrystalline quartz through EBSD, TEM, and NanoSIMS examination of low temperature silica. University of Liverpool.
- French, M.W., Worden, R.H., Mariani, E., Larese, R.E., Mueller, R.R., and Kliewer, C.E. (2012) Microcrystalline Quartz Generation and the Preservation of Porosity In Sandstones: Evidence from the Upper Cretaceous of the Subhercynian Basin, Germany. *Journal of Sedimentary Research*, 82, 422–434.
- Freyer, D., and Voigt, W. (2003) Crystallization and Phase Stability of CaSO₄ and CaSO₄ - Based Salts. *Monatshefte für Chemie / Chemical Monthly*, 134, 693–719.
- Fusseis, F., Schrank, C., Liu, J., Karrech, A., Llana-Fúnez, S., Xiao, X., and Regenauer-Lieb, K. (2012) Pore formation during dehydration of a polycrystalline gypsum sample observed and quantified in a time-series synchrotron X-ray micro-tomography experiment. *Solid Earth*, 3, 71–86.
- Gazdič, D., Hájková, I., and Magrla, R. (2013) Monitoring of Calcium Sulphate Phase Transformations Using High-Temperature X-Ray Diffraction. *Advanced Materials Research*, 864–867, 621–624.
- Goldstein, R.H., and Rossi, C. (2007) Recrystallization in Quartz Overgrowths. *Journal of Sedimentary Research*, 72, 432–440.
- Golmohamadi, S., Mohsenzadeh, A., Hajjalilu, M., and Maleki, M. (2016) Effects of Biocementation Method on Direct Shear Stress and Unconfined Compressive Stress of Sand. *Indian Journal of Science and Technology*, 9.
- Gomez, M.G., Graddy, C.M.R., DeJong, J.T., Nelson, D.C., and Tsesarsky, M. (2017) Stimulation of Native Microorganisms for Biocementation in Samples Recovered from Field-Scale Treatment Depths. *Journal of Geotechnical and Geoenvironmental Engineering*, 144, 04017098.
- Google Earth Pro V 7.3.2 (24.3.2018). Arran, Scotland. 55° 35' 57.21" N, 5° 08' 17.91" E, Eye alt 10m. DigitalGlobe 2019. <http://www.earth.google.com> [February 2, 2019].
- Google Earth Pro V 7.3.2 (24.3.2018). Etes, Hungary. 48° 06' 18.29" N, 19° 43' 41.96" E, Eye alt 460m. DigitalGlobe 2019. <http://www.earth.google.com> [February 2, 2019].
- Google Earth Pro V 7.3.2 (24.3.2018). Utah, USA. 38° 42' 27.16" N, 110° 26' 52.75" W, Eye alt 1422m. DigitalGlobe 2019. <http://www.earth.google.com> [February 2, 2019].

References

- Griffiths, J., Faulkner, D.R., Edwards, A.P., and Worden, R.H. (2018) Deformation band development as a function of intrinsic host-rock properties in Triassic Sherwood Sandstone. Geological Society, London, Special Publications, 435, 161–176.
- Griggs, A.J., Davies, S.M., Abbott, P.M., Coleman, M., Palmer, A.P., Rasmussen, T.L., and Johnston, R. (2015) Visualizing tephra deposits and sedimentary processes in the marine environment: The potential of X-ray microtomography. *Geochemistry, geophysics, geosystems* : G(3), 16, 4329–4343.
- Habibbeygi, F., and Nikraz, H. (2018) Effect of shear rate on the residual shear strength of pre-sheared clays. (S. Irene Torri, Ed.) *Cogent Geoscience*, 4.
- Hall, S.A., Bornert, M., Desrues, J., Pannier, Y., Lenoir, N., Viggiani, G., and Bésuelle, P. (2010) Discrete and continuum analysis of localised deformation in sand using X-ray μ CT and volumetric digital image correlation. *Géotechnique*, 60, 315–322.
- Hamdan, N., and Kavazanjian, E. (2016) Enzyme-induced carbonate mineral precipitation for fugitive dust control. *Géotechnique*, 66, 546–555.
- Hamilton, A. (2005) Sodium sulphate crystallisation, water transport and stone decay.
- Hand, R.J. (1994) The kinetics of hydration of calcium sulphate hemihydrate: A critical comparison of the models in the literature. *Cement and Concrete Research*, 24, 885–895.
- Hanna, R.D., and Ketcham, R.A. (2017) X-ray computed tomography of planetary materials: A primer and review of recent studies. *Geochemistry*, 77, 547–572.
- Harkes, M.P., van Paassen, L.A., Booster, J.L., Whiffin, V.S., and van Loosdrecht, M.C.M. (2010) Fixation and distribution of bacterial activity in sand to induce carbonate precipitation for ground reinforcement. *Ecological Engineering*, 36, 112–117.
- Harrison, T.N. (2012) Experimental VNIR reflectance spectroscopy of gypsum dehydration: Investigating the gypsum to bassanite transition. *American Mineralogist*, 97, 598–609.
- Heap, M.J., Brantut, N., Baud, P., and Meredith, P.G. (2015) Time-dependent compaction band formation in sandstone. *Journal of Geophysical Research: Solid Earth*, 120, 4808–4830.
- Heather-Cooley, M.E. (2017) Faults as episodic conduits for hydrocarbons, CO₂ and groundwater in sandstones. University of Strathclyde.

References

- Hendee, W. (1979) *Medical Radiation Physics*, 2nd ed., 517 p. Year Book Medical Publishers, Chicago.
- Henderson, P., and Henderson, G.M. (2009) *Earth Science Data*, First., 277 p. Cambridge University Press.
- Hernigou, P. (2016) *Plaster of Paris: the orthopaedic surgeon heritage*. International orthopaedics.
- Hildyard, R.C., Llana-Funez, S., Wheeler, J., Faulkner, D.R., and Prior, D.J. (2011) Electron Backscatter Diffraction (EBSD) Analysis of Bassanite Transformation Textures and Crystal Structure Produced from Experimentally Deformed and Dehydrated Gypsum. *Journal of Petrology*, 52, 839–856.
- Hill, A.E. (1937) The Transition Temperature of Gypsum to Anhydrite. *Journal of the American Chemical Society*, 59, 2242–2244.
- Holcomb, D., Rudnicki, J.W., Issen, K.A., and Sternlof, K. (2007) Compaction localization in the Earth and the laboratory: State of the research and research directions. *Acta Geotechnica*, 2, 1–15.
- Holt, R.M., Unander, T.E., and Kenter, C.J. (1993) Constitutive mechanical behaviour of synthetic sandstone formed under stress. *International Journal of Rock Mechanics and Mining Sciences* and, 30, 719–722.
- Horváth, F., Musitz, B., Balázs, A., Végh, A., Uhrin, A., Nádor, A., Koroknai, B., Pap, N., Tóth, T., and Wórum, G. (2015) Evolution of the Pannonian basin and its geothermal resources. *Geothermics*, 53, 328–352.
- Huang, J.T., and Airey, D.W. (1991) The manufacture and index testing of cemented carbonate soils. In *9th Asian Regional Conference Soil Mechanics* pp. 143–146. Foundation Engineering, Bangkok.
- Ingraham, M.D., Issen, K.A., and Holcomb, D.J. (2013) Response of Castlegate sandstone to true triaxial states of stress. *Journal of Geophysical Research: Solid Earth*, 118, 536–552.
- Ismail, M.A., Joer, H.A., Sim, W.H., and Randolph, M.F. (2002) Effect of Cement Type on Shear Behavior of Cemented Calcareous Soil. *Journal of Geotechnical and Geoenvironmental Engineering*, 128, 520–529.
- Jacques, S.D.M., González-Saborido, A., Leynaud, O., Bensted, J., Tyrer, M., Greaves, R.I.W., and Barnes, P. (2009) Structural evolution during the dehydration of gypsum materials. *Mineralogical Magazine*, 73, 421–432.

References

- Johansen, T.E.S., Fossen, H., and Kluge, R. (2005) The impact of syn-faulting porosity reduction on damage zone architecture in porous sandstone: an outcrop example from the Moab Fault, Utah. *Journal of Structural Geology*, 27, 1469–1485.
- Joiret, S., Pillier, F., and Lemarchand, A. (2014) Submicrometric Picture of Plaster Hydration: Dynamic and Space-Resolved Raman Spectroscopy versus Kinetic Monte Carlo Simulations. *The Journal of Physical Chemistry C*, 118, 28730–28738.
- Jones, F. (2012) Infrared investigation of barite and gypsum crystallization: Evidence for an amorphous to crystalline transition. *CrystEngComm*, 14, 8374.
- Kak, A.C., and Slaney, M. (2001) *Principles of Computerized Tomographic Imaging*. Society of Industrial and Applied Mathematics.
- Kaproth, B.M., Cashman, S.M., and Marone, C. (2010) Deformation band formation and strength evolution in unlithified sand: The role of grain breakage. *Journal of Geophysical Research*, 115, B12103.
- Kareem, R., Cubillas, P., Gluyas, J., Bowen, L., Hillier, S., and Greenwell, H.C. (2017) Multi-technique approach to the petrophysical characterization of Berea sandstone core plugs (Cleveland Quarries, USA). *Journal of Petroleum Science and Engineering*, 149, 436–455.
- Katahara, K.W. (1996) Clay mineral elastic properties. In Presented at the 66th Ann. Internat. Mtg., Soc. Expl. Geophys. Society of Exploration Geophysicists.
- Kelley, K.K., Southard, J.C., Anderson, C.T. (1941) *Thermodynamic Properties of Gypsum and Its Dehydration Products*, 73 p. U.S. Government Printing Office.
- Ketcham, R.A., and Carlson, W.D. (2001) Acquisition, optimization and interpretation of x-ray computed tomographic imagery: Applications to the geosciences. *Computers and Geosciences*, 27, 381–400.
- Khaleghi, M., and Rowshanzamir, M.A. (2019) Biologic improvement of a sandy soil using single and mixed cultures: A comparison study. *Soil and Tillage Research*, 186, 112–119.
- Khidas, Y., and Jia, X. (2012) Probing the shear-band formation in granular media with sound waves. *Physical Review E - Statistical, Nonlinear, and Soft Matter Physics*, 85, 1–6.
- Kilian, R., Heilbronner, R., and Stünitz, H. (2011) Quartz microstructures and crystallographic preferred orientation: Which shear sense do they indicate? *Journal of Structural Geology*, 33, 1446–1466.

References

- Kimura, S., Kaneko, H., Noda, S., Ito, T., and Minagawa, H. (2018) Shear-induced permeability reduction and shear-zone development of sand under high vertical stress. *Engineering Geology*, 238, 86–98.
- Klimczak, C., and Schultz, R.A. (2013) Shear-enhanced compaction in dilating granular materials. *International Journal of Rock Mechanics and Mining Sciences*, 64, 139–147.
- Kobchenko, M., Panahi, H., Renard, F., Dysthe, D.K., Malthe-Sørensen, A., Mazzini, A., Scheibert, J., Jamtveit, B., and Meakin, P. (2011) 4D imaging of fracturing in organic-rich shales during heating. *Journal of Geophysical Research*, 116, B12201.
- Kristensen, M.B., Childs, C., Olesen, N.Ø., and Korstgård, J.A. (2013) The microstructure and internal architecture of shear bands in sand–clay sequences. *Journal of Structural Geology*, 46, 129–141.
- Krumgalz, B.S. (2018) Temperature Dependence of Mineral Solubility in Water. Part 3. Alkaline and Alkaline Earth Sulfates. *Journal of Physical and Chemical Reference Data* Vol. 47.
- Kuhinek, D. (2011) Strength and Deformability of Rock Samples, 11, 112–117.
- Lander, R.H., and Walderhaug, O. (1999) Predicting porosity through simulating sandstone compaction and quartz cementation. *AAPG Bulletin* (American Association of Petroleum Geologists), 83, 433–449.
- Lander, R.H., Larese, R.E., and Bonnell, L.M. (2008) Toward more accurate quartz cement models: The importance of euhedral versus noneuhedral growth rates. *AAPG Bulletin*, 92, 1537–1563.
- Landis, E.N., and Keane, D.T. (2010) X-ray microtomography. *Materials Characterization*, 61, 1305–1316.
- Laubach, S.E., Olson, J.E., and Gale, J.F.W. (2004a) Are open fractures necessarily aligned with maximum horizontal stress? *Earth and Planetary Science Letters*, 222, 191–195.
- Laubach, S.E., Reed, R.M., Olson, J.E., Lander, R.H., and Bonnell, L.M. (2004b) Coevolution of crack-seal texture and fracture porosity in sedimentary rocks: Cathodoluminescence observations of regional fractures. *Journal of Structural Geology*, 26, 967–982.
- Lewry, A.J., and Williamson, J. (1994) The setting of gypsum plaster. *Journal of Materials Science*, 29, 5279–5284.

References

- Li, C., Yao, D., Liu, S., Zhou, T., Bai, S., Gao, Y., and Li, L. (2018) Improvement of Geomechanical Properties of Bio-remediated Aeolian Sand. *Geomicrobiology Journal*, 35, 132–140.
- Lin, J., Wu, W., and Borja, R.I. (2015) Micropolar hypoplasticity for persistent shear band in heterogeneous granular materials. *Computer Methods in Applied Mechanics and Engineering*, 289, 24–43.
- Lin, M.L., Jeng, F.S., Tsai, L.S., and Huang, T.H. (2005) Wetting weakening of tertiary sandstones - Microscopic mechanism. *Environmental Geology*, 48, 265–275.
- Lioliou, M.G., Paraskeva, C.A., Koutsoukos, P.G., and Payatakes, A.C. (2006) Calcium sulfate precipitation in the presence of water-soluble polymers. *Journal of Colloid and Interface Science*, 303, 164–170.
- Lommatzsch, M., Exner, U., Gier, S., and Grasemann, B. (2015) Dilatant shear band formation and diagenesis in calcareous, arkosic sandstones, Vienna Basin (Austria). *Marine and Petroleum Geology*, 62, 144–160.
- Lothe, A.E., Gabrielsen, R.H., Hagen, N.B., and Larsen, B.T. (2002) An experimental study of the texture of deformation bands: effects on the porosity and permeability of sandstones. *Petroleum Geoscience*, 8, 195–207.
- Lou, W., Guan, B., and Wu, Z. (2011) Dehydration behavior of FGD gypsum by simultaneous TG and DSC analysis. *Journal of Thermal Analysis and Calorimetry*, 104, 661–669.
- Louis, L., Wong, T., Baud, P., and Tembe, S. (2006) Imaging strain localization by X-ray computed tomography: discrete compaction bands in Diemelstadt sandstone. *Journal of Structural Geology*, 28, 762–775.
- Louis, L., Wong, T.-F., and Baud, P. (2007) Imaging strain localization by X-ray radiography and digital image correlation: Deformation bands in Rothbach sandstone. *Journal of Structural Geology*, 29, 129–140.
- Lukács, R., Harangi, S., Guillong, M., Bachmann, O., Fodor, L., Buret, Y., Dunkl, I., Sliwinski, J., von Quadt, A., Peytcheva, I., and others (2018) Early to Mid-Miocene syn-extensional massive silicic volcanism in the Pannonian Basin (East-Central Europe): Eruption chronology, correlation potential and geodynamic implications. *Earth-Science Reviews*, 179, 1–19.
- Ma, X., and Haimson, B.C. (2013) Failure characteristics of two porous sandstones subjected to true triaxial testing. *Rock Characterisation, Modelling and Engineering Design Methods - Proceedings of the 3rd ISRM SINOROCK 2013 Symposium*, 6477–6498.

References

- Ma, X., and Haimson, B.C. (2016) Failure characteristics of two porous sandstones subjected to true triaxial stresses. *Journal of Geophysical Research: Solid Earth*, 121, 6477–6498.
- Macente, A., Fousseis, F., Menegon, L., Xianghui, X., and John, T. (2017) The strain-dependent spatial evolution of garnet in a high- P ductile shear zone from the Western Gneiss Region (Norway): a synchrotron X-ray microtomography study. *Journal of Metamorphic Geology*, 35, 565–583.
- MacLachlan, E. (2017) Development of a microbially induced calcite and silica biogrowth for the sealing of fine aperture fractures. University of Strathclyde.
- Mahawish, A., Bouazza, A., and Gates, W.P. (2018) Improvement of Coarse Sand Engineering Properties by Microbially Induced Calcite Precipitation. *Geomicrobiology Journal*, 35, 887–897.
- Main, I.G., Kwon, O., Ngwenya, B.T., and Elphick, S.C. (2000) Fault sealing during deformation-band growth in porous sandstone. *Geology*, 28, 1131–1134.
- Mair, K. (2002) Influence of grain characteristics on the friction of granular shear zones. *Journal of Geophysical Research*, 107, 2219.
- Mair, K., Main, I., and Elphick, S. (2000) Sequential growth of deformation bands in the laboratory. *Journal of Structural Geology*, 22, 25–42.
- Mandl, G., Jong, L.N.J., and Maltha, A. (1977) Shear zones in granular material. *Rock Mechanics Felsmechanik Mecanique des Roches*, 9, 95–144.
- Mauz, B., Vacchi, M., Green, A., Hoffmann, G., and Cooper, A. (2015) Beachrock: A tool for reconstructing relative sea level in the far-field. *Marine Geology*, 362, 1–16.
- McCartney, E., and Alexander, A. (1958) The effect of additives upon the process of crystallization. *Journal of Colloid Science*, 13, 383–396.
- McClay, K.R., and Ellis, P.G. (1987) Analogue models of extensional fault geometries. Geological Society, London, Special Publications, 28, 109–125.
- McKeever, P.J. (1992) Petrography and diagenesis of the Permo-Triassic of Scotland. Geological Society, London, Special Publications, 62, 71–96.
- Medeiros, W.E., do Nascimento, A.F., Alves da Silva, F.C., Destro, N., and Demétrio, J.G.A. (2010) Evidence of hydraulic connectivity across deformation bands from field pumping tests: Two examples from Tucano Basin, NE Brazil. *Journal of Structural Geology*, 32, 1783–1791.

References

- Milliken, K.L., Reed, R.M., and Laubach, S.E. (2005) Quantifying compaction and cementation in deformation bands in porous sandstones. *AAPG Memoir*, 85, 237–249.
- Minto, J.M., Hingerl, F.F., Benson, S.M., and Lunn, R.J. (2017) X-ray CT and multiphase flow characterization of a ‘bio-grouted’ sandstone core: The effect of dissolution on seal longevity. *International Journal of Greenhouse Gas Control*, 64, 152–162.
- Minto, J.M., Maclachlan, E., El Mountassir, G., and Lunn, R.J. (2016) Rock fracture grouting with microbially induced carbonate precipitation. *Water Resources Research*, 8827–8844.
- Mitchell, J.K., and Santamarina, J.C. (2005) Biological Considerations in Geotechnical Engineering. *Journal of Geotechnical and Geoenvironmental Engineering*, 131, 1222–1233.
- Mohsin, A.K.M., and Airey, D.W. (2005) Influence of cementation and density on G_{max} for sand. *Proceedings of 16th International Conference on Soil Mechanics and Geotechnical Engineering*, 413–416.
- Molenaar, N., and Venmans, A.A.M. (1993) Calcium carbonate cementation of sand: A method for producing artificially cemented samples for geotechnical testing and a comparison with natural cementation processes. *Engineering Geology*, 35, 103–122.
- Mollema, P.N., and Antonellini, M.A. (1996) Compaction bands: a structural analog for anti-mode I cracks in aeolian sandstone. *Tectonophysics*, 267, 209–228.
- Mortensen, B.M., Haber, M.J., DeJong, J.T., Caslake, L.F., and Nelson, D.C. (2011) Effects of environmental factors on microbial induced calcium carbonate precipitation. *Journal of Applied Microbiology*, 111, 338–349.
- Mujah, D., Shahin, M.A., and Cheng, L. (2017) State-of-the-Art Review of Biocementation by Microbially Induced Calcite Precipitation (MICP) for Soil Stabilization. *Geomicrobiology Journal*, 34, 524–537.
- Nemati, M., Greene, E.A., and Voordouw, G. (2005) Permeability profile modification using bacterially formed calcium carbonate: comparison with enzymic option. *Process Biochemistry*, 40, 925–933.
- Newman, E.S. (1941) Behavior of calcium sulfate at high temperatures. *Journal of Research of the National Bureau of Standards*, 27, 191.

References

- Ngwenya, B.T., Kwon, O., Elphick, S.C., and Main, I.G. (2003) Permeability evolution during progressive development of deformation bands in porous sandstones. *Journal of Geophysical Research: Solid Earth*, 108, n/a-n/a.
- Ogilvie, S.R., and Glover, P.W.. (2001) The petrophysical properties of deformation bands in relation to their microstructure. *Earth and Planetary Science Letters*, 193, 129–142.
- Olsson, W.A. (1999) Theoretical and experimental investigation of compaction bands in porous rock. *Journal of Geophysical Research*, 104, 7219–7228.
- Packter, A. (1974) The precipitation of calcium sulphate dihydrate from aqueous solution. *Journal of Crystal Growth*, 21, 191–194.
- Palchik, V. (1999) Influence of porosity and elastic modulus on uniaxial compressive strength in soft brittle porous sandstones. *Rock Mechanics and Rock Engineering*, 32, 303–309.
- Partridge, E.P., and White, A.H. (1929) The solubility of calcium sulfate from 0 TO 200°. *Journal of the American Chemical Society*, 51, 360–370.
- Peng, S., Marone, F., and Dultz, S. (2014) Resolution effect in X-ray microcomputed tomography imaging and small pore's contribution to permeability for a Berea sandstone. *Journal of Hydrology*, 510, 403–411.
- Petrik, A., Beke, B., and Fodor, L. (2014) Combined analysis of faults and deformation bands reveals the Cenozoic structural evolution of the southern Bükk foreland (Hungary). *Tectonophysics*, 633, 43–62.
- Petrik, A., Beke, B., Fodor, L., and Lukács, R. (2016) Cenozoic structural evolution of the southwestern Bükk Mts. and the southern part of the Darnó Deformation Belt (NE Hungary). *Geologica Carpathica*, 67, 83–104.
- Pettijohn, F.J. (1975) *Sedimentary Rocks*, 3rd ed., 628 p. Harper & Row Publishers Inc., Baltimore.
- Philit, S., Soliva, R., Castilla, R., Ballas, G., and Taillefer, A. (2018) Clusters of cataclastic deformation bands in porous sandstones. *Journal of Structural Geology*, 114, 235–250.
- Philit, S., Soliva, R., Labaume, P., Gout, C., and Wibberley, C. (2015) Relations between shallow cataclastic faulting and cementation in porous sandstones: First insight from a groundwater environmental context. *Journal of Structural Geology*, 81, 89–105.

References

- Plachý, T., Hana, N.Č., Tesárek, P., Hájková, A., and Polák, M. (2011) Determination of Poisson's ratio of gypsum materials. *Experimentalni Analýza Napeti*.
- Prasad, P.S.R. (2005) Direct formation of the -CaSO_4 phase in dehydration process of gypsum: In situ FTIR study. *American Mineralogist*, 90, 672–678.
- Putnis, A., Winkler, B., and Fernandez-Diaz, L. (1990) In Situ IR Spectroscopic and Thermogravimetric Study of the Dehydration of Gypsum. *Mineralogical Magazine*, 54, 123–128.
- Qabany, A.A., and Soga, K. (2013) Effect of chemical treatment used in MICP on engineering properties of cemented soils. *Géotechnique*, 63, 331–339.
- Qian, C., Yu, X., and Wang, X. (2018) A study on the cementation interface of bio-cement. *Materials Characterization*, 136, 122–127.
- Qu, D., and Tveranger, J. (2017) Incorporation of deformation band fault damage zones in reservoir models. *AAPG Bulletin*, 101, 423–443.
- Radzik, N., Świerczewska, A., and Krzyżak, A. (2015) Identification of tectonic microstructures in flysch sandstones of the Outer Carpathians using X-ray nanotomography and nuclear magnetic resonance – first results. *Geology, Geophysics & Environment*, 41, 127.
- Ramm, M., and Bjørlykke, K. (1994) Porosity/depth trends in reservoir sandstones: assessing the quantitative effects of varying pore-pressure, temperature history and mineralogy, Norwegian Shelf data. *Clay Minerals*, 29, 475–490.
- Rathore, J.S., Fjaer, E., Holt, R.M., and Renlie, L. (1995) P- and S-wave anisotropy of a synthetic sandstone with controlled crack geometry. *Geophysical Prospecting*, 43, 711–728.
- Rawling, G.C., and Goodwin, L.B. (2003) Cataclasis and particulate flow in faulted, poorly lithified sediments. *Journal of Structural Geology*, 25, 317–331.
- Renard, F., Ortoleva, P., and Gratier, J.P. (1997) Pressure solution in sandstones: Influence of clays and dependence on temperature and stress. *Tectonophysics*, 280, 257–266.
- Rendel, P.M., Gavrieli, I., Wolff-Boenisch, D., and Ganor, J. (2018) Towards establishing a combined rate law of nucleation and crystal growth – The case study of gypsum precipitation. *Journal of Crystal Growth*, 485, 28–40.

References

- Richey, D.J. (2013) Fault Seal Analysis for CO₂ Storage: Fault Zone Architecture, Fault Permeability, and Fluid Migration Pathways in Exposed Analogs in Southeastern Utah. Utah State University.
- Ridge, M.J. (1964) Hydration of Calcium Sulphate Hemihydrate. *Nature*, 204, 70–71.
- Robertson, K., and Bish, D. (2007) The dehydration kinetics of gypsum: the effect of relative humidity on its stability and implications in the martian environment. *Lunar and Planetary Science XXXVIII*, 1432.
- Romano, C., Minto, J.M., Shipton, Z.K., and Lunn, R.J. (2019) Automated high accuracy, rapid beam hardening correction in X-Ray Computed Tomography of multi-mineral, heterogenous core samples. *Computers and Geosciences Journal*.
- Roscoe, K.H. (1970) The Influence of Strains in Soil Mechanics. *Géotechnique*, 20, 129–170.
- Royden, L., Horváth, F., Nagymarosy, A., and Stegena, L. (1983) Evolution of the Pannonian Basin System: 2. Subsidence and thermal history. *Tectonics*, 2, 91–137.
- Rykkelid, E., and Skurtveit, E. (2018) Deformation in a North Sea Jurassic trap analysed using a triaxial plane strain experiment. *Geological Society, London, Special Publications*, 459, 35–57.
- Saha, A., Lee, J., Pancera, S.M., Bräeu, M.F., Kempter, A., Tripathi, A., and Bose, A. (2012) New insights into the transformation of calcium sulfate hemihydrate to gypsum using time-resolved cryogenic transmission electron microscopy. *Langmuir : the ACS journal of surfaces and colloids*, 28, 11182–7.
- Saidi, F., Bernabé, Y., and Reuschlé, T. (2005) Uniaxial compression of synthetic, poorly consolidated granular rock with a bimodal grain-size distribution. *Rock Mechanics and Rock Engineering*, 38, 129–144.
- Saillet, E., and Wibberley, C.A.J. (2013) Permeability and flow impact of faults and deformation bands in high-porosity sand reservoirs: Southeast Basin, France, analog. *AAPG Bulletin*, 97, 437–464.
- Salifu, E., MacLachlan, E., Iyer, K.R., Knapp, C.W., and Tarantino, A. (2016) Application of microbially induced calcite precipitation in erosion mitigation and stabilisation of sandy soil foreshore slopes: A preliminary investigation. *Engineering Geology*, 201, 96–105.
- Samson, E., Marchland, J., and Snyder, K. (2003) Calculation of ionic diffusion coefficients on the basis of migration test results. *Materials and Structures/Materiaux et Constructions*, 36, 156–165.

References

- Sarma, L.P., Prasad, P.S.R., and Ravikumar, N. (1998) Raman spectroscopic study of phase transitions in natural gypsum. *Journal of Raman Spectroscopy*, 29, 851–856.
- Sassa, K., Fukuoka, H., Wang, G., and Ishikawa, N. (2004) Undrained dynamic-loading ring-shear apparatus and its application to landslide dynamics. *Landslides*, 1, 7–19.
- Saxena, V., Krief, M., and Adam, L. (2018) Rock Strength And Stress Analysis, 281–325 p. *Handbook of Borehole Acoustics and Rock Physics for Reservoir Characterization Vol. 281*.
- Scherer, M. (1987) Parameters Influencing Porosity in Sandstones: A Model for Sandstone Porosity Prediction: REPLY. *AAPG Bulletin*, 71, 485–491.
- Schiller, K. (1962) Mechanism of re-crystallisation in calcium sulphate hemihydrate plasters. *Journal of Applied Chemistry*, 12, 135–144.
- Scholle, P.A., and Ulmer-Scholle, D. (1979) Cements and cementation. In *Sedimentology* pp. 174–190. Springer Netherlands, Dordrecht.
- Scholz, C.H. (Christopher H.). (2002) *The Mechanics of Earthquakes and Faulting.*, 505 p. Cambridge University Press.
- Schultz, R.A. (2009) Scaling and paleodepth of compaction bands, Nevada and Utah. *Journal of Geophysical Research*, 114, 1–13.
- Selley, R.C. (1976) *Introduction to Sedimentology*, 408 p. Academic Press Inc.
- Selley, R.C., and Sonnenberg, S.A. (2015) *Elements of Petroleum Geology*, 3rd ed., 507 p.
- Sharma, P. V. (1997) *Environmental and engineering geophysics*. Cambridge University Press, Cambridge.
- Shipton, Z.K., and Cowie, P. A. (2001) Damage zone and slip-surface evolution over μm to km scales in high-porosity Navajo sandstone, Utah. *Journal of Structural Geology*, 23, 1825–1844.
- Shipton, Z.K., Evans, J.P., and Thompson, L.B. (2005) The geometry and thickness of deformation-band fault core and its influence on sealing characteristics of deformation-band fault zones. *American Association of Petroleum Geologists*.

References

- Shipton, Z.K., Meghraoui, M., and Monro, L. (2017) Seismic slip on the west flank of the Upper Rhine Graben (France–Germany): evidence from tectonic morphology and cataclastic deformation bands. *Geological Society, London, Special Publications*, 432, 147–161.
- Shtukenberg, A.G., Punin, Y.O., Gunn, E., and Kahr, B. (2012) Spherulites. *Chemical Reviews*, 112, 1805–1838.
- Sibson, R.H. (1983) Continental fault structure and the shallow earthquake source. *Journal of the Geological Society*, 140, 741–767.
- Sigda, J.M., and Wilson, J.L. (2003) Are faults preferential flow paths through semiarid and arid vadose zones? *Water Resources Research*, 39, n/a-n/a.
- Singh, N.B., and Middendorf, B. (2007) Calcium sulphate hemihydrate hydration leading to gypsum crystallization. *Progress in Crystal Growth and Characterization of Materials*, 53, 57–77.
- Sippel, R.. (1968) Sandstone Petrology, Evidence from Luminescence Petrography. *SEPM Journal of Sedimentary Research*, Vol. 38, 530–554.
- Skurtveit, E., Torabi, A., Gabrielsen, R.H., and Zoback, M.D. (2013) Experimental investigation of deformation mechanisms during shear-enhanced compaction in poorly lithified sandstone and sand. *Journal of Geophysical Research: Solid Earth*, 118, 4083–4100.
- Stawski, T.M., van Driessche, A.E.S., Ossorio, M., Diego Rodriguez-Blanco, J., Besselink, R., and Benning, L.G. (2016) Formation of calcium sulfate through the aggregation of sub-3 nanometre primary species. *Nature Communications*, 7, 1–9.
- Stretton, I.C., Schofield, P.F., Hull, S., and Knight, K.S. (1997) The static compressibility of gypsum. *Geophys. Res. Lett*, 24, 1267–1270.
- Strydom, C.A., Hudson-Lamb, D.L., Potgieter, J.H., and Dagg, E. (1995) The thermal dehydration of synthetic gypsum. *Thermochimica Acta*, 269–270, 631–638.
- Tadros, M.E., and Mayes, I. (1979) Linear growth rates of calcium sulfate dihydrate crystals in the presence of additives. *Journal of Colloid and Interface Science*, 72, 245–254.
- Tembe, S., Baud, P., and Wong, T. (2008) Stress conditions for the propagation of discrete compaction bands in porous sandstone. *Journal of Geophysical Research*, 113, B09409.

References

- Terzis, D., and Laloui, L. (2017) *Advances in Laboratory Testing and Modelling of Soils and Shales (ATMSS)*.
- Terzis, D., and Laloui, L. (2018) 3-D micro-architecture and mechanical response of soil cemented via microbial-induced calcite precipitation. *Scientific Reports*, 8, 1–11.
- Terzis, D., and Laloui, L. (2019) A decade of progress and turning points in the understanding of bio-improved soils: A review. *Geomechanics for Energy and the Environment*, 19.
- Thompson, A., McNally, D., Maskery, I., and Leach, R.K. (2017) X-ray computed tomography and additive manufacturing in medicine: a review. *International Journal of Metrology and Quality Engineering*, 8, 17.
- Tindall, S.E. (2014) Simple calculations of fluid flow across jointed cataclastic deformation bands. *Marine and Petroleum Geology*, 57, 152–159.
- Tobler, D.J., Maclachlan, E., and Phoenix, V.R. (2012) Microbially mediated plugging of porous media and the impact of differing injection strategies. *Ecological Engineering*, 42, 270–278.
- Tobler, D.J., Minto, J.M., El Mountassir, G., Lunn, R.J., and Phoenix, V.R. (2018) Microscale analysis of fractured rock sealed with microbially induced CaCO₃ precipitation: influence on hydraulic and mechanical performance. *Water Resources Research*.
- Tondi, E., Antonellini, M., Aydin, A., Marchegiani, L., and Cello, G. (2006) The role of deformation bands, stylolites and sheared stylolites in fault development in carbonate grainstones of Majella Mountain, Italy. *Journal of Structural Geology*, 28, 376–391.
- Torabi, A., Braathen, A., Cuisiat, F., and Fossen, H. (2007) Shear zones in porous sand: Insights from ring-shear experiments and naturally deformed sandstones. *Tectonophysics*, 437, 37–50.
- Torabi, A., and Fossen, H. (2009) Spatial variation of microstructure and petrophysical properties along deformation bands in reservoir sandstones. *AAPG Bulletin*, 93, 919–938.
- Torabi, A. (2014) Cataclastic bands in immature and poorly lithified sandstone, examples from Corsica, France. *Tectonophysics*, 630, 91–102.
- Torabi, A., Ando, E., Alikarami, R., and Viggiani, G. (2014) Compaction and shear localization in porous sandstone and sand. In *International Symposium on Geomechanics from Micro to Macro* pp. 1213–1217.

References

- Tucker, M. (2001) *Sedimentary Petrology*, 3rd ed., 262 p. Blackwell Science Ltd.
- Twiss, R.J., and Moores, E. (1992) *Structural Geology*, 532 p. W.H. Freeman and Company, New York.
- Tydlitát, V., Medved', I., and Černý, R. (2011) Determination of a partial phase composition in calcined gypsum by calorimetric analysis of hydration kinetics. *Journal of Thermal Analysis and Calorimetry*, 109, 57–62.
- Underhill, J.R., and Woodcock, N.H. (1987) *Faulting mechanisms in high-porosity sandstones; New Red Sandstone, Arran, Scotland*. Geological Society, London, *Special Publications*, 29, 91–105.
- Van Driessche, A.E.S., Benning, L.G., Rodriguez-Blanco, J.D., Ossorio, M., Bots, P., and García-Ruiz, J.M. (2012) The role and implications of bassanite as a stable precursor phase to gypsum precipitation. *Science (New York, N.Y.)*, 336, 69–72.
- van Paassen, L.A., Daza, C.M., Staal, M., Sorokin, D.Y., van der Zon, W., and van Loosdrecht, M.C.M. (2010) Potential soil reinforcement by biological denitrification. *Ecological Engineering*, 36, 168–175.
- van Paassen, L.A., Ghose, R., van der Linden, T.J.M., van der Star, W.R.L., and van Loosdrecht, M.C.M. (2010) Quantifying Biomediated Ground Improvement by Ureolysis: Large-Scale Biogrout Experiment. *Journal of Geotechnical and Geoenvironmental Engineering*, 136, 1721–1728.
- Vangla, P., and Latha Gali, M. (2016) Effect of particle size of sand and surface asperities of reinforcement on their interface shear behaviour. *Geotextiles and Geomembranes*, 44, 254–268.
- Vaniman, D. T., Bish, D. L., and Chipera, S. J. (2008) Calcium Sulfate Hydration, Stability and Transformation on Mars. 39th Lunar and Planetary Science Conference.
- Walderhaug, O. (1996) Kinetic Modeling of Quartz Cementation and Porosity Loss in Deeply Buried Sandstone Reservoirs. *AAPG Bulletin*, 80, 731–745.
- Wang, W., Kravchenko, A.N., Smucker, A.J.M., and Rivers, M.L. (2011) Comparison of image segmentation methods in simulated 2D and 3D microtomographic images of soil aggregates. *Geoderma*, 162, 231–241.
- Wang, Y.-W., Kim, Y.-Y., Christenson, H.K., and Meldrum, F.C. (2012) A new precipitation pathway for calcium sulfate dihydrate (gypsum) via amorphous and hemihydrate intermediates. *Chemical communications (Cambridge, England)*, 48, 504–6.

References

- Warke, M. (2017) Stratigraphic and geochemical framework of the Palaeoproterozoic rise in atmospheric oxygen: Transvaal Supergroup (South Africa). The University of Manchester, Manchester, UK.
- Weiss, H., and Bräu, M.F. (2009) How much water does calcined gypsum contain? *Angewandte Chemie - International Edition*, 48, 3520–3524.
- Wen, B.P., and Aydin, A. (2004) Deformation history of a landslide slip zone in light of soil microstructure. *Environmental and Engineering Geoscience*, 10, 123–149.
- Weng, M.C., Jeng, F.S., Huang, T.H., and Lin, M.L. (2005) Characterizing the deformation behavior of Tertiary sandstones. *International Journal of Rock Mechanics and Mining Sciences*, 42, 388–401.
- Weng, M.C., Jeng, F.S., Hsieh, Y.M., and Huang, T.H. (2008) A simple model for stress-induced anisotropic softening of weak sandstones. *International Journal of Rock Mechanics and Mining Sciences*, 45, 155–166.
- Wennberg, O.P., and Rennan, L. (2017) A brief introduction to the use of X-ray computed tomography (CT) for analysis of natural deformation structures in reservoir rocks. Geological Society, London, Special Publications, 459, SP459.10.
- Whiffin, V.S. (2004) Microbial CaCO₃ Precipitation for the Production of Biocement. Phd Thesis, 1–162.
- Whiffin, V.S., van Paassen, L.A., and Harkes, M.P. (2007) Microbial carbonate precipitation as a soil improvement technique. *Geomicrobiology Journal*, 24, 417–423.
- Wildenschild, D., and Sheppard, A.P. (2013) X-ray imaging and analysis techniques for quantifying pore-scale structure and processes in subsurface porous medium systems. *Advances in Water Resources*, 51, 217–246.
- Williams, R.T., Farver, J.R., Onasch, C.M., and Winslow, D.F. (2015) An experimental investigation of the role of microfracture surfaces in controlling quartz precipitation rate: Applications to fault zone diagenesis. *Journal of Structural Geology*, 74, 24–30.
- Wirsching, F. (2000) Calcium Sulphate, 520–550 p. Ullmann's Encyclopedia of Industrial Chemistry Vol. 6. Wiley-VCH Verlag GmbH & Co. KGaA.
- Wirsching, F. (2000) Calcium Sulphate, 520–550 p. Ullmann's Encyclopedia of Industrial Chemistry Vol. 6. Wiley-VCH Verlag GmbH & Co. KGaA.

References

- Wong, T., and Baud, P. (2012) The brittle-ductile transition in porous rock: A review. *Journal of Structural Geology*, 44, 25–53.
- Wong, T., and Zhu, W. (1999) Brittle Faulting and Permeability Evolution : Hydromechanical Measurement, Microstructural Observation, and Network Modeling. *Faults and subsurface fluid flow in the shallow crust: American Geophysical Union Geophysical Monograph*, 113, 83–99.
- Wong, T., David, C., and Zhu, W. (1997) The transition from brittle faulting to cataclastic flow in porous sandstones: Mechanical deformation. *Journal of Geophysical Research*, 102, 3009.
- Woodcock, N.H., and Underhill, J.R. (1987) Emplacement-related fault patterns around the Northern Granite, Arran, Scotland. *Geological Society of America Bulletin*, 98, 515.
- Wooldridge, L.J., Worden, R.H., Griffiths, J., Utley, J.E.P., and Thompson, A. (2018) The origin of clay-coated sand grains and sediment heterogeneity in tidal flats. *Sedimentary Geology*.
- Wu, L., Bao, Y., Wang, Y., and Zhang, L. (2015) The Application on Shale Reservoir Based on X-CT Scan Technology. *Acta Geologica Sinica - English Edition*, 89, 347–348.
- Yan, Y., Tang, Y., Xu, G., Lian, J., and Fu, D. (2019) Study on the Relationship between Mechanical Properties and Mesostucture of Microbial Cemented Sand Bodies. *Advances in Materials Science and Engineering*, 2019, 1–13.
- Yang, S., and Jiang, Y. (2010) Triaxial mechanical creep behavior of sandstone. *Mining Science and Technology (China)*, 20, 339–349.
- Yavari, N., Tang, A.M., Pereira, J.-M., and Hassen, G. (2016) Effect of temperature on the shear strength of soils and the soil–structure interface. *Canadian Geotechnical Journal*, 53, 1186–1194.
- Zambrano, M., Tondi, E., Mancini, L., Arzilli, F., Lanzafame, G., Materazzi, M., and Torrieri, S. (2017) 3D Pore-network quantitative analysis in deformed carbonate grainstones. *Marine and Petroleum Geology*, 82, 251–264.
- Zhang, L. (2017) Strength. In *Engineering Properties of Rocks* pp. 251–338. Butterworth-Heinemann.
- Zhao, Q., Li, L., Li, C., Li, M., Amini, F., and Zhang, H. (2014) Factors Affecting Improvement of Engineering Properties of MICP-Treated Soil Catalyzed by Bacteria and Urease. *Journal of Materials in Civil Engineering*, 26, 04014094.

References

Zuluaga, L.F., Fossen, H., and Rotevatn, A. (2014) Progressive evolution of deformation band populations during Laramide fault-propagation folding: Navajo Sandstone, San Rafael monocline, Utah, U.S.A. *Journal of Structural Geology*, 68, 66–81.

Zuluaga, L.F., Fossen, H., Ballas, G., and Rotevatn, A. (2018) Structural and petrophysical effects of overthrusting on highly porous sandstones: the Aztec Sandstone in the Buffington window, SE Nevada, USA. Geological Society, London, Special Publications, 459, 59–77.

Appendices

Appendix 1

Summary of individual deformation bands from multiple studies included in Figure 2.7. Dominant deformation mechanism or kinematics is listed.

		Deformation mechanism	Kinematics
1	Balsamo and Storti. 2011	C	N
2	Brandes and Tanner. 2012	DG	S
3	Cashman and Cashman 2000	C	S
4	Cashman et al. 2007	C	S
5	Du Bernard et al. 2002	C	D
6	Exner and Tschegg. 2012	C	C
7	Kristensen et al. 2013	C	S
8	Kristensen et al. 2013	DG	S
9	Petrik et al. 2014	C	N
10	Petrik et al. 2014	DG	N
11	Petrik et al. 2014	C	S
12	Petrik et al. 2014	N	D
13	Rawling and Goodwin. 2003	C	N
14	Rawling and Goodwin. 2006	C	N
15	Saillet and Wibberley. 2013	C	S
16	Sigda and Wilson. 2003	C	C
17	Torabi 2014	C	C
18	Ballas et al. 2013	C	C
19	Davis 1999	N	C
20	Davis 1999	C	D
21	Davis 1999	C	S
22	Edwards et al. 1993	C	C
23	Eichhubl et al. 2010	C	S
24	Eichhubl et al. 2010	C	C
25	Eichhubl et al. 2010	C	C
26	Fossen et al. 2011	C	C
27	Fossen et al. 2011	D	C
28	Fossen et al. 2015	C	S
29	Fossen et al. 2015	C	C
30	Fossen et al 2015.	C	C
31	Healy et al. 2006	C	S
32	Johnson 1995	C	S
33	Klimczak & Schultz 2013	C	S
34	Klimczak et al. 2011	C	S
35	Liu et al. 2015	N	C
36	Lommatzsch et al. 2015	C	D

37	Milliken and Reed 2002	C	S
38	Mollema & Antonellini 1996	N	C
39	Olsson 1999	N	C
40	Olsson 1999	N	S
41	Olsson et al. 2004	C	S
42	Ord et al. 1991	C	S
43	Philit et al. 2015	C	S
44	Pittman 1981	C	N
45	Ravier et al. 2015	C	C
46	Rochford et al. 1995	C	N
47	Rodrigues et al. 2015	C	C
48	Rotevatn et al. 2008	C	S
49	Salomon et al. 2016	C	N
50	Salomon et al. 2016	D	N
51	Schultz 2009	N	C
52	Schultz and Soliva 2012	C	C
53	Shipton and Cowie 2001	C	S
54	Shipton and Cowie 2003	C	N
55	Soliva et al. 2013	C	C
56	Soliva et al. 2013	C	S
57	Soliva et al. 2013	C	S
58	Solum et al. 2010	C	S
59	Solum et al. 2010	C	C
60	Sternlof et al. 2005	N	C
61	Tindall and Eckert 2015	C	N
62	Torabi et al. 2014	DG	C
63	Tueckmantel et al. 2010	C	S
64	Underhill and Woodcock 1987	C	S
65	Zuluaga et al. 2014	C	C
66	Zuluaga et al. 2014	C	S

Key	
Deformation mechanism	C Cataclasis
	DG Dis-aggregation
	D Dissolution
	N Not reported
Kinematics	S Shear
	C Compaction
	D Dilation
	N Not reported

Appendices

Appendix 2

Individual X-CT scan parameters for all scanned samples.

Description of samples	Sample detail	Sample name	Voxel size (mm)	Detector pixel size	Projections	kV	uA	Date scanned	Minimum voxel size (mm³)
Deformation band sandstones	HN11	HN11_040218	0.004	0.2	3141	135	26	04/02/2018	5.0E-08
	AR01	AR01_230218	0.005	0.2	3141	130	38	23/02/2018	1.6E-07
	UT02	UT02_200118	0.006	0.2	3141	120	41	20/02/2018	1.9E-07
Comparison between scan resolutions	HN11_7um	HN11_7_130218	0.007	0.2	3141	122	55	13/02/2018	3.4E-07
	HN11_10um	HN11_10_130218	0.010	0.2	3141	130	69	13/02/2018	9.7E-07
Gypsum synthetic sandstone	10	10B	0.003	0.2	3141	150	20	11/04/2019	4.1E-08
	15	15B	0.005	0.2	3141	150	20	11/04/2019	1.1E-07
	20	20B	0.004	0.2	3141	150	20	01/04/2019	5.5E-08
	25	25B	0.005	0.2	3141	150	20	11/04/2019	1.1E-07
MICP synthetic sandstones	120	L7	0.004	0.2	3141	130	31	21/03/2018	7.7E-08
	160	M7	0.004	0.2	3141	130	31	21/03/2018	7.7E-08
	200	H6	0.004	0.2	3141	130	31	21/03/2018	7.7E-08

Appendix 3

K_{urea} results for each bacterial solution used to make the MICP cemented synthetic sandstones. Each of the bacterial solutions conductivity was measured for 6 minutes and the results were recorded every 30 seconds.

